Behaviour and Design of Reinforced Concrete Core-Slab-Frame Structures

by

Kyriakos Charles Manatakos

Department of Civil Engineering and Applied Mechanics
McGill University
Montréal, Canada

June 1996

A dissertation submitted to the Faculty of Graduate Studies and Research
in partial fulfillment of the requirements for the
degree of Doctor of Philosophy

0-612-30330-6

Dedicated To:

the *Kopella*

from the *Old Man*

"Though I know I'll never lose affection,
For people and things that went before,
I know I'll often stop and think about them,
In My Life, I love you more."

The Beatles

Abstract

This dissertation examines the response and design of reinforced concrete core-slab-frame structures subjected to monotonically increasing earthquake and gravity loads throughout the entire load range until failure, presenting findings from three separate studies by Manatakos and Mirza (1995) continuing the M. Eng. thesis research by Manatakos (1989). A typical building is selected consisting of a central core substructure composed of elevator, staircase and infilled slab cores, with coupling and lintel beams, and surrounding slabs joining to a frame substructure composed of slab-band girders, slabs and columns.

Stage 1 concentrates on the elastic response and Stage 3 examines the nonlinear response of the core-slab-frame structure considering the effects of cracking and crushing of concrete, strain-hardening of the reinforcement, and tension-stiffening. Analyses involve three-dimensional elastic and nonlinear finite element modeling techniques of the structure to investigate the contribution and influence of the various structural components. The structural response is examined for the deformations, the concentrated reinforcement strains and concrete stresses in the cores, the force and stress distributions in the structural members, and the failure mode.

Stage 2 focuses on the design and detailing of the core-slab-frame structure following seismic provisions of building code requirements for reinforced concrete structures where applicable as given in the CSA Standard CAN3-A23.3-M84 (1984), the ACI Standard ACI 318M-83 (1983) and the New Zealand Standard NZS3101 (1982). Assumptions made in the conventional design procedures and any shortcomings encountered are examined. Suitable design procedures and reinforcement details are suggested where no provisions exist in the codes.

Findings demonstrate complex three-dimensional interaction among the cores, beams, slabs and frames in resisting the lateral and gravity loads, and show considerable strength, ductility and energy absorption capability of the structure. Critical areas for design include the joints and junctions near the vicinity of core wall-slab-beams ends and corners. Plastic hinging extends over the lower 25% to 33% height of the structure with the majority of inelastic action and damage concentrated in the bottom 10% to 15% height, predicting an ultimate load of 3.4 to 5.9 times the design earthquake load with top drifts of the structure between 750 mm to 1375 mm.

Résumé

Cette dissertation examine le comportement complet ainsi que les calculs sismiques des bâtiments immeubles en béton armé composés des cages de noyau, dalles, et cadres, soumis à des charges monotoniques de séismes et de gravité à toutes les phases de chargement jusqu'à la charge ultime. Ces résultants proviennent de trois rapports par Manatakos et Mirza (1995) suite à la recherche de Manatakos (1989). Pour l'étude, un immeuble caractéristique de construction moderne en béton armé est choisi, comportant des cages de noyau pour ascenseur, pour escaliers, et avec dalles, avec des poutres d'accouplement et linteaux d'ascenseur, et des dalles adjacentes connectées à des cadres composés de poutres-dalles, dalles, et des poteaux.

La réponse globale dans la gamme élastique est étudiée dans la première phase. Pour la troisième phase, le comportement non-linéaire est examiné en considérant les effets de fissuration et d'écrasement du béton, d'écoulement et d'écrouissage de l'armature d'acier, et du raidissement sous tension. La contribution et l'influence des divers éléments structuraux de l'immeuble sont étudiées en utilisant des analyses tri-dimensionnelles complètes par éléments finis représentant la structure entière. La réponse structurale est évaluée selon divers niveaux de charge pour les courbes charges-déformations, les allongements de l'acier concentré et les contraintes du béton dans les cages de noyau, la distribution des forces résultantes des éléments structuraux, et le mode d'écroulement.

La deuxième phase de l'étude se concentre sur les principes de calcul sismique pour les immeubles en béton armé selon les normes et règlements des codes Canadiens CSA CAN3-A23.3-M84 (1984), Americain ACI 318M-83 (1983) et Néo Zelandais NZS3101 (1982). Les hypothèses conventionnelles pour les méthodes de calcul et les déficiences rencontrées sont examinées. Des directives et des suggestions appropriées sont proposées en matière de calculs et détails d'armature d'acier au besoin.

Le comportement complet de l'immeuble démontre des effets tri-dimensionnels complexes d'interaction et d'accouplement entre les cages de noyau, poutres, dalles, et cadres, en plus de démontrer une résistance, une ductilité, et capacité d'absorption d'énergie considérable. Parmi les régions importantes pour les calculs sismiques, on dénote les joints et les jonctions á proximité des coins et des extrémités des cages de noyau-dalles-poutres. La région des rotules plastiques couvre de 25% à 33% de la base de la structure, engendrant la majorité des déformations inélastiques et des dommages structuraux aux premiers 10% à 15% de la hauteur de la structure. La charge ultime est évaluée de 3.4 à 5.9 fois plus élevée que les valeurs des calculs sismiques et le déplacement latéral du haut de la structure entre 750 mm et 1375 mm.

Acknowledgements

The author wishes to express his deepest gratitude to Professor M. S. Mirza, research director, for his guidance, valuable suggestions, constant encouragement, and his advice during the course of this investigation and during the preparation and writing of this thesis. Also, for his confidence in providing me with the opportunity to teach workshops and short courses in Bejing, China and throughout Canada enabling me to gain invaluable consulting and professional experience.

Special thanks are expressed to Dr. William D. Cook for his computer expertise, advise, extremely generous help, contribution to the preparation of the final draft of the thesis, and great deal of patience, encouragement and support throughout the research programme.

The following staff members of the Department of Civil Engineering Technology at Dawson College are acknowledged for their assistance, support and encouragement throughout this research programme:

Mr. Steve Babb, P. Eng. Chairman,

Mr. Dan Danielescu, P. Eng., Mr. Costa Maletskas, P. Eng., Mrs. Ruth Shannon,

Mr. René Degraaf, Mathematics Department,

Mr. Jim Luckow, P. Eng. Chairman of Mechanical Engineering Technology.

Deepest gratitude is extended to Dr. Michael Lichter, M. D., F.R.C.P. (C), Gastroenterologist-in-Chief at the Jewish General Hospital and Associate Professor of Medicine at McGill University for the medical treatment in my recovery. An experience I will never forget.

The author would also like to thank Mr. C. Michael Allen, P. Eng. of the consulting firm of Adjeleian and Associates Inc., Ottawa, Ontario, for providing the building structures investigated in this study and for his guidance and assistance.

Thanks are extended to Professor A. G. Razaqpur and Dr. Mostafa Nofal of the Department of Civil Engineering, Carleton University, Ottawa, Ontario, for providing the NONLACS computer program used in the nonlinear analyses.

Gratitude is extended to Mr. P.G. Whitwill, P.Eng., Senior Partner of Oliver, Mangione, McCalla and Associates Ltd. Consulting Engineers, Nepean, Ottawa, Ontario for the invaluable consulting experience obtained working on the World Exchange Plaza project.

Thanks are extended to the staff members and consultants of the McGill University Computing Centre for their assistance and expertise, and for the computer funds, storage and computer time provided without which the analyses would not have been possible.
Special thanks to Mr. Herong Yang

And to the following people:
Mr. Alan Greenberg, Mr. Howard Heitner, Mr. Mike Head, Mr. Sander Wasser,
Mr. Micheal Wood, Mr. Angelo Miele, Mr. Micheal Walsh,
Ms. Joan Brown, Ms. Debra Simpson.

At the McGill University Computer Store:
Mrs. Michèle Raymond, Mrs. Joan Edgar, Mr. Bernard Eckhardt.

To the following people at the Computing Centre Operations:
Mr. George Lebovics, Mr. Mark Brown, Mr. David German, Mr. David Hood,
and to:
Mr. Jerry Persaud, Mr. Eddy Santucci, Mr. Dennis Bancroft, Mr. Elias Daskalakis,
Mr. Agustin Bascao, Mr. Giovanni Mendicino, Ms. Carlette Walker, Mr. Dimitrios Daskalakis.

Finally, this research work and my educational goals would never have been accomplished without the patience, encouragement and support, love and understanding and thoughtfulness of the following people:

Mrs. Ann Bless,
Mrs. Susan Siavala, Mrs. Sandy Shewchuk-Boyd, Mrs. Anna Dinolfo, Ms. Lily Nardini,
Mr. Albert Lim and Anne Marie, Mr. Sheng Chew, Mrs. Lamya Amleh,
Mr. Werner Lex, Ms. Diane Playle, Mr. Arif Mirza, Mr. Dominic Forest, Mr. Dave Fortier,
Ms. Ivy Kwan.

The continuing support of the National Sciences and Engineering Research Council to the ongoing programs at McGill University is gratefully acknowledged.

Contents

List of Figures

List of Tables

Notation

The following is a list of symbols of the principal notations which are common in the various chapters of the text; other symbols are used in individual chapters. In general, subscripts and/or superscripts are added to the symbols defined below. All symbols are defined in the text when they first appear. Note that some symbols have several definitions depending on the context in which they are being used.

Roman Letter Symbols: Upper Case

A	Cross-sectional area; area
AE	Axial rigidity
C	Axial compressive force
C_w	Warping constant
$[C]$	Elasticity matrix
D	Flexural rigidity of a plate or shell
E	Young's modulus of elasticity (in tension and compression)
EI	Flexural rigidity
EC_w	Warping rigidity
F	A generalized force; a concentrated load
G	Modulus of elasticity in shear
GA	Shear rigidity
GJ	Torsional rigidity
H	Height of structure
I	Moment of inertia of cross-sectional area (second moment of cross-sectional area)
I_{xx}, I_{yy}, I_{zz}	Moments of inertia of a plane area with respect to the x, y, and z axes, respectively
I_{xy}	Product of inertia of a plane area with respect to the x and y axes
I_{vertical}	Moment of inertia of cross-sectional area in the vertical plane
$I_{\text{horizontal}}$	Moment of inertia of cross-sectional area in the horizontal plane

$I_{\text{torsional}}$	Torsional moment of inertia of cross-sectional area
J_c, J_o	Polar moments of inertia of a plane area with respect to the centroid and the shear centre, respectively
J	St. Venant torsional constant
K	Stiffness factor for flexural member
L	Length of member; span length
M	Bending moment at a section; moment of force (or couple); end moment of member; bending or twisting stress-couples in plates and shells
M_t	Twisting moment
M_{XX}, M_{YY}	Bending moments at a section of a plate/shell perpendicular to x and y axes, respectively
M_{XY}, M_{YX}	Twisting moments at a section of a plate/shell perpendicular to x and y axes, respectively
N	Normal force; axial force at a section; membrane stress-resultants in in plates and shells
N_X, N_Y	Membrane forces per unit length at a section of a plate/shell perpendicular to x and y directions, respectively
N_{XY}	Shear force in direction of y axis per unit length of a section of a plate/shell perpendicular to x axis
P	Force; concentrated load
Q	Force; concentrated load; statical moment of area; transverse shear stress-resultant in plates and shells
Q_X, Q_Y	Shearing forces parallel to z axis per unit length of sections of a plate/shell perpendicular to x and y axes, respectively
R	Reaction; resultant
S	Distance or length; stress resultant
S_{XX}, S_{YY}	Principal normal stresses per unit area at a section of a plate/shell perpendicular to x and y directions, respectively
S_{XY}	Principal shearing stress force in direction of y axis per unit area of a section of a plate/shell perpendicular to x axis
T	Axial tensile force; torque or twisting moment
V	Shearing force at a section
W	Weight; total load

Roman Letter Symbols: Lower Case

a	Length or distance
b	Length or distance; breadth or width of cross-section
c	Length or distance; distance from neutral axis (centroid) or from centre of twist to extreme fibre
d	Length or distance; diameter; depth of cross-section
e	Eccentricity
f	Numerical factor; flexibility factor for flexural members; computed stress
g	Numerical factor; gravitational acceleration constant
h	Numerical factor; height of a storey or an element; depth of a girder (beam); thickness; distance
i, j	Coefficient; integer
k	Coefficient; numerical factor; constant; sping constant
l	Numerical factor; coefficient; length or distance
ℓ	Length or distance; span
m	Integer; numerical factor; coefficient; length or distance; mass
m_{xx}, m_{yy}	Bending moments per unit length of sections of a plate/shell perpendicular to x and y axes, respectively
m_{xy}, m_{yx}	Twisting moments per unit length of sections of a plate/shell perpendicular to x and y axes, respectively
m_z	Intensity of torque per unit distance along z axis
n	Number; integer; coefficient
p	Pressure intensity per unit area
q	Distributed load intensity
r	Radius; coefficient; integer
s	Distance; coefficient; integer
t	Thickness; width
w	Weight per unit volume; intensity of uniformly distributed load per unit length
w_T	Maximum intensity of triangularly distributed load per unit length
u, v, w	Displacement components corresponding to x, y, and z coordinate directions, respectively
x, y, z	Orthogonal coordinate axis

Greek Letter Symbols

α, β	Angles; numerical factors; coefficients; ratios
γ	Shearing unit strain; weight per unit volume; numerical factor; coefficient
γ_{xy}, γ_{xz}, γ_{yz}	Shearing strain components corresponding to the unit shear stress components
δ	Net deflection; change in deformation
Δ	Total deformation or deflection
Δ_x, Δ_y, Δ_z	Translational degrees of freedom in the x, y, and z directions, respectively
ε	Unit normal strain (tensile or compressive)
ε_{xx}, ε_{yy}, ε_{zz}	Unit normal strains in the x, y, and z directions, respectively
θ	Slope angle for elastic curve; angle of inclination; angle of twist per unit length
θ_x, θ_y, θ_z	Rotational degrees of freedom about the x, y, and z axes, respectively
Θ	Total angle of twist or inclination
ξ, η, λ, μ	Numerical factors; coefficients; ratios
χ, ψ, ω, ζ	Numerical factors; coefficients; ratios
ϕ	Angle of twist
ν	Poisson's ratio
ρ	Radius of curvature
κ	Curvature
σ	Unit normal stress (tensile or compressive)
σ_x, σ_y, σ_z	Normal components of stress in the x, y, and z directions, respectively
τ	Unit shear stress
τ_{xy}, τ_{yz}, τ_{zx}	Unit shear stress components on planes perpendicular to the x, y, and z axes and parallel to the y, z, and x axes

Abbreviations

To facilitate the presentation of the text, the discussions and comparisons of the results in the various figures and tables, the following abbreviations are used (Fig. 1.1):

Core section = Infilled-slab core section

Elev section = Elevator core section

Stair section = Stairwell core section

CB = Coupling beam(s)

LB = Lintel beam(s)

I-E coupling beams = Coupling beams spanning between the Infilled-slab and Elevator core sections flange walls

E-S coupling beams = Coupling beams spanning between the Elevator and Stairwell core sections flange walls

S-slabs = Surrounding slabs around the core sections perimeter

E-slabs = Enclosed slabs with the core sections

E-S-slabs = Enclosed and surrounding slabs

Thesis

Chapter 1

Introduction

1.1 General

Modern low-, medium- and high-rise reinforced concrete buildings typically employ a configuration of the core-slab-frame structural system to satisfy architectural and structural needs, and other requirements aimed at efficient use of the structure. Overall building dimensions, the structural system selected, the floor plans and layout are governed by several factors including municipal bylaws, structural code provisions and architectural requirements for large column-free open spaces. Sizes of the various structural elements must comply with the minimum dimensional requirements to meet the design and construction constraints for placement of the reinforcement with adequate spacing and clear cover, and to ensure overall stability and safety of the structure. The frame substructure consists of columns, beams/girders and a slab system. Core substructures are normally located in the central region of a building and generally consist of a combination of various rectangular, I-, L-, U-, C- configuration cores and walls with openings providing vertical transportation (elevators and stairs) and the various services, and cores with *enclosed* slabs (portions of the slab within the cores). Certain restrictions are imposed on the structural cores to allow for circulation within a building requiring openings for passageways and corridors resulting in deep coupling beams connecting the cores, and lintel beams spanning across the core openings. A *surrounding* slab (portions of the slab around the perimeter of the cores) is present joining the core and frame substructures creating interaction between the two, forming a core-slab-frame structure.

Once the building structural system is selected, elastic analysis techniques are traditionally employed to evaluate the deformations and the design forces in the structural elements due to the imposed loading. Current building codes require the use of the ultimate strength design method for designing and detailing structural members for the factored loads at the ultimate limit state, while satisfying the serviceability limit state criteria. Many alternatives are available in the literature for the idealization of the structure and its substructures for analysis, ranging from simple hand methods of solution and computer modeling techniques for preliminary analyses, to sophisticated finite element techniques idealizing the entire building or substructures for a more detailed and refined analysis [Manatakos (1989)]. The latter type of analysis is generally used for investigative purposes and is neither feasible nor practical for use in the design office. No guidelines exist giving well defined procedures for the type of modeling of a structure and the method of analysis to be employed.

Selection of the analysis method and idealization of a structure should be based on the accuracy of knowledge of the externally applied loading and on the stage of the analysis and design (preliminary or refined) being performed. Traditional simplified planar methods of analysis are not always conservative and the contribution of all of the members in a building should be considered. At the ground level and below, all horizontal translations are typically restrained and the structure base is considered essentially fixed to the underlying foundations with all translations and rotations restrained. It is difficult to examine the influence of such complex boundary conditions and their stiffening effects unless detailed three-dimensional analyses of the structure are undertaken.

The realistic response of a reinforced concrete core-slab-frame structure is very complex as it is subjected to increasing lateral and gravity loads, from zero load through the linear and the nonlinear ranges, to the ultimate load stage until failure. Three-dimensional interaction between the structural components and the nonstructural elements exists, and these are quite difficult to be considered accurately in any analysis and design. Tools and procedures are also lacking for seismic design of such structures taking into consideration the three-dimensional response.

1.2 Identification of the Problem

1.2.1 Linear Elastic Response and Design

Previous studies on core structures have focussed on the response of single cell cores subjected to lateral loads producing torsion in the elastic range [Stafford Smith and Taranath (1972), Heidebrecht and Stafford Smith (1973) and Khan and Stafford Smith (1975)]. Cores are classified as either open-sections when no lintel beams exist across the openings (typically, a slab is present creating a partially closed-section) and closed-sections when lintel beams are present spanning across the openings (generally these beams are of depth equal to about one-third of the storey height). The actual response of a core is between these two limits and is influenced by the core shape and the presence of beams and slabs, making the analysis very complex and difficult. Torsional and warping deformations occur in core structures resulting in torsional moments and bimoments producing torsional shear and longitudinal warping stresses in addition to the direct, flexural, shear and St. Venant shear stresses normally considered. These additional warping stresses can be critical in core structures and must be considered in their analysis and design. More details relating to the theory of torsional analysis of cores have been provided by Vlasov (1961), Zbirohowski-Koŝcia (1967) and Kollbrunner and Basler (1969).

Previous studies on slab-core structures have focussed on interior panels of floor slabs with similar supports, columns or structural walls/cores, subjected to lateral load in the elastic range to determine the effective slab width for a lateral load analysis [Khan and Sbarounis (1964), Qadeer and Stafford Smith (1969), Pecknold (1975), Coull and El Hag (1975) and Alan and Darvell (1974)] and some studies have dealt with mixed column-wall-core supports [Tso and Mahmoud (1977)]. Long and Kirk (1980) examined the influence of gravity loads on the effective slab widths. It is normally assumed that slabs have large in-plane stiffness so that the in-plane deformations can be considered to be negligible (rigid floor slab method) to simplify the analysis by using effective slab widths for lateral load analysis and centre-to-centre panel widths for gravity load analysis. Few investigations have been performed on slab-core structures subject to lateral loads producing torsion. Taranath (1975, 1976) examined the torsional response of a simple symmetric flat plate-core structure, but only for the core actions in the elastic range with simplifying assumptions for the slab-core connection.

In present day analysis and design, it is common practice to employ simplified two- or three-dimensional analyses of a structure incorporating lumping and reduction techniques, and equivalent substitute structures for frames, structural walls/cores and slabs to determine the interactive forces between the various components, to minimize the analysis work and to facilitate the design process. A substructure analysis is then performed using the more refined finite element method isolating a particular building component, incorporating simplifications, imposing the appropriate boundary conditions and applying the corresponding substructure forces. Therefore, two different idealizations of a structure are required for analysis, one idealization for lateral load analysis and another idealization for gravity load analysis. In the lateral load analysis, the applied loads are assumed to be resisted entirely by the structural walls/cores typically as a central core system, or in combination with a frame system forming equivalent frames using effective slab widths. In the gravity load analysis, the loads are resisted by a slab-beam/girder-column-wall/core system, a typical floor and the supporting members are considered using the centre-to-centre panel widths to form frames representing the entire floor slab. Unfortunately, employing these analysis concepts does not always yield conservative results, and quite often it leads to overdesign of the lateral load resisting elements and possible under-design of the gravity load resisting elements. The response of a structure subjected to lateral loads, due to earthquake or wind, and gravity loads is very complex since the *effective* stiffness of the structure varies for each response considered separately. Therefore, a single idealization *cannot* be used for both lateral and gravity load analyses.

Determination of the deformations and forces in a structure for design is not a simple undertaking. Many modeling techniques and methods of analysis of building structures for lateral and gravity loads are available in the literature. Selection of an appropriate method is the responsibility of the structural engineer, a task which can be a difficult one. Current concrete design codes do not provide adequate design procedures and requirements for the design of individual and coupled cores, open-, closed- and partially-closed sections, slabs surrounding and enclosed within cores, coupling and lintel beams connected to cores, and the various slab-core wall-beam connections and regions, taking into consideration the three-dimensional structural behaviour.

Limits and restrictions on the allowable deformations and stresses due to lateral and gravity loads in the various structural components and the overall structure are generally imposed by building codes or by the structural engineer. It should be noted that these imposed restrictions do not take into consideration the method of idealization or the degree of refinement required (simplified or detailed) for the analysis. The question arises: How meaningful are these imposed limitations and restrictions? The governing factors in design for lateral loads are the net inter-storey drift and the overall drift of a building. Maximum allowable drift indices, the ratio of the storey drift to the storey height and that of the drift to the total building height, are specified with typical values of 1/500 and 1/500 to 1/1000, respectively, the latter value being dependent on the height of the structure. From a survey of several buildings, Fintel (1975) noticed differences of several hundred percent in the prediction of the drift of the structure depending on the analysis technique selected. Quite often, the use of a simplified analysis method can result in values which exceed the prescribed deformation and stress limits, whereas, a more detailed sophisticated three-dimensional finite element analysis of the entire structure may give results for these deformations and stresses well within the prescribed limits due to the consideration of the three-dimensional response of the structure [Manatakos (1989)].

Findings by Manatakos (1989) [M. Eng. investigation, details given in the following section] and subsequent work by Chew (1991), demonstrate that the response of a core-slab-frame structure and the resulting deformations and forces in the various substructures due to lateral and gravity loads, vary depending on the method of analysis and the modeling technique used for the analysis. Sophisticated finite element analyses predict a more realistic response of a structure and demonstrate actions which cannot be determined otherwise and may be critical in the analysis and design of core-slab-frame structures. As the idealization of a structure takes into consideration the various structural components, proceeding from a linked planar model to a simplified three-dimensional model to a more detailed three-dimensional finite element model, a considerable increase is noted in the overall stiffness of the structure.

The lateral and gravity load response of core-slab-frame structures is very complex with three-dimensional interaction occurring among the core and frame substructures, and their components, the slabs, columns, and coupling and lintel beams, influencing the structural response which is a critical factor in analysis and design. Factors requiring further study include torsional and warping deformations due to lateral and gravity loads, and the effects and influence of the core-slab-frame components on each other and on the overall structural response. Existing literature shows no research on slab-core regions which takes these effects into consideration. The finite element method appears to be a logical method of efficiently tackling this problem, in order to determine the various actions in core-slab-frame structures.

1.2.2 Previous M. Eng. Investigation

A comprehensive review examining the various linear elastic modeling and analysis techniques of reinforced concrete buildings subjected to lateral and gravity loads, giving complete details and literature reviews, was undertaken by Manatakos (1989). Two buildings reflecting the current trends in design and construction were selected for the investigation: a 20 storey medium-rise building and a 4 storey low-rise building, and their substructures consisting of frames, individual and coupled structural cores/walls, frame-cores/walls, coupled structural cores/walls and flat slab-core/wall structures. The analyses performed range from hand methods of solution, simplified two- and three-dimensional computer modeling (assuming rigid floor slabs) employing lumping and reduction techniques for preliminary analysis and design, to sophisticated three-dimensional finite element analysis techniques idealizing the entire low-rise building and the substructures of the medium-rise building (rigid floor slab assumed) for more detailed analyses. A summary of the various idealization techniques and analysis methods examined is listed below.

I. Frame Structures

a) Hand methods of analysis for determining the drift:

[i] Shear-flexure effects in frames – Goldberg (1974)

b) Hand methods of analysis for calculating the member forces:

[i] Cantilever method – Wilson (1908)

[ii] Simplified portal method – Smith (1915)

[iii] Modified portal method – Bowman (1950)

[iv] K-factor method – Wilbur (1934)

c) Computer Methods of Analysis:

[i] Equivalent one-bay substitute frame – Khan and Sbarounis (1964)

[ii] Lumped girder reduction technique – PCA (1971)

[iii] Member-for-member idealization based on centerline dimensions – PCA (1971)

[iv] Consideration of the dimensions of the beam-column joints
based on clear member lengths – PCA (1971)

II. Structural Wall/Core Structures

a) Hand methods of analysis:

[i] Stick idealization using simple bending theory

[ii] Continuous medium analogy for coupled structural walls
– Coull and Choudhury (1967), Coull and Puri (1967, 1968),
Coull and Adams (1973)

b) Computer methods of analysis:

[i] Lumped column idealization – Khan and Sbarounis (1964)

[ii] Wide column idealization – MacLeod (1970)

[iii] Finite element method (rigid floor slab)

III. Frame-Structural Wall/Core Structures

a) Hand methods of analysis:

[i] Equivalent one-bay substitute frame, and stick idealization of walls/cores – Khan and Sbarounis (1964)

[ii] Shear-flexure effects in frames and structural walls/cores – Heidebrecht and Stafford Smith (1973), Basu and Nagpol (1980)

b) Computer methods of analysis:

[i] Idealization of frames and walls/cores by equivalent or substitute structures as listed in I and II above.

[ii] Simplified two- and three-dimensional analyses (rigid floor slab)

[iii] Finite element method (rigid floor slab)

IV. Slab Structures

a) Lateral load analysis

[i] Simplified two- and three-dimensional analyses assuming rigid in-plane floor slab idealized as equivalent beams with effective slab widths determined using the available charts and tables for similar end support conditions consisting of columns, walls, or cores.
– Khan and Sbarounis (1964), Qadeer and Stafford Smith (1969), Pecknold (1975), Coull and El Hag (1975), Tso and Mahmoud (1977), Alan and Darvell (1974)

[ii] Finite element method

b) Gravity load analysis

[i] Simplified code method: the direct design method
– Nichols (1914), Lord (1910), Westergaard and Slater (1921), CSA Standard CAN3-A23.3-M84 (1984)

[ii] Planar equivalent frame representation of the floor slab substructure and the supporting members: the equivalent frame method
– Corley and Jirsa (1970), Simmonds and Misic (1971), CSA Standard (1984)

[iii] Finite element method

Accuracy of the methods and the response of the various substructures was examined in terms of the deformations, the individual and lumped member forces, the forces and stresses, and the distribution of forces in the different structural elements.

The three-dimensional response of the core-slab-frame structure [Manatakos (1989)] is approximately 4 times stiffer than the aggregation of planar systems basically due to the interaction between the various components. The drift of the structure decreases to about 20% to 25% of the maximum drift given by a planar idealization. Force distributions in the cores for the interactive forces, and the bending moments and shear forces demonstrate a transfer of up to 15% additional shear forces to the cores substructure, indicating an increased stiffness throughout the core height. Stresses in the cores show a reduction by as much as 45% when the three-dimensional structural response is taken into consideration in the analysis.

Results for the low-rise building response [Manatakos (1989)] for the deflected shapes of the slabs due to gravity loads demonstrate complex surfaces showing rapidly changing slopes in panels with mixed support conditions present, illustrating one-way action along structural core walls and two-way action around columns, ends and corners of walls/cores. Earthquake loading results demonstrated that the slab response is influenced by the type of supports : flexible column or stiff wall/core supporting members, and the adjacent slab panels. Thus, very complex deflected surfaces develop in panels with mixed support conditions. Distribution of the in-plane slab stresses due to earthquake loads illustrate shear lag effects with large stresses near regions of stiff structural wall/core ends and corners, and stress reversals where variations in slab stiffness occur due to the presence of walls/cores and openings. As a result, problems may arise in these regions due to the sudden transfer of forces from the slab to the wall/core. In panels with mixed support conditions – columns and walls/cores – irregular bending and twisting moment distributions are noted in a slab due to the earthquake and gravity loads, with larger moments near the ends and corners of walls/cores and moment reversals along the regions of wall/core supports. Slab twisting moments are as significant and larger in magnitude as the slab bending moments in panels with mixed supports; these trends also occur in stiffer slab regions for earthquake loads and in flexible slab regions for gravity loads. The magnitude of the slab bending and twisting moments due to earthquake loads, can be as large as those due to gravity loads in the vicinity of structural cores where mixed panel support conditions exist.

Findings demonstrate that the deformations and forces in a building and its substructures due to lateral and gravity loads can vary widely depending on the method of analysis and the modeling technique employed. The actual structural response is very complex with three-dimensional interaction occurring between the various structural components resulting in all the components participating in the lateral and the gravity loads resistance, irrespective of the idealization and the assumptions employed for analysis and design. Contributions of the various structural components to the overall structural response *must be* taken into consideration in the analysis for an efficient and economical design. It must be emphasized that even the sophisticated finite element methods used for determining the deformations and forces in a structure should *not be* accepted unquestionably as giving the *correct* final results. Approximate methods of analysis provide numbers such as deflections and overall force distributions to perform a quick check on the *reasonableness* of the results obtained using the more sophisticated methods.

1.2.3 Nonlinear Inelastic Behaviour

In present day philosophy, reinforced concrete structures are analyzed using elastic analysis techniques following the building code regulations for equivalent static representation of the ultimate loads. lateral and gravity loads, and are designed for the resulting forces. Concrete is assumed to be an uncracked. homogeneous and isotropic material. How good is this rationale and how reliable are the traditional analysis and design methods for buildings compared with the observed response in practice? Nonlinear analyses of structures are rarely considered by the practising engineer. being impractical and very expensive. and are employed typically for investigative analyses of existing building substructures with serious problems.

The general state of a reinforced concrete building is not the same throughout the structure. Properties and strength of the concrete and the steel reinforcement vary, and cracking of the various structural elements (columns, girders, beams, structural walls/cores, slabs) may occur under service loads. Typically cracked section properties for the various building components are used in elastic analyses, where the reduced stiffness values are determined based on analytical studies and test results of the response of planar individual frames, structural walls/cores subject to lateral loadings. Park and Paulay (1975) have suggested using the following reduced flexural rigidities (based on the gross section properties) for cracked section elastic analysis :

For girders/beams : $$EI_{\text{girder/beam}_{\text{cracked}}} = (0.40 \text{ to } 0.60)\, EI_{\text{girder/beam}_{\text{uncracked}}}$$

For columns : $$EI_{\text{column}_{\text{cracked}}} = (0.70 \text{ to } 0.80)\, EI_{\text{column}_{\text{uncracked}}}$$

For structural walls/cores : $$EI_{\text{wall/core}_{\text{cracked}}} = (0.40 \text{ to } 0.75)\, EI_{\text{wall/core}_{\text{uncracked}}}$$

At higher load levels. it is recommended [Park and Paulay (1975)] that the flexural rigidities of the vertical lateral load resisting elements be further reduced to $EI_{\text{cracked}} = 0.25EI_{\text{uncracked}}$ at the base region of the structure. In addition, cracking due to lateral loads causes the stiffness to change along the length of the individual structural elements. As a consequence, the flexural rigidity of the structural members and components varies along the height of the structure, being smaller in value near the base region where most of the cracking occurs due to lateral loads (potential plastic hinging region for structural walls, cores and columns) and larger in value in the upper regions since cracking is not as severe. Therefore, many values of the flexural rigidity may have to be assigned for the same component or member in a structure along the building height for a lateral load analysis. Guidelines providing such values do not exist.

The nonlinear response of a reinforced concrete slab system subjected to lateral and gravity loads is very complex involving material and geometric nonlinearities, redistribution of forces due to cracking, tension stiffening, arching and membrane action, and inelastic response at higher load levels. Influence of these factors on the overall slab response is dependent on the degree of restraint present and the stiffness of the supporting members, columns, beams or structural core walls around the panel perimeter [Cope and Clarke (1984) and Park and Gamble (1980)].

1.3 Research Needs

Previous studies and investigations of core and slab-core structures have focussed on the linear elastic response of single cores and of isolated symmetric simple slab-core structures. These are not representative of realistic reinforced concrete core-slab-frame structures. To the best of the author's knowledge, the cracking patterns, plastic hinging regions in the various structural components and the failure modes of core-slab-frame structures have not been investigated. No analytical or experimental investigations of a complete three-dimensional reinforced concrete structure or core-slab substructure have been reported.

Based on the findings of the previous investigation by Manatakos (1989), consultations with practicing engineers and from a survey of the existing literature, further research is needed to study the behaviour of modern reinforced concrete core-slab-frame structures subjected to lateral and gravity loads to failure. Various actions must be examined in detail for the different phenomena including: three-dimensional interaction of the various structural components – cores, coupling and lintel beams, enclosed and surrounding slabs, and frames on the overall structural response. Design procedures and reinforcement detailing are lacking in current concrete design codes for lateral and gravity loads design of individual and coupled cores, open-, closed- and partially-closed sections, slabs surrounding and enclosed within cores, coupling and lintel beams connected to cores, and the various slab-core wall-beam connections and regions taking into consideration the three-dimensional structural behaviour.

1.4 Scope and Objectives of the Present Study

The basic objectives and scope of this research program are:

1. To study the behaviour reinforced concrete core-slab-frame structures subjected to lateral and gravity loads to failure.
2. To investigate the three-dimensional interaction of the core-slab-frame structural components and their influence on the overall structural response.
3. To develop practical design recommendations and procedures for the various structural components: core sections, coupling and lintel beams, slabs surrounding and enclosing cores, and their connections.
4. To provide an improved understanding of the complex behaviour of reinforced concrete core-slab-frame structures.

1.5 Description of the Structure

The structure is chosen to represent the current construction trends for reinforced concrete core-slab-frame buildings, designed for interaction of cores and frames to lateral loads.

The core-slab-frame structure Fig. 1.1. is 20 storeys above and one storey below the ground level with storey heights of $4.88\,m$ ($16\,ft$) for the main and roof storeys, $3.50\,m$ ($11\,ft - 6\,in$) for typical interior storeys and $3.66\,m$ ($12\,ft$) for the basement storey. It is of non-rectangular floor plan with 6 bays of $6.10\,m$ ($20\,ft$) each in the short direction, and 4 bays, two of $9.14\,m$ ($30\,ft$) and two of $10.67\,m$ ($35\,ft$) in the long direction of the building.

A central core substructure is present consisting of three cores: an "infilled-slab" core (Core) so termed since it has no opening with a $203\,mm$ ($8\,in$) thick enclosed slab within the core section, an elevator core (Elev) with $203\,mm$ ($8\,in$) wide by $914\,mm$ ($36\,in$) deep lintel beams spanning across the opening, and a stairwell core (Stair) with a staircase opening and partial enclosed slabs. Cross-sectional dimensions of the cores include: web walls of $7.62\,m$ ($25\,ft$) width for each core, two flange walls each of $3.66\,m$ ($12\,ft$), $2.74\,m$ ($9\,ft$) and $1.52\,m$ ($5\,ft$) for the Core, Elev and Stair sections, respectively, and wall thicknesses of $305\,mm$ ($12\,in$) for all but the Elev section web wall which is $254\,mm$ ($10\,in$) thick. The cores are connected in the building short direction at the floor levels by coupling beams of dimensions $305\,mm$ ($12\,in$) wide by $914\,mm$ ($36\,in$) deep (one-third the storey height) with spans of $3.05\,m$ ($10\,ft$) for the I-E coupling beams spanning between the Core and Elev sections flange wall ends, and $1.22\,m$ ($4\,ft$) for the the E-S coupling beams spanning between the Elev section flange-web corners and the Stair section flange wall ends.

A frame substructure is present in the building long direction composed of columns with uniform member properties and cross-sectional dimensions $610\,mm$ by $610\,mm$ ($24\,in \times 24\,in$) throughout the height. To minimize the storey heights (maximizing the clear storey heights), normal beams (girders) are not used, instead "slab-band girders" are used to form the frame system. Three types of "slab-band girders" are present of width-to-depth dimensions: $1.83\,m$ by $356\,mm$ ($6\,ft \times 1\,ft - 2\,in$) for girders SB1, $2.44\,m$ by $356\,mm$ ($8\,ft \times 1\,ft - 2\,in$) for girders SB2, and $2.44\,m$ by $457\,mm$ ($8\,ft \times 1\,ft - 6\,in$) for girders SB3, forming three different sets of frame-bents with the columns: two exterior frame-bents of two-bays, two interior frame-bents of four-bays and three core frame-bents of one-bay each on both sides of the core webs. The frame substructure is connected to the core substructure by a $152\,mm$ ($6\,in$) thick slab around the core sections, termed the "surrounding slabs".

It is noted that in the original design of the structure, the main lateral load resisting elements were considered to be the linked planar frames-core web walls in the building long direction, and the planar coupled Core-Elev flange walls in the building short direction.

1.6 Current Research Program

An analytical investigation is performed using linear elastic and nonlinear inelastic finite element analyses permitting a detailed study of the response of the core-slab-frame structure (Fig. 1.1) subject to Q_X and Q_Y earthquake loadings (in the X- and Y-directions) and gravity loads for the complete response to failure. All analyses involve three-dimensional finite element modeling of the structure, and for each idealization, the model sophistication is increased gradually to take into consideration the various structural components.

The response of the core-slab-frame structure is examined through the various loading stages, linear elastic, nonlinear inelastic, to failure, in terms of the deformations and actions, force distributions, stresses, forces and moments, effects of cracking on the reduction of stiffness and redistribution of forces, and the ultimate load and failure modes. The contribution and interaction of the structural components, the cores, coupling and lintel beams, enclosed and surrounding slabs, and frame substructure on the structural response are also investigated.

1.6.1 Linear Elastic Response

Stage 1 of the current research program concentrates on the three-dimensional linear elastic response of core-slab-frame structures subjected to earthquake and gravity loads. A detailed three-dimensional finite element model of the entire structure is developed, from which four different models are derived for the various analyses performed using the SUPERSAP [SAP IV] computer program (1974). Complete details for the linear elastic finite element modeling and analyses of the core-slab-frame structure under investigation can be found in the report by Manatakos and Mirza (1995).

The contribution and influence of the cores, coupling and lintel beams, enclosed and surrounding slabs, and frames is examined in terms of the interaction among the components and on the structural response. The results are examined for the profiles along the height and at ground level for the drifts, twists, shear forces and interactive forces; the stresses, forces and moments; and three-dimensional distributions and topographical contours for the stresses, forces and moments in the core sections, the enclosed and surrounding slabs, and the coupling and lintel beams.

Simplified two- and three-dimensional elastic finite element modeling and analyses of the structure under investigation have been performed by Manatakos (1989).

1.6.2 Design Considerations

Stage 2 of the investigation involves the design of core-slab-frame structures, with the design forces determined from the elastic analyses performed in Stage 1. Complete design details of the core-slab-frame structure under investigation can be found in the report by Manatakos and Mirza (1995). Highlights of important design considerations, comments and recommendations are presented in this thesis for brevity along with the suggested design procedures. Nonlinear inelastic analysis findings from Stage 3 of this investigation are incorporated in evaluating and modifying the design process where needed.

Design of the core sections, the coupling and lintel beams, the core wall-slab-beam junctions, end and corner regions, and the enclosed and surrounding slabs is performed following the CSA Standard CAN3-A23.3-M84 (1984) requirements of Clause 21, Special Provisions for Seismic Design where applicable. In addition, seismic design provisions from the ACI Standard ACI 318M-83 (1983) Building Code Requirements for Reinforced Concrete and the New Zealand Standard NZS3101 (1982) Code of Practice for the Design of Concrete Structures are used where needed. All references to the Code or to clauses such as Cl 21.5.3 or to notes to the clauses such as N 21.5.3 are with reference to the CSA Standard and the Commentary to the CSA Standard, unless stipulated otherwise. Assumptions made in the conventional design procedures and any shortcomings encountered are examined.

In areas where building codes are not applicable and offer no provisions, reference to the work by the various researchers is made and design procedures and reinforcement details are suggested taking into consideration the various three-dimensional actions which are present in the structure complicating the design.

1.6.3 Nonlinear Inelastic Behaviour

Stage 3 of the current research program focuses on the nonlinear inelastic behaviour of core-slab-frame structures. The core-slab substructure (Fig. 1.1) as designed and detailed in Stage 2 is examined, subjected to monotonically increasing earthquake loads and gravity loads until failure. A detailed three-dimensional finite element model of the core-slab substructure is developed from which the different models are derived for the various analyses performed using the NONLACS computer program [Razaqpur and Nofal (1988)]. Nonlinear analysis findings are also incorporated in modifying the design where needed. Complete details for the nonlinear inelastic finite element modeling and analyses of the core-slab substructure under investigation can be found in the report by Manatakos and Mirza (1995).

The contribution and influence of the cores, coupling and lintel beams, enclosed and surrounding slabs is examined in terms of the interaction among the components and on the structural response. The results are examined for the profiles along the height and at ground level for the structural deformations - drifts, twists, vertical slab-core deflections, the strains in the concentrated reinforcement of the cores; and three-dimensional distributions and topographical contours for the concrete stresses in the cores at the ground level.

1.7 Organization of Thesis

Complete details and results of the present investigation of the behaviour and design of reinforced concrete core-slab-frame structures subject to lateral and gravity loads to failure, can be found in three reports by Manatakos and Mirza (1995):

1. "*Elastic Behaviour of Reinforced Concrete Core-Slab-Frame Structures*"
2. "*Nonlinear Behaviour of Reinforced Concrete Core-Slab-Frame Structures*"
3. "*Design of Reinforced Concrete Core-Slab-Frame Structures*"

This research is a continuation of the previous M. Eng. investigation by the author entitled "Analyses of Low- and Medium-Rise Buildings" Manatakos (1989) in which further details are given relating to linear elastic analyses of reinforced concrete core-slab-frame structures.

This thesis is divided into 7 chapters presenting a summary of the research work:

Chapter 1 presents a general introduction, identification of the problem, a summarized literature survey, main objectives and the scope of this study.

Linear elastic response of core-slab-frame structures are presented in Chapter 2 giving details of the different finite element modeling techniques of the structural components, problems encountered and remedies employed, analyses performed and the applied loadings for the analytical study and design considerations.

Design details are summarized in Chapter 3, giving highlights of important design considerations, with recommendations presented for design procedures and detailing of reinforcement for core sections, slabs enclosing and surrounding cores, coupling and lintel beams, and slab-core wall-beam connections.

Nonlinear inelastic behaviour of core-slab substructures are presented in Chapter 4, giving details of the various finite element modeling techniques for the structural components and material characteristics, problems encountered and remedies employed, analyses performed, and the applied earthquake and gravity loadings.

Discussions of the linear elastic and the nonlinear inelastic behaviour and finite element analyses results are presented in Chapters 5 and 6, respectively, in the form of two- and three-dimensional graphs and surface distributions of the various deformations, forces and stresses in the structural elements throughout the entire load range until failure of the structure.

Conclusions and recommendations are summarized in Chapter 7, from the linear elastic and nonlinear inelastic behaviour and the design, providing useful information and an improved understanding of the complex response of reinforced concrete core-slab-frame structures. Areas requiring future research and investigation are also outlined.

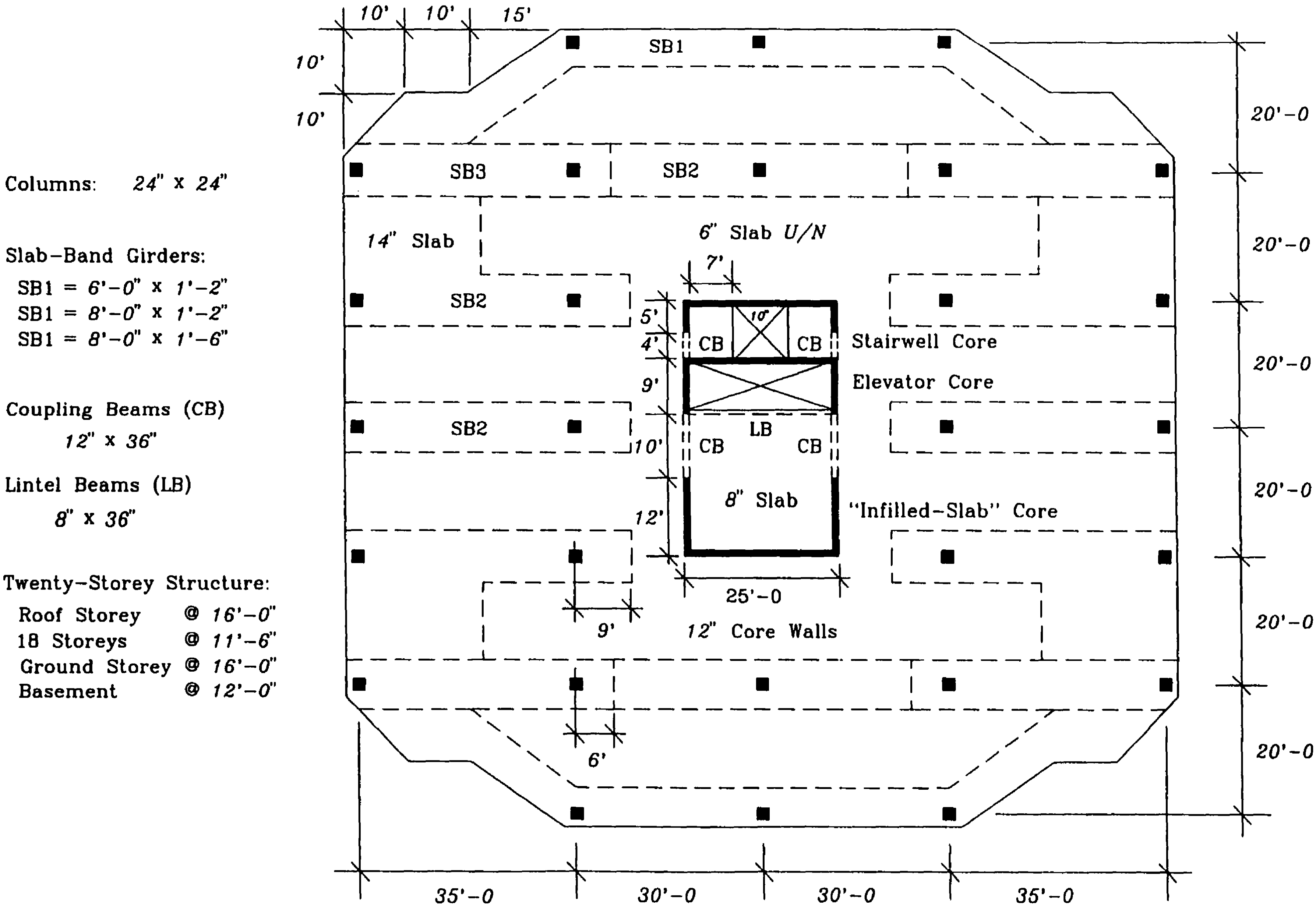

Figure 1.1 Core-Slab-Frame Structure – Typical Floor Plan Details

Chapter 2

Linear Elastic Response

Stage 1 of the current research program concentrates on the three-dimensional linear elastic response of the core-slab-frame structure (Fig. 1.1) subject to earthquake and gravity loads. Simplified two- and three-dimensional elastic finite element modeling and analyses of the structure under investigation have been performed by Manatakos (1989). Findings have demonstrated that the structure responds as a complex three-dimensional assemblage of cores, beams, slabs and frames in resisting the lateral and gravity loads. The contribution and influence of the cores, coupling and lintel beams, enclosed and surrounding slabs, and frames is examined in terms of the interaction among the components and on the structural response. A detailed three-dimensional finite element model of the entire structure is developed from which four different models are derived for the various analyses performed. Complete details for the linear elastic finite element modeling and analyses of the core-slab-frame structure under investigation can be found in the report by Manatakos and Mirza (1995).

The finite element analysis is implemented for both the lateral and gravity loads permitting a direct comparison with the results of the previous investigation by Manatakos (1989). Design forces in the structure are determined to examine and to comment on seismic design of the cores, coupling and lintel beams, and the slabs which is undertaken in Stage 2 of this study.

2.1 Elastic Analysis Computer Program

To perform the elastic analyses of the core-slab-frame structure, the SAP IV computer program [Reference Manual (1974)] is selected. Finite elements in the computer program library include: the beam element (Type 2), the quadrilateral plane stress membrane element (Type 3), the quadrilateral plate/shell element (Type 6) and the boundary element (Type 7). Details of the derivation of the elements and their stiffness matrices can be found in standard texts on the finite element method such as those by Cook (1981) and Zienkiewicz (1977).

2.2 Core-Slab-Frame Building Model Description

Table 2.1 summarizes the material properties for concrete with a compressive strength of 30 MPa used in the various elastic analyses.

2.2.1 Cores, Slabs and Slab-Band Girders Idealization

Figures 2.1 and 2.2 show the elastic modeling details of the core sections along the height, and of the slabs and slab-band beams for a typical floor level.

A division of 4 elements is chosen across the core sections web walls. Across the Core and Elev sections flange walls a 2 elements division is selected, while for the short Stair section flange walls a 1 element division is used to model the entire wall width. Along the cores height for the web and flange walls, in typical storeys and the basement storey, a 2 elements division with heights equal to one-half of the storey heights is used. For the ground and top storeys, a 3 elements division each equal to one-third of the storey height is selected to obtain a more detailed distribution of the core stresses and forces in the lower regions. Element aspect ratios are maintained at values less than 2 and as close to unity as possible.

Selection of the slabs mesh division is influenced by many factors including the modeling technique: planar, simplified, partial or detailed three-dimensional analyses; and requirements of the direct design method and the equivalent frame method of analysis [Manatakos (1989)].

For the panel slabs connecting the frame-bents, each panel slab is divided into one-half column strips and one-half middle strips giving a uniform mesh of 4 by 4 elements per slab panel. In the direction of the frame-bents, column strip widths are equal to the slab-band girder widths and middle strip widths are equal to the slab portions between the slab-band girders. In the direction perpendicular to the frame-bents, the slab panels are divided into 4 approximately equal elements following the column and middle strip definitions. The enclosed slabs within the Core section, the I-E coupling beams and the lintel beams are divided into a mesh of 4 by 4 elements and the two enclosed slab portions within the Elev and Stair sections and the E-S coupling beams are divided at the Stair flange wall end-coupling beam joint into 2 elements each. For the surrounding slabs, the mesh is divided in accordance with the selected 4 by 4 mesh of the other slabs. Aspect ratios for all the elements are kept to values less than 2.5 to 1.

Slab-band girders $SB1$, $SB2$, and $SB3$ of the exterior, the interior and the core frame-bents labeled in Fig. 2.3, are wide, shallow girders and are part of the slab system. Hence, the 4 by 4 mesh division for the slab panels divides the slab-band girders into 2 elements across their widths to form one-half of the column strips. The element aspect ratios are maintained at values less than 2.5 and as close to unity as possible.

Quadrilateral shell elements are used to model the core sections, slabs and slab-band girders with the appropriate thickness and element dimensions determined from the mesh divisions and the properties for E, ν, and G as listed in Table 2.1.

2.2.2 Columns, Coupling and Lintel Beams Idealization

Columns comprising the exterior, the interior and the core frame-bents in Figures 2.3 and 2.4. are of uniform dimensions and modeled for the full storey heights (nodes at each floor level).

For the I-E and E-S coupling beams and the lintel beams of constant cross-sectional dimensions, a mesh division is chosen to match the core and slab mesh. Along the I-E coupling beams span a 2 elements division is selected, while for the short, deep E-S coupling beams a 1 element division modeling the entire beam is used. The lintel beams are divided into 4 equal elements each along the span as shown in Figures 2.1 and 2.2.

Beam elements are used to model the columns, coupling and lintel beams with dimensions corresponding to the mesh divisions and sectional properties as listed in Table 2.2.

2.2.3 Modeling the Core St. Venant Torsional Properties

A problem encountered in the three-dimensional modeling of the cores is that the quadrilateral shell element models the axial, shear and flexural stiffnesses, however, it cannot account for the St. Venant torsional characteristics of the core section. Khan and Stafford Smith (1975) suggest the following equations for calculating the core section St. Venant torsional constant (J):

a) Open-section cores:

$$J = \sum \frac{bt^3}{3} \tag{2.1}$$

b) Closed-section cores:

$$J = \sum \frac{bt^3}{3} + \frac{4A^2}{\oint ds/t} \tag{2.2}$$

where:

b	=	total length measured along the core cross-section centerline.
t	=	thickness of the core wall.
A	=	cross-sectional area of the core within the wall centerlines.
ds	=	elemental length measured along the core cross-section centerline.

In the modeling, St. Venant torsional characteristics of a core section can be considered by the addition of auxiliary elements (J-columns) with a torsional second moment of area equal to the core St. Venant torsional value, vertically orientated along one of the mesh lines of each core section as shown in Fig. 2.1. These J-columns are modeled by soft-flexible beam elements which have negligible axial and flexural stiffnesses and are assigned the following properties:

$$A = 0.0001\, mm^2$$
$$I = 0.0001\, mm^4$$

$$I_{sv} = \text{St. Venant } J - \text{value for the core } (mm^4)$$

Table 2.2 summarizes the St. Venant torsional J-values for the core sections.

2.2.4 Characteristics of the Elastic Finite Element Model

Details of the three-dimensional elastic finite element idealization of the core-slab-frame structure are given in Figures 2.1 to 2.4 for the core sections, frame-bents, coupling and lintel beams, and the slabs. The model is characterized as follows:

- 6 degrees of freedom per node = Δ_x, Δ_y, Δ_z, θ_x, θ_y, θ_z
- Total number of nodes = 9525
- Total number of material properties = 25
- Total number of element stiffness properties = 80
- Total number of beam elements = 3310
  - 588 elements for the columns
  - 126 elements for the coupling beams
  - 84 elements for the lintel beams
  - 132 elements for the auxiliary St. Venant torsional J-columns
  - 2380 elements for the auxiliary elements (rigid, soft)
- Total number of quadrilateral shell/plate elements = 8780
- Total number of quadrilateral shell elements for the cores = 968
  - 352 elements for the infilled-slab core
  - 352 elements for the elevator core
  - 264 elements for the stairwell core
- Total number of quadrilateral plate elements for the slabs = 7812
  * 372 plate elements per slab (21 floors in total)
    - 420 elements (20 per level) for the enclosed slabs
    - 2016 elements (96 per level) for the surrounding slabs
    - 5376 elements (256 per level) for the frame panel slabs
      * 2940 elements (140 per level) for the slab-band girders
      * 2436 elements (116 per level) for the panel slabs
- Total number of quadrilateral plane stress membrane elements = 2016
  - 2016 elements (96 per level) for the surrounding slabs

Boundary conditions involve: all translations and rotations restrained for the nodes at the base level, horizontal translations Δ_x and Δ_y restrained for the perimeter nodes at the ground level. and all 6 degrees of freedom Δ_x, Δ_y, Δ_z, θ_x, θ_y, θ_z are permitted for all other nodes.

Output from the analyses consists of the nodal deflections and rotations for the entire structure: the axial forces, shear forces, bending and twisting moments in the columns, the coupling and the lintel beams: the axial and shear stresses, and the flexural and twisting moments per unit length for the cores and slabs shell/plate elements.

2.3 Applied Loadings

Loadings for the elastic analyses of the core-slab-frame structure consist of the Q_X and Q_Y earthquake loads in the X- and Y-directions and the gravity dead and live loads as obtained from the National Building Code of Canada (1985) and the CSA Standard CAN3-A23.3-M84 (1984). More details relating to the calculation of the loadings are presented by Manatakos (1989).

2.3.1 Earthquake Loads

For the various elastic analyses performed, the equivalent static earthquake loads are applied as determined from the base shear calculations for both principal directions of the structure. The total Q_X and Q_Y earthquake loading at a floor level is divided into discrete concentrated loads distributed to the columns and the core wall ends and corners (nodes) across each floor level in proportion to the tributary floor area supported by each node. Table 2.3 summarizes the Q_X and Q_Y earthquake loads on the core-slab-frame structure.

2.3.2 Gravity Loads

Gravity loading consists of the dead and live loads in a typical office building with service loads for the core-slab-frame structure being:

Concrete density γ_c	=	$2400\,kg/m^3$	$(150\,lb/ft^3)$
Superimposed dead load	=	$1.5\,kN/m^2$	$(30\,lb/ft^2)$
Live load at ground level	=	$4.8\,kN/m^2$	$(100\,lb/ft^2)$
Live load at a typical level	=	$2.4\,kN/m^2$	$(50\,lb/ft^2)$
Mechanical roof load	=	$3.6\,kN/m^2$	$(75\,lb/ft^2)$
Snow load	=	$2.9\,kN/m^2$	$(60\,lb/ft^2)$

The gravity loads are applied as a pressure over the surface of each slab element and as a self weight and fixed end forces (shears and moments) on the cores, the coupling and lintel beams, and the columns.

2.4 Elastic Analyses Performed

2.4.1 Analytical Study

To investigate the three-dimensional elastic response of the core-slab-frame structure subject to earthquake and gravity loads, four idealizations of the structure are derived from the complete finite element model developed in the previous section. The contribution and influence of the core sections, coupling and lintel beams, enclosed and surrounding slabs and frames are studied in terms of the interaction among the various structural components and on the structure response. Details of the four models are as follows:

1. FCS Model:

   Core-slab-frame structure.

   The most detailed idealization of the structure taking into consideration all structural elements, cores, slabs, beams and frames. This model is regarded as the "exact" analysis (reference model).

2. ESC Model:

   Enclosed slab-core-frame structure.

   Out-of-plane flexural actions of the surrounding slabs are not considered, by modeling these slabs using quadrilateral plane stress membrane elements. This results in a coupled core substructure linked to frames substructure model.

3. SSC Model:

   Surrounding slab-core-frame structure.

   Enclosed slabs, coupling and lintel beams are eliminated. This results in a linked cores substructure coupled to frames substructure model.

4. LFCS Model:

   Linked core-slab-frame structure.

   The reductions employed in the ESC and SSC models are combined. Out-of-plane flexural actions of the surrounding slabs, along with the enclosed slabs, the coupling and lintel beams are eliminated.

Unfactored service earthquake loads Q_X and Q_Y in the principal directions of the structure and dead and live loads, are applied in the elastic analyses for the following load cases:

Case 1 :	D
Case 2 :	L
Case 3 :	$D + L$
Case 4 :	Q_X
Case 5 :	Q_Y
Case 6 :	$D + Q_X$
Case 7 :	$D + Q_Y$
Case 8 :	$D + 0.7[L + Q_X]$
Case 9 :	$D + 0.7[L + Q_Y]$

The live loads are applied over the central core-slab substructure region, i.e. over the enclosed and surrounding slabs.

2.4.2 Determination of Design Forces

Design forces for the core-slab-frame structure are obtained from the FCS model results in terms of the axial and shear stresses, flexural and twisting moments per unit length in the core sections and the slabs: and the axial and shear forces, bending and twisting moments in the coupling and lintel beams, and the columns.

From the requirements of the NBCC (1985) and the CSA Standard CAN3-A23.3-M84 (1984) for the ultimate limit states criteria and the uplift loading conditions, various combinations of the dead and live loads and the Q_X and Q_Y earthquake loadings are considered:

Case 1 :	$1.25\,D$
Case 2 :	$1.25\,D + 1.5\,L$
Case 3 :	$1.25\,D + 1.5\,Q_X$
Case 4 :	$1.25\,D + 1.5\,Q_Y$
Case 5 :	$1.25\,D + 0.7[1.5\,L + 1.5\,Q_X]$
Case 6 :	$1.25\,D + 0.7[1.5\,L + 1.5\,Q_Y]$
Case 7 :	$0.85\,D + 1.5\,Q_X$
Case 8 :	$0.85\,D + 1.5\,Q_Y$

From these load combinations, the worst factored loadings are determined for seismic design of the core substructure components.

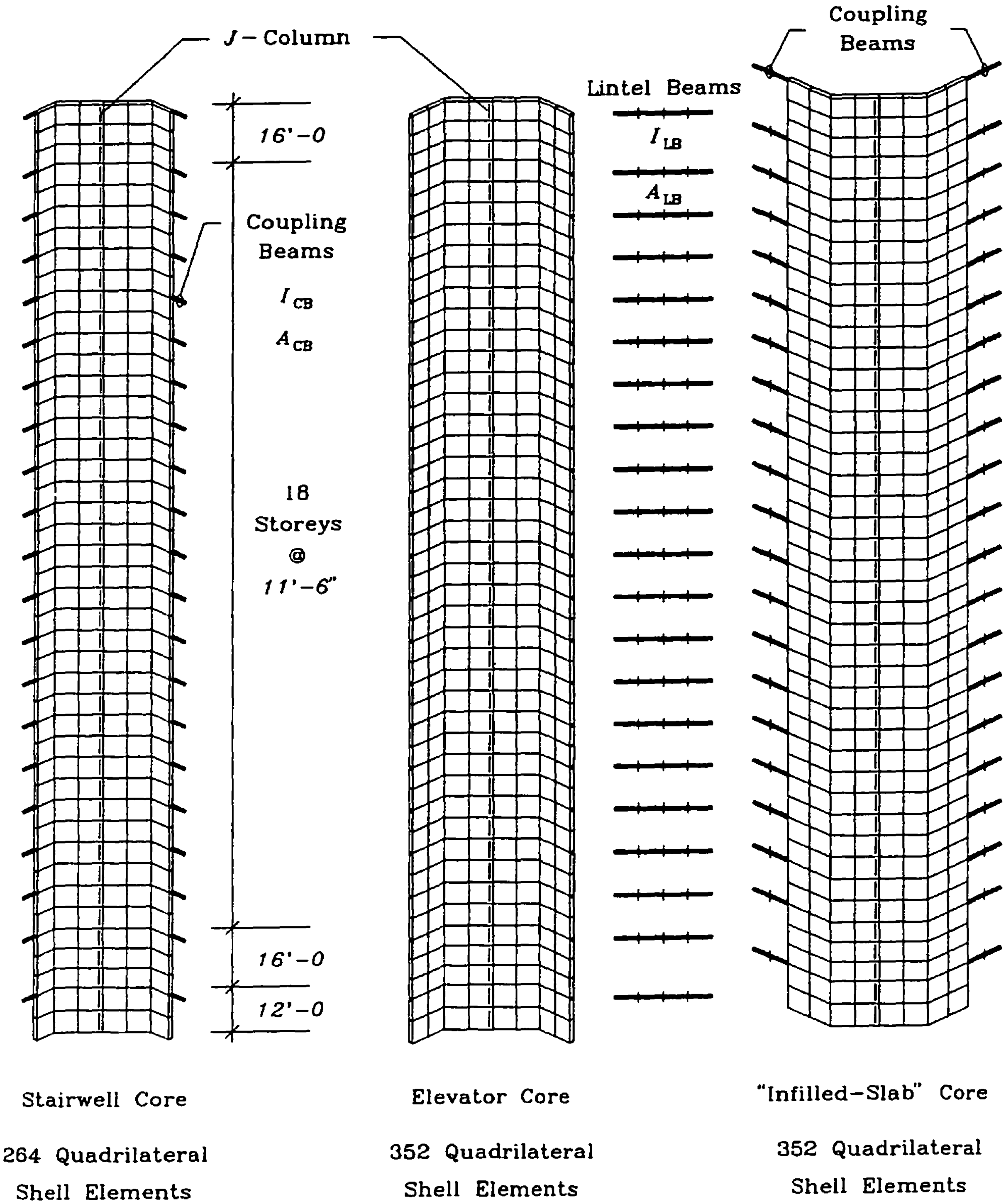

Figure 2.1 Elastic Finite Element Modeling Details of the Cores Substructure – Elevational View

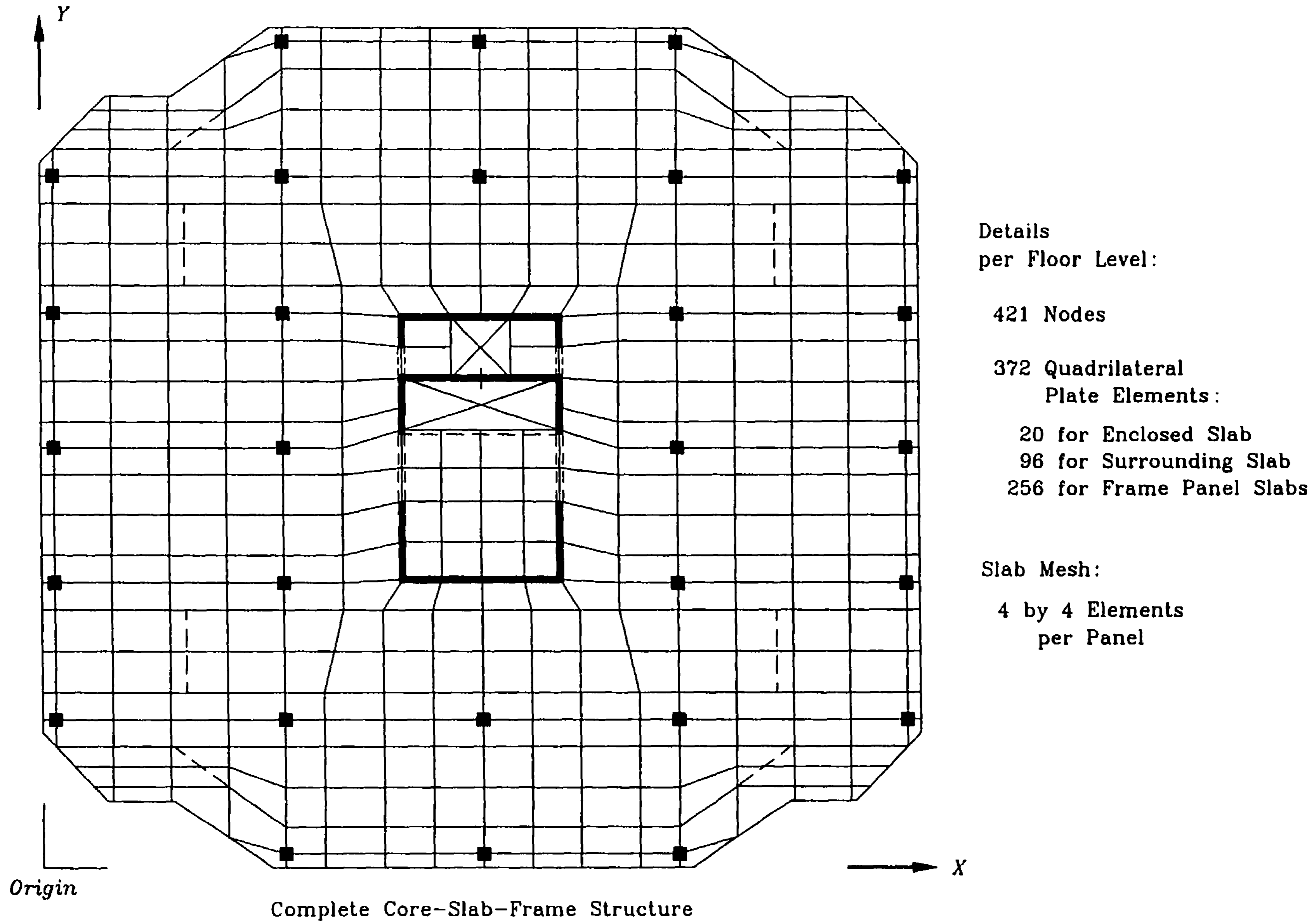

Figure 2.2 Complete Core-Slab-Frame Structure FCS Model
– Elastic Finite Element Modeling Details of the Floor Slab (Typical Level)

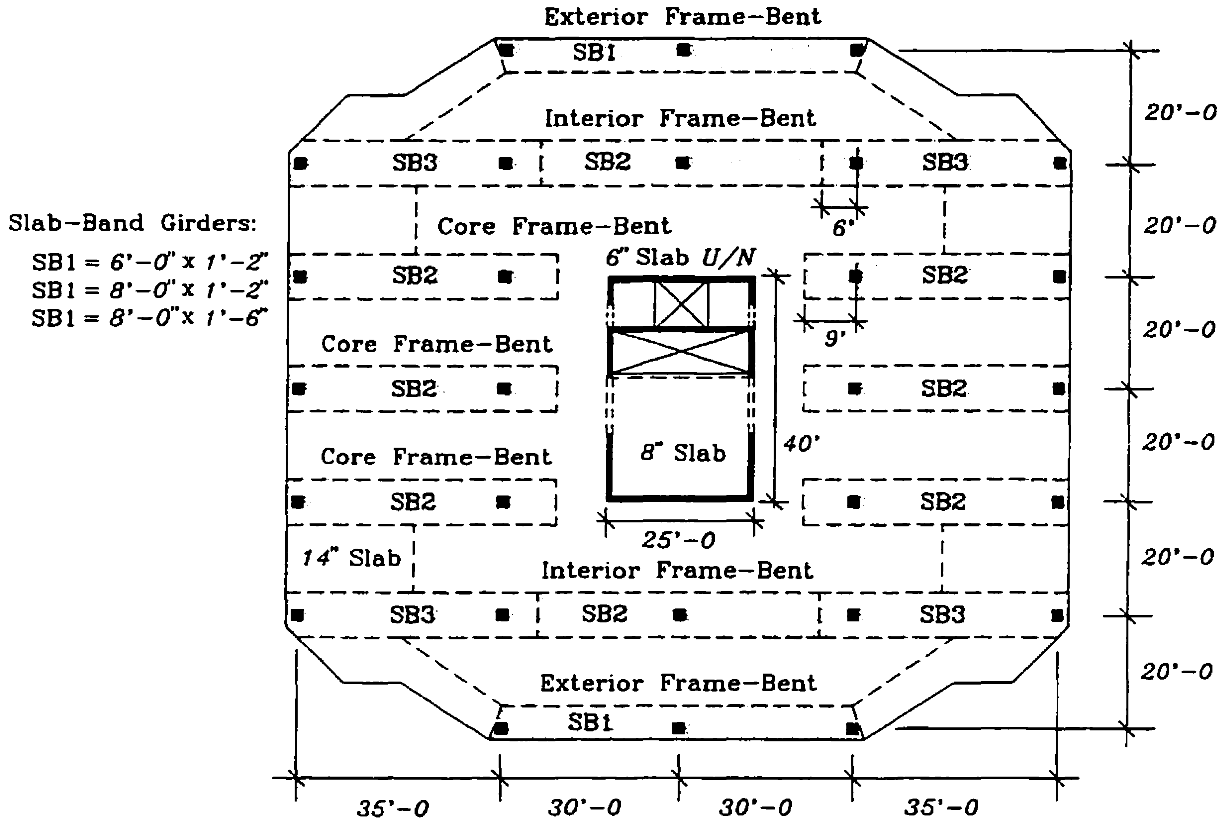

Figure 2.3 Exterior, Interior and Core Frame-Bent Details – Plan View

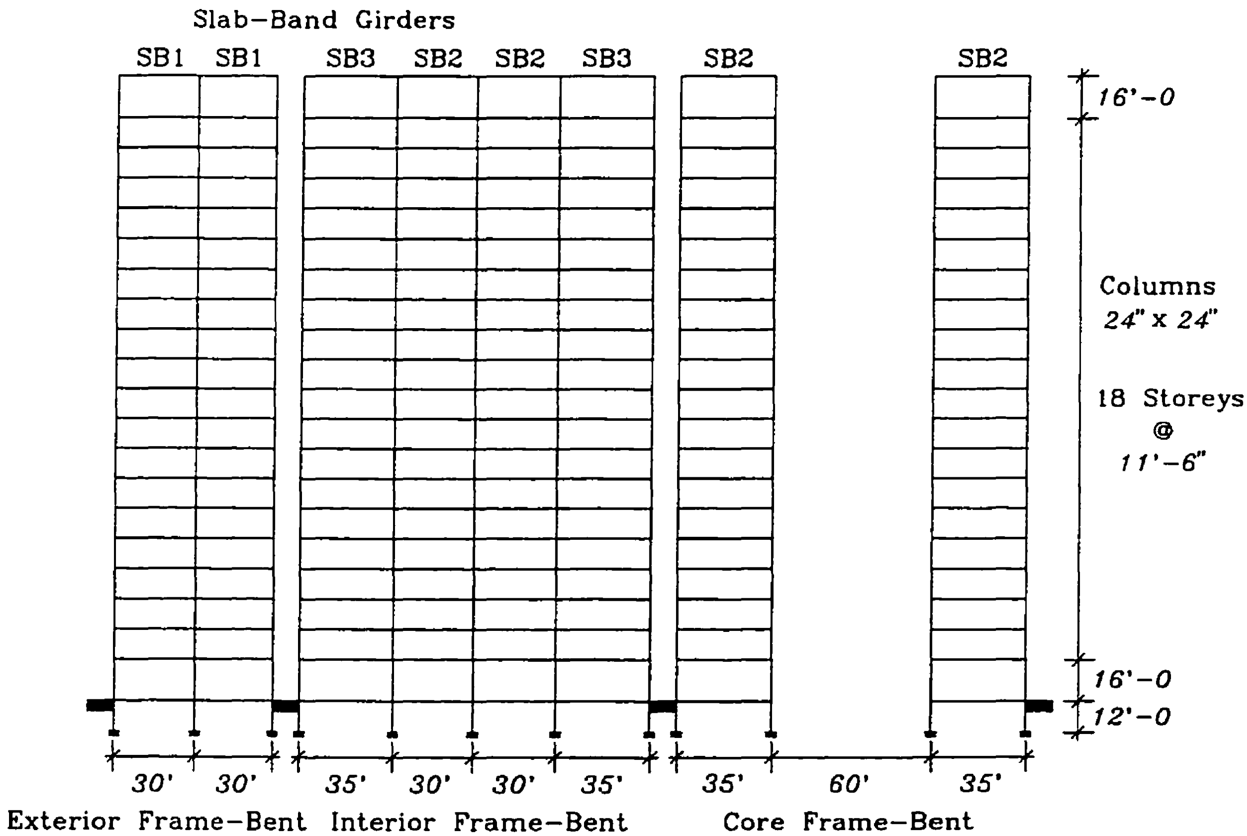

Figure 2.4 Elastic Finite Element Modeling Details of the Frame-Bents – Elevational View

Table 2.1: Concrete Constitutive Material Properties: Elastic Finite Element Analyses

Concrete Property	Theoretical Value			Range of Values	Value Used
Normal Density Concrete	γ_c	=	$2400\,kg/m^3$ $(150\,lb/ft^3)$		$2400\,kg/m^3$
Poisson's Ratio	ν	=		0.15 to 0.22	0.17
Compressive Strength	f'_c	=			$30\,MPa$
Modulus of Elasticity	E_c	=	$5000\sqrt{f'_c}$ (MPa)		$27{,}386\,MPa$
Elastic Shear Modulus	G	=	$E/2(1+\nu)$ (MPa)		$11{,}703\,MPa$

Elasticity Matrix $[C]$ – Plane Stress Condition					
Coefficients:	C_{xx}	=	$E/(1-\nu^2)$		$28{,}201\,MPa$
	C_{xy}	=	$C_{yx} = \nu C_{xx}$		$4{,}794\,MPa$
	C_{xs}	=	C_{sx}		0
	C_{yy}	=	C_{xx}		$28{,}201\,MPa$
	C_{ys}	=	C_{sy}		0
	G_{xy}	=	$E/2(1+\nu)$		$11{,}703\,MPa$

Table 2.2: Core-Slab-Frame Structure:
Geometric Properties of the Cores, Columns and Beams

Property	Infilled-Slab Core	Elevator Core	Stairwell Core
A	$4.37 \times 10^6\, mm^2$	$3.45 \times 10^6\, mm^2$	$3.07 \times 10^6\, mm^2$
I_{XX}	$38.60 \times 10^{12}\, mm^4$	$29.70 \times 10^{12}\, mm^4$	$21.20 \times 10^{12}\, mm^4$
I_{YY}	$5.57 \times 10^{12}\, mm^4$	$2.39 \times 10^{12}\, mm^4$	$4.37 \times 10^{11}\, mm^4$
J	$102.00 \times 10^9\, mm^4$	$89.40 \times 10^9\, mm^4$	$82.00 \times 10^9\, mm^4$

Property	Columns	Coupling Beams	Lintel Beams
A	$371.62 \times 10^3\, mm^2$	$278.71 \times 10^3\, mm^2$	$185.81 \times 10^3\, mm^2$
A_v	$247.74 \times 10^3\, mm^2$	$185.81 \times 10^3\, mm^2$	$123.87 \times 10^3\, mm^2$
I_c	$11.51 \times 10^9\, mm^4$	–	–
I_{vertical}	–	$19.42 \times 10^9\, mm^4$	$12.95 \times 10^9\, mm^4$
$I_{\text{horizontal}}$	–	$2.16 \times 10^9\, mm^4$	$639.33 \times 10^6\, mm^4$
I_J	$17.03 \times 10^9\, mm^4$	$6.82 \times 10^9\, mm^4$	$2.20 \times 10^9\, mm^4$

Table 2.3: Core-Slab-Frame Structure:
Elastic Finite Element Analyses
– Q_X and Q_Y Earthquake Loadings

	Applied Earthquake Loadings	
Floor Level	Q_X (N)	Q_Y (N)
20	383,054	375,470
19	320,063	313,726
18	303,311	297,305
17	286,928	281,247
16	270,541	265,184
15	254,158	249,126
14	237,406	232,705
13	221,023	216,647
12	204,636	200,584
11	187,884	184,164
10	171,501	168,105
9	155,114	152,043
8	138,366	135,627
7	121,979	119,564
6	105,596	103,505
5	88,844	87,085
4	72,462	71,027
3	56,074	54,964
2	39,327	38,548
1	22,939	22,485
V_{Base}	3,641 kN	3,569 kN

Chapter 3

Design Considerations

Stage 2 of the core-slab-frame building response studies, involves the design of the core-slab substructure with the design forces determined from the elastic analyses performed in Stage 1. Complete design details of the core-slab-frame structure under investigation can be found in the report by Manatakos and Mirza (1995). Highlights of important design considerations, comments and recommendations are presented in this thesis for brevity along with the suggested design procedures. Nonlinear inelastic analysis findings from Stage 3 of this investigation are also incorporated in evaluating and modifying the design as needed.

Design of the core sections, the coupling and lintel beams, the core wall-slab-beam junctions, end and corner regions, and the enclosed and surrounding slabs is performed following the CSA Standard CAN3-A23.3-M84 (1984) requirements of Clause 21, Special Provisions for Seismic Design where applicable. In addition, seismic design provisions from the ACI Standard ACI 318M-83 (1983) Building Code Requirements for Reinforced Concrete and the New Zealand Standard NZS3101 (1982) Code of Practice for the Design of Concrete Structures are used where needed. All references to the Code or to clauses such as Cl 21.5.3 or to notes to the clauses such as N 21.5.3 are with reference to the CSA Standard and the Commentary to the CSA Standard, unless stipulated otherwise.

In areas where building codes are not applicable and offer no provisions, reference to the work by the various researchers is made, and design procedures and reinforcement details are suggested taking into consideration the various three-dimensional actions which are present in the structure complicating the design.

3.1 Core Design

3.1.1 Dimensional Requirements

Structural cores have large height and width compared to the thickness of the web and flange walls. hence. they are thin-walled sections subject to axial. shearing. flexural. torsional and warping stresses [Vlasov (1963). Kollbrunner and Basler (1969). Zbirohowski-Koŝcia (1967)]. Nonlinear response of cores at higher load levels leads to concrete cracking. yielding of the reinforcement and formation of plastic hinges in the lower storeys resulting in degradation of stiffness of the core section. At these high load levels. large deformations in the core section can result in very large strains in the reinforcement in the post-yielding range together with large concrete compressive strains in the core walls. These actions can lead to instability of the core section in the highly stressed wall regions.

Some basic dimensional limitations (slenderness requirements) are provided by the CSA Standard for the core section wall geometry in regions where the concrete compressive strain is $\epsilon_c \geq 0.0015$ to check if the required compression zone is adequate and also for effective flange walls in providing lateral support to the core section in the compression regions of the walls Cl 21.5.3 (N 21.5.3) and Fig. N21.11.

In determining the core wall thickness in the plastic hinging regions, the effective flange widths providing lateral support and the unsupported heights of core walls. several factors influence the core section response which must be taken into consideration. These factors include the three-dimensional interaction between the flange and web walls along with the coupling and lintel beams. the enclosed and surrounding slabs. and the frame substructure as observed in the current investigation and previously by Manatakos (1989).

3.1.2 Core Wall Thickness in Plastic Hinging Regions

Except for the core flange walls in typical storeys (2 to 19) the minimum required wall thicknesses in plastic hinge regions (Cl 21.5.3) of 259 mm and 396 mm for typical and the ground storeys. are clearly not satisfied for the other parts of the core sections. The flange and web wall thicknesses are 12 in (305 mm) for all but the 10 in (254 mm) thick Elev section web wall.

CSA Standard provisions for dimensional limitations of structural walls Cl 21.5.3 give conservative values for the wall thicknesses and are not based on consideration of the "actual" complex three-dimensional behaviour of a core substructure, that behave quite differently compared with the actions of individual planar flexural core walls.

3.1.3 Effective Flange/Web Wall Widths

Lateral buckling of compression zones of core sections is critical where large compressive forces are present. The Core section has an enclosed slab within its cross-section and combined with the interaction of the coupling and lintel beams, this core behaves as a closed box-section. Elev section is stiffened by the lintel beams and the surrounding slabs, and responds as a partially closed-section. Stair section has a partial enclosed slab within the web-flange wall regions and due to the interaction with the coupling beams, it behaves as a closed-section. Hence, the entire flange wall length of each core section is considered effective in the lateral load response.

3.1.4 Effective Slab Width for Lateral Loads Analysis

An important factor not considered in the CSA Standard dimensional requirements and in determining the effective flange wall width for response to lateral loads are the effects of the slabs within and surrounding the core sections. Portions of these slabs participate along with the core walls and beams to resist the lateral load, and their influence must be taken into consideration in evaluating the structural response. Determination of these effective slab widths for lateral load analysis has been examined by Manatakos (1989) for flat slab structures composed of various shaped core sections and column support conditions. The effective slab widths are found to be influenced by the geometry and types of supports present, layout of the floor slab, adjacent panels and supports, location of the panel (interior or exterior) and the height along the building (lower, middle or upper floor levels). Further research involving analytical and experimental studies is required in this area.

3.1.5 Post-Cracking Behaviour of Cores

To ensure that a core section possesses adequate post-cracking capacity to prevent collapse, Cl 21.5.6.4.2 requires that the flexural resistance of the cracked section exceeds the flexural strength of the uncracked section; i.e. the factored design core flexural resistance must be greater than the cracked core section flexural strength for the uplift loading conditions of axial dead loads. Since the cracked second moment of area of the core section is required in this calculation, it is assumed that separation occurs between the core and slab junctions in the post-cracking range.

To calculate the cracking moment of each core section, its cracked second moment of area should be used to obtain "realistic" results. The stiffness of a core section subjected to lateral forces (earthquake loads) varies along the core height. At the base region where the majority of cracking and damage occur due to plastic hinging, the core flexural stiffness is reduced significantly. Determination of the cracked stiffness values for cores is very complex and is dependent on the core configuration, the structural elements connecting to the core section and the type and level of loading. Studies by Park and Paulay (1975) have shown that at the ultimate load, the flexural stiffness of core walls is reduced dramatically to approximately 15% to 25% of its uncracked value. Hence, this degradation and loss of stiffness must be taken into consideration in investigating the inelastic response of a core section.

The flexural strengths of the individual core sections and the coupled cores substructure are determined for three values of the second moment of area: the uncracked value $I_{\text{uncracked}}$, and 15% and 25% of $I_{\text{uncracked}}$ values all of which satisfy the requirements of Cl 21.5.6.4.2.

3.1.6 Concentrated Reinforcement Core Wall Region Requirements

CSA Standard provides no guidance for calculating the maximum area of concentrated reinforcement in a structural core wall region, i.e. in determining the corresponding cross-sectional area of the core wall to be used. One dimension is the wall thickness, however, no recommendations are provided on the wall length. Provisions of Cl 21.5.6.4 for calculating the minimum area of concentrated reinforcement in the plastic hinge regions require that $A_{s_{\min}} \geq 0.002 b_w l_w$ and define l_w as the horizontal length of the wall. Park and Paulay (1980) suggest a maximum value for the concentrated wall length of $l_w = 2b_w$. In other words, the central 80% of the wall cross-sectional area should contain uniformly distributed reinforcement, while the concentrated reinforcement regions are kept to 5% to 10% of the core wall ends (corners).

Previous findings by Manatakos (1989) and the present study for the cores substructure lateral load response indicate that an effective flange wall width participates with the web walls in the building long direction and that an effective web wall width participates with the flange walls in the building short direction. Stress distributions along the core walls at the base indicate a concentration of resistance at the wall end and corner regions, and that the interaction between the flange and web walls influence the value of l_w. An effective core wall length is observed at the wall ends and corners that participates as a concentrated area for the lateral load resistance. The Code definition of l_w should take into consideration the three-dimensional core section response and the core configuration and layout in the structure. Effective flange/web wall widths need to be considered along with the other core walls in determining the effective cross-sectional area of the core participating in the lateral load resistance.

For the core-frame-slab structure under investigation, the concentrated core wall regions are calculated for the individual web and flange walls and for the total core cross-sections, which are both checked for the existing CSA Standard requirements.

3.1.7 Confined Core Wall Regions

Analyses of the core-slab-frame structure show a coupled cores substructure box-section response in the building short direction, therefore, provisions of Cl 21.5.7, Eqn. (21-5) cannot be applied to determine the confined compression region of the core flange walls. Provisions of Cl 21.5.8.1 and N 21.5.8.1 require that a ductile coupled structural wall system shall be proportioned so that a significant amount of the overturning moment due to the earthquake loads is resisted by axial loads resulting from the vertical shear in the coupling beams. The primary seismic load energy absorbing elements should be the coupling beams and the limits on the value of the confined compression core wall region given by Cl 21.5.7 need not apply.

Results for the coupled core-slab-frame structure response to Q_X and Q_Y earthquake loadings show a uniform distribution of axial stresses along the core web and flange walls, while the linked core sections response demonstrates shear lag effects in the web and flange walls. These stress results indicate that the entire flange walls of the Stair section and a large part of the Core and Elev sections flange walls must be confined. The "actual" core-slab-frame structural response varies from the elastic range to the nonlinear range to failure. In the low load range. the cores substructure responds as a single unit coupled cores box-action showing uniform stress distributions in the core walls. At higher load levels. the effects of the concrete cracking and yielding of the reinforcement alter the cores behavior significantly and is accompanied by stiffness deterioration and plastic hinging in the lower core regions. This behaviour results in a redistribution of stresses in the core walls tending to an individual core sections response as the structure approaches the ultimate load.

Taking into consideration Cl 21.5.3 requirements for dimensional stability of structural walls. the ductility requirements of Cl 21.5.7. N21.5.7 and Fig. N21.15 to ensure post-cracking integrity of structural walls. and the resulting axial stress distributions in the core walls. the following limits are suggested for the minimum value of the wall compression zone:

$$c_{c_{\min}} \geq 3b_w \tag{3.1}$$

$$c_{c_{\min}} \geq l_w/5 \tag{3.2}$$

where l_w is the horizontal length of the core wall and b_w is the wall thickness.

In addition, the complex three-dimensional interaction involving coupling and stiffening between the core sections, beams, slabs and columns, the effective core section cross-walls providing lateral support and the interaction of the slabs and the structural cores resulting in equivalent beams or effective slab widths participating in the lateral load response [Manatakos (1989)] should be taken into consideration in determining the confined core wall regions.

3.1.8 Plastic Hinging Regions in Cores

CSA Standard Cl 21.5.2 requirement stipulates that plastic hinge regions must be considered for the analysis and design of a structural wall. Cl 21.5.2.1 requires detailing for plastic hinge regions to occur at any location in a structural wall unless a detailed rational analysis is performed. Clearly. this requirement would be too stringent for typical core/wall systems used in practice. Only for structural walls with varying geometry and stiffness throughout their height are such special design detailing needed. Cl 21.5.2.2 takes into consideration lateral load resisting systems with no abrupt changes in strength and stiffness, and locates potential plastic hinging regions in the lower half of the wall height. However, no further guidance is given. The Commentary to the CSA Standard N 21.5.2.1, N 21.5.2.2, Figures N21.9 and N21.10 suggest for uniform uncoupled walls, the plastic hinge region length equal to $l_w \geq h_w/6$ and $\leq 2l_w$ where l_w is the wall length in the earthquake loading direction and h_w is the wall height.

To accurately determine the plastic hinge regions of core-slab-frame structures. one must perform detailed nonlinear finite element analysis and carry out experimental studies. Park and Paulay (1975) have conducted several experiments on planar single walls and coupled wall systems. Their findings show that hinging occurs in the lower storeys of the walls over a height ranging from l_w to $2l_w$, where l_w is the length of the core wall in the direction of the applied earthquake loading. Also, for coupled walls, plastic hinging occurs at the coupling beam ends with the critical beam located at approximately one-third of the height from the wall base in addition to the plastic hinging at the wall base. A major part of inelastic deformations, cracking and damage in structural cores occurs in the lower storeys.

Nonlinear analysis results show considerable cracking and inelastic action in the lower 4 to 5 storeys of the core-slab-frame structure during a severe earthquake. In the building long direction along the core web walls, the cores substructure forms plastic hinges at the ground level and hinging extends over the lower storeys. In the building short direction along the core flange walls, plastic hinges form at the ground level of each core section and since the cores substructure responds as a coupled section due to the influence of the slabs and coupling beams, plastic hinges also form at the coupling beam ends. As cracking and stiffness degradation of the core sections increases due to inelastic action in the lower storeys at the higher load stages, the cores substructure response varies from a coupled cores box-action to individual core sections.

Other factors that influence plastic hinge development include three-dimensional interaction occurring among the cores, the coupling and lintel beams, and the enclosed and surrounding slabs. Problem regions such as core-slab, core-beam, beam-slab, core-beam-slab joints, core junctions, regions of load reversal and varying boundary conditions must also be examined.

3.1.9 Confined Wall Regions and Joints Within Plastic Hinging Regions

Seismic design requirements for transverse reinforcement of structural core walls need confinement of concrete and lateral support for the longitudinal reinforcement. In concentrated reinforcement regions of vertical reinforcement as defined by Cl 21.5.6 and confined compression wall regions as required by Cl 21.5.7, transverse reinforcement is needed for the confinement of these regions as equivalent columns according to Cl 21.4.4. Provisions of Cl 21.5.8.3 for coupled structural walls require that concentrated vertical reinforcement shall be provided in the core walls at the ends of the coupling beams for inelastic response. From Cl 21.5.6.5, Cl 7.6 and Cl 21.4.4.3, the transverse reinforcement shall consist of rectangular hoops and cross-ties overlapping at core wall ends and corners with the maximum spacing limitations fulfilled.

For seismic design, the concentrated reinforcement regions and the confined compression regions at the structural core wall ends, corners and junctions are considered as equivalent confined columns that must preserve their integrity at higher load levels and possess adequate post-cracking strength to ensure ductility in the plastic hinging regions. Proper confinement must be ensured to permit inelastic actions to take place at the joints and to allow development of plastic hinges at the core wall confined regions and joints. Placement of transverse reinforcement along the length of the core wall confined regions and concentrated reinforcement regions, from the face of core wall-beam joints and core wall-slab junctions is designed in accordance with Cl 21.4.4.5, Fig. N21.8 and Cl 21.4.4.6 along the full length of the plastic hinge region, i.e. the lower 4 to 5 storeys of the structure.

3.2 Coupling Beam Design

3.2.1 Ductility Requirements

Seismic response of coupled structural walls subjected to earthquake loads undergoing inelastic load reversals, demonstrate that for diagonally reinforced deep coupling beams the diagonal reinforcement resists the shear and flexural forces as equal alternating diagonal tensile and compressive forces. Studies by Park and Paulay (1975) in the case of short deep coupling beams with span-to-depth ratio of less than 1.5 to 2 have demonstrated that diagonal reinforcement results in a substantial improvement in the behaviour of coupling beams up to a limit of the span-to-depth ratio equal to 5, and also that the gravity load effects can be considered negligible compared to the earthquake load effects. For longer span coupling beams, flexural response due to gravity loads dominates and the resistance cannot be provided effectively by using diagonal reinforcement alone and conventional reinforcement must be used. They showed that providing equal amounts of tension and compression diagonal reinforcement results in the loss of the contribution of the concrete not being significant in the overall member strength, as long as the diagonal compression bars do not become unstable. Coupling beam stiffness reduces to approximately one-fifth of the uncracked stiffness due to the onset of diagonal cracking as a result of the cyclic loading.

Shiu at al (1978) demonstrated that for coupling beams with span-to-depth ratios equal to 2.5 and less than 5, diagonal reinforcement greatly improves the section ductility. They also considered a combination of conventional reinforcement throughout a coupling beam with additional diagonal bars in the plastic hinging end regions at the structural wall joints. Deterioration caused by sliding shear failure at the coupling beam ends was eliminated, however, the overall performance was not improved substantially and using such a combined reinforcement detailing is not practical.

Coupling beams undergo several load reversals due to earthquake loading and as a result lead to the complete "breaking-up" of the concrete and loss of lateral restraint provided by the concrete around the diagonal bars. To prevent buckling of the diagonal bars and to provide confinement of the enclosed diagonal reinforcement concrete core region, transverse hoops and cross-ties must be provided enclosing the diagonal bars along their entire length in the coupling beams and within the core flange walls. This hoop confinement ensures plastic hinging action permitting yielding of the diagonal bars in compression and the integrity of the structural wall and coupling beam joint regions. Near the ultimate load, the resulting shearing forces in the coupling beams must be transferred safely across the concrete compression zone into the structural walls to prevent sliding shear failure at the joint. However, the concrete will have been severely cracked due to the preceding seismic load cycles, hence, the concrete capacity to transfer shear is drastically reduced leading to the break down of the aggregate interlock mechanism.

For the core-slab-frame structure under investigation, the span-to-depth ratios for the I-E and E-S coupling beams are 3.33 and 1.33, respectively, and are within the limiting span-to-depth ratio requirements of less than 5 to qualify for diagonal reinforcement. CSA Standard seismic design provisions of Cl 21.5.8.2 require that coupling beams connecting structural walls in a coupled wall system shall be designed for the entire factored in-plane shear and flexure to be resisted by the diagonal reinforcement. According to Cl 21.5.8.2 requirements and the elastic analysis results for earthquake and gravity loads, the E-S coupling beams must be designed using diagonal reinforcement while the I-E coupling beams may be designed following conventional reinforcement requirements for ductility following Cl 21.3. However, since the coupling beams are deep beams and are an integral part of the cores substructure, they must maintain their strength and develop plastic hinges at their ends while undergoing load reversals in the inelastic load range. Also, the I-E coupling beams connect to the Elev section flange wall ends which join with the E-S coupling beams at the Elev section web-flange corners creating a combined complex system of three core flange walls connected together by two sets of coupling beams. Therefore, all of the coupling beams are designed using diagonal reinforcement for seismic ductility requirements.

It is noted that the CSA Standard seismic requirements Cl 21 provide no specific detailed guideline for the design of deep coupling beams other than the requirement for diagonal reinforcement confined by hoops or spirals in Cl 21.5.8. For this reason, the design procedures suggested by Park and Paulay (1975) and the requirements of the New Zealand Standard are also incorporated in the coupling beams design.

3.2.2 Diagonal Reinforcement Limitations

No limitations on the amount of diagonal reinforcement for coupling beams design in terms of minimum and maximum reinforcement are given in the CSA Standard Cl 21 seismic design provisions. In the higher load range, plastic hinging due to the seismic inelastic action occurs thereby, reducing the coupling beam stiffness. Gravity loads are always present before and after plastic hinging occurs resulting in a flexural response in the coupling beams. Hence, there should be limits stipulated on the amount of diagonal reinforcement for minimum strength and for ductility requirements. Such limits should take into consideration the design of the coupling beam-core wall joints which are heavily congested with reinforcing bars.

CSA Standard seismic design restrictions on minimum and maximum longitudinal reinforcement include Cl 21.4.3.1, N 21.4.3.1 and Cl 21.3.2.1 requirements for design of ductile columns and beams. These reinforcement limitations take into consideration the effects of inelastic deformations, provide for post-cracking strength and ductility, and help to reduce excessive joint stressing and reinforcement congestion. The primary action of diagonal reinforcement is to resist the combined earthquake and gravity load forces (shear and flexure) by diagonal tension-compression resultants due to the short-deep coupling beam behaviour. Hence, since the diagonal reinforcement acts as a column subjected to equal alternating tension and compression forces, this results in one-half of the coupling beam cross-section experiencing compression and the other half in tension when the diagonal load resistance is generated. Therefore, based on the above considerations, one-half of the cross-sectional area Cl 21.4.3.1 requirements are used. Suggested diagonal reinforcement requirements in coupling beams are:

1. Minimum area of diagonal reinforcement:

$$A_{s_{\text{min diag}}} \geq 0.01 \left(\frac{A_g}{2}\right) \tag{3.3}$$

2. Maximum area of diagonal reinforcement:

$$A_{s_{\text{max diag}}} \leq 0.06 \left(\frac{A_g}{2}\right) \tag{3.4}$$

3.2.3 Development of Diagonal Reinforcement

Experimental studies by Park and Paulay (1975) and Shiu et al (1978) have demonstrated that for improved response of coupling beams with span-to-width ratios of 2.5 to 5, the diagonal reinforcement must extend into the structural walls using a straight development length for plastic hinging permitting inelastic load reversals. Developing the reinforcement with a 45° bend starting at the core wall is not practical and creates localized problems at the bend regions in the walls. The entire development length of the diagonal reinforcement must be confined by hoops and the confined concrete core region in the coupling beams should be as large as possible. Some provisions for the design of coupling beams are given in the New Zealand Standard. It is noted that the CSA Standard does not offer any special guidance or direct requirements for the development of diagonal reinforcement in coupling beams.

3.2.4 Secondary Cage Reinforcement

Additional light secondary cage hoop reinforcement consisting of transverse hoops and longitudinal bars must be provided throughout the coupling beam to hold the broken concrete pieces together and to maintain the structural integrity of the member subjected to inelastic load reversals. The confined concrete provides lateral flexural rigidity and does not contribute significantly to the overall coupling beam strength and stiffness. CSA Standard seismic ductility requirements of Cl 21.5.8 give no design provisions for cage reinforcement in diagonally reinforced coupling beams. Studies by Park and Paulay (1975) on coupled structural walls with diagonally reinforced coupling beams have found that a light cage reinforcement is satisfactory to confine the concrete. They suggest using #3 hoops at $150\,mm$ ($6\,in$) spacings. Note that a #3 bar has a diameter $d_b = 9.5mm$ and cross-sectional area $A_b = 71mm^2$.

3.2.5 Torsion Reinforcement Requirements

Elastic analysis results show that the torsional moments in the coupling beams due to earthquake and gravity loads are significant and must be considered in design requiring additional transverse reinforcement. No special provisions exist for ductile design of reinforced concrete members subject to torsion due to seismic loading in the CSA Standard Cl 21. Provisions given in the simplified method for torsion design Cl 11.3.7 are applied for the coupling beam design.

3.3 Lintel Beam Design

The lintel beams of the core-slab-frame structure under investigation do not satisfy the dimensional requirements of Cl 21.3.1 (c) and (d) for the cross-section width and width-to-span ratio to qualify as ductile lateral load resisting elements. According to the CSA Standard, the lintel beams must be designed following the requirements of Cl 21.8 for frame members and shall not be considered part of the lateral force resisting system. Provisions of Cl 21.8 and N 21.8 are intended to ensure that gravity load resisting members of a structure will maintain their strength and integrity when subjected to earthquake loading. Therefore, a minimum level of ductility and proper reinforcement detailing must be provided in the design so that adequate rotational capacity is ensured for the plastic hinges development in the lintel beams acting together with the lateral load resisting elements. N 21.8.2 suggests that following Cl 21.3.2 requirements for the flexural reinforcement design and Cl 21.3.3 requirements for the transverse reinforcement design, would ensure adequate rotational capacity of the member under consideration. In effect, the CSA Standard is allowing design of members that are not considered to be part of the lateral load resisting system, following the provisions of Cl 21.3 for seismic design of ductile frame members even if the members do not satisfy the dimensional requirements of Cl 21.3.1.

Analysis results of the core-slab-frame structure show that the lintel beam forces due to earthquake loads are as significant as those due to the gravity loads. In addition, the lintel beams frame into the Elev section confined flange wall ends which also join with the coupling beams, thus, converting Elev into a partially closed-section. This resulting interaction causes the lintel beams to participate in the lateral load resistance becoming an integral part of the structure. Provisions of Cl 21.2.2.1 state that linear and nonlinear behaviour and interaction of all structural and non-structural members shall be considered in the analysis for seismic design. Dimensional requirements of Cl 21.3.1 do not take into consideration the three-dimensional behaviour of reinforced concrete structures. Therefore, the lintel beams must be designed as ductile members following the CSA Standard seismic design provisions in Cl 21.3 and Cl 21.8 for earthquake loading, and the beams should possess adequate ductility to undergo inelastic deformations and load reversals.

Another factor influencing the lintel beam seismic response is that the lintel beams have a slab present on one side converting them into equivalent one-half T-beams (L-beams) across the Elev section, with a portion of the enclosed slabs in the Core section participating in the lateral load resistance. Determination of the equivalent slab widths participating in lateral load resistance have been investigated by Manatakos (1989).

It is noted that no special provisions exist for ductile design of reinforced concrete members subjected to torsion due to seismic loading in the CSA Standard Cl 21, thus, the simplified method for torsion design Cl 11.3.7 are applied for the lintel beam design.

3.4 Core Wall–Beam Joint Ductility Requirements

3.4.1 Ductility Considerations

Several types of joints are present in core-slab-frame structures including: beam-column, structural wall-coupling/lintel beam, core wall-slab, confined core wall end region-coupling/lintel beam, and combination core wall-beam-slab ends, corners and junctions. All such joints must be designed and detailed properly for ductility and structural integrity (Cl 21.6) for inelastic seismic response and adequate deformations to obtain a desirable hinging pattern and failure mechanism to achieve a "strong structural wall/column-weak beam" design philosophy (Cl 21). To attain the complete failure mechanism of a core-slab-frame structure involving beam-slab hinging sidesway mechanism, yielding and plastic hinging will develop at the base and the lower regions of the columns and the core walls at the ultimate load requiring the lower storeys to be designed for ductility with stringent transverse hoop confinement requirements over the entire hinging region (Cl 21.4 and Cl 21.5).

In the seismic design of core-slab-frame structures, ductility requirements and inelastic actions of all of the individual structural components must be taken into consideration. In addition, the failure mechanism of the structure should be investigated as a whole and not for the individual parts as planar substructures. Building code requirements for seismic design fall short of taking into consideration the "realistic" behaviour of the complete building structure and the engineer must call upon other resources for guidance in analysis and design.

In the analysis and design of the core substructure under investigation, there are two different types of core wall-beam joints present as discussed below.

Coupling beams are present connecting the Core, Elev and Stair sections flange walls. First type of joints are the coupling beam-core flange wall joints which consist of diagonally reinforced deep coupling beams framing into the core confined flange wall ends and web-flange corners. The inelastic behaviour of these joints is considerably different from a typical conventionally reinforced beam-column joint (Cl 21.4.2). No specific ductility design provisions exist in the CSA Standard for such joints, excepting for the requirement that the factored resistance of the structural core walls are greater than the nominal resistance of the coupling beams for formation of plastic hinges in the coupling beams (Cl 21.5.8). Following the design procedures for coupled structural walls with diagonally reinforced coupling beams, joint design and ductility for proper hinging mechanism have been considered in the design of these joints.

Lintel beams span across the Elev section opening and join to the flange wall ends. Second type of joints are the Elev section confined flange wall end-lintel beam joints, with the lintel beams being conventionally reinforced (Cl 21.3). However, this is a deep joint due to the lintel beams having a depth equal to one-third of the storey height, thus, the behaviour is different from the ductility conditions for beam-column joints given by Cl 21.4.2.2 and Cl 21.6. As observed from the analysis results, a three-dimensional partially closed-section Elev flange wall confined column region-lintel beam-slab behaviour occurs with complex interaction developing between the structural members. In the higher nonlinear load range, this response is difficult to be taken into consideration in the design and requires further study.

3.4.2 "Strong Core Wall-Weak Coupling Beam" Ductility Requirements

Coupled structural wall systems subjected to earthquake loads are designed following the ductility requirements of Cl 21.5.8 to achieve a desirable failure mechanism in which yielding occurs and plastic hinges form at the coupling beam ends prior to their formation in the structural walls. The coupling beams are capable of undergoing large inelastic displacements and they can absorb and dissipate energy without collapse of the structure. A "strong structural wall-weak coupling beam" design philosophy (Cl 21.5.8.4) is required with the preferred use of diagonal reinforcement in coupling beams to resist shear and flexural forces (Cl 21.5.8). To attain the complete sidesway failure mechanism of a coupled wall structure, yielding and plastic hinging will develop at the base of the structural walls requiring the lower storeys of the walls to be designed for ductility with stringent transverse hoop confinement requirements over their entire height as for columns (Cl 21.4).

The cores substructure under investigation is a coupled core system with complex three-dimensional interaction among the various structural components as demonstrated in the current analyses and earlier by Manatakos (1989). Cl N 21.5.8.4 is intended for planar coupled structural wall systems with one wall in tension and the other wall in compression. Here, due to the interaction between the cores the coupling and lintel beams, and the enclosed and surrounding slabs, a complex three-dimensional cores substructure box-section response is observed which is very different from that in Cl 21.5.8.4. Seismic ductility provisions of Cl 21.5 for the structural cores design have been satisfied for plastic hinging to develop at the core wall base after plastic hinges form in the coupling beams.

3.4.3 "Strong Elevator Core Flange Wall-Weak Lintel Beam" Ductility Requirements

At the Elev section flange wall-lintel beam joint, analysis results show that there are shear forces and flexural moments introduced in the lintel beams as a result of the vertical movement of the Elev section flange walls subjected to earthquake loading.

To ensure that plastic hinging occurs in the lintel beams and not in the Elev section flange walls for a desired ductile failure mechanism, the "strong core flange wall-weak lintel beam" seismic design approach requirements of Cl 21.4.2.2 and Eqn. 21-1 are followed. The factored resistance of the structural core walls shall be greater than the nominal resistance of the lintel beams at a joint. One difficulty in applying Cl 21.4.2.2 requirements in this situation is that the entire Elev section flange wall participates in flexure with the lintel beam ends. Further research is required to study the local effects and variations which occur at the confined column Elev section flange wall end region-lintel beam joints.

Finite element analysis results also demonstrate that a three-dimensional partially closed-section Elev core response develops with the lintel beams along with a portion of the enclosed and surrounding slabs participating in the lateral load resistance.

3.4.4 Transverse Reinforcement in the Elevator Core Flange Wall Confined Column End Region

Proper confinement of concrete within a joint core region must be provided to permit transfer of shear forces through the joint and to ensure structural integrity of the joint. Confinement of the joint is in the form of cage reinforcement consisting of transverse hoops and cross-ties (Cl 21.6.2, N 21.6.2) surrounding the longitudinal column (confined core wall region) reinforcement uniformly distributed along the joint faces (Cl 21.6.3, N 21.6.3). Detailing of the confinement reinforcement in a joint is essential for ductility to permit inelastic deformations and plastic hinging in the joint beam-slab members without a sliding shear failure occurring (Cl 21.6.4, N 21.6.4). The Elev section flange wall lintel-beam joints must be checked for the shear forces in the confined core wall region due to the moments in the lintel beams (Cl 21.6).

For the Elev section flange wall, one can argue that only the confined column flange wall end region should be considered as being effective in acting with the lintel beams. This approach is conservative but it is not realistic as compared to the actual three-dimensional partially closed-section Elev response observed. Another approach is to determine an effective flange wall width participating with the lintel beams in the lateral load response. One important factor not considered in determining the effective core flange wall width are the effects of the slabs within and surrounding the core sections resulting in an effective slab width participating with the core walls and beams in the lateral load resistance. Manatakos (1989) noted that the effective core wall widths in lateral load resistance are influenced by the effective slab widths. Further analytical and experimental research is required in this area.

For the Elev section under investigation, three different effective flange wall widths (effective cross-sections) participating with the lintel beams response are examined: the confined column Elev section flange wall end region, 50% effective Elev section flange wall width, and the entire Elev section flange wall width. Thus, ductility requirements of Cl 21.4.2.2 are satisfied for the Elev section flange wall-lintel beam joint taking into consideration the entire flange wall as being effective and properly confined. It is noted that considering only the confined Elev section flange wall end region would not satisfy the ductility requirements of Cl 21.4.2.2.

3.5 Slab Design

3.5.1 Ductility Requirements

No provisions or guidelines exist in the CSA Standard Cl 21 for seismic design of ductile two-way slabs subject to both gravity and earthquake loads. A note to Cl 21.9.1 states that:

> "Requirements for the qualification of two-way floor systems without beams are not given. The ability of such structures to sustain their resistance to lateral loads when subjected to deformation reversals in the inelastic range has yet to be established."

Design provisions of Cl 13 for two-way slab systems require that flexural reinforcement shall be provided in each (orthogonal) direction in the slab as determined by analysis (Cl 13.4.1). Finite element analyses give slab bending moments m_{xx} and m_{yy} in orthogonal directions and the corresponding twisting moments m_{yx} and m_{xy}, respectively. The Commentary to the CSA Standard N 13.4.1 suggests that the slab design moments in orthogonal X- and Y-directions can be determined conservatively as the addition of the absolute values of the corresponding flexural and twisting moments as:

$$|m_{xx}| + |m_{yx}| \quad \text{and} \quad |m_{yy}| + |m_{xy}| \tag{3.5}$$

In the ACI Standard, special provisions are given for the seismic design of two-way slabs without beams in Appendix A.9.6 based on ductility considerations, nonlinear behaviour and the yield line theory. These requirements relate to the detailing and placement of the flexural reinforcement for moment reversals, redistribution of negative and positive slab moments, structural integrity at slab supports, and effective slab band widths in column strips.

In the present investigation and earlier work by Manatakos (1989) on the core-slab-frame structure subjected to earthquake and gravity loads, the results show complex three-dimensional interaction between the cores, coupling and lintel beams, slabs and frames. As a result, the enclosed and surrounding slabs transfer not only in-plane forces but also out-of-plane flexural forces between the cores and frames substructures. The resulting distribution of the slab moments demonstrate that the slabs are subjected to flexural and twisting moments, experiencing load and moment reversals. The twisting moments in a two-way slab can be as significant as the flexural moments in regions of slab-core wall corner and end supports.

Critical slab regions are observed at the slab-structural core wall ends, corners and junctions, and the lintel and coupling beam connections. Large negative moment concentrations are present indicating that a large reinforcement content is required in these areas and that uniformly distributed reinforcement may not ensure serviceability of the slab near the supports. To ensure that yielding of the reinforcement does not occur at the service loads, the reinforcement layout should follow the elastic moment distribution in the slabs. However, ductility of slabs at the higher inelastic load range must be ensured, thus, limiting the amount of uniformly distributed reinforcement provided in the critical slab regions. If large differences exist between the actual moment resistance of the slab compared with the required design moments, cracking at the service load level will be excessive because of the low steel content at the highly stressed slab sections which may lead to large values of steel stresses and large crack widths. How far the actual slab reinforcement arrangement can differ from the elastic moment distribution and still result in a serviceable slab, has not been conclusively determined. Elastic analyses of two-way slabs in core-slab-frame structures subjected to earthquake and gravity loads are not representative of the "realistic" behaviour of the structure during a severe earthquake. At low load levels, before cracking of the slab occurs, the distribution of moments and forces is in accordance with the elastic theory. At the higher load stages near the ultimate load, the distribution of inelastic slab moments depends on the flexural strength, the slab support conditions and the type of loading. The CSA Standard permits an elastic redistribution of 20% for the negative moments in Cl 8.4. A reduced flexural rigidity equal to $0.6E_cI_g$ for two-way slabs is suggested in Cl N8.6.1. Cl N10.11.7 suggests a reduced flexural rigidity value based on the state of the structure just prior to reaching the ultimate load, equal to $0.5E_cI_g$ for columns, beams, structural walls and $0.33E_cI_g$ for flat plates. It is noted that these suggested values for the flexural rigidity are based on the uncracked values of the second moments of cross-sectional area for the slab.

Due to the nonlinear post-cracking behaviour of two-way slabs, a significant redistribution of moments occurs at the critical slab regions. Park and Paulay (1975) have found that due to nonlinear response at higher load levels near the ultimate load, a considerable loss of stiffness is observed in structural cores/walls to values as low as 25% of the uncracked stiffness at the base region where plastic hinging occurs. This loss of stiffness also occurs in the slabs at the critical slab-core wall regions and must be taken into consideration in analysis and design at the higher load levels to ensure ductility and structural integrity of the slab. The "actual" flexural rigidity (EI) of a reinforced concrete two-way slab at the higher nonlinear load range is difficult to determine due to the low reinforcement ratio typically used in design and should be representative of the degree of cracking and the load level.

CSA Standard seismic design provisions are based on conditions of a concrete section subjected to uniaxial compression for typical members with a compressive concrete strain at failure of $\epsilon_c \geq 0.003$. Two-way slabs in a core-frame-slab structure respond in a complex three-dimensional manner with axial, flexure, twisting and membrane actions present. At the critical slab-structural wall corner and end regions where the slab moments peak to very large values (stress concentrations are present) the concrete sections at these joints experience biaxial and triaxial conditions in compression and tension, and confinement due to the joint configuration of slab-core wall corner, end, junction and beams present which are not considered directly in analysis and design. Thus, a value for the ultimate concrete compressive strain of $\epsilon_c = 0.004$ to 0.0045 may be more realistic. Other effects influencing the strength and ductility of two-way slab structures typically not taken into consideration in design include: strain hardening of the reinforcement, the presence of compression steel, and the provision of transverse hoop confinement around the longitudinal reinforcement in the critical slab regions over effective slab band widths and plastic hinge lengths for lateral load resistance. Membrane action in two-way slabs, compression and tension from the slab supporting members, can increase the ultimate load capacity and ductility significantly. Tests by Ockleston (1958) and Liebenberg (1963) have demonstrated that slabs possess considerable ductility and strength, provided that a logical reinforcement layout is used to ensure that the serviceability requirements are fulfilled. They found that lateral restraint provided by stiff surrounding beams and slab panels can increase the ultimate load to values between 2 to 3 times that predicted by yield line theory.

3.5.2 Maximum Spacing of Flexural Reinforcement for Seismic Design of Two-Way Slabs

Structural integrity of two-way slabs must be maintained in the post-cracking inelastic load range in the vicinity of the slab supports and critical regions along the slab-structural core wall-beam ends, corners and junctions due to the development of plastic hinges and possible load reversals. CSA Standard requirements for longitudinal reinforcement in slabs given by Cl 13.4.2, Cl 7.8.2, N 7.8.2 and Fig. N7.5 for cracking control, limit the maximum bar spacings in slabs at the critical sections to:

$$s_{\text{max}} \leq 2h_{\text{slab}} \leq 200\,mm \tag{3.6}$$

For seismic design of ductile structural walls, the requirements of Cl 21.5.5.1 sets maximum spacing limits of uniformly distributed longitudinal and transverse reinforcement within and outside plastic hinge regions. Since two-way slabs are subjected to similar bending and twisting moments as structural walls and both are thin-walled plate/shell members, and plastic hinging will occur in the slabs due to load reversals, the maximum spacing of slab reinforcement should be limited to provide for structural integrity of the slab. Spacing requirements for longitudinal reinforcement in structural walls (Cl 21.5.5.1) are applied to the seismic design of two-way slabs.

[i] Within plastic hinging regions: $s_{\text{max}} \leq 300\,mm$

[ii] Outside plastic hinging regions: $s_{\text{max}} \leq 450\,mm$

3.5.3 Maximum Flexural Reinforcement for Ductility Requirements of Two-Way Slabs

Ductility is crucial in seismic design of two-way slabs and generally a significant moment re-distribution is assumed to take place safely in the slab at the higher inelastic load range. To satisfy ductility requirements for two-way slabs based on the distribution of slab moments, serviceability requirements, building code design provisions and the yield line theory, Park and Gamble (1980) and the European Concrete Committee [CEB] (1978) the following ratios of the average negative to average positive ultimate slab moments are suggested:

$$m^{-\text{ive}}_{\text{ult}_x} \leq 1.5 \text{ to } 2.0\, m^{+\text{ive}}_{\text{ult}_x} \tag{3.7}$$

$$m^{-\text{ive}}_{\text{ult}_y} \leq 1.5 \text{ to } 2.0\, m^{+\text{ive}}_{\text{ult}_y} \tag{3.8}$$

$$m^{+}_{\text{ult}_x} \leq 1.0 \text{ to } 1.5\, m^{+}_{\text{ult}_y} \tag{3.9}$$

In the vicinity of slab supports, columns and structural core walls ends, corners and junctions, uniformly distributed reinforcement is not acceptable due to the large negative slab moments. Thus, more heavily concentrated longitudinal reinforcement is needed to follow the elastic moment distribution in these critical slab regions. Park and Gamble (1980) relating experiments on slabs developing collapse mechanisms to the CEB-FIB Model Code (1972) requirements and the ACI Standard (CSA Standard) design factors, and based on the yield line theory, suggest that a maximum tension reinforcement ratio should be maintained throughout the slab to ensure adequate ductility :

$$\rho_{\text{max}} < 0.4\,\rho_{\text{bal}} \tag{3.10}$$

with an upper limit at critical slab sections equal to $0.6\,\rho_{\text{bal}}$.

3.5.4 Reinforcement in Slab-Core Wall Corner and End Regions

Elastic moment distributions in the slabs demonstrate large bending and twisting moment concentrations and reversals at the critical slab-core-beam regions, thus, requiring special slab reinforcement not only at the structural core wall ends and corners, but also along the slab-core wall junctions. The total required reinforcement in the critical slab regions is quite large and would result in over-designed highly brittle slab sections which are not appropriate for the seismic design and ductility requirements.

Top and bottom steel should be provided in two-way slab corner regions to restrain the corner from lifting off the supports, to control cracking and to develop negative corner slab moment resistance. Wood and Jones (1967) have shown that corner effects in slabs cause yield lines that tend to fork with fanning cracks in the slab corners due to the absence of top steel, and reduce the ultimate slab resistance by about 10% to 12%. Park and Gamble (1979) suggest that the amount of top corner slab reinforcement provided is dependent on the edge support conditions ranging from 0.33 to 0.50 of $m_{ult}^{+\text{ive}}$ in the slab at simply supported edges and $m_{ult}^{+\text{ive}}$ in the slab at restrained edges. CSA Standard Cl 13.4.6 provisions require special corner reinforcement in slabs equal to the maximum positive slab moment for cracking control to extend a distance equal to 0.2 of the longer span in both directions measured from the slab edges.

Nonlinear response at the higher load stages due to seismic loads result in a considerable reduction of the slab stiffness (and in structural walls) at critical slab-core wall joints and regions causing a corresponding redistribution of the moments. The actual amount of moment redistribution in two-way slabs can vary greatly from 20% to 30% and it can be as high as 40% as observed by Park and Gamble (1979) depending on the slab configuration and reinforcement details provided. Therefore, special longitudinal reinforcement must be provided in the enclosed and surrounding slabs in two mats in orthogonal directions with a maximum steel content of 0.6 to 0.75 ρ_{bal} to confine the concrete and to provide structural integrity at the slab-core wall flange wall end and flange-web corner regions over a distance of at least one-fifth of the span in each direction or 3 to 5 b_w (the core wall thickness).

3.5.5 Serviceability Requirements for Two-Way Slabs

Serviceability requirements of two-way slabs must be checked to ensure that the slab deformations and stresses (strains) in the reinforcement are not excessive at the service load level. Presently, no CSA Standard (ACI Standard) design provisions or recommendations exist for deflection and crack control of two-way slabs at the serviceability limit state. In absence of such design guidelines, Park and Gamble (1980) suggest using the empirical Gergely-Lutz expression (CSA Standard Cl 10.6.4 crack control parameter) in terms of the steel stresses of beams and one-way slabs.

To control cracking in two-way slabs, more closely spaced fine cracks are preferred as compared with fewer wider cracks. Therefore, smaller diameter bars at close spacings should preferably be used and for uniformly distributed slab reinforcement limit the reinforcement spacings at the critical slab sections as required by Cl 13.4.2 for skin reinforcement Cl 7.8, N 7.8.2, Cl 10.6.7 and Fig. N7.5 in plastic hinging regions to $s_{\text{max}} \leq 2h_{\text{slab}} \leq 200\,mm$.

3.5.6 Ductility of Slab-Structural Wall/Column Connections

Two-way slabs are subjected to repeated load reversals and moments which lead to a degradation of the shear strength at the slab-support connections and a possible shear failure must be avoided. Slab-core/column supports must possess sufficient ductility to absorb and dissipate energy by inelastic deformations without collapse. Ideally for two-way slabs without shear reinforcement, the slab-support connection should contain sufficient continuous longitudinal reinforcement providing some post failure resistance to hold the connection together after punching shear failure of the slab occurs and to prevent the slab from slipping down the column or core wall support. Bottom longitudinal reinforcement is more effective than the top steel due to the concrete slab cover spalling off at higher load levels [Park and Gamble (1980)]. This reinforcement acts as a suspension mechanism stopping slab movement and permitting redistribution of the load to the other parts of the slab.

Studies by Criswell (1980) of two-way slab reinforcement behaviour in providing post punching resistance of slab connections have shown that closed stirrup-ties or hoops around the main longitudinal bars greatly improve the slab-column response. Carpenter, Kaar and Corley (1973), and Islam and Park (1976) have demonstrated that provision of stirrups-ties in a slab result in a substantial increase in the ductility of the slab connection. Hoops or closed stirrup-ties around the slab reinforcement in the critical slab-support regions, over an effective slab band width, provide confinement of the longitudinal reinforcement (top and bottom) and provide flexural and torsional shear resistance at large inelastic deformations in the slab.

Structural integrity and ductility of the critical slab-structural core wall regions must be ensured in the inelastic response to failure permitting large deformations, moment redistribution and formation of plastic hinging without a punching shear failure. Therefore, in the seismic ductile design of two-way slabs, closed transverse hoops should be provided around the longitudinal reinforcement for confinement at the critical slab-core wall connections.

3.5.7 Hoop Confinement of Longitudinal Reinforcement in Slabs

Seismic design provisions of the CSA Standard require transverse hoops and cross-tie reinforcement for shear, stability, confinement of concrete, restraint of longitudinal reinforcement within confined member regions and plastic hinging regions by Cl 21.3.3.4, Cl 21.7.3.3 and Cl 21.5.7 in ductile flexural members. Spacing requirements and limitations for the hoops and cross-ties are given for: ductile frame members Cl 21.4.4.4, N 21.4.4.4, Fig. N21.7; confined regions of structural walls Cl 21.5.7, Cl 21.4.4.3, Cl 7.6.5.2; concentrated reinforcement regions of structural walls Cl 21.5.6.5; diagonal reinforcement in coupling beams Cl 21.5.8.2; with the most stringent spacing of $d/4$ to $d/2$. Plastic hinging regions for confined regions and joints in structural walls Cl 21.4.4.5, Fig. N21.8, and in flexural members (beams and columns) Cl 21.3.3.2, Cl 21.3.3.3 and N 21.3.3, must have transverse hoops provided over a minimum specified distance from the joint equal to $l_o \geq 2d$ of the member effective depth, or $\geq \frac{1}{6}^{th}$ of the clear span or $450\,mm$.

Carpenter, Kaar and Hanson (1970) studied provisions for shear in seismic design of two-way slabs and recommended that for improved ductility at the ultimate load, hoops or stirrup-ties confining the slab longitudinal reinforcement should be provided in a slab at a maximum spacing of $s_{\text{max}} = d/2$, one-half of the effective slab depth. A longitudinal reinforcing bar must be present in each corner of the hoops or stirrup-ties, and the hoops must be properly anchored at each bar to develop the tensile yield strength, as recommended by Park and Gamble (1980). Experimental studies by Lim (1989) on ductility of coupled slab-structural wall structures subjected to reversing displacements, simulating earthquake loadings, demonstrated that the maximum spacing of hoop confinement of slab longitudinal reinforcement should be limited to $d/2$ to $2d/3$ of the effective slab depth. The cracked effective slab width participating in the lateral load resistance ranged from 0.18 to 0.24 of the corridor distance between the coupled structural walls. He also found that the stiffness of the coupled slab-structural wall systems reinforced with stirrups in the slab, is reduced to values between 0.30 to 0.10 of the initial uncracked stiffness when subjected to light to heavy earthquake loadings.

A problem encountered in selecting and detailing the arrangement of the hoops in two-way slabs, is in determining the "cracked" effective slab width due to earthquake loads developed with the structural core wall section at the critical slab-core wall end and flange-web corner regions. Transverse hoop reinforcement must be provided in the slab at the critical slab-core wall connections across the entire cracked effective slab width to provide confinement of the longitudinal reinforcement for large forces and moments, and load reversals in the critical slab sections. Clearly, hoops in critical slab regions should be provided over a distance equal to the moment reversal zone as indicated by finite element analysis results.

Current findings and earlier work by Manatakos (1989) demonstrate that the effective slab widths of flat slabs participating in lateral load resistance in the linear range are dependent on several factors: the location of the span (end or interior), the floor slab location (upper, intermediate, or lower levels), characteristics of the adjacent spans, size and shape of the structural core wall supports, and the interaction between the various structural components – cores, beams, slabs and frames. Values for the effective slab widths varied from one-tenth to the full panel width and the various charts and tables developed by several researchers such as Tso and Mahmoud (1977) and Pecknold (1977) are suitable only for interior spans of interior panels in the interior floor levels.

Therefore, to ensure slab ductility and inelastic response to failure, confinement of the slab longitudinal reinforcement should be provided in the form of closed hoops and cross-ties at the slab-core wall critical regions allowing development of cracked effective slab widths as follows:

1. Hoops should have a minimum 4-legged configuration forming a cage confining the longitudinal slab reinforcement. The maximum spacing between hoop legs should be less than or equal to the core wall thickness to ensure confinement of the slab reinforcement, with $s_{\mathbf{max}} = 300\,mm$.

2. Hoops should be of minimum width equal to $\frac{3}{4}$ to $1\frac{1}{2}$ times the wall thickness on either side of the structural wall, to a maximum width equal to 3 to 5 times the wall thickness.

3. Hoops should extend from the slab-structural wall face outward a distance equal to 0.20 to 0.30 of the span, for a minimum distance of $4d$ to $6d$ of the slab.

4. Maximum spacing between hoops should be equal to $d/2$ for a distance of $2d$ from the slab core wall support, and at spacings of $(2/3)d$ to $(3/4)$d for the remainder of the confinement length.

For the transverse shear reinforcement in the enclosed and surrounding slabs, 10M bars are selected in the form of 4-legged hoops and cross-ties along the span in the plastic hinging critical slab regions between slab supports over the effective slab band widths.

3.6 Design Summary

3.6.1 Core Design

Figures 3.1, 3.2 and 3.3 show cross-sectional views of the infilled-slab, elevator and stairwell cores at the base level and lower storeys showing details of the uniformly distributed vertical and horizontal reinforcement, the concentrated vertical bars at the confined core wall corners and ends, and the transverse hoops and cross-ties at the confined core wall regions.

Figures 3.4, 3.5 and 3.6 depict elevational views of the infilled-slab, elevator and stairwell cores showing details of the concentrated vertical bars at the confined core wall corners and ends, and spacings of the transverse hoops and cross-ties in the confined core wall regions in the lower storeys plastic hinging regions.

3.6.2 Coupling Beam Design

Figures 3.7 and 3.8 present elevational views of the I-E and E-S coupling beams, respectively, showing details of the diagonal reinforcement and hoop confinement, and the secondary cage reinforcement layout.

Figure 3.9 shows the cross-sectional views of the I-E and E-S coupling beams giving details of the placement of the diagonal reinforcement and hoop confinement, and the secondary cage reinforcement consisting of hoops and longitudinal bars.

3.6.3 Lintel Beam Design

Figure 3.10 illustrates an elevational view of a lintel beam showing details of the placement and spacings of the longitudinal flexural and skin reinforcement, and the transverse hoop and cross-tie reinforcement for shear, torsion and confinement within and outside of plastic hinge regions.

Figure 3.11 shows cross-sectional views of the lintel beams at the end supports and the midspan showing details of the longitudinal flexural and skin reinforcement, and the transverse hoop and cross-tie reinforcement for shear, torsion and confinement.

3.6.4 Core Wall–Beam Joint Design

Figure 3.12 illustrates top front and side views, and elevation front and side views, respectively, of the elevator core flange wall end equivalent confined column region-lintel beam end joints giving details of the core wall concentrated vertical bars and the transverse hoop and cross-tie reinforcement within the joint region.

3.6.5 Enclosed and Surrounding Slabs Design

Figures 3.13 and 3.14 show plan views of the enclosed and surrounding slabs showing details of the placement and spacings of the uniformly distributed bottom and top reinforcement mats in orthogonal directions.

Figures 3.15 and 3.16 present plan views of the enclosed and surrounding slabs showing details of the placement and spacings of the uniformly distributed special bottom and top reinforcement mats at the critical slab-core wall regions (slab-structural core ends, corners and junctions) in orthogonal directions.

Figure 3.17 illustrates a plan view of the enclosed and surrounding slabs illustrating the details of the arrangement, placement and spacings of the transverse hoop and cross-tie cage reinforcement confinement of the slab longitudinal bars in effective slab widths for lateral load resistance over plastic hinging lengths at the critical slab-core wall regions, slab-structural core ends, corners and junctions.

3.7 Design Procedure

Suggested design steps for the different structural components of the core-slab-frame structure are given below.

3.7.1 Core Design

1. Dimensional Limitations

   [i] Wall thickness in plastic hinge regions

   [ii] Exceptions to wall thickness requirements in plastic hinge regions

   [iii] Effective flange wall widths

   [iv] Width of effective flange wall providing lateral support

2. Maximum Reinforcement Bar Sizes

3. Distributed Reinforcement

   [i] Minimum uniformly distributed reinforcement

   [ii] Confinement of horizontal distributed reinforcement

   [iii] Requirement for two curtains of distributed reinforcement

4. Concentrated Reinforcement

   [i] Location of concentrated reinforcement

   [ii] Minimum and maximum area of concentrated reinforcement

5. Flexural Reinforcement

   [i] Post-cracking capacity minimum reinforcement requirements

   [ii] Cracked flexural strengths of the core sections

6. Ductility Requirements

   [i] Limits on the depth of the compression zone

   [ii] Confined compression wall regions for vertical reinforcement

   [iii] Determination of confined regions in core sections

   - Calculation of confined compression web wall regions
   - Selection of confinement regions in core walls
   - Minimum vertical reinforcement in confined wall regions

7. Transverse Hoop and Cross-tie Reinforcement in Confined Core Wall Regions

    [i] Horizontal spacing between legs of hoops and cross-ties

    [ii] Maximum vertical spacing of transverse reinforcement

        - Within confined wall regions

        - Within concentrated reinforcement regions

    [iii] Confined regions and joints within plastic hinge regions

8. Shear Reinforcement

    [i] Ductility requirements for shear

    [ii] Design base shear

    [iii] Simplified method for shear design

        - Dimensional limitations

        - Calculating required shear reinforcement

    [iv] Anchorage of horizontal shear reinforcement

    [v] Placement of horizontal shear reinforcement

9. Determination of Plastic Hinge Regions in Core Sections

10. Sliding Shear Resistance at Construction Joints

11. Variation in Uniformly Distributed Reinforcement Along the Wall Height

    [i] Maximum spacing of uniformly distributed reinforcement

    [ii] Minimum shear reinforcement requirements

    [iii] Changes in uniformly distributed reinforcement

    [iv] Confinement of vertical uniformly distributed reinforcement

3.7.2 Coupling Beam Design

1. Diagonal Reinforcement

   [i] Minimum factored shear stress requirement

   [ii] Required diagonal reinforcement

   [iii] Limitations and restrictions on diagonal reinforcement

   [iv] Development of diagonal reinforcement

   [v] Hoop confinement of diagonal reinforcement

2. Transverse Reinforcement

   [i] Shear reinforcement requirements

   [ii] Torsion reinforcement requirements

   [iii] Dimensional limitations

   [iv] Spacing limitations for transverse reinforcement

3. Distributed Longitudinal Bar Requirements for Torsion

4. Skin Reinforcement for Crack Control of Deep Flexural Members

5. Reinforcement Requirements for Deep Shear Spans

6. Stability and Confinement Requirements of Longitudinal Bars Using Transverse Hoops

7. Secondary Cage Reinforcement – Transverse Hoops and Longitudinal Bars

3.7.3 Lintel Beam Design

1. Flexural Reinforcement

   [i] Consideration for ductile design of joints

   [ii] Bar sizes, spacings and development lengths

   [iii] Minimum and maximum reinforcement requirements

   [iv] Allowances for possible moment redistribution

   [v] Skin reinforcement for crack control of deep flexural members

   [vi] Seismic requirements for negative and positive moment resistance

   [vii] Development of longitudinal reinforcement

2. Shear Reinforcement

   [i] Probable moment of resistance at joint faces

   [ii] Determination of shear forces corresponding to plastic hinging

   [iii] Hoop and cross-tie requirements and leg spacings

   [iv] Simplified method for shear design
   - Dimensional limitations
   - Required shear reinforcement
   - Minimum shear reinforcement requirements
   - Spacing limitations

3. Torsion Reinforcement

   [i] Consideration of torsion

   [ii] Hoop and cross-tie requirements and leg spacings

   [iii] Simplified method for torsion design
   - Required torsion reinforcement
   - Spacing limitations
   - Distributed longitudinal bar requirements for torsion

4. Transverse Reinforcement for Combined Shear and Torsion

   [i] Dimensional limitations

   [ii] Spacing limitations

5. Stability and Confinement Requirements of Longitudinal Bars Using Transverse Hoops

3.7.4 Core Wall-Beam Joint Ductility Requirements

1. "Strong Core Wall-Weak Coupling Beam" Ductility Requirements

    [i] Axial load-moment interaction diagrams for the flange walls

    [ii] Nominal flexural resistance of the coupling beams

    [iii] Strong core wall-weak coupling beam requirements

    [iv] Ductile coupled core walls response

2. "Strong Elevator Core Flange Wall-Weak Lintel Beam" Ductility Requirements

    [i] Axial load-moment interaction diagram for elevator flange wall

    [ii] Nominal flexural resistance of the lintel beams

    [iii] Strong elevator core flange wall-weak lintel beam requirements

    [iv] Transverse reinforcement in elevator wall confined end region

3. Elevator Core Flange Wall End-Lintel Beam Joint Ductility Requirements

    [i] Equivalent elevator core flange wall end-lintel beam joint

    - Factored shear force in the joint
    - Shear resistance of the joint
    - Transverse reinforcement in the joint

3.7.5 Slab Design

1. Slab Flexural Reinforcement - General Design Requirements

2. Two-Way Slab Design - CSA Standard Requirements

   [i] Maximum reinforcement bar sizes

   [ii] Minimum longitudinal reinforcement

   - Shrinkage and temperature reinforcement
   - Skin reinforcement for crack control
   - Maximum spacing of flexural reinforcement

   [iii] Maximum spacing of longitudinal reinforcement at slab critical sections

   [iv] Maximum flexural reinforcement

   [v] Positive moment reinforcement

   [vi] Negative moment reinforcement

   [vii] Special exterior corner reinforcement

   - Top and bottom corner reinforcement
   - Placement of corner reinforcement
   - Extent of corner reinforcement

   [viii] Minimum bottom flexural reinforcement requirements for structural integrity of slabs

   - Minimum bottom reinforcement
   - Continuous reinforcement requirements

3. Special Provisions for Seismic Design of Two-Way Slabs Without Beams - ACI Standard Requirements

   [i] Moment reversals in slabs

   [ii] Redistribution of negative and positive slab moments

   [iii] Structural integrity at slab supports

   [iv] Effective slab band widths in column strips

4. Ultimate, Nominal and Probable Flexural Resistance of Slabs

5. Serviceability Requirements for Two-Way Slabs

6. Shear Provisions in Two-Way Slabs for Seismic Design

7. Ductility Requirements of Slab-Core Wall Supports

8. Hoop Confinement of Longitudinal Reinforcement in Slabs

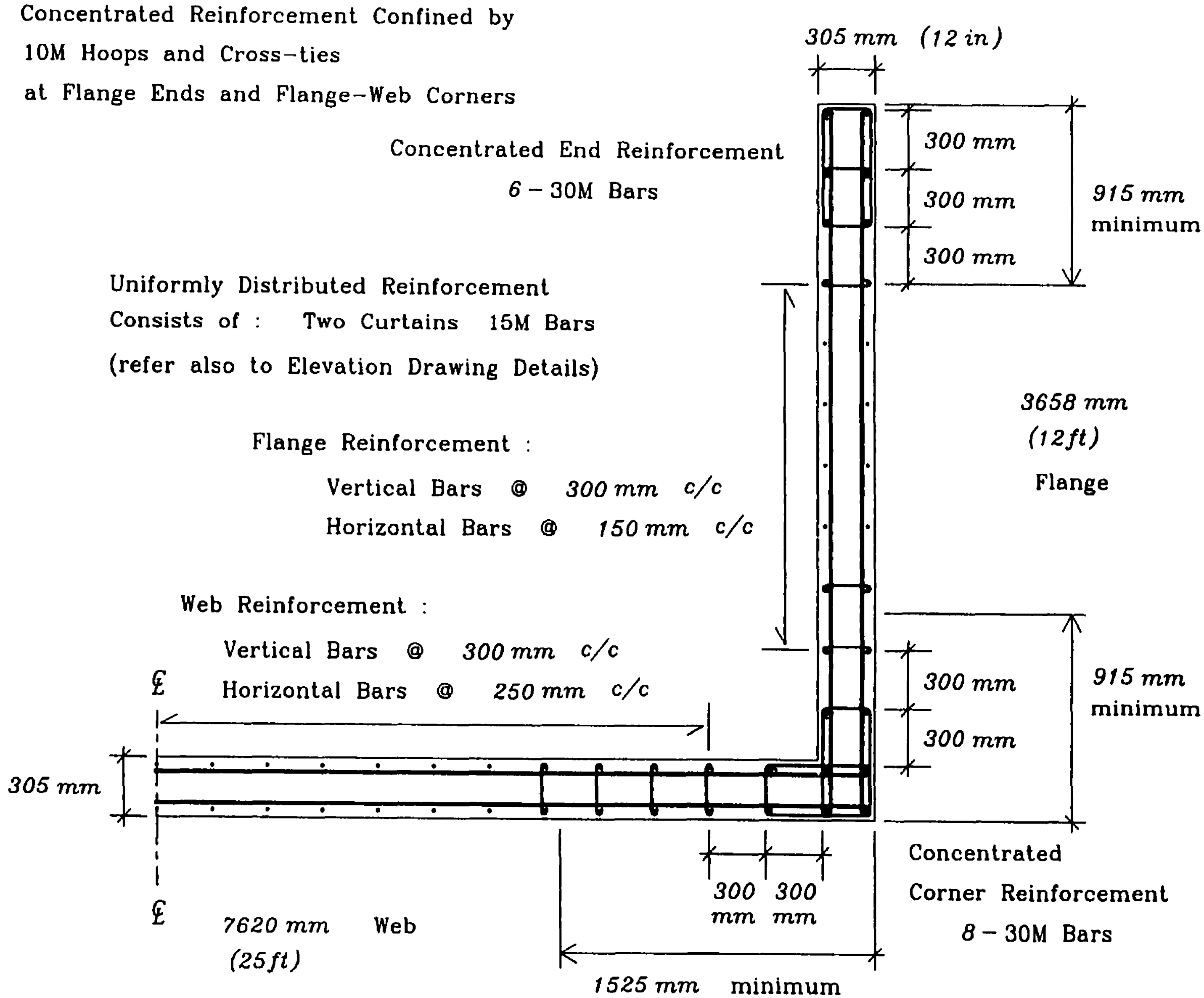

Figure 3.1 Reinforcement Details for the Infilled-Slab Core – Cross-sectional View at the Lower Storeys

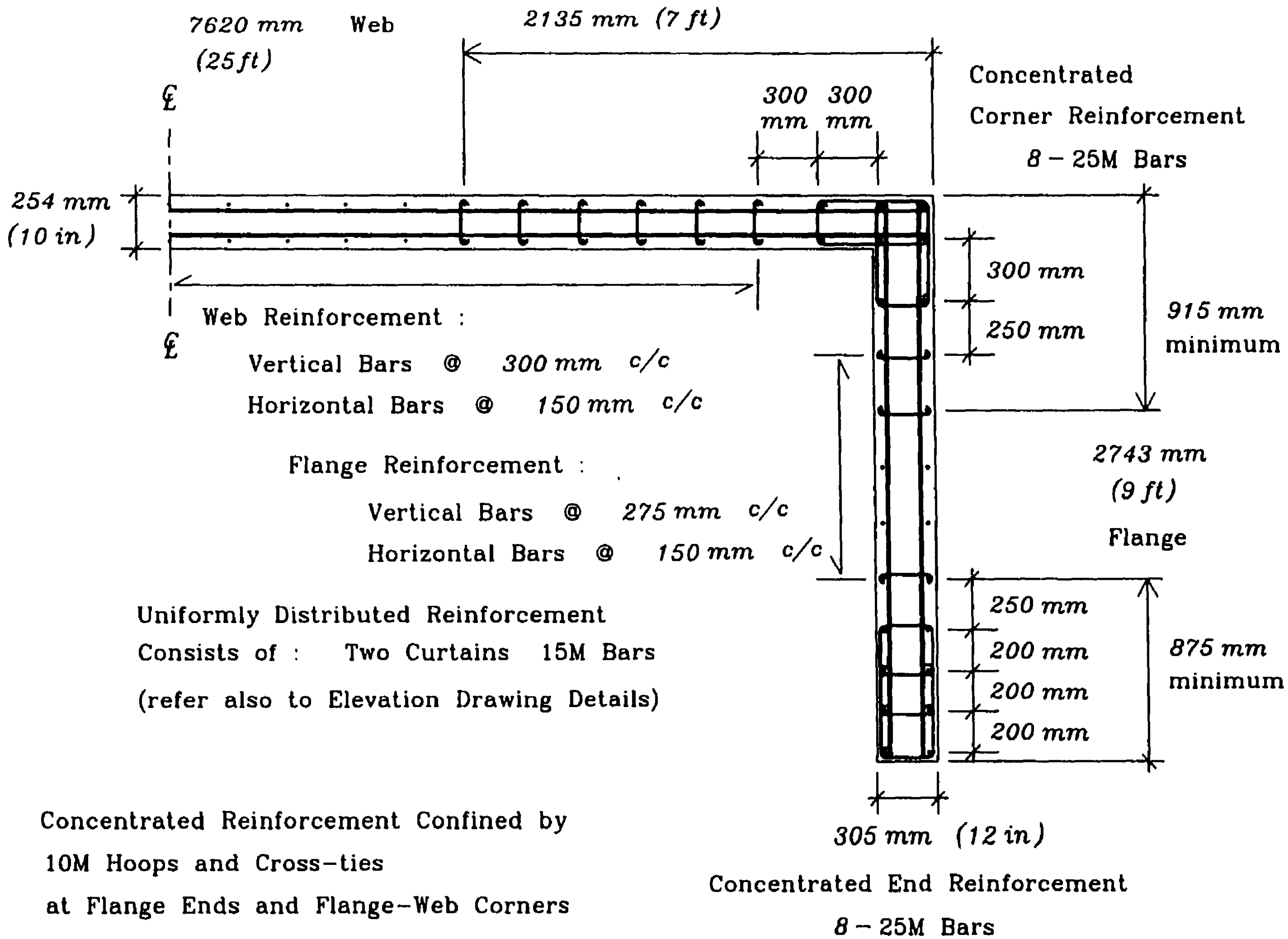

Figure 3.2 Reinforcement Details for the Elevator Core – Cross-sectional View at the Lower Storeys

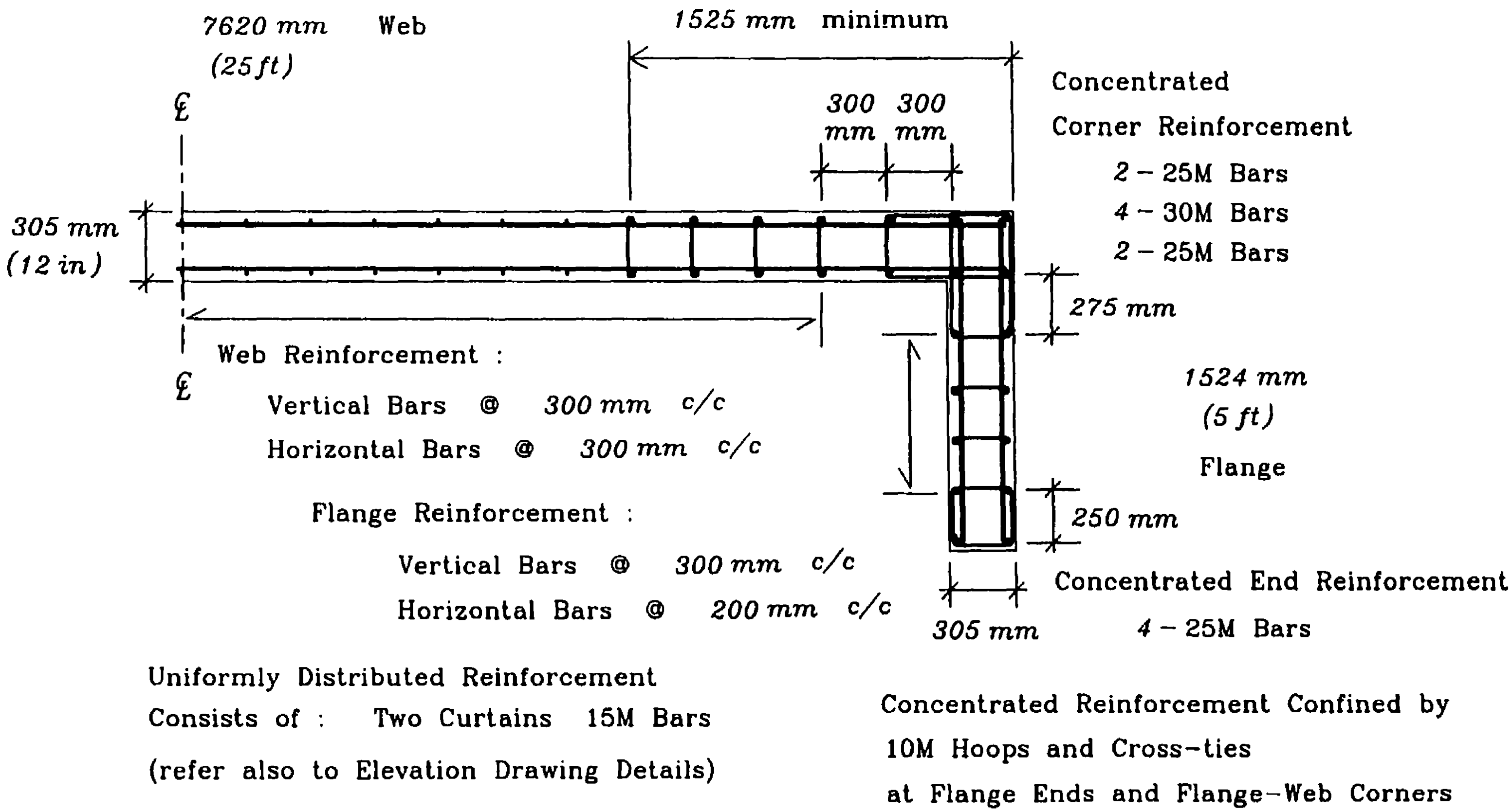

Figure 3.3 Reinforcement Details for the Stairwell Core – Cross-sectional View at the Lower Storeys

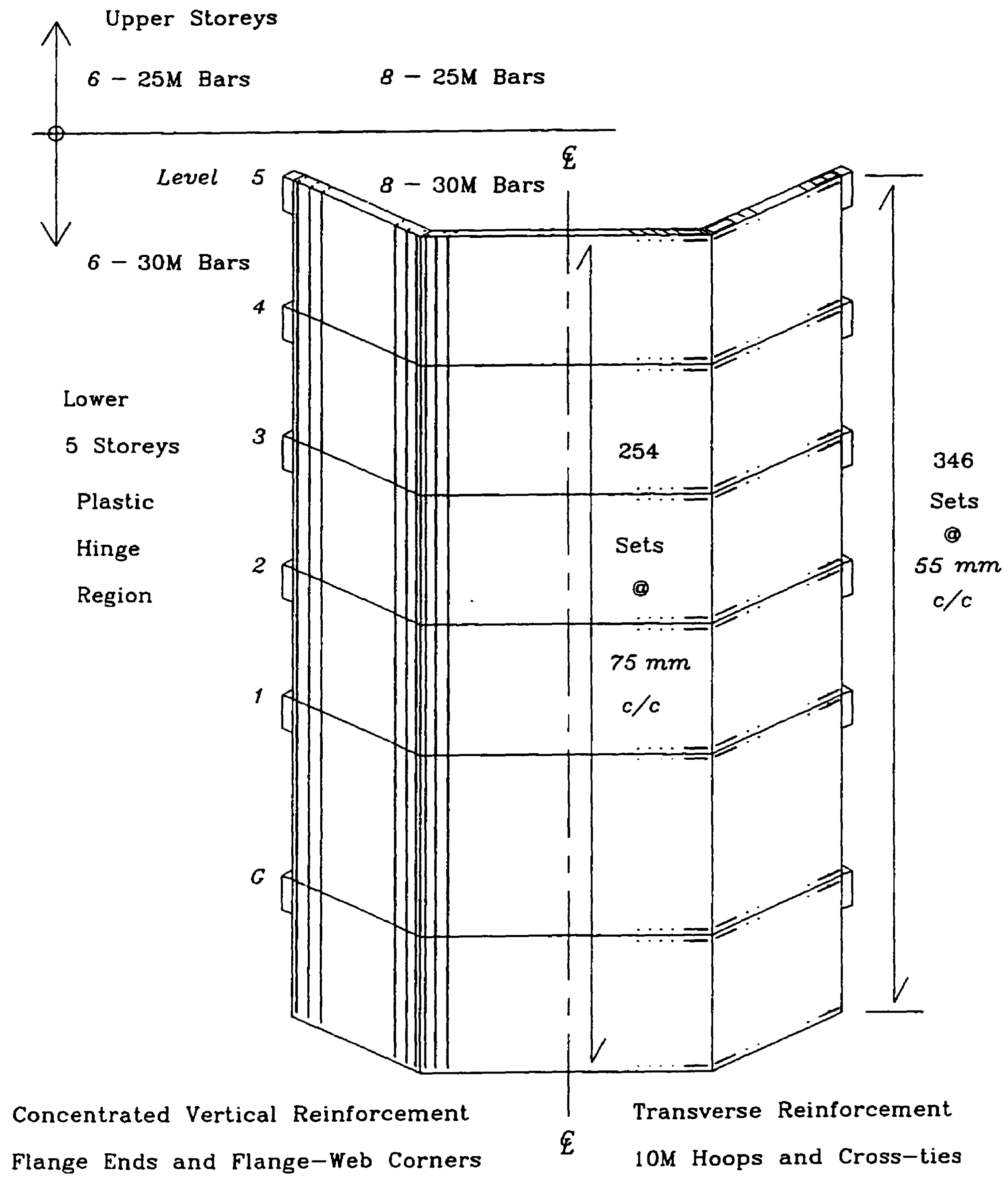

Figure 3.4 Concentrated and Hoop and Cross-tie Reinforcement Details for the Infilled-Slab Core – Elevational View for the Confined Wall Regions in the Lower 5 Storeys

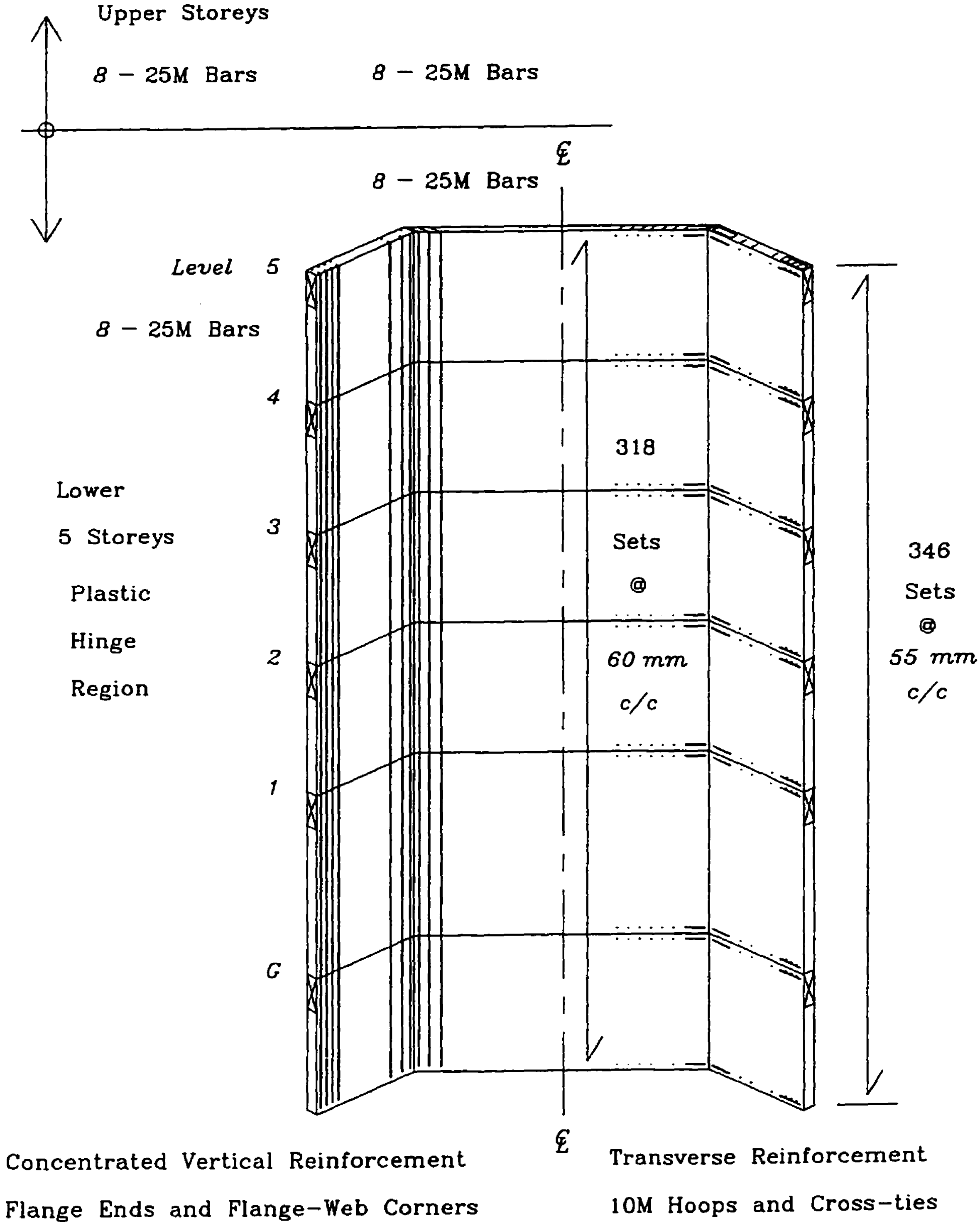

Figure 3.5 Concentrated and Hoop and Cross-tie Reinforcement Details for the Elevator Core – Elevational View for the Confined Wall Regions in the Lower 5 Storeys

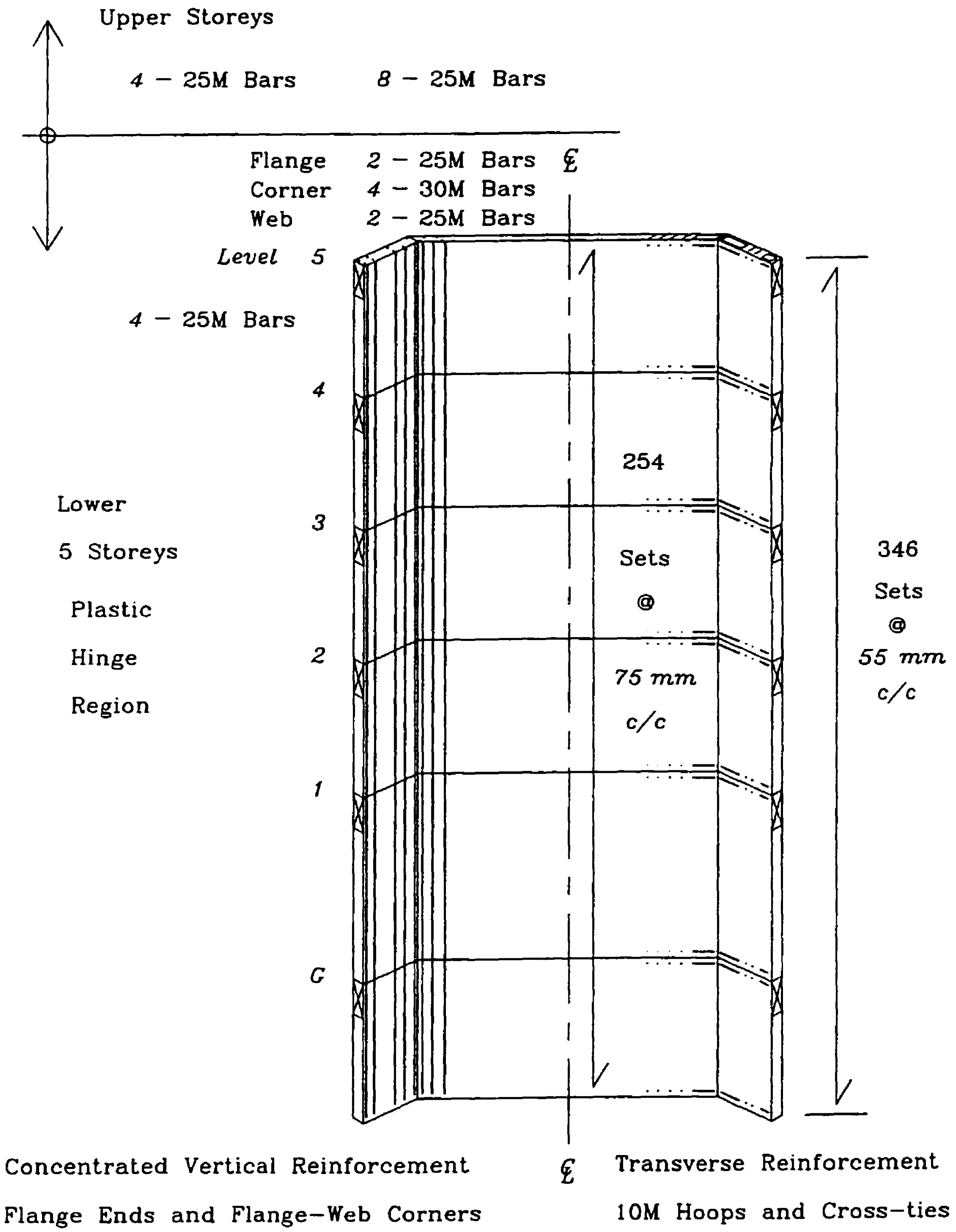

Figure 3.6 Concentrated and Hoop and Cross-tie Reinforcement Details for the Stairwell Core – Elevational View for the Confined Wall Regions in the Lower 5 Storeys

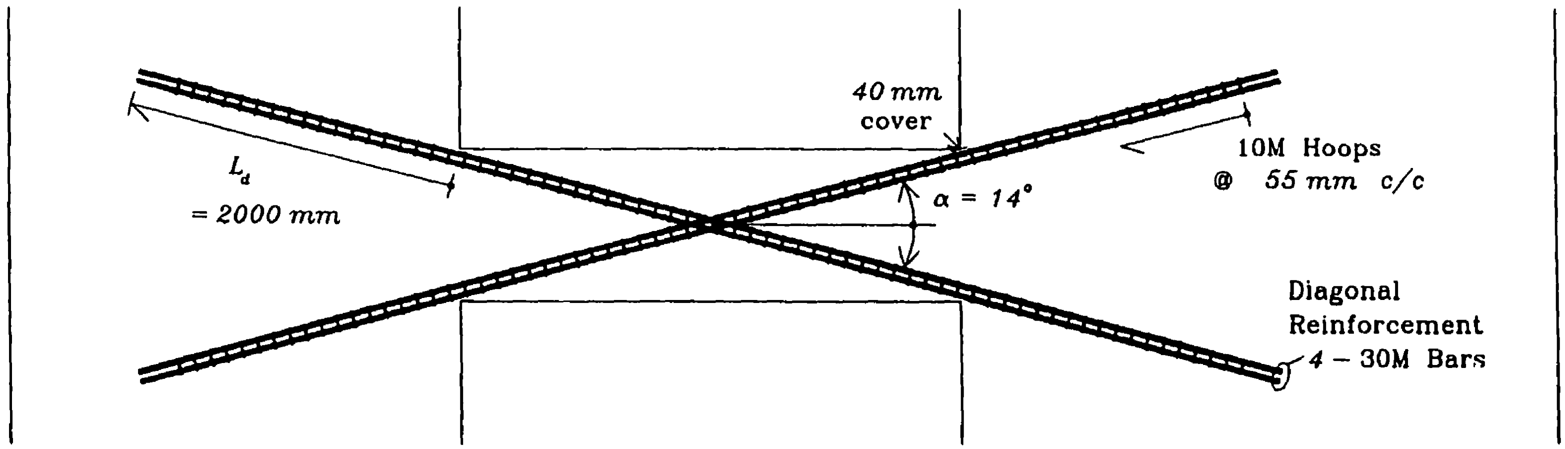

a) Details of Diagonal Reinforcement and Hoop Confinement

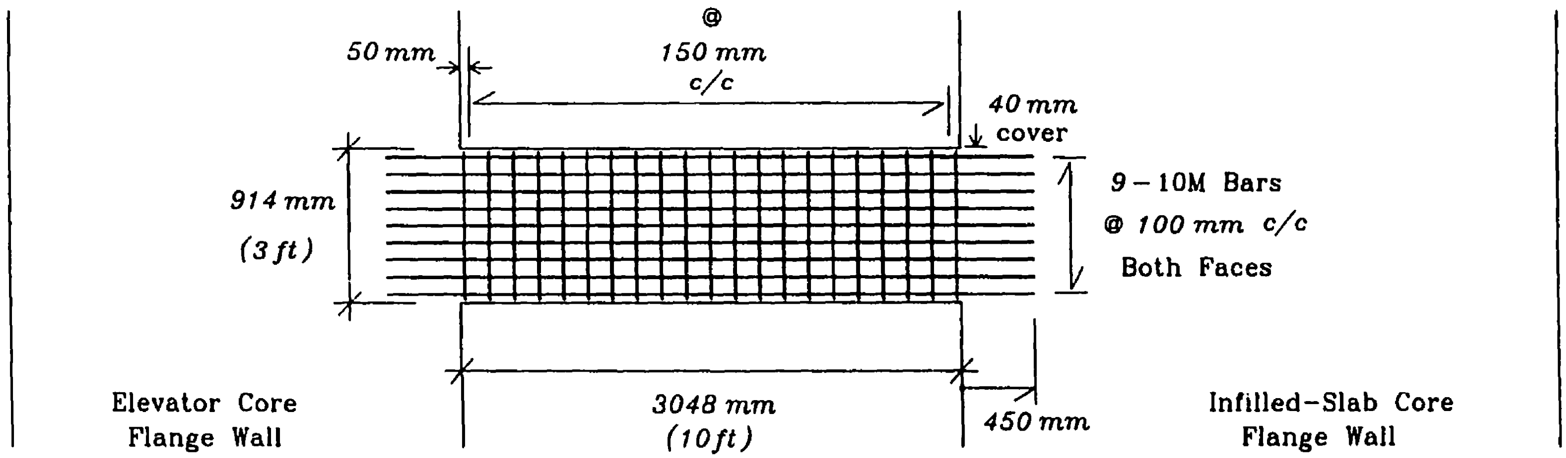

b) Details of Cage Reinforcement : Longitudinal Bars and Transverse Hoops

Figure 3.7 Diagonal, Hoop and Secondary Cage Reinforcement Details for the I-E Coupling Beams – Elevational View Including the Core Flange walls

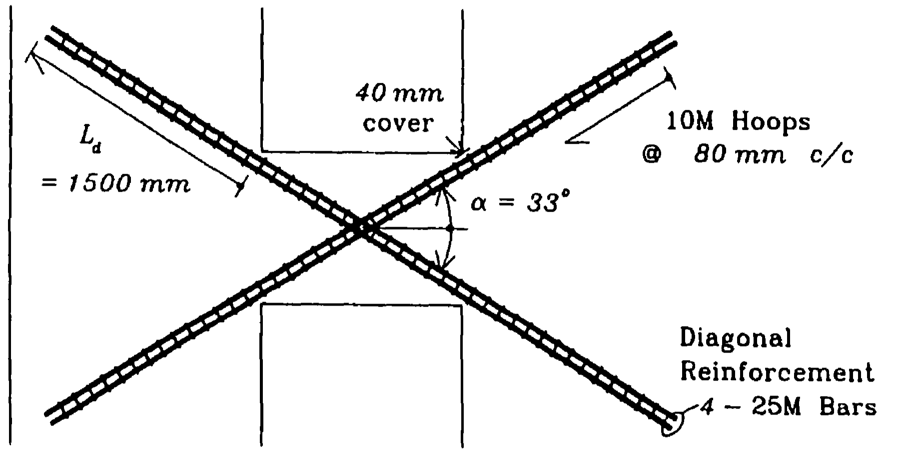

a) Details of Diagonal Reinforcement and Hoop Confinement

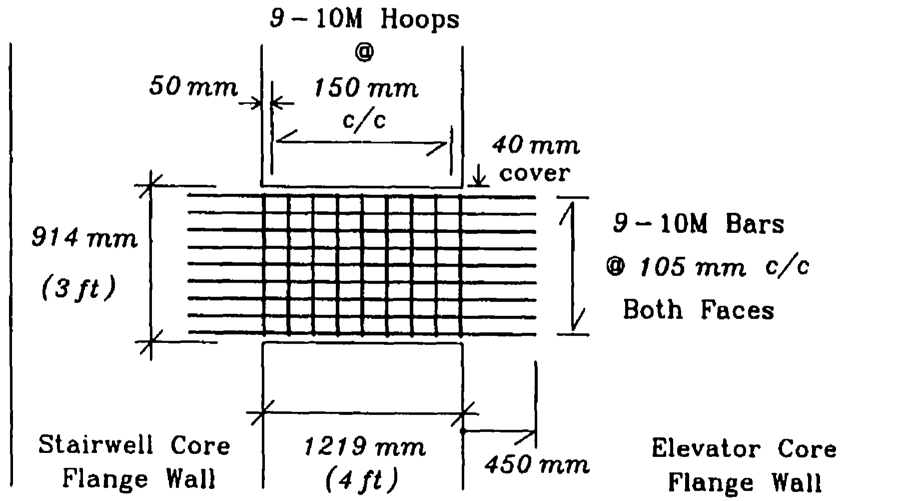

b) Details of Cage Reinforcement : Longitudinal Bars and Transverse Hoops

Figure 3.8 Diagonal, Hoop and Secondary Cage Reinforcement Details for the E-S Coupling Beams – Elevational View Including the Core Flange walls

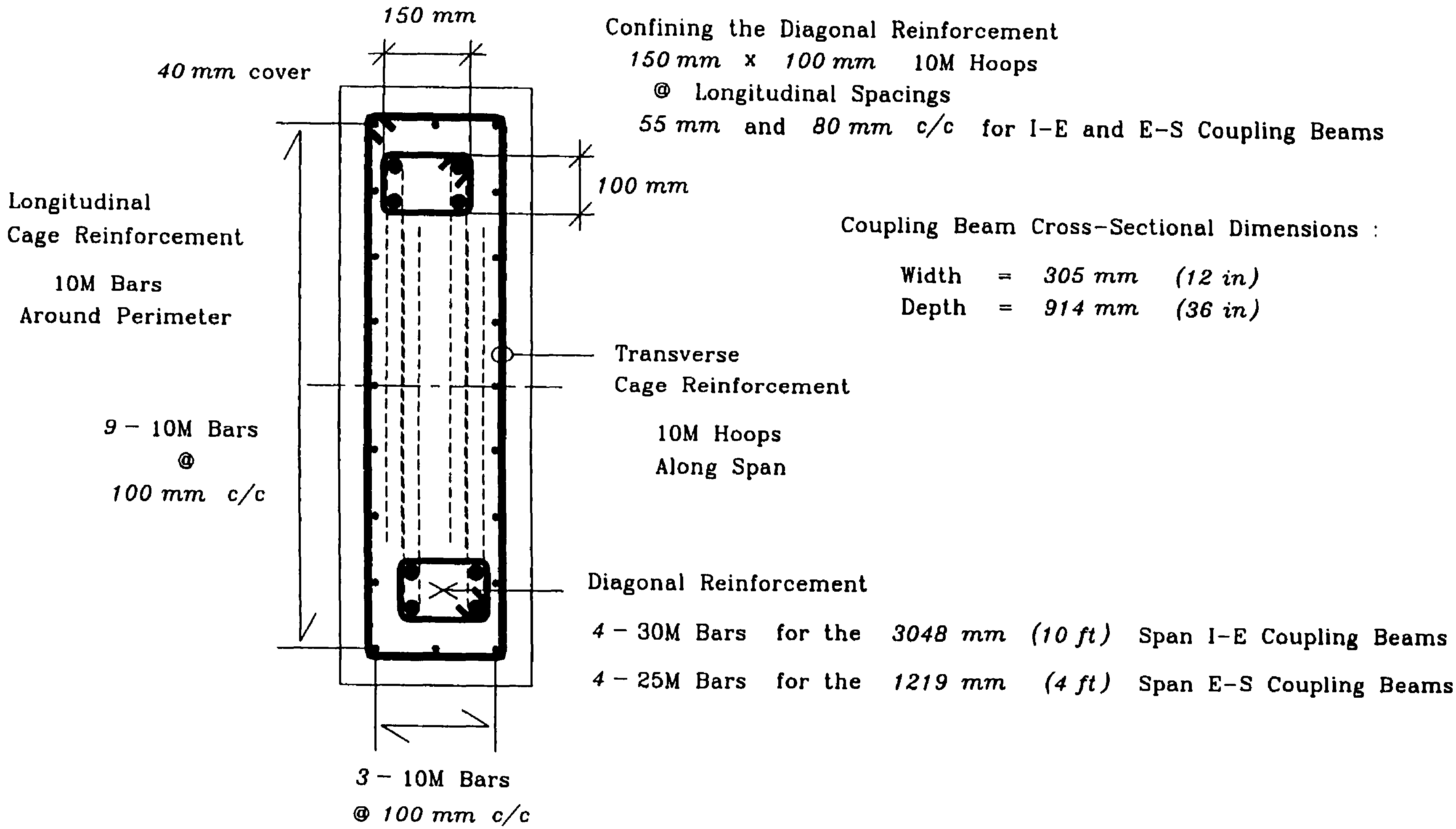

Figure 3.9 Diagonal, Hoop and Secondary Cage Reinforcement Details for the I-E and E-S Coupling Beams
– Cross-sectional View at the Supports

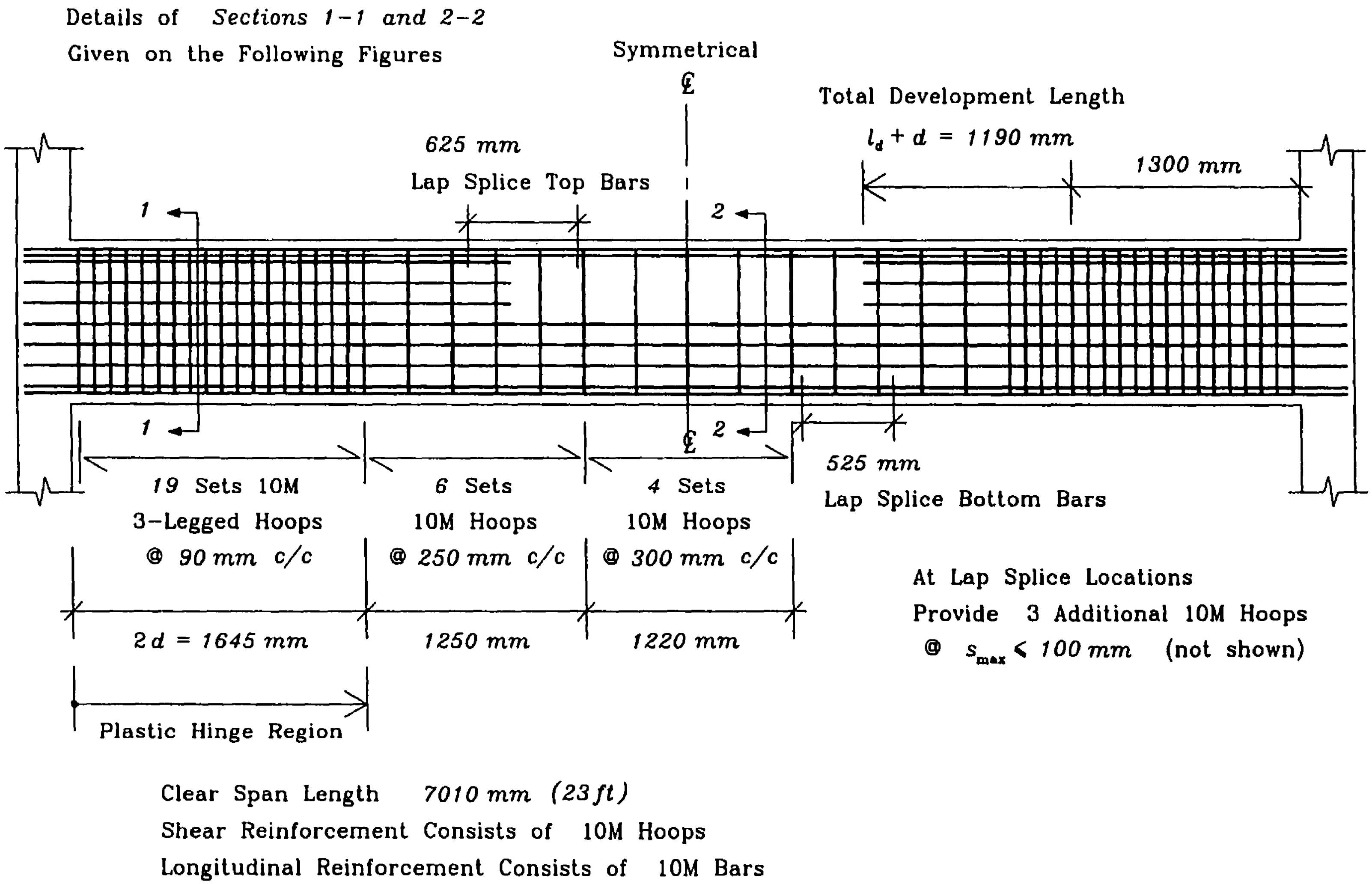

Figure 3.10 Reinforcement Details for the Lintel Beams
– Elevational View Spanning Between the Elevator Core Flange Walls

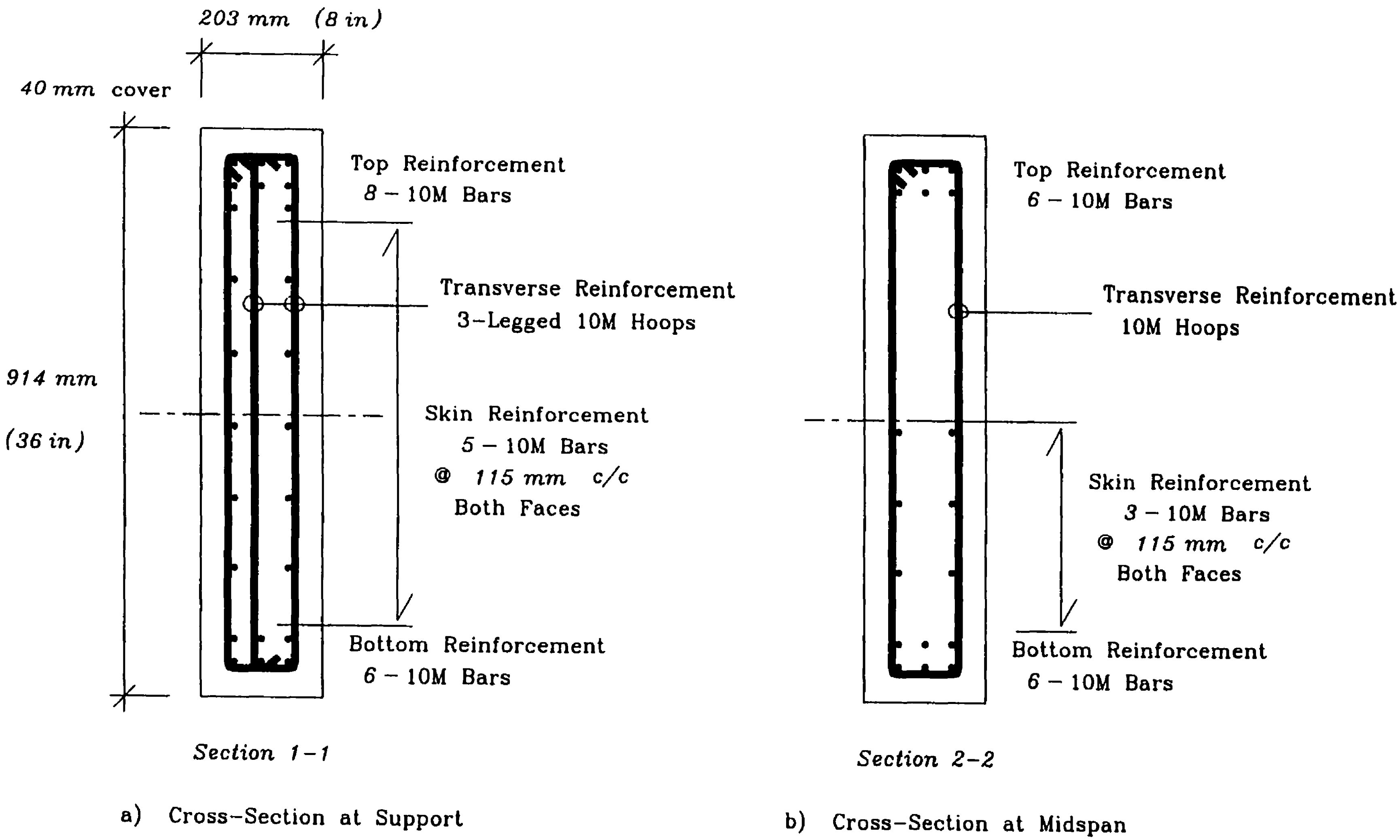

Figure 3.11 Reinforcement Details for the Lintel Beams
– Cross-sectional Views at the Support and the Midspan

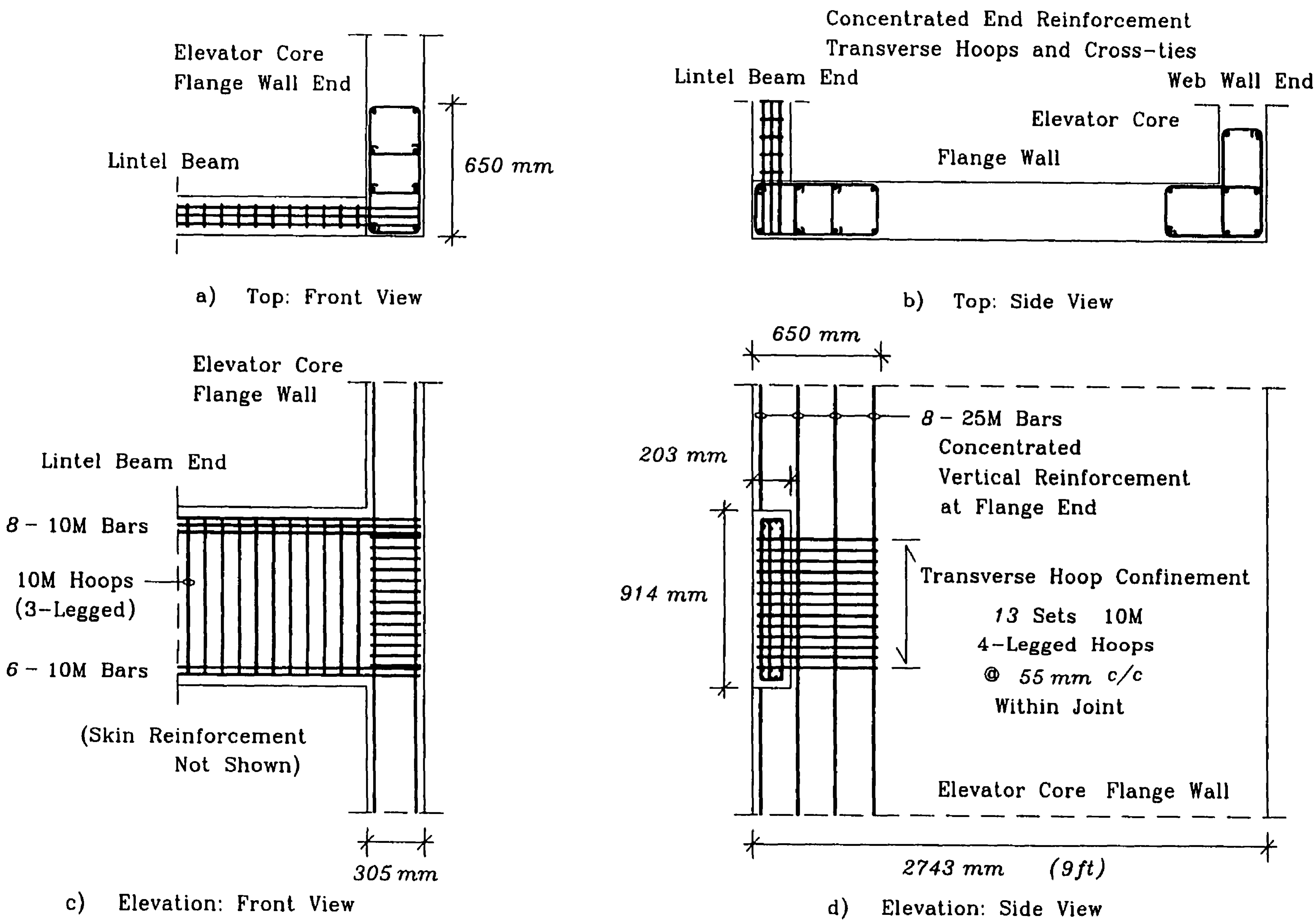

Figure 3.12 Reinforcement Details for the Elevator Flange Wall End Confined Column Region-Lintel Beam End Joints

Slab Reinforcement Consists of 15M Bars @ c/c Spacings as Indicated

Number of Bars and Bar Lengths (*ft*) Also Given

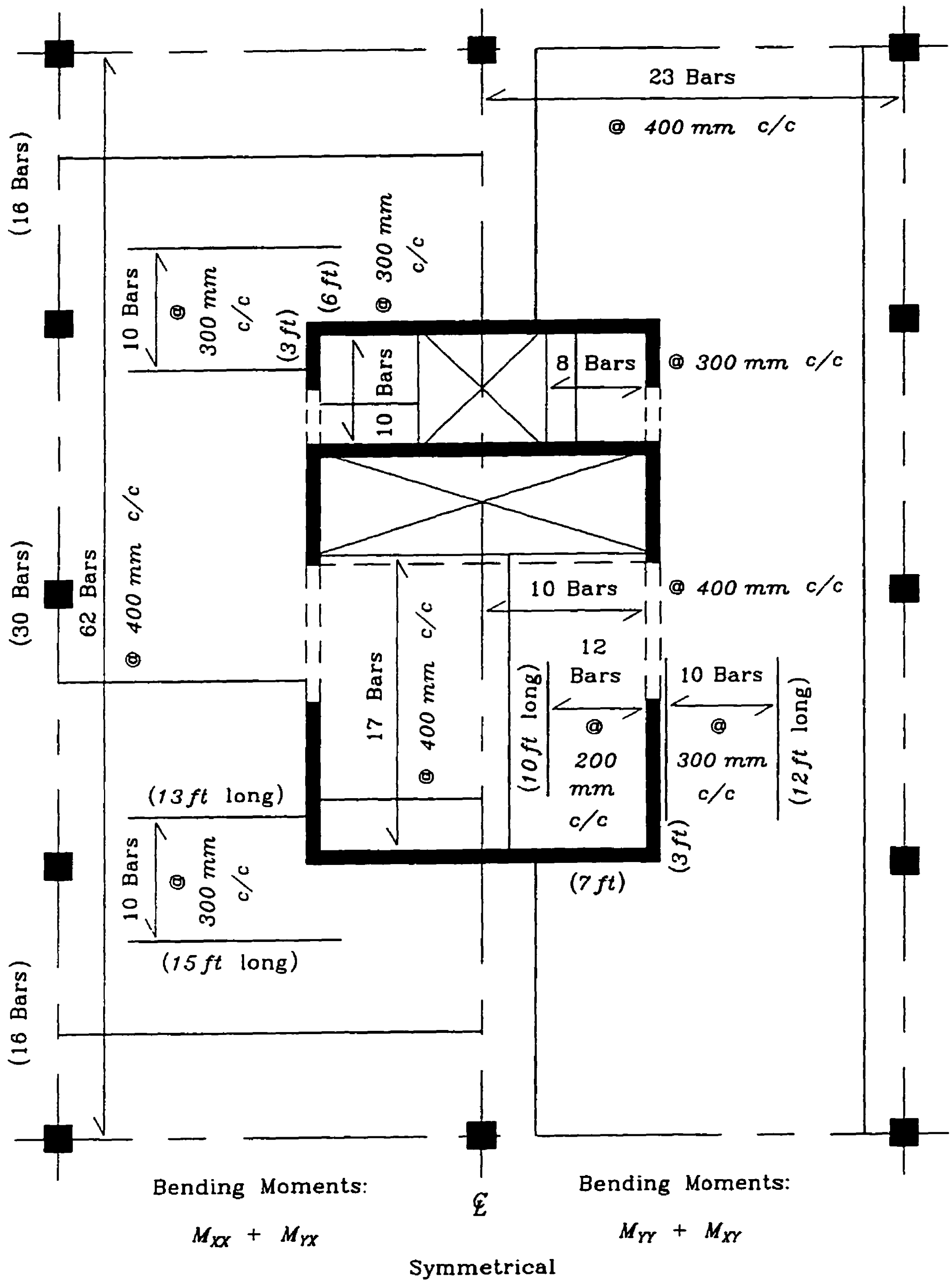

Figure 3.13 Uniformly Distributed Bottom Reinforcement Details for the Enclosed and Surrounding Slabs - Plan View Typical Floor Level

Slab Reinforcement Consists of 15M Bars @ c/c Spacings as Indicated
Number of Bars and Bar Lengths (*ft*) Also Given

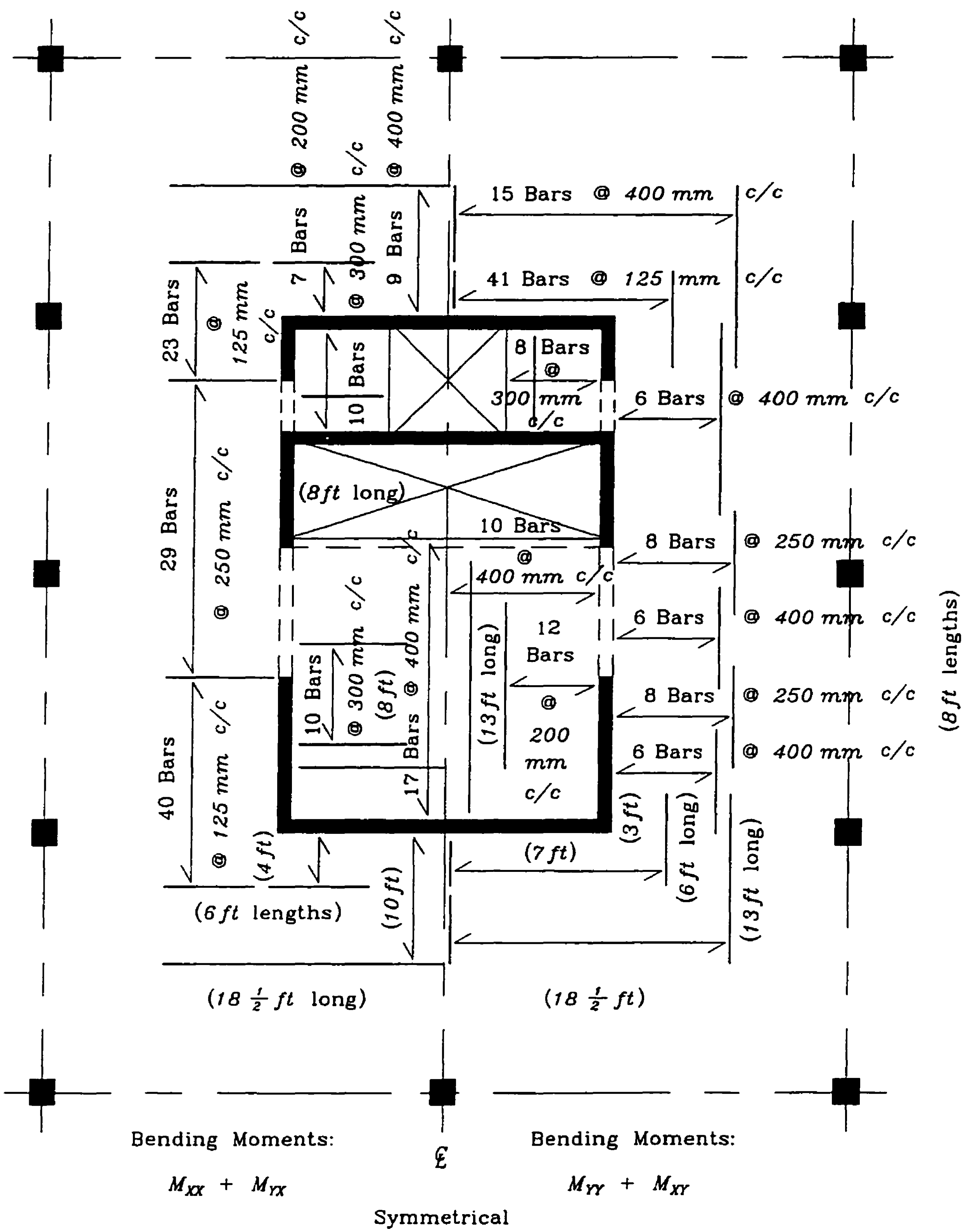

Figure 3.14 Uniformly Distributed Top Reinforcement Details for the Enclosed and Surrounding Slabs - Plan View Typical Floor Level

Slab Reinforcement Consists of 15M Bars @ c/c Spacings as Indicated
Number of Bars and Bar Lengths (*ft*) Also Given

Note: All Spacings = 15M Bars @ *200 mm* c/c

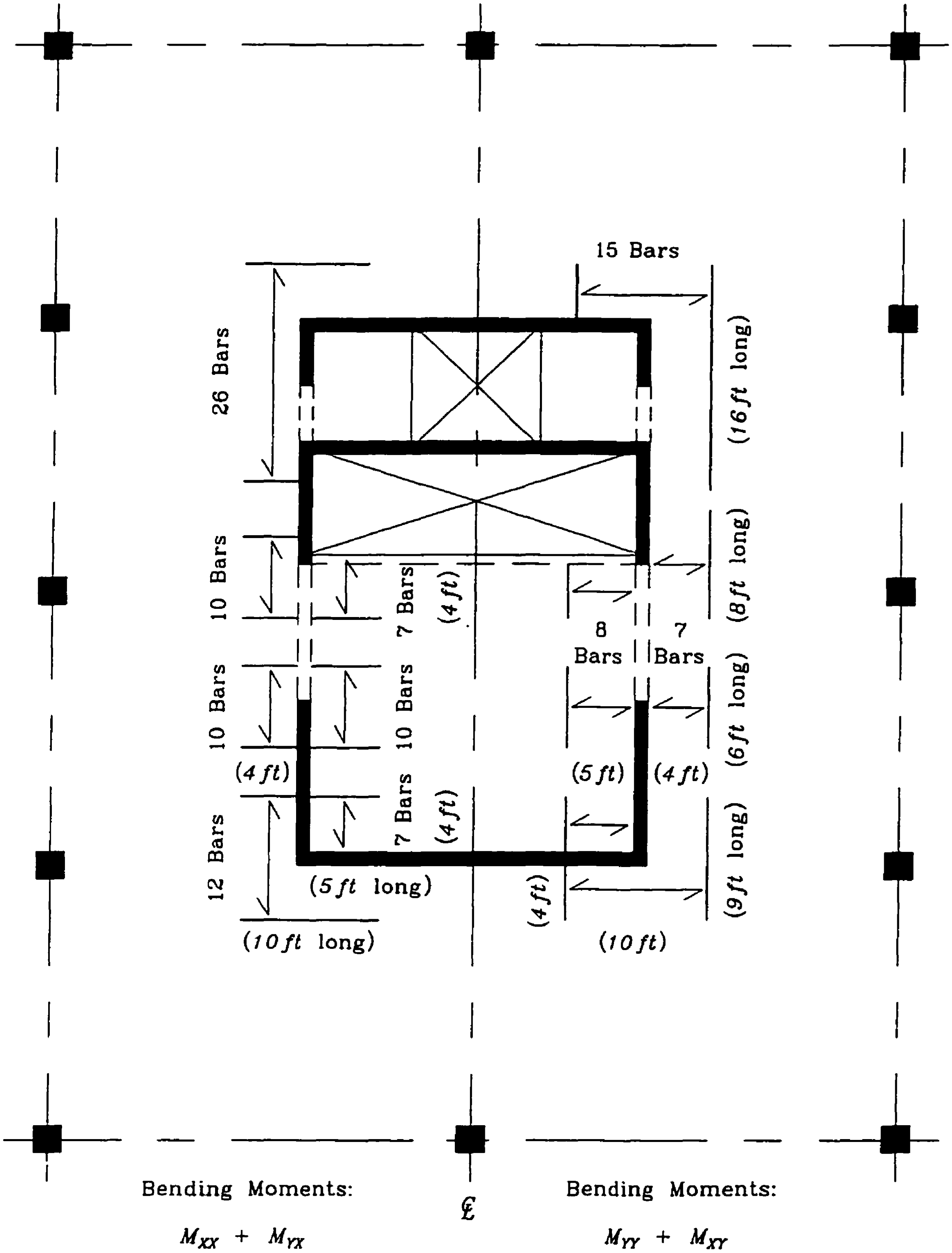

Figure 3.15 Additional Uniformly Distributed Bottom Reinforcement Details at the Critical Slab-Core Ends, Corners and Junctions for the Enclosed and Surrounding Slabs - Plan View Typical Floor Level

Slab Reinforcement Consists of 15M Bars @ c/c Spacings as Indicated

Number of Bars and Bar Lengths (*ft*) Also Given

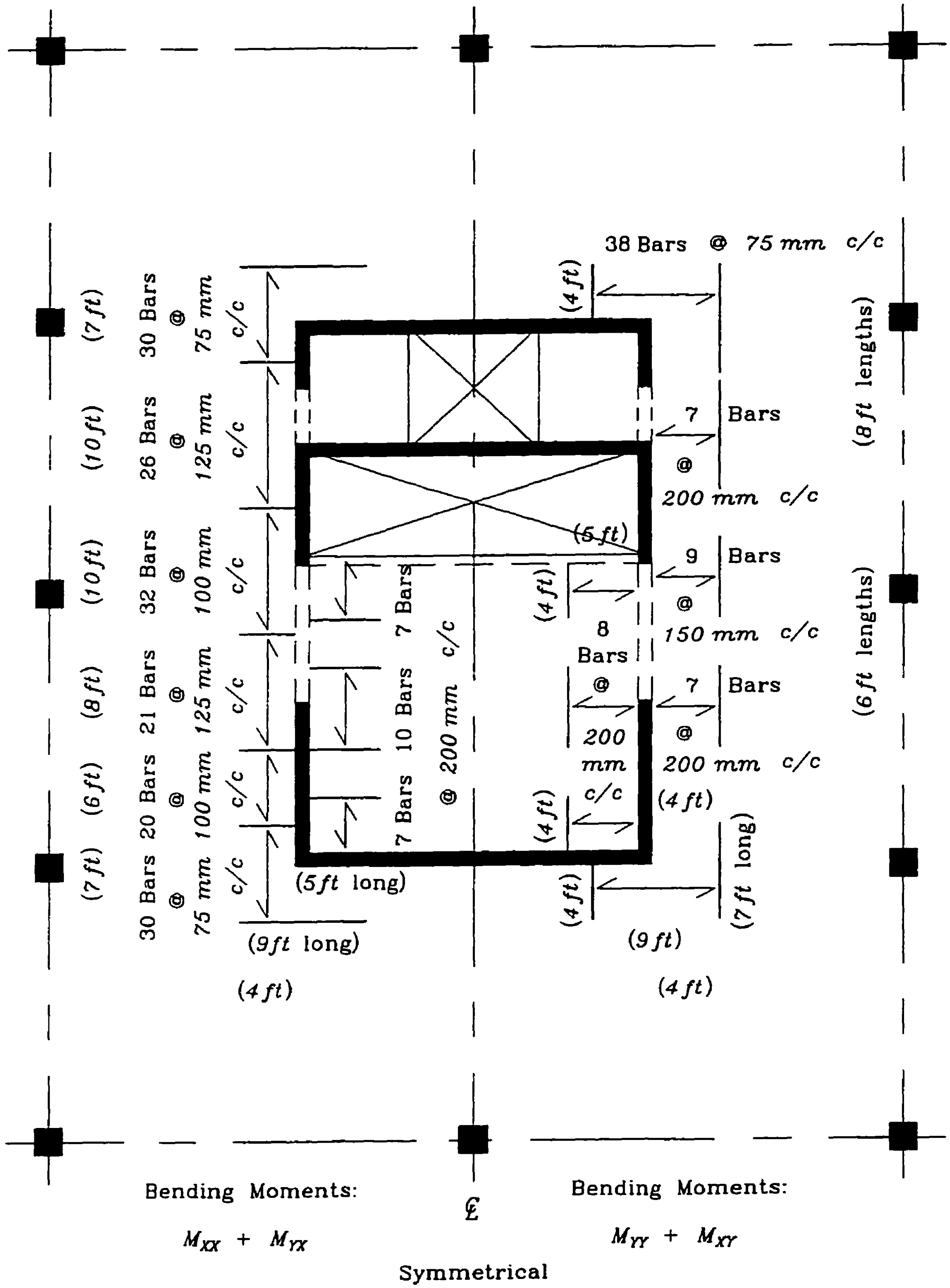

Figure 3.16 Additional Uniformly Distributed Top Reinforcement Details at the Critical Slab-Core Ends, Corners and Junctions for the Enclosed and Surrounding Slabs – Plan View Typical Floor Level

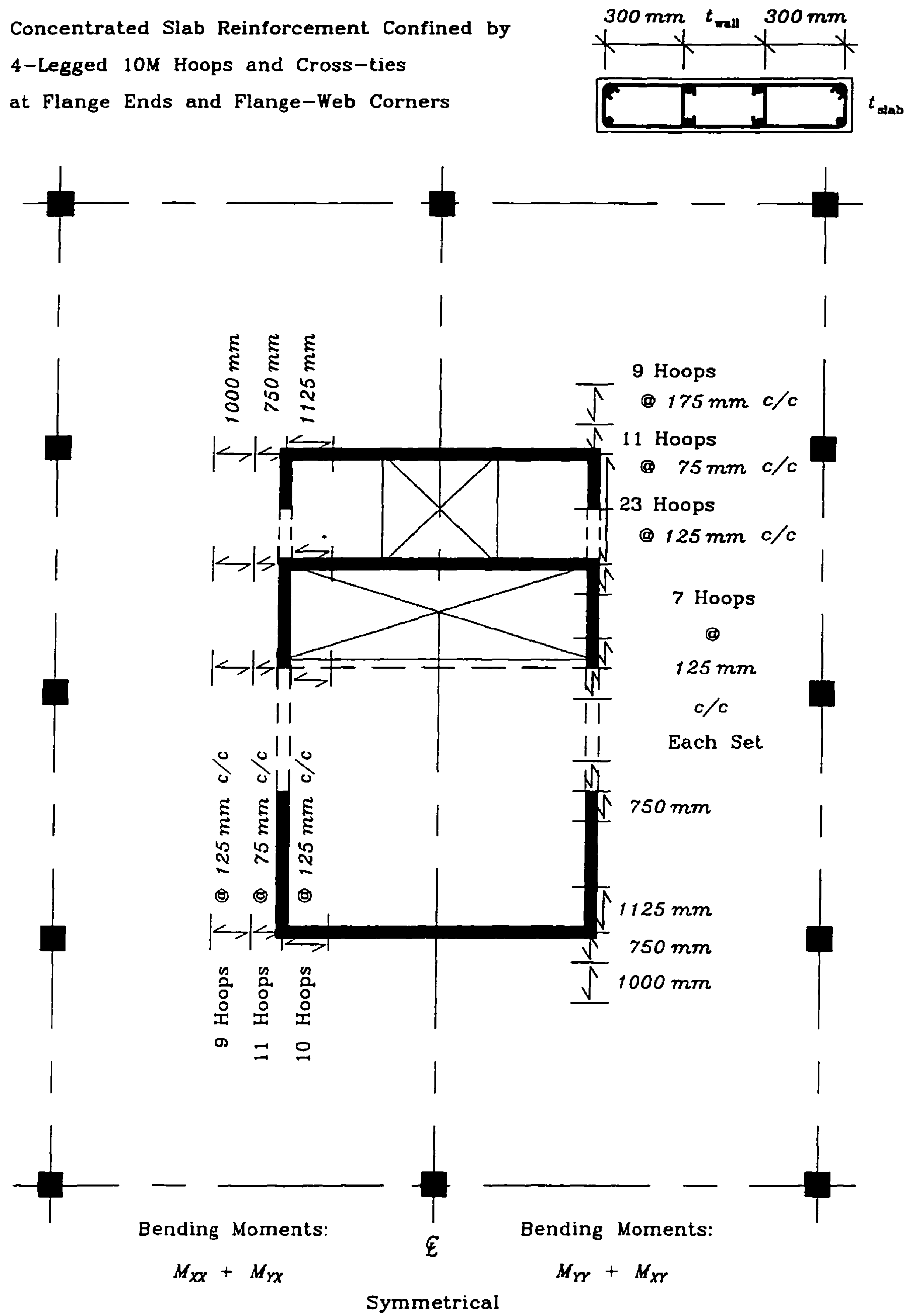

Figure 3.17 Transverse Hoop and Cross-tie Cage Reinforcement Details Confining the Slab Longitudinal Bars in the Slab-Core Ends, Corners and Junctions for the Enclosed and Surrounding Slabs – Plan View Typical Floor Level

Chapter 4

Nonlinear Inelastic Behaviour

Stage 3 of the core-slab-frame building response studies focusses on the nonlinear inelastic behaviour of the core-slab substructure (Fig. 1.1) as designed and detailed in Stage 2, throughout the entire load range, subjected to monotonically increasing earthquake and gravity loads until failure. The contribution and influence of the cores, coupling and lintel beams, enclosed and surrounding slabs is examined in terms of the interaction among the components and on the structure responsal. A detailed three-dimensional finite element model of the core-slab substructure is developed from which the different models are derived for the various analyses performed. Complete details for the nonlinear inelastic finite element modeling and analyses of the core-slab substructure under investigation can be found in the report by Manatakos and Mirza (1995).

4.1 Nonlinear Analysis Method

4.1.1 Computer Program

To evaluate the nonlinear response of the slab-core substructure until failure, the NONLACS computer program (NONLinear Analysis of Concrete and Steel structures) is selected which takes into consideration the effects of cracking of concrete, yielding of reinforcement and other nonlinear phenomena in structural concrete. Details of the computer program, its origin and development are presented by Nofal (1988), Razaqpur and Nofal (1988) and Ghoneim (1978). The NONLACS program can be used to analyze and trace the nonlinear response and failure mode of any plain, reinforced or prestressed concrete, steel or composite concrete-steel structure that can be idealized as an assemblage of thin plates and/or shells subjected to monotonically increasing loads. Such structures include beams, plates, shells, folded plates, box girders, cores and slabs. The program employs an incremental-iterative procedure based on the tangent stiffness method to trace the nonlinear response of the structure, solving the nonlinear problem in a series of incrementally linear analyses.

Verification of the computer program involving extensive analytical investigations for predicting the nonlinear response and failure modes of a wide variety of structures including steel plates, simply supported and cantilever beams, flat slabs, prestressed double T-beams, single- and two-cell prestressed concrete box girder bridges, and composite concrete slab on steel (multi-) girder bridges has been demonstrated by several researchers including Ghoneim (1978), Nofal (1988), Razaqpur and Nofal (1988), and Razaqpur, Nofal and Mirza (1989). Comparisons of the theoretical predictions with the experimental results have shown, in general, very good agreement establishing confidence and reliability of the NONLACS program.

4.1.2 Finite Elements Incorporated

1. Quadrilateral facet shell plate element (QFSE): Fig. 4.1

   The quadrilateral facet shell plate element in the NONLACS program is a 4 node, high order element with a cubic displacement field [Razaqpur and Nofal (1988)], with 6 degrees of freedom per node including 3 translations Δ_x, Δ_y, Δ_z and 3 rotations θ_x, θ_y, θ_z. Due to the material nonlinearity, this element is an anisotropic shell with coupled in-plane membrane and plate bending actions.

2. Uniaxial bar element: Fig. 4.1

   A standard 2 node, uniaxial bar (truss) element with a linear displacement field and 3 translational degrees of freedom Δ_x, Δ_y, Δ_z per node is used which can be orientated in any direction in the global axes.

4.1.3 Modeling of Concrete and Reinforcement

For the nonlinear modeling, concrete layers and smeared steel layered techniques are employed where quadrilateral shell plate elements are divided into layers across their thickness, composed of concrete and smeared steel reinforcement or continuous steel plate, as illustrated in Fig. 4.1 for a typical quadrilateral shell element with respect to the element local axes (u, v) and the local coordinates (η, ξ). Each layer i is located within the shell element thickness as measured from the reference centroidal surface (z-value) to the outer faces and the centroid of each individual layer. A typical concrete element is divided into a number of layers n_{c_i} of thickness t_{c_i} each. Uniformly distributed reinforcement within the concrete element is modeled using smeared steel layers n_{s_i} of an equivalent layer thickness calculated from:

$$t_{s_i} = \frac{\text{area of one bar}}{\text{center} - \text{to} - \text{center spacing between bars}} \tag{4.1}$$

Continuous steel plate is modeled as discrete steel layers of corresponding thickness at their appropriate locations. Smeared reinforcement layers are located within each shell element, measured from the neutral surface to the centroid of the respective uniformly distributed reinforcement being modeled. Concentrated reinforcing bars, prestressing steel tendons and truss members are modeled by bar elements located within the shell element (a maximum of 4 bar elements per shell element), or as separate bar elements attached to two specified nodes in the mesh in the plane of the centroidal element surface ($z = 0$). Thus, compatibility is enforced at the nodes. Bar elements are orientated in the shell element by the local coordinates (η, ξ) of the bar ends within the shell element.

Due to the modeling of the concrete and the steel reinforcement, stress-induced orthotropic properties are present in each shell element as a result of the constitutive material properties. Assumptions in nonlinear modeling include a constant state of plane stress and constant material properties to exist within each layer, and perfect bond between concrete and steel for compatibility. The total shell element stiffness is equal to the summation of the contribution of all of the different concrete, smeared steel reinforcement, continuous steel plate layers and reinforcement bar elements.

4.2 Concrete Constitutive Material Modeling

4.2.1 Compressive Stress-Strain Curve

A uniaxial compressive stress-strain curve for concrete is used Fig. 4.2 in the principal stress directions. The intrinsic shape of the curve consists of two parts. Part I, the initial portion of the curve upto the maximum compressive concrete stress level (f_c') is represented by the Saenz model (1964). Part II, the descending branch of the curve for the inelastic concrete strain-softening response is given by the Smith-Young model (1955).
Parameters required to define the complete concrete compressive stress-strain curve include:

f_c'	=	maximum concrete compressive stress.
ϵ_c'	=	concrete compressive strain at f_c'.
$\epsilon_{c_{ult}}$	=	ultimate concrete compressive strain.
E_c	=	initial tangent modulus of elasticity of concrete in compression.
E_{cs}	=	secant modulus of elasticity of concrete at f_c'.

These parameters are dependent on the ratio of the principal stresses. Hence, concrete is considered as a stress-induced orthotropic material.

4.2.2 Tensile Stress-Strain Curve

A uniaxial tensile stress-strain curve for concrete is used Fig. 4.3 in the principal stress directions. The shape of the curve is considered as a bilinear representation with a linear elastic portion upto the tensile cracking stress level f_t' and a linear unloading descending portion tracing the tension-stiffening phenomenon in stress and strain increments using the Kabir model (1976). Parameters required to define the complete concrete tensile stress-strain curve include:

f_t' = concrete tensile cracking stress.

$\epsilon_{t_{cr}}'$ = concrete tensile strain at f_t'.

$\epsilon_{t_{ult}}$ = ultimate tensile concrete strain.

E_{ct} = tangent modulus of elasticity of concrete in tension.

Razaqpur (1988) has shown that this bilinear tension constitutive model for concrete gives reasonable results for structures with normal amounts of steel reinforcement.

4.2.3 Biaxial Stress State – Failure Envelope

Experimental values for the biaxial concrete strength for constant values of the ratio (α) of the principal stresses (σ_1/σ_2) have been determined by Kupfer. Hilsdorf and Rush (1969), and an analytical representation of the biaxial failure envelope for concrete has been developed by Kupler and Gerstle (1973) as shown in Fig. 4.4. The equivalent uniaxial strain concept by Darwin and Pecknold (1977) uses experimental data from uniaxial compressive and tensile tests of concrete, relating mathematically to the different parts of the biaxial failure envelope for concrete. Thus, the biaxial problem is treated as two equivalent uniaxial stress states in the principal directions for E_1, E_2, σ_1 and σ_2 from which the uniaxial compressive and tensile stress-strain concrete curves can be derived.
For uncracked concrete, the constitutive matrix $[D]$ is given by:

$$[D] = \frac{1}{1-\nu^2}\begin{bmatrix} E_1 & \nu\sqrt{E_1E_2} & 0 \\ \nu\sqrt{E_1E_2} & E_2 & 0 \\ 0 & 0 & \frac{1}{4}(E_1 + E_2 - 2\nu\sqrt{E_1E_2}) \end{bmatrix} \tag{4.2}$$

where:

ν = Poisson's ratio for concrete.

E_1 E_2 = tangent moduli for concrete in the principal directions 1 and 2.

Crushing of concrete occurs when the compressive stress in either principal stress direction exceeds the ultimate compressive concrete stress, thus, the constitutive matrix becomes null.

4.2.4 Concrete Cracking

For uncracked concrete, the principal directions of a concrete element for the tangent moduli E_1 and E_2 coincide with the major $\sigma_{1_{major}}$ and minor $\sigma_{2_{minor}}$ principal stress directions. For cracked concrete, Fig. 4.5, the principal directions of the concrete element rotate becoming parallel and normal to the direction of the cracks. Formation of a crack leads to zero stiffness perpendicular to the crack, however, the concrete resists some tension between the cracks due to tension-stiffening taking into consideration the descending portion of the concrete tensile stress-strain curve (Fig. 4.3). The constitutive matrix $[D]$ is modified for concrete cracking. If a crack forms in the direction 1 then $E_1 = 0$, and for a second crack forming perpendicular to σ_1 then $E_2 = 0$. The effects of cracking in a shell element (per layer) are taken into consideration through the smeared cracking technique by replacing the elastic shear modulus G of the concrete by a reduced value βG which considers the effects due to aggregate interlock and dowel action using a shear retention factor of $\beta = 0.10 - 1.0$ [Lin (1973) and Link et al. (1988)]. Razaqpur (1982) found that using a value of β equal to 0.10 to 0.50 is adequate.

4.2.5 Concrete Constitutive Material Properties

A summary of the constitutive material properties for concrete is presented in Table 4.1 giving typical values and formulae for their determination, for the following:

Density γ_c

Poisson's ratio ν

Young's modulus of elasticity in compression and in tension E_c and E_{ct}

Shear modulus of elasticity G

Maximum compressive strength and strain at the onset of crushing f'_c and ϵ'_c

Ultimate compressive strength and strain $f_{c_{ult}}$ and $\epsilon_{c_{ult}}$

the descending strain-softening branch of the stress-strain curve;

Tensile strength given by:

Direct tensile strength f'_t

Split cylinder (Indirect) tensile strength f_{ct}

Flexural tensile strength - modulus of rupture f_{rt}

Maximum tensile cracking strain $\epsilon_{t_{cr}}$

Ultimate tensile strain $\epsilon_{t_{ult}}$

the descending portion of the curve considering the tension stiffening phenomenon.

More details relating to the constitutive material properties for concrete can be found in the following references: ASCE Task Committee State of the Art (1982), Chen (1982), Park and Paulay (1975), Park and Gamble (1980), Wang and Salmon (1985), Fintel (1985), Sabnis, Harris, White and Mirza (1983), Winter and Nilson (1979), Wischers (1978), Huges and Chapman (1966), Evans and Marathe (1968), Gopalaratnam and Shah (1985), Kupfer et al. (1969), Liu et al. (1972), Nelissen (1972), Kupfer and Gerstle (1973), Darwin and Peknold (1976,1977) and Paulay and Priestley (1992).

4.3 Reinforcing Steel Constitutive Material Modeling

4.3.1 Tensile Stress-Strain Curve

A bilinear elastic-strain hardening stress-strain relationship Fig. 4.6, is used for the steel reinforcement with initial elastic and strain-hardening moduli of elasticity E_s and E_s^*.

4.3.2 Smeared Steel Layer Technique

For the modeling of uniformly distributed reinforcement as smeared steel layers, the constitutive matrix $[D]$ is a function of the stress level and is defined in the local coordinate system (s, t) of the distributed steel reinforcement shown in Fig. 4.7 and is given by:

$$[D] = \begin{bmatrix} E_s & 0 & 0 \\ 0 & 0 & 0 \\ 0 & 0 & 0 \end{bmatrix} \tag{4.3}$$

where:

E_s = modulus of elasticity of the reinforcement (E_s or E_s^*).

(s, t) = local axes directions normal and parallel to the reinforcement.

4.3.3 Reinforcing Steel Constitutive Material Properties

A summary of the constitutive material properties for the steel reinforcement is presented in Table 4.2 giving typical values and formulae for their determination, for the following:

Poisson's ratio ν
Elastic modulus of elasticity E_s
Strain-hardening modulus of elasticity E_{st} or E_s^*
Yield strength and strain f_y and ϵ_y
Maximum yield strain (length of the yield plateau) $\epsilon_{st_{max}}$
Maximum tensile strength at the peak of the strain-hardening range $f_{s_{max}}$
Ultimate (Fracture) tensile strain $\epsilon_{s_{ult}}$
depending on the ductility and strain-hardening capability.

More details relating to the constitutive material properties for reinforcing steel can be found in the following references: ASCE Task Committee State of the Art (1982), Chen (1982), Park and Paulay (1975), Park and Gamble (1980), Wang and Salmon (1985), Fintel (1985), Sabnis, Harris, White and Mirza (1983) and Mirza and MacGregor (1979).

4.4 Core-Slab Substructure Nonlinear Model Description

For the nonlinear analyses, values of the constitutive material properties used for concrete with a compressive strength of 30 MPa and for the steel reinforcement with a specified yield strength of 400 MPa are summarized in Tables 4.1 and 4.2, respectively.

4.4.1 Cores Idealization

Figures 4.8 to 4.11 show details for the nonlinear modeling of the core sections.

4.4.1.1 Mesh Division

Referring to Fig. 4.8, a division of 4 elements is used across the core sections web walls. Across the Core and Elev sections flange walls, a 2 elements division is selected taking into consideration the depth of the coupling and lintel beam joints, and to match the slab mesh. For the short Stair section flange walls, a 1 element division is used modeling the entire wall width. Along the cores height for the web and flange walls, in typical storeys and the basement storey, a 2 elements division is used with the upper wall elements height equal to the coupling and lintel beams depth, and the lower wall elements height equal to the remainder of the storey heights. For the ground and top storeys, a 3 elements division is selected with the upper wall elements height equal to the beam depth and the remainder of the storey heights are divided into 2 lower wall elements to obtain a more detailed distribution of the core stresses in the lower storeys. Element aspect ratios are maintained at values of less than 2 and as close to unity as possible.

4.4.1.2 Concrete Layer Systems

Shell elements are divided into 8 concrete layers across the core wall thicknesses resulting in 2 different concrete layer systems, one for the 12 in thick web and flange walls and one for the 10 in thick Elev section web wall, as shown in Figures 4.9 to 4.11 for each core section.

4.4.1.3 Smeared Reinforcing Steel Layer Systems

Both vertical (outer bars) and horizontal (inner bars) uniformly distributed wall reinforcement consist of 2 curtains of 15M bars at various spacings in the cores design. (Note that in the DQXX model, 2 curtains of 10M vertical uniformly distributed reinforcement are used.) Four layers of equivalent smeared reinforcement are required in each wall element, a smeared steel layer for each of the 2 curtains of vertical and horizontal uniformly distributed reinforcement located at both core wall faces. Values of the equivalent smeared steel layer thicknesses for the different uniformly distributed wall reinforcement bar spacings are listed in Table 4.3. There are a total of 9 different sets of vertical and horizontal uniformly distributed reinforcement spacing arrangements using 15M bars in the cores design as summarized in Table 4.4, thus, requiring

9 different smeared reinforcement steel layer systems in the modeling. Details of the smeared reinforcing steel layers in the core sections flange and web walls are shown in Figures 4.9 to 4.11.

4.4.1.4 Concentrated Steel Reinforcement Bar Element Systems

Concentrated reinforcement at the confined, end and corner wall regions of the core sections is modeled using equivalent bar elements located at the centroid of each set of concentrated reinforcing bars considered as lumped together.

A total of 14 different sets of concentrated steel reinforcement bar element systems with 2 to 4 bar elements arrangements are required to model the concentrated reinforcement in the confined end and corner regions of the web and flange walls of the core sections as shown in Figures 4.9 to 4.11. In the web walls, the concentrated reinforcement bars located at the corner (end) regions are modeled by 2 equivalent bar elements each in the wall shell elements. In the flange walls for the Core and Elev sections, 2 equivalent bar elements are used at the wall end and corner concentrated reinforcement regions; while for the Stair section flange walls modeled by a 1 full width shell element, the concentrated reinforcement at the end and corner regions are modeled by 1 equivalent bar element each. An additional 2 equivalent bar elements are added within all of the core flange wall shell elements to model the coupling beam diagonal reinforcement that extends into the flange walls (Fig. 4.14). Thus, each flange wall shell element has a total of 4 equivalent bar elements.

For the planar analyses of the core-slab substructure, a total of 5 and 9 different sets of concentrated steel reinforcement bar element systems with 2 bar elements arrangements in each shell element are required in the PDQX and PDQY models, respectively. In the direction along the core sections web walls for the PDQX model, all of the concentrated reinforcement at the flange-web wall confined corner regions is considered to be concentrated at the web wall ends (corners). In the direction along the core sections flange walls for the PDQY model, all of the concentrated reinforcement at the flange-web wall confined corner regions is considered to be concentrated at the flange wall ends and corners.

4.4.2 Coupling Beams Idealization

Figures 4.8 and 4.12 to 4.14 show details for the nonlinear modeling of the coupling beams.

4.4.2.1 Mesh Division

For the I-E and E-S coupling beams, a mesh division is chosen to match the core and slab mesh (Figures 4.8 and 4.17). Along the I-E coupling beams span, a 2 elements division is selected with element heights equal to the beam depth, Fig. 4.12. The short, deep E-S coupling beams are modeled by a 1 element division for each beam, Fig. 4.13. Element aspect ratios are kept to values of less than 2.

4.4.2.2 Concrete Layer Systems

Shell elements are divided into 6 concrete layers across the 12 *in* coupling beam width (element thickness) requiring 1 concrete layer system, shown in Figures 4.12 and 4.13.

4.4.2.3 Smeared Reinforcing Steel Layer Systems

Cage reinforcement in the I-E and E-S coupling beams for concrete confinement, crack control and torsion consists of 10M transverse hoops and 10M longitudinal bars uniformly spaced along the span and around the cross-sectional perimeter. Four layers of equivalent smeared reinforcement are required in each coupling beam element, one smeared steel layer for each side of the vertical transverse hoop bar legs and one smeared steel layer for each set of the horizontal longitudinal reinforcing bars, located at both faces of the beams as shown in Figures 4.12 and 4.13 for the I-E and E-S coupling beams. A total of 2 smeared reinforcing steel layer systems are required to model the uniformly distributed vertical and horizontal reinforcement cage arrangements in the coupling beams, one system for each beam type.

4.4.2.4 Diagonal Reinforcement Bar Element Systems

Diagonal reinforcement in the I-E and E-S coupling beams consists of 4-30M bars and 4-25M bars for each beam type, respectively. Development of the diagonal reinforcement bars is provided through straight extensions into the core sections flange walls.

The diagonal reinforcement is considered as concentrated reinforcement bars and is modeled using equivalent bar elements located at the centroid of each set of diagonal reinforcing bars, requiring a total of 2 different sets of concentrated steel reinforcement bar element systems with 2 bar elements arrangements each. To idealize the diagonal reinforcement development lengths appropriately, these equivalent bar elements are extended the required development lengths into the shell elements modeling the core sections flange walls. This results in an additional 2 equivalent bar elements for a total of 4 bar elements within each flange wall shell element as shown in Fig. 4.14 for the ground, a typical and the top storey coupling beams.

4.4.3 Lintel Beams Idealization

Figures 4.8 and 4.15 show details for the nonlinear modeling of the lintel beams.

4.4.3.1 Mesh Division

The lintel beams are divided into 4 equal elements along their span, with element heights equal to the beam depth as shown in Fig. 4.15. This mesh is chosen to match the core and slab mesh (Figures 4.8 and 4.17). Element aspect ratios are maintained at values of less than 2.

4.4.3.2 Concrete Layer Systems

Shell elements are divided into 6 concrete layers across the 8 *in* lintel beam widths (element thickness) requiring 1 concrete layer system, shown in Fig. 4.15.

4.4.3.3 Smeared Reinforcing Steel Layer Systems

In the lintel beams design, the reinforcement consists of 3- and 2-legged 10M transverse hoops and cross-ties shear-torsion reinforcement and longitudinal 10M bars skin reinforcement uniformly placed around the cross-section perimeter. Five and four layers of equivalent smeared steel reinforcement are required in the lintel beam elements (Fig. 4.15), one smeared steel layer for each side of the vertical 3- and 2-legged transverse hoop bar legs and one smeared steel layer for each set of the horizontal longitudinal skin reinforcement bars located at both beam faces. Note that in the central region of the lintel beams, skin reinforcement is present only on the lower tension faces. Since a smeared steel reinforcement layer extends across the entire shell element face (Fig 4.1), the calculated value of the smeared steel thickness (t_{s_i}) must be divided in half to smear the equivalent steel layer over the entire lintel beam side faces.

A total of 2 sets of smeared reinforcement steel layer systems are required in the lintel beams. One set consisting of 5 smeared steel layers for the 3-legged 10M hoops in the plastic hinging regions and 10M skin reinforcement, and one set consisting of 4 smeared steel layers for the 2-legged 10M hoops in the midspan regions and 10M skin reinforcement, as shown in Fig. 4.15.

4.4.3.4 Main Flexural Reinforcement Bar Element Systems

Main flexural reinforcement in the lintel beams consists of top 6-10M upper bars and 2-10M lower bars, and 6-10M bottom bars which are each considered as concentrated reinforcement bar groups and are modeled using equivalent bar elements located at the respective centroids of each set of reinforcing bars. A total of 2 different sets of concentrated steel reinforcement bar element systems with 3 bar elements arrangement each are required for the modeling. The top and bottom 6-10M equivalent bar elements flexural reinforcement extend across the entire lintel beams span, while the top lower 2-10M equivalent bar elements terminate in the central region of the lintel beams as shown in Fig. 4.15.

4.4.4 Enclosed and Surrounding Slabs Idealization

Figures 4.16 and 4.17 show details for the nonlinear modeling of the enclosed and surrounding slabs. A portion of the surrounding slabs is considered extending upto one-half of the panel in all directions around the core sections perimeter, thus, requiring appropriate boundary conditions to be imposed at the cut slab panel edges to prevent cantilever action. The cut slab edges are constrained for the vertical deflections Δ_z and the rotations θ_x and θ_y by limiting the maximum deformations to the values obtained from the cracked elastic gravity load analysis, equal to approximately 2 to 3 times the uncracked elastic analyses values. These boundary conditions are achieved through the addition of boundary elements representing vertical and rotational springs along the cut slab panel edges.

4.4.4.1 Mesh Selection

Enclosed slabs within the Core section, the I-E coupling beams and the lintel beams are divided into a 4 by 4 mesh. The two enclosed slab portions within the Elev and Stair sections, and the E-S coupling beams are divided at the Stair flange wall end-coupling beam joint into 2 slab elements each. For the surrounding slabs, the mesh is divided in accordance with the enclosed slabs, the cores and the coupling and lintel beams meshes as shown in Fig. 4.17 for a typical floor level. Element aspect ratios are maintained to values of less than 2.5 and as close to unity as possible.

4.4.4.2 Concrete Layer Systems

Shell elements are divided into 6 concrete layers across the slab thicknesses of 8 *in* and 6 *in* each, resulting in 2 different concrete layer systems (Fig. 4.16).

4.4.4.3 Smeared Reinforcing Steel Layer Systems

Uniformly distributed top and bottom reinforcement in the enclosed and surrounding slabs consist of 2 orthogonal mats of 15M bars at various spacings in the slabs. Four layers of equivalent smeared reinforcement are required in the slab elements, a smeared steel layer for each of the top and bottom (outer and inner mats) uniformly distributed reinforcement located at both slab faces (Fig. 4.16). Values of the equivalent smeared steel layer thicknesses for the different top and bottom slab reinforcement bar spacings used are listed in Table 4.3. There are 7 different sets of uniformly distributed orthogonal reinforcement bar spacing arrangements used in the design of the slabs considered in the nonlinear modeling, as summarized in Table 4.5. Note that the additional top and bottom distributed reinforcement for cracking control due to the seismic action at the critical slab regions, is not included in the modeling.

4.4.5 Characteristics of the Nonlinear Finite Element Model

Details of the three-dimensional nonlinear finite element idealization of the core-slab substructure are given in Figures 4.8 to 4.17 for the core sections, the coupling and lintel beams, and the enclosed and surrounding slabs. The model is characterized as follows:

- 6 degrees of freedom per node = $\Delta_x, \Delta_y, \Delta_z, \theta_x, \theta_y, \theta_z$
- Total number of nodes = 2238
- Total number of concrete and reinforcing steel material properties = 2
- Total number of quadrilateral facet shell plate elements = 2186
- Total number of quadrilateral facet shell elements for the cores = 968
  - 352 elements for the infilled-slab core
  - 352 elements for the elevator core
  - 264 elements for the stairwell core

  * Concrete layer systems = 2
  * Smeared reinforcing steel layer systems = 9
  * Concentrated steel reinforcement bar element systems = 14
    - Bar element arrangements = 2 to 4 bars
- Total number of quadrilateral facet shell elements for the coupling beams = 126
  - 84 elements for the I-E coupling beams
  - 42 elements for the E-S coupling beams

  * Concrete layer systems = 1
  * Smeared reinforcing steel layer systems = 2
  * Concentrated steel reinforcement bar element systems = 2
    - Bar element arrangements = 2 bars
- Total number of quadrilateral facet shell elements for the lintel beams = 84
  * Concrete layer systems = 1
  * Smeared reinforcing steel layer systems = 2
  * Concentrated steel reinforcement bar element systems = 2
    - Bar element arrangements = 2 to 3 bars

- Total number of quadrilateral facet plate elements for the slabs = 1008 (21 floors in total)
  - 420 elements (20 per level) for the enclosed slabs
  - 588 elements (28 per level) for the partial surrounding slabs
  * Concrete layer systems = 2
  * Smeared reinforcing steel layer systems = 7

Boundary conditions consist of: all translations and rotations restrained for the nodes at the base level, horizontal translations Δ_x and Δ_y restrained for the perimeter nodes at the ground level, and all 6 degrees of freedom Δ_x, Δ_y, Δ_z, θ_x, θ_y, θ_z are permitted for all other nodes. For the planar analyses, 3 degrees of freedom are permitted above ground level consisting of Δ_x, Δ_z and θ_y for the PDQX model and Δ_y, Δ_z and θ_x for the PDQY model.

Output from the analyses consists of the nodal deflections and rotations for the entire structure; the axial and shear stresses in the concrete layers of the cores, the coupling and the lintel beams, and the slabs shell/plate elements; and the strains in the concentrated reinforcement bar elements of the core sections.

4.5 Applied Loadings

4.5.1 Earthquake Loads

Earthquake loadings are determined from the interactive shear force distributions in the core sections obtained from the elastic analysis of the core-slab-frame structure (FCS model). The interactive force distributions in the infilled-slab, elevator and stairwell cores are calculated and used as the applied Q_X and Q_Y earthquake loads for the nonlinear analyses, summarized in Tables 4.6 and 4.7. The total interactive earthquake force at a floor level is divided into discrete concentrated loads distributed to the core sections wall ends and corners (nodes) across each floor level in proportion to the tributary floor area supported by each node.

4.5.2 Gravity Loads

Gravity loading consists of the dead and live loads in a typical office building as listed for the elastic analyses. The gravity loads are applied as a pressure over the surface of each slab element and as a self weight on the cores and the coupling and lintel beams.

4.6 Nonlinear Analyses Performed

To study the response of the core-slab substructure subject to earthquake and gravity loads throughout the entire load range until failure, several idealizations of the substructure are derived from the three-dimensional nonlinear finite element model developed in the previous section. The contribution and influence of the core sections, coupling and lintel beams, enclosed and surrounding slabs are studied in terms of the interaction among the various structural components and on the structure response, and the design of the structure is examined. Several loading combinations of the earthquake and the gravity loads are considered in the analyses for strength, serviceability and the ultimate limit state criteria as required by the NBCC (1985) and the CSA Standard CAN3-A23.3-M84 (1984).

The Q_X and Q_Y earthquake loadings are applied as monotonically increasing loads in 30 load increments by increasing the value of the earthquake load factor α_Q from 0.1 to 3.0 – 5.0 (in 30 steps) for an accurate determination of the "failure load" and a well-defined load-deflection response. Tables 4.8 to 4.10 summarize the selected α_Q values for the Q_X and Q_Y earthquake loadings for the various nonlinear analyses.
Details of the nonlinear models and analyses are given in the following sections.

4.6.1 Q_X Earthquake Loading Analyses

The Q_X earthquake loads and dead loads (unless otherwise stated) are applied as:

$$1.25\,D + \alpha_Q\,Q_X$$

1. DQX Model:

   Three-dimensional nonlinear finite element model of the core-slab structure including the cores, coupling and lintel beams, and enclosed and partial surrounding slabs.

2. DQXO Model:

   Model DQX with tension-stiffening response not considered.

3. DQXX Model:

   Model DQX using an alternative arrangement of 2 curtains of 10M bars for the vertical uniformly distributed reinforcement at the maximum spacings throughout the height of the core walls.

4. QX Model:

   Model DQX ignoring the dead loads $\alpha_D = 0$. The applied loading is: $\alpha_Q Q_X$.

5. ESDQX Model:

   Three-dimensional coupled cores, coupling and lintel beams,
   and enclosed slabs substructure model.

   Partial surrounding slabs are eliminated from the model DQX.

6. CCDQX Model:

   Three-dimensional coupled cores, coupling and lintel beams substructure model. Enclosed slabs and partial surrounding slabs are eliminated from the model DQX.

7. PDQX Model:

   Planar idealization of the model DQX in the direction along the core web walls. The flange walls, the coupling and lintel beams, and the enclosed and surrounding slabs are ignored. All of the concentrated reinforcement within the core flange-web wall confined corner regions is placed at the core web wall ends (corners).

8. DLQX Model:

   Model DQX for the factored load combination: $1.25\,D + 0.7(1.5\,L) + \alpha_Q\,Q_X$.

9. DQXU Model:

   Model DQX for the uplift loading condition: $0.85\,D + \alpha_Q\,Q_X$.

4.6.2 Q_Y Earthquake Loading Analyses

The Q_Y earthquake loads and dead loads (unless otherwise stated) are applied as:

$$1.25\,D + \alpha_Q\,Q_Y$$

1. DQY Model:

   Three-dimensional nonlinear finite element model of the core-slab structure including the cores, coupling and lintel beams, and enclosed and partial surrounding slabs.

2. DQYR Model:

   Due to the nonsymmetrical layout of the core sections, the Q_Y earthquake loading is also applied in the reverse direction to the model DQY.

3. QY Model:

   Model DQY ignoring the dead loads $\alpha_D = 0$. The applied loading is: $\alpha_Q Q_Y$.

4. CCDQY Model:

   Three-dimensional coupled cores, coupling and lintel beams substructure model. Enclosed slabs and partial surrounding slabs are eliminated from the model DQY.

5. PDQY Model:

   Planar idealization of the model DQY in the direction along the core flange walls. The web walls, the lintel beams, and the enclosed and surrounding slabs are ignored. All of the concentrated reinforcement within the core flange-web wall confined corner regions is placed at the core flange wall ends and corners.

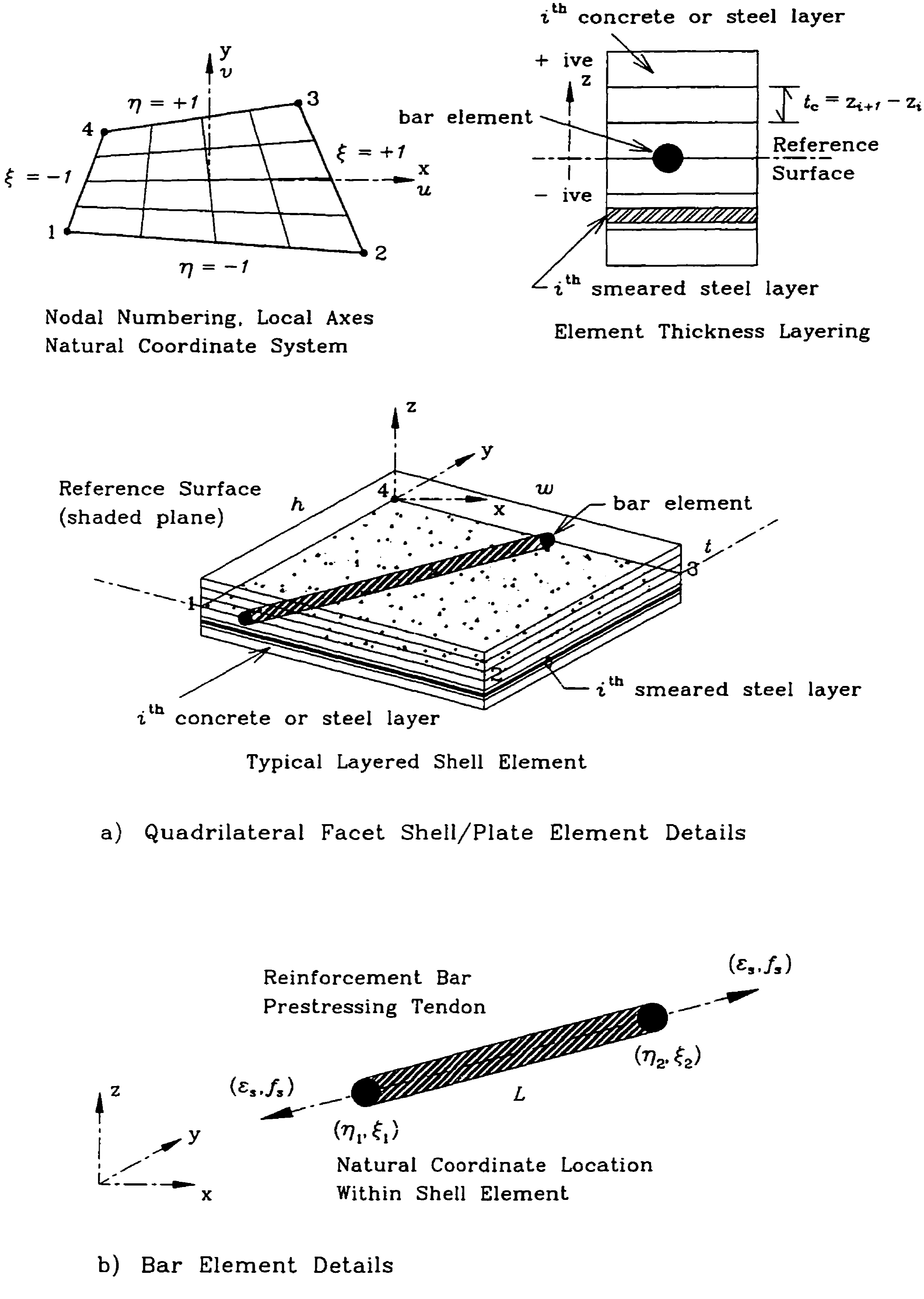

Figure 4.1 Details of the Quadrilateral Facet Shell/Plate and Bar Elements – NONLACS Computer Program

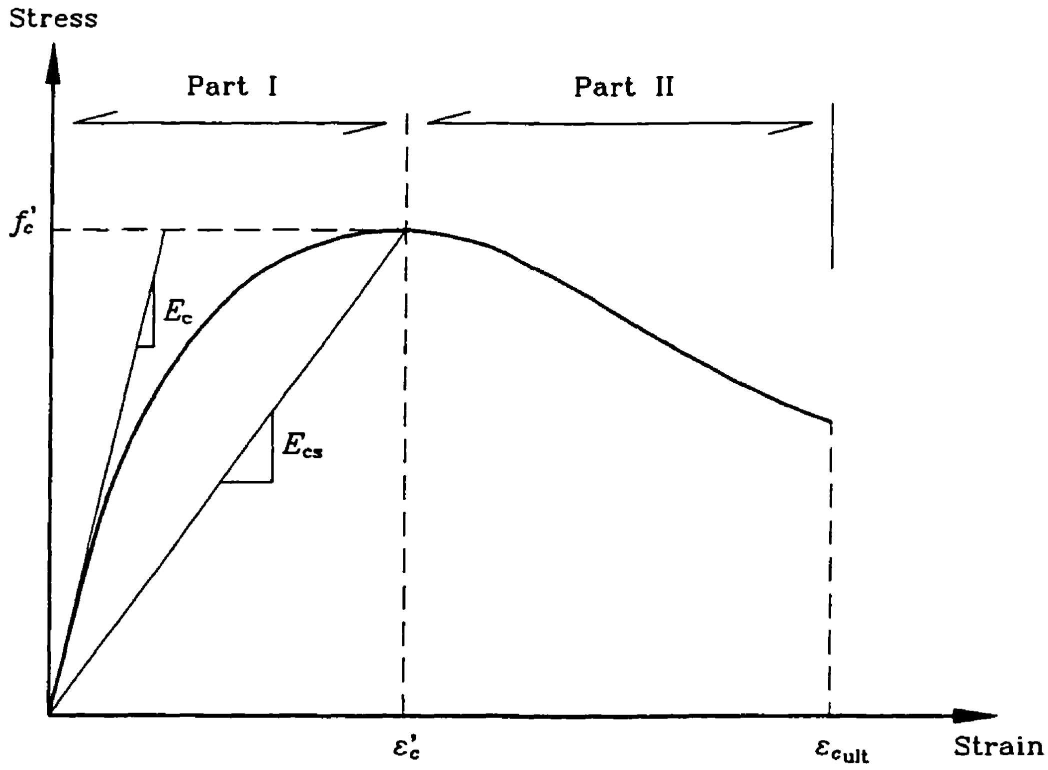

Figure 4.2 Uniaxial Compressive Stress-Strain Curve for Concrete – NONLACS Computer Program

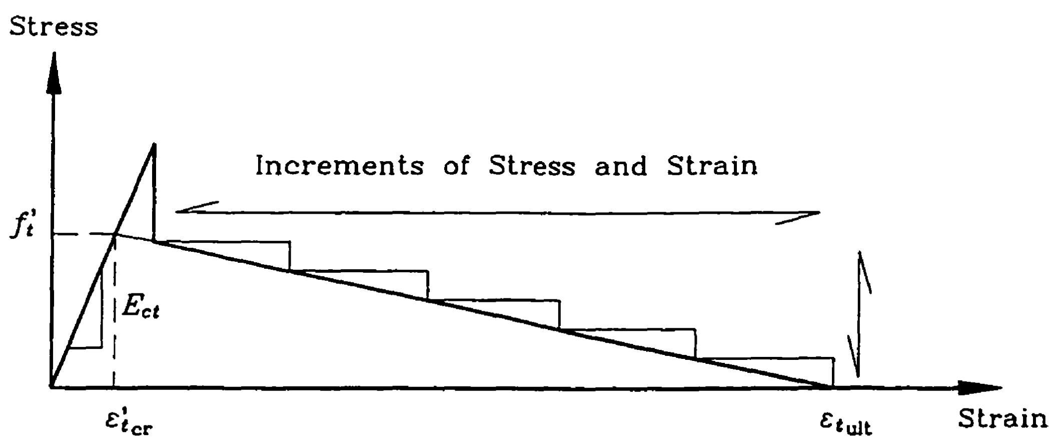

Figure 4.3 Uniaxial Tensile Stress-Strain Curve for Concrete – NONLACS Computer Program

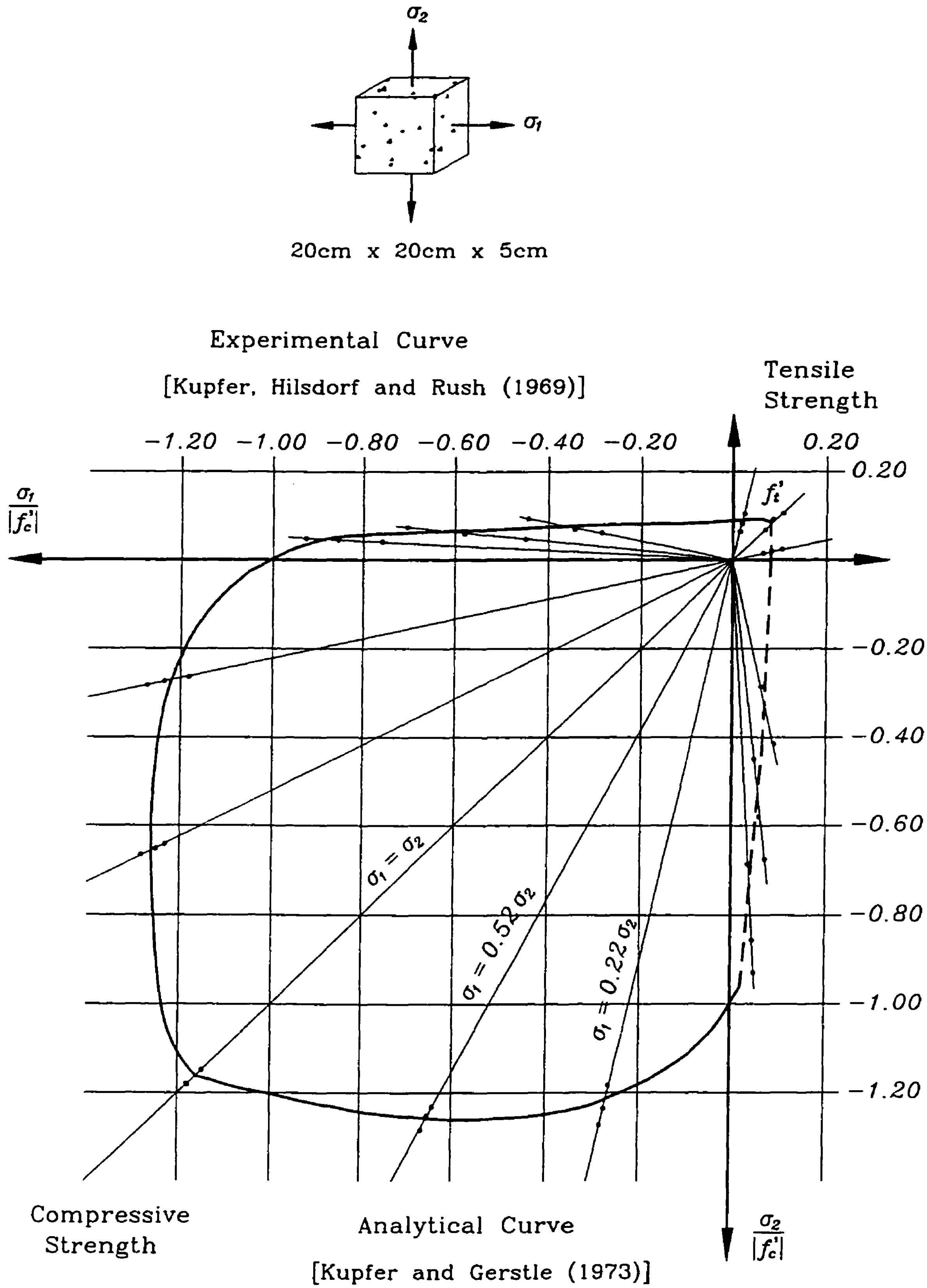

Figure 4.4 Failure Envelope for Concrete Subjected to Biaxial Stresses
– NONLACS Computer Program

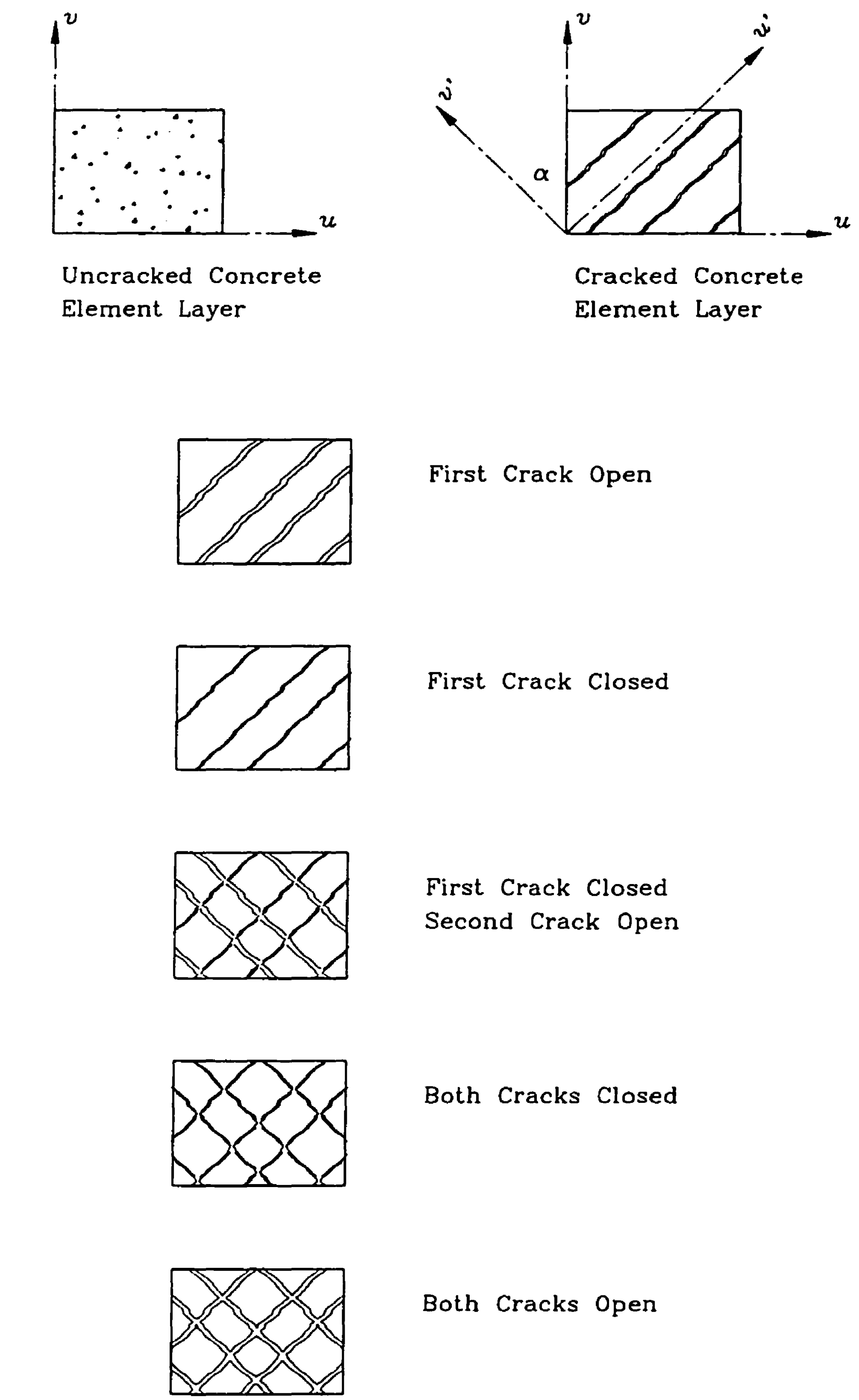

Figure 4.5 Modeling of Concrete Cracking - NONLACS Computer Program

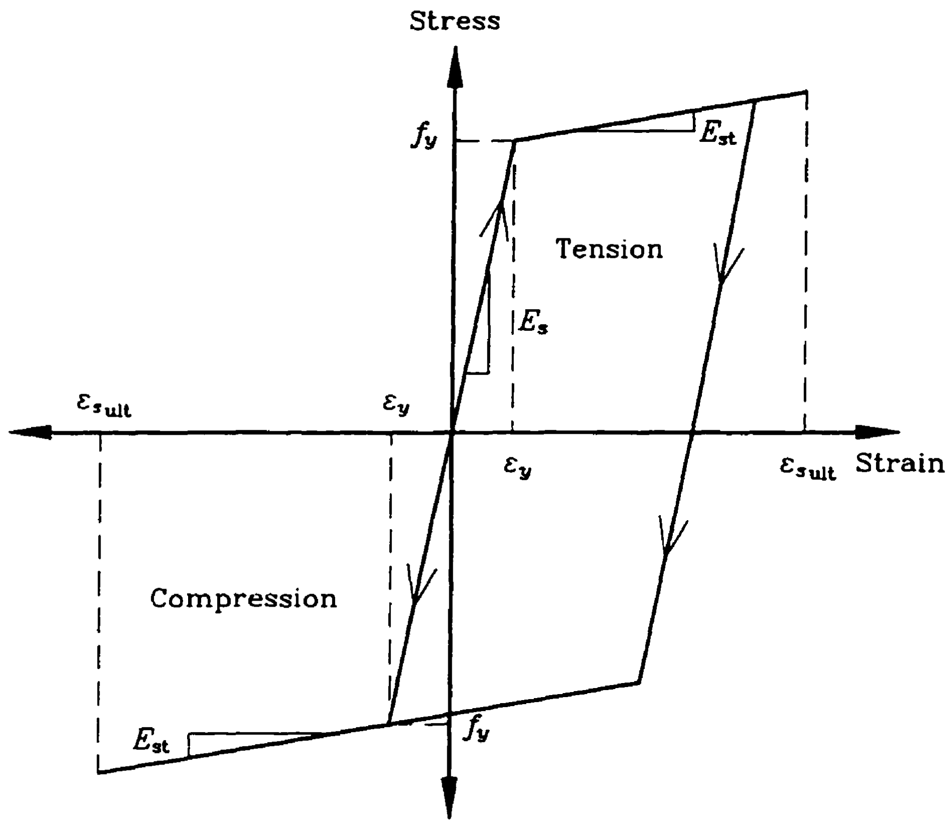

Figure 4.6 Stress-Strain Characteristics for Reinforcing Steel – NONLACS Computer Program

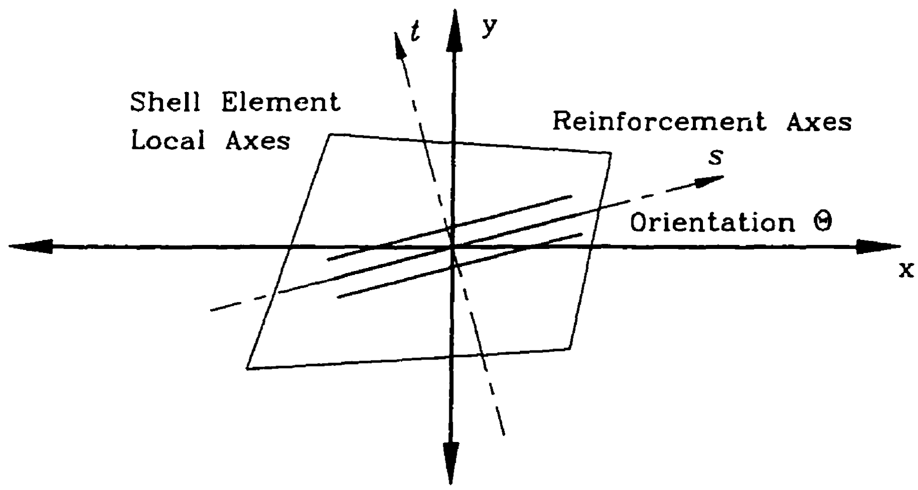

Figure 4.7 Modeling of Uniformly Distributed Reinforcement as Smeared Steel Layers – NONLACS Computer Program

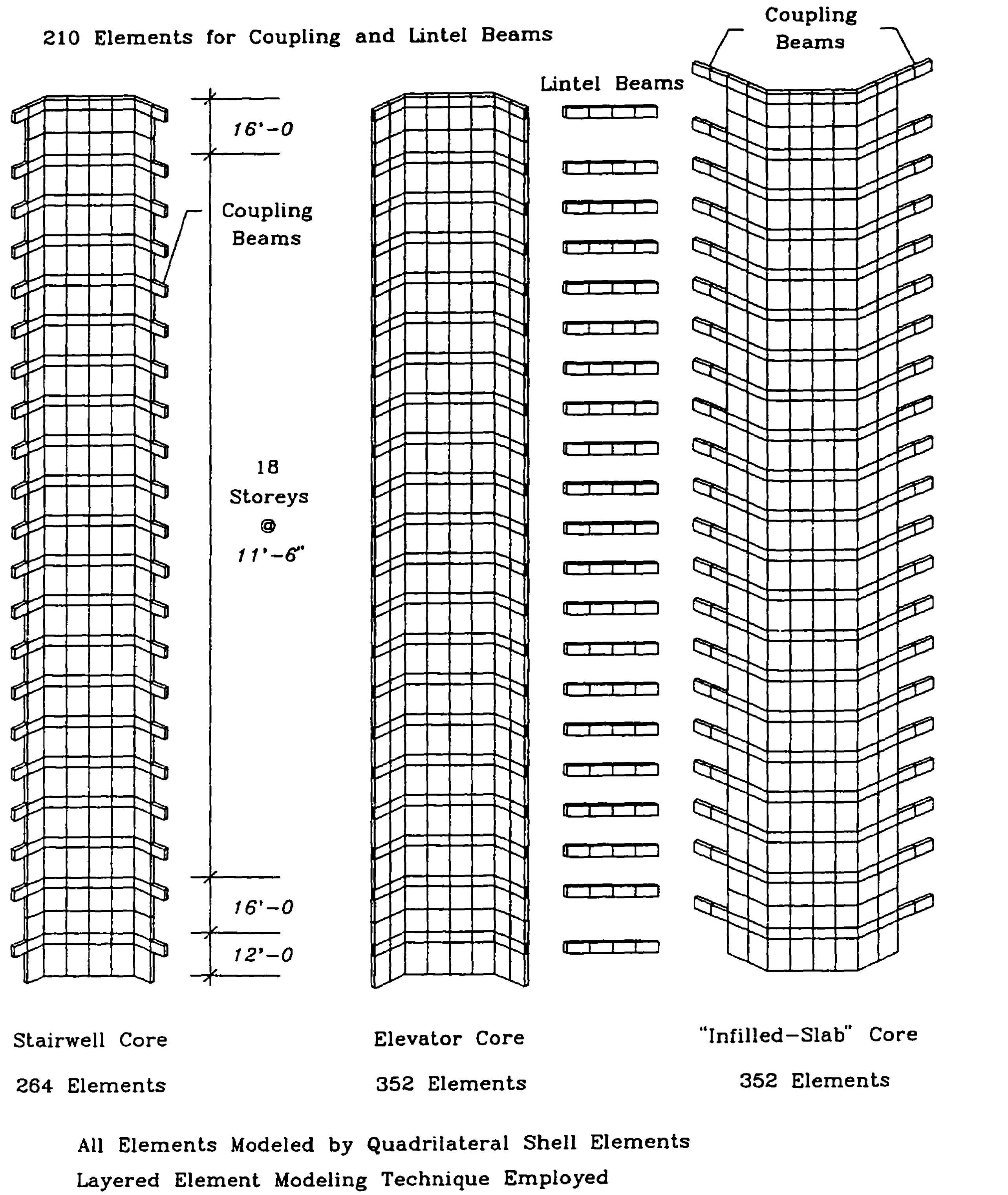

Figure 4.8 Nonlinear Finite Element Modeling Details of the Cores Substructure – Elevational View

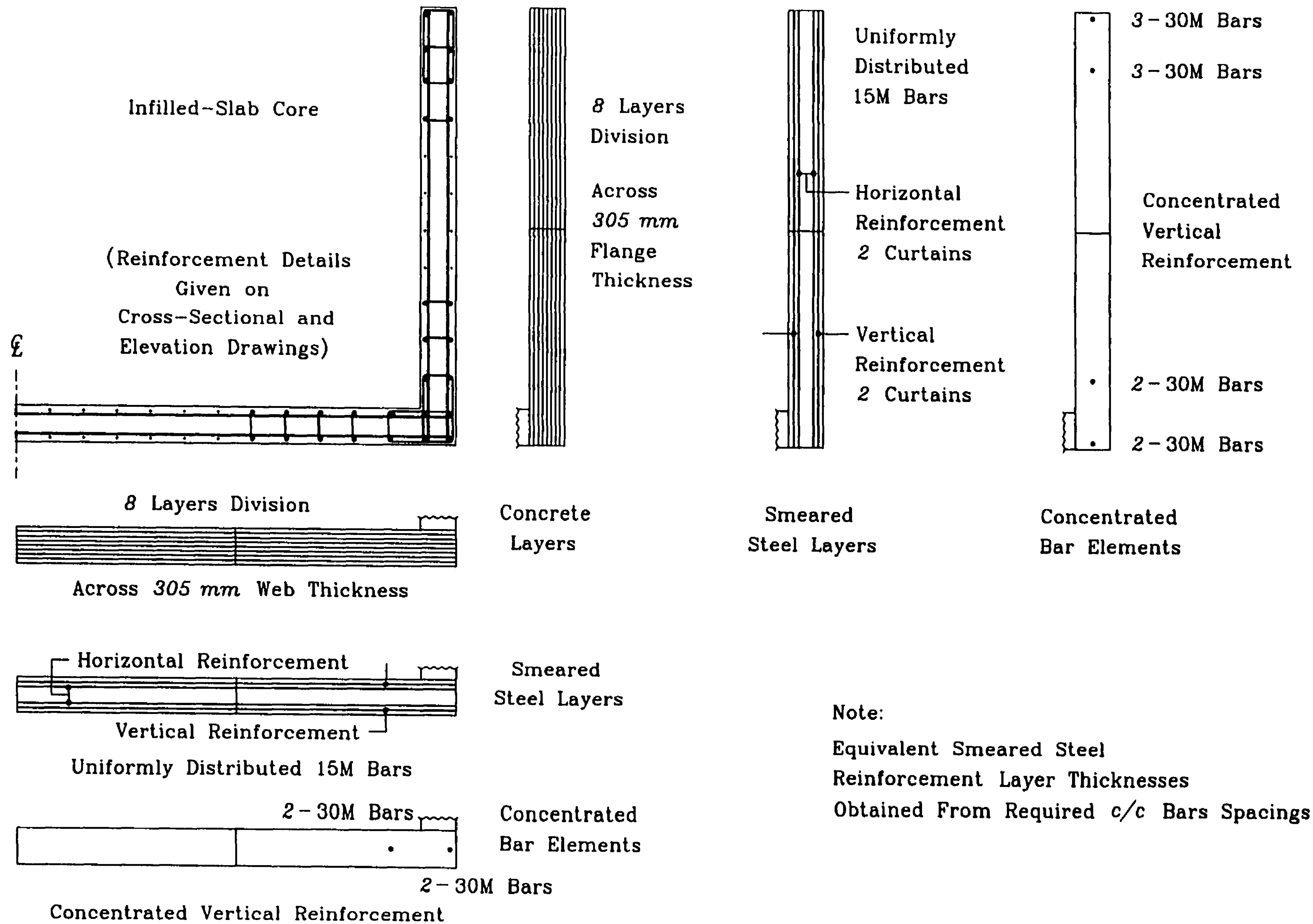

Figure 4.9 Concrete and Reinforcing Steel Modeling Details for the Infilled-Slab Core – Cross-sectional Views at the Base Region

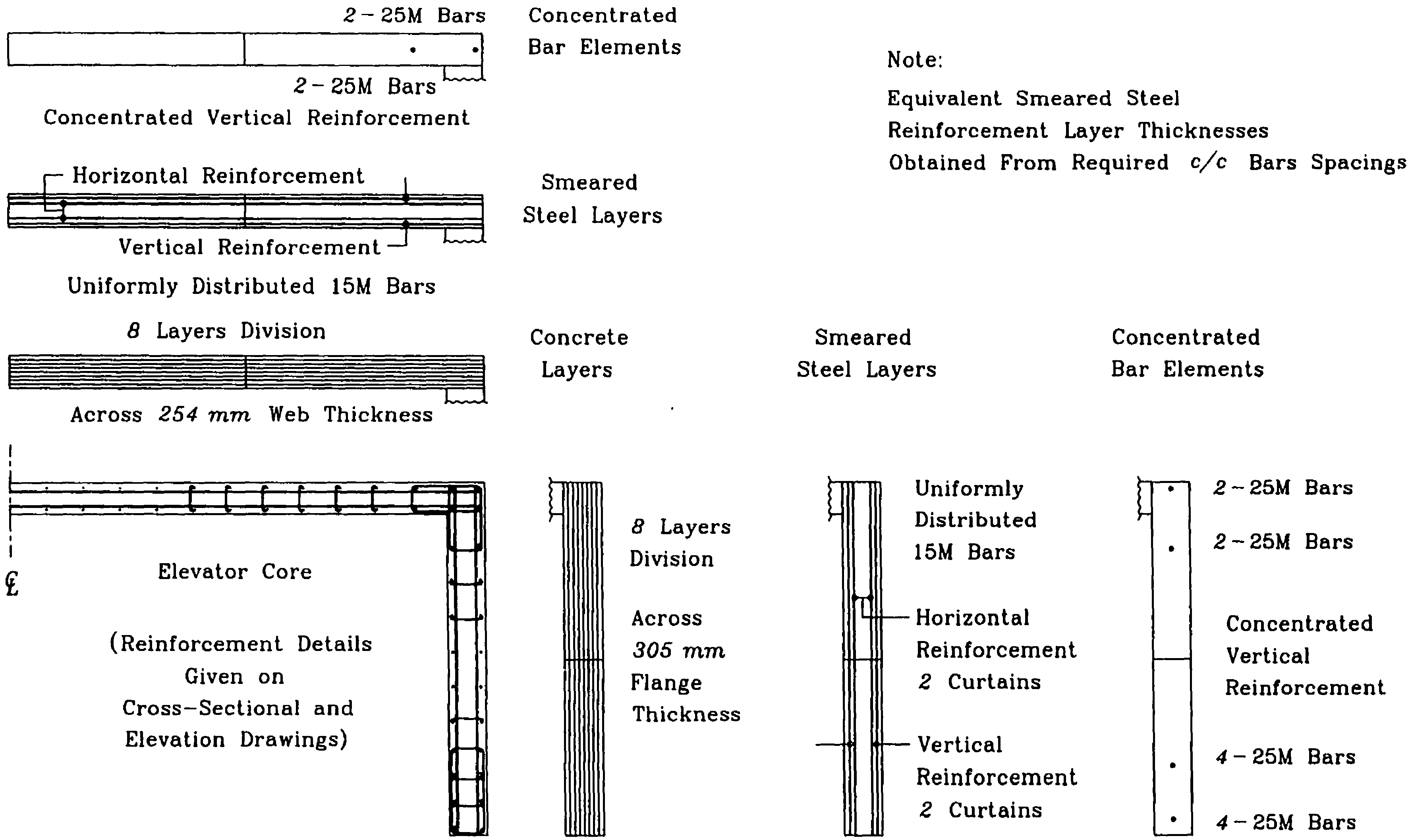

Figure 4.10 Concrete and Reinforcing Steel Modeling Details for the Elevator Core – Cross-sectional Views at the Base Region

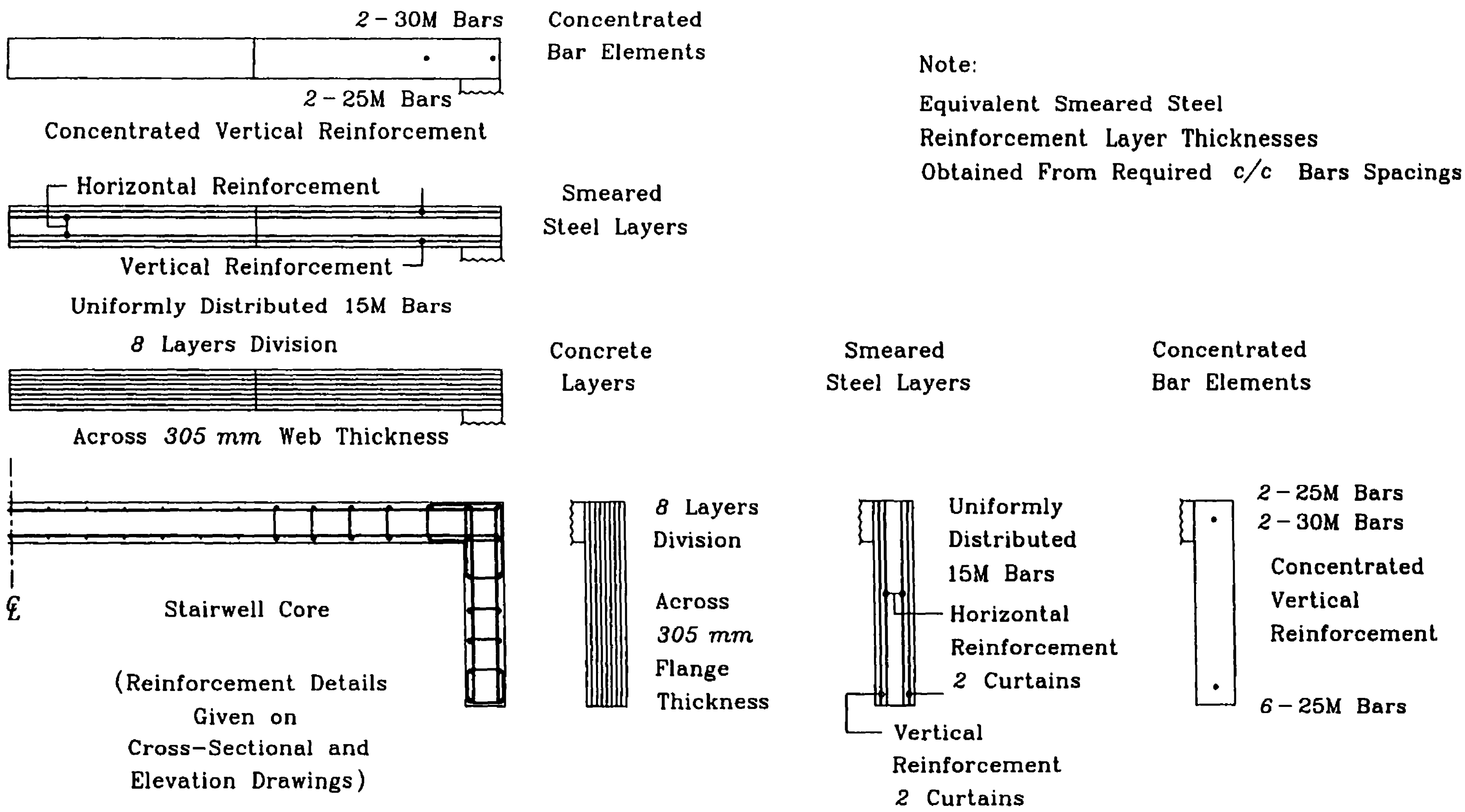

Figure 4.11 Concrete and Reinforcing Steel Modeling Details for the Stairwell Core – Cross-sectional Views at the Base Region

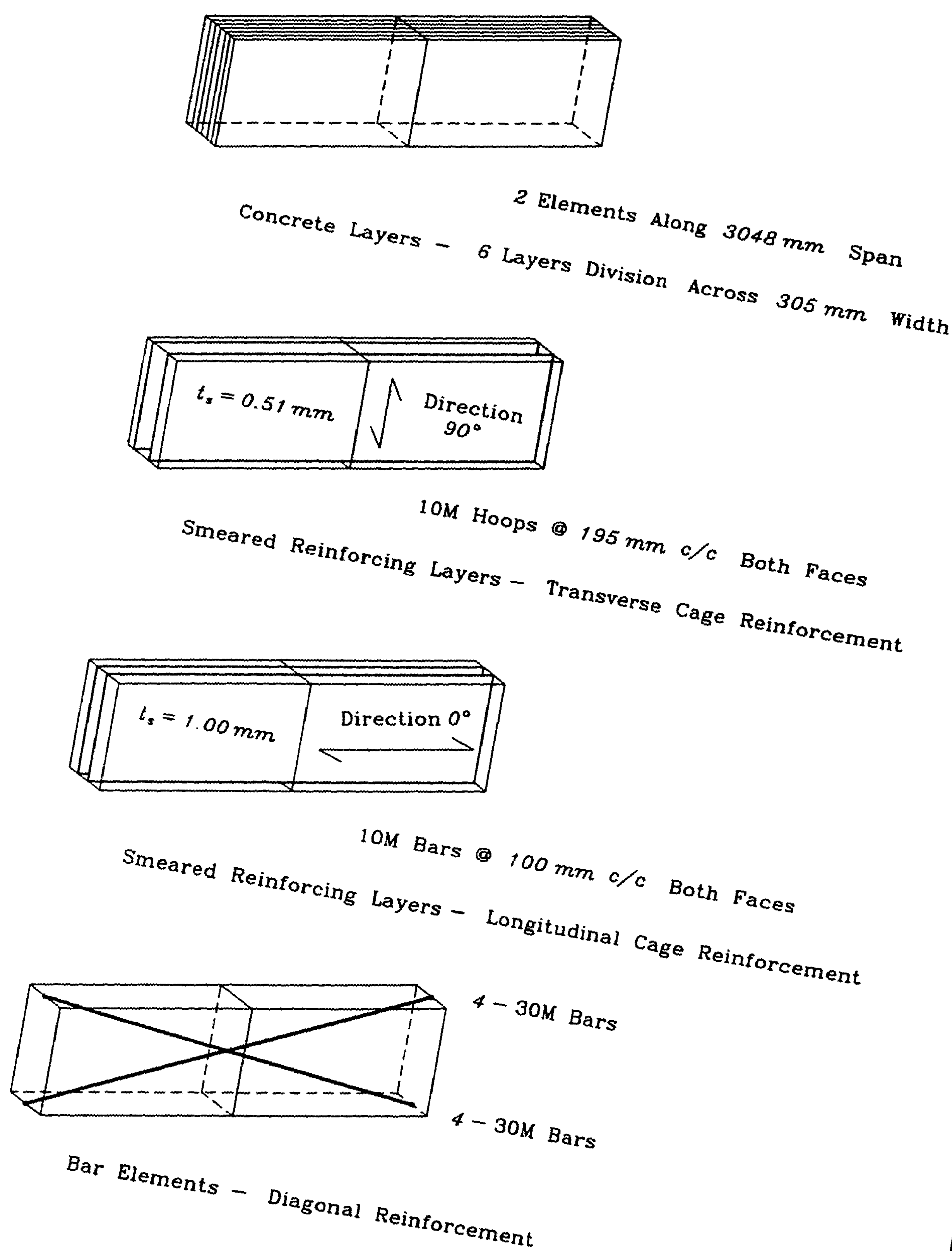

Figure 4.12 Concrete and Reinforcing Steel Modeling Details for the I-E Coupling Beams

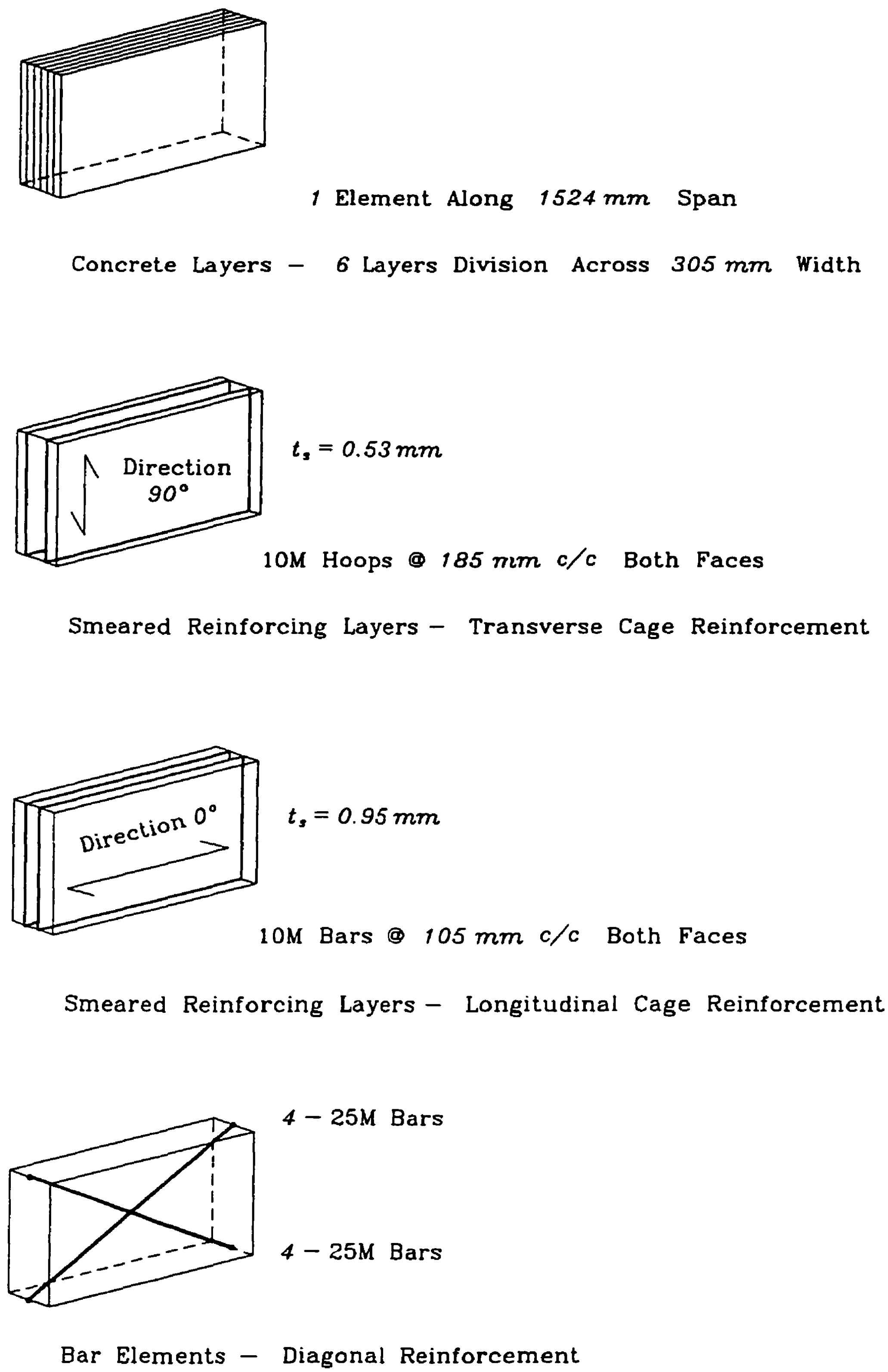

Figure 4.13 Concrete and Reinforcing Steel Modeling Details for the E-S Coupling Beams

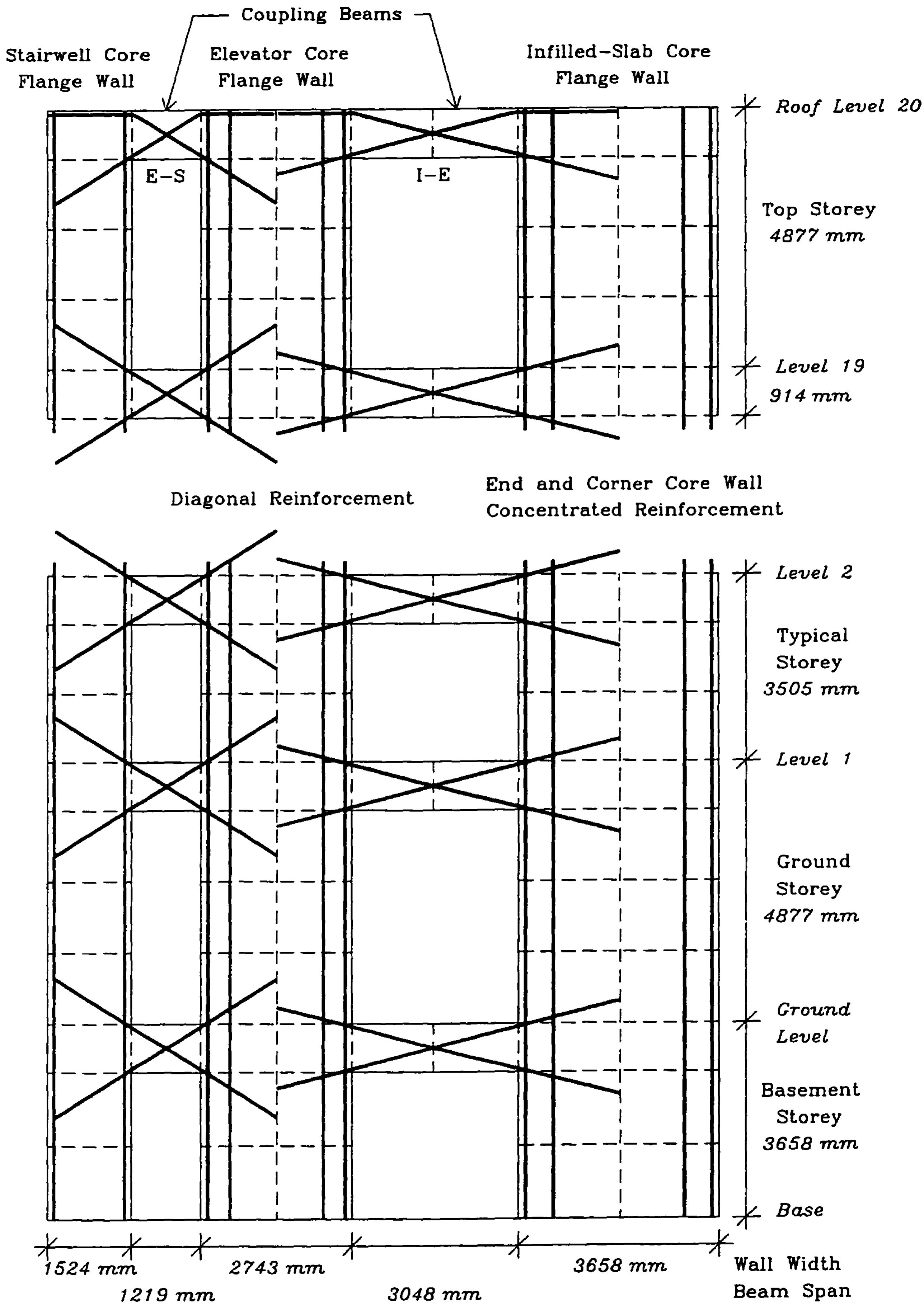

Figure 4.14 Modeling Details of the I-E and E-S Coupling Beam Diagonal Reinforcement within the Core Sections Flange Walls – Lower and Top Storeys

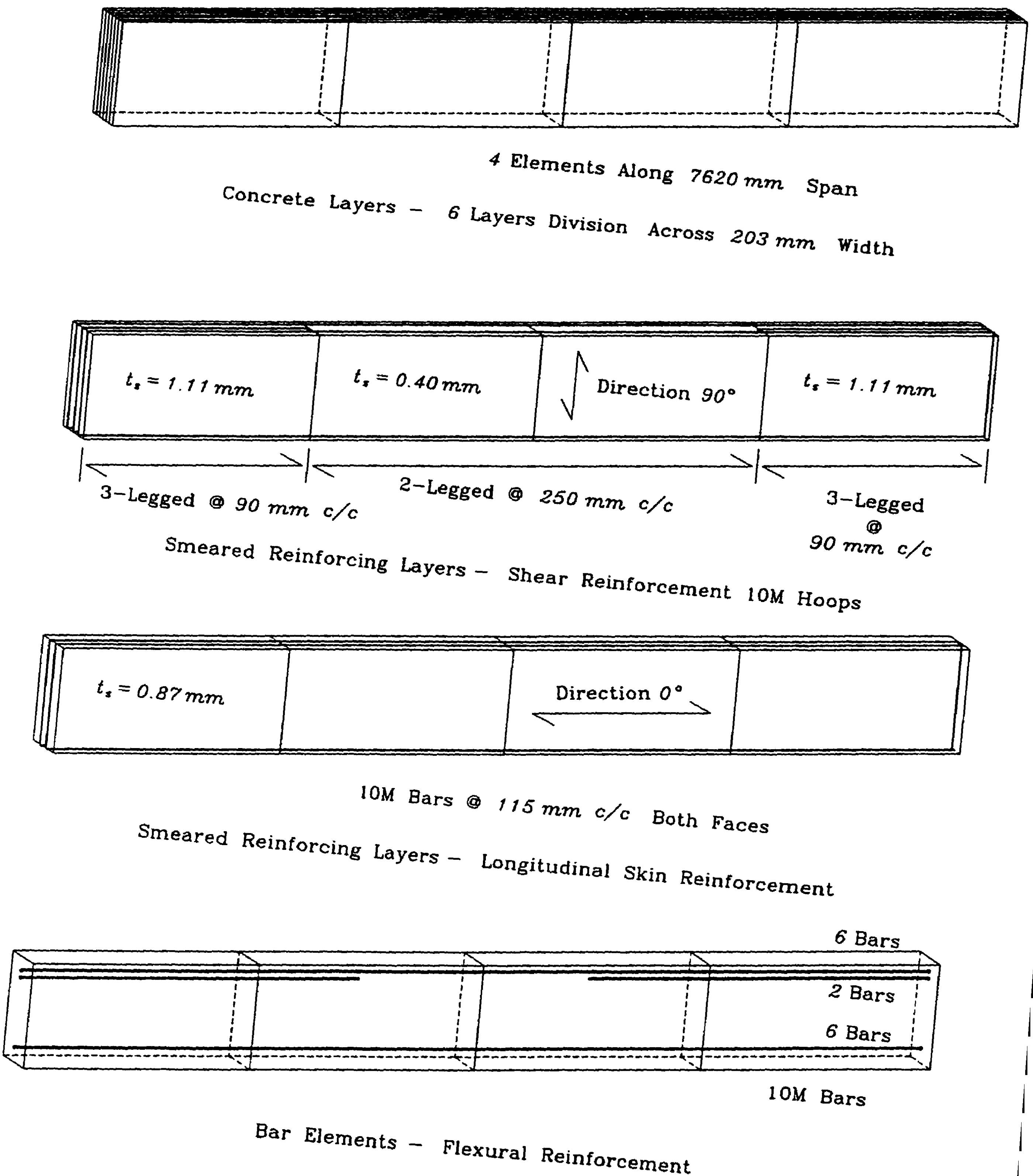

Figure 4.15 Concrete and Reinforcing Steel Modeling Details for the Lintel Beams

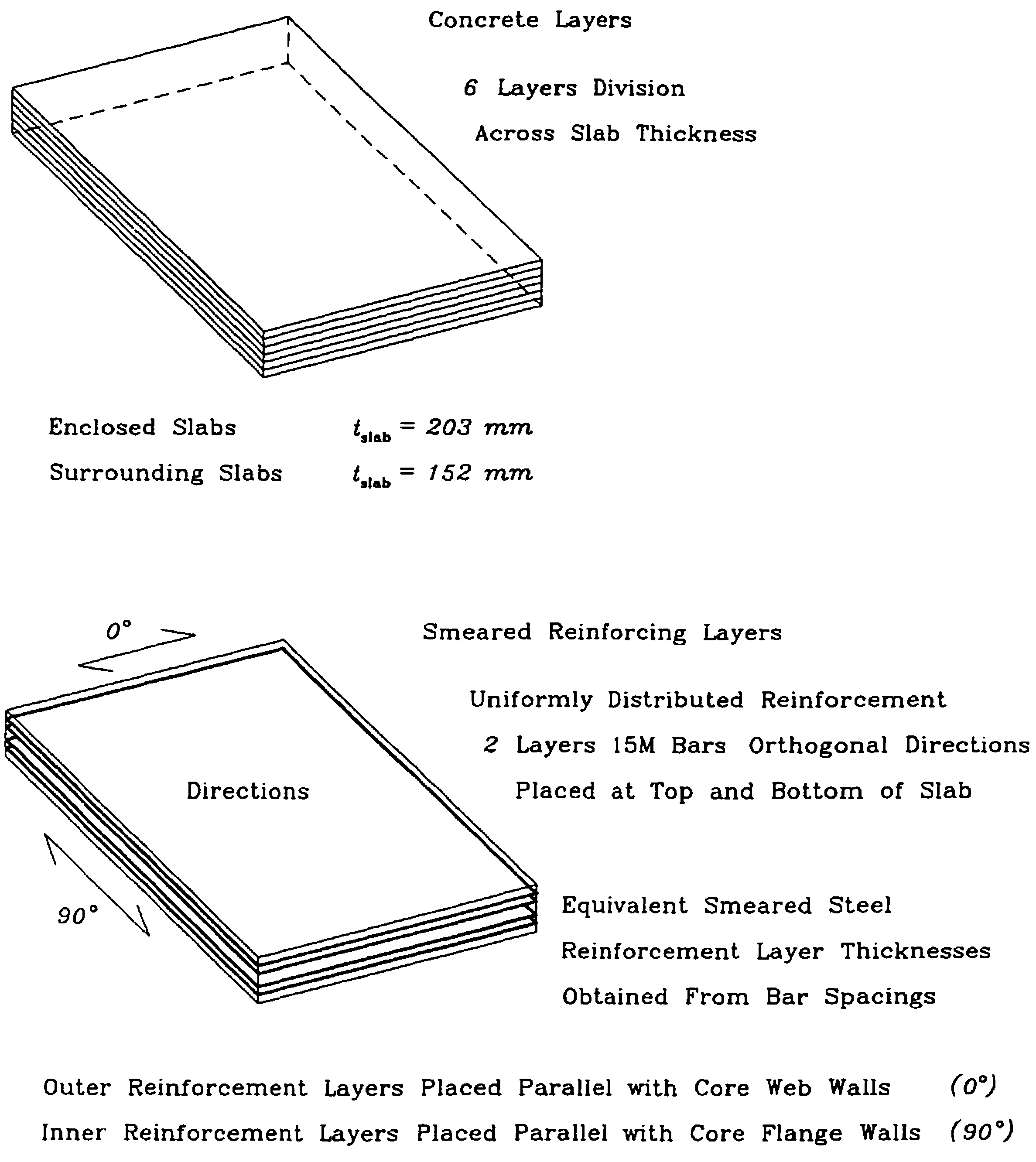

Figure 4.16 Concrete Element and Smeared Steel Layer Modeling Details for the Slabs

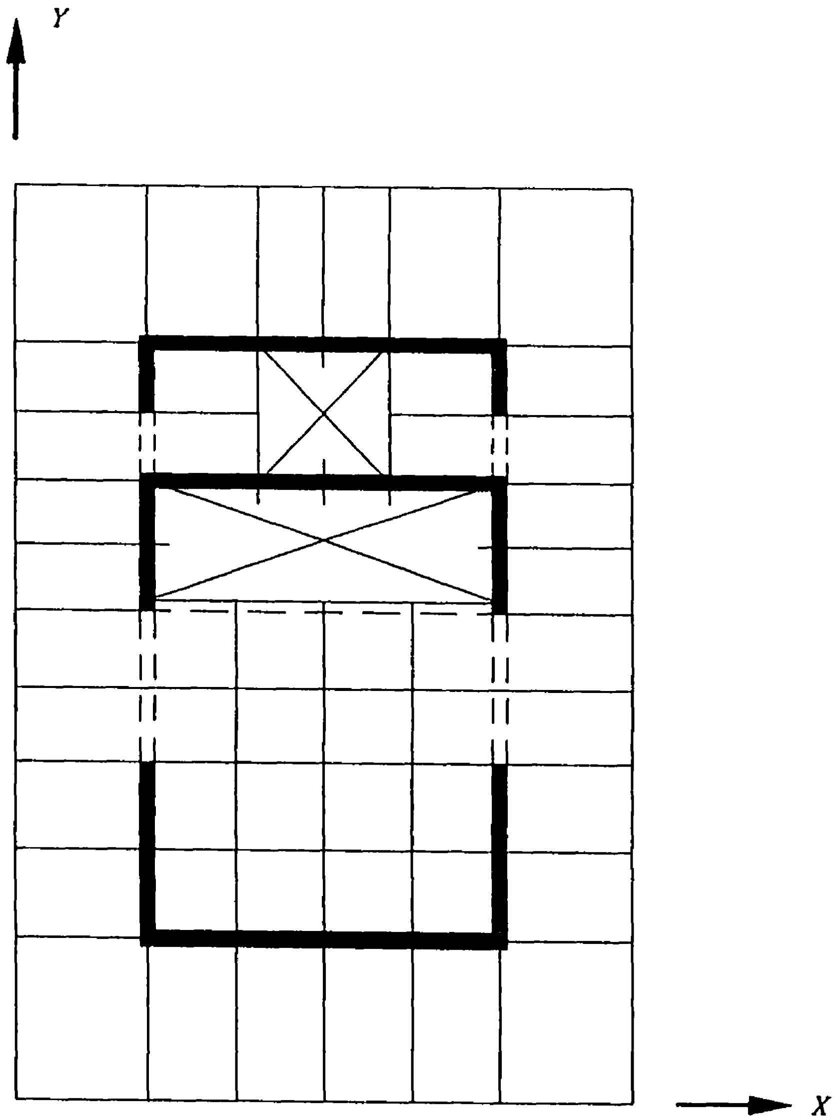

Details
per Floor Level:

73 Nodes

54 Quadrilateral
Plate Elements:

20 for Enclosed Slab
28 for Surrounding Slab
1 per Elevator–Stair Coupling Beam
2 per Core–Elevator Coupling Beam

Modeling Details of
Cores and Beams
Given on Accompanying Figures

Slab Mesh Similar to that
Selected for Elastic Analyses

Coupled Cores – Enclosed and Surrounding Slabs Model

Figure 4.17 Nonlinear Finite Element Modeling Details of the Coupled Cores-Enclosed and Surrounding Slabs Structure – DQX and DQY Models Typical Floor Level

Table 4.1: Concrete Constitutive Material Properties: Nonlinear Finite Element Analyses

Concrete Property			Theoretical Value	Range of Values	Value Used
Normal Density Concrete	γ_c	=	$2400\,kg/m^3$ $(150\,lb/ft^3)$		$2400\,kg/m^3$
Poisson's Ratio	ν	=		0.15 to 0.22	0.17
Compressive Strength	f_c'	=			$30\,MPa$
Young's Modulus in Compression	E_c	=	$5000\sqrt{f_c'}$ (MPa)		$27{,}386\,MPa$
Young's Modulus in Tension	E_{ct}	=	$5500\sqrt{f_c'}$ (MPa)		$30{,}125\,MPa$
Shear Modulus of Elasticity	G	=	$E/2(1+\nu)$ (MPa)		$11{,}703\,MPa$
Shear Retention Factor	β	=		0.10 to 0.50 – 1.00	0.50
Maximum Compressive Strain	ϵ_c'	=		0.002 to 0.0025	0.0020
Ultimate Compressive Strength	$f_{c_{ult}}$	=	0.80 to $0.85f_c'$	$24\,MPa$ to $25.5\,MPa$	$24\,MPa$
Ultimate Compressive Strain	$\epsilon_{c_{ult}}$	=		0.003 to 0.0080 – 0.012	0.0045
Maximum Tensile Strength	f_t'	=	0.04 to 0.10 – $0.15f_c'$	$1.20\,MPa$ to 3.00 – $4.50\,MPa$	$3.40\,MPa$
Direct Tensile Strength	f_t'	=	$0.33\sqrt{f_c'}$ (MPa)	$1.81\,MPa$	–
Split Cylinder Tensile Strength	f_{ct}	=	$0.5\sqrt{f_c'}$ to $0.6\sqrt{f_c'}$ (MPa)	$2.74\,MPa$ to $3.29\,MPa$	–
Modulus of Rupture	f_{rt}	=	$0.62\sqrt{f_c'}$ (MPa)	$3.40\,MPa$	–
Maximum Tensile Strain	$\epsilon_{t_{cr}}$	=	f_t'/E_{ct}		0.000113
Ultimate Tensile Strain	$\epsilon_{t_{ult}}$	=	6 to 10 – $30\epsilon_{t_{cr}}$	0.000125 to 0.003 – 0.012	0.000675

Table 4.2: Steel Reinforcement Constitutive Material Properties: Nonlinear Finite Element Analyses

Steel Reinforcement Property	Theoretical Value			Range of Values	Value Used
Poisson's Ratio	ν	=	0.30		0.30
Elastic Modulus of Elasticity	E_s	=	200,000 MPa		200,000 MPa
Strain-Hardening Modulus of Elasticity	E_{st}	=	E_s/E_{st} = 40 to 42	5,000 MPa to 4,762 MPa	4,762 MPa
Tensile Yield Strength	f_y	=		200 MPa to 400 MPa	400 MPa
Tensile Yield Strain	ϵ_y	=	$\epsilon_y = f_y/E_s$		0.0020
Maximum Tensile Yield Strain Range	$\epsilon_{st_{max}}$	=	8 to 15 – 20ϵ_y	0.0160 to 0.0300 – 0.0400	0.0250
Maximum Tensile Yield Strength	$f_{s_{max}}$	=	1.25 to 2.0f_y = 1.55f_y	500 MPa to 800 MPa = 620 MPa	620 MPa
Ultimate Tensile Strain	$\epsilon_{s_{ult}}$	=	50 to 250 – 300ϵ_y = 0.125	0.1000 to 0.5000 – 0.6000	0.1250

Table 4.3: Equivalent Smeared Reinforcement Layer Thicknesses: Nonlinear Finite Element Modeling – Cores and Slabs

Bar Spacings (mm) c/c	Equivalent Smeared Steel Layer Thickness t_{s_i} (mm) 15M Bars	10M Bars
100	2.0000	–
150	1.3333	–
200	1.0000	–
250	0.8000	0.4000
300	0.6667	0.3333
350	0.5714	–
400	0.5000	–

Table 4.4: Bar Spacing Arrangements for 15M Bars: – Cores Design

Set #	Bar Mesh Spacing Vertical (mm)	×	Horizontal (mm)	Core Wall Thickness (mm)
1	300	×	150	305
2	300	×	200	305
3	300	×	250	305
4	300	×	300	305
5	300	×	300	254
6	400	×	350	305
7	400	×	350	254
8	400	×	400	305
9	400	×	400	254

Table 4.5: Bar Spacing Arrangements for 15M Bars: – Enclosed and Partial Surrounding Slabs Design

Set #	Bar Mesh Spacing (mm)	×	(mm)
1	400	×	400
2, 3	300	×	300
4, 5	250	×	250
6	200	×	200
7	150	×	150

Table 4.6: Core-Slab-Frame Structure:
Q_X Earthquake Loading – FCS Model
Interactive Force Distributions in the Cores

	Interactive Shear Forces in Cores Q_X Earthquake Loading		
Floor Level	Infilled-Slab Core (N)	Elevator Core (N)	Stairwell Core (N)
20	-229,840	-173,970	-156,706
19	+54,393	+23,971	+31,538
18	107,149	67,404	68,569
17	129,643	114,666	90,010
16	94,471	76,291	57,097
15	88,471	71,118	51,986
14	83,155	66,505	47,872
13	78,524	62,453	44,883
12	74,432	59,415	42,138
11	70,749	56,826	40,141
10	68,022	55,029	38,526
9	69,797	53,899	41,137
8	70,753	53,339	42,765
7	70,340	53,339	43,383
6	70,478	53,904	44,878
5	70,615	55,251	47,498
4	70,753	58,739	52,758
3	72,248	55,589	61,710
2	103,603	48,050	89,512
1	130,600	9,226	116,566

Table 4.7: Core-Slab-Frame Structure :
Q_Y Earthquake Loading – FCS Model
Interactive Force Distributions in the Cores

Floor Level	Interactive Shear Forces in Cores Q_Y Earthquake Loading Infilled-Slab Core (N)	Elevator Core (N)	Stairwell Core (N)
20	-125,289	+129,594	-55,727
19	+7,998	-29,056	+27,414
18	96,233	+49,927	49,771
17	83,324	44,736	34,910
16	69,944	38,277	34,589
15	60,878	33,784	33,949
14	53,961	29,977	32,730
13	48,116	26,978	31,516
12	43,504	24,096	30,106
11	39,509	21,445	28,762
10	36,435	19,025	27,414
9	33,820	17,063	26,004
8	32,436	14,759	24,470
7	32,592	13,260	22,548
6	35,052	30,324	19,919
5	40,279	49,807	16,272
4	51,346	60,647	12,233
3	84,396	77,595	+1,415
2	295,931	150,812	-18,963
1	404,619	361,458	+73,151

Table 4.8: Core-Slab Substructure:
Nonlinear Finite Element Analyses – Design
Load Factor Increments α_Q for Q_X Earthquake Loading

Load Step	Core-Slab Substructure Models α_{Q_X} Load Factor Increments				
	DQX	QX	ESQX	CCQX	PDQX
1	0.25	0.10	0.25	0.25	0.10
2	0.50	0.20	0.50	0.50	0.20
3	0.75	0.25	0.75	0.75	0.25
4	1.00	0.30	1.00	1.00	0.30
5	1.10	0.40	1.10	1.10	0.40
6	1.25	0.50	1.25	1.25	0.50
7	1.40	0.60	1.40	1.40	0.60
8	1.50	0.70	1.50	1.50	0.70
9	1.60	0.75	1.60	1.60	0.75
10	1.75	0.80	1.75	1.75	0.80
11	1.90	0.90	1.90	1.90	0.90
12	2.00	1.00	2.00	2.00	1.00
13	2.10	1.10	2.10	2.10	1.10
14	2.20	1.20	2.20	2.20	1.20
15	2.25	1.25	2.25	2.25	–
16	2.30	1.30	2.30	2.30	–
17	2.40	1.40	2.40	2.40	–
18	2.50	1.50	2.50	2.50	–
19	2.60	1.60	2.60	2.60	–
20	2.70	1.70	2.70	2.70	–
21	2.75	–	2.75	2.75	–
22	2.80	–	2.80	2.80	–
23	2.90	–	2.90	2.90	–
24	3.00	–	3.00	3.00	–
25	3.10	–	3.10	3.10	–
26	3.20	–	3.20	3.20	–
27	3.30	–	3.30	–	–
28	3.40	–	3.40	–	–
29	–	–	–	–	–
30	–	–	–	–	–

Table 4.9: Core-Slab Substructure:
Nonlinear Finite Element Analyses
Load Factor Increments α_Q for Q_X Earthquake Loading

Load Step	Core-Slab Substructure Models α_{Q_X} Load Factor Increments DQXO	DQXX	DLQX	DQXU
1	0.25	0.25	0.25	0.25
2	0.50	0.50	0.50	0.50
3	0.75	0.75	0.75	0.75
4	1.00	1.00	1.00	1.00
5	1.10	1.10	1.10	1.10
6	1.25	1.25	1.25	1.25
7	1.40	1.40	1.40	1.40
8	1.50	1.50	1.50	1.50
9	1.60	1.60	1.60	1.60
10	1.75	1.75	1.75	1.75
11	1.90	1.90	1.90	1.90
12	2.00	2.00	2.00	2.00
13	2.10	2.10	2.10	2.10
14	2.20	2.20	2.25	2.20
15	2.25	2.25	2.40	2.25
16	2.30	2.30	2.50	2.30
17	2.40	2.40	2.60	2.40
18	2.50	2.50	2.75	2.50
19	2.60	2.60	2.90	2.60
20	2.70	2.70	3.00	2.70
21	2.75	2.75	3.10	2.75
22	2.80	2.80	3.20	2.80
23	2.90	2.90	3.30	2.90
24	3.00	3.00	3.40	3.00
25	3.10	3.10	3.50	3.10
26	3.20	–	3.60	–
27	3.30	–	3.70	–
28	3.40	–	3.80	–
29	–	–	3.90	–
30	–	–	4.00	–

Table 4.10: Core-Slab Substructure:
Nonlinear Finite Element Analyses
Load Factor Increments α_Q for Q_Y Earthquake Loading

Load Step	Core-Slab Substructure Models α_{Q_Y} Load Factor Increments DQY	DQYR	QY	CCQY	PDQY
1	0.25	0.25	0.25	0.25	0.10
2	0.50	0.50	0.50	0.50	0.20
3	0.75	0.75	0.75	0.75	0.25
4	1.00	1.00	1.00	1.00	0.30
5	1.25	1.25	1.10	1.25	0.40
6	1.50	1.50	1.25	1.50	0.50
7	1.75	1.75	1.40	1.75	0.60
8	2.00	2.00	1.50	2.00	0.70
9	2.25	2.25	1.60	2.25	0.75
10	2.50	2.50	1.75	2.50	0.80
11	2.75	2.75	1.90	2.75	0.90
12	3.00	3.00	2.00	3.00	1.00
13	3.25	3.25	2.10	3.25	1.10
14	3.50	3.50	2.20	3.50	1.20
15	3.75	3.75	2.25	3.75	1.25
16	4.00	4.00	2.30	4.00	1.30
17	4.25	4.25	2.40	4.10	1.40
18	4.50	4.50	2.50	4.25	1.50
19	4.75	4.75	2.60	4.40	1.60
20	5.00	4.80	2.70	4.50	1.70
21	5.25	4.90	2.75	4.60	1.75
22	5.50	5.00	2.80	4.70	1.80
23	5.75	5.10	2.90	–	1.90
24	5.80	–	–	–	–
25	5.90	–	–	–	–
26	–	–	–	–	–
27	–	–	–	–	–
28	–	–	–	–	–
29	–	–	–	–	–
30	–	–	–	–	–

Chapter 5

Linear Elastic Analysis Results – Discussion

Linear elastic analysis results of the core-slab-frame structure subject to Q_X and Q_Y earthquake loads and gravity loads are presented for the total and the inter-storey drift and twist profiles along the structure height. Distributions of the in-plane transverse axial stresses S_{xx}, the longitudinal axial stresses S_{yy} and the shear stresses S_{xy}, the transverse moments M_{xx}, the longitudinal moments M_{yy} and the twisting moments M_{xy} are plotted at the ground level in the infilled-slab (Core), elevator (Elev) and stairwell (Stair) core sections (for the stresses), and in the the enclosed slabs (E-slabs) and the surrounding slabs (S-slabs), referred to as E-S-slabs for both, across the core-slab junctions (locations of largest values) as predicted by the various analyses due to Q_X and Q_Y earthquake loads and dead loads.

Three-dimensional distributions consisting of "*Bird's Eye*" and "*Worm's Eye*" views, and topographical contours of the in-plane transverse axial stresses S_{xx}, the longitudinal axial stresses S_{yy}, the shear stresses S_{xy}, the transverse moments M_{xx}, the longitudinal moments M_{yy} and the twisting moments M_{xy} are plotted throughout the height of the Core, Elev and Stair sections, and in the S-E-slabs at the ground level (locations of largest values) as predicted by the FCS model due to Q_X and Q_Y earthquake loads and dead loads.

The structure response is examined and discussed in terms of the comparison of the different computer models and the individual behaviour of the various structural components for their influence on the structural behaviour. In the discussions, interaction of the cores substructure components consists of the three-dimensional coupling and stiffening actions that occur between the cores, beams and slabs.

More detailed discussions of the linear elastic analysis results for the core-slab-frame structure under investigation can be found in the report by Manatakos and Mirza (1995).

5.1 Core-Slab-Frame Structure Deformations due to Q_X Earthquake Loading

5.1.1 Drifts

Two different drift responses are observed in Fig. 5.1, showing a flexural behaviour with the majority of the deformations in the lower 4 to 5 storeys. Maximum drifts at the top are:

	Drift (mm)			
Level	FCS	ESC	SSC	LFCS
top	$50\,mm$	$73\,mm$	$51\,mm$	$73\,mm$

ESC and LFCS models predict a similar response with a top drift of $73\,mm$ indicating that ignoring the S-slabs flexural actions gives a behaviour similar to that of also ignoring the interaction of the E-slabs, the coupling and lintel beams. FCS and SSC models show similar profiles giving a top drift of approximately $51\,mm$, with FCS model response being slightly stiffer. A much stiffer response is noted for FCS and SSC models compared to ESC and LFCS models with a 46% increase for the top drift in the latter models, $51\,mm$ vs $73\,mm$, respectively.

Eliminating the effects of the E-slabs, coupling and lintel beams resulting in a linked cores substructure coupled to frames substructure (SSC model) has no major impact on the drift response. However, ignoring the S-slabs flexural actions (ESC model) resulting in a coupled cores linked to frames structure, and in addition eliminating the effects of the E-slabs, the coupling and lintel beams (LFCS model) giving a linked core-slab-frame structure, significantly reduces the structure lateral stiffness by as much as 35%.

5.1.2 Inter-Storey Drifts

Two different inter-storey drift responses are observed in Fig. 5.2. FCS and SSC models predict similar, stiffer profiles compared to ESC and LFCS models which show a significant increase in the drift throughout the height. Inter-storey drifts at the top and ground storeys are:

	Inter-Storey Drift (mm)			
Storey	FCS	ESC	SSC	LFCS
top	$3.4\,mm$	$5.6\,mm$	$3.5\,mm$	$5.6\,mm$
ground	$1.6\,mm$	$2.0\,mm$	$1.7\,mm$	$2.1\,mm$

Reversals are noted at the ground and top storeys showing a sharp 36% increase in the inter-storey drifts due to the larger storey heights combined with the fixed boundary conditions and the core-frame interaction at these storeys. All models show a constant increase in the inter-storey drifts from storeys 2 to 11, and an almost uniform profile for the upper half storeys 11 to 19 with a slight reduction or pull-back observed due to the core-frame interaction. The largest inter-storey drift (ignoring the top storey) occurs at storey 13 with values of $2.8\,mm$ and $4.2\,mm$ for FCS (SSC) and ESC (LFCS) models, respectively. This inter-storey drift response demonstrates a 45% decrease in the lateral stiffness of the structure when ignoring the S-slabs flexural actions and eliminating the interaction of the E-slabs and the coupling and lintel beams.

5.1.3 Twists

Twist profiles predicted by the various models are plotted in Fig. 5.3.

	Twist ($\times 10^{-6}$ *rad*)			
Level	FCS	SSC	ESC	LFCS
top	2.25	−1.50	−7.75	−12.50
maximum	5.80 Level 5	5.60 Level 4	4.75 Level 4	4.60 Level 3
contra-twist	none	Storey 17	Storey 10	Storey 9

A reversal in the twists is noted as the models become increasingly detailed from LFCS to FCS, giving top twists of $-12.50 \times 10^{-6}\,rad$ to $2.25 \times 10^{-6}\,rad$. FCS model demonstrates a positive twist throughout the height. Eliminating the interaction of the cores substructure components (SSC model), the S-slabs flexural actions (ESC model) and then combining both these effects (LFCS model), results in a lower contra-twist location ranging from storeys 17 to 10 to 9, respectively. More of the structure is in reverse twisting over the height as the effects of the slabs and the beams are ignored. Locations of maximum twists are at about the one-quarter height, levels 3 to 5, from the structure base with values upto $5.80 \times 10^{-6}\,rad$ in FCS model. Examining the individual core sections twist profiles given by FCS model in Fig. 5.4,

	Twist ($\times 10^{-6}$ *rad*)			
Level	FCS	Core	Elev	Stair
top	2.25	2.00	−1.00	2.50
maximum	5.80 Level 5	5.40 Level 5	14.90 Level 4	7.80 Level 5
contra-twist	none	none	Storey 20	none

it is observed that the Core and Stair section twists are close to the total FCS twist response with the Stair section displaying the larger twists. Elev section response is much more pronounced giving the largest twist profile due to the presence of the elevator opening, with a maximum twist at level 5 of $14.90 \times 10^{-6}\,rad$ which is almost 3 times the total FCS twist of $5.80 \times 10^{-6}\,rad$. Twist values at the top level show that the Core and Stair sections response are close to the total FCS response, while Elev section indicates a twist reversal of $-1.00 \times 10^{-6}\,rad$ due to its open-section response.

Therefore, Core section is the stiffer section in terms of the twist due to the presence of the infilled slabs, followed by the Stair section with the partially E-slabs, and the Elev section which is relatively flexible (3 times more than the Core section) tending toward an open-section response. Maximum twists occur in the lower 5 storeys, one-quarter height of the structure.

5.1.4 Inter-Storey Twists

Inter-storey twist profiles predicted by the models are plotted in Fig. 5.5.

	Inter-Storey Twist ($\times 10^{-6}\,rad$)			
Storey	FCS	SSC	ESC	LFCS
top	−0.25	−0.60	−1.10	−1.25
maximum	−0.375 Storey 8	−0.625 Storey 9	−0.975 Storey 10	−1.30 Storey 9
ground	3.10	3.35	2.75	2.90

Inter-storey twists decrease as the models become more detailed from LFCS to FCS. Ignoring interaction of the cores substructure components (SSC model) doubles the maximum inter-storey twist, while eliminating the S-slabs flexural actions (ESC model) triples the maximum twist, and combining both reductions (LFCS model) increases the maximum twist by about 4 times the value for FCS model. Maximum inter-storey twists occur at about the mid-height at storeys 8 to 10. The majority of twist is noted over the lower 6 storeys, one-third the structure height, with an almost uniform inter-storey twist over the upper half 10 storeys. Increases in the inter-storey twists are observed in the SSC, ESC and LFCS models at the top storey due to core-frame interaction and the largest inter-storey twist increase noted at the ground storey due to the fixed conditions, combined with the larger storey heights in these storeys.
Inter-storey twist profiles for the individual core sections predicted by FCS model in Fig. 5.6,

	Inter-Storey Twist ($\times 10^{-6}\,rad$)			
Storey	FCS	Core	Elev	Stair
top	−0.25	−0.75	−3.10	0.75
maximum	−0.375 Storey 8	−0.375 Storey 8	−1.40 Storey 8	−0.50 Storey 8
ground	3.10	2.50	9.85	4.00

show the Core and Stair section responses close to the total FCS inter-storey twist profile with differences at the top and ground storeys due to the core-frame interaction and fixed boundary conditions, respectively. Elev section response deviates more from the total FCS model twist, more so at the upper and lower storeys, with the maximum inter-storey twist at the ground storey being 3 times the FCS model value. An increase of about 6.00 $\times$ $10^{-6}\,rad$ is noted in storey 1 due to Elev behaving as an open-section. The majority of the inter-storey twists occur in the lower 2 storeys with the twists increasing over the lower 4 storeys, 20% structure height, and then becoming constant upto the top 2 storeys where a twist increase occurs.

Therefore, Core section is the stiffer section in terms of the inter-storey twist due to the presence of the infilled slabs, followed by the Stair section with the partially E-slabs, and the Elev section which is relatively flexible (3 times more than the Core section) tending toward an open-section response. Maximum inter-storey twists occur in the lower 4 storeys, one-fifth height of the structure.

5.2 Core Forces

5.2.1 Core Stresses at Ground Level due to Q_X Earthquake Loading

Figures 5.7 to 5.9 show the S_{xx}. S_{yy} and S_{xy} stress distributions at the ground level of the Core. Elev and Stair sections as given by the FCS. SSC. ESC and LFCS models.

5.2.1.1 Transverse Stresses S_{xx}

Distributions of the S_{xx} stresses at the ground level of the cores in Fig. 5.7 (a), (b) and (c) show similar symmetrical profiles about the web wall center. Across the web walls. the stresses decrease linearly from tension to compression and are largest at the web-flange corners ranging from $\pm 0.25\,MPa$ to $\pm 0.35\,MPa$. Core and Elev section flange walls show an almost linear stress distribution. while in the Stair section a linear stress increase is noted from the flange wall end to the corner. with one flange wall in tension and the opposite wall in compression.

For all three cores. the web wall stresses increase from FCC to ESC to SSC to LFCS models as the S-slabs flexural actions, and the E-slabs. the coupling and lintel beams are eliminated. Maximum corner S_{xx} stresses in the Core section are: $0.25\,MPa$ in FCS. $0.28\,MPa$ in ESC. $0.32\,MPa$ in SSC and $0.34\,MPa$ in LFCS models. Thus. a significant reduction is observed in the corner stresses of upto 35% in the Core section due to the consideration of the three-dimensional interaction of the cores substructure components. Eliminating the interaction of the core components (LFCS model) reduces the S_{xx} stresses in the flange walls by 10%. while eliminating the S-slabs flexural actions (ESC model) increases the stresses in the flange walls by 10%. This response is due to the web walls being less restrained over their length and as a consequence more load is distributed to the flange walls, with the longer flange walls experiencing larger S_{xx} stresses as observed in the Core vs the Stair section results.

Dead load S_{xx} stresses are compressive showing a parabolic distribution in the web walls. being more pronounced in the Core section, and a linear distribution in the flange walls with maximum S_{xx} stresses of $-0.25\,MPa$ in Core, $-0.15\,MPa$ in Elev and $-0.19\,MPa$ in Stair sections which are as significant as the S_{xx} stresses due to Q_X earthquake loads.

5.2.1.2 Longitudinal Stresses S_{yy}

Distributions of the S_{yy} stresses at the ground level of the cores in Fig. 5.8 (a). (b) and (c) demonstrate similar symmetrical profiles about the web wall center. Across the web walls, the stresses vary linearly from tension to compression with the largest values at the corners ranging from $\pm 3.20\,MPa$ to $\pm 4.45\,MPa$. Along the flange walls, an almost constant stress distribution is noted with one wall in tension and the other wall in compression. These results indicate that the flange walls experience essentially equal S_{yy} stresses.

In all three cores, FCS model predicts the lowest S_{yy} stresses, SSC model shows almost equal core stresses, while ESC and LFCS models give essentially similar results predicting the largest stresses. Maximum corner stresses in the Core section are: $3.40\,MPa$ in FCS, $3.50\,MPa$ in

SSC, 4.20 MPa in ESC and 4.10 MPa in LFCS models. Hence, eliminating the interaction of cores substructure components (SSC model) has very little effect on the core section S_{yy} stresses, but eliminating the S-slabs flexural actions (ESC model) or combining both of these reductions (LFCS model) increases the core S_{yy} stresses by approximately 24%.

Dead load S_{yy} stresses are compressive and almost constant across the flange and web walls with values of: -5.25 MPa in Core, -4.50 MPa in Elev and -4.50 MPa in Stair sections which are as significant as the S_{yy} stresses due to Q_X earthquake loads.

5.2.1.3 Shear Stresses S_{xy}

Distributions of the S_{xy} stresses at the ground level of the cores in Fig. 5.9 (a), (b) and (c) illustrate a parabolic stress profile symmetrical about the web wall center. Core and Elev sections show a parabolic stress distribution across the web walls with maximum stresses at the web wall center and a linear stress profile along the flange walls decreasing toward the corners. Stair section demonstrates a parabolic stress distribution across the entire section web and flange walls with maximum stresses located at the web wall center. This variation of the S_{xy} stresses is due to the Stair section having the shortest flange walls. Maximum shear stresses at the web wall center are: 0.68 MPa in Core, 0.58 MPa in Elev and 0.50 MPa in Stair sections.

All models predict essentially similar S_{xy} stress distributions in the cores indicating that the relative shear stiffness of the core sections is about equal. Elimination of the interaction of the cores substructure components has little effect on the resulting relative core section shear stiffnesses. Hence, the core S_{xy} stress distributions demonstrate that the wall dimensions are influential on the resulting shear stresses. Flange walls affect the core response as effective flange wall lengths participating with the web walls in the core shear resistance. Determination of this effective flange wall length is dependent on the three-dimensional behaviour of the core-slab-frame structure.

Dead load S_{xy} stresses demonstrate irregular distributions across the web and flange walls varying from positive to negative values, and are asymmetrical about the web wall center with the maximum stresses occurring near the corners of: ± 0.15 MPa in Core, ± 0.05 MPa in Elev and ± 0.075 MPa in Stair sections which are as significant in the flange walls and the corners compared to the S_{xy} stresses due to Q_X earthquake loads.

5.2.2 Core Stresses at Ground Level due to Q_Y Earthquake Loading

Figure 5.10 (a), (b) and (c) shows the S_{xx}, S_{yy} and S_{xy} stress distributions at the ground level of the Core, Elev and Stair sections as given by the FCS model.

5.2.2.1 Transverse Stresses S_{xx}

Profiles of the S_{xx} stresses across the ground level of the cores in Fig. 5.10 (a) show the web walls in tension for the Core section and in compression for the Elev and Stair sections with a symmetrical parabolic stress distribution about the web wall center. Maximum stresses are located at the web wall center with values of: $0.28\,MPa$ in Core, $-0.06\,MPa$ in Elev and $-0.22\,MPa$ in Stair sections. Along the flange walls, the S_{xx} stresses demonstrate linearly increasing and decreasing distributions toward the wall ends to values of: $-0.21\,MPa$ in Core, $-0.18\,MPa$ in Stair and a stress reversal occurring in the Elev section near the corner from $-0.28\,MPa$ to $0.15\,MPa$ at the flange wall end due to its open-section configuration.

5.2.2.2 Longitudinal Stresses S_{yy}

Profiles of the S_{yy} stresses across the ground level of the cores in Fig. 5.10 (b) illustrate a symmetrical concave distribution across the web walls, with 15% to 50% lower stresses at the more flexible wall center increasing to a local maximum at the stiffer web-flange corners. These non-uniform S_{yy} stress variations are due to the length of the web walls combined with interaction of the cores substructure components.

	S_{yy} Stresses (MPa)		
Location	Core	Elev	Stair
corner	2.75	−1.00	−2.50
mid-web	2.40	−0.50	−2.20
flange end	−3.75	4.50	−0.10

The S_{yy} stresses in the web walls are tensile in the Core section and compressive in the Elev and Stair sections. Flange wall stress profiles vary linearly from the wall end to the corner regions showing stress reversals of compressive to tensile S_{yy} stresses in the Core section, tensile to compressive stresses in the Elev section, and only compressive stresses in the Stair section.

5.2.2.3 Shear Stresses S_{xy}

Profiles of the S_{xy} stresses across the ground level of the cores in Fig. 5.10 (c) show an asymmetrical distribution about the web wall center, varying from positive to negative values in the Elev and Stair sections and from negative to positive values in the Core section.

Nonlinear partially parabolic shear stress distributions are observed with larger stresses in the flange walls increasing toward the corners. Maximum flange wall S_{xy} stresses are located at approximately two-thirds of the distance from the wall end with values: $-0.66\,MPa$ in Core, $0.53\,MPa$ in Elev and $0.45\,MPa$ in Stair sections. A shear stress drop occurs in the web walls from the corners proceeding sharply over one-fifth of the wall length dropping to small values and linearly to zero stresses at the web wall center. This response indicates that the flange walls resist a majority of the S_{xy} stresses with a shear lag effect (larger shear stresses) noted at the stiffer core sections flange-web corners.

5.2.3 Three-Dimensional Distribution of Core Stresses due to Q_X Earthquake Loading

5.2.3.1 Transverse Stresses S_{xx}

Similar S_{xx} stress distributions are obtained for the core sections throughout their heights as shown for the Core section in Fig. 5.11. Maximum stresses occur in the lower 2 to 3 storeys with values of $\pm 0.29\,MPa$ to $\pm 0.22\,MPa$ in the cores at the ground storey. From the stress contours, a symmetrical stress distribution in noted throughout the height of each core section about the web wall centerline with one-half of the core experiencing tensile stresses and the other half being in compression.

The S_{xx} stresses increase over the lower one-third height, 5 to 6 storeys, showing sharp peaked stress reversals and concentrations in the web and flange walls in the lower 2 storeys. In the upper two-thirds cores height, levels 6 to 20, the stresses show a flatter distribution with small values of $\pm 0.010\,MPa$. Elev section demonstrates a stress reversal at the top storey of $\pm 0.075\,MPa$ due to this core being the least restrained (an open-section) with openings for the elevators and the stairwell present in front and behind the Elev web wall.

5.2.3.2 Longitudinal Stresses S_{yy}

Similar S_{yy} stress distributions are obtained for the core sections throughout their heights as illustrated for the Core section in Fig. 5.12. A symmetrical stress distribution is noted about the web wall centerline showing one-half of each core section in tension and the other half in compression. Over the lower one-half of the cores height, levels 1 to 10, the stresses increase uniformly toward the base. Maximum stresses occur in the ground storey at the web-flange corners with values: $\pm 3.57\,MPa$ in Core, $\pm 3.45\,MPa$ in Elev and $\pm 3.63\,MPa$ in Stair sections. Across the web walls, a very steep stress gradient occurs in the lower storeys varying from tension to compression, and then becoming constant across the flange walls. An S_{yy} stress reversal is observed at storey 10 over the upper half of the cores height with a humped surface and giving maximum stresses at level 17 of less than $\pm 0.50\,MPa$, then another stress reversal occurs at the top level due to core-frame interaction. In the upper one-third cores height, the S_{yy} stress surfaces are smooth across the core walls with larger stresses at the web-flange corners.

5.2.3.3 Shear Stresses S_{xy}

Essentially identical S_{xy} stress distributions are obtained throughout the height of the core sections as demonstrated for the Core section in Fig. 5.13. The smallest stresses are located at the three-quarter height, level 16, and then increase uniformly downward to the base. Maximum shear stresses occur at level 1 with values of $0.68\,MPa$ to $0.50\,MPa$ showing a humped parabolic surface increasing toward level 1 centered in the web walls and then decreasing sharply toward the flange wall ends.

At the ground and basement storeys, a stress drop and reversal is observed in the lower storeys to $-0.13\,MPa$ at the base due to the fixity conditions in this region combined with the interaction of the cores substructure components. Shear lag effects in the cores are observed in the ground to basement storeys where the S_{xy} stress distributions are parabolic in shape with a maximum value at the web wall centers and stress reversals at the flange wall ends.

Over the upper 4 storeys, 20% structure height, an S_{xy} stress reversal is noted showing a smaller parabolic hump peaking in the web walls at the top level. This shear stress reversal is due to the core-frame-slab interaction resulting in a restraining force in the cores.

5.2.4 Three-Dimensional Distribution of Core Stresses due to Q_Y Earthquake Loading

5.2.4.1 Transverse Stresses S_{xx}

Figures 5.14 to 5.16 show different S_{xx} stress distributions throughout the height of the core sections. At the top storey, a stress reversal is noted in the web walls showing a small peaked distribution with stresses of $\pm 0.025\,MPa$ at the web wall center and a flat distribution in the flange walls. Over the majority of the cores height, levels 4 to 19, the S_{xx} stress distributions are very flat with a hump at the center of the web walls and decreasing toward the flange wall ends. Stress reversals occur at levels 6, 10 and 11 for the Core, Elev and Stair sections, respectively, with larger stresses at the web wall center and flange wall ends. The stresses increase sharply over the lower one-quarter cores height, 4 to 5 storeys, demonstrating very irregular distributions being symmetrical about the web wall centerline. In the Core section lower storeys 3 large stress peaks are noted, giving values at the ground level of one peak of $-0.21\,MPa$ at each flange wall end increasing sharply toward the web wall center to $0.34\,MPa$. Several stress peaks and reversals occur in the Elev section, being concentrated in the lower 2 storeys giving stress concentrations of $0.21\,MPa$ to $-0.26\,MPa$ at the web-flange corners, with both web and flange walls experiencing a double stress reversal due to the open-section response. A sharp uniform S_{xx} stress increase is observed in the ground and basement storeys of the Stair section with the largest stresses of $-0.28\,MPa$ at the web wall center and no stress reversals due to the short flange walls.

This varied S_{xx} stress distribution in the cores demonstrates that the flange wall lengths as well as the section being open-, partially closed- or closed-section configuration influences the resulting S_{xx} stresses for Q_Y earthquake loading. The magnitude of the core S_{xx} stresses due to the Q_Y earthquake loads are as large as the S_{xx} stresses from the Q_X earthquake loads.

5.2.4.2 Longitudinal Stresses S_{yy}

Figures 5.17 to 5.19 illustrate similar S_{yy} stress distributions throughout the height of the core sections. In the upper two-thirds structure height, levels 7 to 20, a stress reversal is observed in the Core and Elev sections predicting tensile/compressive stresses in the flange walls and compressive/tensile stresses in the web walls. Flatter stress distributions are noted in the web walls with the stresses increasing from the corners toward the flange wall ends. The flange wall stresses in the upper one-third cores height reach a maximum value at about level 13 in Core and level 14 in Elev section. A decreasing S_{yy} stress distribution is then observed in Core and Elev sections upward to the top level and downward to level 7 where a stress reversal occurs. In the Stair section, the S_{yy} stresses are very small at the top level 20 and increase gradually with a smooth flat distribution down toward the lower storeys, showing larger stresses at the flange wall ends and remain essentially uniform across the web wall.

Below level 7, after the stress reversal in the Core and Elev sections and level 6 in the Stair section, the S_{yy} stresses increase sharply toward the base. Core and Elev sections show the larger stresses in the flange walls with maximum values at the wall ends of $-3.82\,MPa$ and $4.43\,MPa$, respectively. Stresses in the Core and Elev sections change sharply in the lower storeys showing closer contours from tension/compression in the flange walls to compression/tension in the web walls, with a humped distribution. A similar humped S_{yy} stress distribution occurs in the Stair section at the lower storeys, but the stresses are compressive across the flange and web walls with no stress reversal due to the short flange walls. Peaks of these S_{yy} stress humps in the lower storeys occur across the web walls at about the one-third to two-thirds of the central wall regions (flatter stress contours observed) giving values of: $2.82\,MPa$ in Core, $-0.96\,MPa$ in Elev and $-2.43\,MPa$ in Stair sections.

5.2.4.3 Shear Stresses S_{xy}

Figures 5.20 to 5.22 demonstrate highly irregular S_{xy} stress distributions throughout the height of the core sections, with asymmetrical distributions about the web walls centerline. Several stress reversals are observed, especially in the ground storey, with maximum stresses at the ground level of $\pm 0.75\,MPa$ in Core, $\pm 0.70\,MPa$ in Elev to $\pm 0.49\,MPa$ in Stair sections.

For the Core section from levels 20 to 2, a double S_{xy} stress reversal occurs at each flange-web corner with irregularly increasing stresses toward the lower storeys. In the lower 2 storeys, the largest peaked S_{xy} stresses occur at the flange-web corners and the flange wall ends with 3 very irregular stress reversals. For the Elev and Stair sections, similar S_{xy} stress distributions are observed throughout the height, with larger stresses in the flange walls dropping sharply toward the corners and remaining almost smooth and flat across the web walls. In the lower 2 storeys, the S_{xy} stresses increase showing sharper stress gradients across the web walls from corner to corner demonstrating an irregular pattern of large stress peaks and 3 sharp stress reversals.

These irregularly peaked S_{xy} stress distributions consisting of several reversals at the lower 2 storeys of the core sections height are due to the three-dimensional core-slab-frame interaction combined with the fixed conditions at the base region stiffening the structure in the lower storeys, and creating shear lag effects caused by the longer web walls stiffened at the corner regions by the flange walls.

5.2.5 Three-Dimensional Distribution of Core Stresses due to Dead Loads

5.2.5.1 Transverse Stresses S_{xx}

Figure 5.23 shows a symmetrical S_{xx} stress distribution in the Core section about the web wall centerline increasing linearly downward throughout the height from level 19 (smallest stresses) to level 2 with a constant stress distribution across the flange walls and a spinal hump in the web walls peaking to a maximum value at the web wall centerline. These stress humps in the web walls have a sharper peak toward the bottom storeys. At the top storey 20, stress reversals occur in the flange-web corners and web walls due to core-frame interaction. A large S_{xx} stress increase in the Core section is observed at the ground and basement storeys, showing a steep gradient to a maximum value of $-0.72\,MPa$ compared to $0.061\,MPa$ in the upper storeys. This sharp ten-fold increase of the S_{xx} stresses in the cores at the lower 2 storeys is due to the fixity created by the fixed boundary conditions at the base combined with the three-dimensional core-slab-frame structure response.

Dead load S_{xx} stresses at the ground storey of $-0.72\,MPa$ are about twice the S_{xx} stresses due to the Q_X and Q_Y earthquake loads of $0.29\,MPa$ and $0.34\,MPa$, respectively.

5.2.5.2 Longitudinal Stresses S_{yy}

Figure 5.24 illustrates a symmetrical S_{yy} stress distribution in the Core section about the web wall centerline increasing linearly downward along the height from levels 20 to ground. Topographical contours show a uniform stress profile (constant in magnitude) across the core cross-section at any level. This stress distribution is expected since the dead and live loading is essentially constant for all floor levels.

Maximum S_{yy} stresses due to gravity loads occur at the base level giving a dead load stress of $-5.58\,MPa$ in the Core section compared to $\pm 3.57\,MPa$ and $\pm 3.82\,MPa$ for the Q_X and Q_Y earthquake loadings, respectively. The S_{yy} stresses due to earthquake loads are as significant as those due to the dead loads for maximum values at the base region. At the ground and basement storeys of the core sections, a nonlinear S_{yy} stress distribution is noted across the web and flange walls due to the dead loads as a result of the fixed conditions at the lower region stiffening the core-slab-frame structure response.

5.2.5.3 Shear Stresses S_{xy}

Very irregular S_{xy} stress distributions are observed in the core sections as shown in Fig. 5.25 for the Core section, being asymmetrical throughout the height about the web wall centerline.

Several S_{xy} stress reversals occur across the core cross-sections demonstrating a folded plate distribution with essentially constant shear stresses (contours) along the height, except at the top and bottom storeys. Shear stress peaks are located at the flange wall ends, the corners and at the one-third web wall lengths. This uniform stress pattern from levels 19 to 2 is due to the gravity loading being essentially constant in value for all of the floor levels. At the top storey 20, larger stress peaks are noted at the flange wall ends and corners due to core-frame interaction. Highly irregular, asymmetrical stresses are observed in the lower 2 to 3 storeys with several reversals and very sharp peaks at the flange wall ends and the corners. Maximum S_{xy} stresses range from $\pm 0.30\,MPa$ to $\pm 0.24\,MPa$. These irregular peaked shear stress distributions in the cores are due to the three-dimensional core-slab-frame interaction combined with fixed conditions at the base region stiffening the structure in the lower storeys, and creating shear lag effects caused by the large width of the web walls stiffened at the corners by the flange walls.

Shear stresses due to Q_X earthquake loads range from $\pm 0.68\,MPa$ to $\pm 0.50\,MPa$, and due to Q_Y earthquake loads from $\pm 0.75\,MPa$ to $\pm 0.49\,MPa$. Thus, the S_{xy} stresses due to dead load are approximately one-half of the S_{xy} stresses due to earthquake loads.

5.2.6 Three-Dimensional Distribution of Core Moments due to Q_X Earthquake Loading

5.2.6.1 Transverse Moments M_{xx}

Figures 5.26 to 5.28 show the M_{xx} moment distributions throughout the height of the core sections. Similar asymmetrical distributions are observed about the web wall centerlines showing flatter moment surfaces in the web walls compared to the flange walls, with one-half of each core section experiencing positive/negative moments and the other half of the core section being in negative/positive moments.

A moment reversal occurs at the mid-height of each core section, levels 9 to 11, more notable in the flange walls with concave/convex moment distributions of maximum values at the one-quarter and three-quarter core heights. However, the humped M_{xx} moment surface reversals are gradual in the flange walls. Moment reversals are noted at the top storey 20 with values increasing to 3 to 5 times the maximum moment hump values. This increase in the core M_{xx} moments is due the larger top storey height combined with the core-frame interaction. Each core demonstrates a different moment distribution at the ground storey. Stair section M_{xx} moments become constant at the ground and basement storeys with small values due to the short flange walls, and the largest moments of $\pm 2208\,N \cdot m$ are at the one-quarter core height. Core and Elev sections show steep moment gradients and reversals in the lower 2 storeys giving large moments at the flange-web corners and flange wall ends with maximum values of $\pm 2404\,N \cdot m$ and $\pm 3760\,N \cdot m$ for each core, respectively. The M_{xx} moments are larger in the Elev open-section configuration which experiences a larger variation in stiffness, with increasing moments in the lower 2 storeys of the structure, due to the influence of the fixity conditions at the ground level combined with the core-slab-frame structure three-dimensional response.

5.2.6.2 Longitudinal Moments M_{yy}

Figures 5.29 to 5.31 illustrate similar M_{yy} moment distributions throughout the height of the core sections, with asymmetrical distributions about the web wall centerlines.

Several irregular humped M_{yy} moment reversals, positive to negative, are noted in the web and flange walls across the web centerline and along the cores height at the mid-height, level 10. The moment surfaces indicate a sharp moment increase from the centre of the web walls to a maximum at the web-flange corners followed by a moment drop toward the flange wall ends. Four humped moment surfaces are observed with maximum values located at the one-quarter and the three-quarter core heights. Sharp moment reversals with steep gradients occur at the top storey and the bottom 2 storeys. At the top storey, the M_{yy} moments are largest in the stiffer Core section, followed by Stair and the more flexible Elev sections. The largest moment reversals are at the ground level showing steep moment gradients over the ground storey and peaks at the web-flange corners giving values of 10,875 $N \cdot m$ in Core, 8,146 $N \cdot m$ in Elev and 10,116 $N \cdot m$ in Stair sections. Hence, interaction of the cores substructure components combined with the fixity conditions at the ground level, stiffen the core flange wall ends and flange-web corner regions and result in M_{yy} moment concentrations and reversals in the cores.

5.2.6.3 Twisting Moments M_{xy}

Figures 5.32 to 5.34 demonstrate similar M_{xy} moment distributions throughout the height of the core sections, showing symmetrical distributions about the web wall centerlines.

Constant M_{xy} moments are noted over the majority of the cores height except for the top, ground and basement storeys. A folded plate moment surface is observed with several moment reversals of steep gradients and sharp peaks located at the web-flange corners, the web walls center and in the flange walls. The M_{xy} moments are approximately equal in the cores at about 2000 $N \cdot m$ in the uniform folded plate regions which is due to the interaction of the cores substructure components with the frames substructure.

At the top storey, the Core and Stair sections demonstrate larger reversals of maximum M_{xy} moment peaks at the web-flange corners dropping sharply toward the flange wall ends. This effect is due to the stiffer core corners created by the presence of the E-slabs. A similar but less pronounced M_{xy} distribution is noted in the Elev section due to its open-section configuration. The largest M_{xy} moments occur at the ground and basement storeys showing a parabolic humped distribution in the web walls, reversing to a peaked moment concentration at the web-flange corners and then reducing sharply to the flange wall ends, giving maximum values of 3756 $N \cdot m$ in Core, 3012 $N \cdot m$ in Elev and -3569 $N \cdot m$ in Stair sections.

The M_{xy} moments in the cores are equal to and larger compared to the M_{xx} moments and are 30% to 40% of the M_{yy} moments, and thus, they must be considered in design.

5.2.7 Three-Dimensional Distribution of Core Moments due to Q_Y Earthquake Loading

5.2.7.1 Transverse Moments M_{xx}

Figures 5.35 to 5.37 show the M_{xx} moment distributions throughout the height of the core sections. Similar symmetrical distributions are observed about the web wall centerline in the Core and Stair sections with a more complex surface noted in the Elev section.

In the Core and Stair sections, a smoother flatter M_{xx} moment surface is observed throughout the core height except in the lower 2 storeys. These cores experience small moment reversals at the top storey in the web wall center region and in the flange walls. A smooth humped moment surface is noted over the upper 6 to 8 storeys with larger moments at the web-flange corners. Moment contours show a more complex M_{xx} moment pattern in the Core section compared to a smoother, flatter moment surface in the Stair section.

Moment reversals occur in storeys 10 to 12 for the Core and Stair sections, showing a humped moment surface over the lower half of the core height increasing gradually toward the bottom 2 storeys. Core section demonstrates a more complex pattern of M_{xx} moments (contours) compared to Stair section, with moment peaks at the web-flange corners and the web wall center. At the web wall center in the ground storey of the Core and Stair sections, a pronounced M_{xx} moment concentration is observed showing a steep moment gradient increasing to 3 to 4 times the values at the center to $4693\,N \cdot m$ and $6465\,N \cdot m$ in each core, respectively. This complex distribution of M_{xx} moments is due to the stiffer Core closed-section configuration resulting from the interaction with the other components and the longer flange walls, compared to the Stair partially closed-section configuration with short flanges and an opening.

In the Elev section, the most complex and irregular M_{xx} moment distribution is observed consisting of several reversals, humped peaks and sharp moment gradients. At the top storey 20, a parabolic moment hump occurs with maximum value at the web wall center and reversals to moment peaks at the web-flange corners. Double humped moment reversals are noted from storeys 20 to 19 and across storeys 10 to 19 along the upper half height of the Elev section with the maximum moments at the web-flange corners and moment reversals of steep gradients toward the web wall center. Similar humped moment reversals occur in the lower half height of the Elev section, with larger gradients from the web-flange corner to the web wall center and maximum moments of about $-3543\,N \cdot m$ at level 2. Another steep moment reversal occurs at level 1 to a peak value of $2848\,N \cdot m$ at the web wall center. This complex and varied M_{xx} moment distribution in the Elev section is due to this open-section core being influenced by the lintel beams and effective width of the E-slabs participating in the lateral load resistance stiffening the Elev section, moreso in the bottom 2 storeys of the structure.

5.2.7.2 Longitudinal Moments M_{yy}

Figures 5.38 to 5.40 illustrate similar M_{yy} moment distributions throughout the height of the core sections, with symmetrical distributions about the web wall centerlines.

Examining the M_{yy} moments in the Core and Stair sections, a flatter surface is noted over the upper half of the cores height, levels 10 to 20, with moment peaks of less than 3000 $N \cdot m$ at the web walls center. At the top storey, a moment reversal occurs from levels 19 to 20 with a steep gradient and larger values at the flange-web corners, and then becoming constant across the web walls. Over the lower half of the cores height, a moment reversal is observed gradually increasing in a hump shape toward the one-quarter height (level 5) in the Core section showing maximum moments in the web wall. In the Stair section, the moments increase uniformly downward to the lower storeys. At the ground and basement storeys, both Core and Stair sections demonstrate a large pronounced humped moment concentration with a very steep gradient to a maximum in the web walls of 20 $kN \cdot m$ and 24 $kN \cdot m$, respectively, and then dropping to small values at the base level. These complex M_{yy} moment distributions in the Core and Stair sections are due to the stiffer core configurations with closed- and partially closed-sections, respectively.

In the Elev section, the M_{yy} moments demonstrate very complex and irregular distributions composed of several humps, peaks and reversals occurring throughout the core height and across the core walls. At the top storey, a small moment reversal is noted from levels 19 to 20, then the moments increase gradually in a folded hump over the upper half of the core height, 10 storeys. Small moments occur in the flange walls with sharp humps at the flange-web corners descending toward the web wall center. Maximum humped moment peaks are located at approximately two-thirds of the core height, level 12, with a value of 5 $kN \cdot m$. Over the lower half of the Elev section, a moment reversal occurs at level 10 with sharply increasing moments downward in a hump shape along the web-flange corners to a maximum of $-22\,kN \cdot m$ at level 1. From levels 1 to ground, a sharp parabolic moment reversal occurs across the web wall with a maximum value of 12 $kN \cdot m$ at the web wall center and then the moment gradient reduces to small values toward the base level. This complex and varied M_{yy} moment distribution in the Elev section is due its open-section being influenced by the lintel beams and the effective width of the E-slabs participating in the lateral load resistance stiffening the Elev section.

5.2.7.3 Twisting Moments M_{xy}

Figures 5.41 to 5.43 demonstrate highly irregular M_{xy} moment distributions throughout the height of the core sections, showing asymmetrical distributions about the web wall centerlines.

Along the Core section height from levels 19 to 2, a folded plate M_{xy} moment distribution is noted demonstrating moment reversals at the web-flange corners and at the one-third web wall lengths. The moments peak at the flange-web corners and the web wall center to values of $\pm 1500\,N \cdot m$. At the top storey 20, a moment reversal with a steep gradient occurs in the flange and web walls showing a sharp peak at the web wall center. Several moment reversals are observed in the bottom 2 storeys across the web and flange walls. This irregular M_{xy} moment reversal, shows peak moments of $\pm 1715\, N \cdot m$ located at the Core section web wall center which are due to interaction of the core substructure components combined with the fixed boundary conditions at the base region stiffening the core.

In the Elev section, the M_{xy} distributions demonstrate a folded plate surface gradually increasing from the top to the lower storeys showing larger moments at the flange wall ends and the corners. A folded hump moment surface is observed along the web wall centerline with the largest value of $\pm 5383\, N \cdot m$ at level 1 and steep moment gradients toward the web-flange corners, and a double moment reversal in the basement storey across the flange and web walls.

Along the Stair section, steep M_{xy} moment reversals are observed at the top storey 20 over the short flange wall length. The moments reduce downward to the core mid-height, level 11, in a folded plate distribution across the core section being flatter in the web walls. At level 11, a moment reversal is noted increasing linearly down to the lower region level 1 to a peak value of $\pm 1359\, N \cdot m$ at the web-flange corner. Several irregular moment reversals occur between level 1 to the base with maximum values of $\pm 1250\, N \cdot m$ at the corners and the web wall center. This complex variation of M_{xy} moments in the Stair section is due to the partially closed-section being influenced by the coupling beams and the partially E-slabs stiffening the short flange walls and one-third of the web wall regions in the lateral load resistance.

In the Core and Stair sections, the M_{xy} moments are small with maximum values of $\pm 1715\, N \cdot m$ and $\pm 1359\, N \cdot m$, respectively, which are about 25% of the M_{xx} moments and 10% of the M_{yy} moments; while the Elev section maximum M_{xy} moments $\pm 5383\, N \cdot m$ are about twice the M_{xx} moments and 50% the M_{yy} moments.

5.2.8 Three-Dimensional Distribution of Core Moments due to Dead Loads

5.2.8.1 Transverse Moments M_{xx}

Similar M_{xx} moment distributions are obtained for the core sections being symmetrical about the web wall centerline throughout the height, as shown for the Core Section in Fig. 5.44.

At the base of the cores, the M_{xx} moments are small with values of $2000\, N \cdot m$ at the flange wall ends. The moments increase gradually from level 1, peaking at about the one-quarter core height and then decrease to a contra-flexure point at about the core mid-height. A smooth, folded plate surface is noted with larger moments at the flange wall ends, the flange-web corners and the web wall center. This smooth moment distribution is reversed in the upper half of the cores height, increasing gradually upward to level 19. At the top storey 20, a sharp increase to 5 times the moments is noted ($\pm 4404\, N \cdot m$ to $\pm 7936\, N \cdot m$) compared to the moments at level 19, due to core-frame interaction. Sharp moment peaks are noted at the flange wall ends and at the web-flange corners in the Core section, at the flange wall ends dropping parabolically toward the web wall center in the Elev section, and across the flange walls increasing parabolically to the web wall center in the Stair section. These complex M_{xx} moment distributions at the top storey are due to the Core closed-section, the Elev open-section and the Stair partially closed-section being influenced by the interaction with the other structural components.

Maximum M_{xx} moments in the cores due to dead loads are: $\pm 5683\, N \cdot m$ in Core, $\pm 4404\, N \cdot m$ in Elev and $\pm 7936\, N \cdot m$ in Stair sections, which are 2 to 3 times the M_{xx} moments due to Q_X earthquake loads, and one-half to the same as the M_{xx} moments due to Q_Y earthquake loads.

5.2.8.2 Longitudinal Moments M_{yy}

Similar M_{yy} moment distributions are obtained for the core sections being symmetrical about the web wall centerline throughout the height, as illustrated for the Core Section in Fig. 5.45.

In the ground and basement storeys, the M_{yy} moment distributions are very flat with slightly larger values in the flange walls. Over the lower half of the cores height, levels 1 to 10, the moments increase gradually upward from the base in a hump shape at the web-flange corner regions and in the flange walls to a maximum of $\pm 15\, kN \cdot m$ to $\pm 20\, kN \cdot m$ located at the one-quarter core height, level 5. In the web walls, flat moment surfaces are noted demonstrating a moment reversal at about the mid-height, level 10, and the moments increase over the upper half of the height in a hump fashion giving larger values at the flange-web wall corner regions.

A sharp increase in the M_{yy} moments with steep gradients occurs from levels 19 to 20. In the Core section, the moments at the top storey 20 show peaks of $32\, kN \cdot m$ at the web-flange corners dropping toward the web wall center with a steep moment reversal to the largest value of $-40\, kN \cdot m$ at the flange wall ends. In the Elev section, a moment reversal occurs at the top level 19 of $-18\, kN \cdot m$ with moment peaks at the flange-web corners and almost constant moments across the flange walls with a value of $23\, kN \cdot m$ at level 20 and a parabolic drop toward the web wall center. The Stair section exhibits a very steep moment reversal from $-36\, kN \cdot m$ at level 19 to $40\, kN \cdot m$ at level 20 with a constant moment across the flange walls and a moment drop toward the web wall center. These complex M_{yy} moment distributions at the top storey are due to the Core closed-section, the Elev open-section and the Stair partially closed-section being influenced by the interaction with the other structural components.

Dead load M_{yy} moments in the cores are 2 to 4 times the M_{yy} moments due to Q_X earthquake loads, and 25% to 50% greater than the M_{yy} moments due to Q_Y earthquake loads.

5.2.8.3 Twisting Moments M_{xy}

Similar irregular M_{xy} moment distributions are obtained in the core sections, asymmetrical about the web wall centerline throughout the height as shown for the Core Section in Fig. 5.46.

A uniform folded plate M_{xy} moment surface is noted with several reversals, consisting of steep moment gradients and peaks at the flange wall ends, the flange-web corners and the web wall center regions. Core and Stair sections demonstrate larger folded plate surfaces throughout the height being flatter in the Stair web wall. Elev section shows a smoother M_{xy} surface with larger moments in the lower half of the core height, levels 1 to 10, due to the stiffening effect on this open-section from the interaction with the other structural components combined with the fixity conditions at the base region.

All of the cores experience large M_{xy} moment reversals and peaks located at the web-flange corners, and in the web wall at the one-third length and the center wall regions, with steep gradients at the top storey. Maximum moments occur at the top level 20 of: $\pm 18\,kN \cdot m$ in Core, $\pm 10\,kN \cdot m$ in Elev and $\pm 17\,kN \cdot m$ in Stair sections. These complex M_{xy} moment distributions are due to the Core closed-section, the Elev open-section and the Stair partially closed-section being influenced by the interaction with the other structural components.

Dead load M_{xy} moments in the cores are 3 to 5 times the M_{xy} moments due to Q_X earthquake loads, and 2 to 10 times the M_{xy} moments due to Q_Y earthquake loads.

5.3 Slab Forces

5.3.1 In-Plane Stresses in the Surrounding Slabs at the Core-Wall Junctions

Figure 5.47 (b), (c) and (d) shows the S_{xx}, S_{yy} and S_{xy} stress distributions in the S-slabs across the core-slab junctions at the ground level as given by the FCS, SSC, ESC and LFCS models due to Q_X earthquake loads and dead loads (FCS model).

5.3.1.1 Transverse Stresses S_{xx}

Examination of the S_{xx} stresses in the S-slabs Fig. 5.47 (b), shows that in slab regions away from the Core and Stair sections, the models predict essentially similar stress distributions increasing toward the core web-flange corner regions to values of about 0.30 MPa.

Across the Core section, the FCS, SSC and ESC models predict a sharp stress peak at the slab-web-flange corner with stresses of 0.68 MPa, 0.84 MPa and 0.875 MPa, respectively, while LFCS model gives the lowest stress of 0.10 MPa. The stresses then drop sharply toward the Core flange wall end and remain constant across the slab to the Elev flange wall end. At the Elev web-flange corner, an increase in the slab stresses is noted to: 0.63 MPa in FCS, 0.67 MPa in SSC, 0.80 MPa in ESC and 0.85 MPa in LFCS models. Except for FCS model, a slightly irregular constant stress profile is observed from the slab-Elev web-flange corner to the slab-Stair web-flange corner. FCS model predicts a stress drop to 0.075 MPa across the Stair flange wall.

The S_{xx} stresses in the S-slabs due to Q_X earthquake loads are 2 to 3 times greater than the dead loads S_{xx} stresses.

Hence, elimination of the S-slabs flexural actions and interaction of the other structural components has the largest affect on the S_{xx} stresses in the S-slabs near the Stair section region increasing the stresses by approximately 10 times the values at the core-slab junctions, while the slab stresses decrease along the Core section region by about 10 times. This creates an equalization or redistribution of slab stresses toward the slab-Stair section region.

5.3.1.2 Longitudinal Stresses S_{yy}

Profiles of the S_{yy} stresses in the S-slabs Fig. 5.47 (c), show similar distributions given by the models indicating that the relative in-plane slab stiffness remains almost constant when ignoring the S-slabs flexural actions and interaction of the cores substructure components.

SSC, ESC and LFCS models show similar S_{yy} stress profiles, but with reduced values due to the redistribution of the stresses. At the slab-core wall junctions, stress peaks of 0.10 MPa to 0.25 MPa are observed at the core flange wall ends and web-flange corners due to the large stiffness in these regions compared with the slab regions between the cores. The S_{yy} stresses in the S-slabs increase by 25% to 50% as the flexural actions and the interaction of the core components are eliminated, proceeding from the FCS to the LFCS model.

The S_{yy} stresses in the S-slabs due to Q_X earthquake loads are approximately equal to the dead loads S_{yy} stresses.

Hence, critical regions in the S-slabs for the in-plane S_{yy} stress distributions are located along slab-core junctions, the slab-core web-flange wall corners and flange wall ends that are stiffened by the coupling and lintel beams and the E-slabs.

5.3.1.3 Shear Stresses S_{xy}

Plots of the S_{xy} stresses in the S-slabs Fig. 5.47 (d), show similar distributions across the slab-core wall junctions as given by all the models.

Very irregular S_{xy} stress distributions are observed with sharp stress concentrations at the slab-core web-flange corners, and stress reversals across each slab-core flange wall from the flange-web corner to the flange wall end. Double shear stress reversals are noted between the Elev web-flange corner and the Stair web-flange corner. The S_{xy} stresses vary from $\pm 0.25\, MPa$ as given by FCS model from one side of a core corner across the wall thickness to the other side of the same corner. A 20% to 60% increase is observed in the S-slabs S_{xy} stresses between the models showing the largest differences at the slab-core web-flange corners with values of: 0.25 MPa in FCS, 0.30 MPa in SSC, 0.35 MPa in ESC and 0.40 MPa in LFCS models.

The S_{xy} stresses in the S-slabs due to Q_X earthquake loads are approximately equal to the dead loads S_{xy} stresses, with stress reversals observed between the core flange walls.

Hence, the S-slabs flexural actions and interaction of the cores components significantly influence the S_{xy} stresses in the S-slabs, decreasing the stresses by about 20% to 40%. Thus, horizontal cracking and separation between the slabs and core walls must be considered in design, since large distress is observed in the slab at the slab-core corner and the end regions.

5.3.2 Three-Dimensional Distribution of Slab Stresses due to Q_X Earthquake Loading

5.3.2.1 Transverse Stresses S_{xx}

Examination of the S_{xx} stresses in the E-S-slabs in Fig. 5.48 demonstrates an asymmetrical distribution about the core sections web walls centerline, with one side of the slabs experiencing tensile stresses and the other side subjected to compressive stresses. This is due to the Q_X earthquake loading being perpendicular to the core flange walls.

For the S-slabs, S_{xx} stress concentrations of $\pm 0.68\,MPa$ are located at the slab-Core web-flange corners (stiffest slab regions) and the slab-Elev flange wall end regions (lintel and coupling beam junctions). Very sharp stress gradients are observed near and around the slab-Core wall regions due to the three-dimensional stiffening created by the Core web-flange wall and corner regions on the S-slabs. At the slab-Stair web-flange corner regions a smoother and flatter S_{xx} stress distribution is noted due to the short flange wall lengths resulting in a smaller slab-corner region stiffness compared to the slab-Elev and slab-Core web-flange corner regions. Further away from the core walls, the S_{xx} stresses become less pronounced with a smoother distribution toward the slab panel center regions, being less influenced by the column supports.

In the E-slabs, smaller S_{xx} stress peaks occur at the interior slabs of the stiffer core web-flange corner regions. A very flat stress surface is noted in the E-slabs between the Core flange wall ends and the lintel beams, with the stresses increasing sharply close to the I-E coupling beams due to this slab-beam-core wall location creating an increased slab stiffness.

5.3.2.2 Longitudinal Stresses S_{yy}

Results of the S_{yy} stresses in the E-S-slabs in Fig. 5.49 show an asymmetrical distribution about the core sections web walls centerline.

A smooth humped S_{yy} stress distribution is noted throughout the slab with maximum values of $\pm 0.17\,MPa$ around the core wall regions, located at the outer slab-core web-flange corners of the Core and Stair sections, that diminish to a very flat stress distribution in the S-slabs over a distance of about 3 to 5 times the core wall thickness from the core walls. Along the S-slab-core flange wall regions the S_{yy} stress surface is humped, showing a steeper gradient adjacent to the flange walls. These stress humps fade outwards in a ponding fashion in the S-slabs as noted from the stress contours. In the E-slabs, the S_{yy} stress humps are located near the Core and Stair section flange walls reducing toward the more flexible center region of the slabs.

Notable S_{yy} stress concentrations in the E-S-slabs are located around the slabs-I-E coupling beams regions and junctions. A pronounced stress distribution is observed extending from the S-slabs toward the E-slabs over the I-E coupling beams, then flattening out in the E-slabs center region due to the varying slab stiffness created by the interaction between the E-S-slabs through the coupling beams, indicating larger S_{yy} stresses in the stiffer slab regions.

5.3.2.3 Shear Stresses S_{xy}

Distributions of the S_{xy} stresses in the E-S-slabs in Fig. 5.50 show a symmetrical surface about the core sections web walls centerline. Very steep stress gradients and concentrations with several reversals are noted along the stiffer slab regions adjacent to the core walls.

Across the S-slab-core web wall regions, an almost constant S_{xy} stress profile is observed forming a very steep gradient over a slab distance of 3 to 5 times the core wall thickness from the web wall. the stresses then drop sharply toward the column supports. In the E-slabs. a similar steep S_{xy} stress gradient occurs near the stiffer Core web wall region dropping sharply toward the more flexible Core flange wall ends. These S_{xy} stress concentrations across the slab-core web wall locations are caused by the varying stiffness of the slab-core flange-web wall regions due to the three-dimensional response of the structure.

Along the S-slab-core web-flange wall regions, the S_{xy} stresses undergo several reversals with stress concentrations at the slab-core web-flange corner, the flange wall end and the mid-flange wall regions due to the increased slab stiffness at the core web-flange corner and flange wall regions created by the interaction of the cores substructure components.

Maximum S_{xy} stresses in the S-E-slabs are located at the stiffer slab-core web-flange corner regions giving values of $\pm 0.42\,MPa$.

5.3.3 Three-Dimensional Distribution of Slab Stresses due to Q_Y Earthquake Loading

5.3.3.1 Transverse Stresses S_{xx}

Examination of the S_{xx} stresses in the E-S-slabs shown in Fig. 5.51 demonstrates a symmetrical distribution about the core sections web walls centerline.

Several peaked and rounded humps are observed in the S_{xx} stress distribution in the S-slabs around the core wall regions. Along the S-slab-core flange wall regions, notable tensile stress peaks of $0.33\,MPa$ are located at the Core and Stair section flange wall ends. These stress peaks reduce sharply toward the slab-core web-flange corners and away from the flange walls. An S_{xx} stress band concentration in the S-slabs is observed of width 2 to 3 times the core wall thickness away from the slab-core flange wall junction. Reversals to compressive stresses occur in the S-slabs across the Stair flange walls and at the Core flange wall corner regions. Along the S-slab-Core and S-slab-Stair web wall regions a smooth distribution with small stresses is observed in the central one-third web wall region toward the column supports (flexible regions).

In the E-slabs, a very flat S_{xx} stress distribution is noted ($< 0.10\,MPa$) showing stress peaks at the slab-Core and slab-Stair web-flange corners and along the slab-lintel beam regions.

The S_{xx} stresses in the S-E-slabs due to Q_Y earthquake loads give a maximum value of $0.33\,MPa$ which are about one-half of the S_{xx} stresses due to Q_X earthquake loads with a maximum value of $0.68\,MPa$.

5.3.3.2 Longitudinal Stresses S_{yy}

Distribution of the S_{yy} stresses in the E-S-slabs in Fig. 5.52 shows a symmetrical surface about the core sections web walls centerline. The S-slabs demonstrate stress concentrations at the stiffer slab-core flange-web corner regions with maximum values ranging from 1.40 MPa to -1.13 MPa and show steep stress gradients toward the more flexible column supports.

The S-E-slabs regions adjacent to and within the Core section experience tensile S_{yy} stresses with steep concentrations across the web walls within a slab width of 2 to 3 times the core wall thickness away from the web walls. Two sharp S_{yy} stress peaks occur, with one peak at each slab-Core web-flange corner region. In the Elev and Stair section regions, the slabs experience compressive stress concentrations along the core walls in a slab width of 2 to 3 times the core wall thickness, with stress peaks at the slab-core web-flange regions where the local slab-core stiffness is large. It is noted that the slab regions around the lintel beams and the I-E coupling beams between the Core and Elev sections, show smooth and flatter S_{yy} stress distributions. However, slab regions around the E-S coupling beams demonstrate an S_{yy} stress band concentration over a slab width of 2 to 3 times the core wall thickness due to the three-dimensional stiffening and influence of the proximity of the Elev and Stair section walls on the S-E-slabs.

The S_{yy} stresses in the S-E-slabs due to Q_Y earthquake loads (1.40 MPa) are more pronounced giving values about 9 times the S_{yy} stresses due to Q_X earthquake loads (0.17 MPa).

5.3.3.3 Shear Stresses S_{xy}

Results of the S_{xy} stress distributions in the E-S-slabs in Fig. 5.53 show an irregular asymmetrical surface about the core sections web walls centerline, with several stress peaks.

In the S-slabs, very steep irregular S_{xy} stress distributions are noted in the shapes of long peaked humps across the slab-core flange wall regions with steep gradients, then reducing toward the column supports. From the stress contours, these long peaked S_{xy} stress humps are concentrated over a slab band width of 2 to 4 times the flange wall thickness adjacent to the flange walls. These shear stress slab bands stretch from the slab-Core to the slab-Stair web-flange corner regions. Several S_{xy} stress reversals are observed across the web walls with smaller humped stress peaks near the slab-web-flange corner regions. In the E-slabs along the core flange walls, several sharp S_{xy} stress peaks occur at the slab-core flange wall end and web-flange corner regions. A large double stress hump is observed in the E-slabs at the stiffer lintel and coupling beams end regions, which then reduces sharply toward the more flexible center beam span-slab regions. These S_{xy} stress concentrations are due to the increased slab stiffness at the core web-flange corner and flange wall regions created by the interaction of the cores substructure components.

The S_{xy} stresses in S-E-slabs give a maximum of ± 0.61 MPa due to Q_Y earthquake loads, which are about 30% larger than the S_{xy} stresses of ± 0.42 MPa due to Q_X earthquake loads.

5.3.4 Three-Dimensional Distribution of Slab Stresses due to Dead Loads

5.3.4.1 Transverse Stresses S_{xx}

Figure 5.54 shows a symmetrical S_{xx} stress distribution in the E-S-slabs about the core sections web walls centerline.

In the S-slabs. a large peaked parabolic shaped tensile S_{xx} stress distribution is observed along the slab-Core and slab-Stair section web walls. decreasing sharply away from the web wall toward the column supports. Maximum stresses are $0.38\,MPa$ located at the center of the slab-core web wall regions. From the S_{xx} stress contours, this parabolic stress surface is concentrated over a slab distance equal to 2 to 3 times the core web wall thickness away from the web walls. Along the flange walls. stress reversals are noted to compressive concentrations of $-0.29\,MPa$ at the slab-Core web-flange corner and near the slab-Stair flange wall end regions. Across the I-E coupling beams span, the S_{xx} stresses show a flat distribution with small values. In the E-slabs, a similar large peaked parabolic shaped tensile S_{xx} stress distribution is observed along the slab-Core web wall region and tensile stress peaks near the slab-Stair flange wall end regions. In the lintel and coupling beam slab regions, the S_{xx} stresses show a flat distribution.

Dead load S_{xx} stresses in the S-E-slabs range from $0.38\,MPa$ to $-0.29\,MPa$. and are about one-half to equal in value compared to the slab S_{xx} stresses of $\pm0.68\,MPa$ for Q_X earthquake loads $\pm0.33\,MPa$ for Q_Y earthquake loads.

5.3.4.2 Longitudinal Stresses S_{yy}

Figure 5.55 illustrates a symmetrical S_{yy} stress distribution in the E-S-slabs about the core sections web walls centerline. Several S_{yy} stress concentrations are noted with reversals from tension to compression around the vicinity of the cores (stiffer slab regions) and very steep stress gradients toward the more flexible column supports.

In the S-slabs, tensile S_{yy} stress peaks occur at the slab-mid-flange wall regions with reversals to compressive peaks between the core sections at the midspan slab regions of the coupling beams. Along the core web walls, compressive stress peaks are noted at the stiffer slab-core web-flange corner regions and the stress surface smooths out rapidly toward the flexible column supports to very small values. In the E-slabs, sharp tensile S_{yy} stress peaks occur along the slab-Core flange walls toward the web-flange corner regions. The stresses then drop to almost zero values at the mid-panel region of the E-slab within the Core section, with a slight tensile stress hump towards the lintel beam regions indicating the stiffer to more flexible slab regions.

Maximum S_{yy} stresses in the S-E-slabs due to dead loads are $\pm0.25\,MPa$ which are larger than the S_{yy} stresses due to Q_X earthquake loads with values of $\pm0.17\,MPa$, and one-sixth of the S_{yy} stresses due to Q_Y earthquake loads with stresses of $\pm1.40\,MPa$.

5.3.4.3 Shear Stresses S_{xy}

Figure 5.56 demonstrates a very irregular, jagged peaked S_{xy} stress distribution in the E-S-slabs being symmetrical about the core sections web walls centerline.

In the S-slabs, irregular S_{xy} stress concentrations of $\pm 0.22\,MPa$ are located at the slab-Core and the slab-Stair web-flange corner regions, the stiffest corners around the cores substructure. Across the slab-Core and slab-Stair web wall regions, a sharp shear stress drop and reversal is observed between the core section web-flange corner to corner locations. Along the slab-core flange walls, smaller S_{xy} stress humps are noted at the mid-flange wall regions with alternating stress reversals. The S-slabs S_{xy} stresses are concentrated over a slab width equal to approximately 2 to 3 times the core wall thickness in the slabs away from the core walls. Beyond this distance, the S_{xy} stresses in the slabs drop sharply to negligible values at the column supports.

In the E-slabs, a double S_{xy} stress reversal is observed within the slab-Core-lintel and coupling beam regions showing stress peaks at the slab-core web-flange corner regions and stress humps near the slab-I-E coupling beam locations. This double S_{xy} stress reversal is due to the rapidly varying slab support conditions and stiffness changing from Core web-flange corner to Core flange wall end to the coupling and lintel beams plus Elev flange wall end supports.

Maximum S_{xy} stresses in the S-E-slabs due to dead loads are $\pm 0.22\,MPa$, which are as significant as the dead load slab S_{xx} and S_{yy} stresses. Compared to the slab S_{xy} stresses of $\pm 0.42\,MPa$ for Q_X earthquake loads and $\pm 0.61\,MPa$ for Q_Y earthquake loads, the dead load slab S_{xy} stresses are 50% to 30% of these values.

5.3.5 Three-Dimensional Distribution of Slab Moments due to Q_X Earthquake Loading

5.3.5.1 Transverse Moments M_{xx}

Examination of the M_{xx} moments in the E-S-slabs in Fig. 5.57 shows an asymmetrical distribution about the core sections web walls centerline.

In the S-slabs, steep conical M_{xx} moment distributions of peak values $\pm 84\,kN \cdot m$ occur around the column supports in the column-column strip slab regions, with positive bending on one side reversing to negative moments on the column line side. These conical moment surfaces decrease sharply over the column-column strip regions to moment reversals and concentrations at the slab-core flange wall supports. The mid-panel slab regions between the columns show very small M_{xx} moments. A line of contra-flexure is located between the column supports and the flange walls at about 0.25 to 0.33 of the slab distance from the core sections flange walls.

Along the S-slabs-core sections flange walls, the M_{xx} moments show longer concentrated peaks of $\pm 40\,kN \cdot m$ to $\pm 60\,kN \cdot m$ across the entire slab-Stair flange wall, at the slab-Elev web-flange corner and flange wall ends, and at the slab-Core web-flange corner regions. These large moment concentrations are due to the varying core sections flange wall lengths and stiffnesses permitting moment redistribution along the slab-core flange wall regions. Across the Core and Stair web walls, the M_{xx} moments peak at the S-slab-core web-flange corner regions being equal and opposite at both ends (moment reversal between the web wall corners). The slab moments then drop sharply to a flat surface over about one-third of the distance to the column supports due to the changing slab stiffness, being more restrained (stiffer) near the core sections web walls and less restrained (more flexible) towards the column supports.

In the E-slabs, the M_{xx} moments are small demonstrating a flat surface throughout the slab regions within the Core section and the lintel beams, and within the Stair section. Small M_{xx} moment concentrations of $\pm 20\,kN \cdot m$ to $\pm 40\,kN \cdot m$ are observed at the E-slabs regions around the coupling and lintel beams joining to the core section flange wall ends and web-flange corners. A very flat M_{xx} moment surface is also noted in the E-slabs between the Core section and the lintel beams, increasing sharply to moment concentrations located close to the coupling and lintel beam joints due to the changing slab stiffness resulting in much less restraint in the slab-beam regions compared to the stiffer slab-core wall-beam regions.

5.3.5.2 Longitudinal Moments M_{yy}

Results of the M_{yy} moments in the E-S-slabs in Fig. 5.58 show an asymmetrical distribution about the core sections web walls centerline.

In the S-slabs, the M_{yy} moments show several humped pyramidal shaped concentrations of $\pm 29\,kN \cdot m$ over the column supports. These moments spread out and decrease radially around the columns over about one-third the slab panel region. Between the columns in the mid-panel slab areas parallel to the core flange walls, the M_{yy} moments drop sharply to small negative values (and vice-versa). For the slab-column regions behind the core sections web walls, the M_{yy} moments are $\pm 28\,kN \cdot m$ reversing from negative to positive bending across the column support and spreading to the center panel slab regions to a flatter distribution in the mid-panel areas parallel to the core sections web walls. Along the S-slabs-core sections flange wall regions, moment reversals are noted to negative bending (and vice-versa) with conical humped M_{yy} moment concentrations of $\pm 20\,kN \cdot m$ located at the stiffer slab-Core and slab-Stair web-flange corners, and at the slab-Stair and slab-Elev flange wall end regions. Across the Core and Stair sections web walls, a moment reversal occurs gradually between the stiffer slab-core flange-web corner to corner regions.

In the E-slabs, the M_{yy} moments are small with a very flat surface noted. However, moment concentrations with large peaks of values $\pm 20\,kN \cdot m$ to $\pm 25\,kN \cdot m$ are observed at the slab-coupling and lintel beam regions joining to the core sections flange wall ends and flange-web corners, due to the varying E-slab support conditions and stiffness, i.e. larger moments at the stiffer slab-core wall-beam regions.

5.3.5.3 Twisting Moments M_{xy}

Distributions of the M_{xy} moments in the E-S-slabs in Fig. 5.59 illustrate a symmetrical surface about the core sections web walls centerline.

Examination of the M_{xy} moments show a flat surface across the slabs with negligible values in the E-slabs and values of $\pm 5\,kN \cdot m$ in the S-slabs regions nearer the core sections. Small moment humps of less than $\pm 10\,kN \cdot m$ are observed at the S-slab-core corner regions and at the S-E-slabs-coupling and lintel beam end regions. In the S-slabs around the columns, the M_{xy} moment distributions are flat in the mid-panel regions showing sharp pyramidal peaks of $\pm 21\,kN \cdot m$ forming around the column supports in the column-column strip panel slab regions. The steepest M_{xy} moment gradient is in the S-slabs corner panel regions furthest from the Core and Stair section web-flange corners, mixed support conditions.

Maximum M_{xy} moments in the E-S-slabs around the slab-core sections wall-coupling and lintel beam regions are approximately $\pm 10\,kN \cdot m$ which are about 50% to 25% of the slab M_{xx} and M_{yy} moments, and therefore, they must be considered in the slab design.

5.3.6 Three-Dimensional Distribution of Slab Moments due to Q_Y Earthquake Loading

5.3.6.1 Transverse Moments M_{xx}

The M_{xx} moments in the E-S-slabs in Fig. 5.60 demonstrate a symmetrical distribution about the core sections web walls centerline. Several moment concentrations are located at the stiffer slab-core wall section end and corner regions.

In the S-slabs along the core flange walls, several M_{xx} moment concentrations of $\pm 20\,kN \cdot m$ are observed at the slab-Core and slab-Stair web-flange corner regions showing steep moment reversals along the core flange walls toward the slab-core flange wall ends. These M_{xx} moment peaks extend a slab width adjacent to the core section flange walls equal to 2 to 4 times the core wall thickness. Across the core web walls, a constant moment surface is noted over the central 80% of the slab-web wall regions increasing sharply to moment concentrations at the stiffer slab-core web-flange corner regions. Larger pyramidal shaped M_{xx} moments of $26\,kN \cdot m$ to $-31\,kN \cdot m$ form over the slab-column supports, concentrated over a column-column strip slab region and descend sharply to the mid-panel slab areas.

In the E-slabs, steep pyramidal shaped M_{xx} moments occur at the slab-Core flange wall end regions decreasing sharply toward the slab-Core web-flange corners and the center slab regions to a small moment reversal. These moment peaks are largest $20\,kN \cdot m$ at the slab-Core flange wall end-coupling and lintel beam regions, indicating distress and possible cracking in these regions. M_{xx} moment peaks are noted at the E-slabs-Stair flange wall end-coupling beam regions.

The most distressed slab region is located at the slab-Core-Elev flange wall ends-coupling and lintel beams regions where a double 90° pyramidal M_{xx} moment peak is noted ($\pm 20\,kN \cdot m$) due to the largest variation in the slab-core wall-beam stiffness.

5.3.6.2 Longitudinal Moments M_{yy}

Examination of the M_{yy} moments in the E-S-slabs in Fig. 5.61 shows a symmetrical distribution about the core sections web walls centerline with peaked concentrations observed throughout.

In the S-slabs along the slab-core flange wall regions, several M_{yy} moment reversals of $\pm 50\,kN \cdot m$ are observed from the slab-Core web-flange corners toward the slab-Core flange wall ends, reversing across the I-E coupling beams and again from the slab-Elev flange wall ends to the slab-Elev web-flange corner regions. A double M_{yy} moment reversal is noted across the slab-E-S coupling beams toward the slab-Stair web-flange corner regions. Across the slab-Core and slab-Stair web walls, an almost constant moment distribution with peaks is observed at the S-slabs-core corners and mid-web wall regions. Column regions of the S-slabs experience large positive pyramidal shaped M_{yy} moment concentrations of $85\,kN \cdot m$ with steep reversals to negative moment peaks of $-120\,kN \cdot m$ at the mid-panel slab regions between the columns.

In the E-slabs, large positive M_{yy} moments of $75\,kN \cdot m$ arranged in a saddle shaped distribution are noted in the slab portion enclosed by the Core section walls showing 2 moment peaks at the slab-Core flange wall end regions and a steep gradient drop toward the slab-Core web wall region. Negative pyramidal moment peaks of $-50\,kN \cdot m$ are observed in the slab portion enclosed within the Stair section walls at the slab-Stair flange wall end regions.

The most complex M_{yy} moment distributions and concentrations in the S-E-slabs occur along the slab-core flange wall ends and web-flange corners, and slab-coupling and lintel beams regions due to the increased slab stiffness at the core web-flange corner and flange wall regions.

5.3.6.3 Twisting Moments M_{xy}

Results of the M_{xy} moment distribution in the E-S-slabs in Fig. 5.62 illustrate a highly irregular asymmetrical surface about the core sections web walls centerline.

In both the S-E-slabs several M_{xy} moment reversals occur with steep gradients at the slab-core web-flange corners and flange wall end regions, and at the slab-coupling and lintel beam locations. At the S-slabs-Core and S-slabs-Stair corner regions, a flat M_{xy} moment surface is observed over one-half of the slab panel due to the large restraint in these regions resulting from the three-dimensional core section interaction.

S-slabs M_{xy} moments are larger in the column supported regions where the moments show peaked pyramids of $\pm 84\,kN \cdot m$ around the columns, with sharp reversals in the slab-column areas further from the core web walls. Along the slab-core sections flange wall regions the M_{xy} moments are of pyramidal shaped concentrations of $\pm 50\,kN \cdot m$ showing several reversals from the slab-Core flange wall end to the slab-Elev flange wall end to the slab-Stair flange wall end regions. Slab regions around the I-E coupling beams, the lintel beams, the Core and Elev flange wall ends demonstrate the most irregular M_{xy} moment surface showing moment peaks and humps of $\pm 50\,kN \cdot m$ and moment reversals along the slab-I-E coupling beams span regions due to the varying slab-core-beam support stiffness.

Maximum M_{xy} moments in the S-E-slabs around the slab-core wall-coupling and lintel beam regions are approximately $\pm 50\,kN \cdot m$, which are about twice the M_{xx} moments and about 75% of the M_{yy} moments. Therefore, they must be considered in the slab design.

5.3.7 Three-Dimensional Distribution of Slab Moments due to Dead Loads

5.3.7.1 Transverse Moments M_{xx}

Figure 5.63 shows a symmetrical M_{xx} moment surface in the E-S-slabs about the core sections web walls centerline.

In the S-slabs along the slab-core sections flange wall regions, negative M_{xx} moments of $-100\,kN \cdot m$ are observed showing a constant distribution across the slab-core flange walls and decreasing moments at the slab-coupling beam joints. These M_{xx} moments adjacent to the core sections flange wall regions are concentrated in a slab band width of 2 to 3 times the core wall thickness. Across the slab-Core and slab-Stair web wall regions the M_{xx} moments are constant with a flat surface over 80% of the slab-web walls, then the moments peak to $-50\,kN \cdot m$ at the stiffer slab-core web-flange corner regions. A flat moment surface is noted in the mid-panel slab regions behind the Core and Stair web walls with a steep negative moment pyramidal shaped drop to $-140\,kN \cdot m$ around the columns. Negative pyramidal shaped M_{xx} moments occur around the columns in the column-column slab regions and positive moment humps are noted in the mid-panel S-slab regions with values ranging from $107\,kN \cdot m$ to $-142\,kN \cdot m$.

In the E-slabs, the M_{xx} moments are small showing a smooth flat surface. Moment concentrations are observed along the slab-coupling beams regions, more notably in the E-slab region of the Elev and Core section flange wall ends and I-E coupling beams, and the slab-lintel beams junctions with negative moment values of $-75\,kN \cdot m$. This variation in the slab M_{xx} moments is due to the changing slab support stiffness.

Dead load M_{xx} moments in the E-S-slabs are approximately 20% to 30% larger than the slab M_{xx} moments due to Q_X earthquake loads, and about 4 to 6 times the slab M_{xx} moments due to Q_Y earthquake loads.

5.3.7.2 Longitudinal Moments M_{yy}

Figure 5.64 illustrates a symmetrical M_{yy} moment surface in the E-S-slabs about the core sections web walls centerline.

In the S-slabs, the M_{yy} moment distribution demonstrates a constant negative moment band of value $-100\,kN \cdot m$ across the slab-Core and slab-Stair web wall regions over the central 80% of the slab-web wall length, and moment peaks of $-125\,kN \cdot m$ at the stiffer slab-core web-flange corner regions. These M_{yy} moments are concentrated over a slab band distance of 2 to 3 times the core wall thickness adjacent to the core walls, and a steep upward moment gradient is observed toward the mid-panel slab region to a constant positive moment of $45\,kN \cdot m$. At the slab-column regions, negative M_{yy} moments of pyramidal shape $-138\,kN \cdot m$ are concentrated over the column-column strip slab regions. Along the S-slab-core flange wall regions, a very irregular negative M_{yy} moment distribution is observed with values of $-50\,kN \cdot m$ along the slab-core flange wall regions to concentrations of $-100\,kN \cdot m$ located at the slab-core flange wall end regions. The moments increase sharply to positive values in the mid-panel slab regions adjacent to the slab-core flange walls with values of $25\,kN \cdot m$ near the column supports. A drop to negative pyramidal shaped M_{yy} moments of $-125\,kN \cdot m$ is noted in the slabs around the column supports.

In the E-slabs. large M_{yy} moment concentrations are observed at the slab-coupling beam end regions with values of $-25\,kN \cdot m$ to $-50\,kN \cdot m$. The slab-I-E coupling beams. slab-lintel beams and the slab-Core and slab-Elev flange wall end regions show the most varied M_{yy} moment distribution. The E-slabs within the Core section are in positive bending showing a moment hump of $25\,kN \cdot m$ at the mid-panel slab region. These variations in the slab M_{yy} moments are due to the changing slab support stiffness.

Dead load M_{yy} moments in the E-S-slabs are 2 to 5 times the M_{yy} moments due to Q_X earthquake loads, and between one-half to equal the M_{yy} moments due to Q_Y earthquake loads.

5.3.7.3 Twisting Moments M_{xy}

Figure 5.65 demonstrates an irregular M_{xy} moment surface in the E-S-slabs, being asymmetrical about the core sections web walls centerline.

The S-slabs experience several peaked M_{xy} moment concentrations and reversals along the slab-core sections flange wall regions. extending from the core web-flange wall corners to the flange wall ends. Double humped M_{xy} moment peaks of $\pm 25\,kN \cdot m$ are located at the slab-Core and slab-Stair web-flange corner regions extending 10% of the slab-web wall length and along 80% of the slab-flange walls. Similar negative/positive M_{xy} moment peaks of $\pm 25\,kN \cdot m$ are present along the slab-coupling and lintel beam end regions. Around the slab-column supports, moment peaks of $\pm 90\,kN \cdot m$ occur with steep gradients concentrated over the column-column strip slab regions, and moment reversals in the mid-panel slab regions being the largest in the corner slab panel next to the Core and Stair sections; i.e. where the largest variation in the slab-core wall-beam stiffness is present.

In the E-slabs. the M_{xy} moments are small demonstrating a very flat surface. This response is due to the three-dimensional cores configuration stiffening and restraining the E-slabs. However. M_{xy} moment peaks do occur at the slab-coupling and lintel beam locations due to the changing slab support conditions.

The M_{xy} moments in the E-S-slabs due to dead loads are about equal to the M_{xx} and the M_{yy} moments. Compared to the slab M_{xy} moments due to Q_X earthquake loads of $\pm 22\,kN \cdot m$ and Q_Y earthquake loads of $\pm 84\,kN \cdot m$. the dead load slab M_{xy} moments $\pm 94\,kN \cdot m$ are as significant and they must be considered in the design.

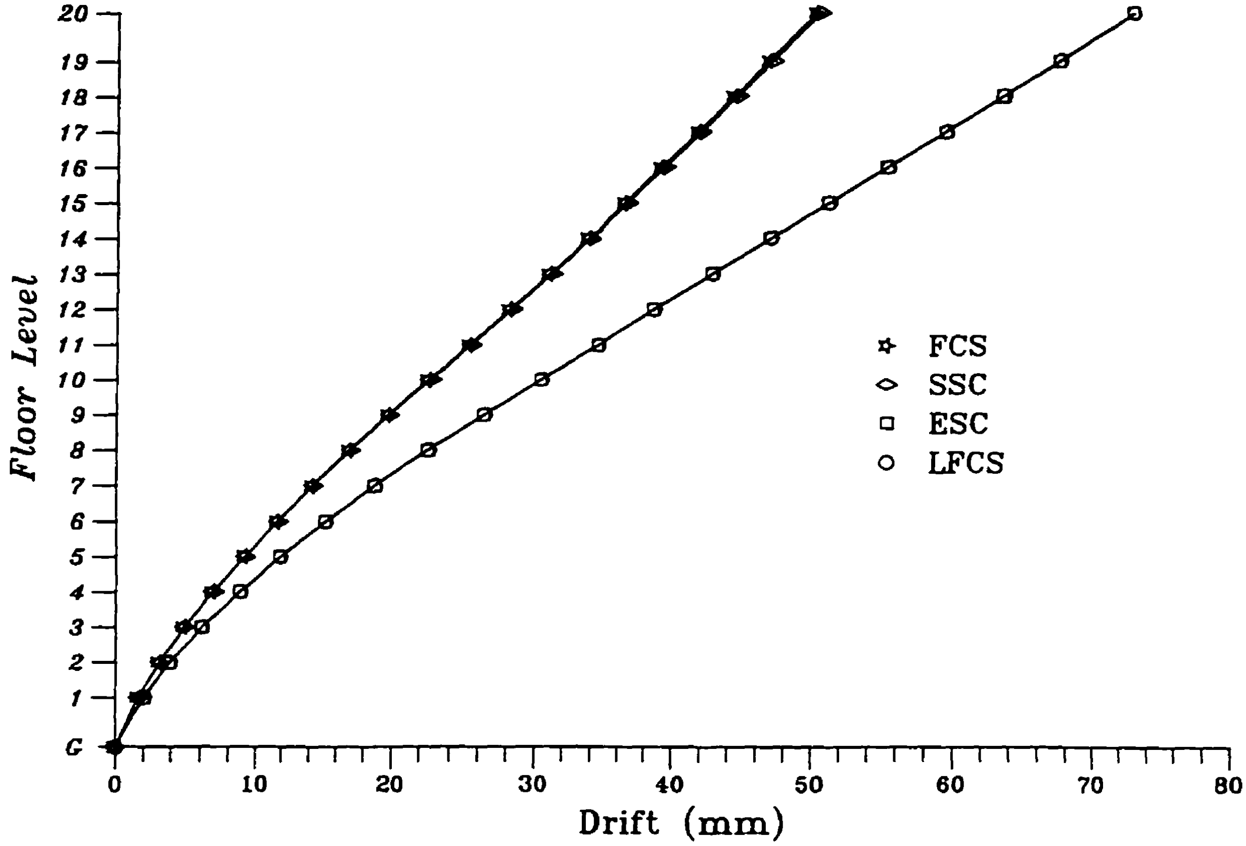

Figure 5.1 Drift Profiles – Q_X Earthquake Loading – Elastic Analyses Model Results

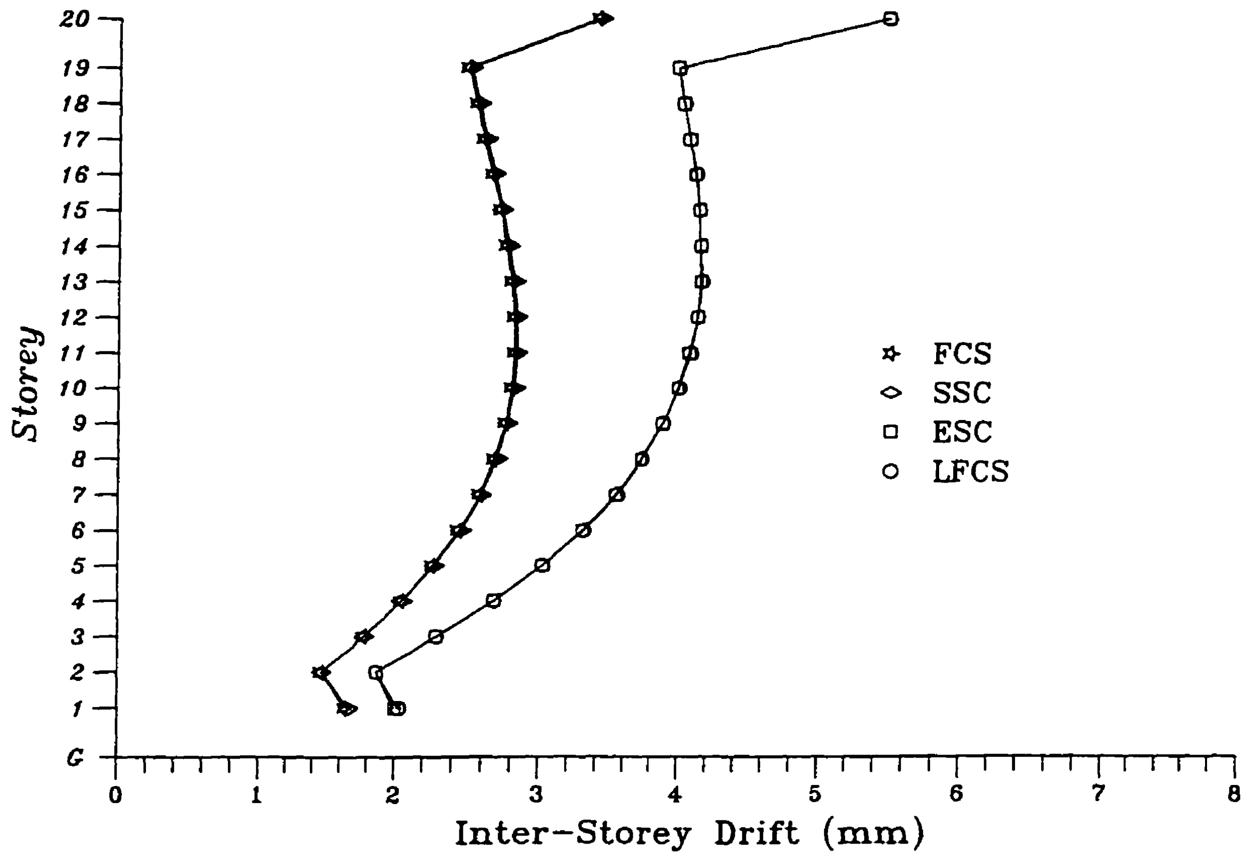

Figure 5.2 Inter-Storey Drift Profiles – Q_X Earthquake Loading – Elastic Analyses Model Results

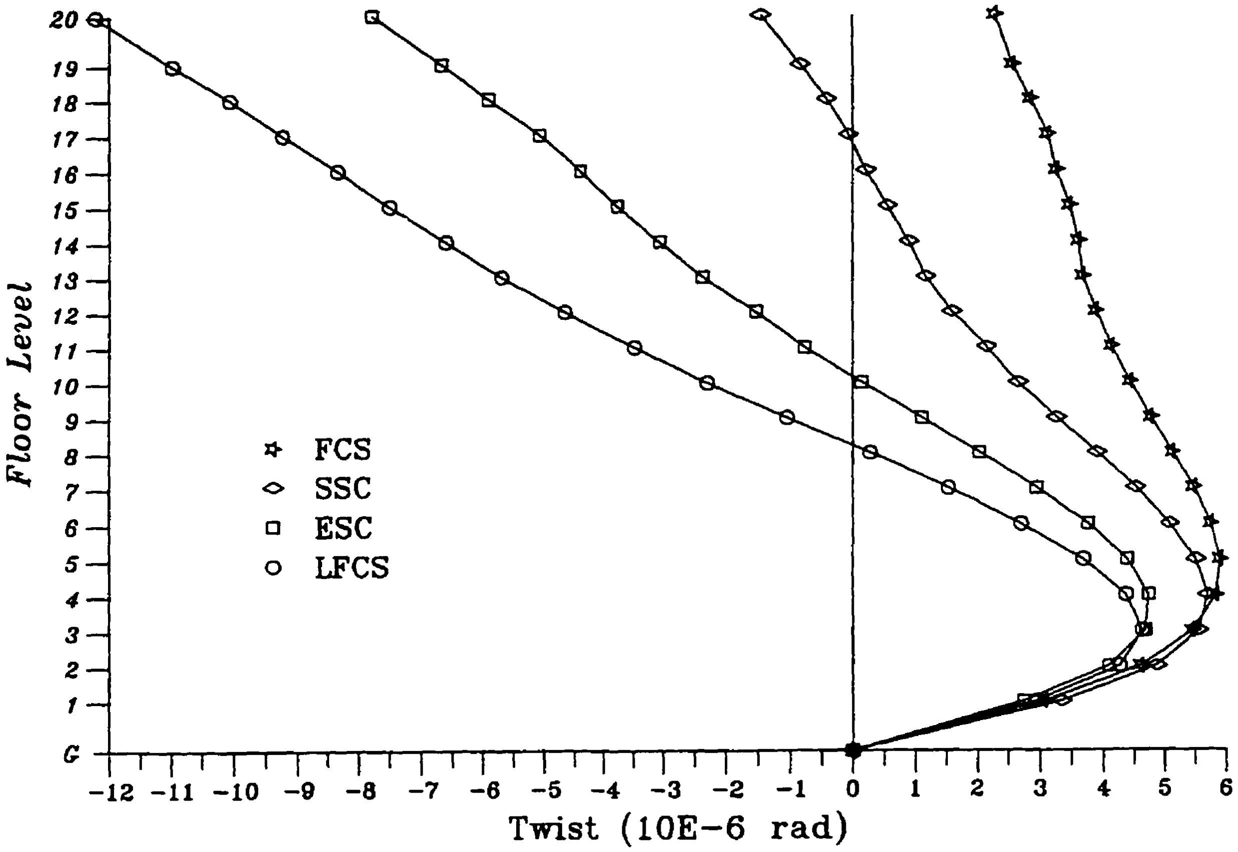

Figure 5.3 Twist Profiles - Q_X Earthquake Loading - Elastic Analyses Model Results

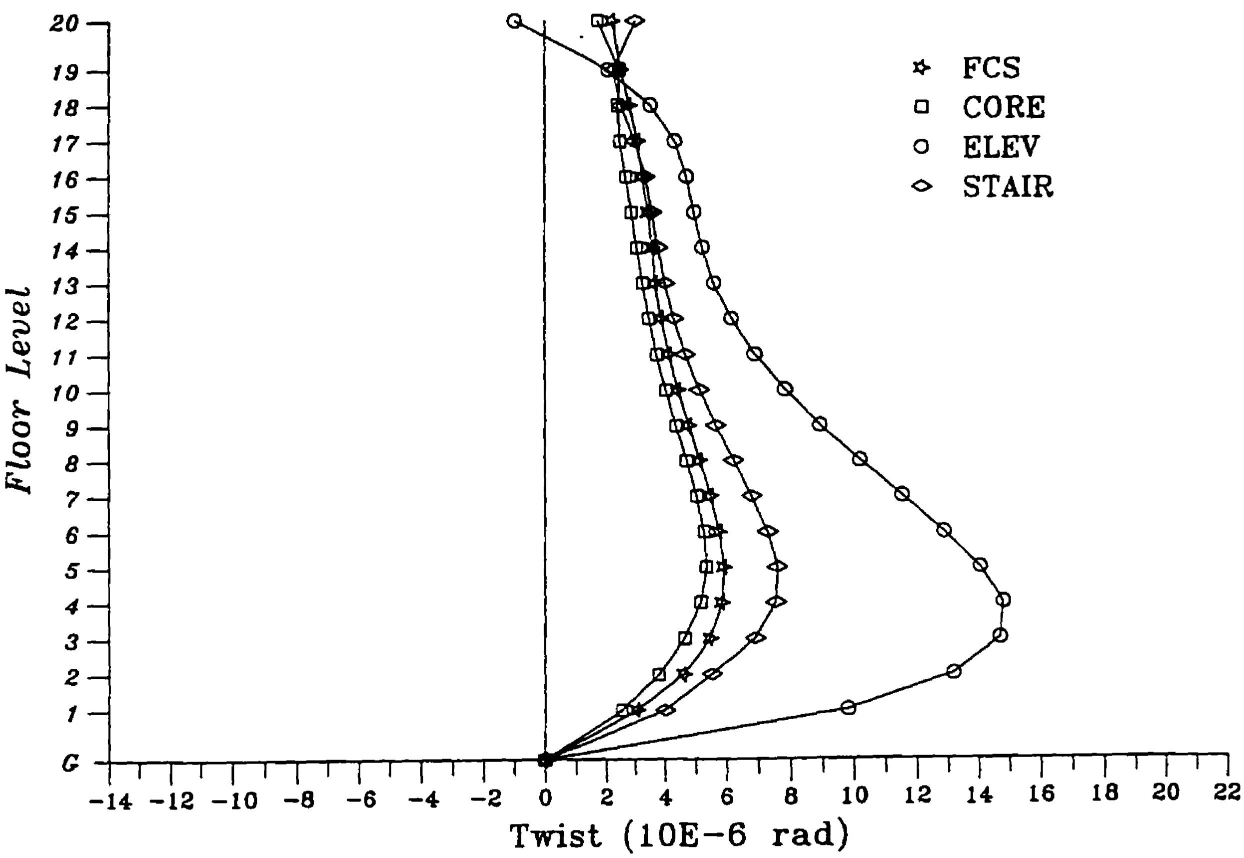

Figure 5.4 Twist Profiles - Q_X Earthquake Loading
- Elastic Analysis FCS Model and Individual Core Sections Results

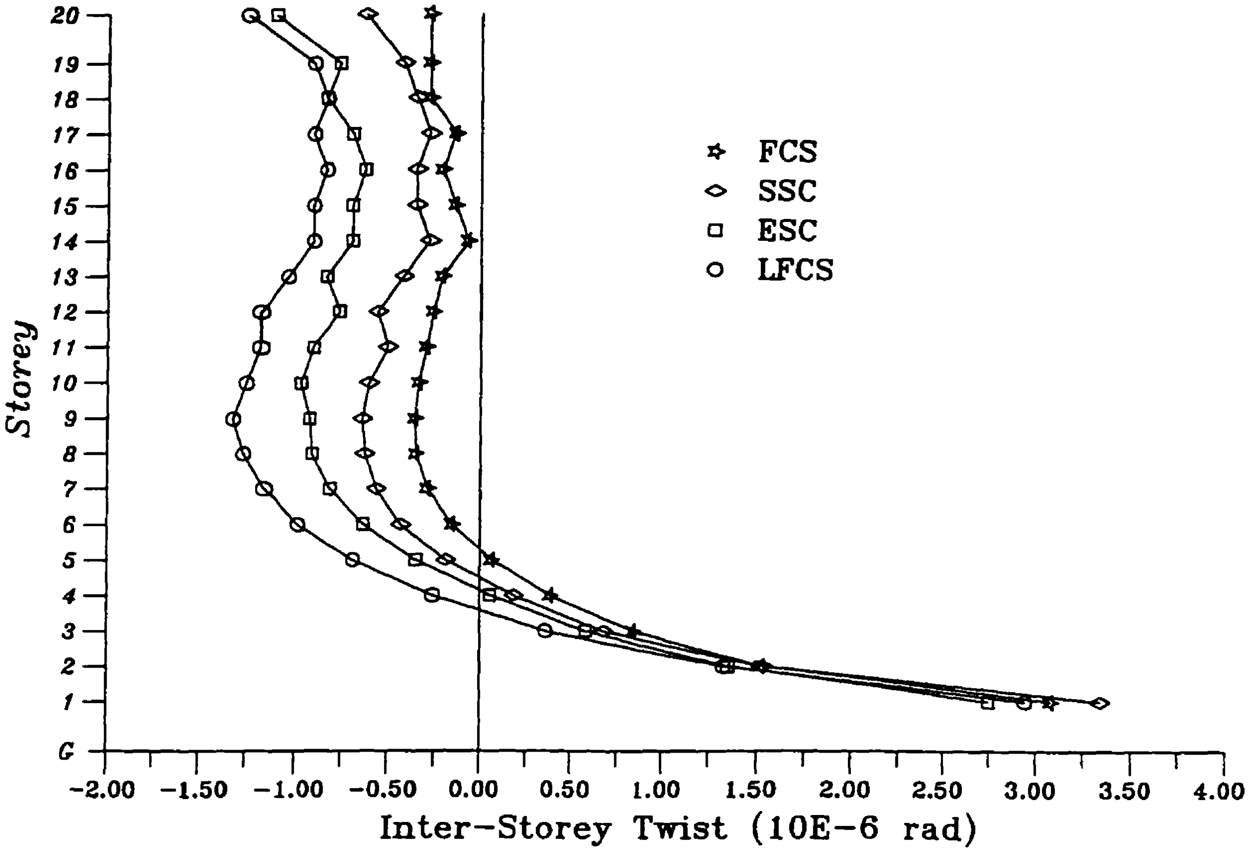

Figure 5.5 Inter-Storey Twist Profiles – Q_X Earthquake Loading – Elastic Analyses Model Results

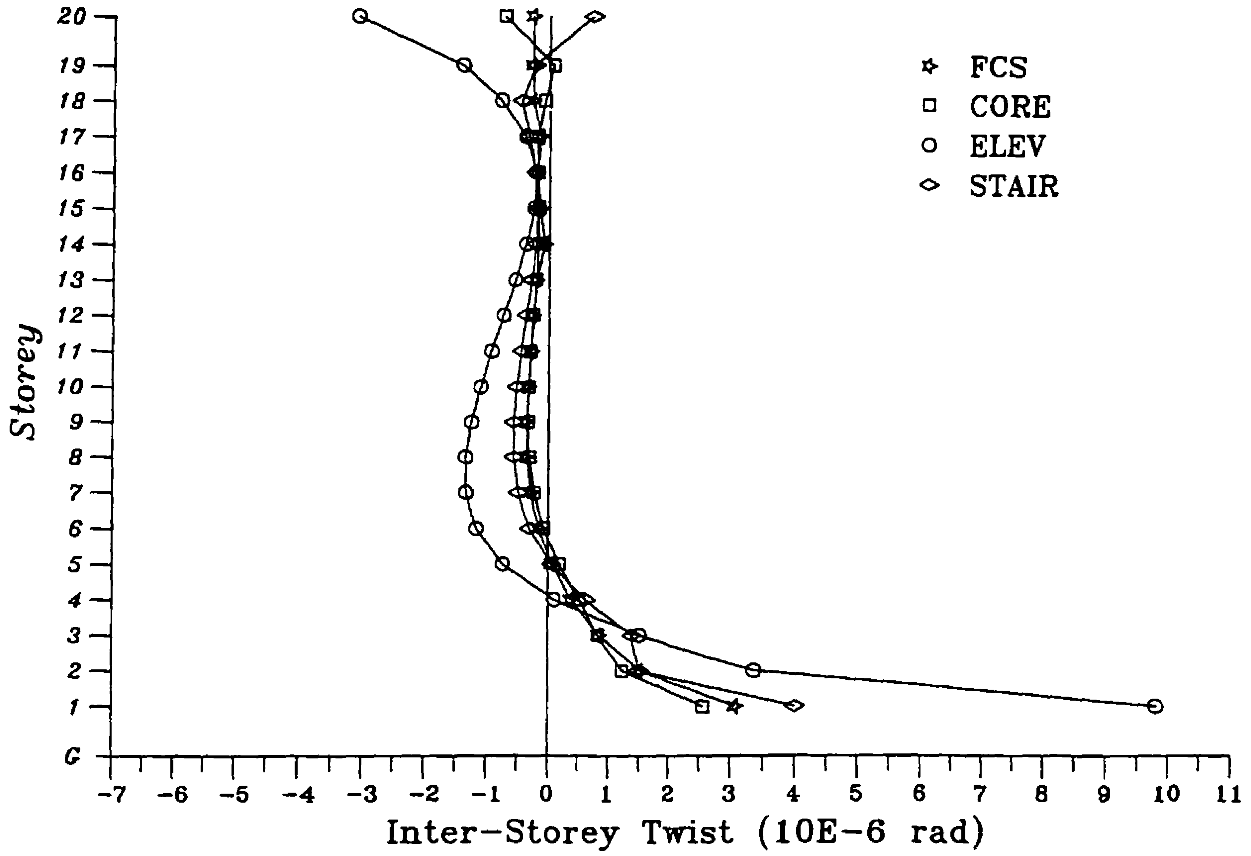

Figure 5.6 Inter-Storey Twist Profiles – Q_X Earthquake Loading – Elastic Analysis FCS Model and Individual Core Sections Results

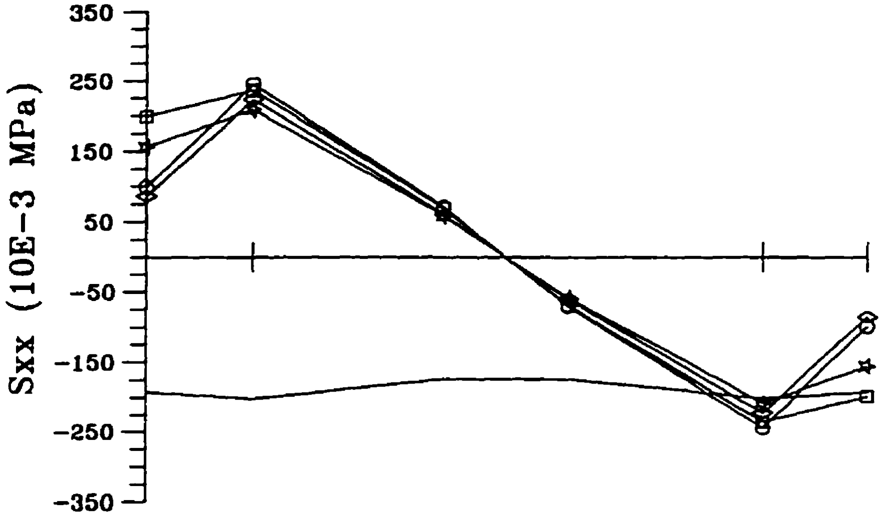

(a) Stairwell Core

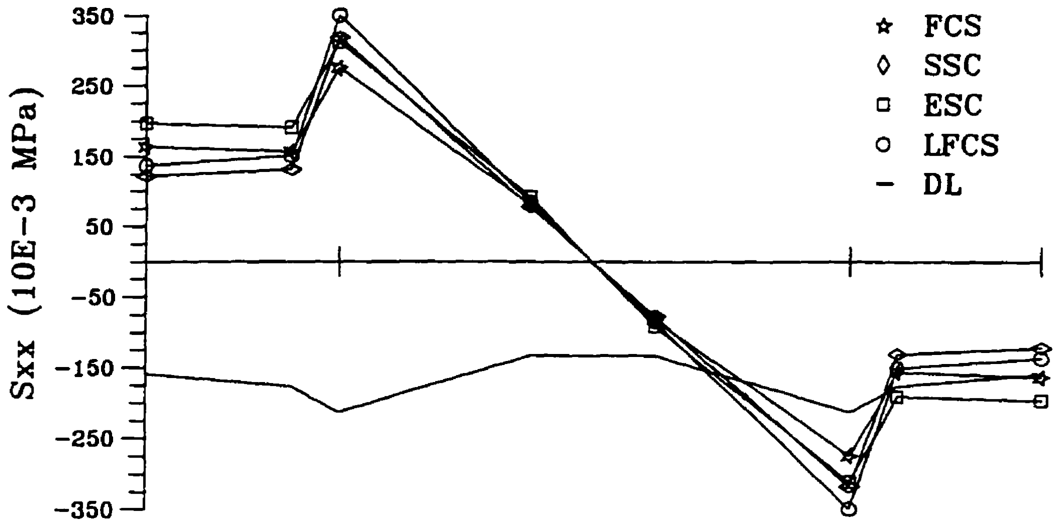

(b) Elevator Core

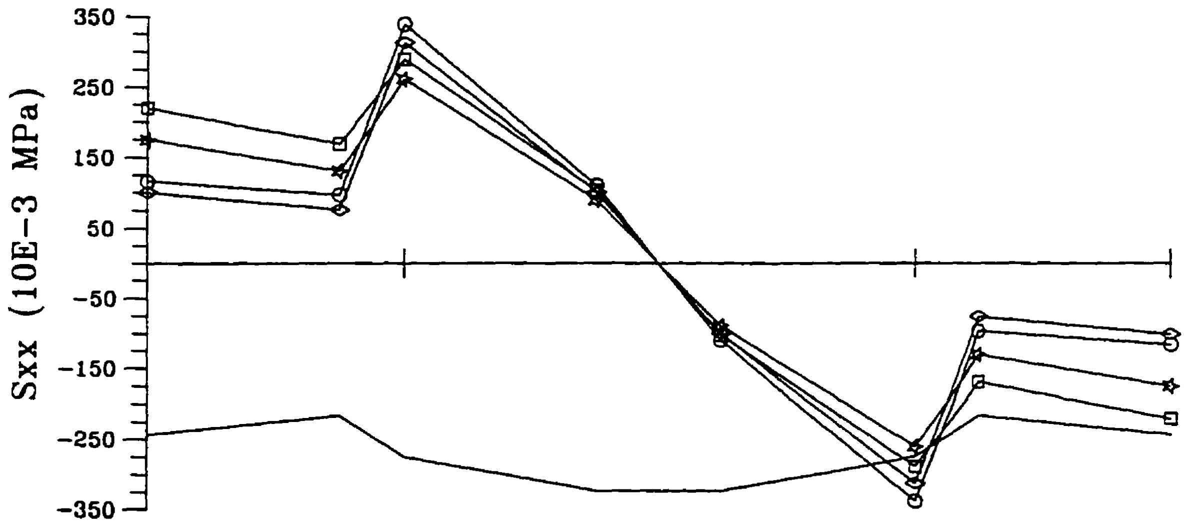

(c) Infilled-Slab Core

Figure 5.7 Distribution of the Transverse Stresses S_{xx} at the Cores Section Base – Q_X Earthquake Loading – Elastic Analyses Model Results

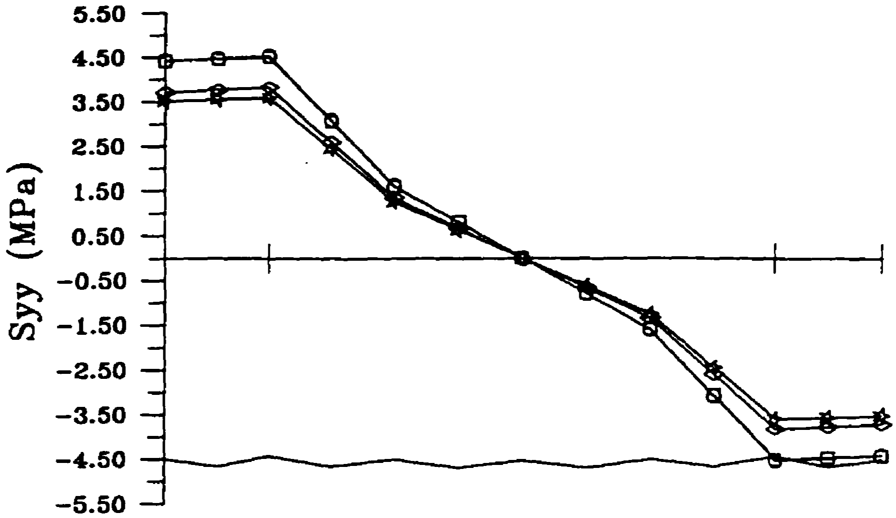

(a) Stairwell Core

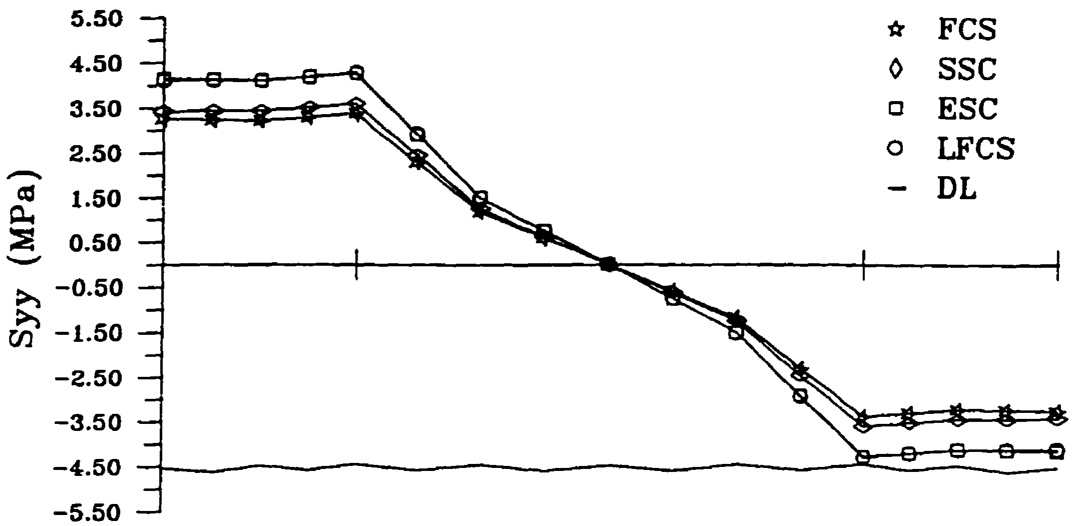

(b) Elevator Core

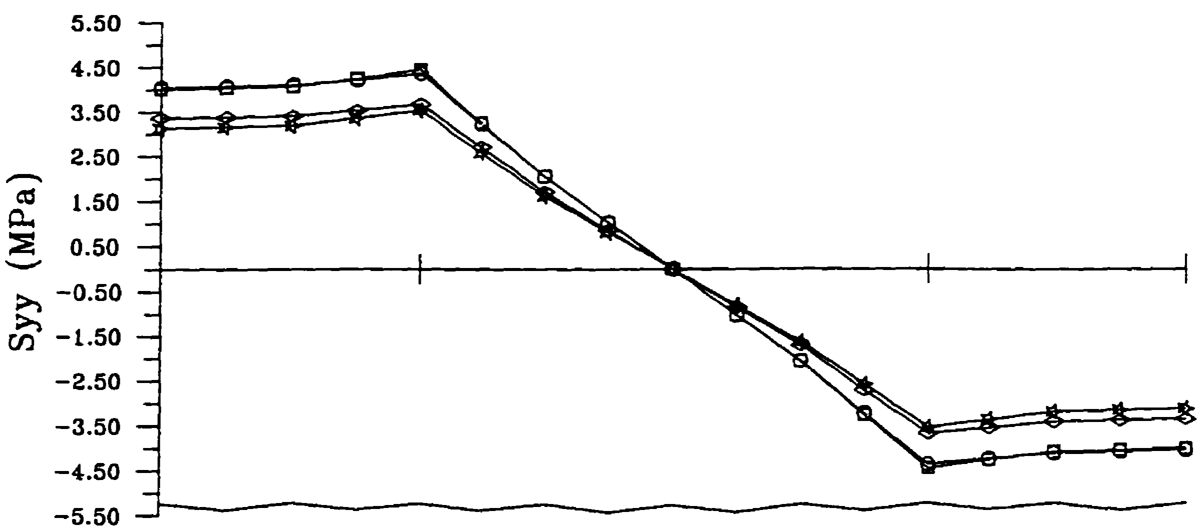

(c) Infilled-Slab Core

Figure 5.8 Distribution of the Longitudinal Stresses S_{yy} at the Cores Section Base – Q_X Earthquake Loading – Elastic Analyses Model Results

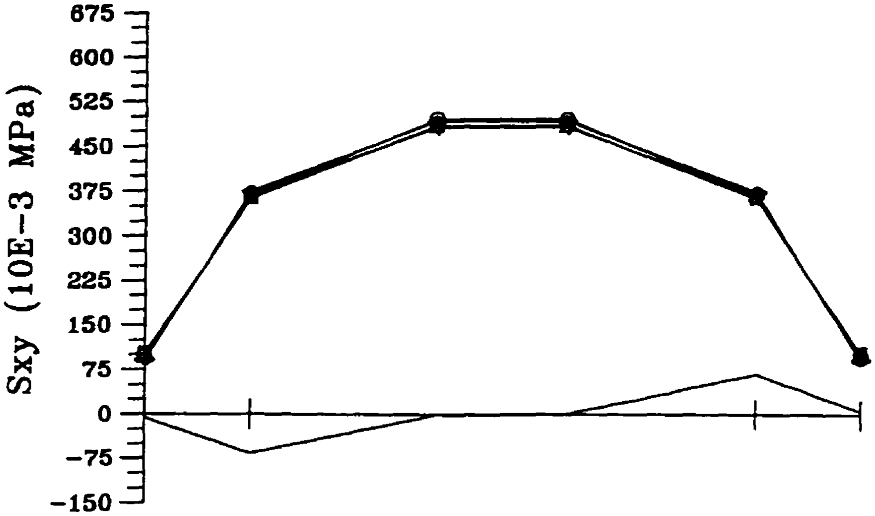

(a) Stairwell Core

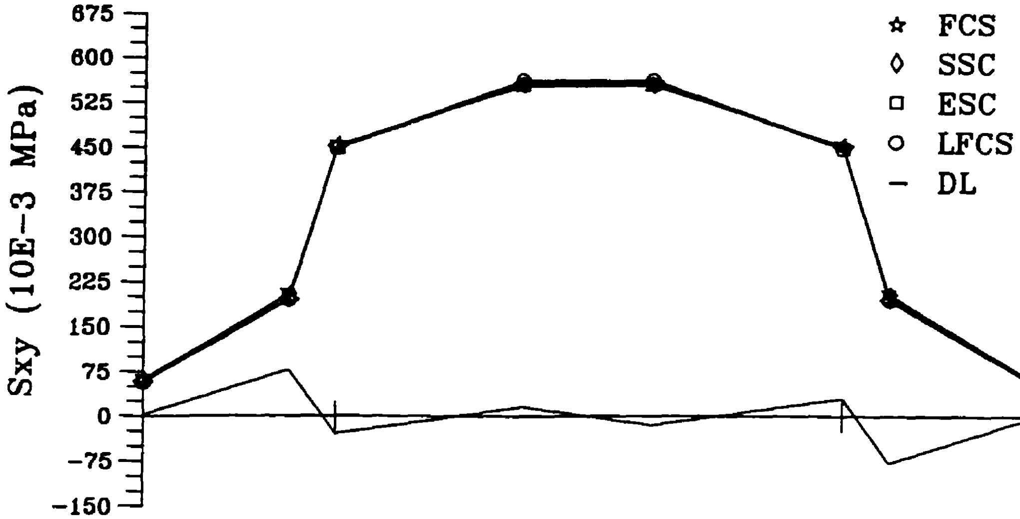

(b) Elevator Core

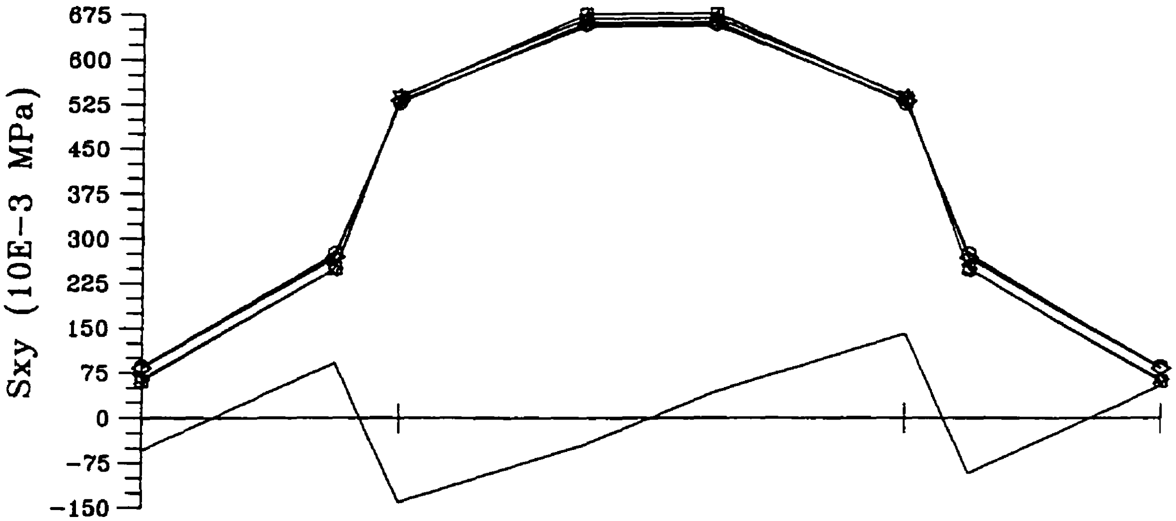

(c) Infilled-Slab Core

Figure 5.9 Distribution of the Shear Stresses S_{xy} at the Cores Section Base – Q_X Earthquake Loading – Elastic Analyses Model Results

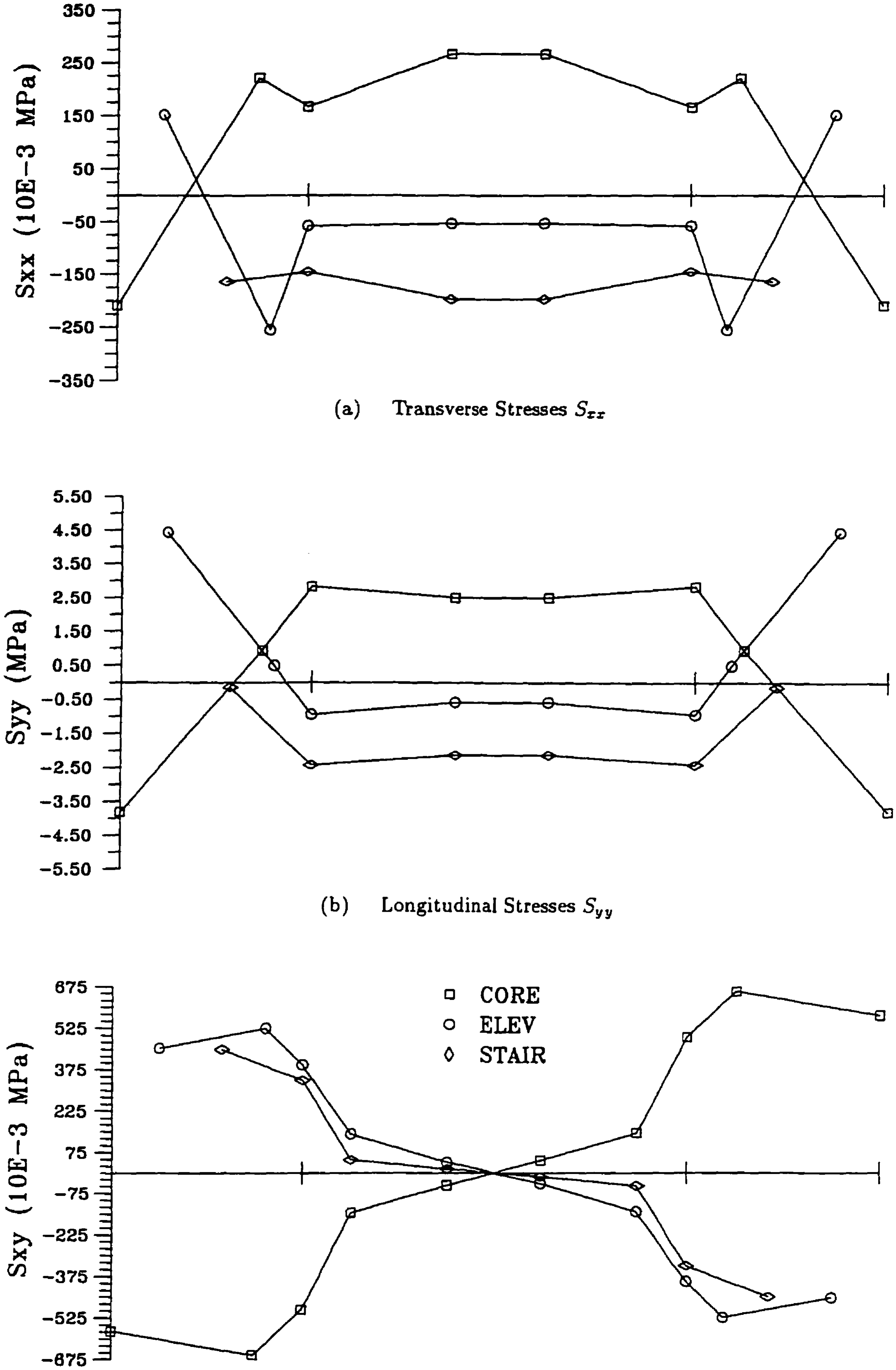

(a) Transverse Stresses S_{xx}

(b) Longitudinal Stresses S_{yy}

(c) Shear Stresses S_{xy}

Figure 5.10 Distribution of the Axial and Shear Stresses at the Cores Section Base – Q_Y Earthquake Loading – Elastic Analysis FCS Model Results

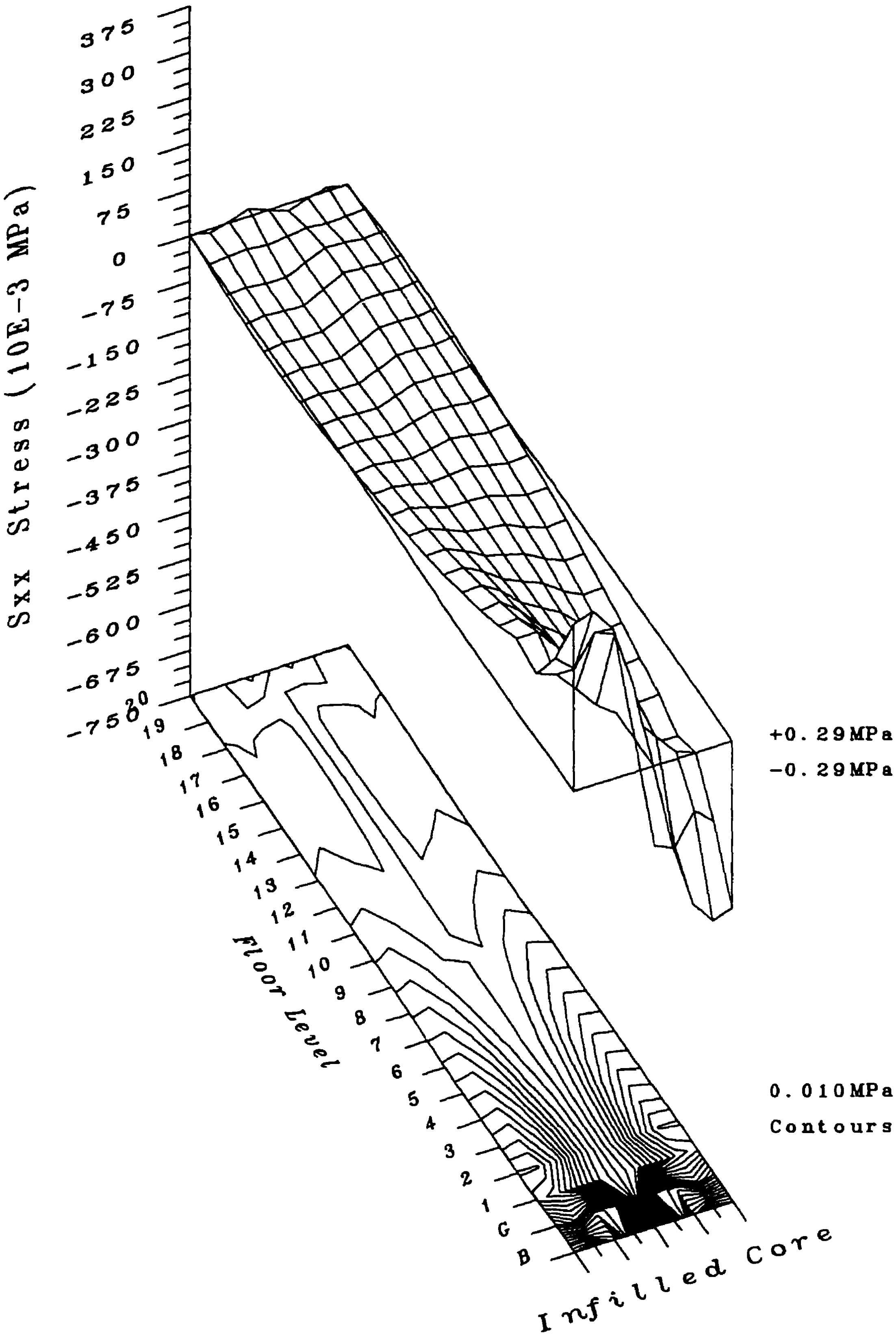

Figure 5.11 Distribution of the Transverse Stresses S_{xx} in the Infilled-Slab Core – Q_X Earthquake Loading – Elastic Analysis FCS Model Results

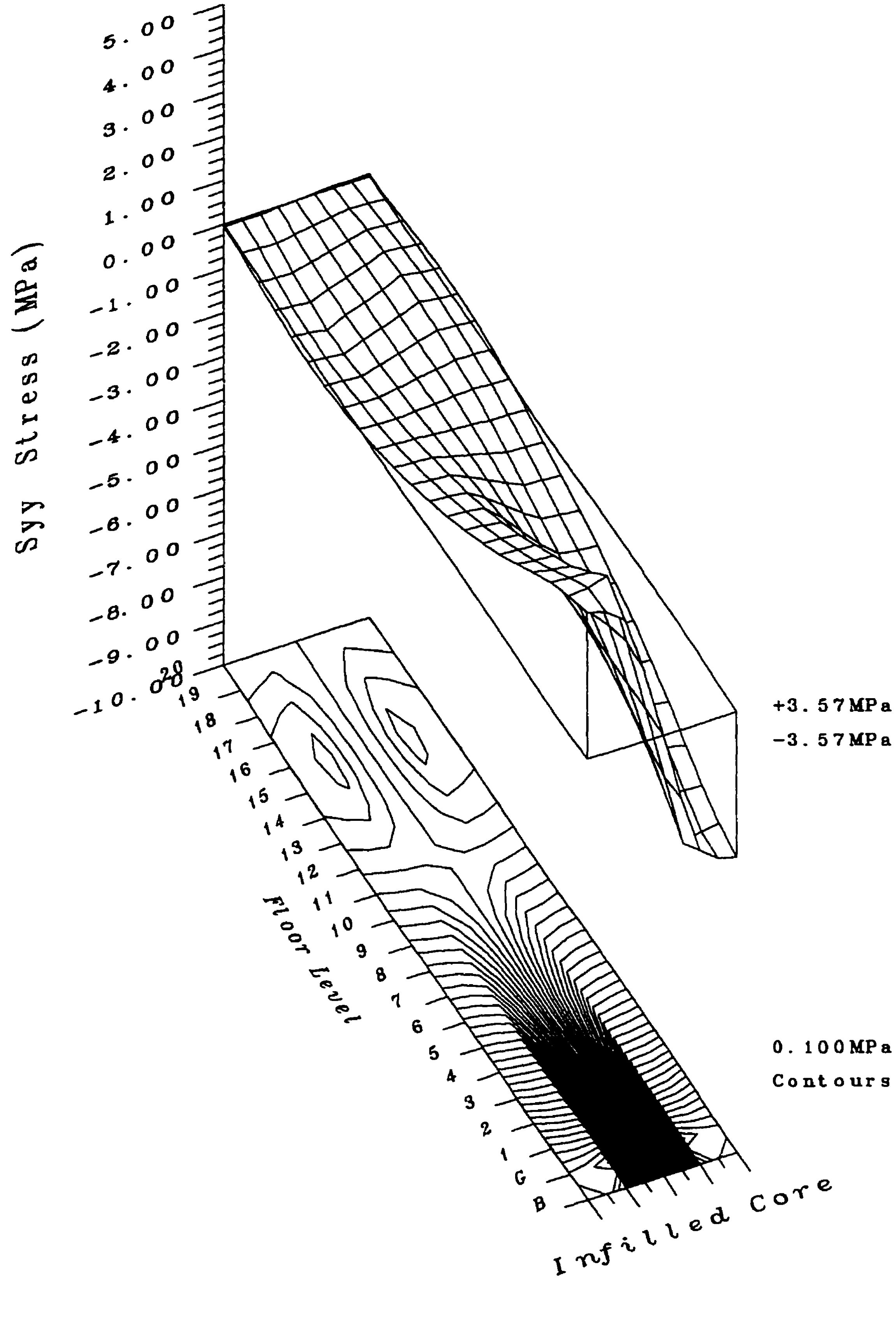

Figure 5.12 Distribution of the Longitudinal Stresses S_{yy} in the Infilled-Slab Core – Q_X Earthquake Loading – Elastic Analysis FCS Model Results

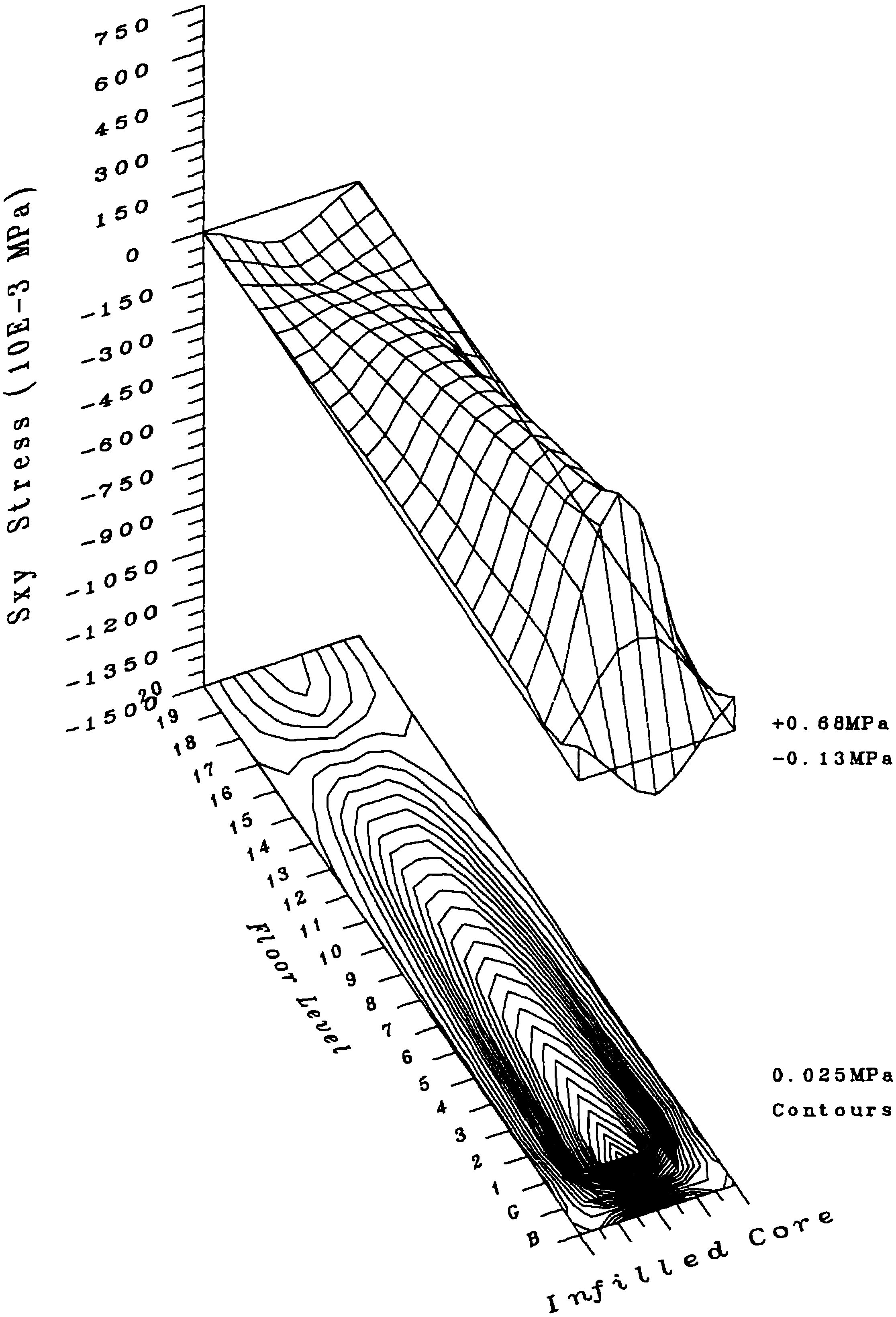

Figure 5.13 Distribution of the Shear Stresses S_{xy} in the Infilled-Slab Core – Q_X Earthquake Loading – Elastic Analysis FCS Model Results

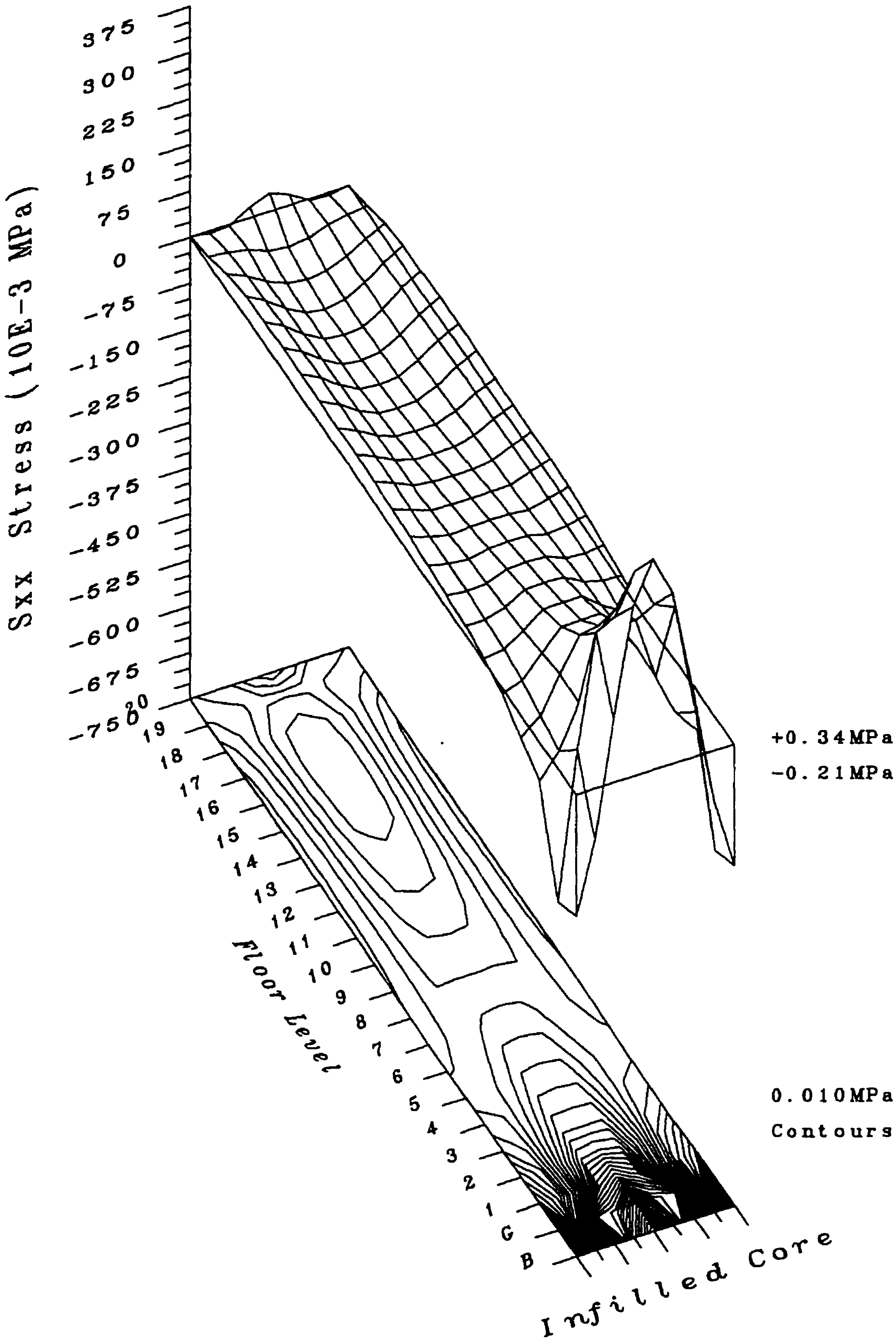

Figure 5.14 Distribution of the Transverse Stresses S_{xx} in the Infilled-Slab Core – Q_Y Earthquake Loading – Elastic Analysis FCS Model Results

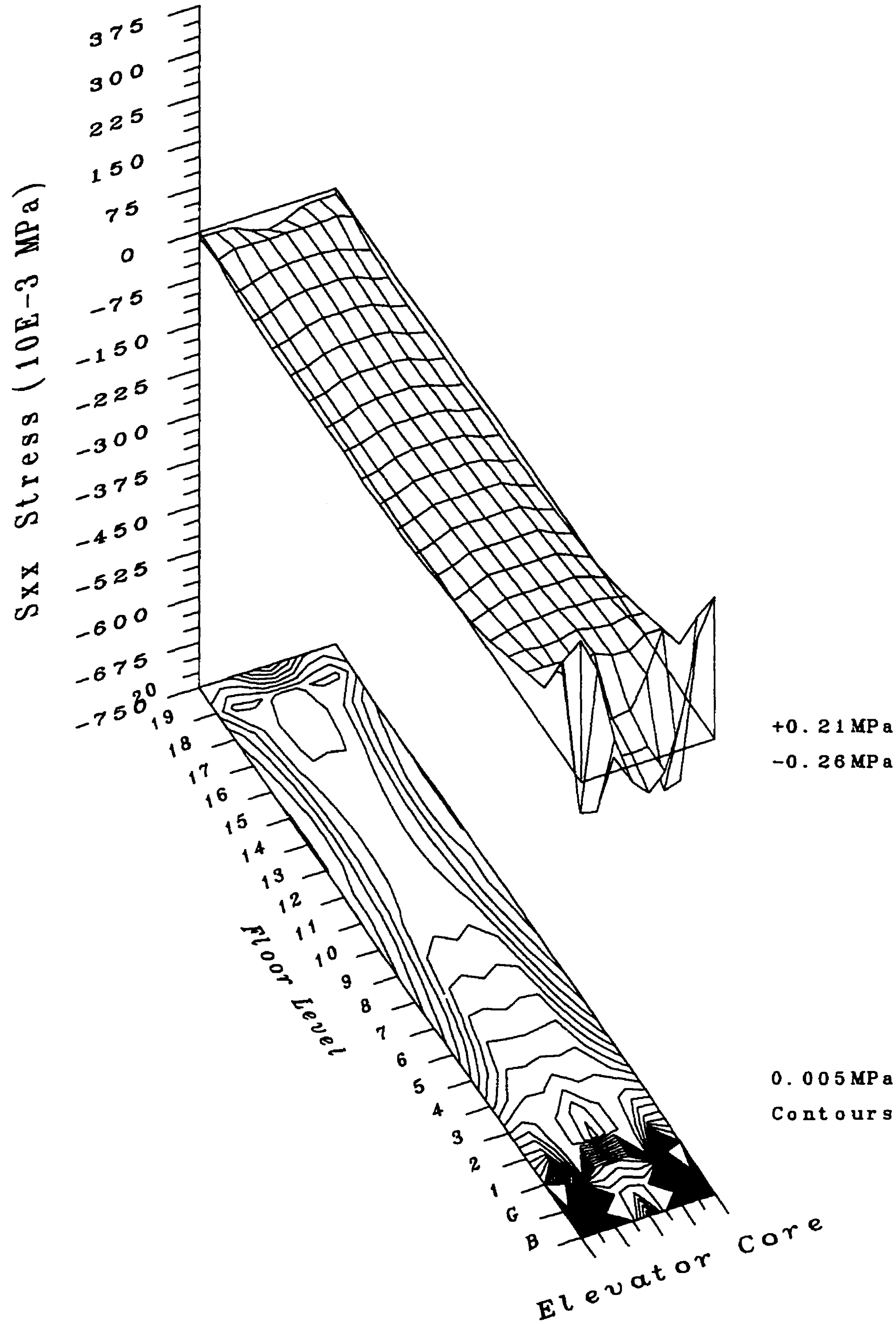

Figure 5.15 Distribution of the Transverse Stresses S_{xx} in the Elevator Core – Q_Y Earthquake Loading – Elastic Analysis FCS Model Results

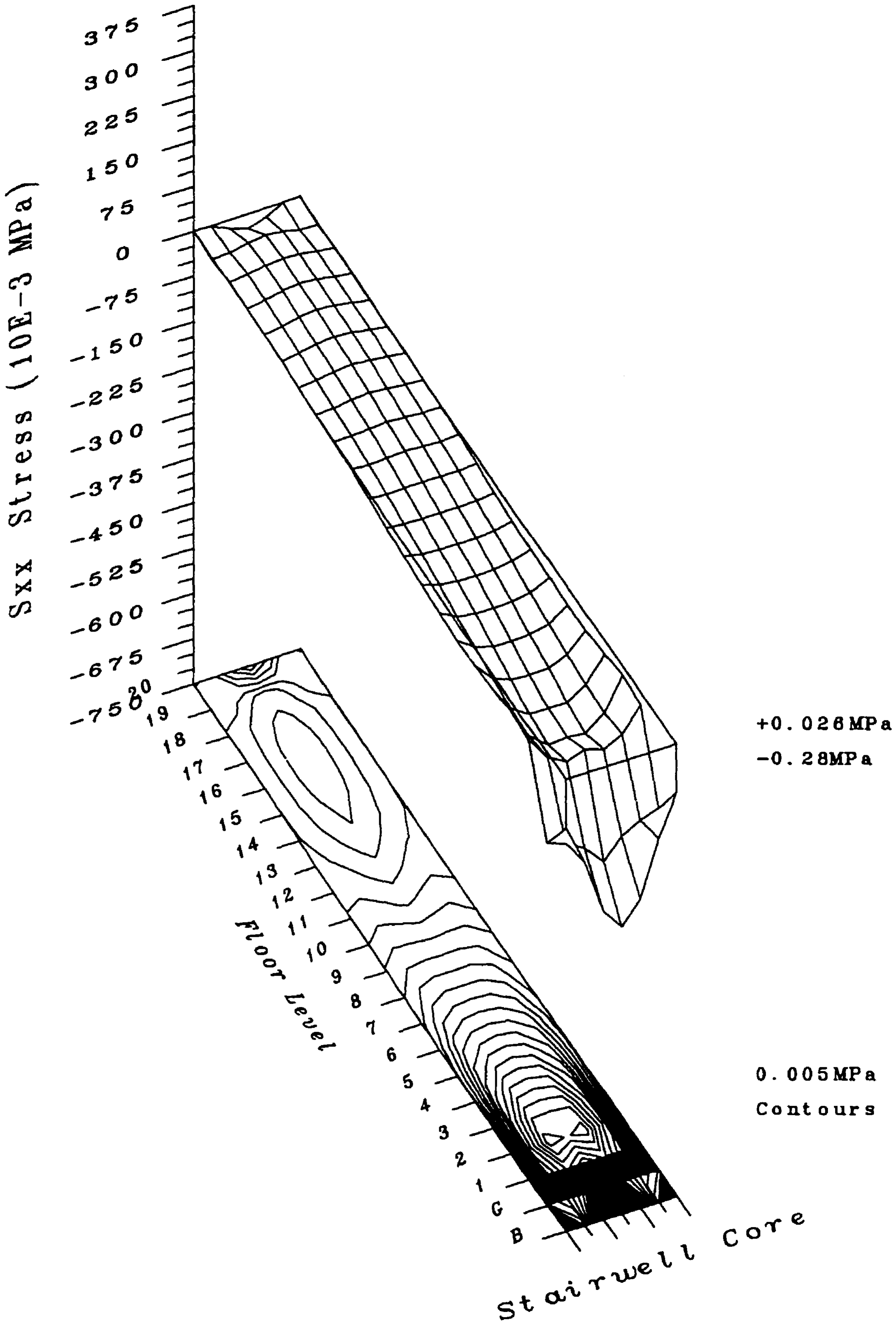

Figure 5.16 Distribution of the Transverse Stresses S_{xx} in the Stairwell Core – Q_Y Earthquake Loading – Elastic Analysis FCS Model Results

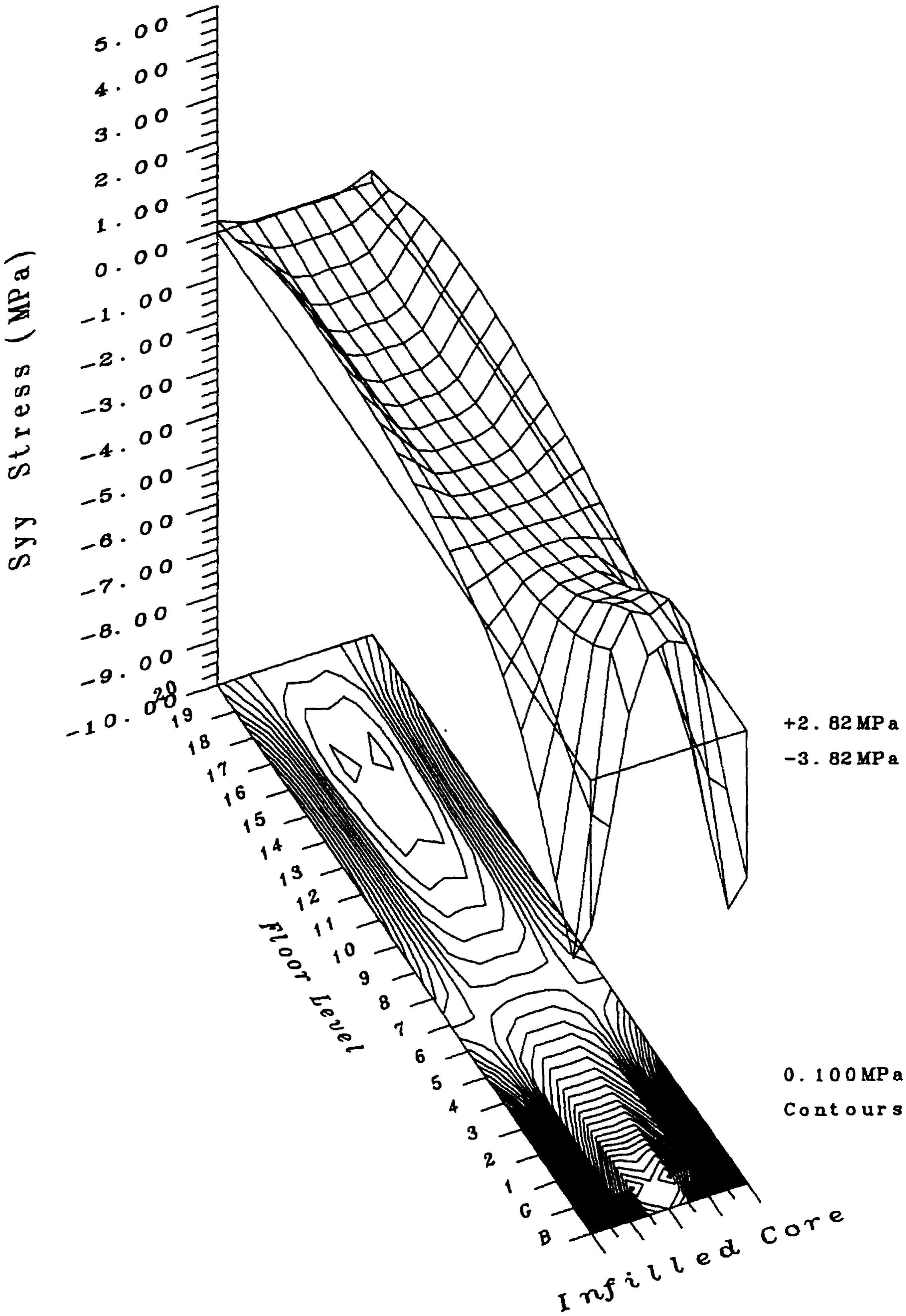

Figure 5.17 Distribution of the Longitudinal Stresses S_{yy} in the Infilled-Slab Core - Q_Y Earthquake Loading - Elastic Analysis FCS Model Results

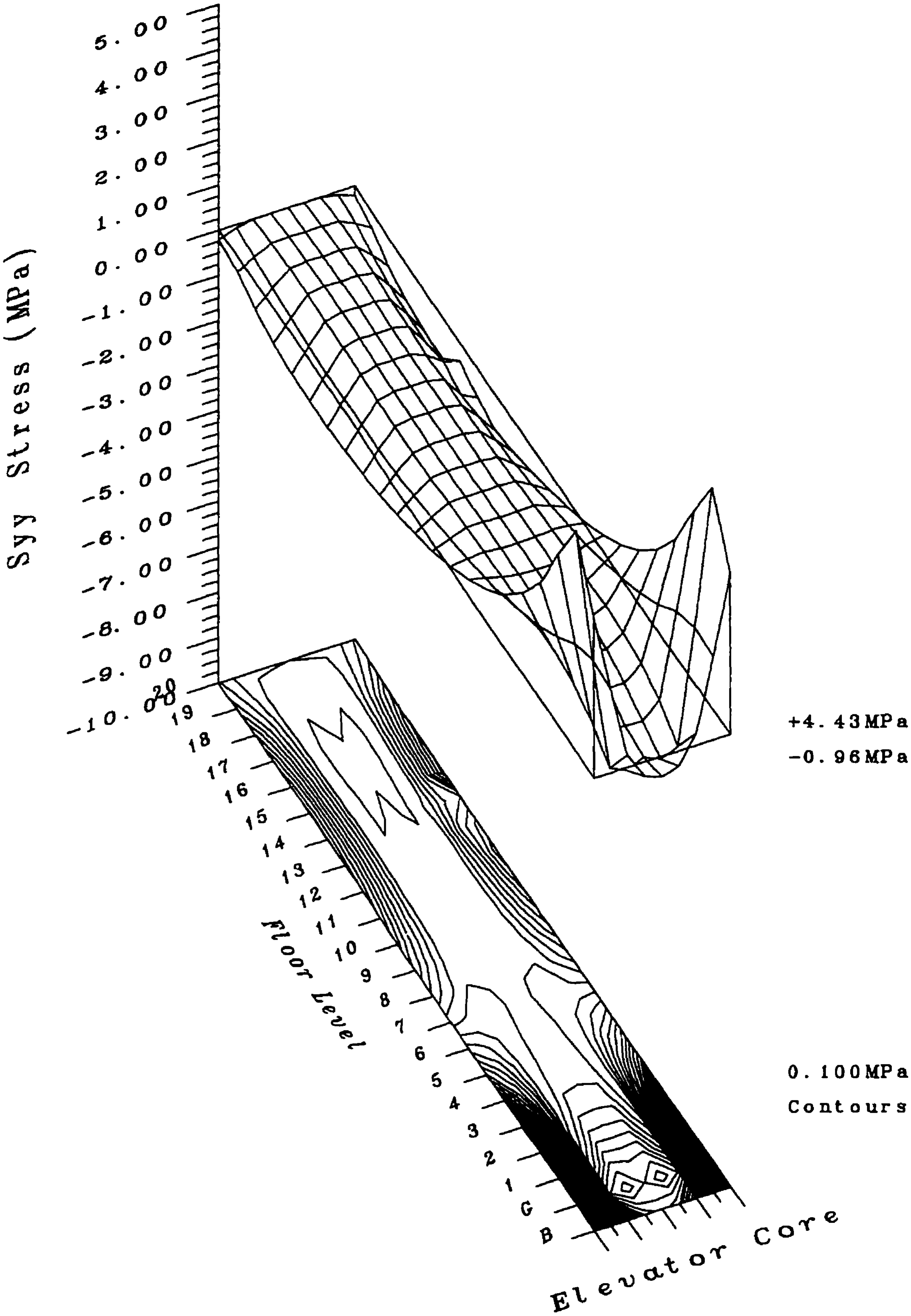

Figure 5.18 Distribution of the Longitudinal Stresses S_{yy} in the Elevator Core – Q_Y Earthquake Loading – Elastic Analysis FCS Model Results

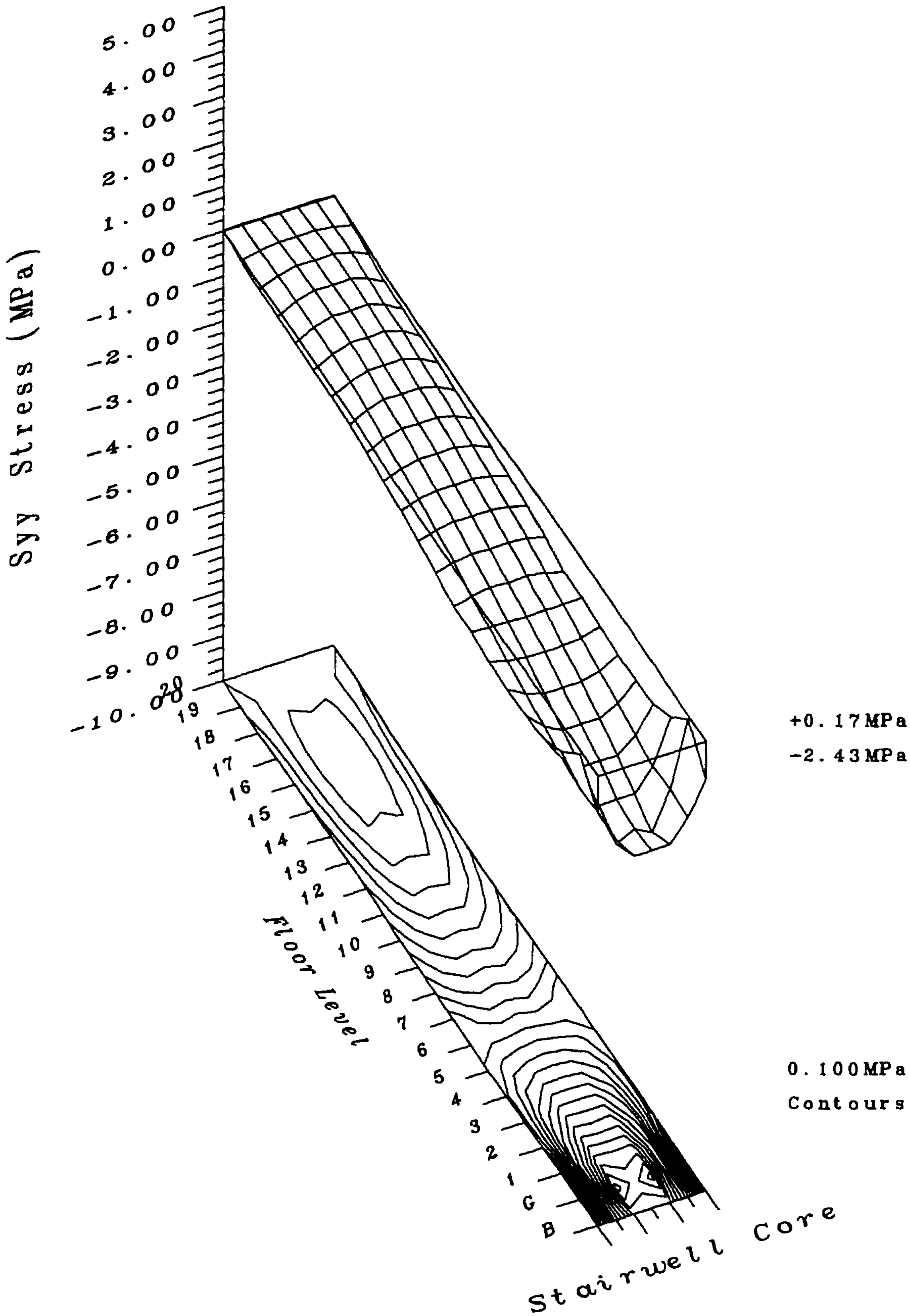

Figure 5.19 Distribution of the Longitudinal Stresses S_{yy} in the Stairwell Core – Q_Y Earthquake Loading – Elastic Analysis FCS Model Results

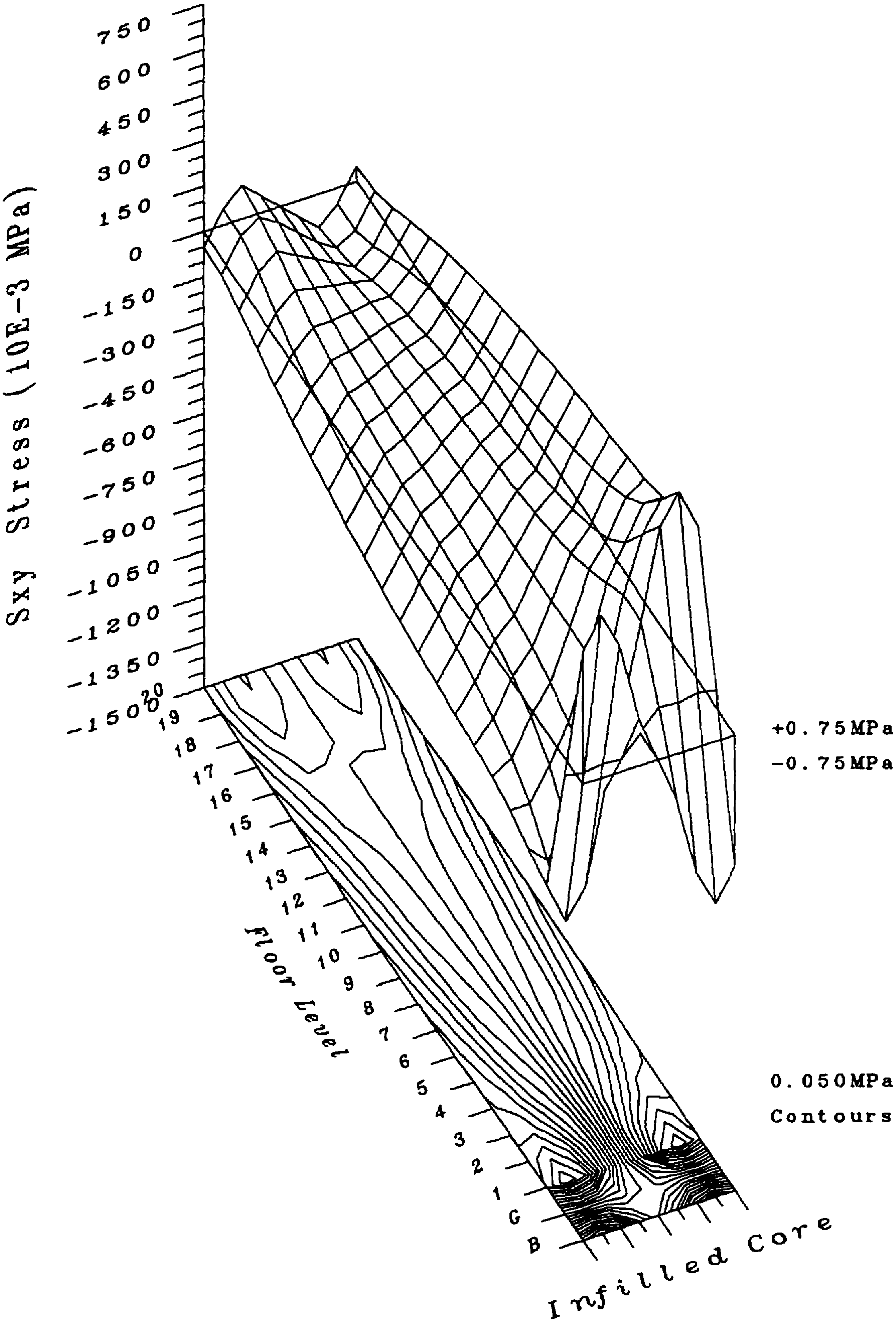

Figure 5.20 Distribution of the Shear Stresses S_{xy} in the Infilled-Slab Core – Q_Y Earthquake Loading – Elastic Analysis FCS Model Results

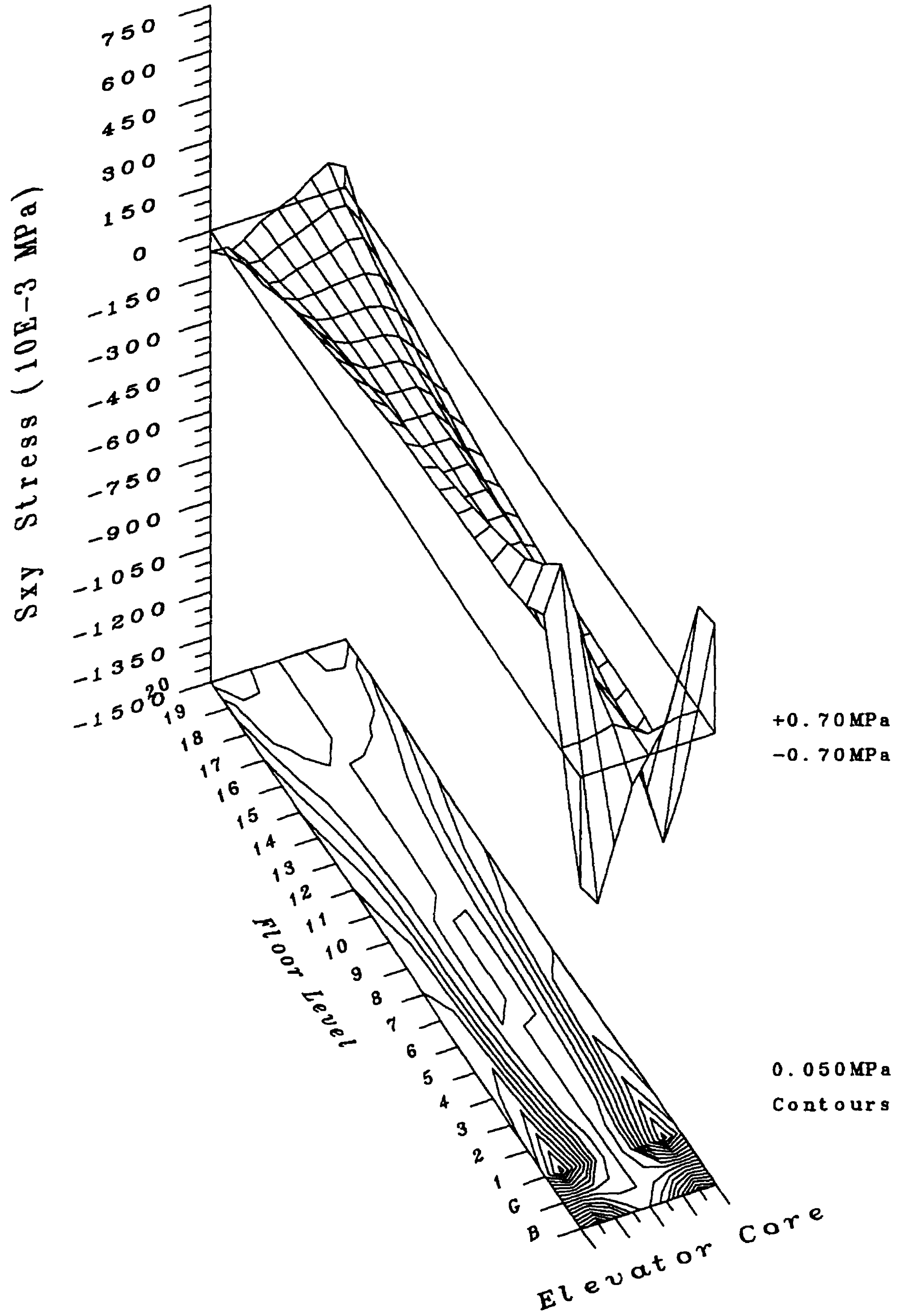

Figure 5.21 Distribution of the Shear Stresses S_{xy} in the Elevator Core – Q_Y Earthquake Loading – Elastic Analysis FCS Model Results

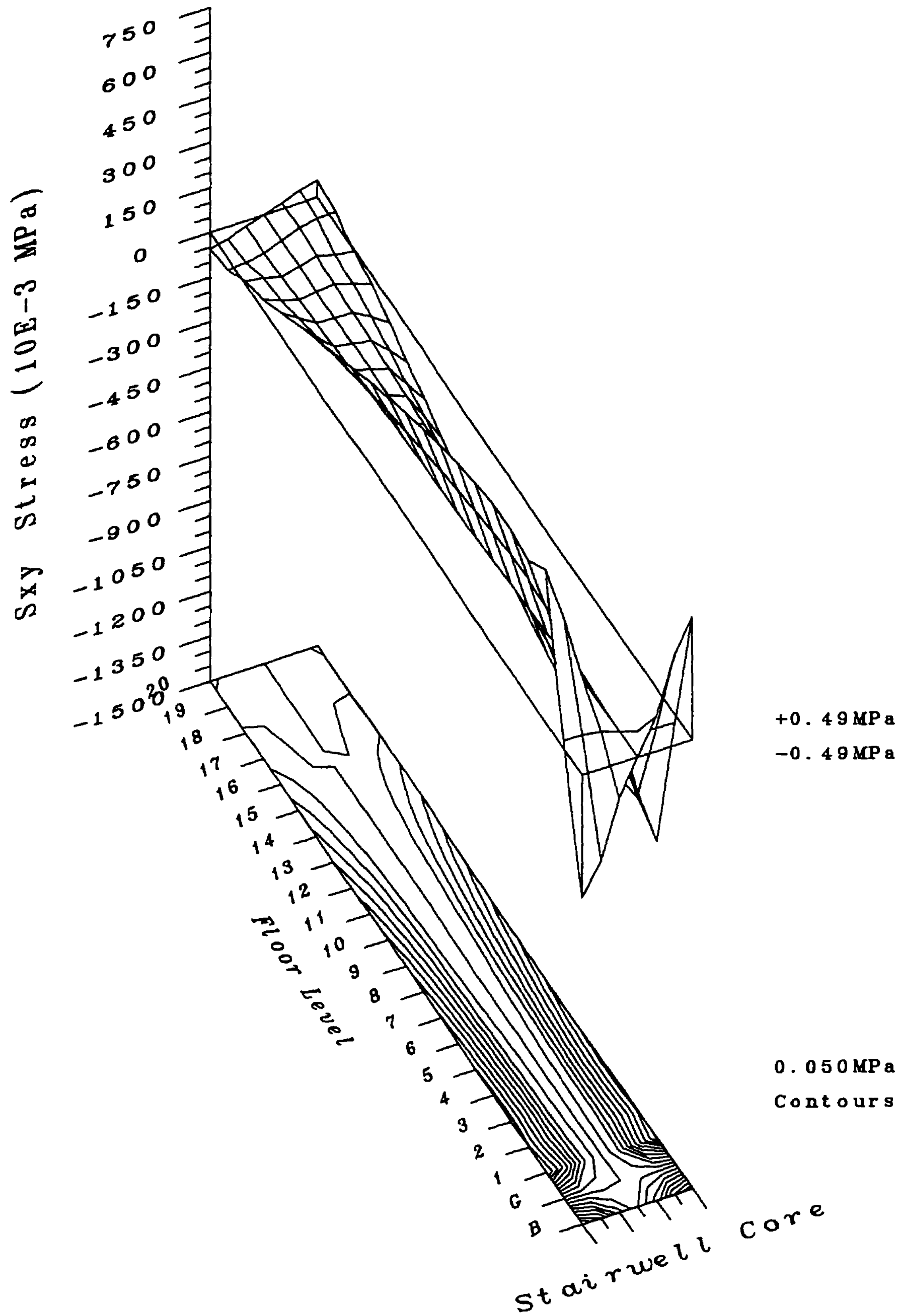

Figure 5.22 Distribution of the Shear Stresses S_{xy} in the Stairwell Core – Q_Y Earthquake Loading – Elastic Analysis FCS Model Results

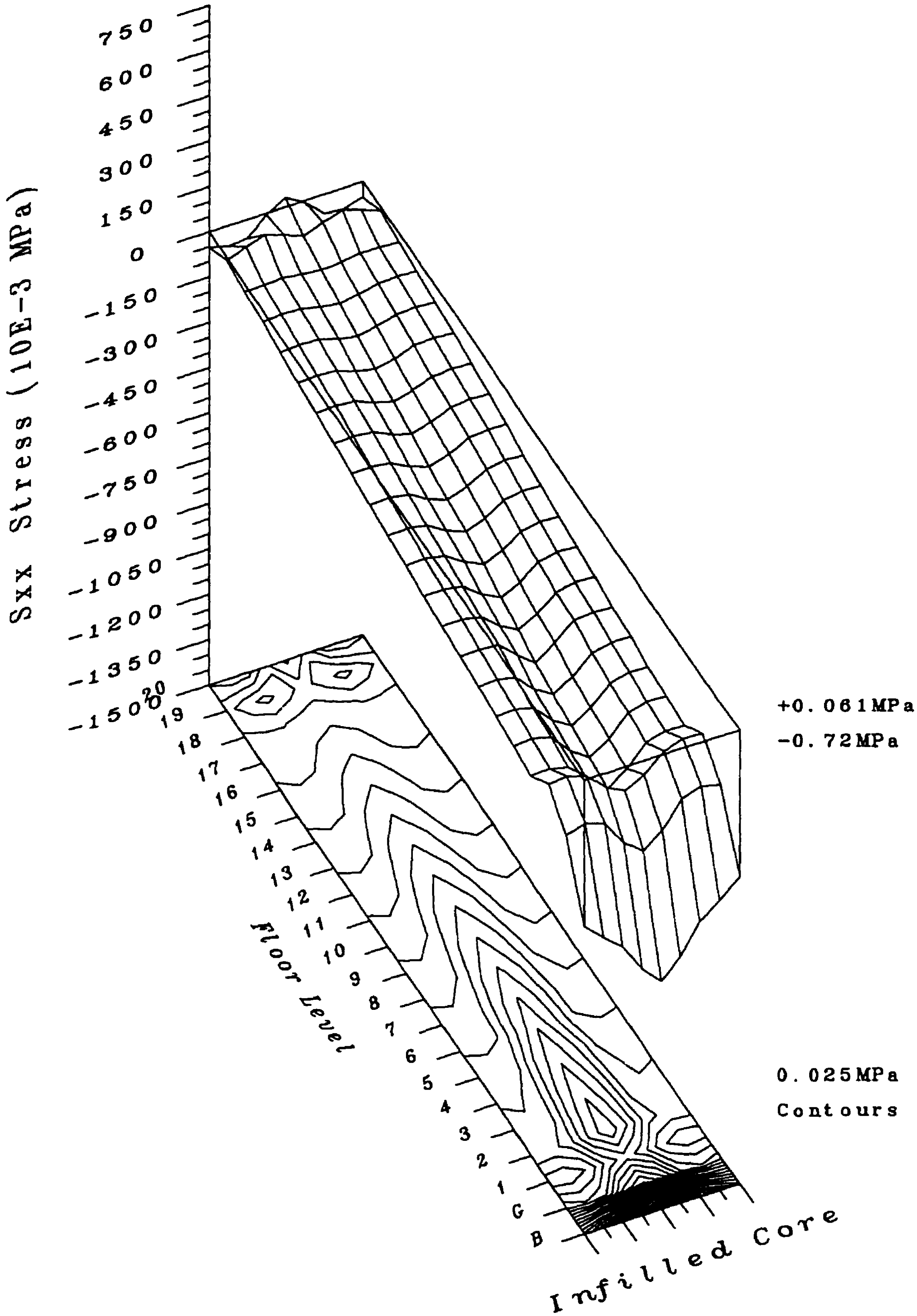

Figure 5.23 Distribution of the Transverse Stresses S_{xx} in the Infilled-Slab Core – Dead Load – Elastic Analysis FCS Model Results

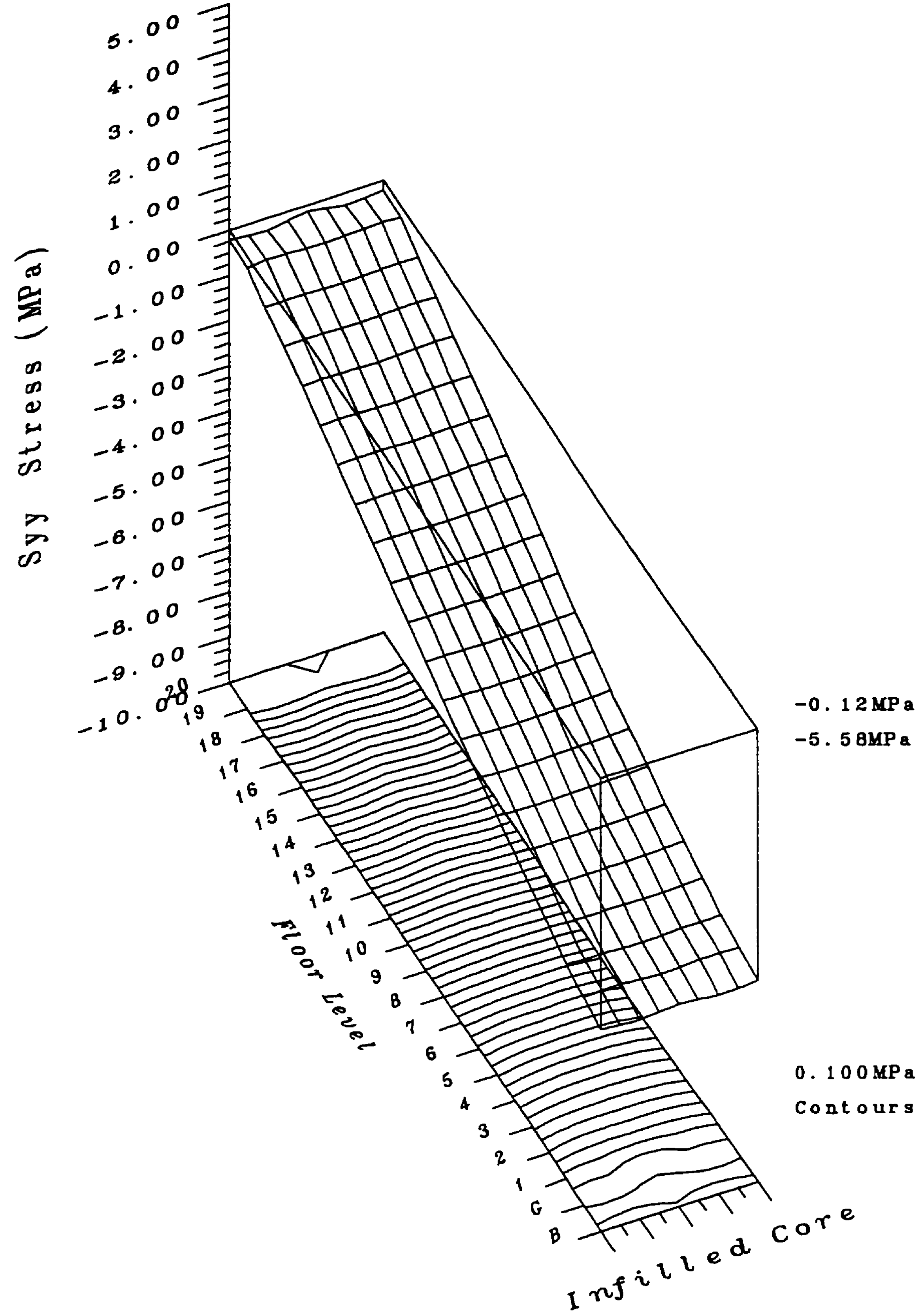

Figure 5.24 Distribution of the Longitudinal Stresses S_{yy} in the Infilled-Slab Core – Dead Load – Elastic Analysis FCS Model Results

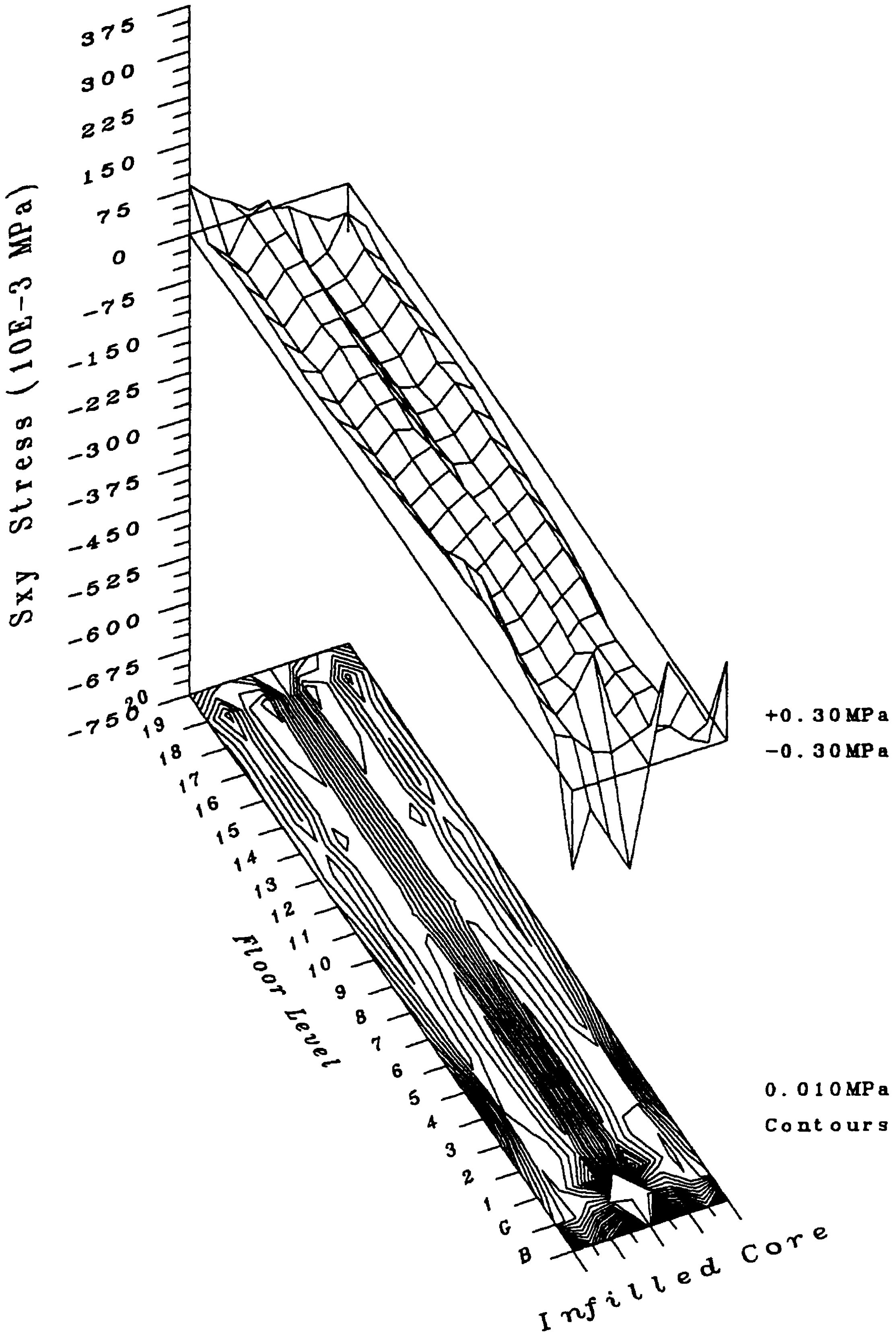

Figure 5.25 Distribution of the Shear Stresses S_{xy} in the Infilled-Slab Core – Dead Load – Elastic Analysis FCS Model Results

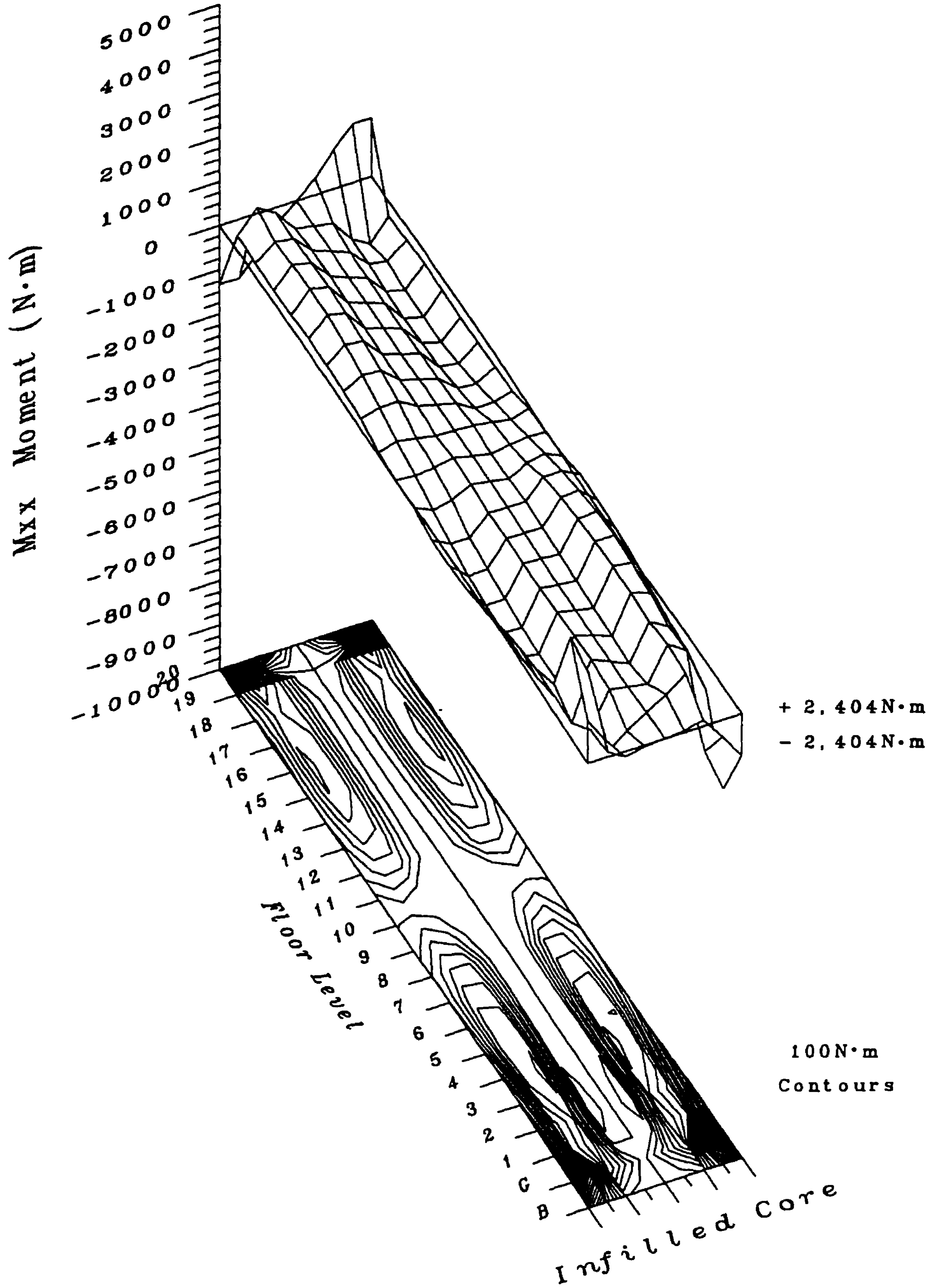

Figure 5.26 Distribution of the M_{xx} Bending Moments in the Infilled-Slab Core - Q_X Earthquake Loading - Elastic Analysis FCS Model Results

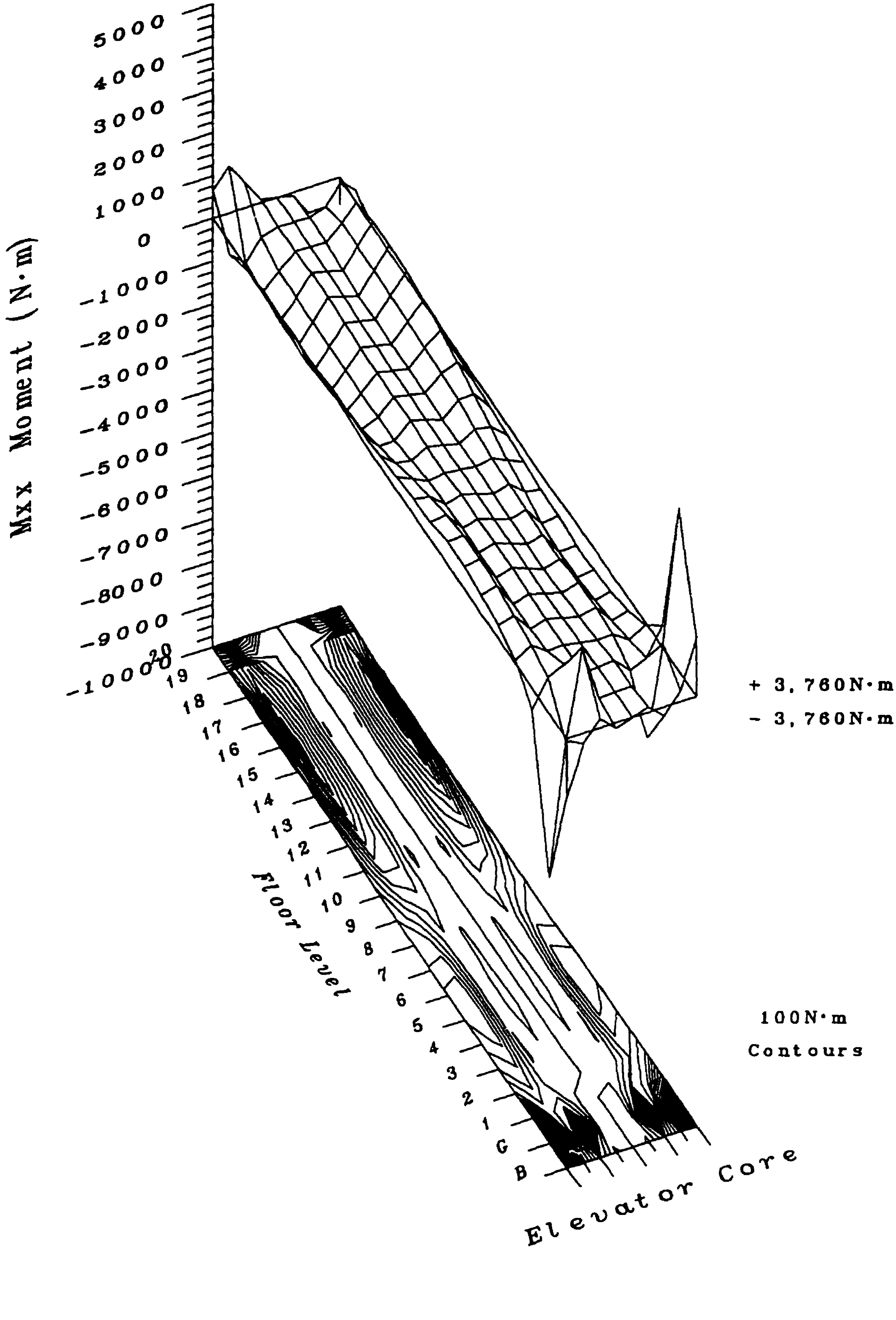

Figure 5.27 Distribution of the M_{xx} Bending Moments in the Elevator Core – Q_X Earthquake Loading – Elastic Analysis FCS Model Results

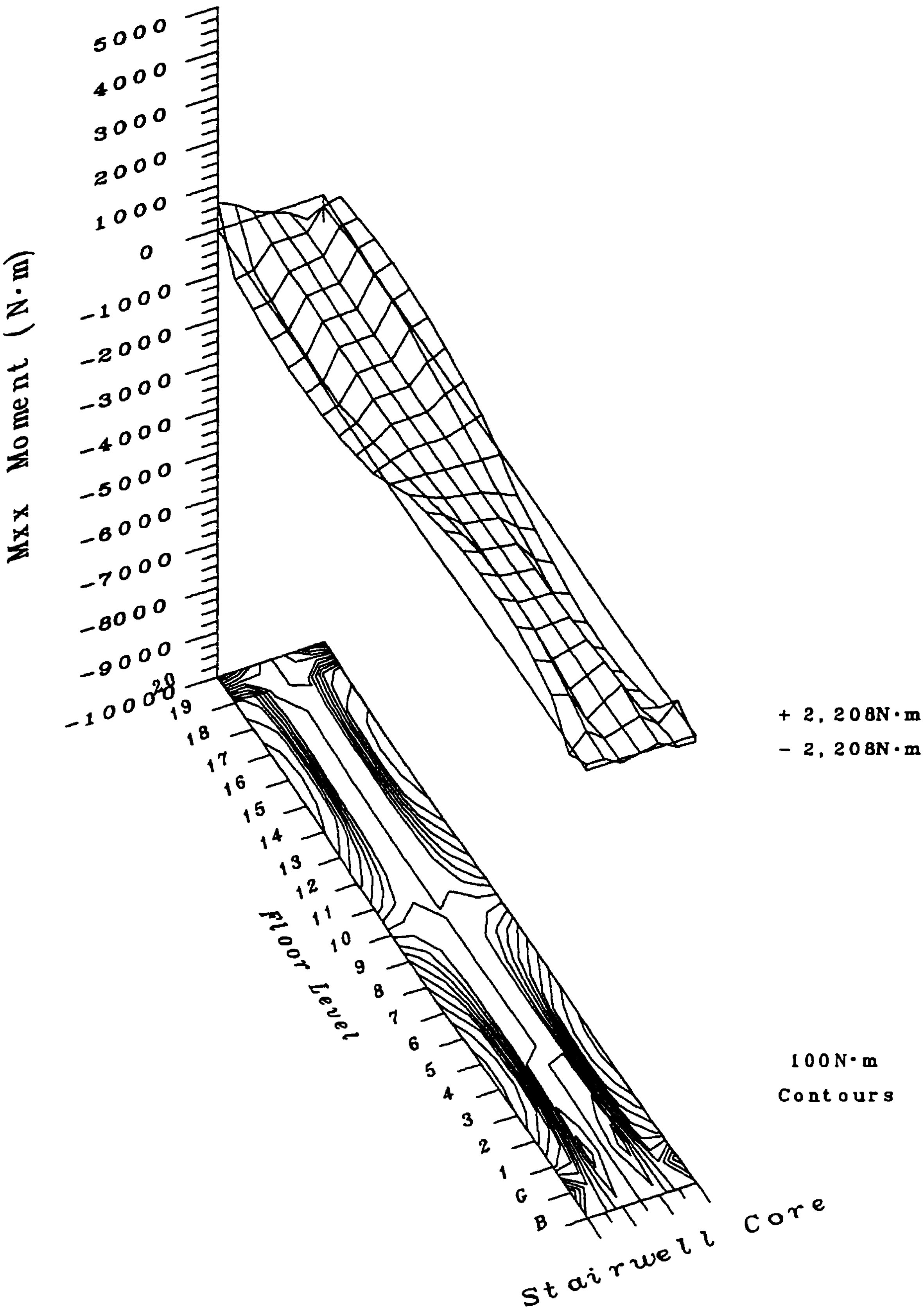

Figure 5.28 Distribution of the M_{xx} Bending Moments in the Stairwell Core – Q_X Earthquake Loading – Elastic Analysis FCS Model Results

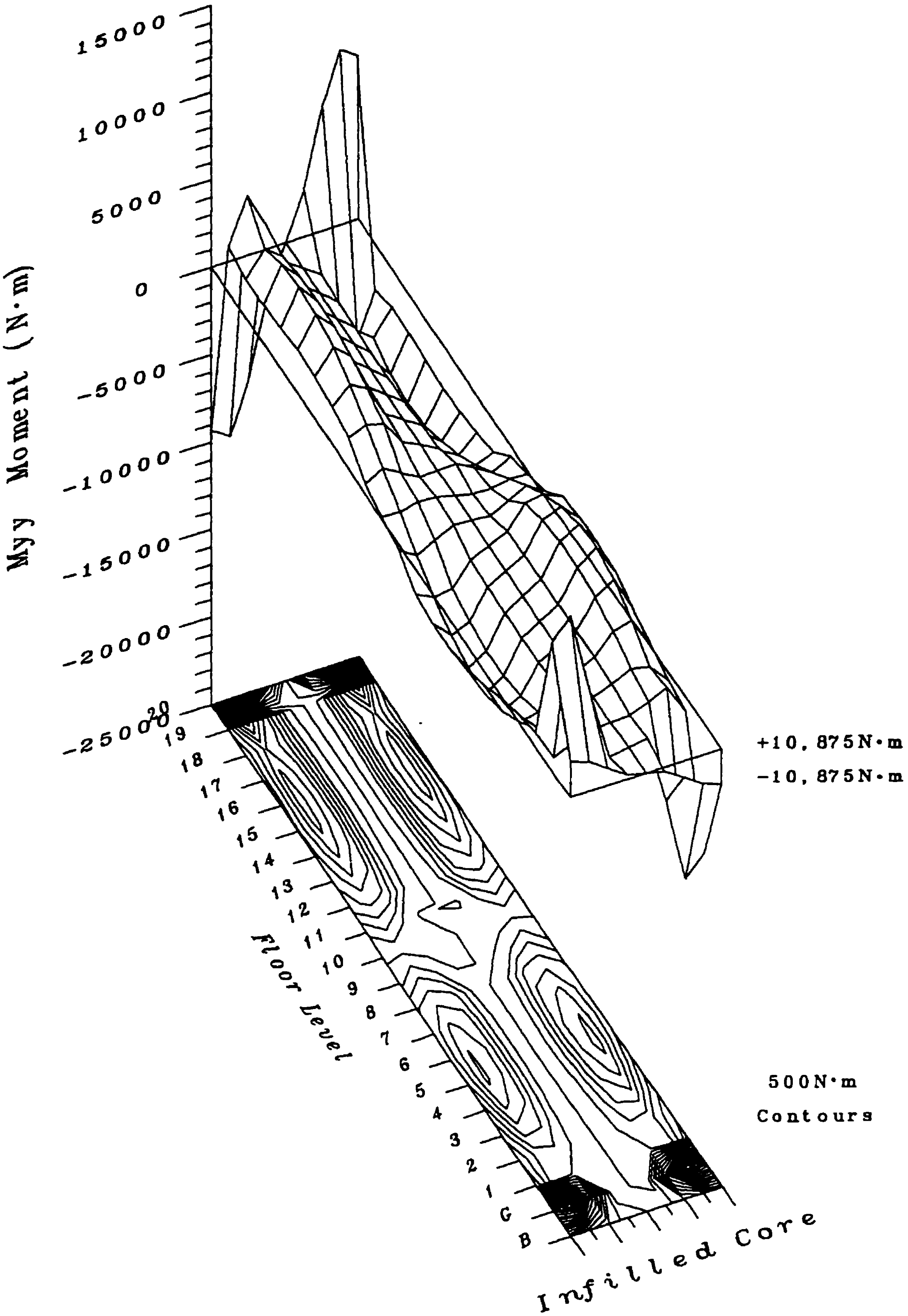

Figure 5.29 Distribution of the M_{yy} Bending Moments in the Infilled-Slab Core – Q_X Earthquake Loading – Elastic Analysis FCS Model Results

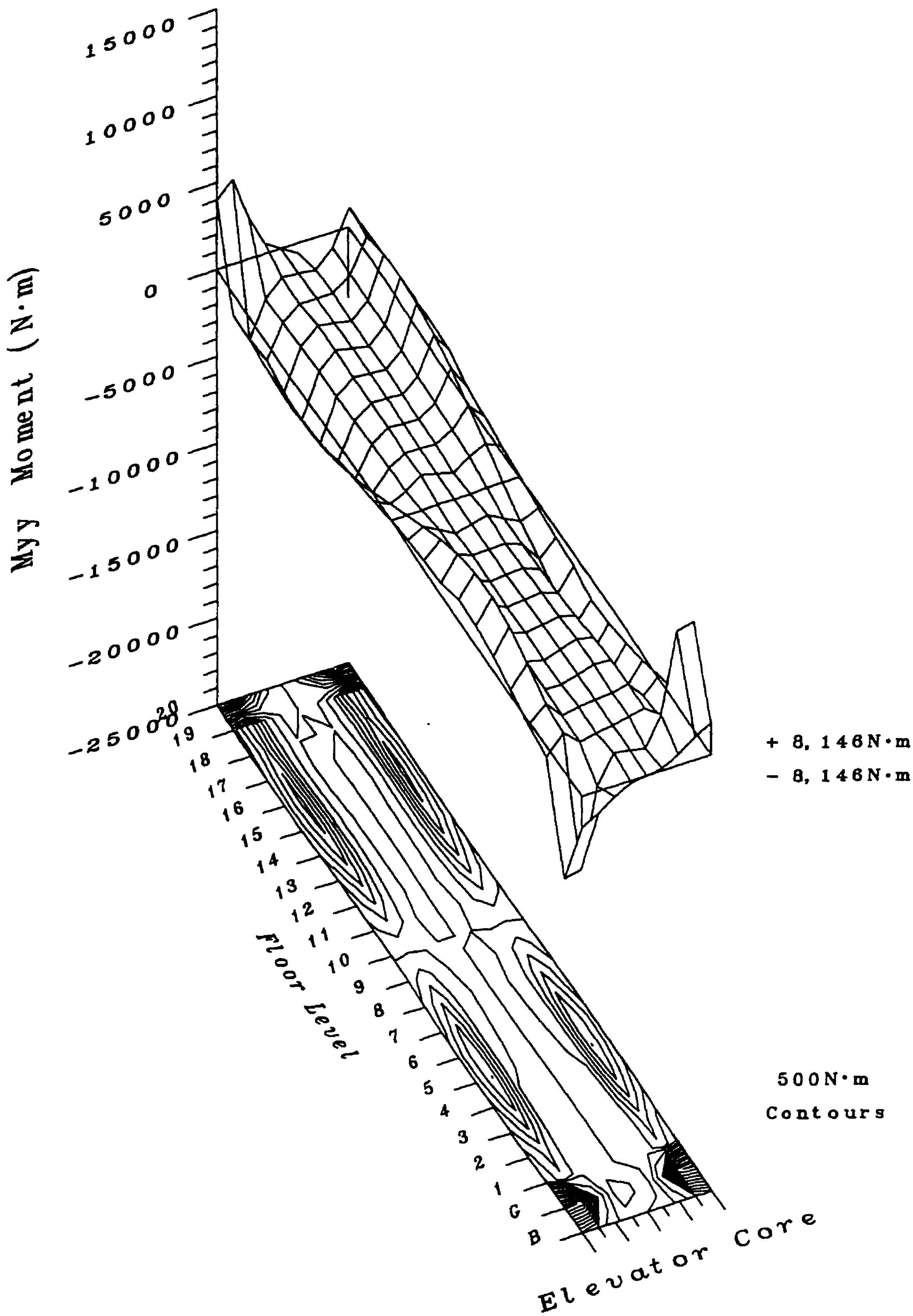

Figure 5.30 Distribution of the M_{yy} Bending Moments in the Elevator Core – Q_X Earthquake Loading – Elastic Analysis FCS Model Results

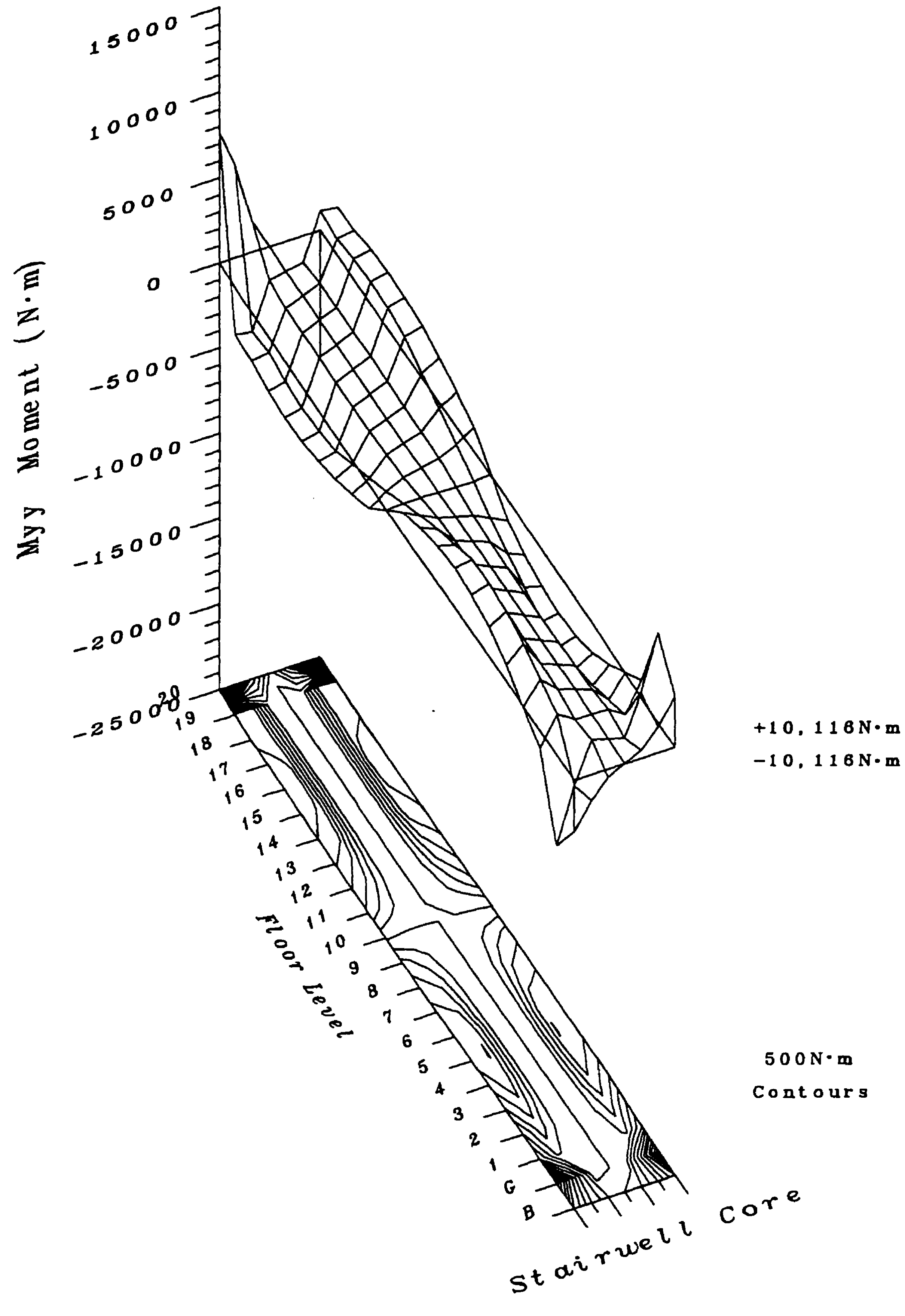

Figure 5.31 Distribution of the M_{yy} Bending Moments in the Stairwell Core – Q_X Earthquake Loading – Elastic Analysis FCS Model Results

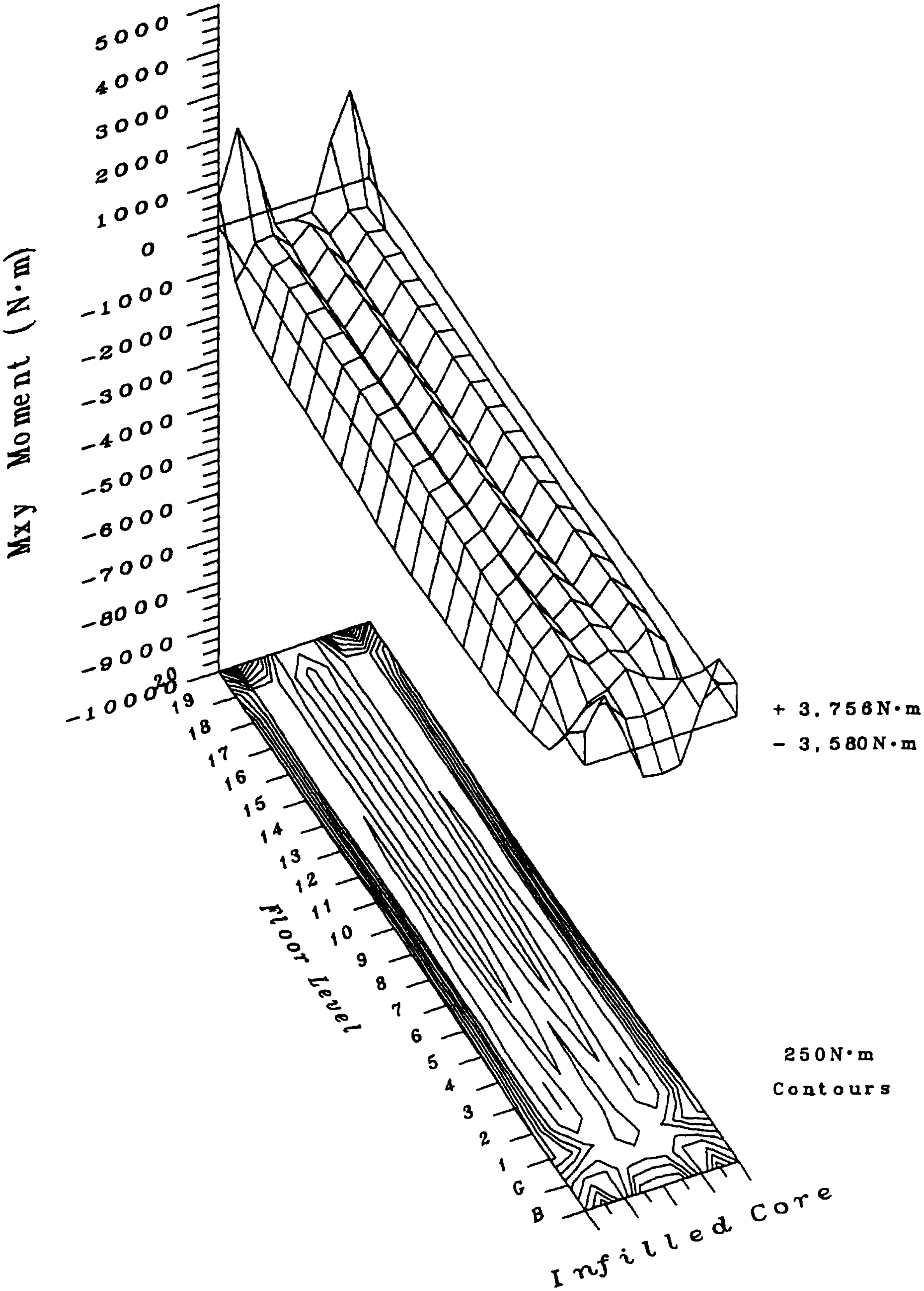

Figure 5.32 Distribution of the M_{xy} Twisting Moments in the Infilled-Slab Core – Q_X Earthquake Loading – Elastic Analysis FCS Model Results

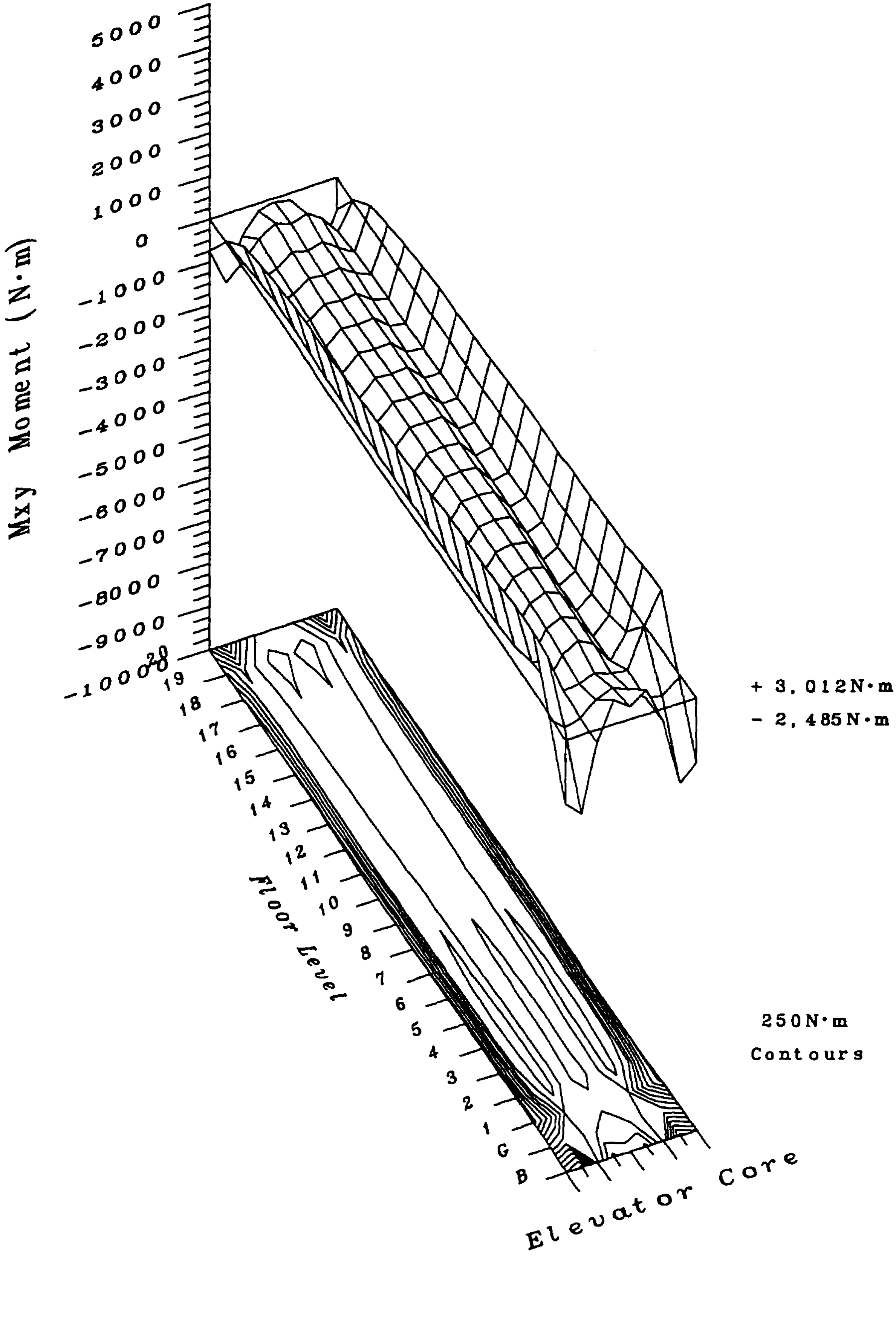

Figure 5.33 Distribution of the M_{xy} Twisting Moments in the Elevator Core - Q_X Earthquake Loading - Elastic Analysis FCS Model Results

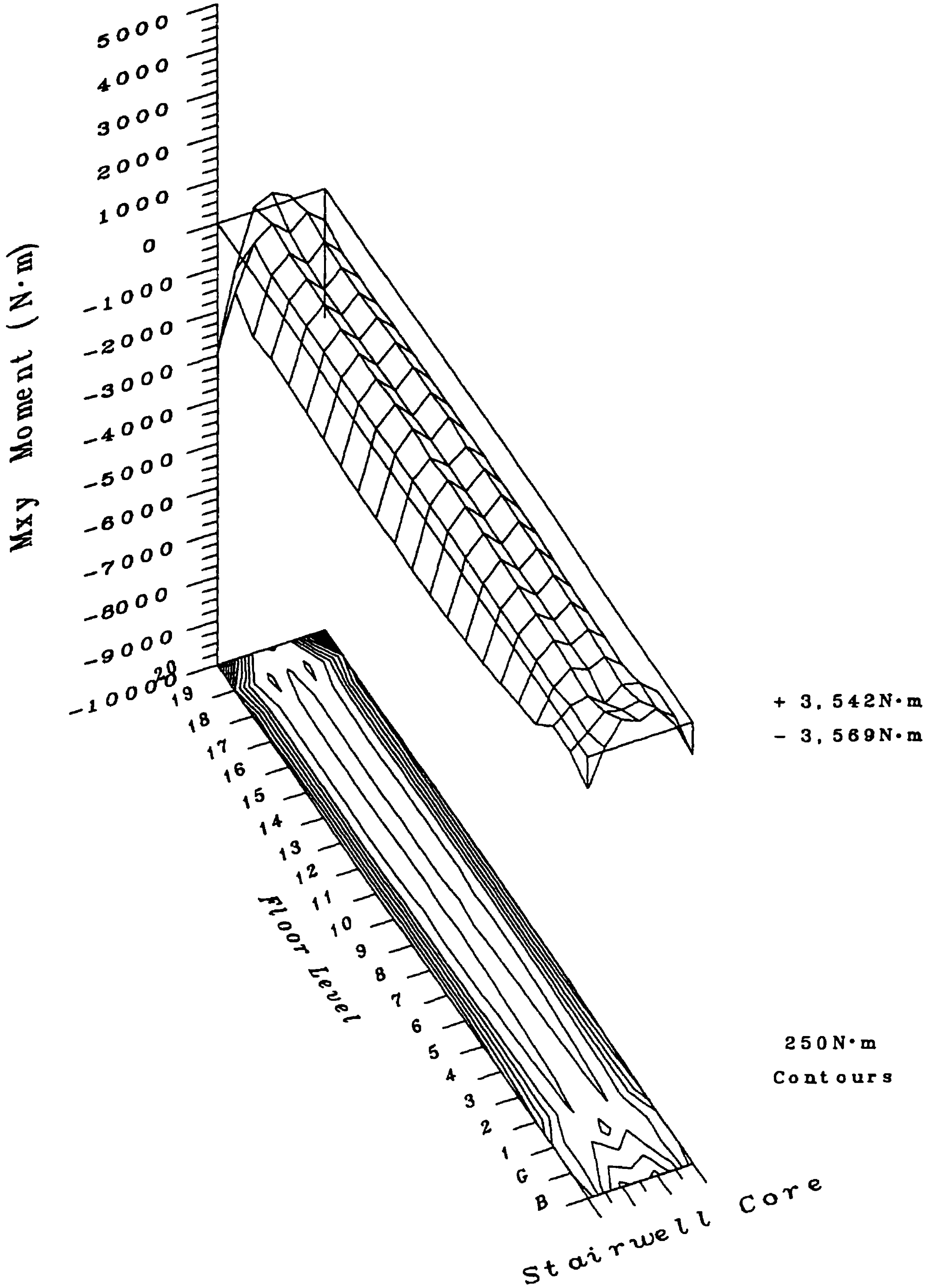

Figure 5.34 Distribution of the M_{xy} Twisting Moments in the Stairwell Core – Q_X Earthquake Loading – Elastic Analysis FCS Model Results

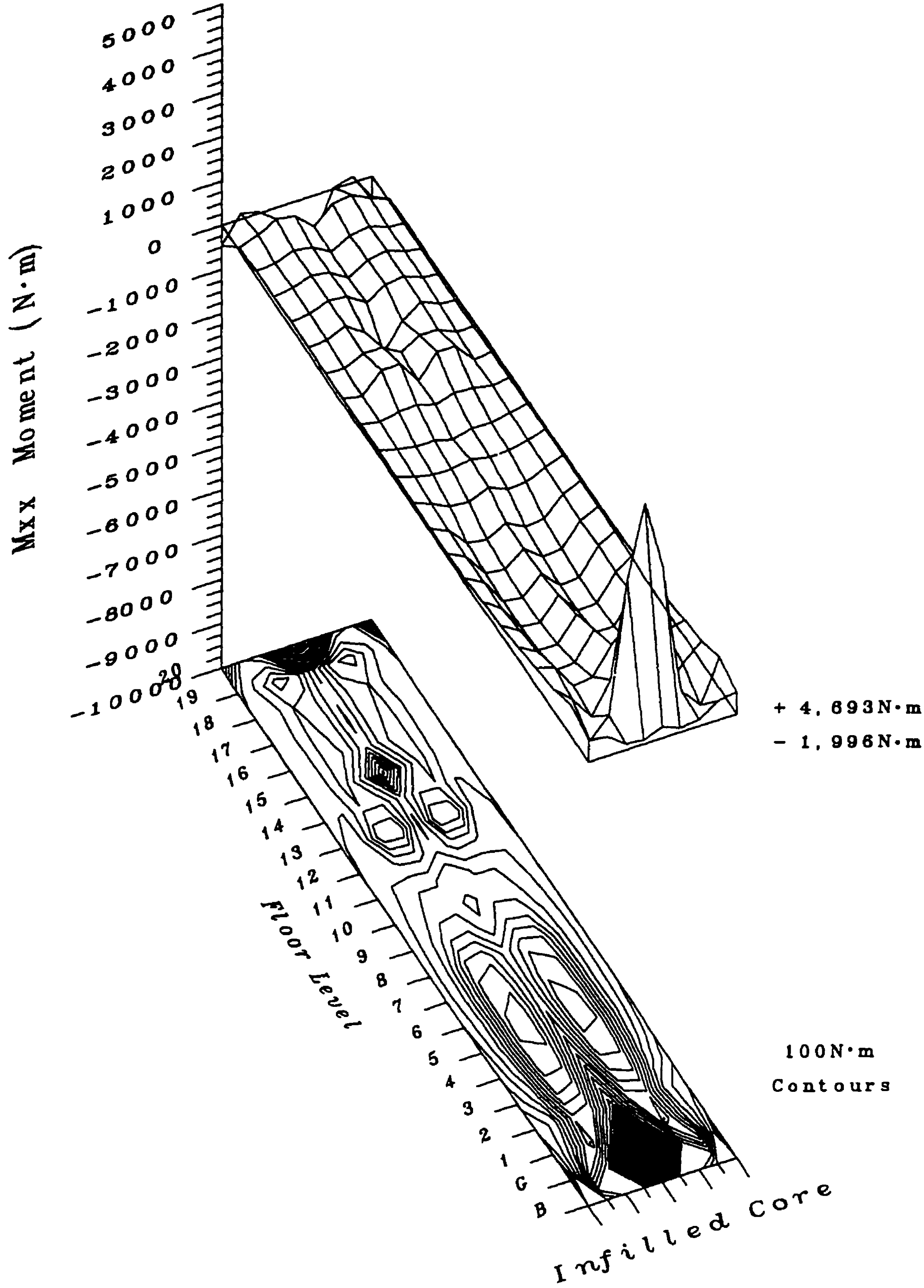

Figure 5.35 Distribution of the M_{xx} Bending Moments in the Infilled-Slab Core – Q_Y Earthquake Loading – Elastic Analysis FCS Model Results

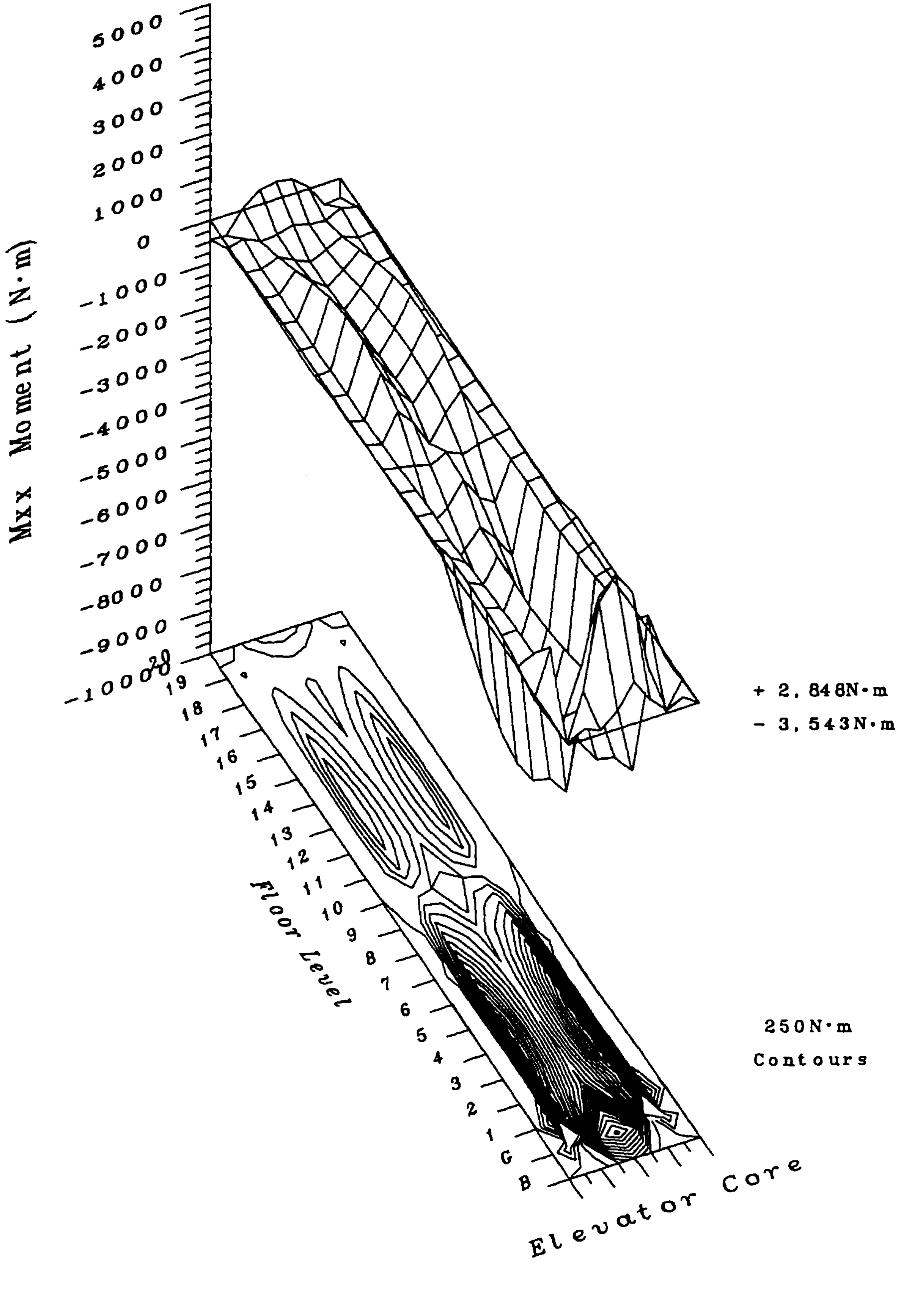

Figure 5.36 Distribution of the M_{xx} Bending Moments in the Elevator Core - Q_Y Earthquake Loading - Elastic Analysis FCS Model Results

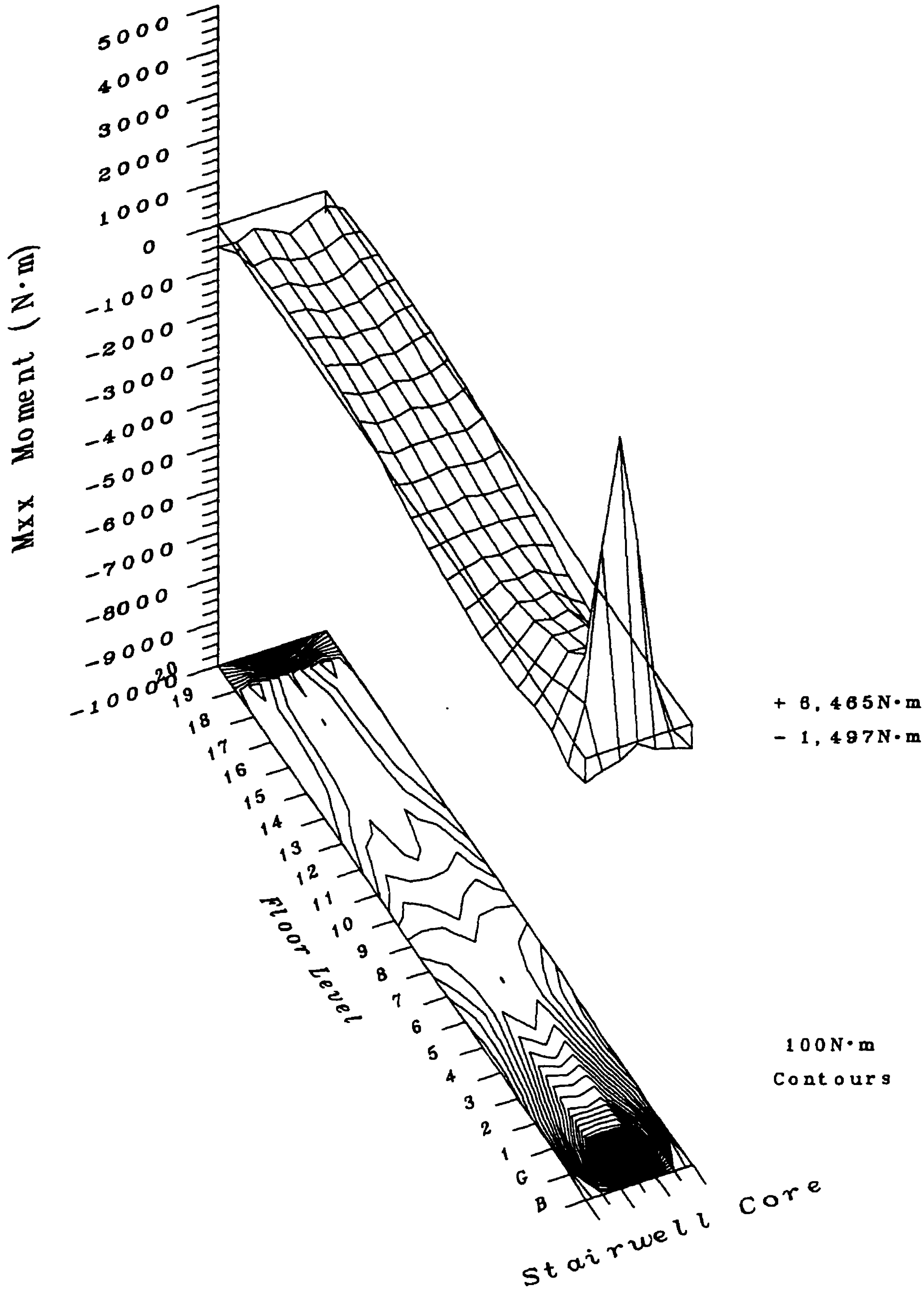

Figure 5.37 Distribution of the M_{xx} Bending Moments in the Stairwell Core – Q_Y Earthquake Loading – Elastic Analysis FCS Model Results

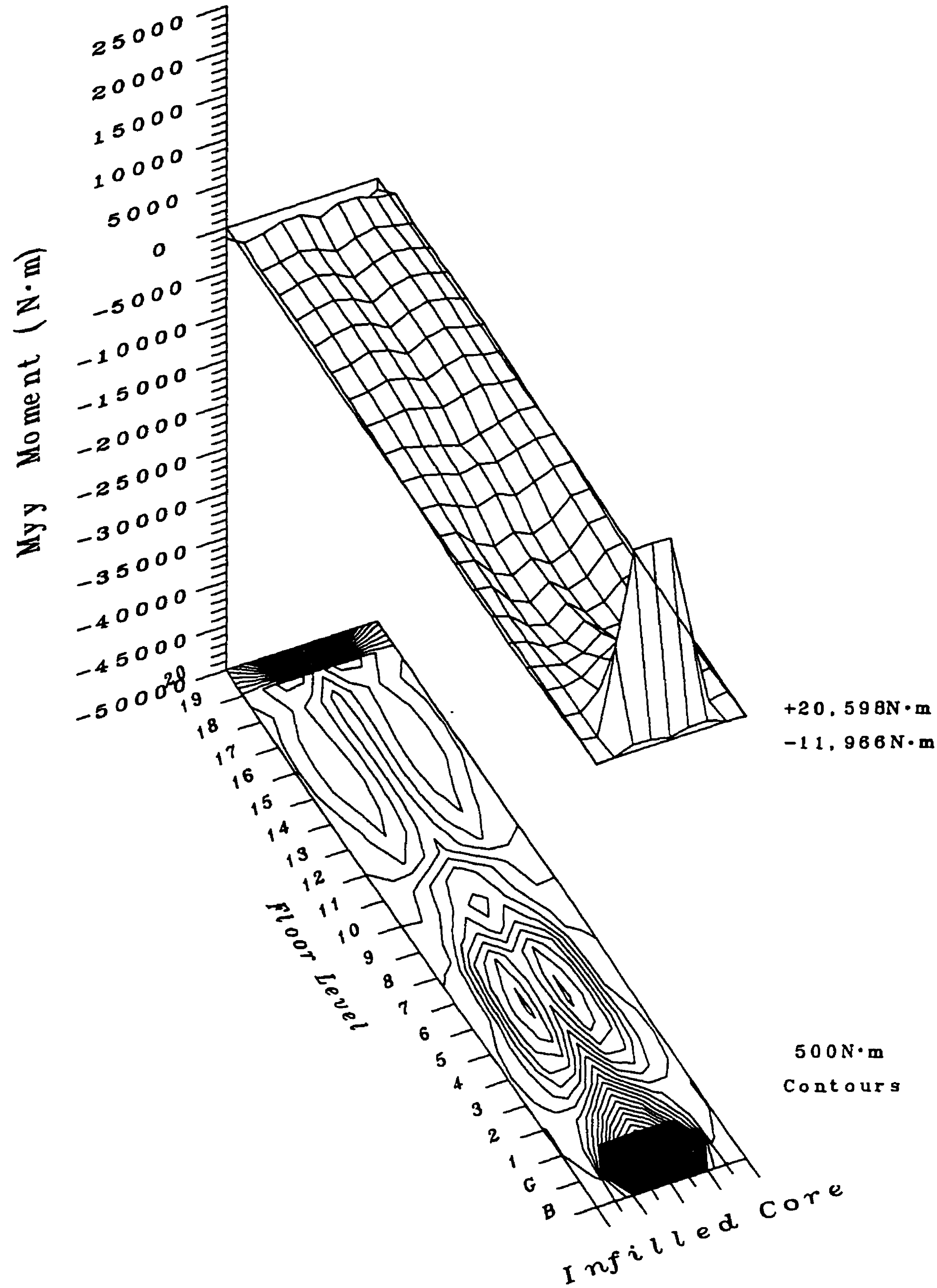

Figure 5.38 Distribution of the M_{yy} Bending Moments in the Infilled-Slab Core – Q_Y Earthquake Loading – Elastic Analysis FCS Model Results

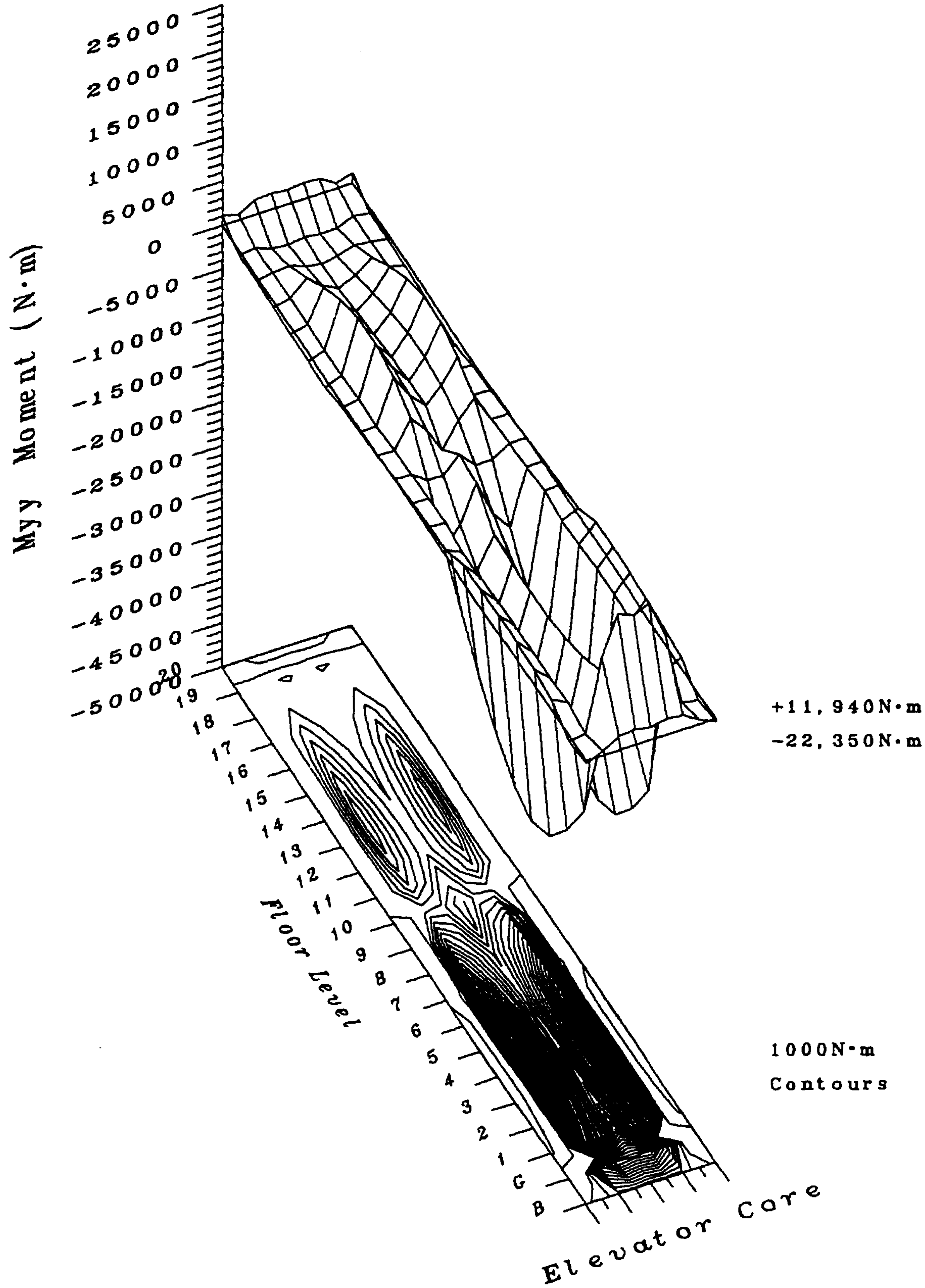

Figure 5.39 Distribution of the M_{yy} Bending Moments in the Elevator Core – Q_Y Earthquake Loading – Elastic Analysis FCS Model Results

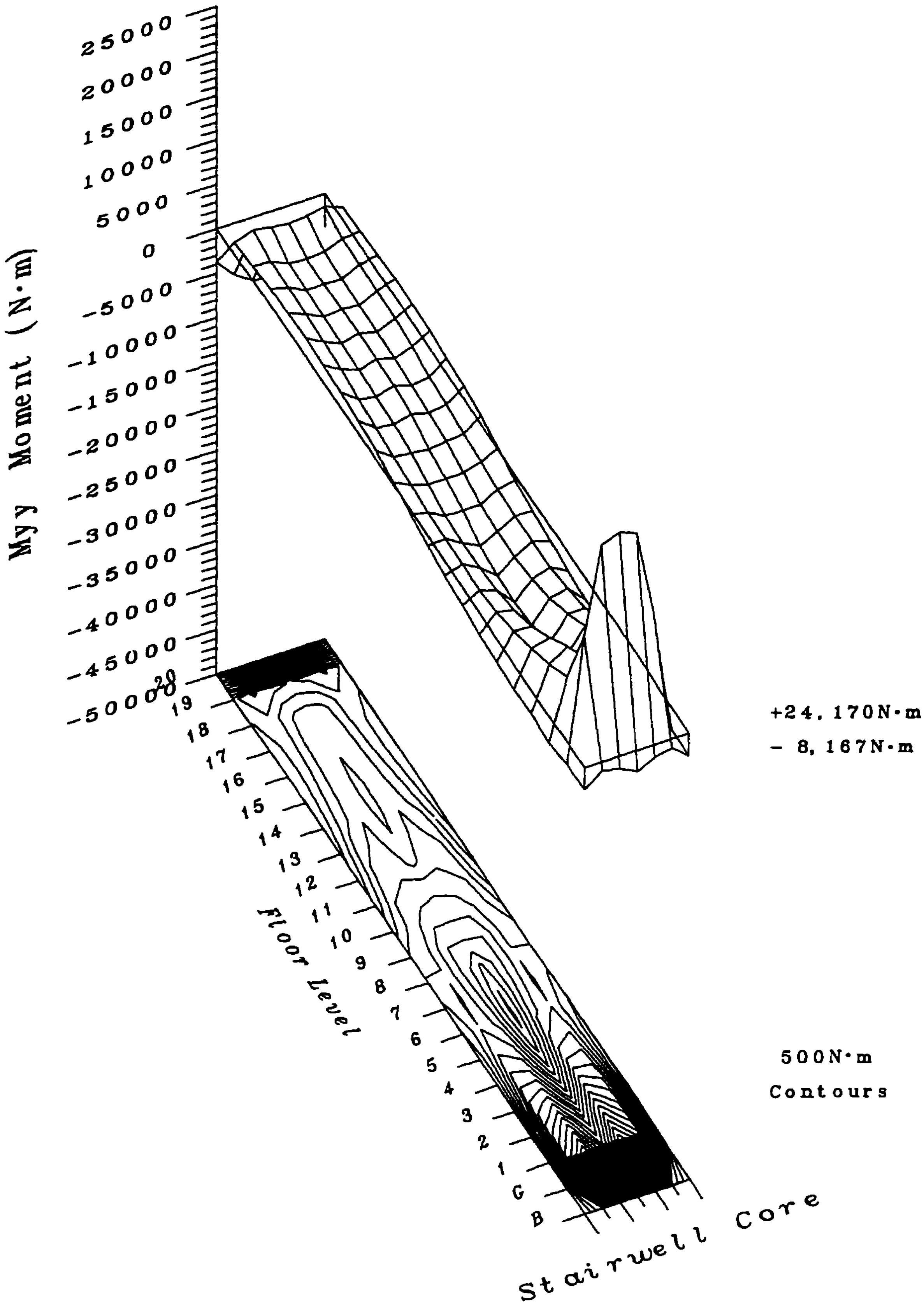

Figure 5.40 Distribution of the M_{yy} Bending Moments in the Stairwell Core – Q_Y Earthquake Loading – Elastic Analysis FCS Model Results

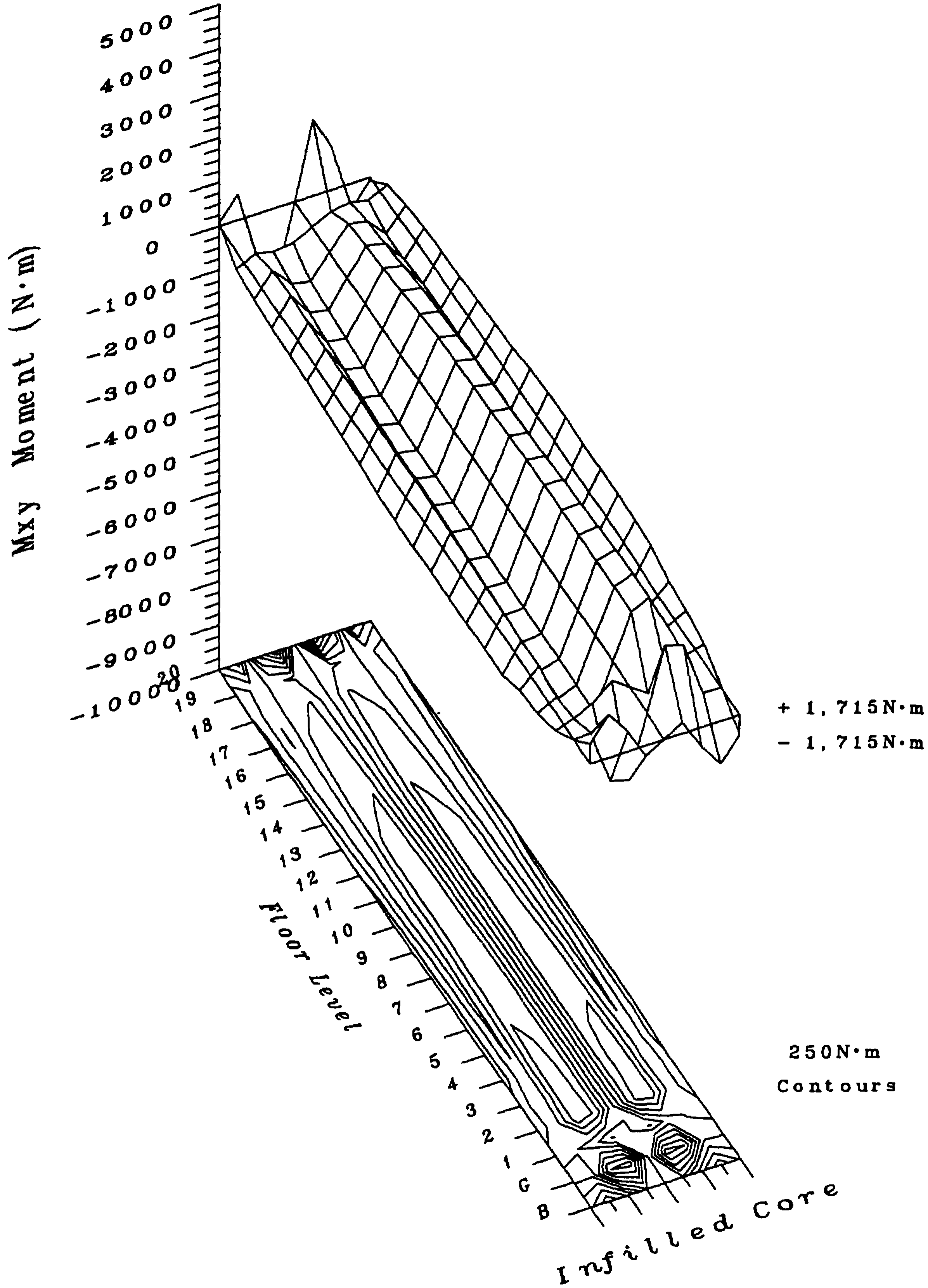

Figure 5.41 Distribution of the M_{xy} Twisting Moments in the Infilled-Slab Core – Q_Y Earthquake Loading – Elastic Analysis FCS Model Results

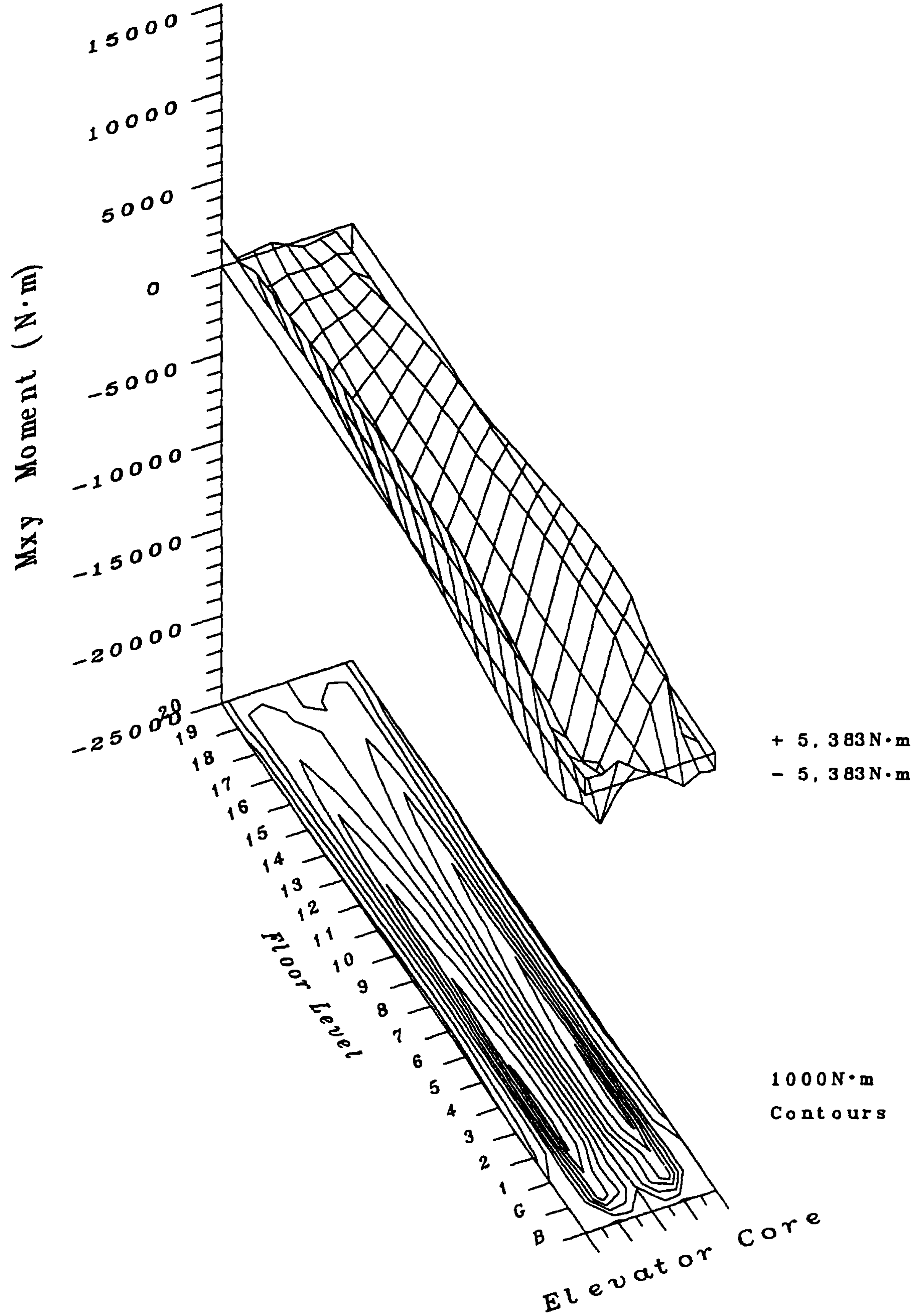

Figure 5.42 Distribution of the M_{xy} Twisting Moments in the Elevator Core – Q_Y Earthquake Loading – Elastic Analysis FCS Model Results

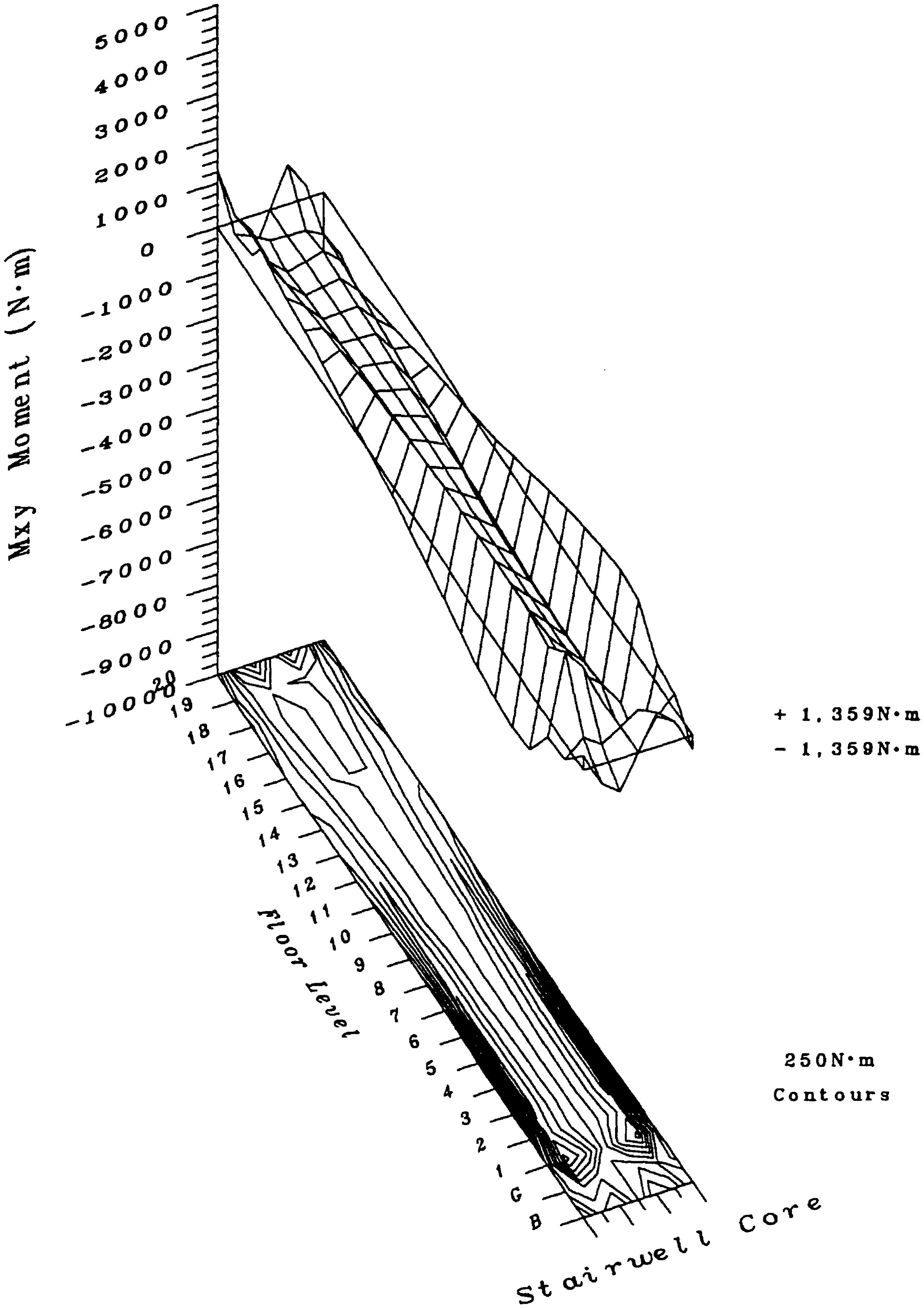

Figure 5.43 Distribution of the M_{xy} Twisting Moments in the Stairwell Core - Q_Y Earthquake Loading - Elastic Analysis FCS Model Results

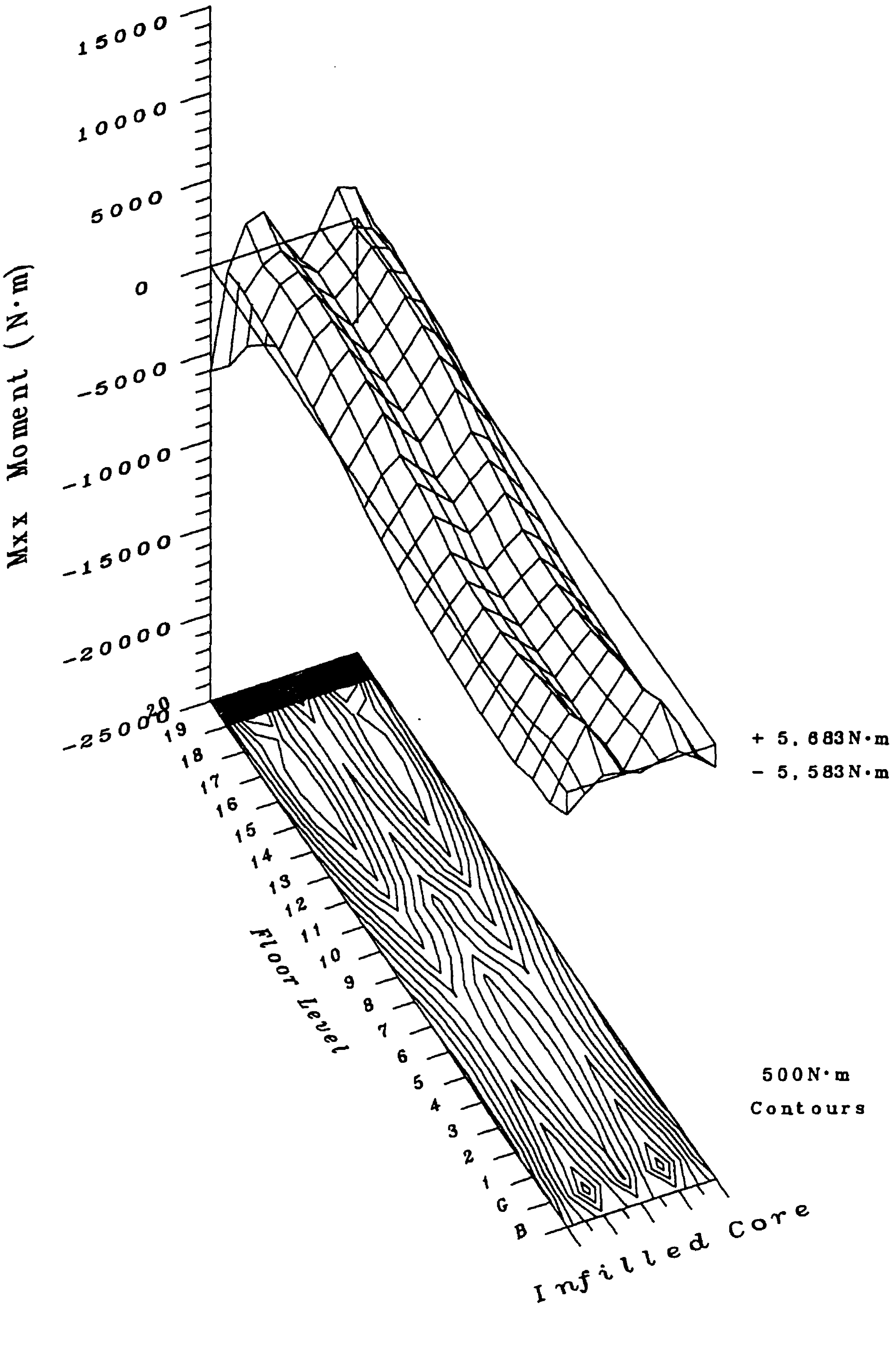

Figure 5.44 Distribution of the M_{xx} Bending Moments in the Infilled-Slab Core - Dead Load - Elastic Analysis FCS Model Results

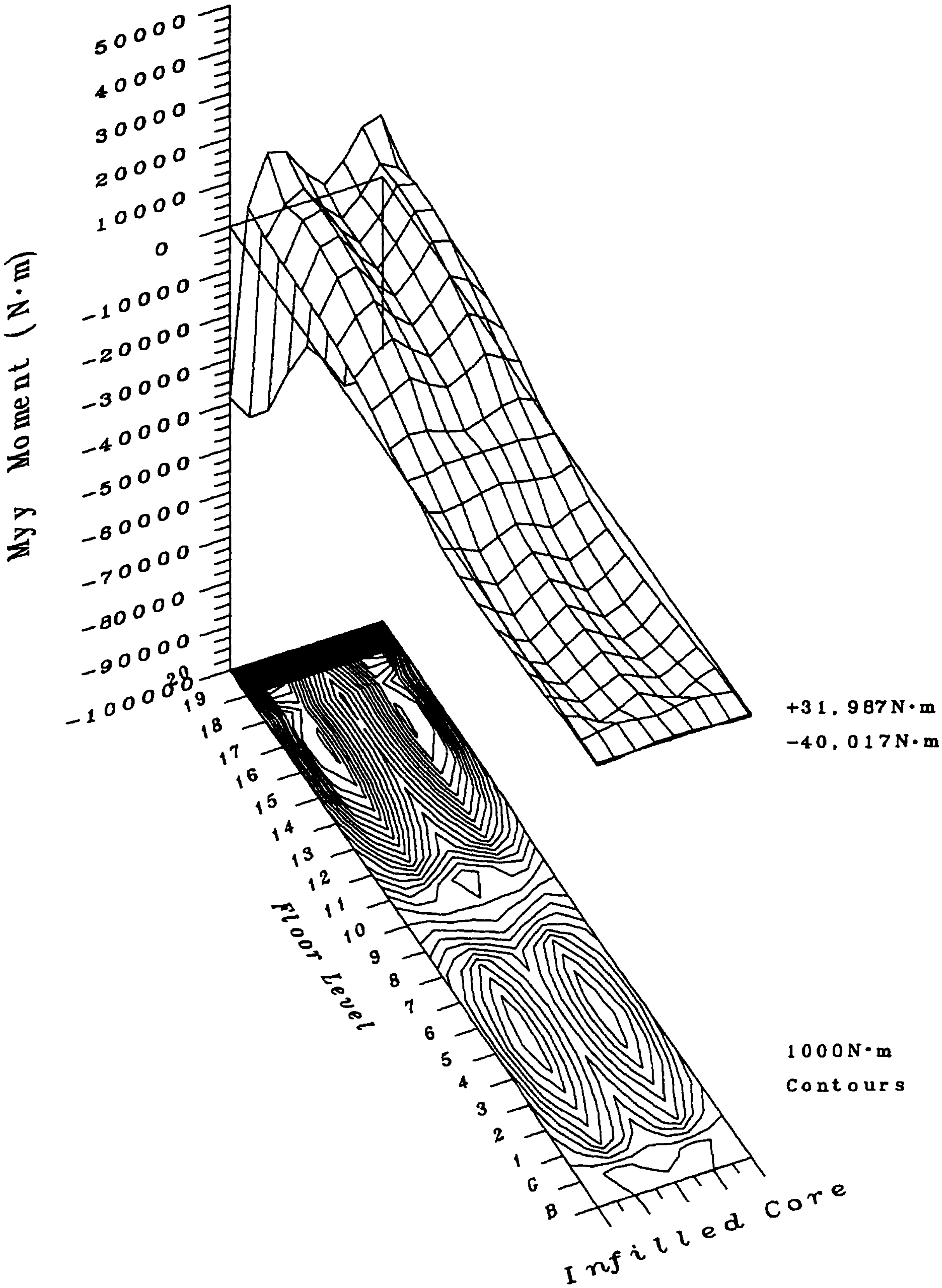

Figure 5.45 Distribution of the M_{yy} Bending Moments in the Infilled-Slab Core – Dead Load – Elastic Analysis FCS Model Results

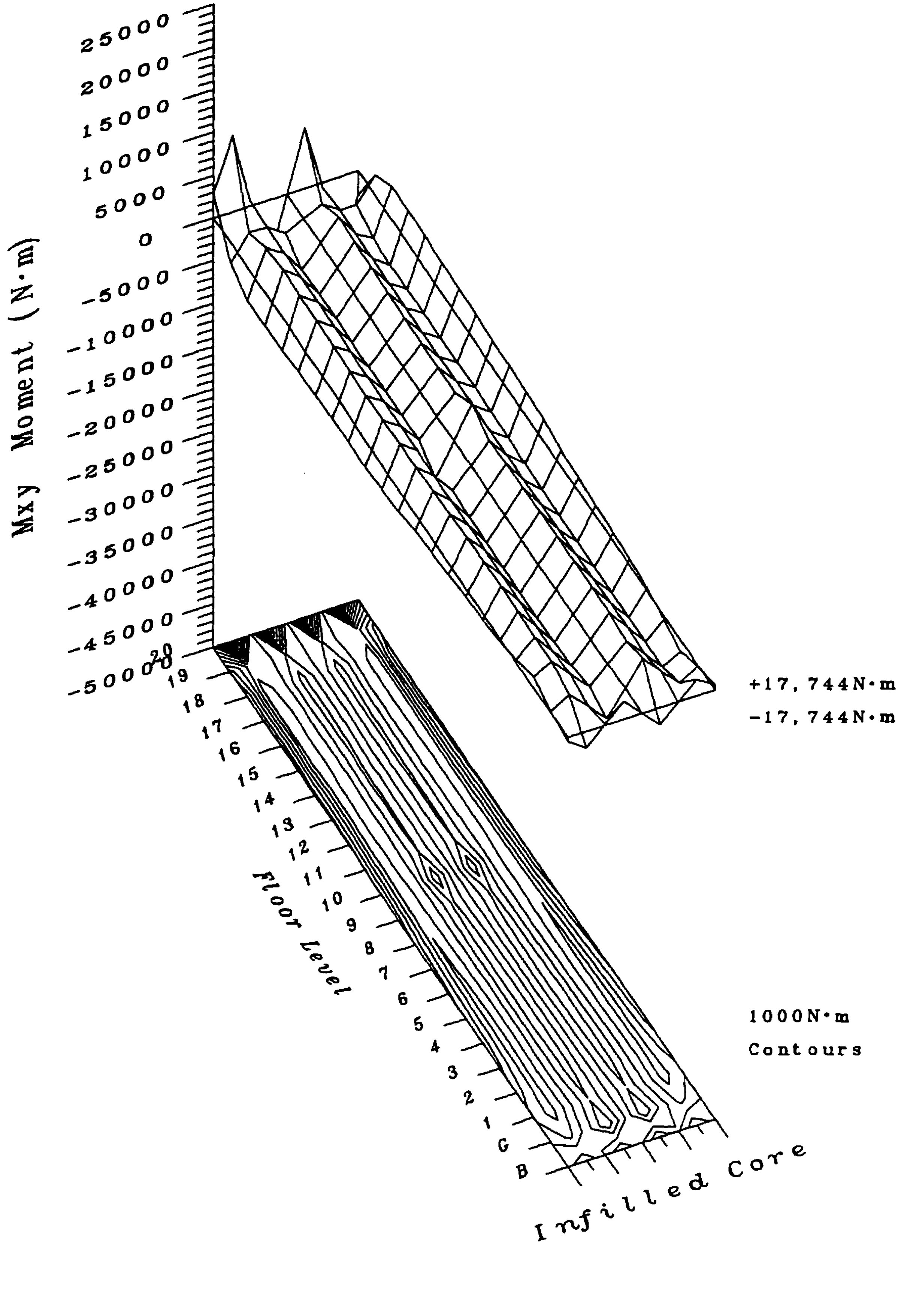

Figure 5.46 Distribution of the M_{xy} Twisting Moments in the Infilled-Slab Core – Dead Load – Elastic Analysis FCS Model Results

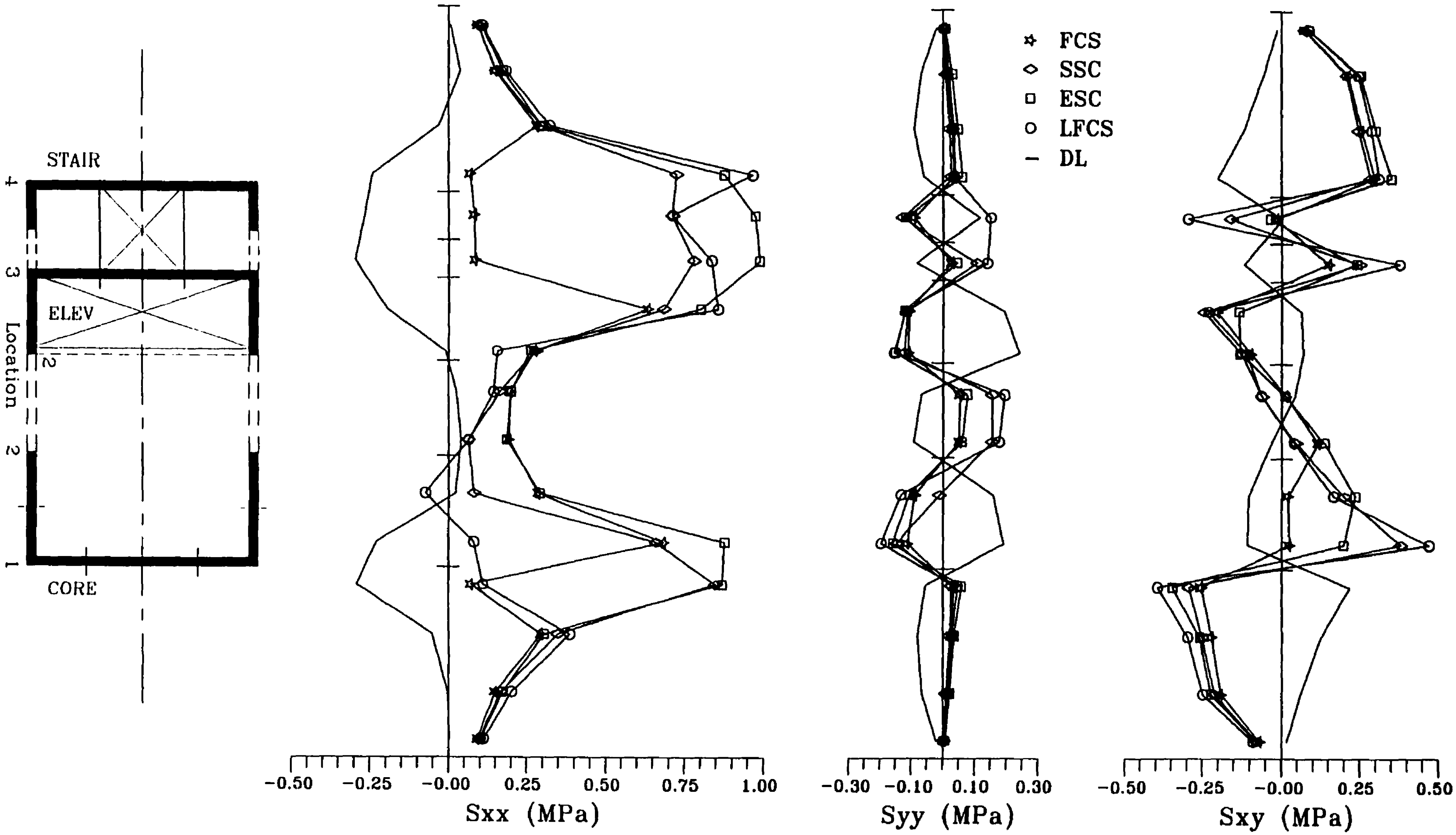

(a) Slab Locations 1 to 4 (b) Transverse Stresses S_{xx} (c) Longitudinal Stresses S_{yy} (d) Shear Stresses S_{xy}

Figure 5.47 Distribution of the In-Plane Axial and Shear Stresses in the Surrounding Slabs Along the Core Wall Junctions – Q_X Earthquake Loading – Elastic Analyses Model Results

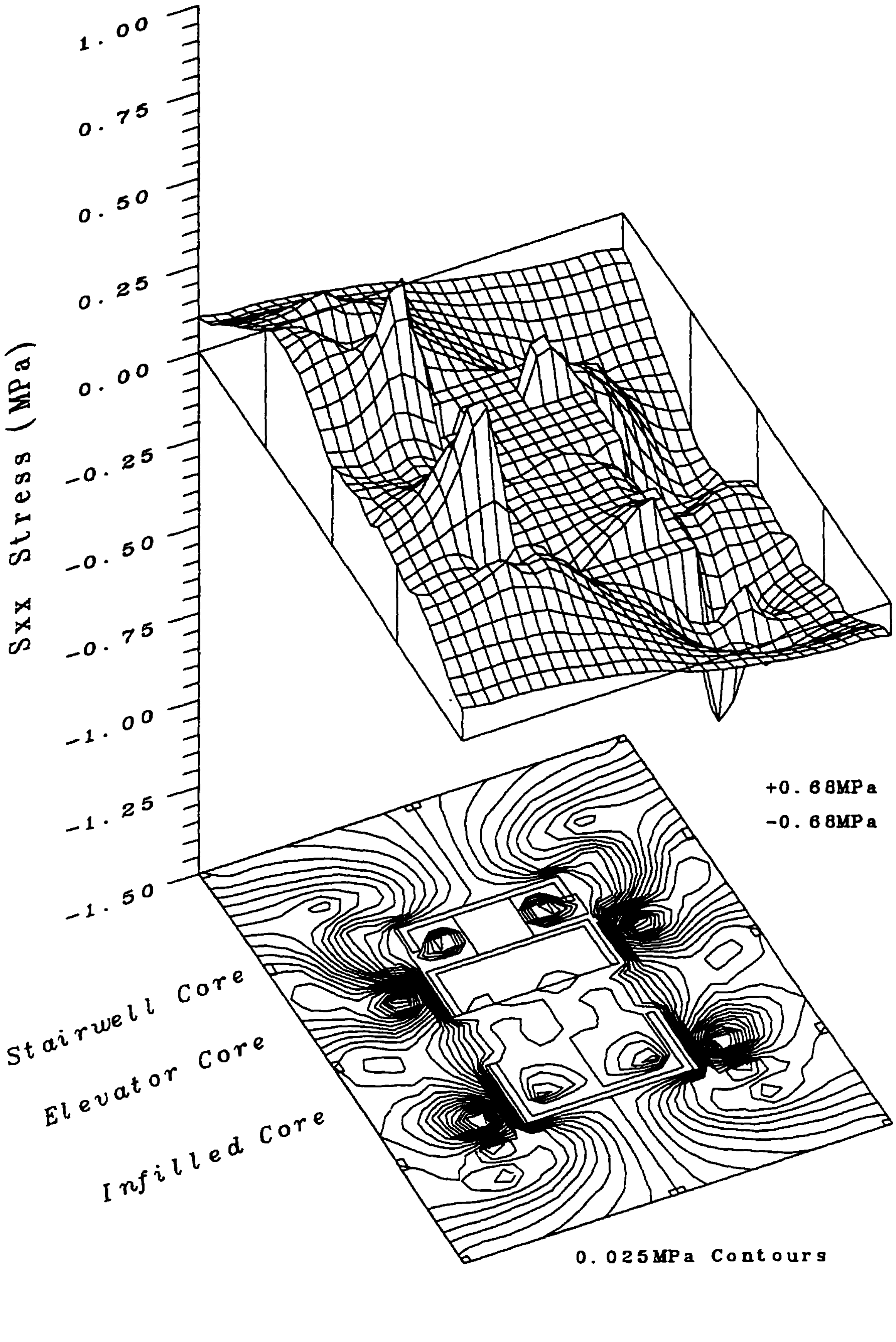

Figure 5.48 Distribution of the Transverse Stresses S_{xx} in the Enclosed and Surrounding Slabs – Q_X Earthquake Loading – Elastic Analysis FCS Model Results

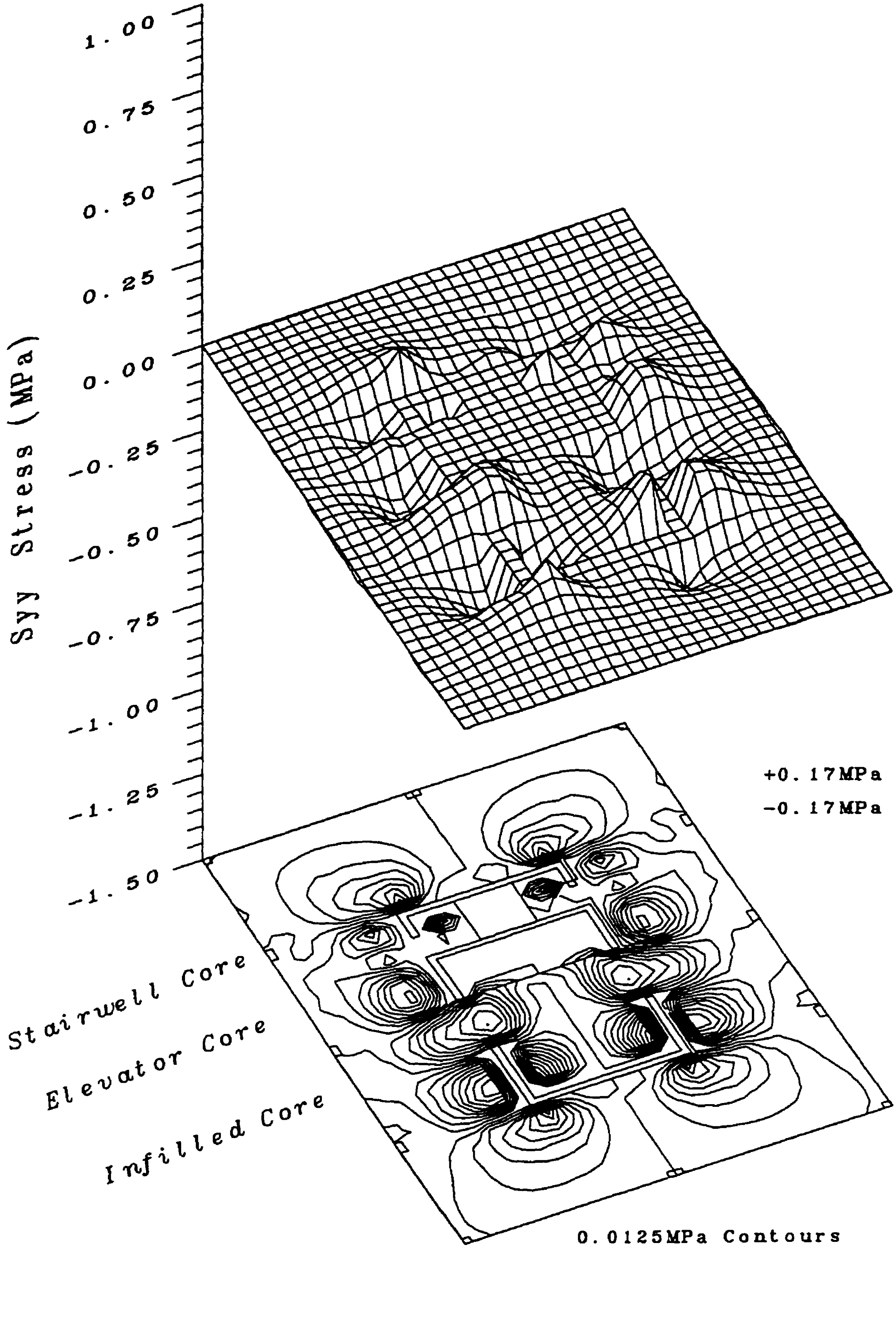

Figure 5.49 Distribution of the Longitudinal Stresses S_{yy} in the Enclosed and Surrounding Slabs – Q_X Earthquake Loading – Elastic Analysis FCS Model Results

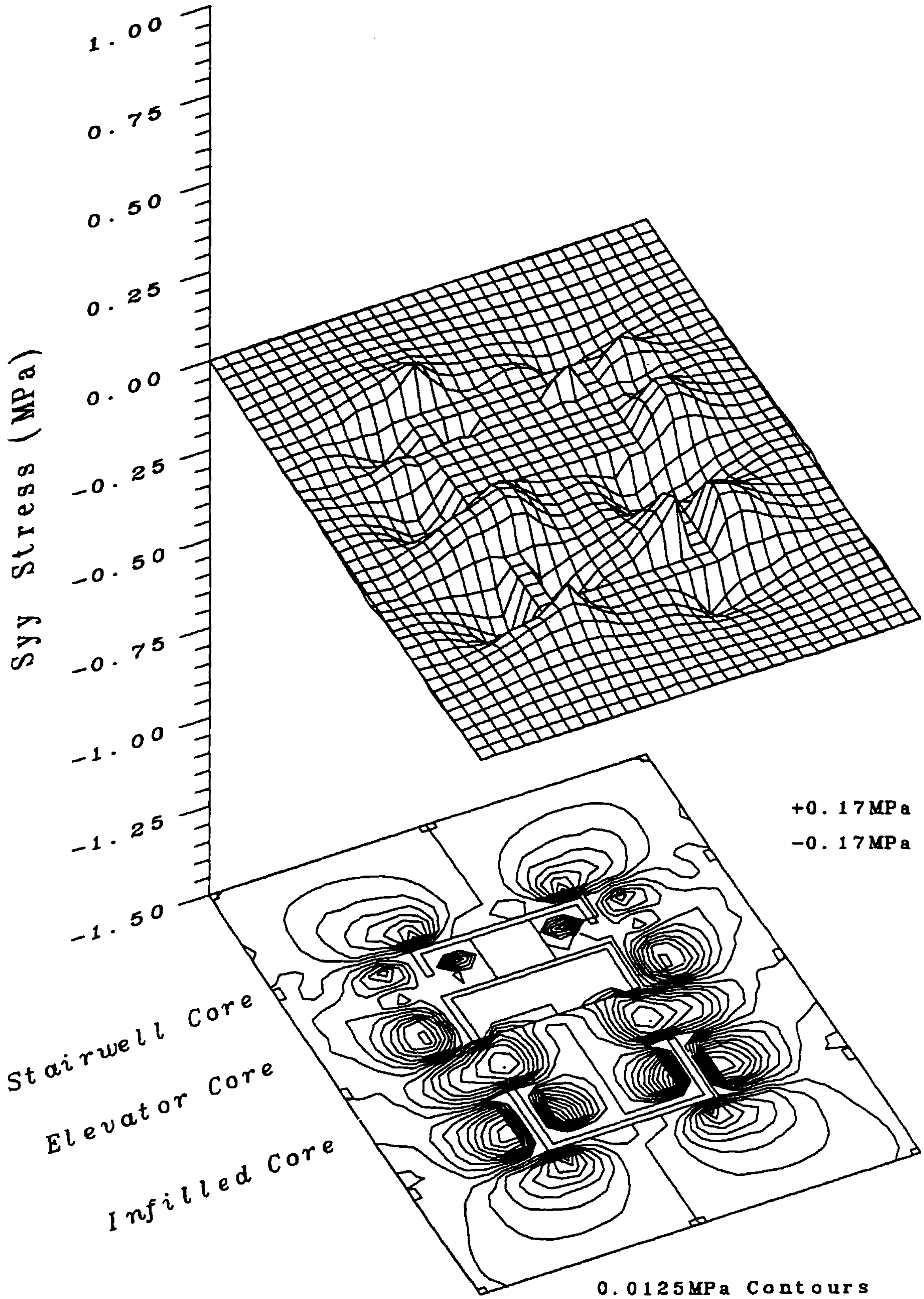

Figure 5.49 Distribution of the Longitudinal Stresses S_{yy} in the Enclosed and Surrounding Slabs – Q_X Earthquake Loading – Elastic Analysis FCS Model Results

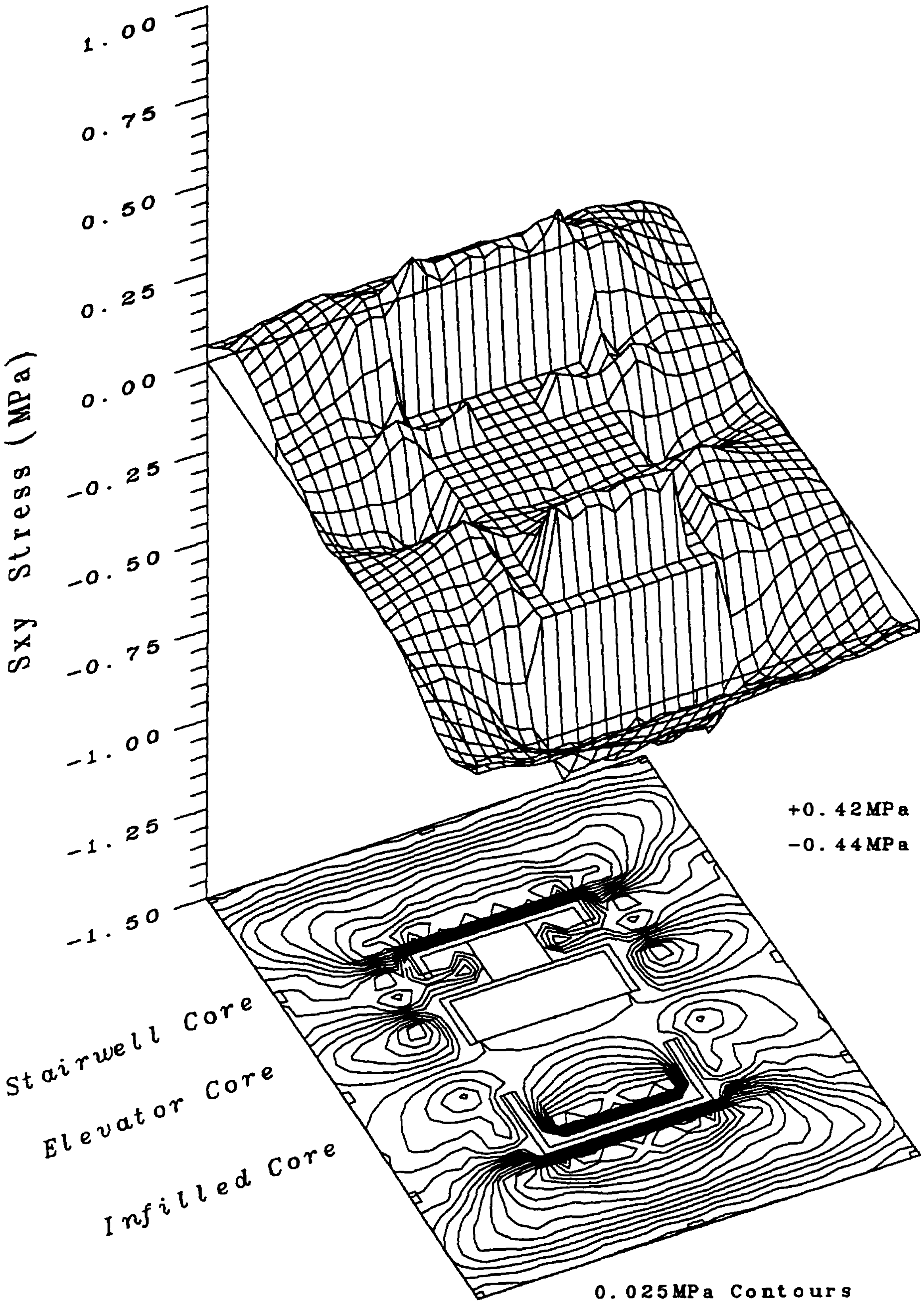

Figure 5.50 Distribution of the Shear Stresses S_{xy} in the Enclosed and Surrounding Slabs – Q_X Earthquake Loading – Elastic Analysis FCS Model Results

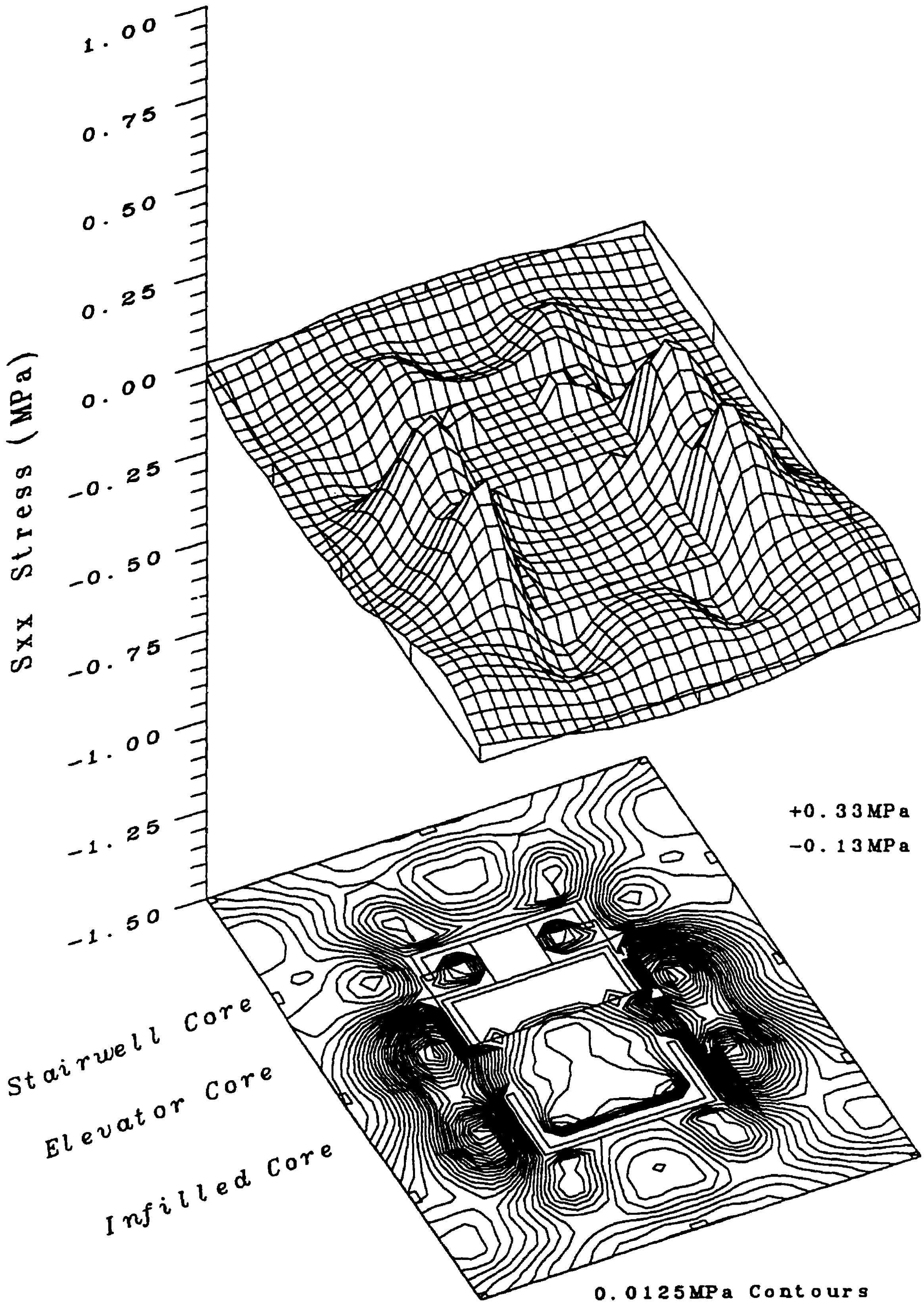

Figure 5.51 Distribution of the Transverse Stresses S_{xx} in the Enclosed and Surrounding Slabs – Q_Y Earthquake Loading – Elastic Analysis FCS Model Results

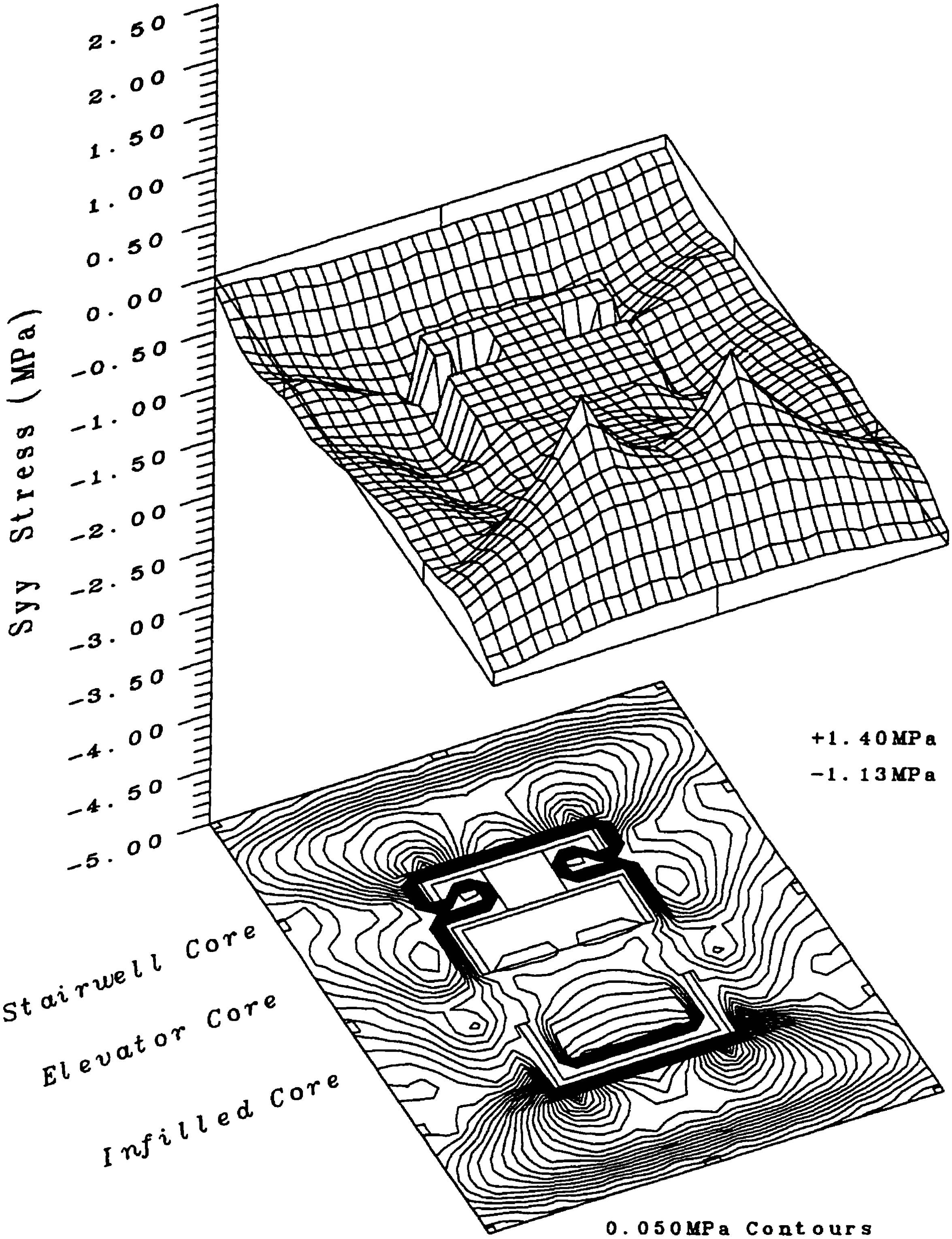

Figure 5.52 Distribution of the Longitudinal Stresses S_{yy} in the Enclosed and Surrounding Slabs – Q_Y Earthquake Loading – Elastic Analysis FCS Model Results

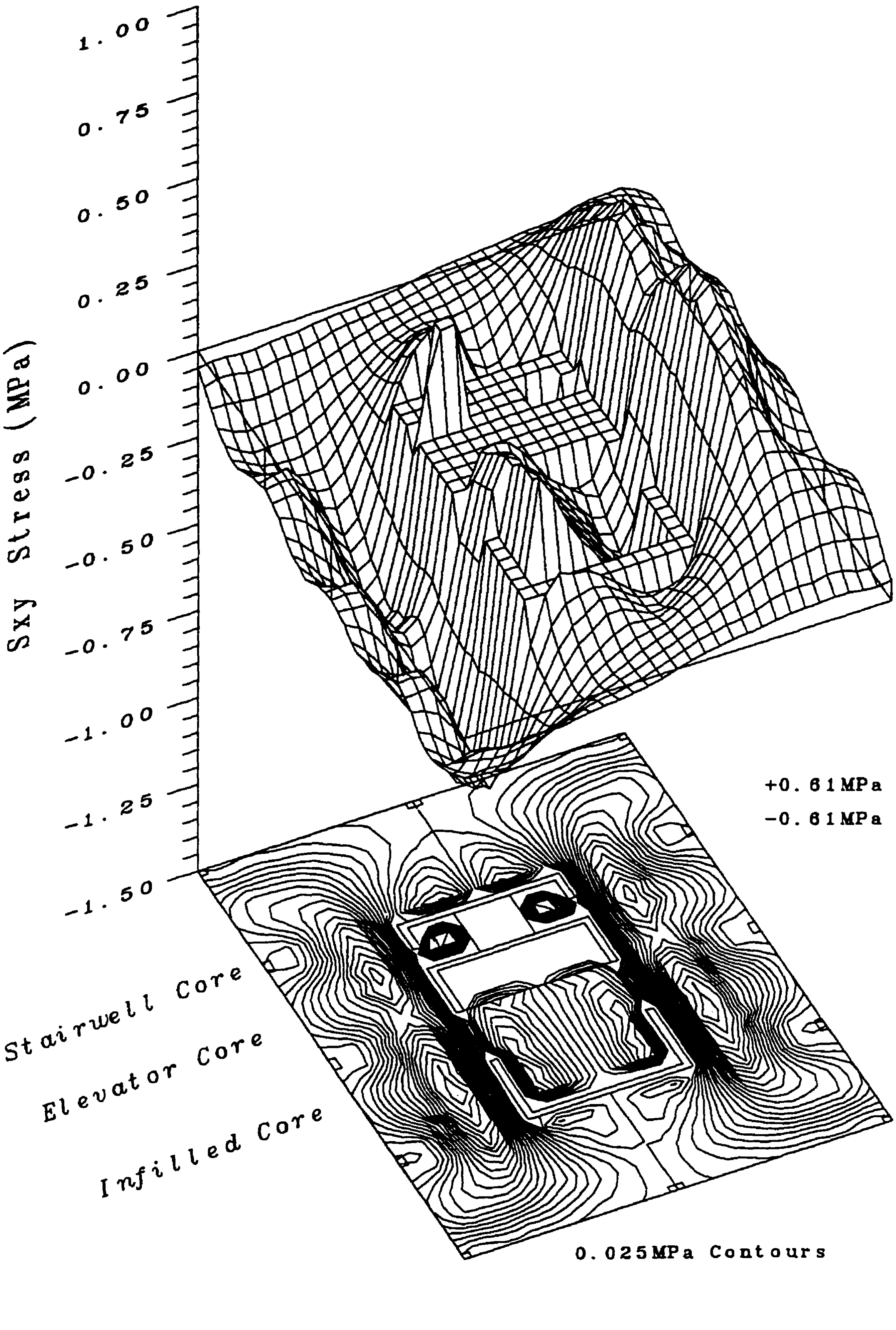

Figure 5.53 Distribution of the Shear Stresses S_{xy} in the Enclosed and Surrounding Slabs – Q_Y Earthquake Loading – Elastic Analysis FCS Model Results

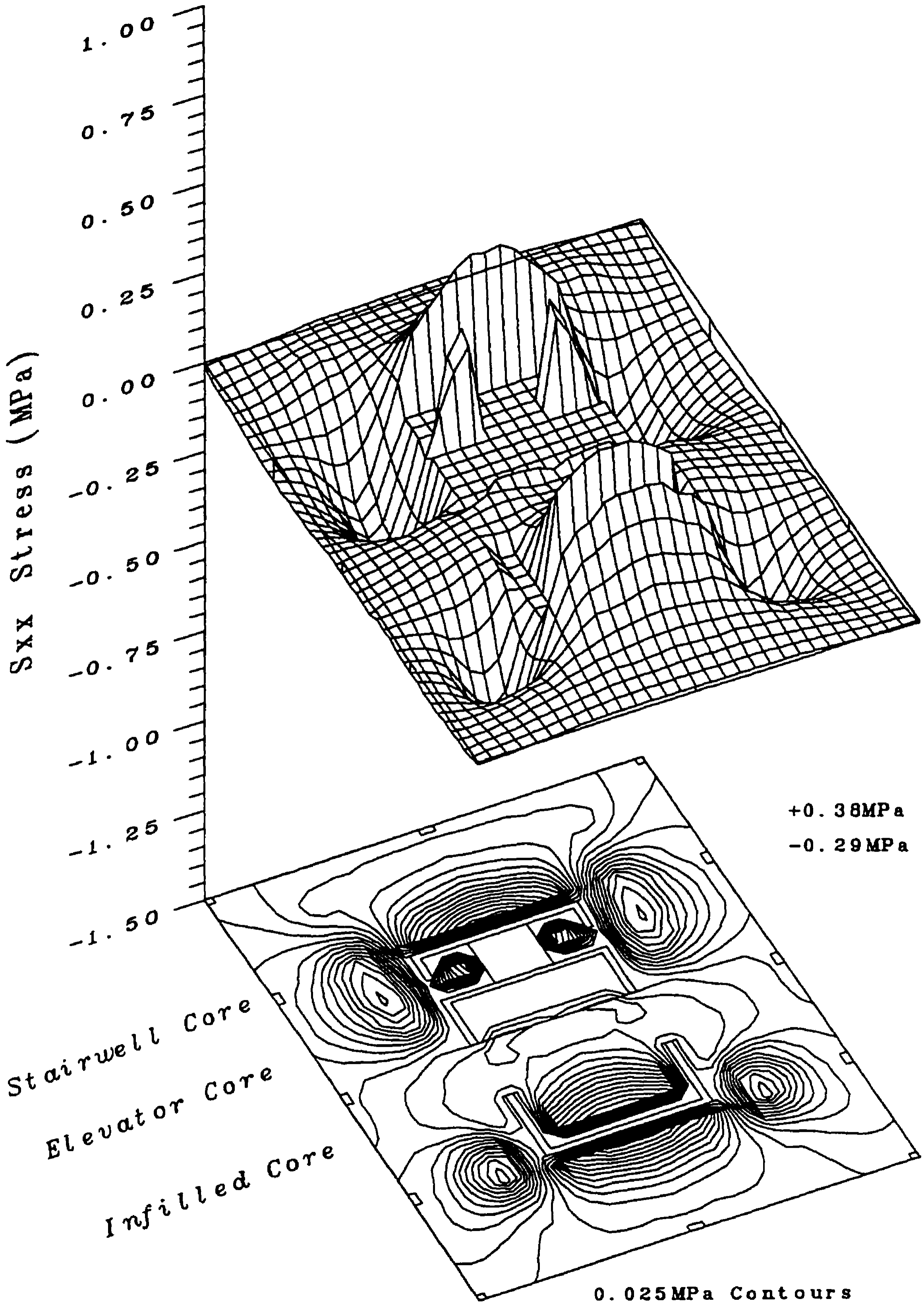

Figure 5.54 Distribution of the Transverse Stresses S_{xx} in the Enclosed and Surrounding Slabs – Dead Load – Elastic Analysis FCS Model Results

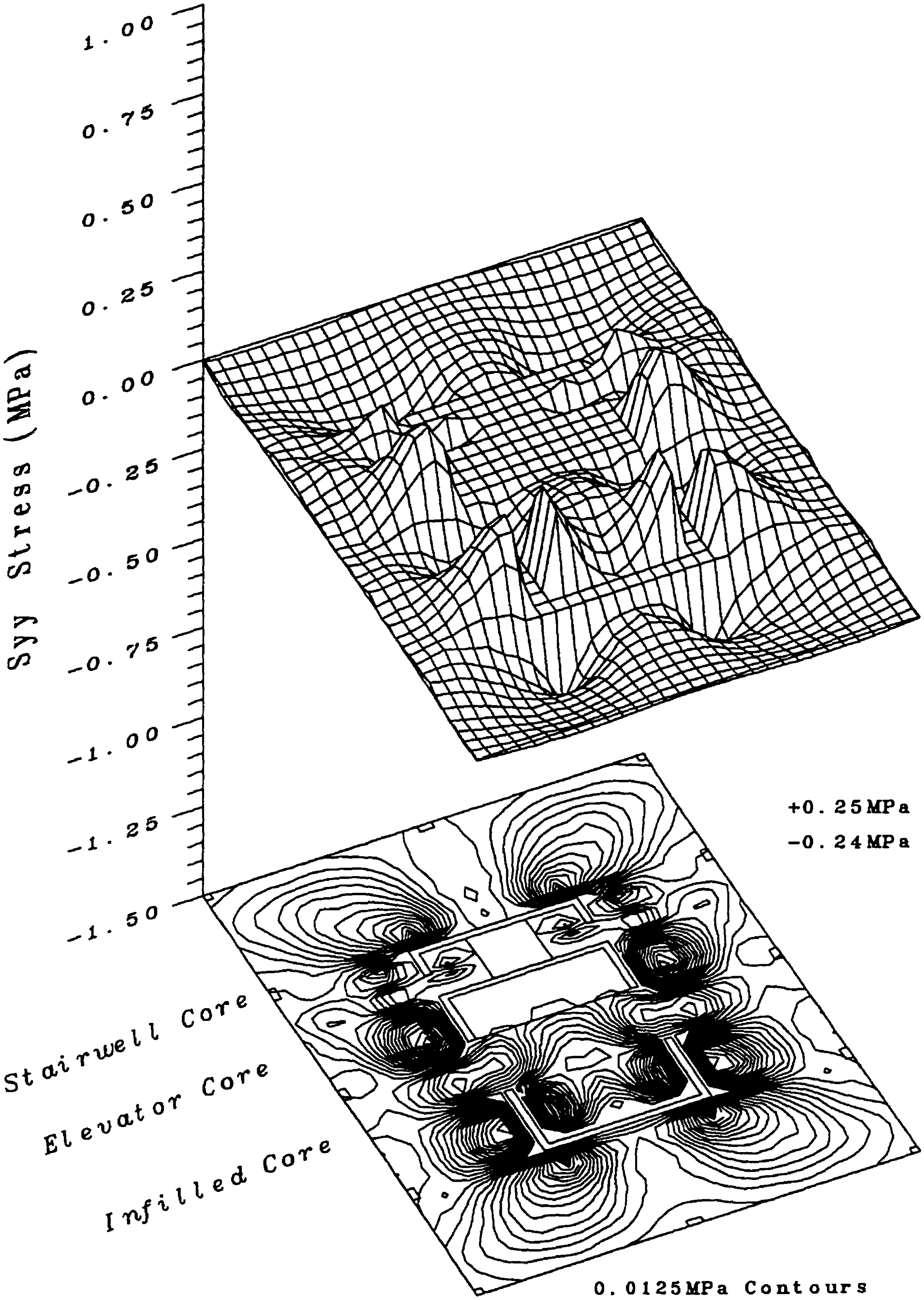

Figure 5.55 Distribution of the Longitudinal Stresses S_{yy} in the Enclosed and Surrounding Slabs – Dead Load – Elastic Analysis FCS Model Results

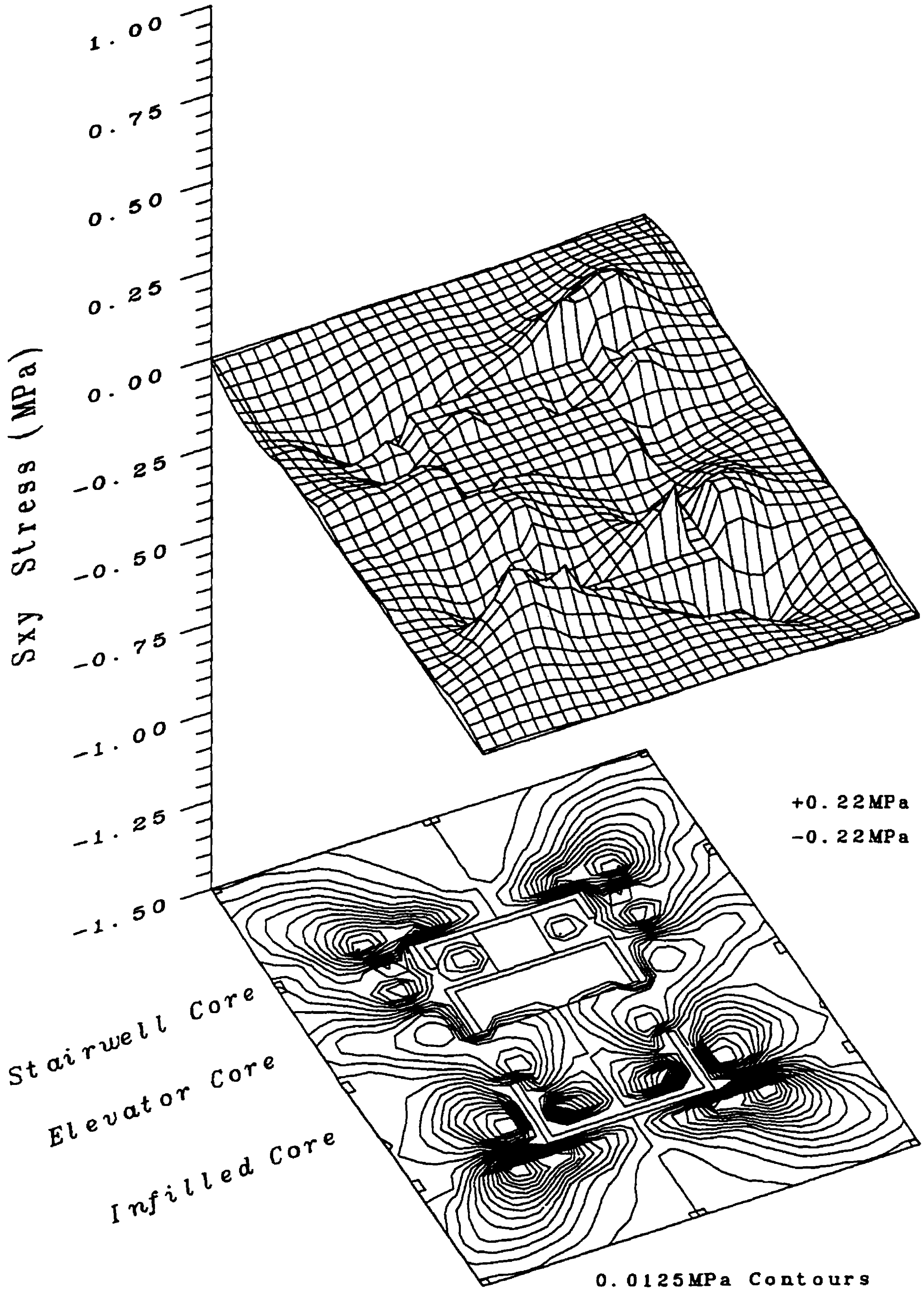

Figure 5.56 Distribution of the Shear Stresses S_{xy} in the Enclosed and Surrounding Slabs – Dead Load – Elastic Analysis FCS Model Results

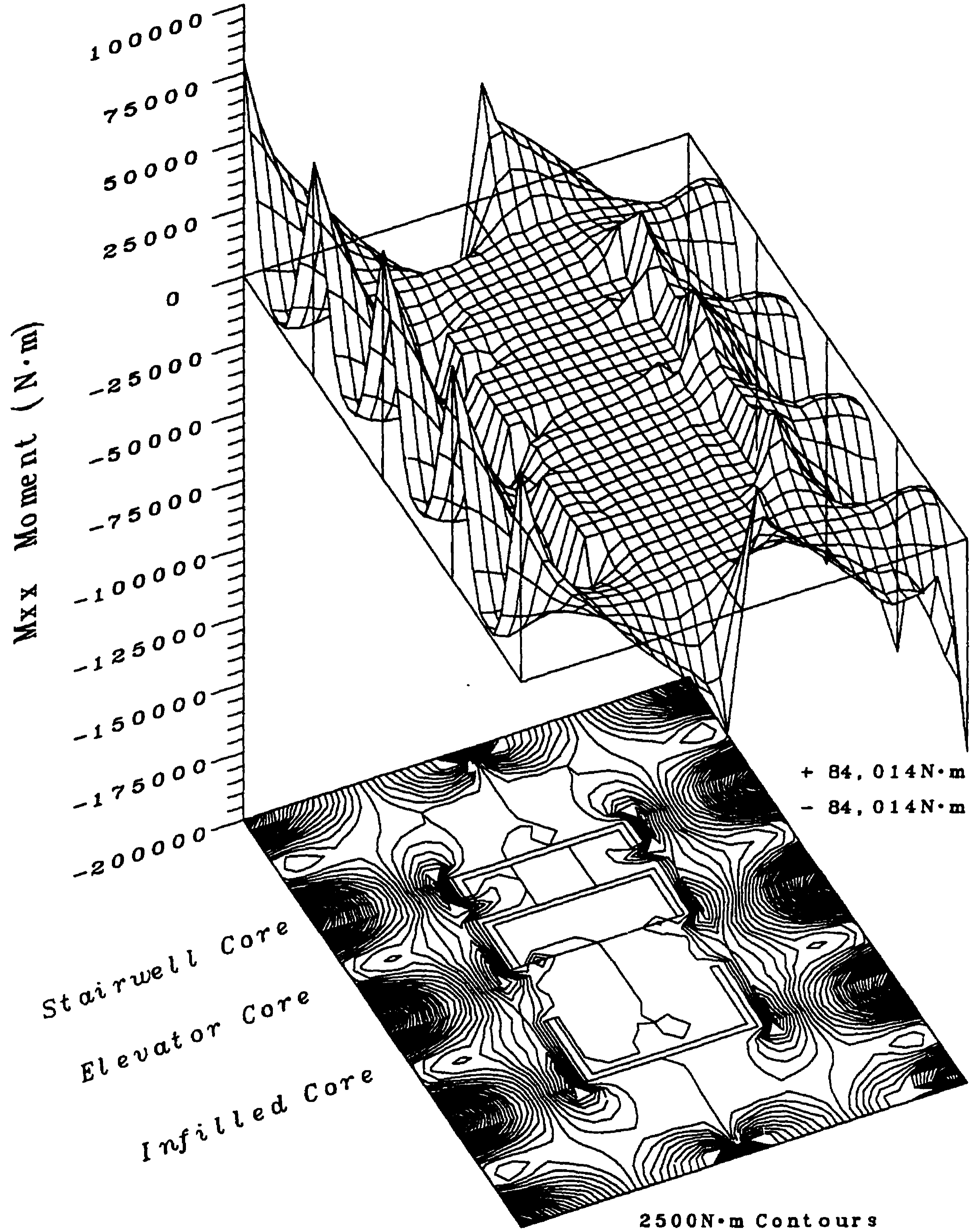

Figure 5.57 Distribution of the M_{xx} Bending Moments in the Enclosed and Surrounding Slabs – Q_X Earthquake Loading – Elastic Analysis FCS Model Results

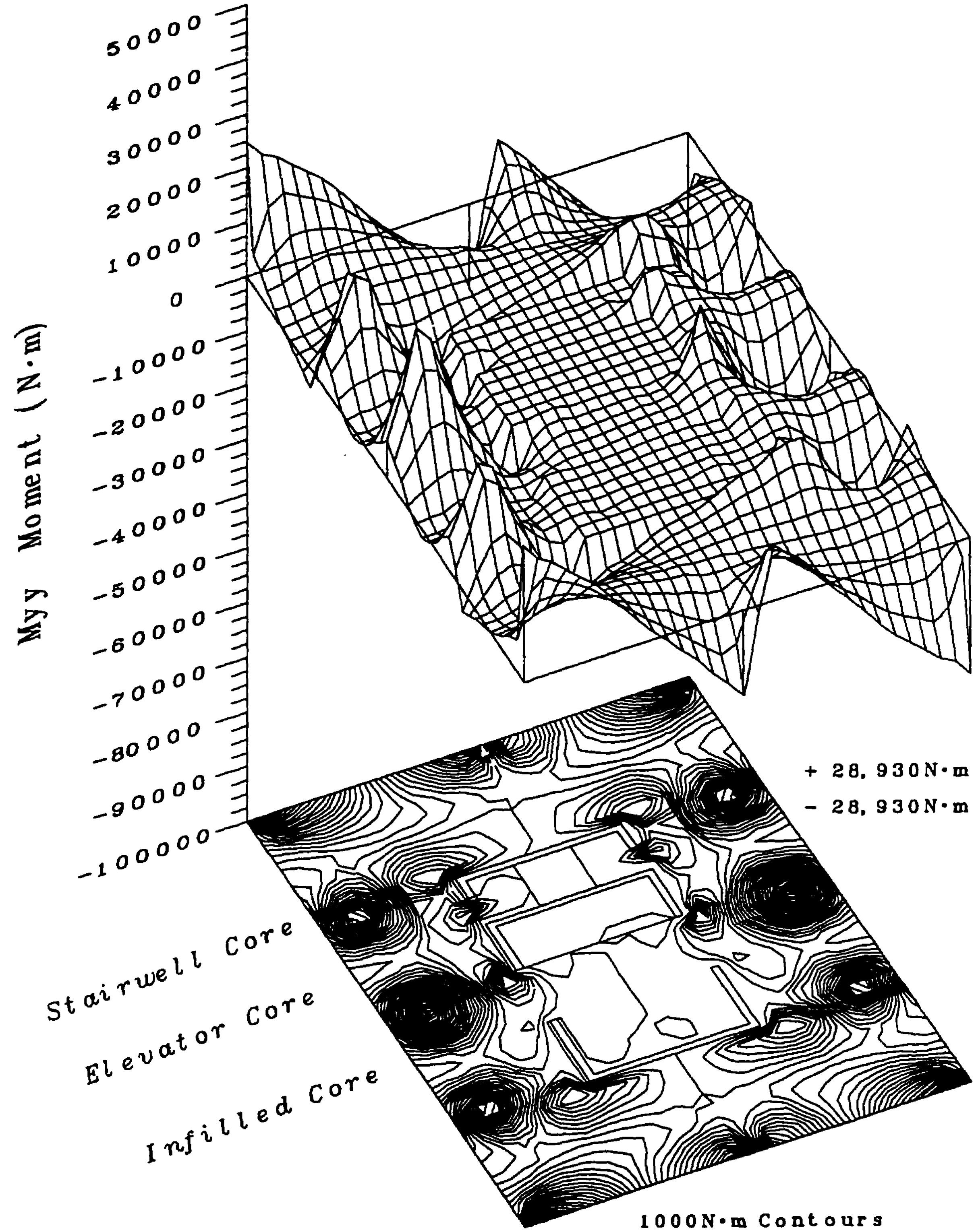

Figure 5.58 Distribution of the M_{yy} Bending Moments in the Enclosed and Surrounding Slabs – Q_X Earthquake Loading – Elastic Analysis FCS Model Results

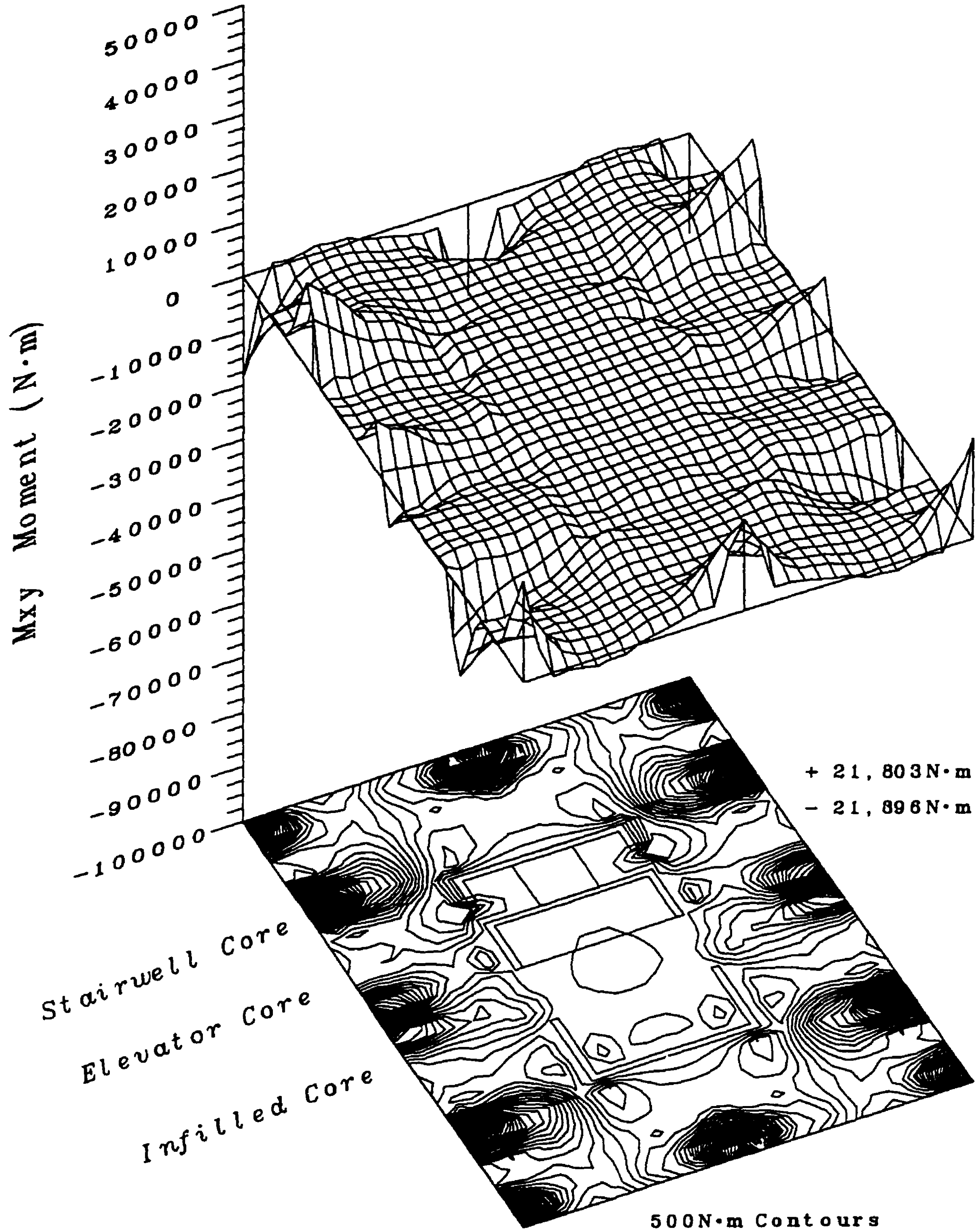

Figure 5.59 Distribution of the M_{xy} Twisting Moments in the Enclosed and Surrounding Slabs - Q_X Earthquake Loading - Elastic Analysis FCS Model Results

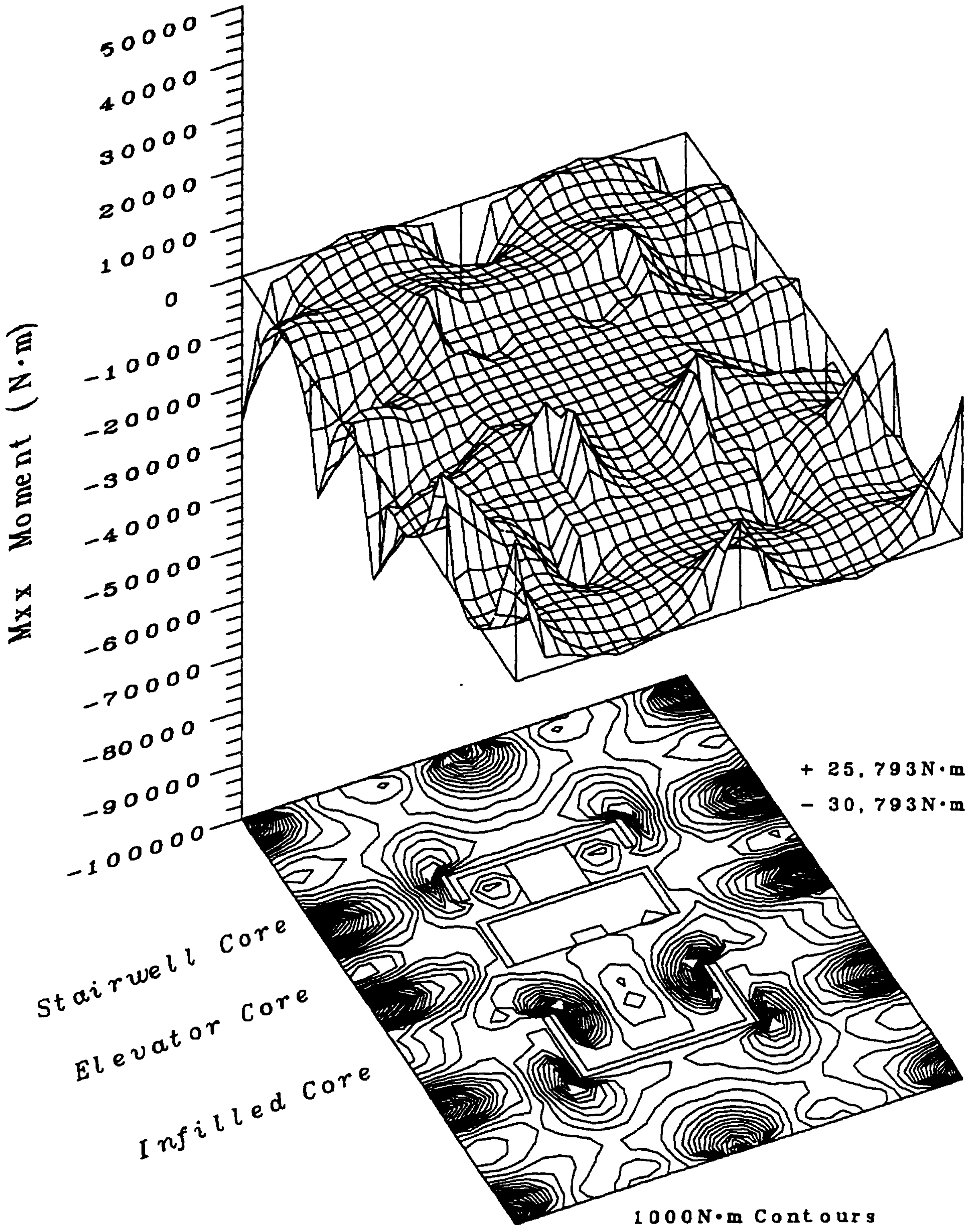

Figure 5.60 Distribution of the M_{xx} Bending Moments in the Enclosed and Surrounding Slabs – Q_Y Earthquake Loading – Elastic Analysis FCS Model Results

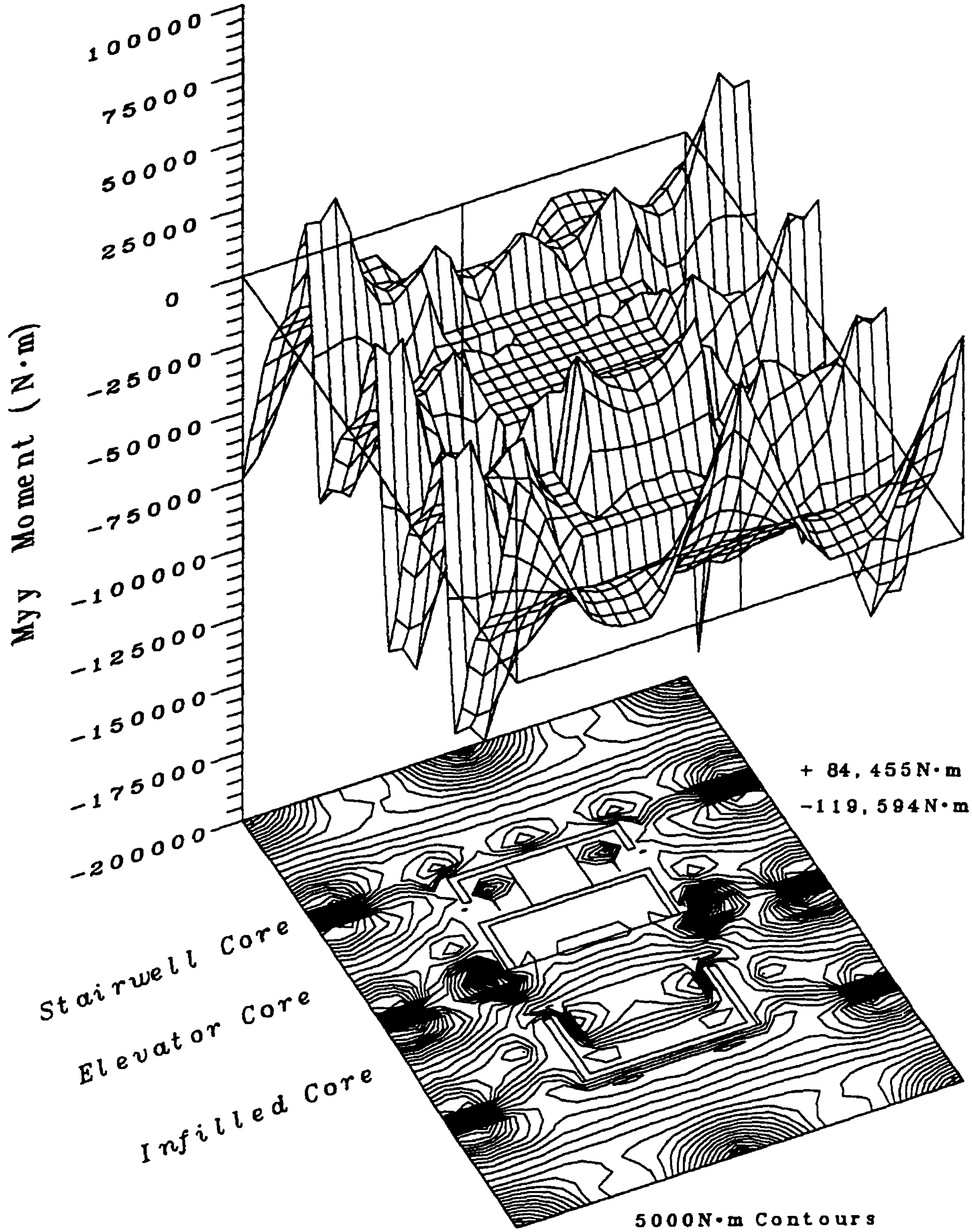

Figure 5.61 Distribution of the M_{yy} Bending Moments in the Enclosed and Surrounding Slabs – Q_Y Earthquake Loading – Elastic Analysis FCS Model Results

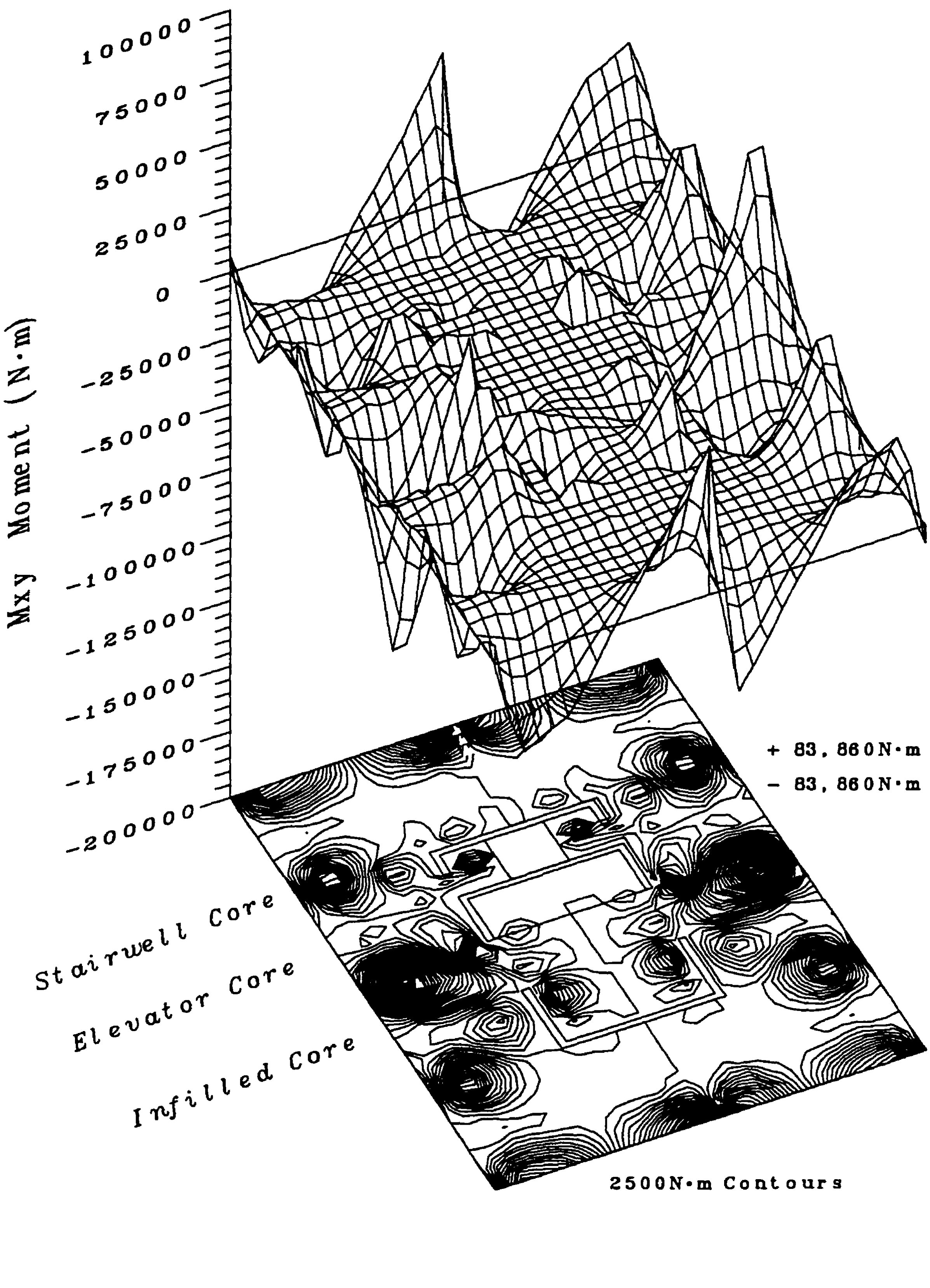

Figure 5.62 Distribution of the M_{xy} Twisting Moments in the Enclosed and Surrounding Slabs – Q_Y Earthquake Loading – Elastic Analysis FCS Model Results

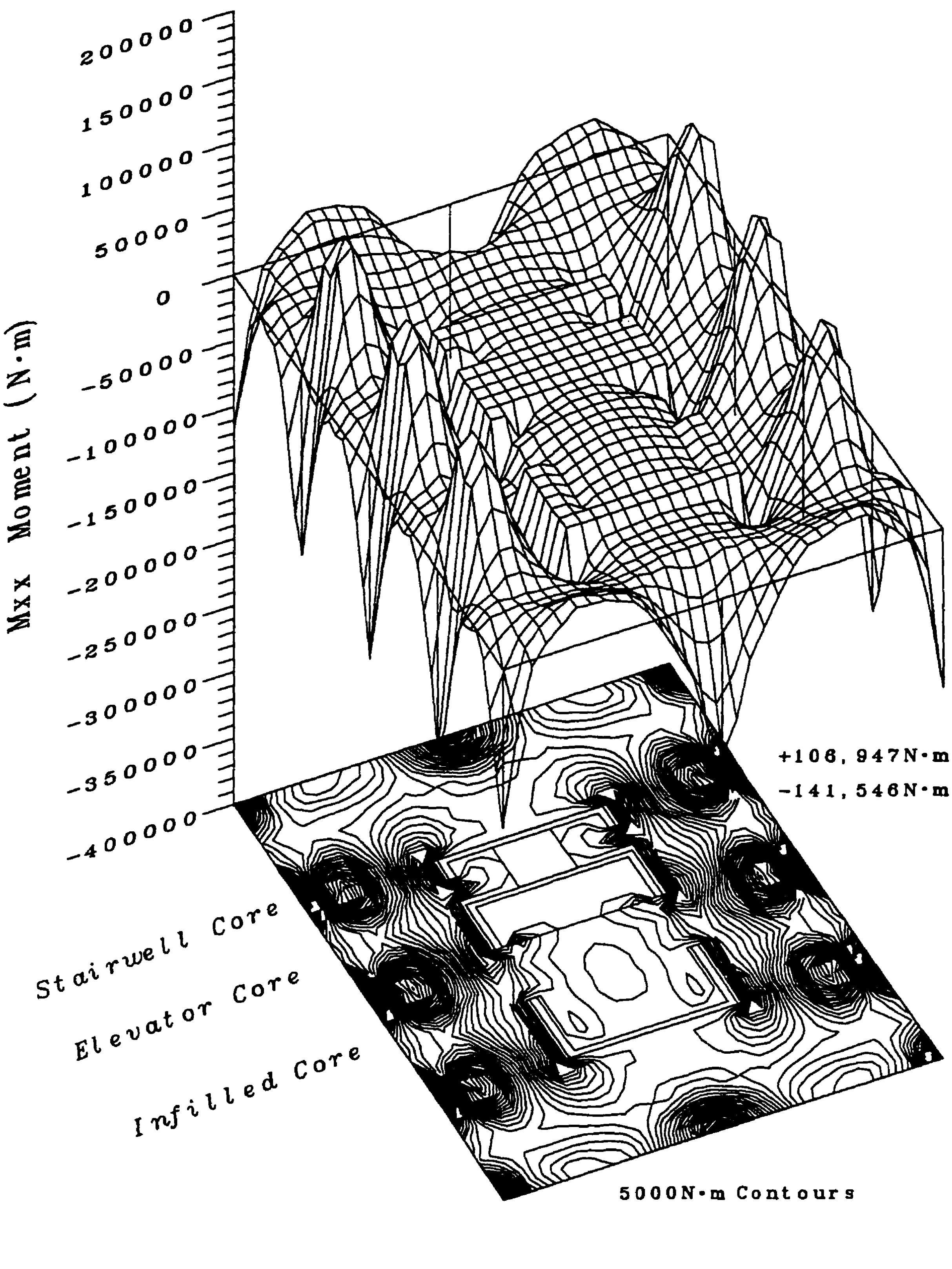

Figure 5.63 Distribution of the M_{xx} Bending Moments in the Enclosed and Surrounding Slabs – Dead Load – Elastic Analysis FCS Model Results

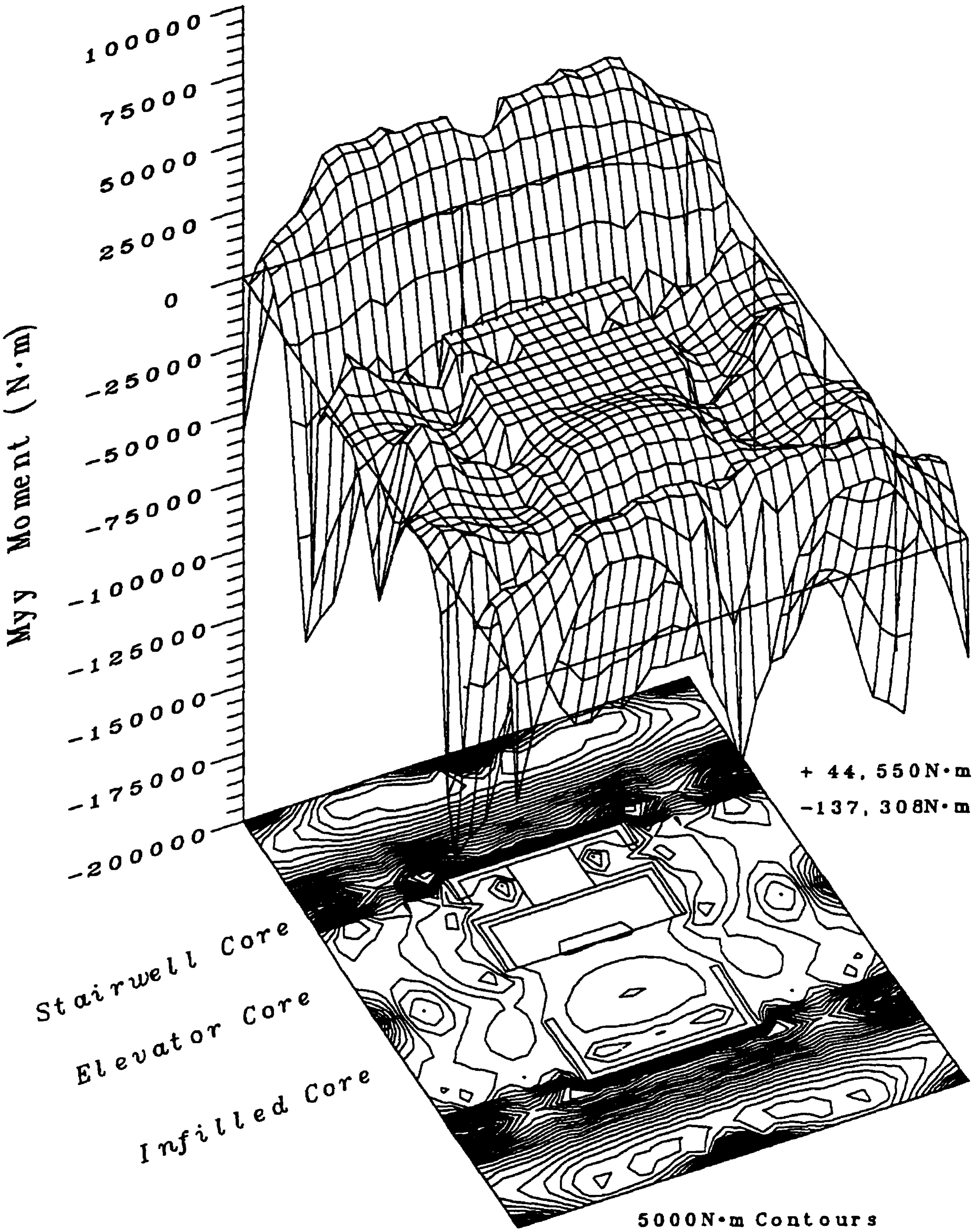

Figure 5.64 Distribution of the M_{yy} Bending Moments in the Enclosed and Surrounding Slabs – Dead Load – Elastic Analysis FCS Model Results

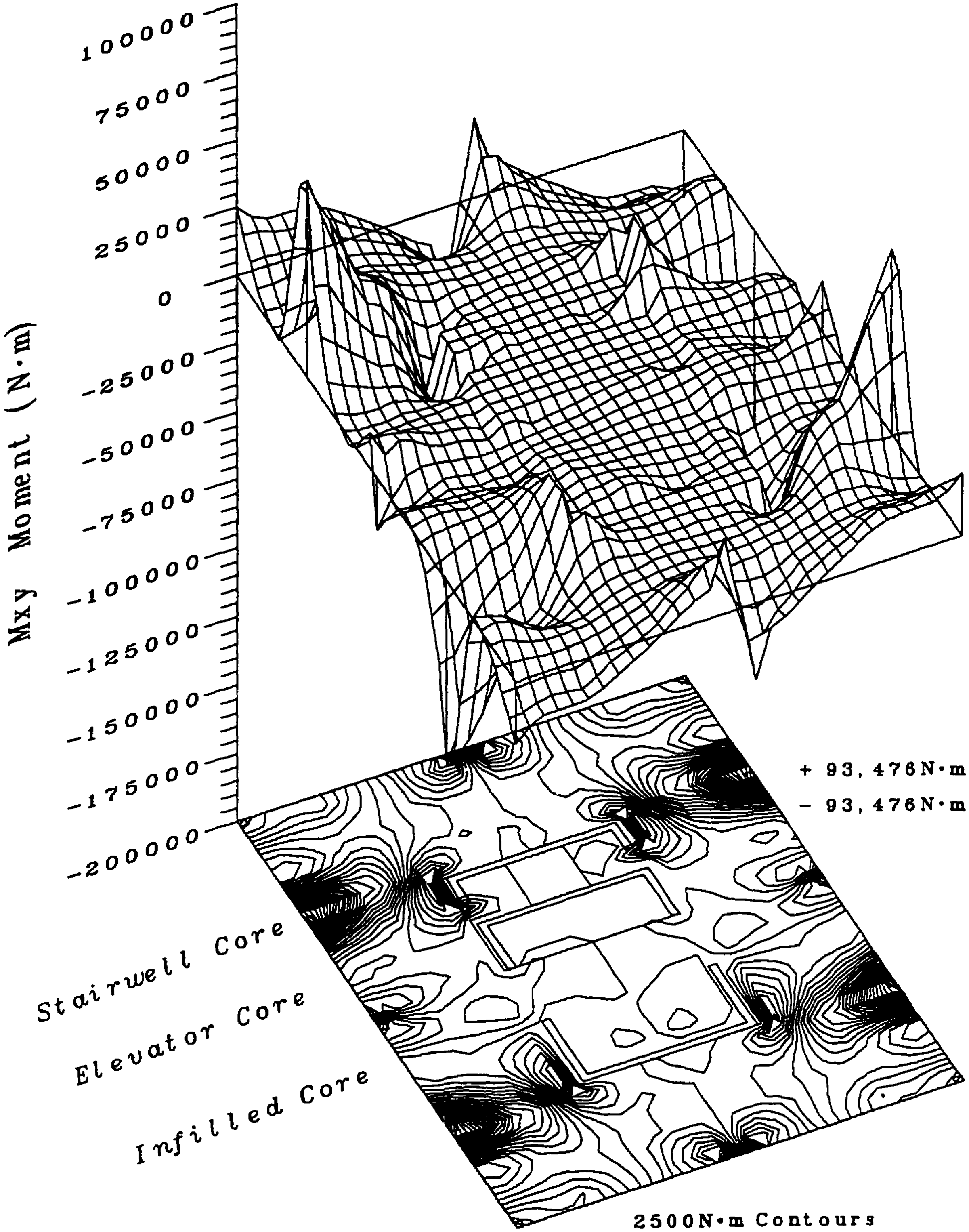

Figure 5.65 Distribution of the M_{xy} Twisting Moments in the Enclosed and Surrounding Slabs – Dead Load – Elastic Analysis FCS Model Results

Chapter 6

Nonlinear Inelastic Analysis Results – Discussion

Nonlinear inelastic analysis results of the core-slab structure subject to Q_X and Q_Y earthquake loadings and gravity loads throughout the entire load range from zero load to failure, are presented for the distributions along the structure height for the drifts, twists and vertical slab-core deflections, and at the ground level for the strains in the concentrated reinforcement of the core sections as predicted by the various models. Three-dimensional distributions of the concrete stresses consisting of "*Bird's Eye*" and "*Worm's Eye*" views, and topographical contours of the in-plane transverse axial stresses S_{xx}, the longitudinal axial stresses S_{yy} and the shear stresses S_{xy} at ground level across the core sections for selected Q_X and Q_Y earthquake load levels and the dead loads are plotted as predicted by the DQX and DQY models.

The structural behaviour is examined and discussed in terms of the comparison of the different computer models and the individual behaviour of the various structural components, the infilled-slab (Core), elevator (Elev) and stairwell (Stair) core sections, the enclosed slabs (E-slabs) and the surrounding slabs (S-slabs), referred to as E-S-slabs for both, and the coupling and lintel beams for their influence on the structural behaviour. In the discussions, interaction of the cores substructure components consists of the three-dimensional coupling and stiffening actions that occur between the cores, beams and slabs.

For discussion purposes, the lateral deformation and core concentrated reinforcement strain responses are divided into four regions as shown in Fig. 6.1. Tables 6.1 to 6.3 summarize the relevant values for the Regions 1 to 4, the failure loads and the ductility ratios for the different analyses performed.

More detailed discussions of the nonlinear inelastic analysis results for the core-slab-frame structure under investigation can be found in the report by Manatakos and Mirza (1995).

6.1 Deformations : Core-Slab Structure

6.1.1 Earthquake Load Level vs Drift – Response to Failure

6.1.1.1 Material Properties and Design Considerations

Earthquake load Q_X vs drift response of the core-slab structure in Fig. 6.2 examines the different material properties and the cores design as predicted by the DQX, DQXO, DQXX, DLQX and DQXU models. A summary of the relevant values is presented in Table 6.1.

Region 2, indicating the linear portion of the response, varies as given by the different models. DQXO model gives the lowest Region 2 limit at $1.60\,Q_X$ as a result of ignoring the tension-stiffening behaviour of the concrete and reinforcement. DQXU model for the uplift conditions for the lowest dead loads, shows a slightly higher Region 2 limit of $1.75\,Q_X$. DQX, DQXX and DLQX models all predict a 25% larger load level of $2.00\,Q_X$ for the end of the linear range due to the consideration of all of the loads and the tension-stiffening effect, resulting in top drifts between $71\,mm$ to $89\,mm$. Region 4 for the highly nonlinear response due to yielding of the reinforcement and/or crushing of the concrete, initiates at $2.90\,Q_X$ for DQXX, $3.00\,Q_X$ for DQXU, $3.20\,Q_X$ for DQXO, $3.30\,Q_X$ for DQX and $3.80\,Q_X$ for DLQX models. These results show that considering the dead and live loads with a varying steel content through the core walls height (DLQX model) gives the highest failure load and the better load-drift response compared with the other models in terms of the largest ultimate load, slower stiffness deterioration and the best energy absorption characteristics. Reducing the dead loads for the uplift conditions (DQXU model) gives the lowest energy absorption capacity with the smallest ultimate load, while using uniform wall reinforcement throughout the cores height (DQXX model) shows the lowest Region 4 load range predicting a 25% lower energy absorption capacity of the structure compared to the DQX model.

Examining the lateral load-drift responses predicted by the different models indicates a failure load above $3.00\,Q_X$. DQX, DQXX and DQXU models response group together through to the middle of Region 3, the nonlinear portion, giving failure loads at $3.40\,Q_X$, $3.10\,Q_X$ and $3.10\,Q_X$ with top drifts of $871\,mm$, $1372\,mm$ and $689\,mm$, respectively. DQXX model with uniform reinforcement throughout the core walls height results in a 10% lower failure load compared to DQX model, but shows more ductility with a 57% larger drift at failure, $1372\,mm$ vs $871\,mm$. DQXU model demonstrates the least ductility and shortest response, giving local failure at $3.10\,Q_X$ due to the smallest axial compressive load (uplift dead load condition) in the cores. DQXO model predicts a failure load of $3.40\,Q_X$ and $1362\,mm$ top drift which is 55% larger (more ductility) than DQX model. However, ignoring the tension-stiffening behaviour of the concrete and reinforcement (DQXO model) gives the lowest response for Region 3. DLQX model with dead and live loads considered, predicts the best overall lateral load-drift response showing a higher Region 3 and good ductility, predicting failure at $4.00\,Q_X$ with $1291\,mm$ top drift, which are 17% and 48% larger compared to the DQX model results.

6.1.1.2 Q_X Earthquake Loads Response

Earthquake load Q_X vs drift response for the core-slab structure as predicted by the DQX, ESDQX, CCDQX, QX and PDQX models are shown in Fig. 6.3, with relevant values summarized in Table 6.2.

Essentially the same load-drift response is predicted by DQX and ESDQX models, giving failure loads with corresponding top drifts of $3.40\,Q_X$ and $871\,mm$ top drift for DQX and $3.40\,Q_X$ and $1326\,mm$ top drift for ESDQX models. Therefore, the contribution of the S-slabs flexural actions shortens the earthquake loads response causing a 50% reduction in the drift at failure, with a 30% decrease in the energy absorption capacity, a less ductile response of the structure and a reduced ductility ratio from 15.07 for ESDQX model compared to 9.90 for DQX model.

CCDQX model gives a load-drift response similar to DQX model but with a 12% lower Region 2 limit of $1.75\,Q_X$ with $77\,mm$ top drift, a lower Region 3 extending the same length to the start of Region 4 at $3.10\,Q_X$ with $554\,mm$ top drift compared to the DQX model giving Region 4 at $3.30\,Q_X$ with $494\,mm$ top drift. CCDQX model predicts a 28% larger top drift of $1113\,mm$ at failure $3.20\,Q_X$ vs the DQX model values of $871\,mm$ top drift at $3.40\,Q_X$ failure load. These results indicate a less effective lateral load response by CCDQX model in the post-cracking range. Therefore, the contribution of the E-S-slabs gives a 10% to 15% higher Region 3 portion and failure load in the Q_X earthquake load-drift response of the core-slab structure, but decreases the energy absorption capacity by about 20% and the ductility ratio from 14.45 for CCDQX model to 9.90 for DQX model.

A large reduction in the load-drift response is noted when ignoring the dead loads in QX model, showing Region 3 starting at one-half the load level at $1.10\,Q_X$ with a $50\,mm$ top drift and the Region 4 beginning at $1.60\,Q_X$ with a $302\,mm$ top drift compared to the DQX model values of Region 3 at $2.00\,Q_X$ with $88\,mm$ top drift and Region 4 at $3.30\,Q_X$ with $494\,mm$ top drift, respectively. QX model predicts a significant top drift of $711\,mm$ at a failure load of $1.70\,Q_X$ with a ductility ratio of 14.22 predicting local buckling of the core flange walls followed by collapse of the structure at $1.75\,Q_X$, which is one-half the failure load given by the DQX model. Also, the energy absorption capacity of the QX model is reduced to approximately 40% of DQX model. Therefore, consideration of the dead loads in the core-slab structure behaviour results in an improved lateral load-drift response, doubling the load levels for the Regions 2 and 3, the failure load and the energy absorption characteristics until failure.

The planar structure PDQX model show 3 individual load-drift responses, one for each core section web wall, giving a failure load of $1.25\,Q_X$ which is about 0.30 of that for the DQX model. Stair section web wall shows a very short Region 3 portion with $136\,mm$ top drift, while the Elev and Core section web walls have a longer nonlinear Region 3 portion with top drifts at failure of $470\,mm$ and $560\,mm$, respectively. PDQX model demonstrates a much reduced lateral stiffness with the Region 3 starting at $0.75\,Q_X$ approximately 0.40 of that for DQX model, and no Region 4 portion obtained in the response. Therefore, consideration of the three-dimensional interaction and influence of the cores (flange and web walls) as open-, partially closed- and closed-sections combined with the E-S-slabs (DQX vs PDQX models) improves the lateral load response of the core-slab structure. The results show an increase of about 3 times for the linear portion Region 2 and the failure load, giving a Region 4 portion and increasing the total energy absorption capacity of the structure by about 9 times, and an increased ductility ratio from 4.5 in PDQX model to 9.90 for DQX model.

6.1.1.3 Q_Y Earthquake Loads Response

Earthquake load Q_Y vs drift response for the core-slab structure as predicted by the DQY, DQYR, CCDQY, QY and PDQY models are shown in Fig. 6.4, with relevant values summarized in Table 6.3.

DQY and DQYR models demonstrate a similar response for Regions 1 and 2 upto a load level of $2.00\,Q_Y$ giving a $50\,mm$ top drift. DQYR model shows a shorter Region 3 portion with a higher load range to Region 4, which starts at $4.90\,Q_Y$ giving a $328\,mm$ top drift, and a failure load of $5.10\,Q_Y$ with $880\,mm$ top drift. DQY model (compared to DQYR model) has a stretched-out Region 3 portion being about 2.5 times longer, Region 4 starting at $5.75\,Q_Y$ (17% higher) with a $852\,mm$ top drift (2.5 times larger) and failure at $5.90\,Q_Y$ (17% larger) with a $1190\,mm$ top drift (26% larger). Thus, the DQY model demonstrates a larger energy absorption capacity than the DQYR model. Hence, the core-slab structure is more effective in the Q_Y earthquake load direction when the Core section is on the tension side for generating the resistance (DQY model). Ductility ratios are 17.25 for DQYR and 25.87 for DQY models, with the latter model demonstrating a better and more ductile lateral load-drift response.

CCDQY model gives a load-drift response similar to DQY model showing a 13% lower Region 2 limit at $1.75\,Q_Y$ with $47\,mm$ top drift, a lower Region 3 extending to the start of Region 4 at $4.60\,Q_Y$ (20% lower) with $552\,mm$ top drift (35% less) compared to the DQY model values for Region 4 at $5.75\,Q_Y$ with $852\,mm$ top drift, respectively. These results indicate a less effective lateral load response in the post-cracking region for the CCDQY model. However, this model demonstrates a 47% larger drift at failure load of $4.70\,Q_Y$ (20% less) with $1749\,mm$ top drift (a 45% increase) compared to DQY model failure load of $5.90\,Q_Y$ with $1190\,mm$ top drift. Therefore, the contribution of the E-S-slabs gives a 15% to 20% higher Region 3 portion and higher failure load for the Q_Y earthquake load-drift response of the core-slab structure, but decreases the energy absorption capacity by about 44% and the ductility ratio from 37.21 for the coupled cores CCDQY model to 25.87 for DQY model.

A large reduction in the load-drift response is noted when ignoring the dead loads in QY model, showing a 30% lower Region 2 limit at $1.40\,Q_Y$ with a $34\,mm$ top drift, and a 50% lower load Region 4 starting at a load of $2.80\,Q_Y$ with $469\,mm$ top drift compared to the DQY model values for the Region 2 limit at $2.00\,Q_Y$ with $46\,mm$ top drift and the start of Region 4 at $5.75\,Q_Y$ with $852\,mm$ top drift. QY model predicts the largest top drift of $2200\,mm$ at a failure load of $2.90\,Q_Y$ with local buckling of the Core and Stair flange walls followed by collapse at $3.00\,Q_Y$ which is about 50% of the failure load and the energy absorption capacity with an 85%

larger top drift compared to the values given by the DQY model. Ductility ratio for QY model is 64.71 which is about twice that predicted by DQY model of 25.87. Therefore, consideration of the dead loads improves the lateral load-drift response of the core-slab structure by increasing the Region 2 linear limit by 30%, doubling the failure load and the energy absorption capacity, but results in a 50% reduction in the top drift and the ductility at failure.

The planar structure PDQY model for the lateral load-drift response, show a much reduced lateral stiffness giving a Region 2 limit at $0.90\,Q_Y$ which is approximately 50% of that for the DQY model, a short Region 3 portion and no Region 4 occurring in the response. PDQY model failure load is $1.90\,Q_Y$ with a $302\,mm$ top drift (25% of the DQY model drift) due to buckling of the core walls followed by collapse at $2.00\,Q_Y$. Therefore, consideration of the three-dimensional interaction and influence of the cores (flange and web walls) as open-, partially closed- and closed-sections combined with the E-S-slabs (DQY vs PDQY models) improves the lateral load response of the core-slab structure. The results show an increase of approximately 2 to 3 times for the linear portion Region 2 and the failure load, giving a Region 4 portion and increasing the total energy absorption capacity of the structure by about 12 times, and an increased ductility ratio from 4.65 in PDQY model to 25.87 for DQY model.

6.1.2 Drift Profiles – Response to Failure

6.1.2.1 Q_X Earthquake Loads Response

Figure 6.5 (Table 6.2) illustrates the drift profiles for load levels $0.50\,Q_X$ to $3.40\,Q_X$ failure load of the core-slab structure as predicted by the DQX model. The Region 2 limit extends upto $2.00\,Q_X$ as can be noted from the constant increase between the drift profiles. Load levels $2.00\,Q_X$ to $3.30\,Q_X$ represent the Region 3 portion, demonstrating larger drift increments and a larger increase in the drifts at storey 1 corresponding to a reduction in the lateral stiffness of the structure. Within Region 3, the top drift increases by about 5 times from $88\,mm$ to $494\,mm$ giving a ductility ratio of 5.61. The curved drift profiles indicate a reducing structure lateral stiffness that extends from the ground storey to storey 4 over the remaining load levels to failure.

At load level $3.30\,Q_X$, Region 4 is reached in the structural response where large steel strains are present in the lower storeys that result in a large increase in the drifts upto failure. At failure load $3.40\,Q_X$, the drift profile shows a much reduced lateral stiffness with the majority of loss of stiffness in the lower 4 storeys of the structure. Top drift doubles from $494\,mm$ at $3.30\,Q_X$ to $871\,mm$ at $3.40\,Q_X$. Failure of the structure occurs due to the rupture of the reinforcement and the concrete crushing in the Core section flange-web corners. The ductility ratio at failure is equal to 9.90.

Damage as a result of concrete cracking, yielding of reinforcement and formation of plastic hinging in the core walls due to Q_X earthquake loading is observed in the lower 20% height, storeys 1 to 4, and is critical in the design and evaluation of the core-slab structure response.

6.1.2.2 Q_Y Earthquake Loads Response

Figure 6.6 (Table 6.3) illustrates the drift profiles for load levels $1.00\,Q_Y$ to $5.90\,Q_Y$ failure load of the core-slab structure as predicted by the DQY model. The Region 2 limit extends upto $2.00\,Q_Y$ as can be noted from the constant increase between the drift profiles. Load levels $2.00\,Q_Y$ to $5.75\,Q_Y$ for Region 3, show larger drift increments and a larger increase in the drift at storey 1 indicating a reducing lateral stiffness extending over the lower one-third structure height, 6 storeys, giving an increased top drift from $46\,mm$ at $2.00\,Q_Y$ to $852\,mm$ at $5.75\,Q_Y$ with a ductility ratio of 18.52. Region 4 of the response extends from load levels $5.75\,Q_Y$ to $5.90\,Q_Y$ failure load, where the drift profiles demonstrate a severe stiffness degradation in the structure as noted by the diminishing flatter slopes in the lower storeys. Top drift increases by 40% from $852\,mm$ at $5.75\,Q_Y$ to $1190\,mm$ at $5.90\,Q_Y$. A large increase in the drift occurs between load levels $5.80\,Q_Y$ to $5.90\,Q_Y$ due to a large increase in the reinforcement strains at the lower storeys of the core sections just prior to failure showing a ductility ratio of 25.87. Failure at $5.90\,Q_Y$ is due to rupture of the concentrated reinforcement in the Core section flange-web corners, leading to collapse of the structure at $6.00\,Q_Y$ due to concrete crushing in the Stair section compression wall regions.

Damage due to concrete cracking, yielding of reinforcement and formation of plastic hinging in the core walls due to Q_Y earthquake loading is observed in the lower one-third height, storeys 1 to 6, and is critical in the design and evaluation of the core-slab structure response.

6.1.3 Inter-Storey Drift Profiles – Response at Failure

6.1.3.1 Q_X Earthquake Loads Response

Inter-storey drift profiles of the core-slab structure at failure due to Q_X earthquake loading are shown in Fig. 6.7 as given by the DQX, CCDQX, QX and PDQX models. Relevant values are summarized below.

Level	Inter-storey Drift (mm) DQX	CCDQX	QX	PDQX
Level 20	$61\,mm$	$77\,mm$	$50\,mm$	$41\,mm$
uniform region Levels 6 – 19	$44\,mm$ Level 12	$56\,mm$ Level 12	$36\,mm$ Level 12	$30\,mm$ Level 13
Level 1	$40\,mm$	$39\,mm$	$23\,mm$	$16\,mm$

Similar inter-storey drift profiles are observed for all of the models excepting with some differences in the lower storeys. An almost constant inter-storey drift is noted between levels 6 to 19, indicating approximately equal drift increments with a local maximum value at level 12.

DQX model predicts a maximum inter-storey drift of 61 mm at $3.40\,Q_X$ failure load. Eliminating the S-slabs flexural actions and the E-slabs (CCDQX model) demonstrates a 27% increase in the maximum inter-storey drift to $77\,mm$ and a 6% decrease in the failure load to $3.20\,Q_X$. Ignoring the dead loads (QX model) results in an 18% lower maximum inter-storey drift of

50 mm at a failure load of $1.70 Q_X$ about 50% that of DQX model. Planar model (PDQX) predicts the lowest maximum inter-storey drift of 41 mm and a failure load of $1.20 Q_X$ which are about 30% smaller than the corresponding values for the DQX model. At the top storey levels 19 to 20, all the profiles indicate a sharp 20% to 25% increase in the inter-storey drifts due to the larger storey height and discontinuous boundary conditions. Large increases in the inter-storey drift profiles are noted in the lower 4 storeys, with the DQX and CCDQX models showing more irregular profiles over levels 1 to 3. Inter-storey drifts for DQX model are 40 mm at level 1, decreasing to 31 mm at level 2, then a sharp increase to 40 mm at level 3. CCDQX model values are 39 mm at level 1, 55 mm at level 2, 53 mm at level 3 and 55 mm at level 4 showing reversals and large increases in the inter-storey drifts in the lower storeys. QX and PDQX models show smoother inter-storey drift profiles with gradually increasing values in the lower storeys, resulting in a doubling of the inter-storey drifts between levels 1 to 4.

The irregular inter-storey drift profiles in the lower one-quarter height of the structure, lower 4 storeys, are due to the concrete cracking, yielding of reinforcement and plastic hinging resulting in a loss of lateral stiffness in the core-slab structure indicating the critical regions for design and the majority of the damage occurs in the lower storeys. Separation occurs between the slabs and core walls resulting in a changing lateral stiffness throughout the height, being considerably reduced in the lower storeys of the structure.

6.1.3.2 Q_Y Earthquake Loads Response

Inter-storey drift profiles of the core-slab structure at failure due to Q_Y earthquake loading are shown in Fig. 6.8 as given by the DQY, CCDQY, QY and PDQY models. Relevant values are summarized below.

	Inter-storey Drift (mm)			
Level	DQY	CCDQY	QY	PDQY
Level 20	76 mm	112 mm	145 mm	22 mm
uniform region Level 8 - 19	57 mm	85 mm	105 mm	17 mm
Level 1	81 mm	97 mm	140 mm	11 mm

Similar inter-storey drift profiles are observed for all the models in the upper two-thirds structure height, with differences occurring in the lower one-third structure height.

DQY model demonstrates a slight decrease in the inter-storey drifts from levels 8 to 19 with the larger value of 57 mm at level 8 at $5.90 Q_Y$ failure load. CCDQY model also shows this trend with a larger inter-storey drift of 85 mm at level 8 at the failure load of $4.70 Q_Y$ indicating a 30% increase in the inter-storey drifts and a 20% lower failure load compared to DQY model, due to the elimination of the contribution of the S-slabs flexural actions and the E-slabs. QY model shows an almost constant inter-storey drift in the upper two-thirds structure height with the larger value of 105 mm at level 8 at $2.90 Q_Y$ failure load and an 84% increase in the inter-storey drift at approximately 50% of the failure load for the DQY model, due to the exclusion of the dead loads. PDQY model gives the lowest inter-storey drifts with a value of 17 mm at the mid-height and 1.90 Q_Y failure load, being one-third of the DQY model values as a result of the planar modeling. At the top storey, the inter-storey drift profiles indicate large drift increases from levels 19 to 20, depending on the model, giving a 30% increase for DQY model to a 50% increase for PDQY model caused by the larger storey height and discontinuous boundary conditions. Over the lower one-third structure height, levels 1 to 8, nonlinear irregular inter-storey drift profiles are observed for the DQY, CCDQY and QY models. PDQY model shows an almost smooth profile decreasing toward level 1 to a value of 11 mm and a slight reduction at level 2 caused by the planar modeling which ignores any three-dimensional actions between the structural components.

DQY model inter-storey drift at failure, at level 1 is 81 mm which decreases nonlinearly upward to 59 mm at level 4, remains constant to level 7 and then drops to 57 mm at level 8. This profile illustrates the formation of the plastic hinging region in the cores extending from the ground level to level 4 and upto the one-third of the structure height, levels 7 to 8, as a result of the coupled cores substructure response. CCDQY model gives inter-storey drifts of 97 mm at level 1 increasing to 101 mm at level 3 and then decreases in a nonlinear profile to 85 mm at level 7. Nonlinear inter-storey drift profiles demonstrating increases and reductions in the drifts, occur in the lower 4 storeys at failure caused by elimination of the E-slabs and the S-slabs flexural actions. QY model inter-storey drifts are 140 mm at level 1 reducing sharply to 103 mm at level 3, a 25% drop over 2 storeys, demonstrating the largest loss of lateral stiffness in the structure due to ignoring the dead loads.

Irregular inter-storey drift profiles in the lower one-third structure height, lower 6 storeys, are due to the concrete cracking, yielding of the reinforcement and plastic hinging resulting in a loss of lateral stiffness in the core-slab structure indicating the critical regions for design and the majority of the damage occurs in the lower storeys. Separation occurs between the slabs and core walls resulting in a changing lateral stiffness throughout the height, being considerably reduced in the lower storeys of the structure.

6.1.4 Inter-Storey Drift Profiles – Response to Failure

6.1.4.1 Q_X Earthquake Loads Response

Figure 6.9 illustrates the inter-storey drift profiles for load levels 1.00 Q_X to 3.40 Q_X failure load of the core-slab structure as predicted by the DQX model.

The Region 2 limit is noted upto 2.00 Q_X from the constant profiles and a nearly uniform increase in the inter-storey drifts. Load levels 2.00 Q_X to 3.30 Q_X represent the Region 3 portion, demonstrating larger inter-storey drift increments indicating a reduction in the structure lateral stiffness, principally in the lower 4 storeys. Increasingly nonlinear inter-storey drift profiles are observed extending from level 1 upwards along the structure height for each increasing earthquake load level, caused by the cracking of the concrete elements and yielding of reinforcement at the higher load range. At level 1, the inter-storey drift increases by about 9 times, from 2 mm

at $2.00\,Q_X$ to $18\,mm$ at $3.30\,Q_X$ indicating a significant reduction in the lateral stiffness of the cores substructure.

From load level $3.30\,Q_X$ to $3.40\,Q_X$ at failure, the Region 4 portion, the inter-storey drift doubles throughout the height of the structure. At $3.40\,Q_X$, a large drop in the inter-storey drift is noted at level 2 showing a 25% decrease to $30\,mm$ from $40\,mm$ at level 1. This response indicates a considerable reduction in the lateral stiffness in the lower 2 storeys of the structure near failure, with the plastic hinging region extending over the lower one-quarter structure height to level 6. The upper three-quarters of the structure height show a smooth constant inter-storey drift profile at failure load $3.40\,Q_X$, indicating that no damage has occurred in this region.

Damage as a result of concrete cracking, yielding of reinforcement and formation of plastic hinging in the core walls due to Q_X earthquake loading is observed in the lower 20% height, storeys 1 to 4, and is critical in the design and evaluation of the core-slab structure response.

6.1.4.2 Q_Y Earthquake Loads Response

Figure 6.10 illustrates the inter-storey drift profiles for load levels $1.00\,Q_Y$ to $5.90\,Q_Y$ failure load of the core-slab structure as predicted by the DQY model.

The Region 2 limit is reached at $2.00\,Q_Y$ giving an inter-storey drift of $2\,mm$ at level 1 with a nearly constant profile throughout the height. Load levels $3.00\,Q_Y$ to $5.75\,Q_Y$ within the Region 3 portion, demonstrate larger inter-storey drift increments with increasingly steeper slopes at the top and bottom storeys. At level 1, the inter-storey drifts increase by 11 times from $5\,mm$ at $3.00\,Q_Y$ to $55\,mm$ at $5.75\,Q_Y$. The lower storeys of the structure demonstrate a more irregular nonlinear profile, with increasing inter-storey drifts, extending upwards from levels 1 to 7 for successively increasing load levels. This nonlinear inter-storey drift profile in the lower one-third structure height indicates the reduction of the structure lateral stiffness in the higher load stages due to the concrete cracking, yielding of reinforcement and plastic hinging.

Region 4 portion extends from load level $5.75\,Q_Y$ to $5.90\,Q_Y$ failure load, demonstrating a 40% increase in the inter-storey drift at level 1 from $56\,mm$ at $5.80\,Q_Y$ to $80\,mm$ at $5.90\,Q_Y$. In the lower one-third height of the structure, principally in storeys 1 to 4, the inter-storey drift profiles show a very nonlinear response with large drift increases and reversals, from $57\,mm$ at level 1 to $80\,mm$ at level 4. These inter-storey drift results demonstrate a severe degradation of the lateral stiffness of the structure and the plastic hinging region extending over approximately the lower 2 to 6 storeys, one-third height, of the structure.

Damage due to concrete cracking, yielding of reinforcement and formation of plastic hinging in the core walls due to Q_Y earthquake loading is observed in the lower one-third height, storeys 1 to 6, and is critical in the design and evaluation of the core-slab structure response.

6.1.5 Twist Profiles – Response at Failure

Twist profiles of the core-slab structure at failure due to Q_X earthquake loading are shown in Fig. 6.11 as given by the DQX, CCDQX and QX models.

DQX and QX models show similar twist profiles with the latter model predicting a negative (clockwise) twist throughout the structure height, giving failure loads of $3.40\,Q_X$ for DQX and $1.70\,Q_X$ for QX models. A constant twist is noted along the upper two-thirds structure height, levels 4 to 20, giving twists of $1575 \times 10^{-6}\,rad$ and $-350 \times 10^{-6}\,rad$ for DQX and QX models, respectively. These twist profiles indicate that the majority of twisting upto failure occurs in the lower 20% height, the lower 4 storeys, of the structure.

In the DQX model, the largest twist at failure occurs at level 1, where the twist increases sharply to $1450 \times 10^{-6}\,rad$ demonstrating a flat slope and indicating a large reduction in the torsional stiffness in the lower region of the structure. From levels 1 to 3, the twist decreases nonlinearly to a slightly lower value of $1400 \times 10^{-6}\,rad$ due to the severe cracking of the concrete and yielding of the reinforcement. The twist then increases to $1500 \times 10^{-6}\,rad$ at level 4. This twist response demonstrates that the majority of damage near failure occurs in the lower one-fifth of the structure height, lower 4 storeys, and more extensively in the bottom 2 storeys causing a considerable loss of torsional stiffness for the coupled cores substructure system.

For the QX model, a reversal or negative (clockwise) twist distribution is obtained at failure. The largest twist occurs in the lower 4 storeys, predicting maximum twists of $-325 \times 10^{-6}\,rad$ at level 1 and $-400 \times 10^{-6}\,rad$ at level 2, then dropping slightly toward level 4 to $-375 \times 10^{-6}\,rad$ and becoming a uniform twist from levels 6 to 20. The largest torsional deformation occurs in the lower 3 storeys of the structure, with the ground storey indicating the largest loss of torsional stiffness. Ignoring the compressive effects of the dead loads (QX model) results in a reduction of torsional stiffness of the structure in terms of the twist to about one-third to one-quarter of the uncracked stiffness, and a failure load of one-half of that given by the DQX model.

Eliminating the E-slabs and the S-slabs flexural actions (CCDQX model) gives an increased top twist at failure from $1575 \times 10^{-6}\,rad$ in DQX to $1850 \times 10^{-6}\,rad$ in CCDQX models. At level 1, the twist increases sharply to $625 \times 10^{-6}\,rad$ (about 50% of the DQX model value) resulting in a very flat slope indicating a low torsional stiffness. The slope of the twist profile then increases gradually between levels 1 to 5, indicating a much reduced torsional stiffness in this region. From levels 5 to 20, the upper two-thirds of the structure height, the twists increase from $1050 \times 10^{-6}\,rad$ to a maximum of $1850 \times 10^{-6}\,rad$ showing a smooth profile. Thus, the CCDQX model predicts an increasing twist along the structure height, being larger in the upper half, with the majority of loss of torsional stiffness occurring in the lower 4 storeys giving a 6% smaller failure load compared to the DQX model.

6.1.6 Inter-Storey Twist Profiles – Response at Failure

Inter-storey twist profiles of the core-slab structure at failure due to Q_X earthquake loading are shown in Fig. 6.12 as given by the DQX, CCDQX and QX models.

DQX and QX models show almost identical inter-storey twist profiles from storeys 5 to 20 with values less than $25 \times 10^{-6}\,rad$ at storey 6. CCDQX model illustrates an inter-storey twist profile similar to that of the DQX model, but with the upper three-quarters of the structure height showing a maximum inter-storey twist of $75 \times 10^{-6}\,rad$ at storey 5 (3 times that of the DQX model). Thus, consideration of the E-slabs and the S-slabs flexural actions (DQX model) results in a stiffer three-dimensional core-slab structure response and reduces the inter-storey twists to one-third of the CCDQX model values. In the lower 5 storeys of the structure, nonlinear reversing inter-storey twist profiles are observed with a local peak at storey 4, then reducing (reversal of inter-storey twist) toward storey 2 and increasing sharply with a flat slope to a maximum at storey 1 of $1450 \times 10^{-6}\,rad$ for DQX, $625 \times 10^{-6}\,rad$ for CCDQX and $-325 \times 10^{-6}\,rad$ for QX models. At failure, the profiles at level 1 show that DQX model (failure load of $3.40\,Q_X$) predicts the largest inter-storey twist of $1450 \times 10^{-6}\,rad$, CCDQX model (failure load of $3.20\,Q_X$) gives approximately one-half the inter-storey twists and QX ($1.70\,Q_X$ failure load) shows a twist reversal in the bottom 3 storeys.

Hence, consideration of the E-slabs and the S-slabs flexural actions in the core-slab structure increases the torsional stiffness resulting in twice the inter-storey twists in the lower 4 storeys, 20% structure height, at failure. Also, the dead load compressive effects are beneficial in increasing the ductility and the maximum torsional deformation at the base region of the structure by a factor of upto 5 times prior to failure. Therefore, the inter-storey twist profiles indicate that torsional cracking occur in the lower one-quarter structure height, lower 5 storeys, with the majority of loss of torsional stiffness being concentrated in the lower 2 storeys.

6.1.7 Inter-Storey Twist Profiles – Response to Failure

Figure 6.13 illustrates the inter-storey twist profiles for load levels $1.00\,Q_X$ to $3.40\,Q_X$ failure load (indicated by the star symbol) of the core-slab structure as predicted by the DQX model.

Region 2 portion of the response extends upto load level $2.00\,Q_X$ giving very small inter-storey twists with a maximum value of $5 \times 10^{-6}\,rad$ at storey 1. Within the Region 3 portion, between load levels $2.00\,Q_X$ to $3.30\,Q_X$, the upper storeys 5 to 20 experience small inter-storey twists of less than $8 \times 10^{-6}\,rad$. Thus, the upper three-quarters of the structure height does not experience torsional distress. In the lower 5 storeys, one-quarter of the structure height, as the load level increases to $3.30\,Q_X$ attainment of Region 4, the inter-storey twists increase sharply between storeys 2 to 4 showing flatter slopes indicating the extent of the loss of torsional stiffness in the structure. At storey 1, a reversal develops in the inter-storey twist profiles at load level $2.50\,Q_X$ which becomes increasingly pronounced to load level $3.30\,Q_X$. The inter-storey twist at storey 2 increases 12 times from $5 \times 10^{-6}\,rad$ at $2.00\,Q_X$ to $67 \times 10^{-6}\,rad$ at $2.75\,Q_X$ and then reduces to $45 \times 10^{-6}\,rad$ at $3.30\,Q_X$. From load levels $3.30\,Q_X$ to $3.40\,Q_X$ failure load, the inter-storey twist profile demonstrates a double twist reversal with a very flat slope and reversal at storey 4 of value $110 \times 10^{-6}\, rad$ and storey 2 of $-13 \times 10^{-6}\, rad$ and a maximum inter-storey twist of $1450 \times 10^{-6}\, rad$ at storey 1.

Thus, these nonlinear reversing inter-storey twist profiles response indicates that the majority of torsional damage due to Q_X earthquake loading occurs in the lower 10% to 20% of the structure height, lower 2 to 4 storeys, with the maximum loss of torsional stiffness reducing the stiffness values to about one-tenth of the uncracked stiffness at the ground storey caused by the concrete cracking, yielding of reinforcement and plastic hinging in the lower storeys.

6.1.8 Inter-Storey Vertical Deflection Profiles of Slab-Core Corner – Response to Failure

6.1.8.1 Q_X Earthquake Loads Response

Figures 6.14 and 6.15 show the inter-storey vertical deflection profiles of the slab-Core and slab-Stair web-flange corners (Fig. 1.1) along the height for Q_X earthquake loading as obtained from the DQX model for load levels $1.00\,Q_X$ to $3.40\,Q_X$ failure load.

Examining Fig. 6.14, the slab-Core corner (tension side) inter-storey vertical deflections in the upper levels 5 to 20, a maximum value of $1\,mm$ at the Region 2 limit at $2.00\,Q_X$ is noted indicating no severe cracking or separation of the slab-Core joints. In the lower 5 storeys of the structure height, within Region 3 between load levels $2.25\,Q_X$ to $3.30\,Q_X$, the deflections increase 10 times from $2.25\,mm$ to $24.25\,mm$ at storey 1. Flatter profiles and large reversals are observed in the later load levels, with an increasing inter-storey vertical deflection propagating upwards over the lower 4 storeys of the structure. Between $3.30\,Q_X$ to failure load $3.40\,Q_X$ in Region 4, the inter-storey vertical deflections at storey 1 double from $24.25\,mm$ to $53\,mm$ due to rupture of the Core section corner concentrated reinforcement. At $3.40\,Q_X$ failure load, the inter-storey vertical deflection profile demonstrates a double reversal between storeys 2 to 4 giving a $53\,mm$ uplift of the slab-Core joint. This nonlinear response is due to the concrete cracking of the slab-Core junction and yielding of the reinforcement causing separation of the core section and slab. Thus, resulting in loss of slab-core wall joint stiffness and integrity as observed by the degrading flatter slope of the inter-storey vertical deflection profiles in the lower one-quarter height of the structure, lower 4 storeys.

Figure 6.15 for the slab-Stair corner (compression side) demonstrates similar inter-storey vertical deflection profiles to failure. In the upper one-quarter structure height (storeys 15 to 20) the deflections are less than $0.50\,mm$ increasing uniformly downward over storeys 15 to 5 to a maximum value at the base. At storey 1, the largest deflection is noted with a very flat slope indicating loss of slab-Stair wall joint stiffness as a result of the large concrete compressive stresses in the higher load levels, giving deflections of: $-2.8\,mm$ at $2.00\,Q_X$, $-5.5\,mm$ at $3.00\,Q_X$, $-6.4\,mm$ at $3.30\,Q_X$ and $-7.6\,mm$ at $3.40\,Q_X$ failure load. The largest differences in the slab-Stair corner inter-storey vertical deflections occur in the lower 2 storeys of the structure, demonstrating a very flat and nonlinear slope extending upto storey 4 at failure of the structure.

6.2 Core Concentrated Reinforcement Strains at the Base Region – Response to Failure

6.2.1 Q_X Earthquake Loads Response

Earthquake loading Q_X vs concentrated reinforcement strains response to failure, at the ground level of the core sections for the DQX model are illustrated in Figures 6.16 to 6.19.

Examining the concentrated tension reinforcement strain profiles in Figures 6.16 to 6.18, a similar behaviour is observed in all of the cores to failure. Upto load levels $0.60\,Q_X$ to $1.00\,Q_X$ for the Region 1 limit, the strain profiles are linear and show a slight discontinuity with strains of about $50 \times 10^{-6}\,mm/mm$ indicating initial cracking of the concrete in the Core web wall and the Elev and Stair flange wall end elements. The strain profiles remain approximately linear to load level $2.00\,Q_X$ representing the Region 2 limit, where all of the concentrated reinforcement experiences a larger strain increase to $150 - 200 \times 10^{-6}\,mm/mm$ in the following load level. From the earthquake load-drift response (Fig. 6.2) and the concrete stress distributions in the core sections at the ground level (discussed in the next section) a redistribution of load occurs in the cores along with a shift of the neutral axis, toward the compression side of the core sections. Nonlinearly increasing concentrated reinforcement strain profiles are observed in the Region 3 portion which extends from load levels $2.00\,Q_X$ to $3.10 - 3.30\,Q_X$ in Core, $2.75 - 3.00\,Q_X$ in Elev and $2.90 - 3.00\,Q_X$ in Stair sections. The latter strain values indicate the varying yield load levels ($0.002\,mm/mm$ strain) for the concentrated reinforcement depending on their location: flange wall end, flange wall corner and web wall corner; and on the core-slab-beam stiffness in the vicinity of the concentrated reinforcement bars. Region 4 portion of the strain profiles starts at approximately a load level of $3.30\,Q_X$ in Core and $3.00\,Q_X$ in Elev and Stair sections, and illustrates flatter strain profiles increasing from the yield strain to values of $2700 \times 10^{-6}\,mm/mm$ in Core, $4200 \times 10^{-6}\,mm/mm$ in Elev and $3600 \times 10^{-6}\,mm/mm$ in Stair sections.

At failure load $3.40\,Q_X$, a very large strain increase is noted in the concentrated reinforcement at the flange wall end and the flange-web corner locations. In the Core section (Fig. 6.16), the flange wall end reinforcement strain is $0.035\,mm/mm$ (17 times the yield strain) with a strain reversal in the flange-web corner to $-0.011\,mm/mm$ (5 times the yield strain) indicating the presence of significant strength and ductility. Also, this concentrated reinforcement has not ruptured at failure of the structure. The strain reversal in the Core flange-web corner concentrated reinforcement is due to the failure of the Stair and Elev sections causing the Core section to be pulled inward in the lower 2 storeys. Elev section (Fig. 6.17) shows a peak strain of $0.012\,mm/mm$ (6 times the yield strain) in the web-flange corner concentrated reinforcement and a large strain reversal in the flange wall end reinforcement due to rupture of this reinforcement and collapse of the core wall at failure. Stair section (Fig. 6.18) shows the largest strain in the flange wall end concentrated reinforcement of $0.0083\,mm/mm$ (4 times the yield strain) and a strain reversal in the flange-web corner concentrated reinforcement as a direct result of the rupture of the Elev flange wall end concentrated reinforcement causing a redistribution of forces to the Stair and Core sections. Since the Stair section has the shortest flange walls and the smallest stiffness of the cores, the Stair corner region concentrated reinforcement yields followed by buckling of the flange wall corner region. Therefore, between load levels $3.10\,Q_X$ to $3.40\,Q_X$ at failure of the structure, the concentrated reinforcement strains increase substantially from the yield strain to $0.0083 - 0.030\,mm/mm$ in the core sections indicating large ductility of the core-slab structure due to its three-dimensional response. At failure, the Stair concentrated tension reinforcement ruptures at the flange wall end causing buckling of the compression flange-web corner wall regions in the Stair and Elev sections. Failure is due to rupture of the core concentrated tension reinforcement at the flange-web corners and the flange wall ends, followed by local buckling of the core flange-web wall corners in the lower 2 storeys caused by the instability and deterioration of stiffness in each of the core sections.

In summary, for the DQX model with a failure load of $3.40\,Q_X$: initial cracking of the concrete wall layer elements occurs at load levels $0.60\,Q_X$ to $1.00\,Q_X$, the Region 1 limit, or 18% to 30% of the failure load giving concentrated reinforcement strains which are only 2.5% of the yield strain. The Region 2 limit indicating that the first cracked concrete-smeared steel layer core wall elements, starts at $2.00\,Q_X$ or 60% of the failure load, with concentrated reinforcement strains in the range of 7.5% to 10% of the yield strain. Region 3 of the response extends upto load levels $2.75\,Q_X$ to $3.10\,Q_X$, or 81% to 91% of the failure load, with yielding of the reinforcement. Region 4 portion extends for the remainder 10% to 20% of the failure load giving concentrated reinforcement strains at failure between 5 to 20 times the yield strain.

Strain profiles of the concentrated compression reinforcement show a similar response in the cores upto failure as illustrated for the Core section in Fig. 6.19. Linear strain profiles are observed with a slight discontinuity at about the $0.75\,Q_X$ to $1.00\,Q_X$ load level range indicating the Region 1 limit, with strains of $-250 \times 10^{-6}\,mm/mm$. Region 2 of the response extends upto a load of $2.00\,Q_X$ showing a linear profile with a slight increase in the reinforcement strains to $-300 \times 10^{-6}\,mm/mm$. Within the Region 3 portion, between load levels $2.00\,Q_X$ to $2.75\,Q_X - 3.10\,Q_X$ depending on the core section, the concentrated reinforcement strains increase in a linear fashion to $-750 \times 10^{-6}\,mm/mm$ excepting in the web wall corners which show non-linear strain profiles increasing to values of $-300 \times 10^{-6}\,mm/mm$ and $-500 \times 10^{-6}\,mm/mm$. The Region 4 portion of the response extends between load levels $2.75\,Q_X - 3.10\,Q_X$ to $3.40\,Q_X$ at failure, showing a larger increase in the strains. A flat slope is demonstrated for all except the web wall corner reinforcement which experience a strain drop to an almost zero value in the Elev section. This strain drop is due to the rupture of the Stair flange wall end concentrated tension reinforcement creating lateral instability of the Stair and Elev sections flange-web corner regions and concrete crushing at the web wall corner regions at failure. The maximum concentrated compression reinforcement strains at failure are $-950 \times 10^{-6}\,mm/mm$ in Core, $-1000 \times 10^{-6}\,mm/mm$ in Elev and $-1150 \times 10^{-6}\,mm/mm$ in Stair sections, which are about 50% of the yield strain.

6.2.2 Q_Y Earthquake Loads Response

Earthquake loading Q_Y vs concentrated reinforcement strains response to failure, at the ground level of the core sections for the DQY model are illustrated in Figures 6.20 to 6.22. The strain profiles are symmetrical about the core sections web wall center.

In the Core section, the concentrated reinforcement undergoes compressive strains in the linear range and tensile strains in the post-cracking range to failure at load level $5.90\,Q_Y$, as observed in Fig. 6.20. The Region 1 linear portion extends upto load level $0.60\,Q_Y$ to $1.00\,Q_Y$, or 10% to 17% of the failure load, where a slight discontinuity is noted with strains of $-100 \times 10^{-6}\,mm/mm$ to $-200 \times 10^{-6}\,mm/mm$ corresponding to the cracking of the Core section outer concrete web wall element layers in tension while the inner concrete layers remain in compression. Region 2 of the response is reached at about load level $2.00\,Q_Y$ or 33% of the failure load, where the Core flange-web corner reinforcement strain profiles show a further discontinuity to a strain of $100 \times 10^{-6}\,mm/mm$ or 5% of the yield strain. At this load level, the Core corner web wall elements crack causing a redistribution of the load within the Core section with a shift of the neutral axis toward the flange wall ends. Between load levels $3.00\,Q_Y$ and $4.00\,Q_Y$ representing the Region 3 portion, or 50% to 68% of the failure load, the concentrated reinforcement strain profiles flatten out and become nonlinear showing large strains. The flange-web corner reinforcement experience larger tensile strains compared to the flange wall end reinforcement due to the cracking of the Core web wall. Thus, the load level at which the concentrated reinforcement yields varies: the flange wall corners at $4.00\,Q_Y$ or 68% of the failure load, followed by the web wall corners at $4.25\,Q_Y$ to $4.75\,Q_Y$ or 72% to 81% of the failure load, and the flange wall ends at $5.25\,Q_Y$ to $5.75\,Q_Y$ or 89% to 97% of the failure load. Region 4 of the strain response begins at load level $4.00\,Q_Y$ and extends to $5.75\,Q_Y$, showing a considerable strain increase at the flange wall corners demonstrating very flat strain profiles with strains varying from $2000 \times 10^{-6}\,mm/mm$ to $8000 \times 10^{-6}\,mm/mm$. From load levels $5.75\,Q_Y$ to $5.90\,Q_Y$ at failure, for the remainder 5% to 10% of the failure load, the Core section concrete elements in the lower web-flange corner regions crack severely causing the concentrated reinforcement strains to increase substantially to values of $0.010\,mm/mm$ to $0.10\,mm/mm$, or 5 to 50 times the yield strain, until the rupture of the corner concentrated reinforcement demonstrating large ductility. At failure of the structure, the Core section concentrated reinforcement at the flange wall ends show a strain reversal from tension $3000 \times 10^{-6}\,mm/mm$ to very large compressive strains, indicating concrete crushing at the flange wall end regions due to the tensile rupture of the web wall corner concentrated reinforcement.

Elev section demonstrates a similar concentrated reinforcement strain response in Fig. 6.21, as for the Core section but with the Elev flange wall end reinforcement rupturing at failure load of $5.90\,Q_Y$ and compression buckling of the corner reinforcement due to instability of the Core section at failure. Region 1 portion of the strain response extends upto a load level of $0.60\,Q_Y$ to $1.00\,Q_Y$, or 10% to 17% of the failure load. The Region 2 linear limit progresses to load level $2.00\,Q_Y$, or 33% of the failure load, giving concentrated reinforcement strains of

$100 \times 10^{-6}\, mm/mm$ or 5% of the yield strain. Region 3 of the concentrated reinforcement strain response is noted upto load level $4.25\, Q_Y$ or 72% of the failure load, showing a nonlinear profile. The Elev web-flange corner concentrated reinforcement does not yield at failure of the structure, except for one set of concentrated reinforcement bars in the flange wall corner that yield at the start of Region 4 at load level $5.75\, Q_Y$. This strain behaviour is caused by the three-dimensional coupled cores response due to the interaction of the various cores substructure components. Region 4 portion begins at load level $5.75\, Q_Y$ and extends the remainder 3% to 5% of the failure load giving concentrated reinforcement strains just prior to failure of $8000 \times 10^{-6}\, mm/mm$ or 4 times the yield strain. At failure $5.90\, Q_Y$, the Elev flange wall end concentrated reinforcement ruptures showing a substantial increase in the strain from $0.010\, mm/mm$ to $0.10\, mm/mm$, or 5 to 50 times the yield strain, and the flange-web corner regions buckle in compression in the lower 2 storeys.

Stair section flange-web concentrated reinforcement undergoes compressive strains throughout the entire load range to failure of the structure, Fig. 6.22. A linear strain response with a slight discontinuity is observed at load $1.00\, Q_Y$ for the Region 1 limit corresponding to the initial cracking of concrete in the Core section, and the Region 2 linear portion of the response extends to load level $2.00\, Q_Y$. The concentrated reinforcement strain profiles become nonlinear beyond $2.00\, Q_Y$ as the Region 3 portion begins in the Core and Elev sections. Concentrated reinforcement strains at the Stair section flange-web corners increase to $-1500 \times 10^{-6}\, mm/mm$ at the failure load of $5.90\, Q_Y$. For the flange wall end concentrated reinforcement, the Region 1 limit is reached between load levels $0.60\, Q_Y$ to $1.00\, Q_Y$, or 10% to 17% of the failure load. Region 3 portion of the response starts at load level $2.00\, Q_Y$ or 33% of the failure load, giving concentrated reinforcement strains of $100 \times 10^{-6}\, mm/mm$ or 5% of the yield strain, and extends upto load level $4.25\, Q_Y$ or 72% of the failure load, and the Region 4 portion begins at load level $5.00\, Q_Y$ or 85% of the failure load. At the failure load $5.90\, Q_Y$, the Stair section flange wall end concentrated reinforcement strains increase to $6700 \times 10^{-6}\, mm/mm$ (over 3 times the yield strain). The Stair section flange-web corner concentrated compression reinforcement experience a strain reversal to very large tensile strains and the flange wall end concentrated tension reinforcement a reversal to large compressive strains, indicating that due to the rupture of the concentrated tensile reinforcement in the Core and Elev sections, buckling and concrete crushing at the Stair flange-web corner wall regions occur in the lower 2 storeys of the structure.

6.3 Core Concrete Stresses : Distributions at Base Region – Response to Failure

6.3.1 Q_X Earthquake Loads Response – DQX Model

6.3.1.1 Transverse Stresses S_{xx}

The concrete S_{xx} stresses in the cores demonstrate similar distributions for all load levels within the linear response range upto the Region 2 limit at $2.00\,Q_X$, as for the Core section stresses in Fig. 6.23. The tension flange walls show a uniform stress surface consisting of a series of small peaks and valleys from the flange wall end to the flange-web corner with maximum stresses of $0.67\,MPa$ to $0.85\,MPa$. Across the web walls, the tensile stresses decrease linearly from the flange-web corners to zero stresses located at about one-quarter of the distance from the tension corners. Beyond this point, at approximately the three-quarter length of the web walls, the concrete stresses become compressive increasing linearly in a series of several peaks and valleys to maximum values of $-2.00\,MPa$ to $-2.20\,MPa$ at the opposite flange-web corner regions. Along the compression flange walls, almost uniform stress distributions consisting of a series of peaks are observed from the corner to the wall end with a maximum stress of $-2.20\,MPa$. This concrete S_{xx} stress distribution consisting of peaks and valleys is due to the presence of the uniformly distributed reinforcement in the core walls and deformation compatibility between the concrete and the reinforcement.

Between load levels $2.00\,Q_X$ to $3.30\,Q_X$ for the nonlinear Region 3 portion of the response, the concrete S_{xx} stress distributions change substantially becoming nonlinear with several sharp peaks and reversals due to the concrete cracking and the yielding of the reinforcement.

Core section left flange wall concrete S_{xx} stresses, Figures 6.24 and 6.25, show a nonlinear reversal to compressive stresses consisting of sharp peaks and valleys with values of $-3\,MPa$ at $2.50\,Q_X$ to $-5\,MPa$ at $3.30\,Q_X$ over the two-thirds flange wall length toward the flange-web corner region. The remaining one-third of the flange wall end region shows a humped tensile stress distribution peaking at the flange wall center region with stresses of $1.00\,MPa$ at $2.50\,Q_X$ to $0.01\,MPa$ at $3.30\,Q_X$. Elev section left flange wall concrete S_{xx} stresses, Figures 6.26 and 6.27, are compressive at the flange-web corner, the flange wall middle and end regions with a peaked tensile stress distribution inbetween these locations. Maximum stresses range from $-1.75\,MPa$ and $1.00\,MPa$ at $2.50\,Q_X$ to $-3.25\,MPa$ and $1.25\,MPa$ at $3.30\,Q_X$. Stair section left flange wall concrete S_{xx} stress distributions are similar to those for the Elev section response, showing an almost constant tensile hump of $1\,MPa$ across the outer two-thirds of the flange wall length and a stress reversal to compression at the one-third flange-web corner region length with the stresses increasing from $-0.50\,MPa$ at $2.50\,Q_X$ to $1.50\,MPa$ at $3.30\,Q_X$.

Across the Core web wall between load levels $2.50\,Q_X$ to $3.30\,Q_X$, Figures 6.24 and 6.25, small compressive concrete S_{xx} stresses occur over the left side one-third to one-quarter length of the web wall region. The right web wall region shows tensile and compressive stress humps of values 1.50 MPa to a maximum of $-3\,MPa$ at the web-flange corner region at $2.50\,Q_X$. As the earthquake loading increases to $3.30\,Q_X$, the concrete stresses in the right half of the web wall increase showing a pronounced compressive peaked distribution at the web wall center and several smaller sharp peaks and valleys decreasing toward the web-flange corner region. Values of the compressive stress peak and the web-flange corner stress peak increase from $-3.50\,MPa$ and $-3.00\,MPa$ at $2.50\,Q_X$ to $-11.32\,MPa$ and $-5.00\,MPa$ at $3.30\,Q_X$. Across the Elev web wall, the concrete S_{xx} stresses Figures 6.26 and 6.27, are compressive consisting of several sharp peaks and valleys. This irregular concrete stress distribution increases at the web-wall central region and the right web-flange corner regions with values ranging from $-2.50\,MPa$ and $-3.45\,MPa$ at $2.50\,Q_X$ to $-8.51\,MPa$ and $-6.50\,MPa$ at $3.30\,Q_X$. Stair web wall concrete S_{xx} stresses are compressive demonstrating larger peaks and valleys over the one-third length of the web wall end regions and larger stresses at the right web-flange corner region with values of $-2.50\,MPa$ and $-3.25\,MPa$ at $2.50\,Q_X$, respectively. As the earthquake load increases, larger stress peaks develop in the central web wall region showing more irregular peaks and valleys toward the right web-flange corner region with values increasing to $-7.35\,MPa$ and $-6.50\,MPa$ at $3.30\,Q_X$, respectively.

At the failure load of $3.40\,Q_X$, the concrete S_{xx} stresses in the core sections illustrated in Figures 6.28 to 6.30, respectively, demonstrate very irregular distributions with essentially the entire core sections in compression except the flange-web corner regions of the Core and Stair sections that are in tension with maximum stresses of $> 5\,MPa$ and $3\,MPa$, respectively. The compressive concrete S_{xx} stress distributions consist of several sharp peaks ($> -30\,MPa$) and valleys along the core walls being more pronounced across the left flange and web wall regions, indicating concrete crushing in the Core section at the web-flange corner region and in the Elev section at the left flange wall end region. Over the remainder of the core wall regions, the maximum compressive concrete S_{xx} stresses at failure are about $-20\,MPa$ in Core and Elev, and $-15\,MPa$ in Stair sections.

6.3.1.2 Longitudinal Stresses S_{yy}

For all load levels within the linear response range upto $2.00\,Q_X$ representing the Region 2 limit, similar concrete S_{yy} stress distributions are obtained in the cores as for the Core section stresses in Fig. 6.31. Along the tension flange walls, almost uniform stress distributions are noted consisting of several closely spaced peaks with maximum values of $3.80\,MPa$ at $2.00\,Q_X$ indicating that concrete has reached the cracking stress level of $3.40\,MPa$. Across the web walls, the concrete stresses peak in tension at the left flange-web corner regions and decrease linearly to zero stress at approximately one-third of the distance from the left flange-web corner region. Beyond this zero stress point, toward the right flange-web corner region, over two-thirds of the web wall length, a linearly increasing compressive stress distribution composed of several larger stress peaks and valleys is observed with a maximum value of $-13\,MPa$ at the right web wall corner region. Along the compression flange walls, an almost constant stress distribution is observed composed of peaks and drops with slightly larger values of $-13\,MPa$ at the flange wall corner and the flange wall end regions. This concrete S_{yy} stress distribution consisting of peaks and valleys is due to the presence of the uniformly distributed wall reinforcement and the deformation compatibility between the concrete and the reinforcement.

Within the nonlinear Region 3 portion of the response, between load levels $2.00\,Q_X$ to $3.30\,Q_X$, the concrete S_{yy} stress distributions in the cores become nonlinear demonstrating larger stress peaks and reversals. After load level $2.00\,Q_X$, the concrete stresses in the tension flange walls drop significantly due to the cracking of the concrete. At load level $2.50\,Q_X$ for the Core section stresses Fig. 6.32, almost zero stresses occur near the one-third distance of the tension flange wall end region. A very irregular stress distribution consisting of sharp peaks of $4\,MPa$ and valleys is noted over the remaining two-thirds length of the Core section flange wall corner region, while the Elev (Fig. 6.33) and Stair section tension flange walls show similar responses of very small to almost no tensile stresses at load level $2.50\,Q_X$. Along the cores web walls, after cracking of the concrete elements in the flange walls, approximately two-thirds length of the web walls are subjected to tensile stresses showing a distribution consisting of irregularly spaced humps of maximum values of $2\,MPa$ to $4\,MPa$ and large gaps of very small stresses inbetween. At about the two-thirds length of the web wall from the tension flange-web corner regions, the core sections web walls demonstrate a stress reversal to compression increasing linearly in a series of irregular steep peaks and valleys toward the compression flange walls. Maximum concrete stresses are about $-18\,MPa$ to $-20\,MPa$ located at the core sections web-flange corners. All of the compression flange walls of the cores demonstrate very irregular compressive concrete S_{yy} stress distributions composed of several jagged peaks and valleys.

At load level $3.30\,Q_X$ for the Region 4 portion of the response, the concrete S_{yy} stress distributions in the cores are similar to those obtained for the Region 3 response but with larger values as illustrated in Figures 6.34 and 6.35 for the Core and Elev sections. Tension stress distributions across the Core section left flange wall are very irregular consisting of sharp peaks ($4\,MPa$) and valleys, while across the Elev and Stair sections left flange walls the concrete has cracked severely showing almost zero stresses. Across the core sections web walls, approximately 80% of the web wall lengths experience tensile stresses demonstrating an irregular distribution consisting of several humps and peaks of maximum values $3\,MPa$ to $> 5\,MPa$ with varying gaps inbetween. The remainder 20% length of the web wall end regions are in compression along with the compression flange walls, showing irregular nonlinear concrete stress distributions composed of several sharp peaks and valleys. Maximum concrete S_{yy} stresses are $-33\,MPa$ at the web-flange corner regions and $-25\,MPa$ at the flange wall end regions indicating that the concrete is near the crushing stress level in these regions.

At the failure load of $3.40\,Q_X$, the concrete S_{yy} stresses in the core sections illustrated in Figures 6.36 to 6.38, respectively, demonstrate very irregular distributions across the core walls. The stress distributions at the cores base region at failure load, must be examined carefully due to the failure of the core-slab structure comprising of the rupture of the concentrated reinforcement in the Core section, instability of the tension flange walls of the Stair and Elev sections and crushing of the opposite flange-web wall regions. Figures 6.36 and 6.37 show very large compressive and tensile concrete S_{yy} stresses and reversals in the Core and Elev section left flange walls with values ranging from $-47\,MPa$ to $> 5\,MPa$. Such large concrete stresses are not possible since the ultimate concrete tensile and compressive (uniaxial) strengths are $3.40\,MPa$ and $-30\,MPa$. Consideration of the biaxial effects in the concrete will result in a higher compressive concrete strength. The resulting concrete S_{yy} stress distributions at failure of the structure mathematically demonstrate that the flange walls in the Core and Elev sections have failed, and from the concentrated reinforcement strain results (discussed in the previous section) rupture of the concentrated reinforcement in these core sections has occurred. Figure 6.38 for Stair section concrete S_{yy} stresses at failure, shows a sharp compressive spiked distribution at the left flange wall end with stresses of about $-16\,MPa$ reflecting the instability failure of the Stair section caused by the buckling of the flange-web corner region. Large irregular tensile S_{yy} stress distributions composed of humps, peaks ($> 5\,MPa$) and valleys are present over 60% to 80% central length of the core sections web walls. These concrete S_{yy} stress distributions illustrate that failure of the structure causes separation of the slab-core web wall junctions, extending across the majority of the flange and web wall lengths. Compressive concrete S_{yy} stress distributions in the core sections right flange walls are irregular consisting of several sharp peaks and valleys with values ranging from $-38\,MPa$ to $-48\,MPa$ indicating that crushing of the concrete has occurred at the Core section flange-web wall corner region, at the Elev section flange-web wall corner and end regions and along the Stair section flange wall.

6.3.1.3 Shear Stresses S_{xy}

For all load levels in the linear response range upto $2.00\,Q_X$ the Region 2 limit, similar concrete S_{xy} stress distributions are obtained in the cores as shown for the Core section stresses in Fig. 6.39. In the flange walls, the concrete stress distributions consist of several conical spikes (positive shear) equally spaced with larger stress peaks located at the stiffer corner and end wall regions. Along the web walls, the stresses are larger demonstrating a distribution of a series of conical spikes with varying gaps of zero stress, increasing nonlinearly from the left to the right web wall corner regions with stresses ranging from $1.00\,MPa$ to $1.33\,MPa$. Core section web wall concrete S_{xy} stresses shows the most number of peaks, followed by the Stair and the Elev section web walls. These peaked concrete S_{xy} stress distributions in the web walls are observed throughout the entire load range until failure indicating that the stiffer Core closed-section resists more shear stresses and the more flexible Elev open-section with unrestrained web wall offers the least shear resistance showing very small shear stresses. Across the cores right flange walls, the concrete S_{xy} stress distributions are nonlinear exhibiting a double stress reversal at the ends and the corner regions, consisting of larger spiked peaks with stresses ranging from $-0.75\,MPa$ to $1.25\,MPa$. A majority of the flange and web walls experience positive S_{xy} stresses upto load level $2.00\,Q_X$ prior to the concrete attaining the cracking stress level.

Between load levels $2.00\,Q_X$ to $3.30\,Q_X$ for the nonlinear Region 3 portion of the response, the concrete S_{xy} stress distributions in the cores become nonlinear demonstrating larger peaks and reversals commencing at a load of $2.50\,Q_X$, after the concrete cracking as illustrated in Fig. 6.40 for the Core section stresses. At load level $3.30\,Q_X$, similar S_{xy} stress distributions are obtained in the cores as shown for the Core section in Fig. 6.41. The left flange walls demonstrate several S_{xy} stress reversals in the Core and Elev sections only, with sharp conical peaked distributions increasing toward the wall corner and end regions. These irregular concrete S_{xy} stresses and reversals are due to the cracking of the concrete core walls and yielding of the reinforcement causing a stress redistribution within the cores. Shear stresses in the left flange walls range from $4.00\,MPa$ to $-11.00\,MPa$ in Core, $\pm 2.50\,MPa$ in Elev and $-2.50\,MPa$ in Stair sections. Along the web walls, approximately one-half of the length (the left flange wall side) of the web walls experience negative concrete S_{xy} stresses due to the cracking of the concrete in the web wall extending upto one-half of the web wall length (as noted in the cores concrete S_{yy} stress distribution response). The right half length of the web walls toward the right corner regions, experience positive concrete S_{xy} stresses created by the associated compressive concrete S_{yy} stresses in these regions. Along the web walls, irregular concrete S_{xy} stress distributions are noted composed of a series of varied spaced humps of maximum value $1.25\,MPa$ and steep peaks of $> 5\,MPa$ showing maximum stresses at the right flange-web corner regions; i.e. larger concrete S_{xy} stresses are concentrated toward the confined concrete compression S_{yy} stress locations of the core sections. Across the right flange walls, the concrete S_{xy} stresses are positive demonstrating a reversed parabolic distribution composed of several smaller peaks in the center wall regions increasing in magnitude toward the wall ends. Maximum shear stresses occur at the flange-web corners with peak values of $> 5\,MPa$ and lower stresses at the flange wall ends of $1\,MPa$ to $4\,MPa$, indicating that tensile cracking of the concrete has occurred.

At the failure load of $3.40\,Q_X$, the concrete S_{xy} stress distributions in the core sections shown in Figures 6.42 to 6.44, respectively, become highly nonlinear demonstrating several reversals and very irregular sharp peaks at varying spacings along the core walls.

In the left flange walls. Core section shows the most irregular concrete S_{xy} stress distributions with stress reversals near the flange wall end and the flange-web corner regions to very large peaks of $-18\,MPa$ and $> 5\,MPa$, respectively. These stress distributions correspond to the rupture of the concentrated tension reinforcement at the Core flange-web corner region and separation of the slab-flange wall junction at the ground level at failure. Elev section left flange wall concrete S_{xy} stresses show a negative peaked stress profile of maximum value $-3\,MPa$ and reversals at the wall end and corner regions with stresses of $1\,MPa$ to $3\,MPa$, respectively, due to the rupture of the concentrated tension reinforcement at the Elev flange-web corner region. Very small shear stresses ($< 0.10\,MPa$) are noted in the Stair section left flange wall with a stress peak of $1.50\,MPa$ at the corner region caused by the separation of the slab-flange wall junction at the ground level and instability of the Stair section at failure.

Across the web walls at failure $3.40\,Q_X$, Core section concrete S_{xy} stress distribution shows several reversals composed of large peaks of $-15\,MPa$ and $> 5\,MPa$ near the web-flange corner regions and smaller peaks of $\pm 4\,MPa$ in the web wall center region. Elev section web wall concrete S_{xy} stresses demonstrate reversals at the mid-length of the web wall, with the stresses increasing to twice the values from $-5\,MPa$ at the left corner to $> 5\,MPa$ at the right corner caused by the separation of the slab-Elev section left flange-web corner and concrete crushing at the right flange-web corner regions. Stair section web wall concrete S_{xy} stresses illustrate distinctive sharp peaks of $-10\,MPa$ near the left flange wall region due to the buckling of the section, a double shear stress reversal at the web wall mid-region from $5\,MPa$ to $-1\,MPa$ and positive shear stresses peaking toward the right web-flange corner to $5\,MPa$.

Along the Core section right flange walls at the failure load $3.40\,Q_X$, the concrete S_{xy} stresses are negative in value $-4\,MPa$ for the majority of the wall length with reversals to positive shear stresses of peaks $> 5\,MPa$ at the stiffer flange-web corner regions. Elev section right flange wall S_{xy} stresses increase nonlinearly from the wall corner to the end regions with values ranging from $2\,MPa$ to $5\,MPa$ indicating a shear stress concentration of $> 5\,MPa$ at the corner region. Stair section right flange wall shows S_{xy} stress concentrations at the corner region of $> 5\,MPa$ with the stress profile decreasing parabolically to the center of the flange wall to $1\,MPa$ and increasing to the wall end region to $2\,MPa$ caused by the crushing of the flange-web corner region at failure.

6.3.2 Q_Y Earthquake Loads Response – DQY Model

6.3.2.1 Transverse Stresses S_{xx}

After concrete attains the cracking stress level in the Core section at a load of $2.00\,Q_Y$ and upto load level $5.75\,Q_Y$, representing the nonlinear Region 3 portion of the response, the concrete S_{xx} stress distributions in the cores change substantially from a constant profile across the walls to a nonlinear profile consisting of several sharp peaks and stress reversals caused by the concrete cracking and yielding of the reinforcement.

Core section concrete S_{xx} stress distributions at load levels $3.00\,Q_Y$ and $4.00\,Q_Y$ are illustrated in Figures 6.45 and 6.46. Across the web wall, small tensile stresses are noted over the entire wall length with reversals to compressive stresses at the web-flange corner regions. Very irregular stress distributions are observed composed of sharp peaked humps with maximum values of $0.88\,MPa$ at the one-third length and the end of the web wall regions, and smaller stress peaks ($0.25\,MPa$) at the web wall center region at load level $3.00\,Q_Y$. As the earthquake load increases, the web wall concrete stresses become compressive from the web-flange corners toward the web-wall center region giving essentially zero stresses in the central one-third web wall regions beginning at load level $4.00\,Q_Y$, indicating a reduction of axial stiffness as a result of concrete cracking in the web wall. Corner web wall region concrete S_{xx} stresses increase from $-0.50\,MPa$ at $3.00\,Q_Y$ to $-10\,MPa$ at $5.75\,Q_Y$ showing a peaked distribution. Along the flange walls, the stress distributions consist of several peaks and valleys increasing nonlinearly in a steep gradient from the corner to the end wall regions giving stresses increasing from $-0.50\,MPa$ and

$-2\,MPa$ at $3.00\,Q_Y$ to $-14\,MPa$ and $-25\,MPa$ at $5.75\,Q_Y$ at each location, respectively.

Elev section concrete S_{xx} stresses at load level $3.00\,Q_Y$ are shown in Fig. 6.47. Across the web wall, the concrete stresses show a series of sharp compressive peaks and valleys in a reversed parabolic profile with a minimum value at the web wall center increasing toward the web-flange corner regions, giving minimum and maximum web wall stresses between $-1.00\,MPa$ and $-2.26\,MPa$. As the earthquake load increases, the concrete stress distributions become a series of fewer peaks spaced further apart showing decreasing stresses in the web wall center and the web-flange end regions, to almost zero stresses at load level $5.50\,Q_Y$ over the central one-fifth region of the web wall region as shown in Fig. 6.48. Two distinct stress peaks form at the one-third lengths of the web wall between load levels $4.00\,Q_Y$ to $5.75\,Q_Y$, with stresses increasing from $-1.25\,MPa$ to $-4.00\,MPa$, respectively. Formation of these S_{xx} stress peaks is influenced by the partial E-slabs between the Stair and Elev sections restraining and stiffening the Elev section web wall. Along the Elev flange walls starting at load level $3.50\,Q_Y$, the S_{xx} stresses become compressive showing a parabolic distribution composed of several sharp peaks with a maximum value at about the one-third distance from the flange wall end. At load level $5.75\,Q_Y$, the concrete stresses increase in the flange wall to $-13\,MPa$ at the corner region, $-22\,MPa$ at the maximum peak and $-17.50\,MPa$ at the end region.

Stair section concrete S_{xx} stresses show that the entire core is in compression until the failure load, with the stress distribution at load level $3.00\,Q_Y$ plotted in Fig. 6.49. Across the web wall, the concrete stresses are composed of a series of sharp compressive stress peaks and valleys in a reversed parabolic shape with a minimum value of $-1.60\,MPa$ at the web wall center increasing to $-2.86\,MPa$ at the web-flange corner regions at $3.00\,Q_Y$, and becoming almost constant in value across the web wall to a stress of $-7.25\,MPa$ at $5.75\,Q_Y$. This concrete S_{xx} stress variation is due to the Stair section accepting a larger compressive loading in the higher load stages resulting from the redistribution of load caused by the concrete cracking in the Core section and the yielding of reinforcement. Along the Stair section flange walls, the S_{xx} stresses increase linearly from the end region to a stress concentration at the flange-web corner region, with values of $-0.50\,MPa$ and $-2.86\,MPa$ at $3.00\,Q_Y$ to $-6.25\,MPa$ and $-9.00\,MPa$ at $5.75\,Q_Y$ at each location, respectively.

Within load levels $5.75\,Q_Y$ to $5.90\,Q_Y$ representing the Region 4 portion of the response, highly nonlinear concrete S_{xx} stress distributions are observed in the cores. It is noted that collapse of the structure occurs at a load of $6.00\,Q_Y$ giving concrete S_{xx} stress distributions in the cores with values greater than $-50\,MPa$ and $5\,MPa$ which are mathematical representations at the collapse of the core-slab structure.

At the failure load of $5.90\,Q_Y$, the Core section concrete S_{xx} stress distribution in Fig. 6.50 shows larger compressive stresses in the flange walls of $-25\,MPa$ at the flange wall ends decreasing to $-5\,MPa$ near the flange-web corner region and increasing to a stress peak of $-17\,MPa$ at the web-flange corner. Across the web wall, large compressive stress peaks are noted at the one-quarter wall distances from the corner regions of values $-11\,MPa$ decreasing parabolically to zero stresses at the web wall center region. The Core section web-flange corner concentrated reinforcement ruptures at failure causing splitting of the flange wall ends at the ground level. indicating the extent of the flange wall tensile splitting zone. Elev section concrete S_{xx} stress distribution at failure load Fig. 6.51, predicts stresses of $-40\,MPa$ at the flange wall ends indicating the crushing of concrete. with decreasing stresses toward the flange-web corner to $-15\,MPa$. Across the web wall, the outer one-third length wall regions demonstrate compressive stress peaks of $-5\,MPa$ and the central one-third length wall region shows tensile stresses of $1\,MPa$. At collapse. crushing of the concrete at the Elev flange wall end occurs due to the large compressive stresses, while the web-flange corner regions are almost unstressed. This concrete S_{xx} stress response indicates that lateral instability of the Elev section flange-web corner region occurs in the lower 2 storeys at failure, leading to the collapse of this core section. Stair section concrete S_{xx} stress distribution at failure load Fig. 6.52, illustrates a parabolic profile of compressive stresses across the web wall with a maximum value of $-8.75\,MPa$ at the wall center reducing to $-5.50\,MPa$ at the web-flange corners. Along the flange walls, the stresses peak at the wall end regions to $-10\,MPa$. At collapse, very large concrete S_{xx} stresses ($> 40\,MPa$) are obtained in the Stair section at the flange-web corner indicating concrete crushing and almost no stresses are noted in the flange walls. This concrete S_{xx} stress response indicates buckling of the Stair section web-flange corner region in the lower 2 storeys at failure of the structure due to the compressive load, leading to collapse of this core section.

6.3.2.2 Longitudinal Stresses S_{yy}

At load level $2.00\,Q_Y$, the cracking of concrete elements occurs in the Core section and similar concrete S_{yy} stress distributions are noted in the cores within the nonlinear Region 3 portion of the response upto a load of $5.80\,Q_Y$ becoming nonlinear and demonstrating several peaks and valleys caused by the concrete cracking and the yielding of reinforcement.

Core section concrete S_{yy} stress distributions at load levels $3.00\,Q_Y$ and $3.50\,Q_Y$ are illustrated in Figures 6.53 and 6.54. Across the web wall, the stresses increase in a parabolic profile toward the web-flange corner regions and larger peaked tensile stresses form with larger gaps of smaller stresses inbetween. These concrete S_{yy} stress peaks increase to values $> 5\,MPa$ progressively covering the entire web wall. The uniaxial concrete tensile strength is $3.40\,MPa$ and such large tensile stresses in the Core web wall are not possible. Mathematically, these large tensile S_{yy} stresses indicate that the outer concrete element layers of the Core web wall elements have cracked on the tension side, while the inner concrete layers of the wall elements are in tension having not yet attained the cracking stress level due to compatibility of the concrete and the smeared steel reinforcement layers. Along the flange walls, the S_{yy} stresses increase in tension from the flange-web corner to the flange end wall regions showing four-fifths length of the flange wall in tension at $5.80\,Q_Y$ and the remainder of the wall in compression of $-4\,MPa$. This varying concrete S_{yy} stress distribution indicates the progression of concrete cracking, from the Core section web wall corner toward the flange wall end regions.

Elev section concrete S_{yy} stresses demonstrate a similar distribution increasing in value from load levels $3.00\,Q_Y$ shown in Fig. 6.55 to $5.00\,Q_Y$. Across the web wall, a parabolic compressive stress distribution composed of several peaks and valleys is noted increasing toward the corner regions forming a steeper parabolic profile at the higher load levels. The concrete stresses increase sharply at the web wall corner regions from $-8\,MPa$ to $-23\,MPa$ and remain fairly constant in the central web wall region at about $-5\,MPa$ within this load range. This parabolic concrete S_{yy} stress profile indicates that the stiffer Elev section web wall region, restrained by the partial E-slabs on the outer Elev web wall side, resists more redistributed load as the cracking of the concrete elements progresses in the Core section. At load level $5.25\,Q_Y$ illustrated in Fig. 6.56, the central portion of the Elev section web wall region undergoes a stress reversal showing a series of tensile stress humps with values increasing to $3\,MPa$ at load level $5.80\,Q_Y$. Along the flange walls, the concrete stresses become tensile at the end wall regions after load level $2.00\,Q_Y$ and extend toward the corner wall regions at load level $5.80\,Q_Y$ with stresses increasing to values $> 5\,MPa$. As the earthquake loading increases and due to redistribution of stresses to the Elev section, after cracking of the concrete elements occurs in the Core section, the Elev section flange walls accept load and cracking of these flange wall concrete elements occurs gradually over the Region 3 portion of the response. Mathematically, these large tensile concrete S_{yy} stresses indicate that the outer concrete element layers of the Elev section flange wall elements have cracked on the tension side, while the inner concrete layers of the wall elements are in tension having not yet attained the cracking stress level due to compatibility of the concrete and the smeared steel reinforcement layers.

Stair section concrete S_{yy} stresses increase in a similar compressive distribution between load levels $3.00\,Q_Y$ shown in Fig. 6.57 to $5.90\,Q_Y$. Across the web wall, the stresses vary parabolically upto load level $5.50\,Q_Y$ consisting of a series of stress peaks and valleys with lowest values at the web wall center and increase toward the web-flange corner regions to values of $-11.50\,MPa$ and $-35\,MPa$ at $3.00\,Q_Y$ and $-18.80\,MPa$ and $-45\,MPa$ at $5.50\,Q_Y$, respectively, at each location. At load level $5.75\,Q_Y$ and beyond, the web wall concrete stresses become an almost constant series of sharp peaks and valleys due to the attainment of the ultimate compressive concrete stress at the web-flange corner regions, redistributing the stresses to the central web wall region resulting in stresses of $-35\,MPa$ to $-40\,MPa$ at load level $5.80\,Q_Y$. These compressive concrete S_{yy} stresses are larger than the ultimate concrete compressive strength ($-30\,MPa$) indicating that the three-dimensional core-slab structure response creates biaxial effects on the concrete at the corners and joint regions of the cores, the E-S-slabs, and the coupling and lintel beams. Along the Stair section flange walls, a series of linear compressive stress peaks are noted with maximum values at the flange-web corner regions increasing to $-40\,MPa$ at load level $5.00\,Q_Y$. The flange wall ends show a peaked tensile stress distribution beyond load level $3.00\,Q_Y$ and cracking of the outer core wall element layers occurring at a load of $4.50\,Q_Y$ giving concrete S_{yy} stresses of $> 5\,MPa$ at $5.80\,Q_Y$.

At the failure load of $5.90\,Q_Y$, very irregular concrete S_{yy} stress distributions are observed in the core sections. Collapse of the structure occurs at a load of $6.00\,Q_Y$ where very large and irregularly distributed compressive and tensile concrete S_{yy} stresses are obtained in the core sections exceeding values of $-50\,MPa$ and $5\,MPa$ which are mathematical representations at collapse of the core-slab structure.

Core section concrete S_{yy} stress distribution at failure load in Fig. 6.58, shows an irregular tensile parabolic profile composed of several peaks and valleys across the web wall with values of $4.50\,MPa$ at the web wall center increasing to $> 5\,MPa$ at the web-flange corner regions. Across the flange walls, one-half of the wall toward the corner experiences tensile stresses $> 5\,MPa$, decreasing sharply and reversing to compressive stresses of $-4\,MPa$ at the flange wall mid-length, then a double stress reversal occurs from tension to compression to $-4.50\,MPa$ at the flange wall ends. These concrete S_{yy} stresses exceed the concrete tensile strength indicating that concrete has cracked through the entire concrete wall element thickness (all concrete layers) in the longitudinal direction, but not in the transverse direction for the concrete S_{xx} stresses and the wall element can resist further loading. At collapse, very large concentrated S_{yy} stress peaks are obtained at the Core flange-web corner locations representing mathematically the effect caused by the rupture of the Core concentrated reinforcement at the flange-web corner locations at the base region, resulting in splitting and separation of the slab-Core section across one-half of the flange wall and one-third of the web wall lengths noted by the near zero concrete S_{yy} stresses at the Core flange-web corners and mid-web wall region.

Elev section concrete S_{yy} stress distribution at failure load in Fig. 6.59, shows almost no stresses in the central web wall region near the stairwell opening and two large irregular compressive stress concentrations of $-35\,MPa$ with sharp gradients located at each web wall corner at the one-quarter length regions. Along the flange walls at the corners, compressive stresses of $-35\,MPa$ are observed but these reverse at the one-quarter flange wall length to very large tensile stresses of $> 5\,MPa$ over the remaining three-quarters end flange wall length. These tensile concrete S_{yy} stresses exceed the concrete tensile strength indicating that concrete has cracked through the entire concrete wall element thickness (all concrete layers) in the longitudinal direction, but not in the transverse direction for the concrete S_{xx} stresses and the wall element can resist further loading. At collapse, the Elev section concrete S_{yy} stresses are nonexistent in the web wall and the web-flange corner regions with a small stress peak at the web wall center region and steep tensile peaks across the flange walls, indicating that the Elev concentrated reinforcement at the flange wall ends has ruptured in tension, the concrete in the flange-web corner regions has crushed and the web wall has buckled as a result of instability of the Elev section in the lower 2 storeys.

Stair section concrete S_{yy} stress distribution at failure load in Fig. 6.60, illustrates an almost uniform compressive stress distribution across the web wall composed of several peaks and valleys with a maximum value of $-45\,MPa$ indicating that crushing of the concrete has occurred. Along the flange walls, tensile stresses of $5\,MPa$ are obtained showing an irregular peaked profile indicating concrete cracking. At collapse, the concrete S_{yy} stress distribution shows a series of compressive sharp peaks and gaps across the web wall and several tensile stress reversals ranging from values of $-46\,MPa$ to $5\,MPa$ with almost no stresses present in the flange walls. This concrete S_{yy} stress distribution indicates that the Stair section fails due to the concrete crushing in the web wall and buckling of the web-flange corner regions and flange walls in the lower 2 storeys of the section.

6.3.2.3 Shear Stresses S_{xy}

After the cracking of the concrete elements in the Core section web wall at load level $2.00\,Q_Y$, the concrete S_{xy} stresses in the core sections reduce to almost zero (less than $0.10\,MPa$) in the web walls with some concentrated stresses ($\pm 0.20\,MPa$) in the Core section web wall near the web-flange corner regions caused by the three-dimensional stiffening created by the interaction of the Core section and the E-S-slabs. In the flange walls, the S_{xy} stress distributions are a series of peaks in the Core and Elev sections of constant values of $\pm 1.32\,MPa$ and $\pm 1.63\,MPa$, respectively, while in the Stair section the stresses increase from ± 0.65 at the flange wall ends to $\pm 1.40\,MPa$ at the flange-web corner regions. It is noted that the Core section concrete S_{xy} stresses vary from negative to positive from the left to the right flange walls, while in the Elev and Stair sections the stresses vary from positive to negative. Thus, after the Region 1 limit of the response when initial concrete cracking occurs, the core sections web wall shear stiffness is reduced significantly and the flange walls resist the majority of the concrete S_{xy} stresses.

Within the nonlinear Region 3 portion of the response between load levels $3.00\,Q_Y$ to $5.75\,Q_Y$, and the Region 4 extending upto load level $5.90\,Q_Y$, similar concrete S_{xy} stress distributions are observed in the core sections. Core section displays asymmetrical concrete S_{xy} stress distributions about the web wall center Fig. 6.61 at load level $3.50\,Q_Y$. Due to the redistribution of stresses after cracking of the concrete elements at the Region 2 limit at $3.00\,Q_Y$, one-third of the web wall corner regions accept stresses showing an almost constant value of $\pm 1.00\,MPa$; while along the flange walls the stresses peak at the wall end regions to $\pm 3.00\,MPa$ and reduce in a parabolic profile to $\pm 1.25\,MPa$ over two-thirds of the flange wall length end regions. As the earthquake loading increases to $5.75\,Q_Y$, very irregular shear stress distributions are noted with several reversals composed of peaks and gaps of maximum values $\pm 5\,MPa$ along the web walls and one-half of the flange wall lengths. Over one-half of the flange wall length end regions, the concrete S_{xy} stresses increase sharply to a large peak. Three distinct stress peaks are observed in the Core section in the higher load range upto $5.80\,Q_Y$ located at the flange wall end, the mid-length flange wall and at the flange-web corner regions with stresses of $-21\,MPa$ and $> 5\,MPa$. The Elev and Stair sections demonstrate similar asymmetrical concrete S_{xy} stress distributions about the web wall center as shown at load level $3.50\,Q_Y$ in Fig. 6.62 for the Elev section. As the earthquake load increases, the web walls show almost no shear stresses near the one-fifth length of the web-flange wall corner regions with a small peak stress of $\pm 5\,MPa$ at $5.80\,Q_Y$. This concrete S_{xy} stress distribution is due to the stiffer web-flange corner region and the presence of the Elev and Stair section openings not providing shear stiffness (restraint and confinement of the core sections) development in the web walls, compared to the Core section with the stiffening action of the E-S-slabs. Across the Elev and Stair sections flange walls, the concrete S_{xy} stresses illustrate very sharp peaks at the flange-web corner regions of values $-12\,MPa$ and $> 5\,MPa$ extending over the two-thirds flange-web corner lengths of the flange walls. Near the remainder one-third of the flange wall end length regions, a shear stress reversal occurs with a steep gradient peak to values of $-12\,MPa$ and $> 5\,MPa$ in Elev and $\pm 1.00\,MPa$ in Stair sections. These large concrete S_{xy} stress peaks are due to the three-dimensional stiffening and confinement due to the lintel and coupling beams, and the E-slabs.

At the failure load of $5.90\,Q_Y$, very irregular concrete S_{xy} stress distributions composed of several reversals, peaks and gaps are observed in the cores sections response.

Core section concrete S_{xy} stress distribution at failure load Fig. 6.63 and collapse are similar to the shear stress distributions obtained in the Region 3 response demonstrating very large distinctive sharp peaks with maximum stresses of $-23\,MPa$ and $> 5\,MPa$ at the flange-web corner regions extending over one-half of the flange wall and one-third of the web wall lengths. These concrete S_{xy} stress distributions correspond to the rupture of the concentrated reinforcement at the Core section flange-web corner regions and the tensile splitting and separation of the slab-Core web-flange corner regions at the ground level at failure. Almost zero shear stresses are obtained in the one-half of the flange wall and the one-third of the mid-web wall regions, indicating a complete loss of shear stiffness of the Core section at failure due to separation of the slab-Core flange-web wall junctions at the ground level.

Elev section concrete S_{xy} stress distribution at failure load Fig. 6.64, demonstrate large stress peaks of $-15\,MPa$ and $> 5\,MPa$ at the flange wall ends and the flange-web corner regions with a shear stress reversal occurring at the mid-length of the flange walls. At collapse, two S_{xy} stress peaks of $-25\,MPa$ and $> 5\,MPa$ each are located at the flange wall ends with almost no stresses in the web and flange-web corner regions corresponding to the rupture of the concentrated reinforcement at the Elev section flange wall ends and the crushing of the concrete leading to collapse of the web-flange corner regions in the lower 2 storeys.

Stair section concrete S_{xy} stress distribution at failure load Fig. 6.65, illustrates stress peaks of $\pm 9.00\,MPa$ over one-half of the length of the flange wall corner regions with smaller peaks at the flange-web corners ($\pm 3.00\,MPa$) and very small stresses at the flange wall ends. At collapse, very steep concrete S_{xy} stress peaks of $-20\,MPa$ and $> 5\,MPa$ occur at the web wall corners extending over one-third of the web wall corner regions with almost no shear stresses in the flange walls, corresponding to the crushing of the concrete in the web-flange wall corner regions leading to collapse of the Stair section in the lower 2 storeys.

Table 6.1: Nonlinear Response Analysis Results: for Q_X Earthquake Loading – Design Models

Model Q_X Load	Region 1		Region 2		Region 3		Region 4 to Failure	Mode	Δ_{top}	Ductility Ratio $(\Delta_{ult}/\Delta_{Region\ 2})$
DQX	0 to	$0.60\,Q_X$	to	$2.00\,Q_X$	to	$3.30\,Q_X$	to	F at $3.40\,Q_X$	$871\,mm$	9.90
	$\Delta_{top} =$	$26\,mm$		$88\,mm$		$494\,mm$				
DQXO	0 to	$0.60\,Q_X$	to	$1.60\,Q_X$	to	$3.20\,Q_X$	to	LF at $3.30\,Q_X$	$853\,mm$	19.18
	$\Delta_{top} =$	$26\,mm$		$71\,mm$		$569\,mm$		F at $3.40\,Q_X$	$1362\,mm$	
DQXX	0 to	$0.60\,Q_X$	to	$2.00\,Q_X$	to	$2.90\,Q_X$	to	LF at $3.00\,Q_X$	$597\,mm$	15.42
	$\Delta_{top} =$	$25\,mm$		$89\,mm$		$310\,mm$		F at $3.10\,Q_X$	$1372\,mm$	
DLQX	0 to	$0.60\,Q_X$	to	$2.00\,Q_X$	to	$3.80\,Q_X$	to	F at $4.00\,Q_X$	$1291\,mm$	14.67
	$\Delta_{top} =$	$26\,mm$		$88\,mm$		$505\,mm$				
DQXU	0 to	$0.50\,Q_X$	to	$1.75\,Q_X$	to	$3.00\,Q_X$	to	LF at $3.10\,Q_X$	$689\,mm$	8.95
	$\Delta_{top} =$	$24\,mm$		$77\,mm$		$437\,mm$		Collapse at $3.20\,Q_X$		

LF = Local failure – buckling of flange-web walls.

F = Failure of structure.

Table 6.2: Nonlinear Response Analysis Results: for Q_X Earthquake Loading Models

Model Q_X Load	Region 1		Region 2		Region 3		Region 4 to Failure		Mode	Δ_{top}	Ductility Ratio ($\Delta_{ult}/\Delta_{Region\ 2}$)
DQX	0	to	$0.60\,Q_X$	to	$2.00\,Q_X$	to	$3.30\,Q_X$	to	F at $3.40\,Q_X$	$871\,mm$	9.90
	Δ_{top} =		$26\,mm$		$88\,mm$		$494\,mm$				
ESDQX	0	to	$0.60\,Q_X$	to	$2.00\,Q_X$	to	$3.30\,Q_X$	to	LF at $3.40\,Q_X$	$1326\,mm$	15.07
	Δ_{top} =		$24\,mm$		$88\,mm$		$514\,mm$		Collapse at $3.50\,Q_X$		
CCDQX	0	to	$0.50\,Q_X$	to	$1.75\,Q_X$	to	$3.10\,Q_X$	to	F at $3.20\,Q_X$	$1113\,mm$	14.45
	Δ_{top} =		$24\,mm$		$77\,mm$		$554\,mm$				
QX	0	to	$0.40\,Q_X$	to	$1.10\,Q_X$	to	$1.60\,Q_X$	to	LF at $1.70\,Q_X$	$711\,mm$	14.22
	Δ_{top} =		$14\,mm$		$50\,mm$		$302\,mm$		Collapse at $1.75\,Q_X$		
PDQX											
Core	0	to	$0.25\,Q_X$	to	$0.75\,Q_X$		None		F at $1.20\,Q_X$	$560\,mm$	4.59
	Δ_{top} =		$33\,mm$		$122\,mm$				Collapse at $1.25\,Q_X$		
Elev	0	to	–	to	$0.75\,Q_X$		None		$1.25\,Q_X$	$470\,mm$	4.52
	Δ_{top} =		–		$104\,mm$				Did Not Fail		
Stair	0	to	–	to	$1.10\,Q_X$		None		$1.25\,Q_X$	$136\,mm$	1.11
	Δ_{top} =		–		$108\,mm$				Did Not Fail		

Table 6.3: Nonlinear Response Analysis Results: for Q_Y Earthquake Loading Models

Model Q_Y Load	Region 1	Region 2	Region 3	Region 4 to Failure Mode	Δ_{top}	Ductility Ratio $(\Delta_{ult}/\Delta_{Region\ 2})$
DQY	0 to $0.60\,Q_Y$	to $2.00\,Q_Y$	to $5.75\,Q_Y$	to F at $5.90\,Q_Y$	$1190\,mm$	25.87
	$\Delta_{top} =$ $18\,mm$	$46\,mm$	$852\,mm$	Collapse at $6.00\,Q_Y$		
DQYR	0 to $0.60\,Q_Y$	to $2.00\,Q_Y$	to $4.90\,Q_Y$	to F at $5.10\,Q_Y$	$880\,mm$	17.25
	$\Delta_{top} =$ $18\,mm$	$51\,mm$	$328\,mm$			
CCDQY	0 to $0.40\,Q_Y$	to $1.75\,Q_Y$	to $4.60\,Q_Y$	to F at $4.70\,Q_Y$	$1749\,mm$	37.21
	$\Delta_{top} =$ $16\,mm$	$47\,mm$	$552\,mm$			
QY	0 to $0.30\,Q_Y$	to $1.40\,Q_Y$	to $2.80\,Q_Y$	to LF at $2.90\,Q_Y$	$2200\,mm$	64.71
	$\Delta_{top} =$ $12\,mm$	$34\,mm$	$469\,mm$	Collapse at $3.00\,Q_Y$		
PDQY	0 to $0.30\,Q_Y$	to $0.90\,Q_Y$	None	LF at $1.90\,Q_Y$	$302\,mm$	4.65
	$\Delta_{top} =$ $26\,mm$	$65\,mm$		Collapse at $2.00\,Q_Y$		

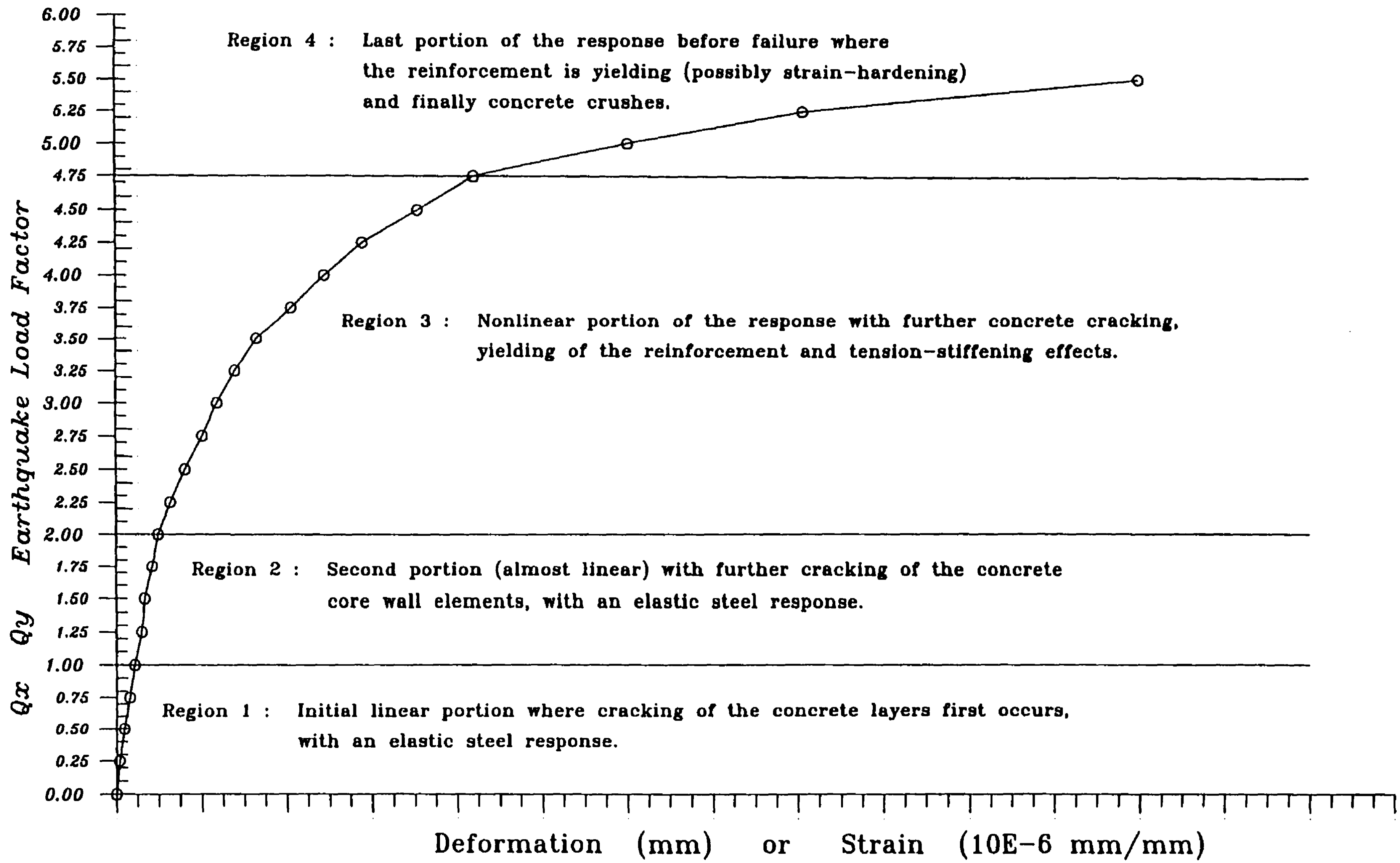

Figure 6.1 Definition of Deformational Behaviour Regions

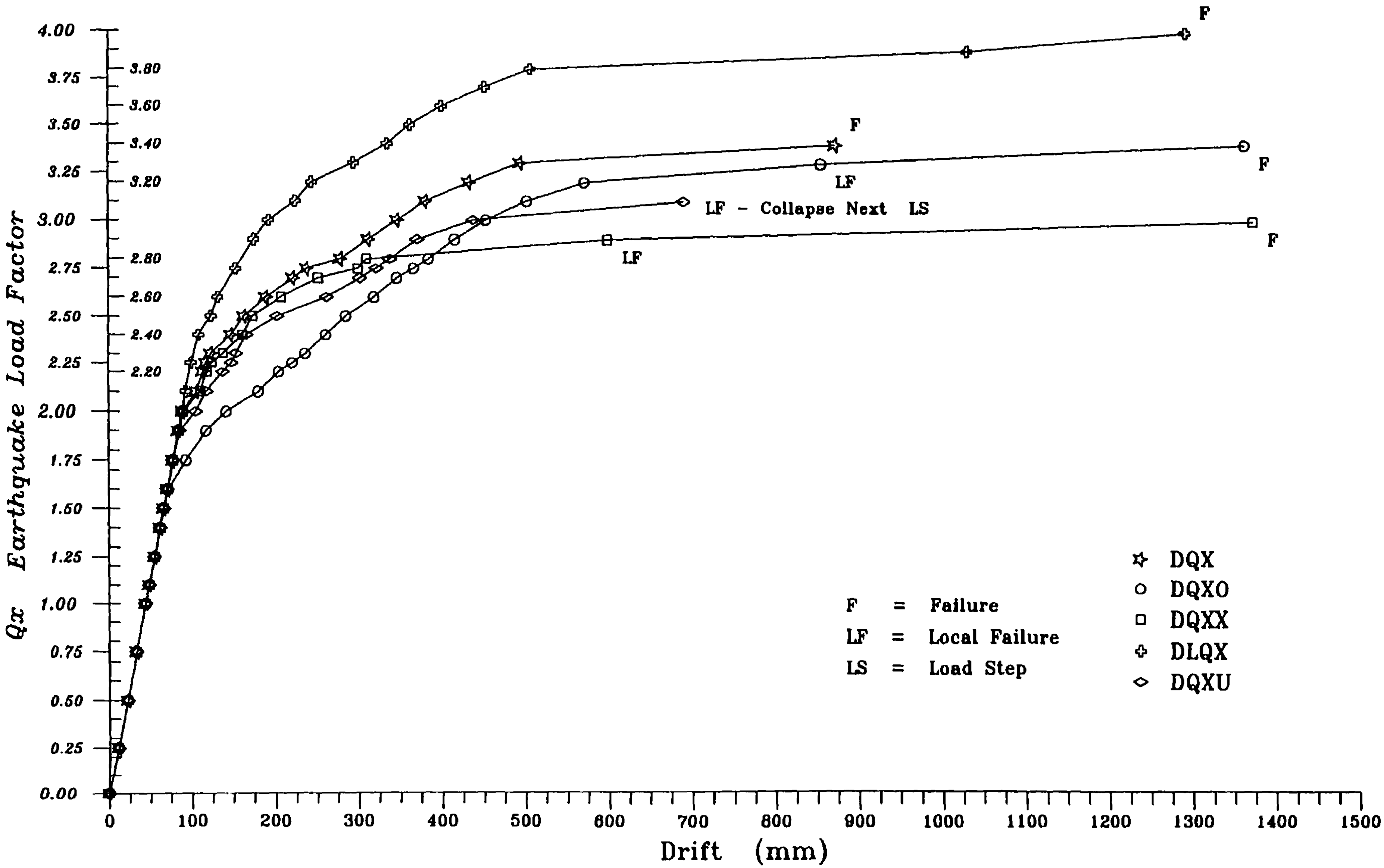

Figure 6.2 Q_X Earthquake Load vs Drift Response - Nonlinear Analyses Model Results - Material Properties and Design Considerations

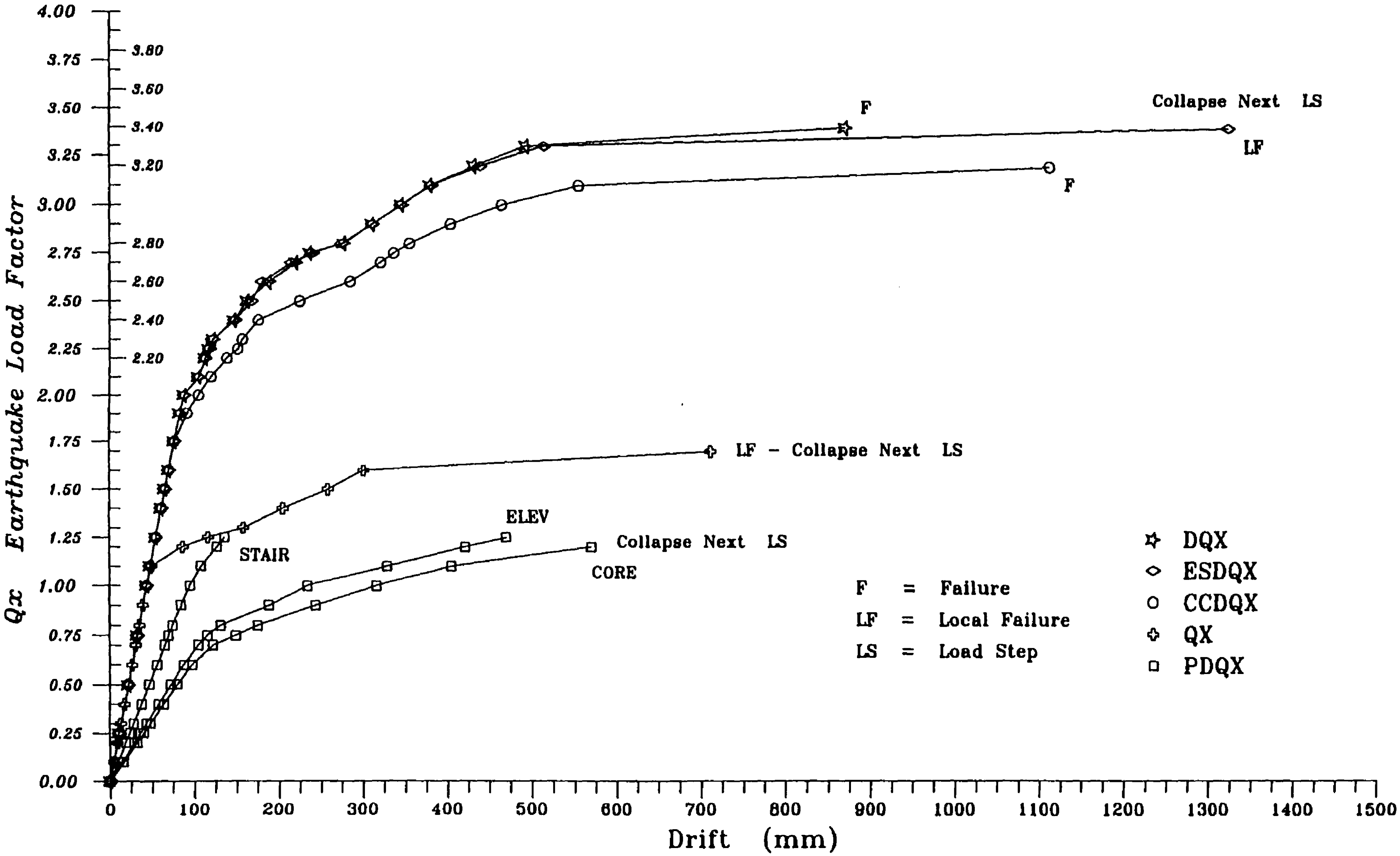

Figure 6.3 Q_X Earthquake Load vs Drift Response – Nonlinear Analyses Model Results

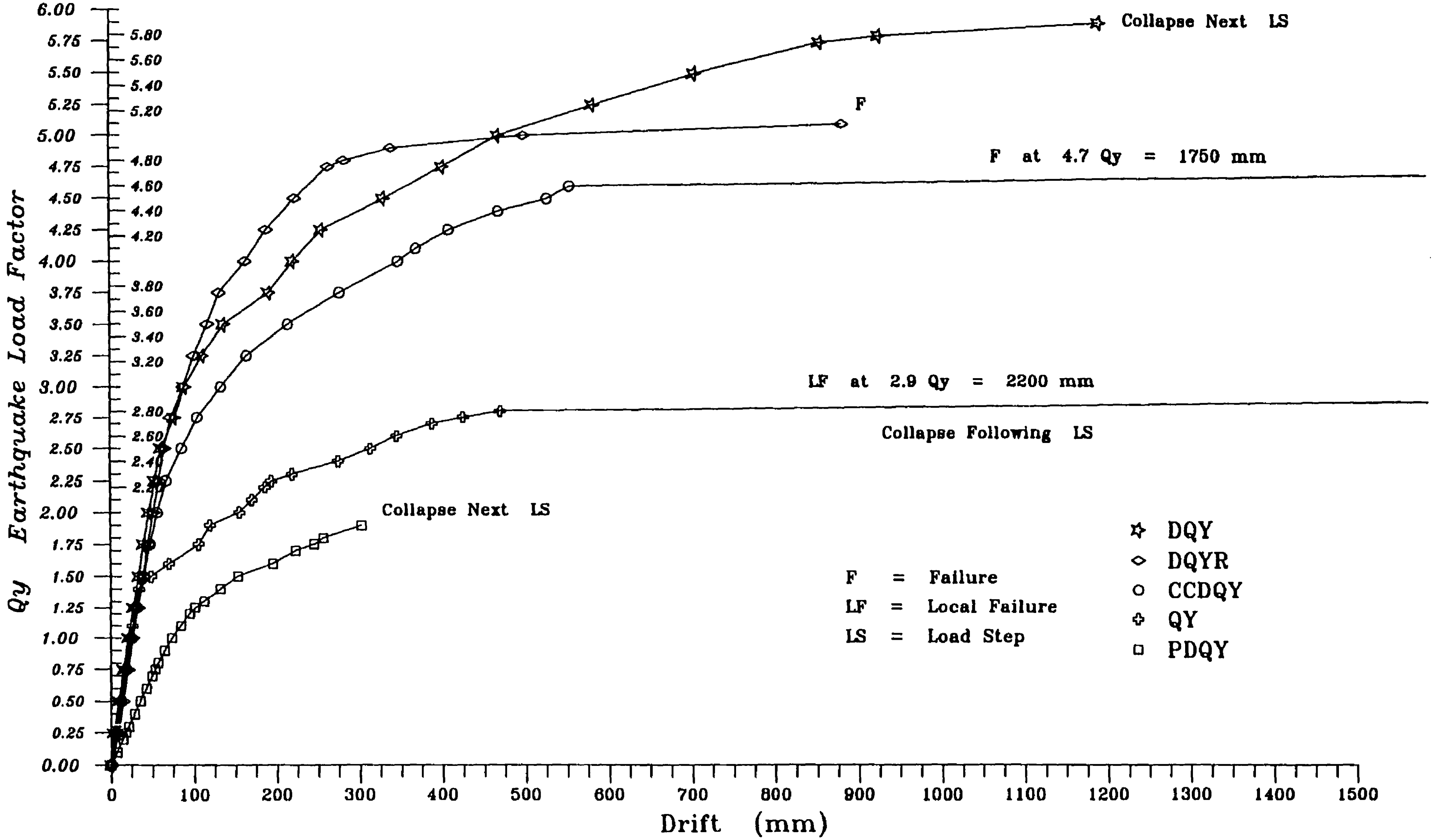

Figure 6.4 Q_Y Earthquake Load vs Drift Response – Nonlinear Analyses Model Results

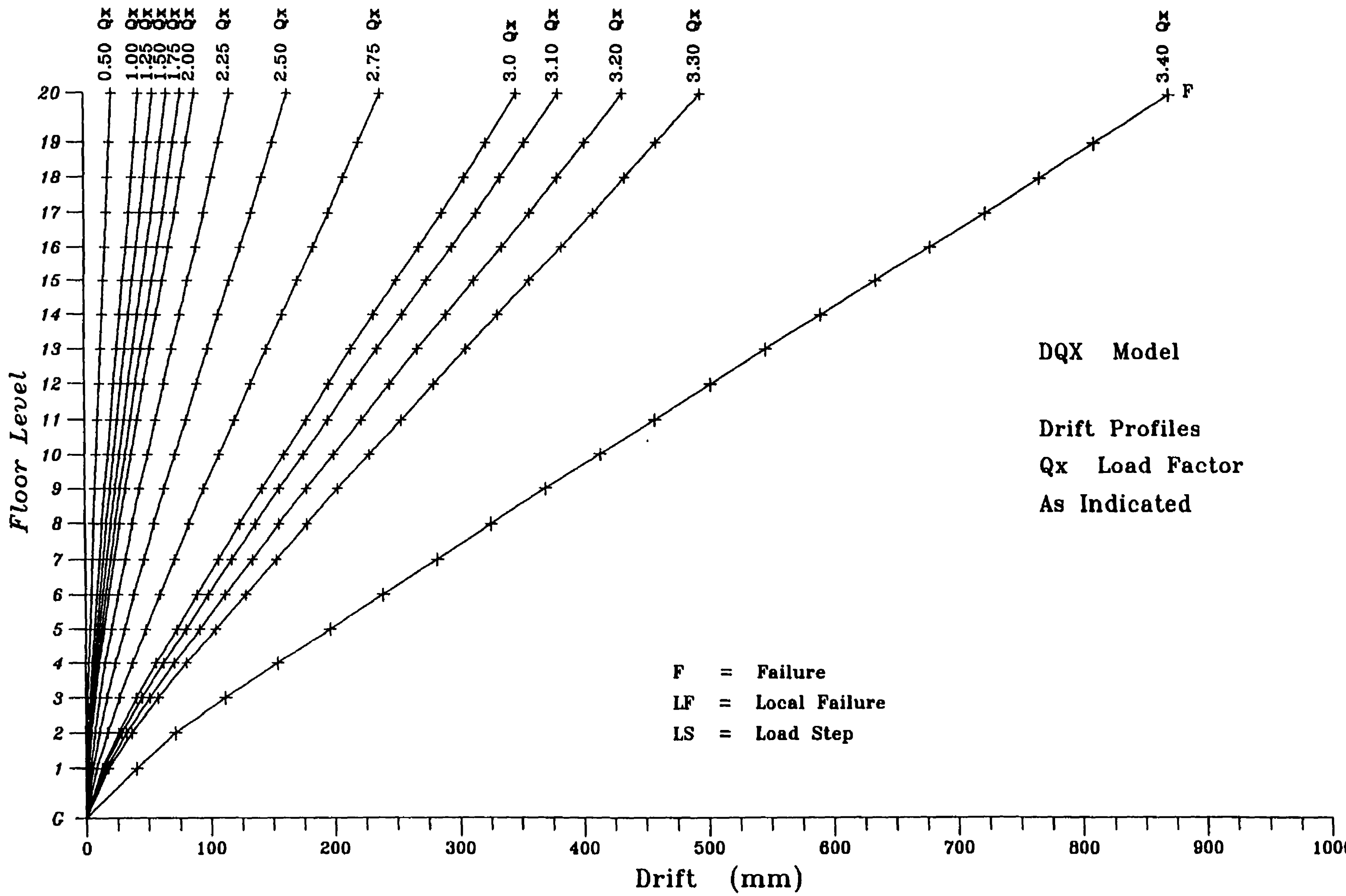

Figure 6.5 Drift Profiles at the Various Q_X Earthquake Load Levels – Nonlinear Analysis DQX Model Results

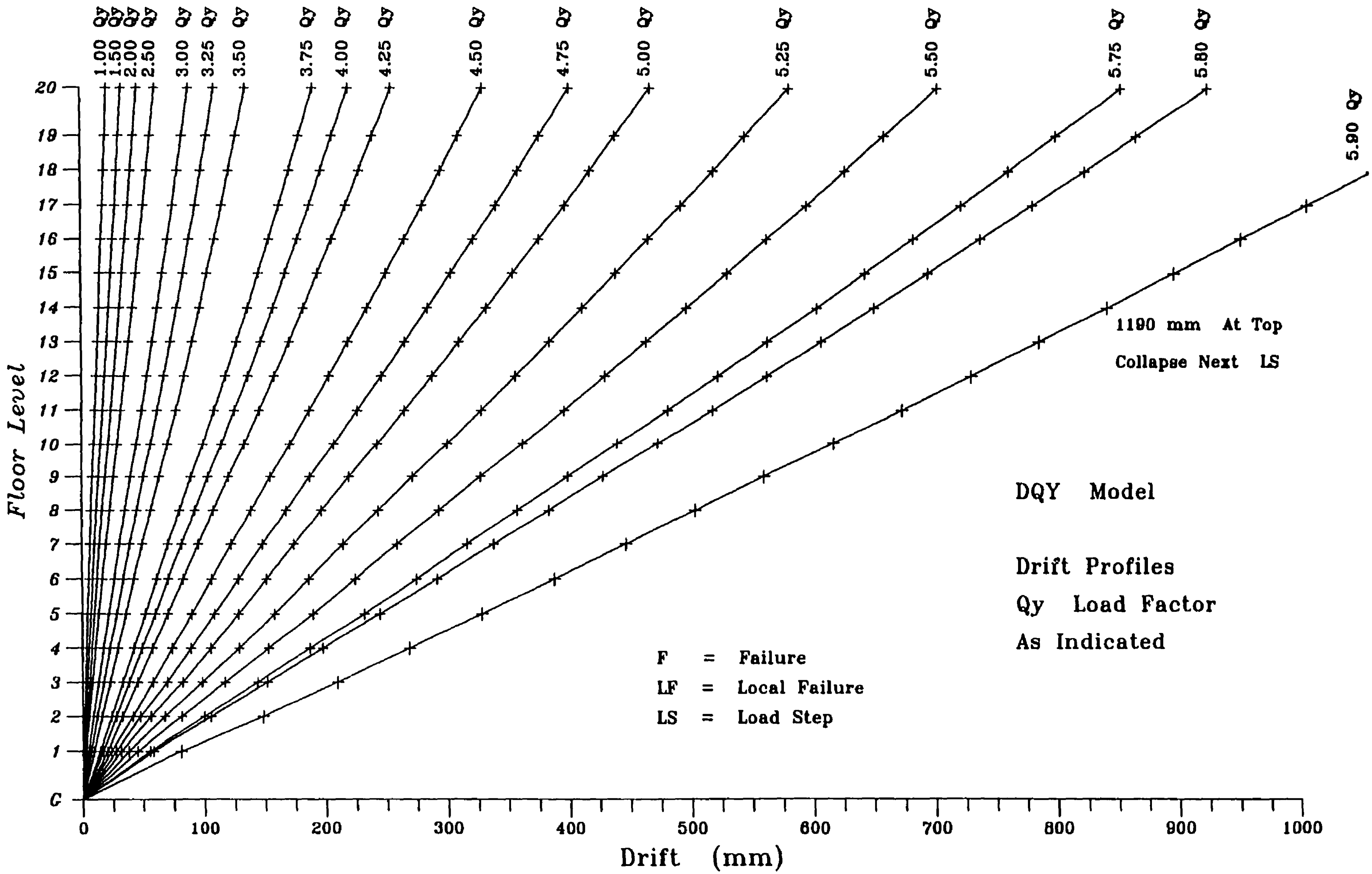

Figure 6.6 Drift Profiles at the Various Q_Y Earthquake Load Levels – Nonlinear Analysis DQY Model Results

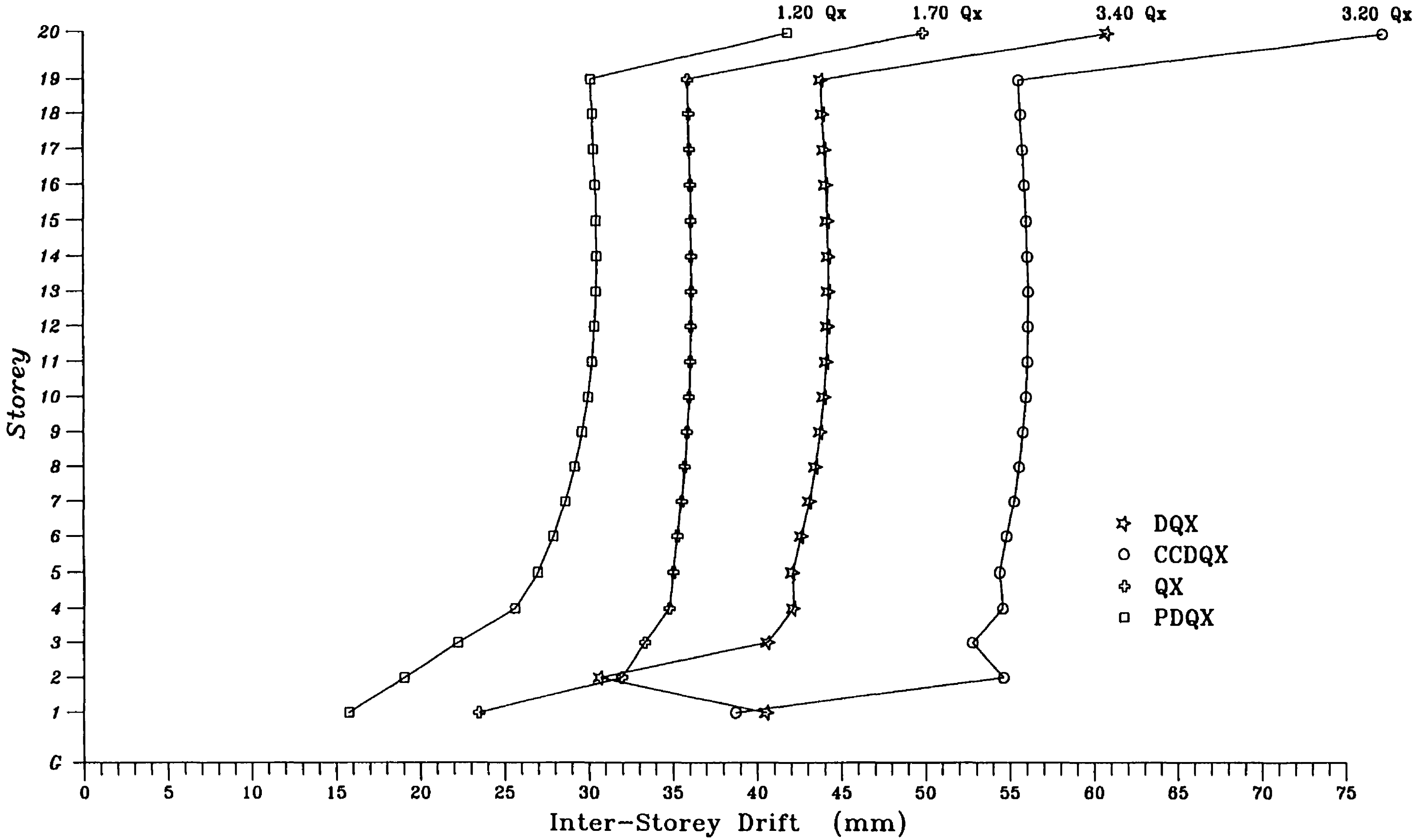

Figure 6.7 Inter-Storey Drift Profiles at the Failure Load - Q_X Earthquake Loading - Nonlinear Analyses Model Results

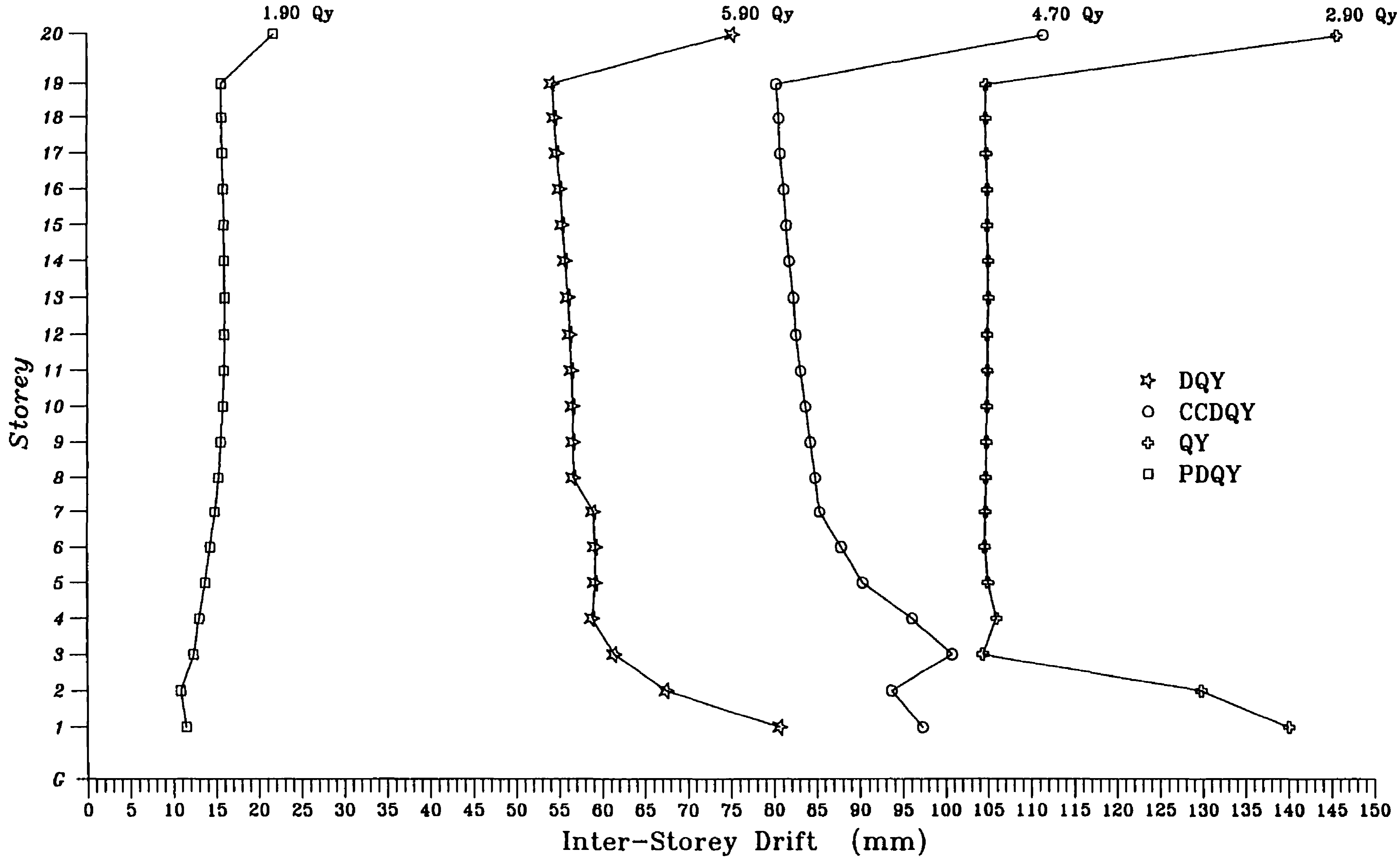

Figure 6.8 Inter-Storey Drift Profiles at the Failure Load – Q_Y Earthquake Loading – Nonlinear Analyses Model Results

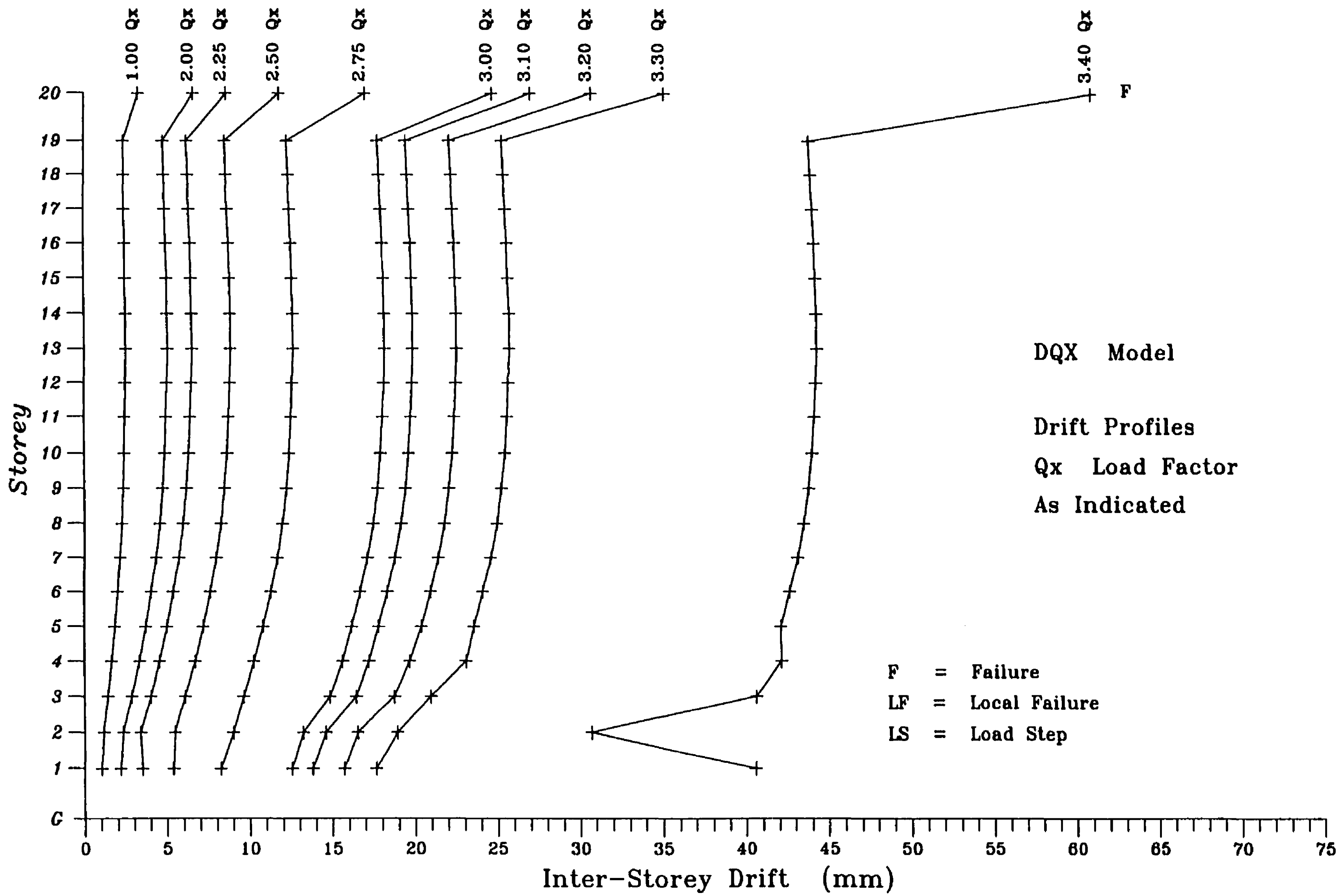

Figure 6.9 Inter-Storey Drift Profiles at the Various Q_X Earthquake Load Levels – Nonlinear Analysis DQX Model Results

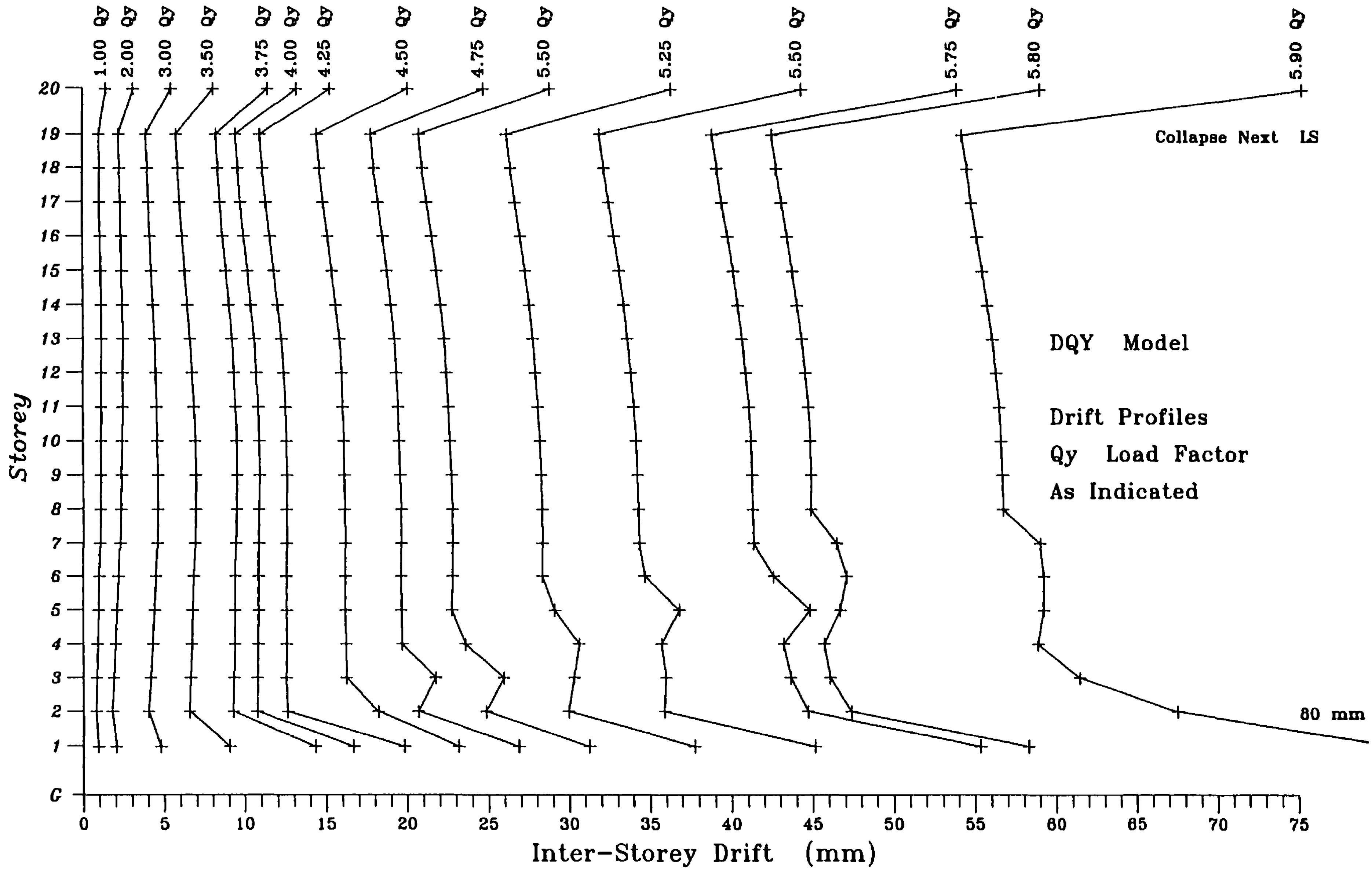

Figure 6.10 Inter-Storey Drift Profiles at the Various Q_Y Earthquake Load Levels – Nonlinear Analysis DQY Model Results

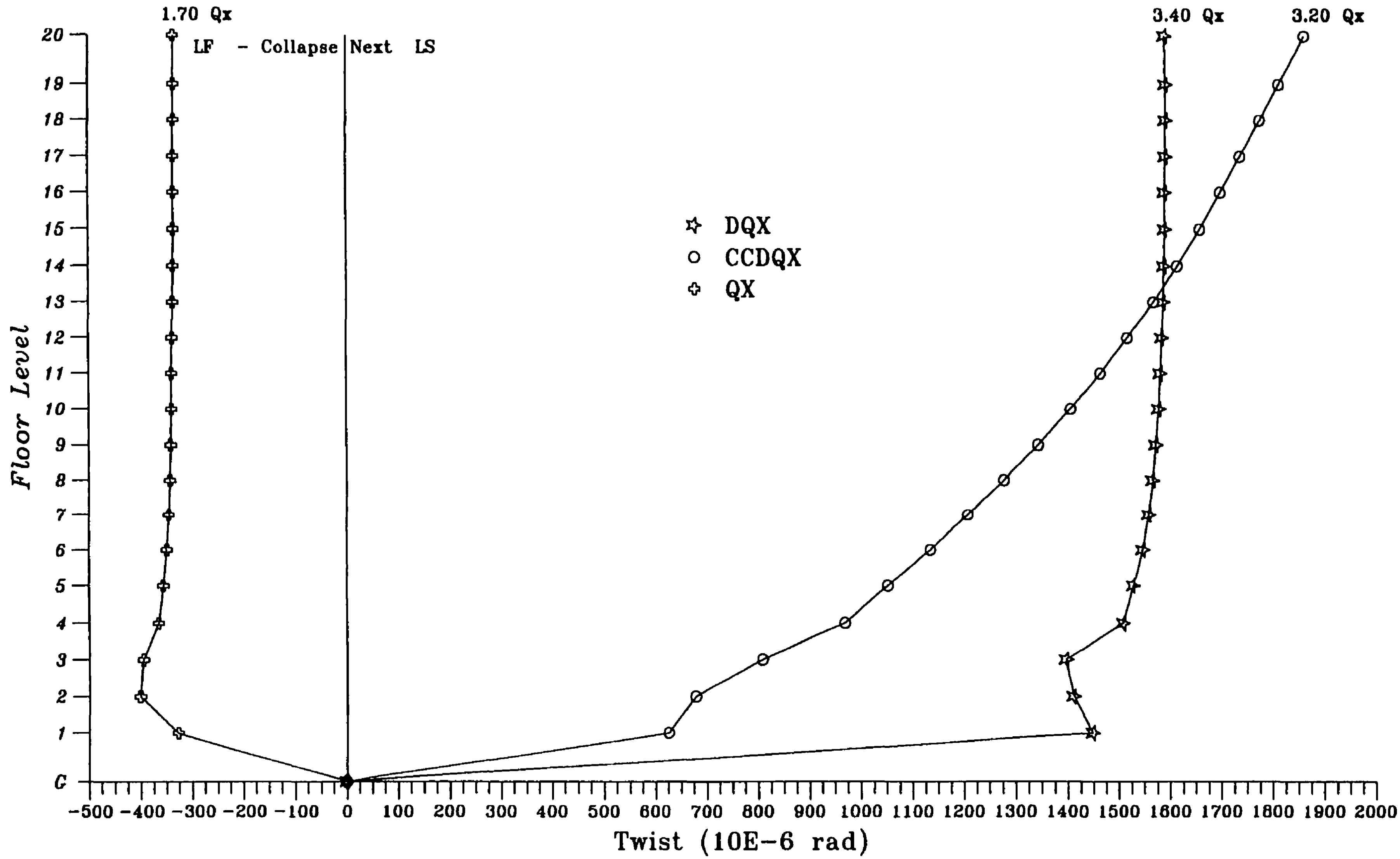

Figure 6.11 Twist Profiles at the Failure Load – Q_X Earthquake Loading – Nonlinear Analyses Model Results

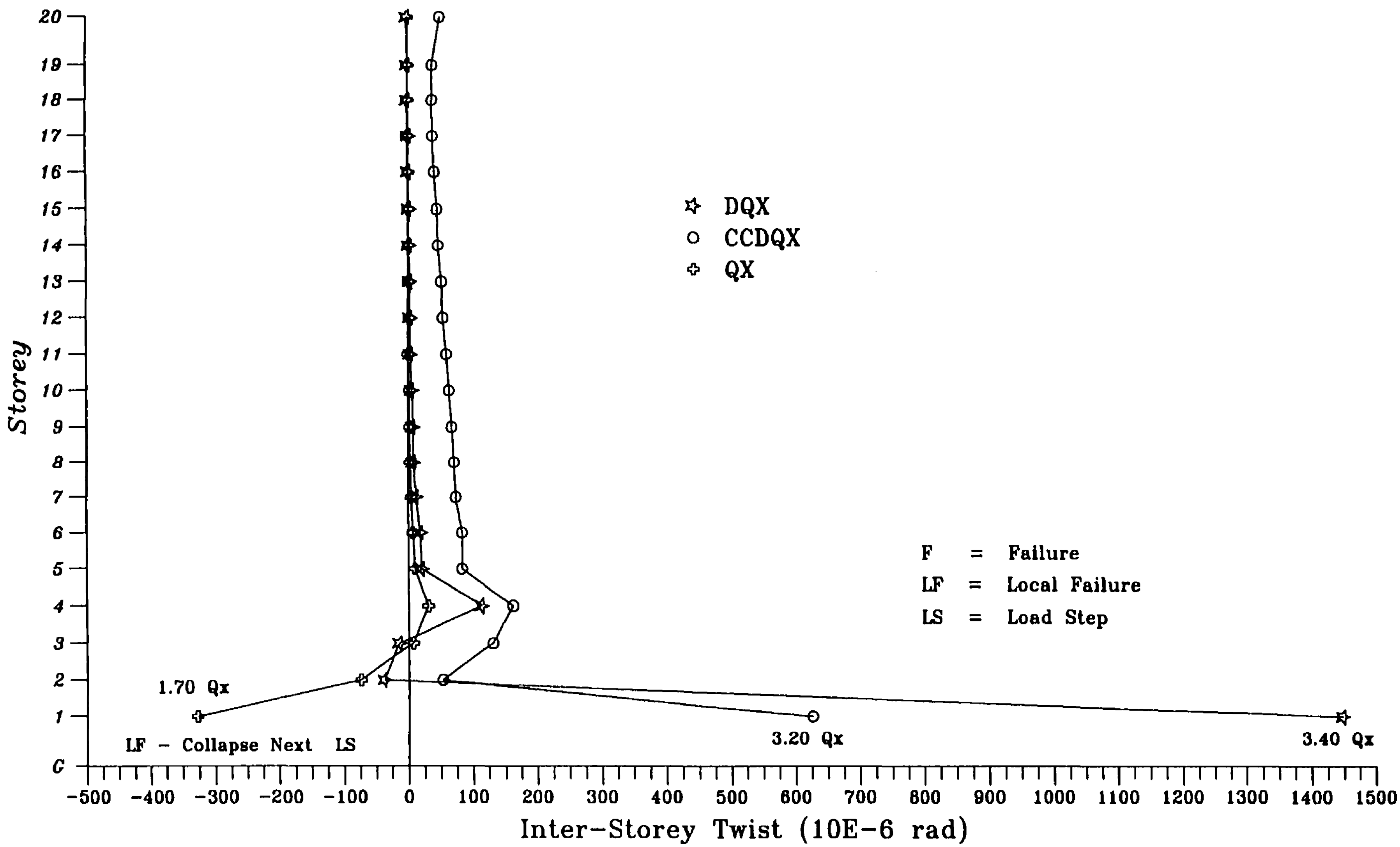

Figure 6.12 Inter-Storey Twist Profiles at the Failure Load – Q_X Earthquake Loading – Nonlinear Analyses Model Results

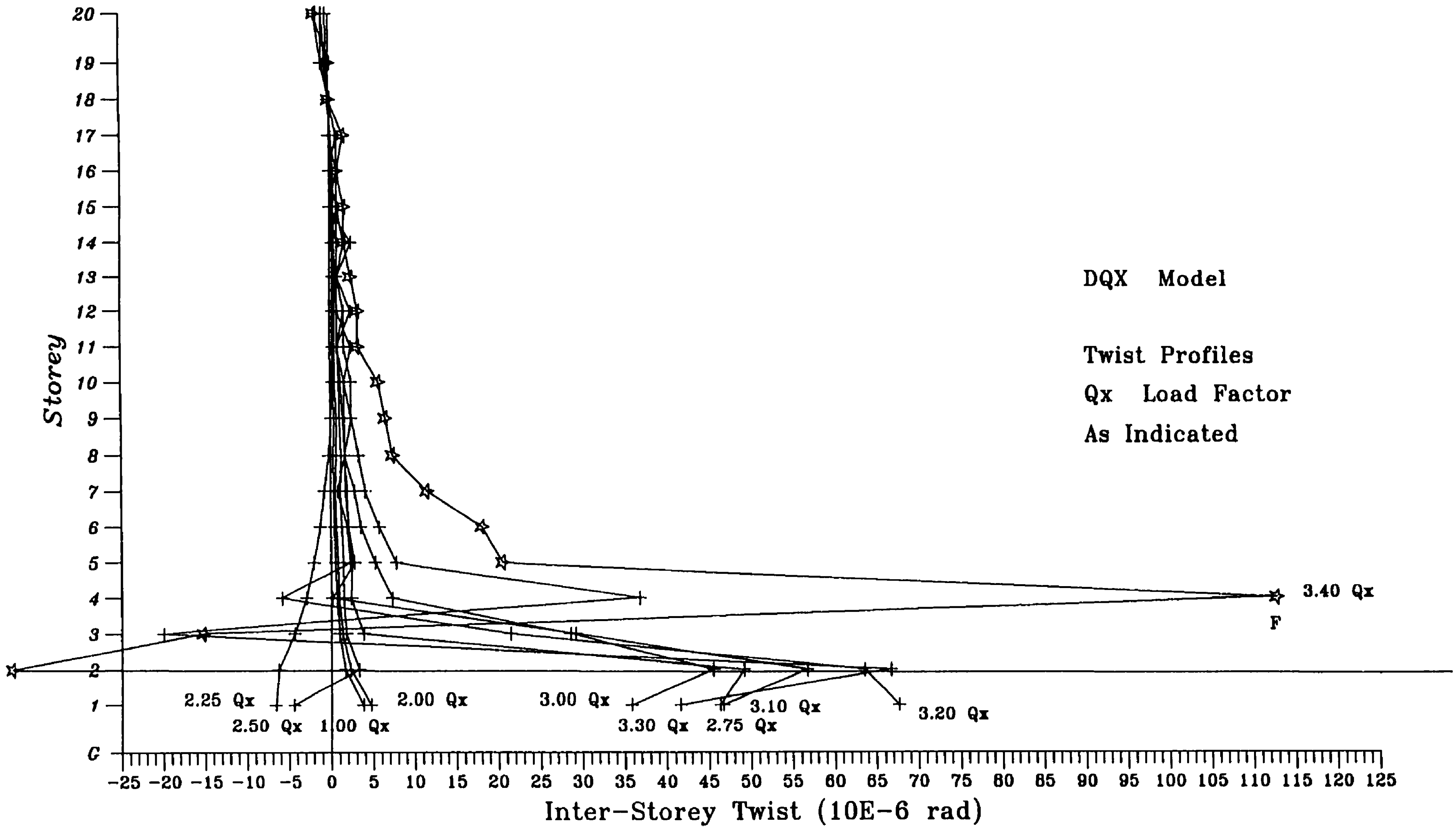

Figure 6.13 Inter-Storey Twist Profiles at the Various Q_X Earthquake Load Levels – Nonlinear Analysis DQX Model Results

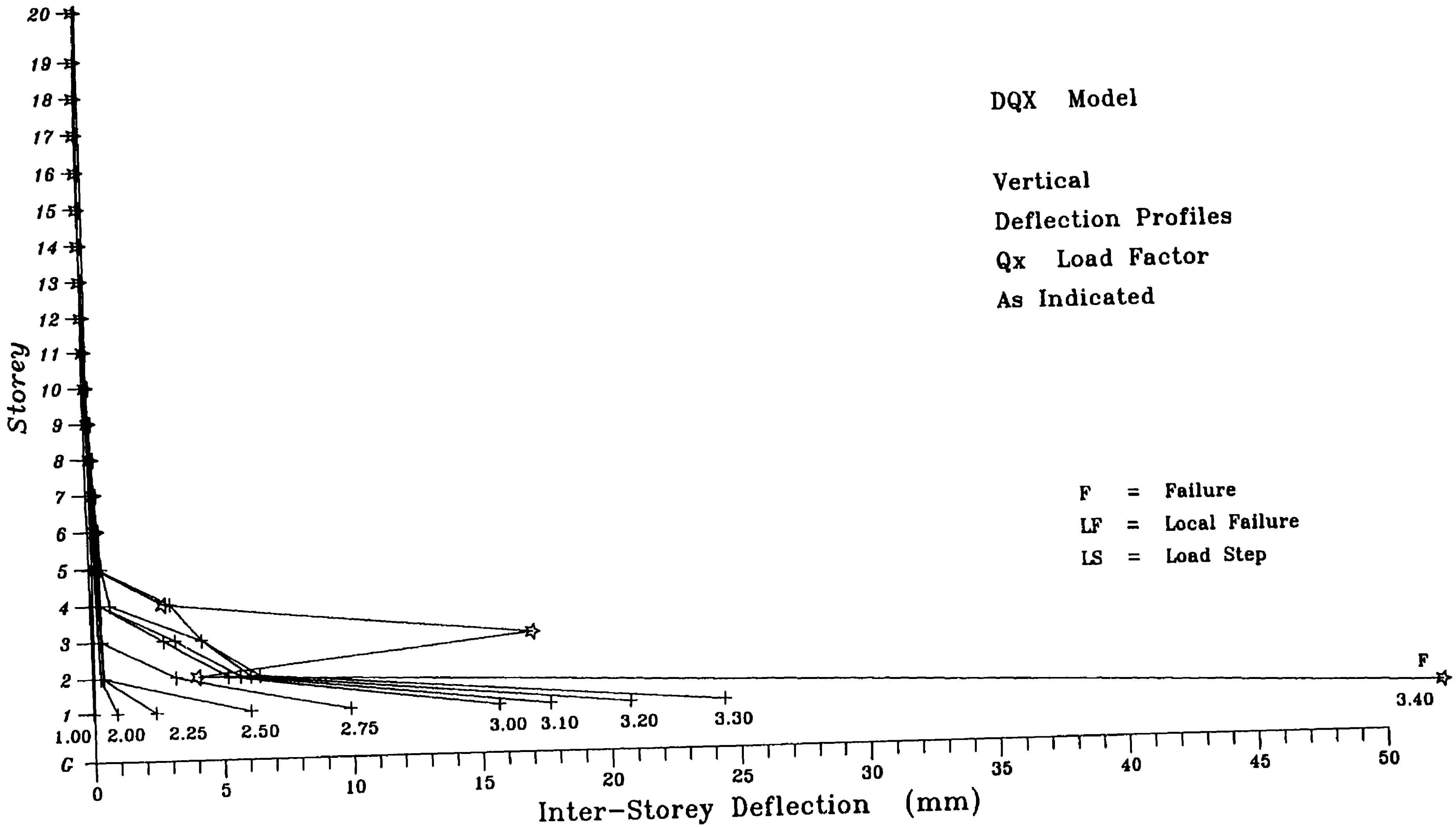

Figure 6.14 Inter-Storey Vertical Deflection Profiles of the Slab-Infilled-Slab Core Corner Along the Structure Height at the Various Q_X Earthquake Load Levels – Nonlinear Analysis DQX Model Results

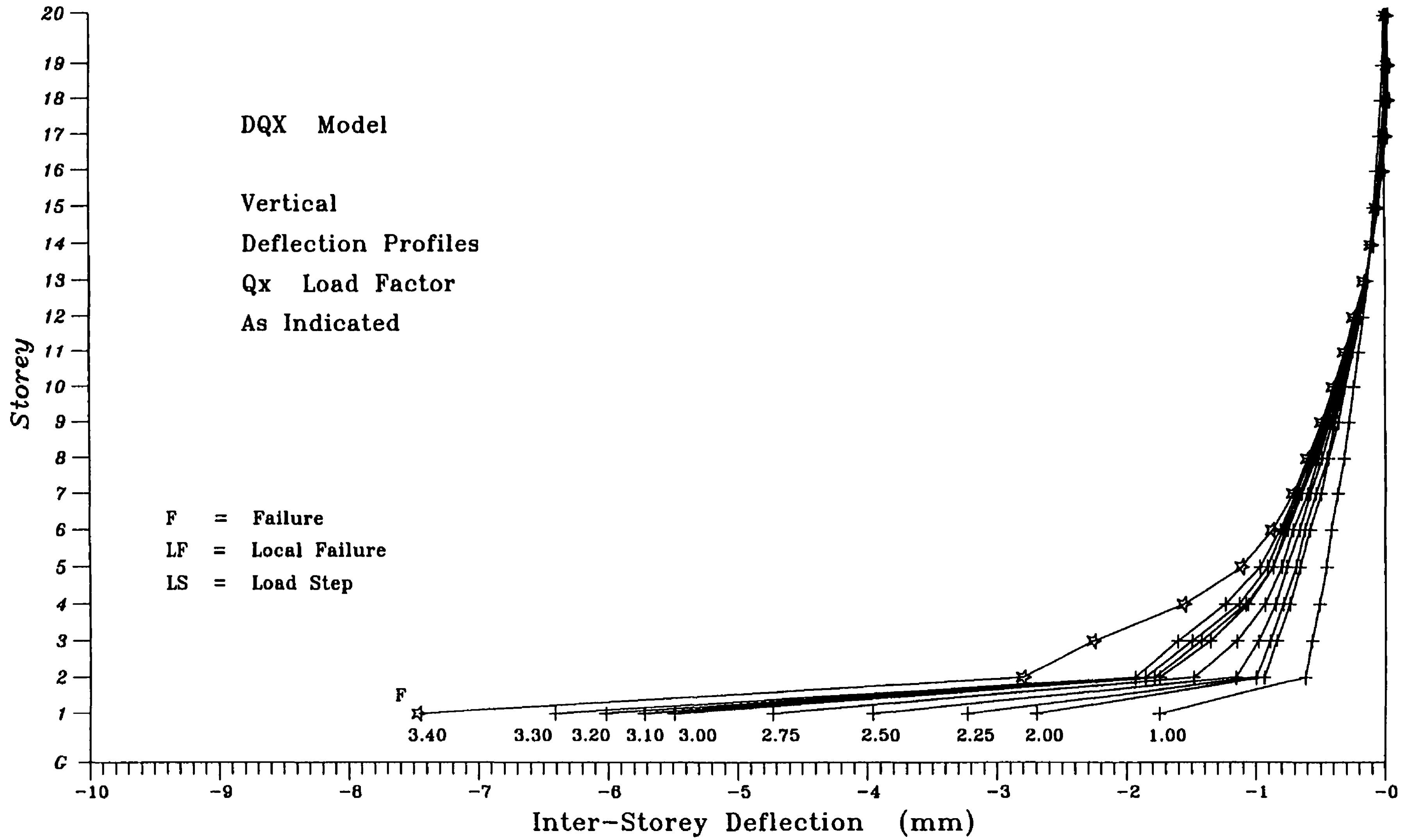

Figure 6.15 Inter-Storey Vertical Deflection Profiles of the Slab-Stairwell Core Corner Along the Structure Height at the Various Q_X Earthquake Load Levels – Nonlinear Analysis DQX Model Results

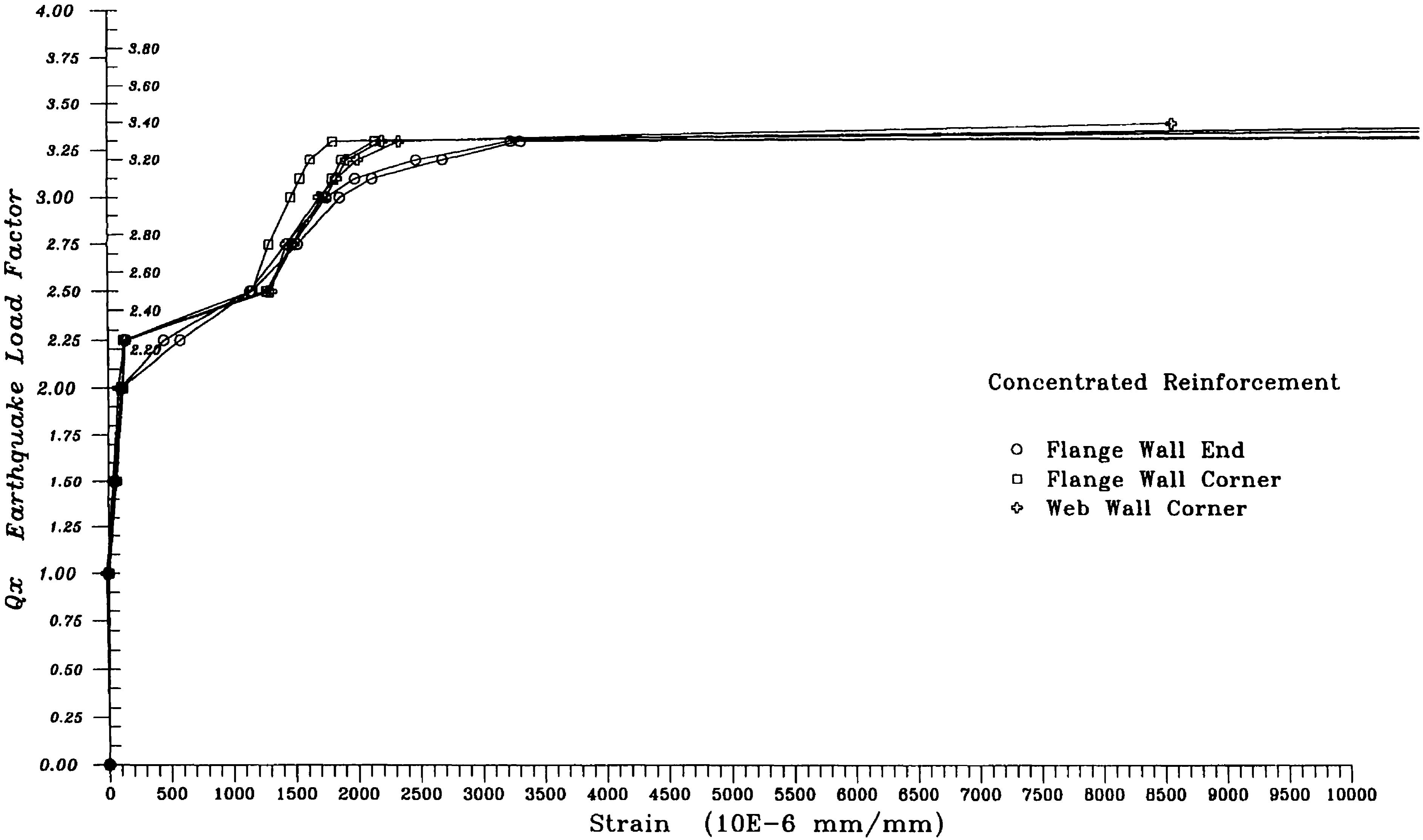

Figure 6.16 Concentrated Reinforcement Strain Response for Q_X Earthquake Loading – Tension (Left) Side of the Infilled-Slab Core Nonlinear Analysis DQX Model Results

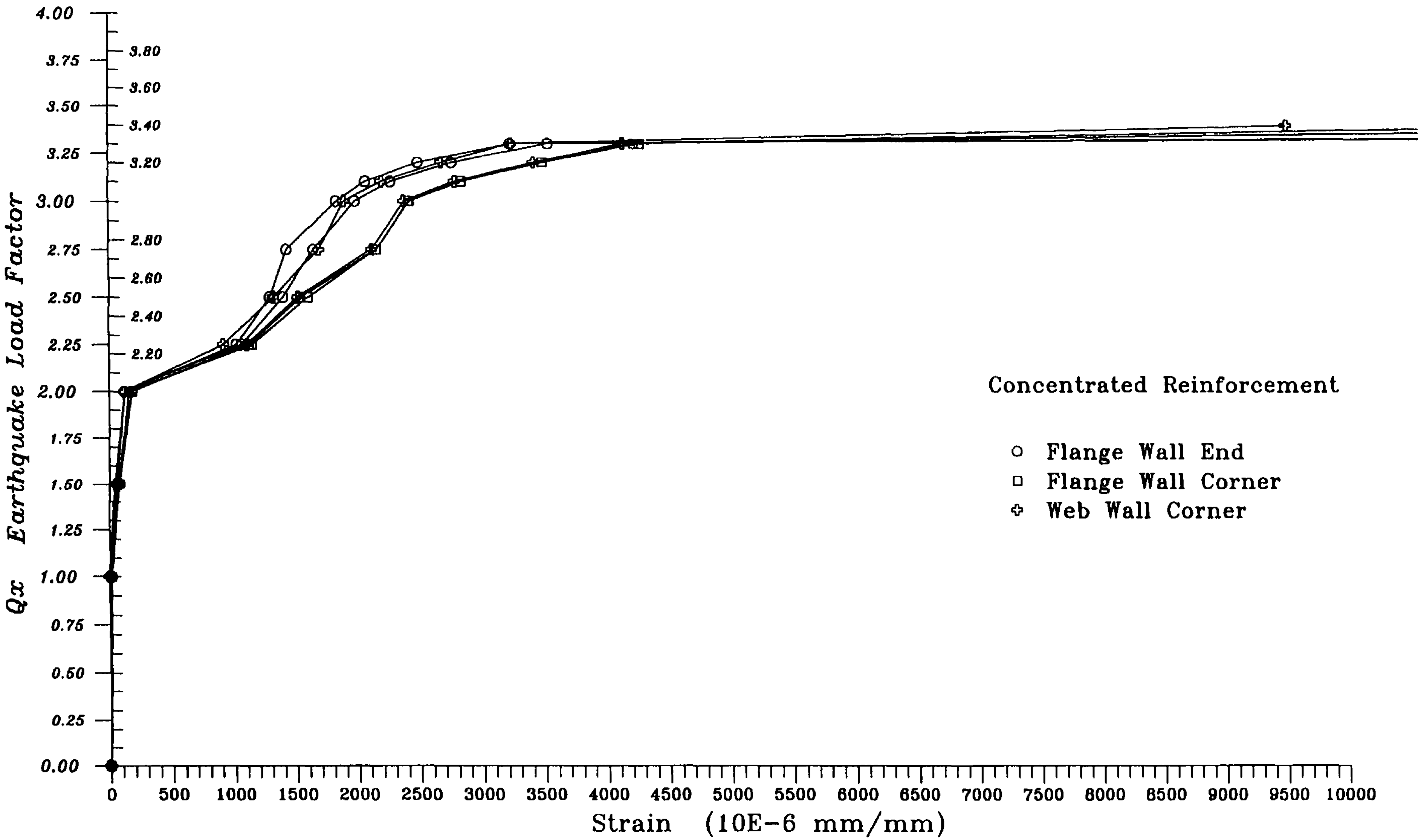

Figure 6.17 Concentrated Reinforcement Strain Response for Q_X Earthquake Loading - Tension (Left) Side of the Elevator Core Nonlinear Analysis DQX Model Results

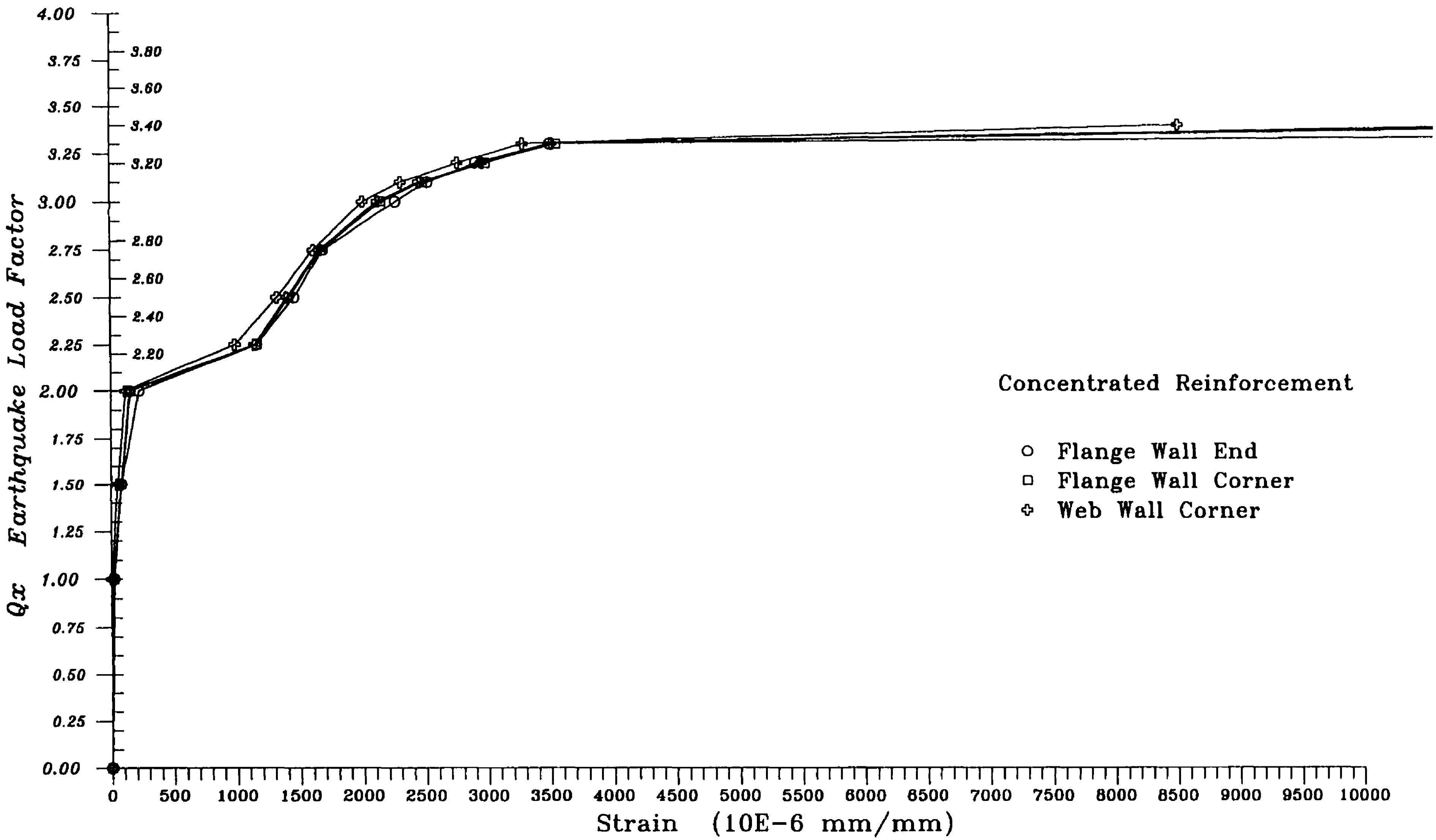

Figure 6.18 Concentrated Reinforcement Strain Response for Q_X Earthquake Loading – Tension (Left) Side of the Stairwell Core Nonlinear Analysis DQX Model Results

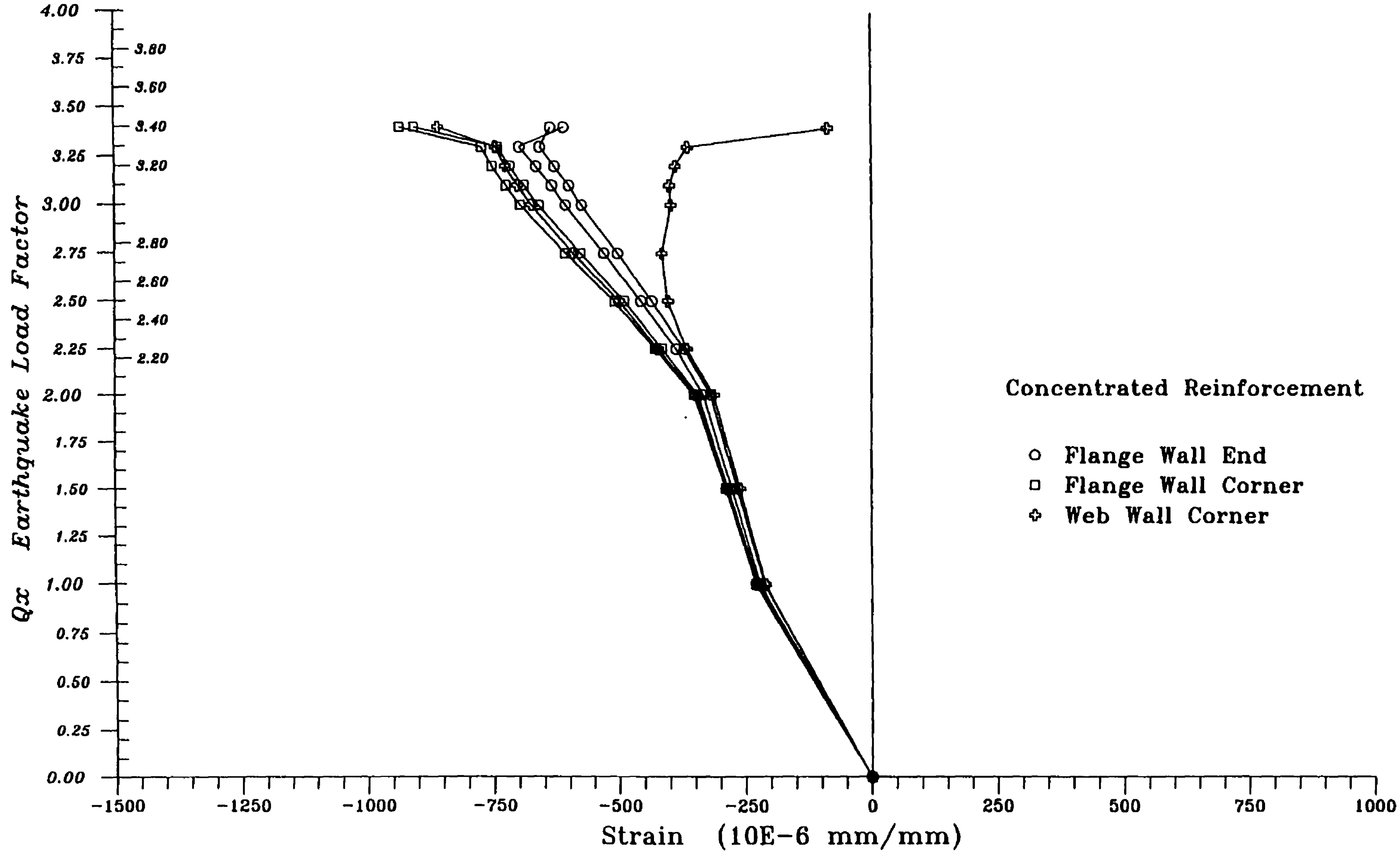

Figure 6.19 Concentrated Reinforcement Strain Response for Q_X Earthquake Loading – Compression (Right) Side of the Infilled-Slab Core – Nonlinear Analysis DQX Model Results

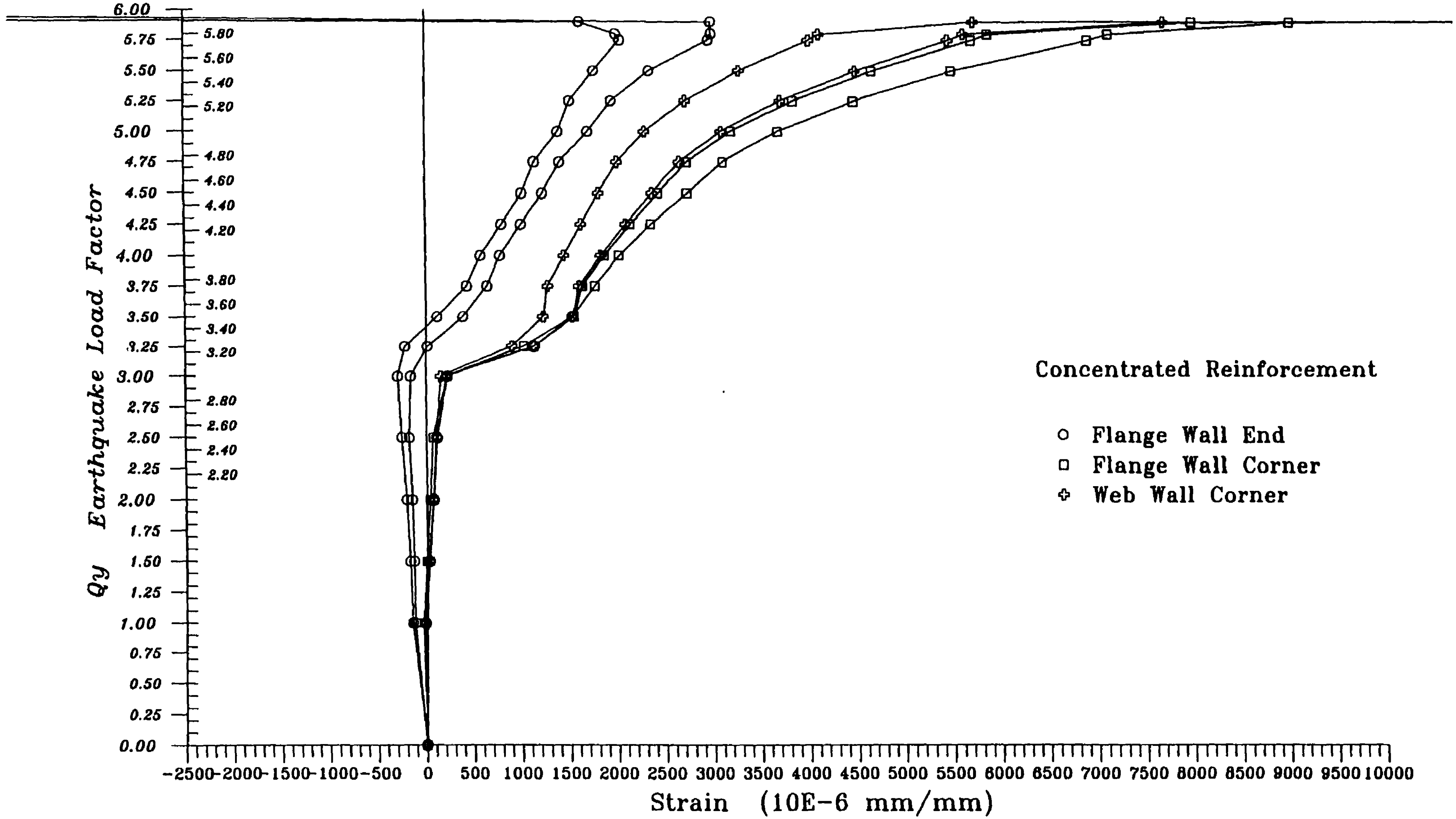

Figure 6.20 Concentrated Reinforcement Strain Response for Q_Y Earthquake Loading – For the Infilled-Slab Core – Nonlinear Analysis DQY Model Results

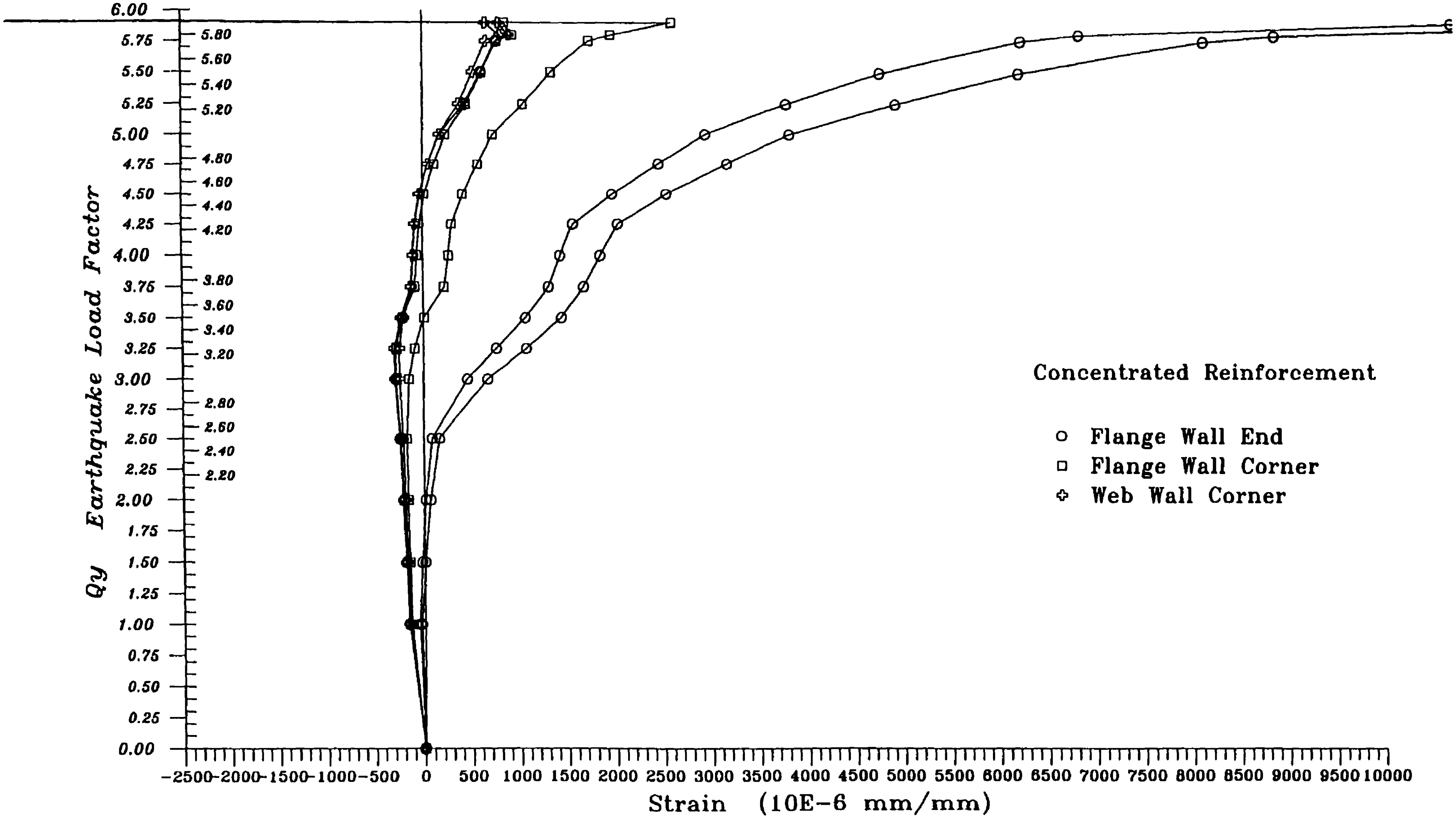

Figure 6.21 Concentrated Reinforcement Strain Response for Q_Y Earthquake Loading – For the Elevator Core – Nonlinear Analysis DQY Model Results

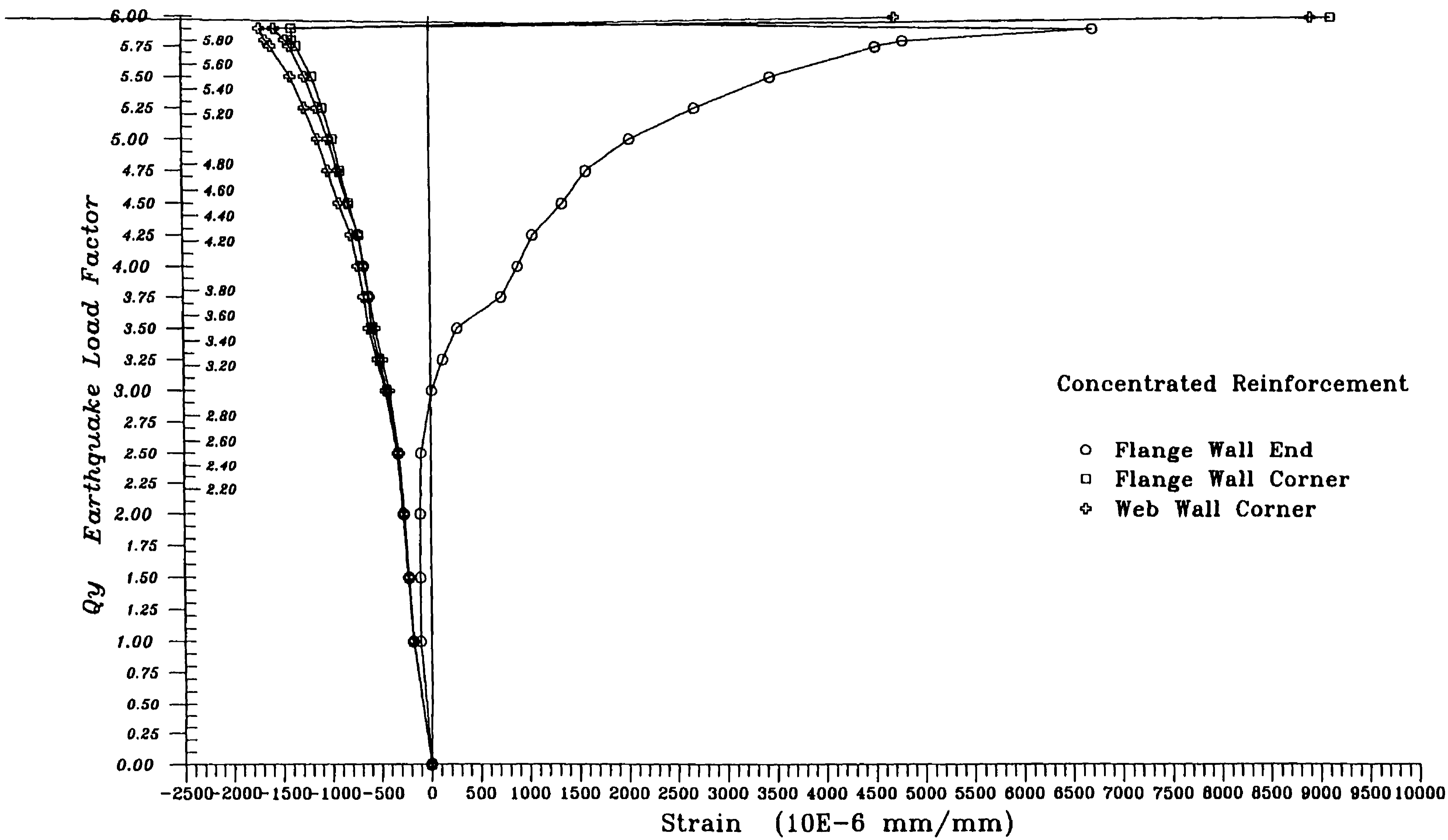

Figure 6.22 Concentrated Reinforcement Strain Response for Q_Y Earthquake Loading – For the Stairwell Core – Nonlinear Analysis DQY Model Results

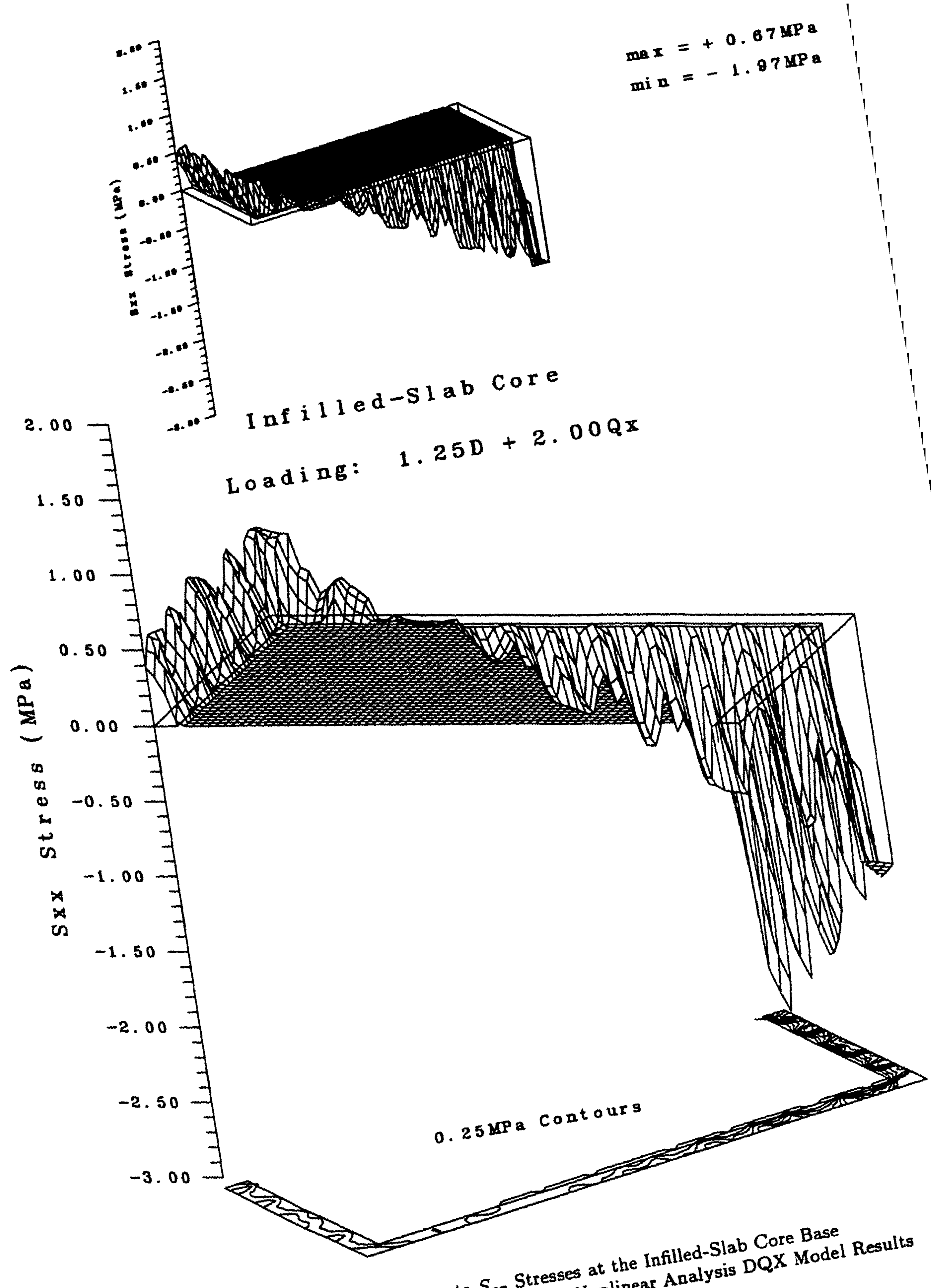

Figure 6.23 Distribution of the Concrete S_{xx} Stresses at the Infilled-Slab Core Base At Load Level $1.25\,D + 2.00\,Qx$ – Nonlinear Analysis DQX Model Results

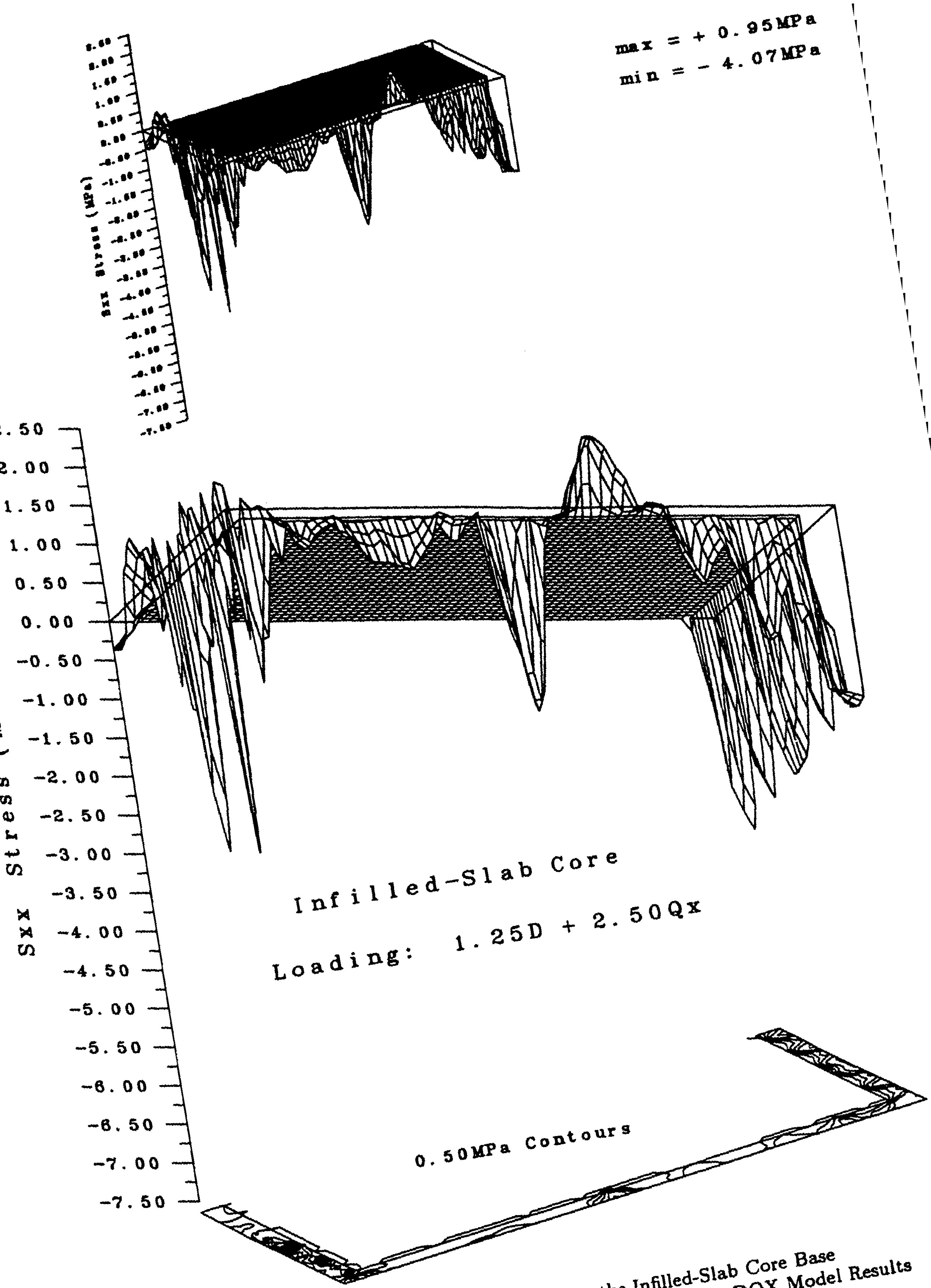

Figure 6.24 Distribution of the Concrete S_{xx} Stresses at the Infilled-Slab Core Base At Load Level $1.25\,D + 2.50Q\,x$ – Nonlinear Analysis DQX Model Results

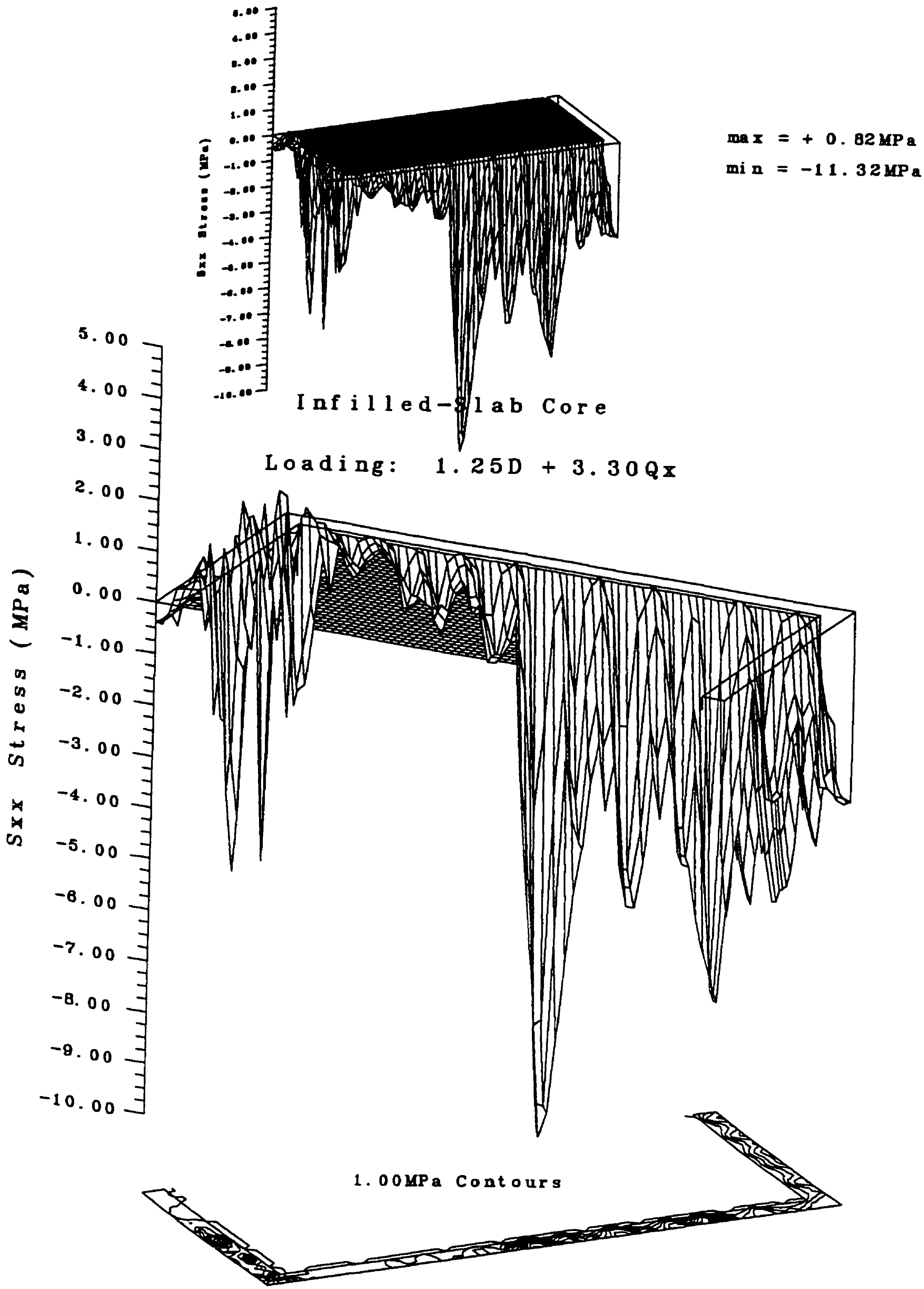

Figure 6.25 Distribution of the Concrete S_{xx} Stresses at the Infilled-Slab Core Base At Load Level $1.25\,D + 3.30\,Q_X$ – Nonlinear Analysis DQX Model Results

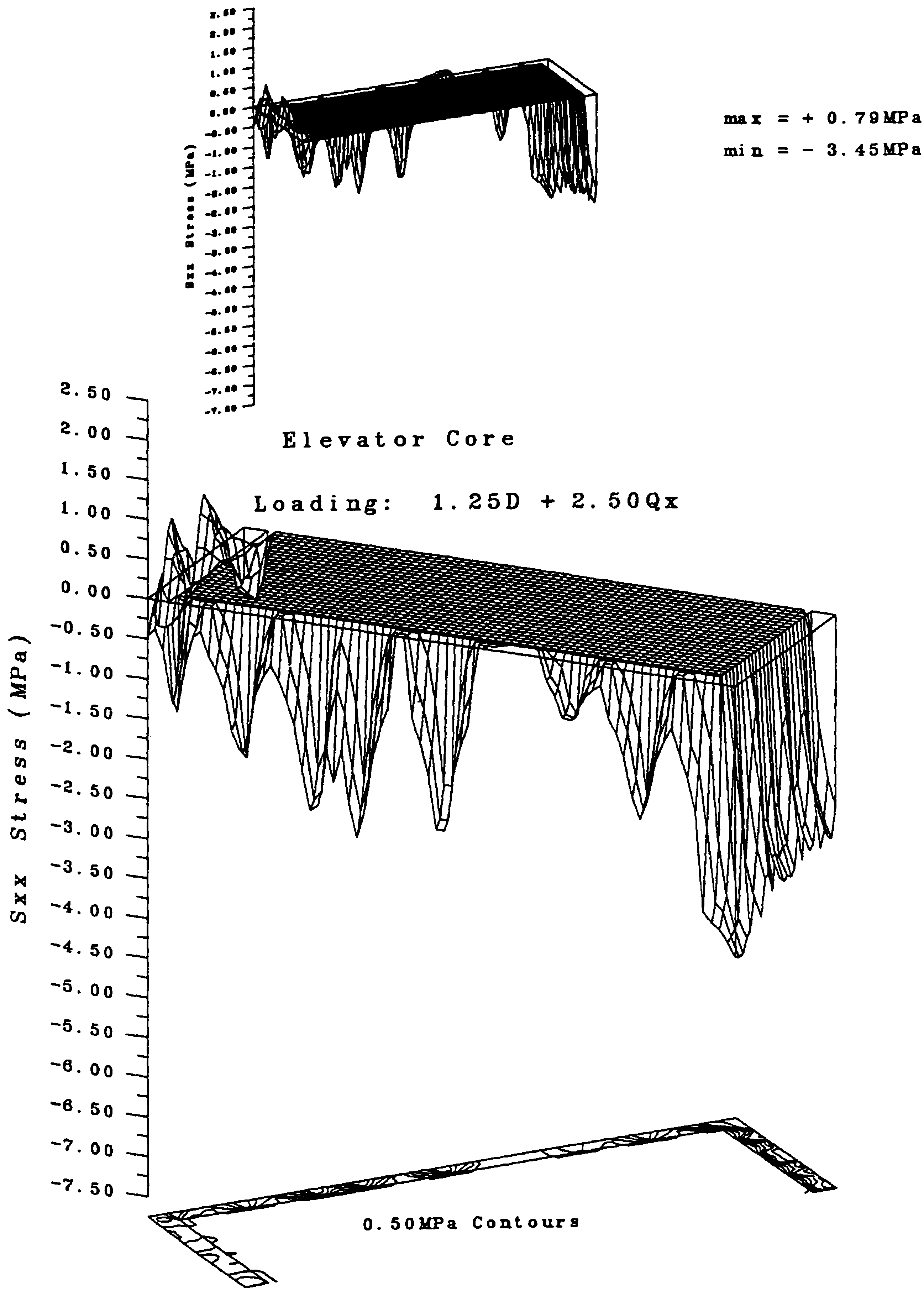

Figure 6.26 Distribution of the Concrete S_{xx} Stresses at the Elevator Core Base At Load Level $1.25\,D + 2.50\,Qx$ – Nonlinear Analysis DQX Model Results

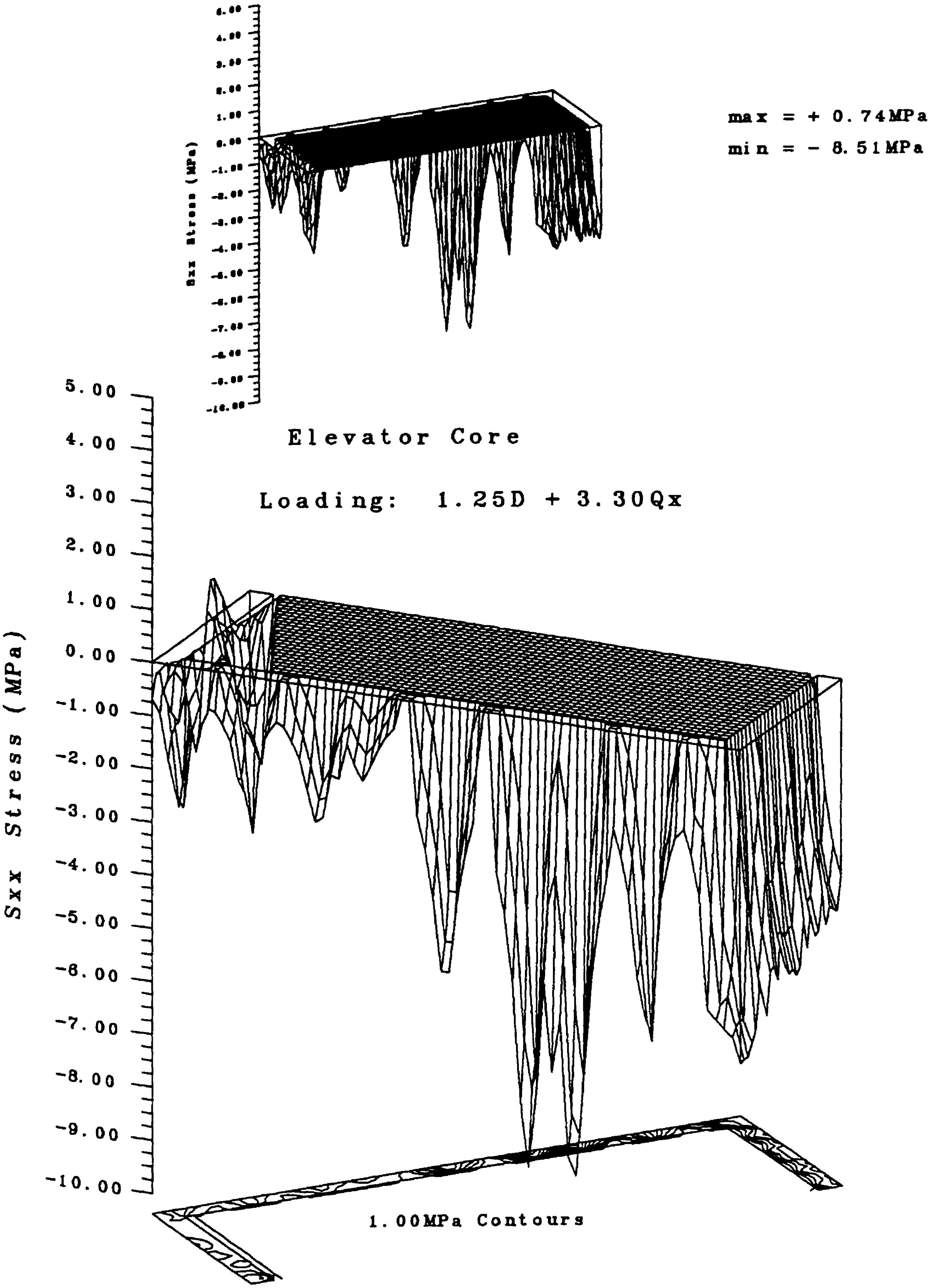

Figure 6.27 Distribution of the Concrete S_{xx} Stresses at the Elevator Core Base At Load Level $1.25\,D + 3.30\,Q_X$ – Nonlinear Analysis DQX Model Results

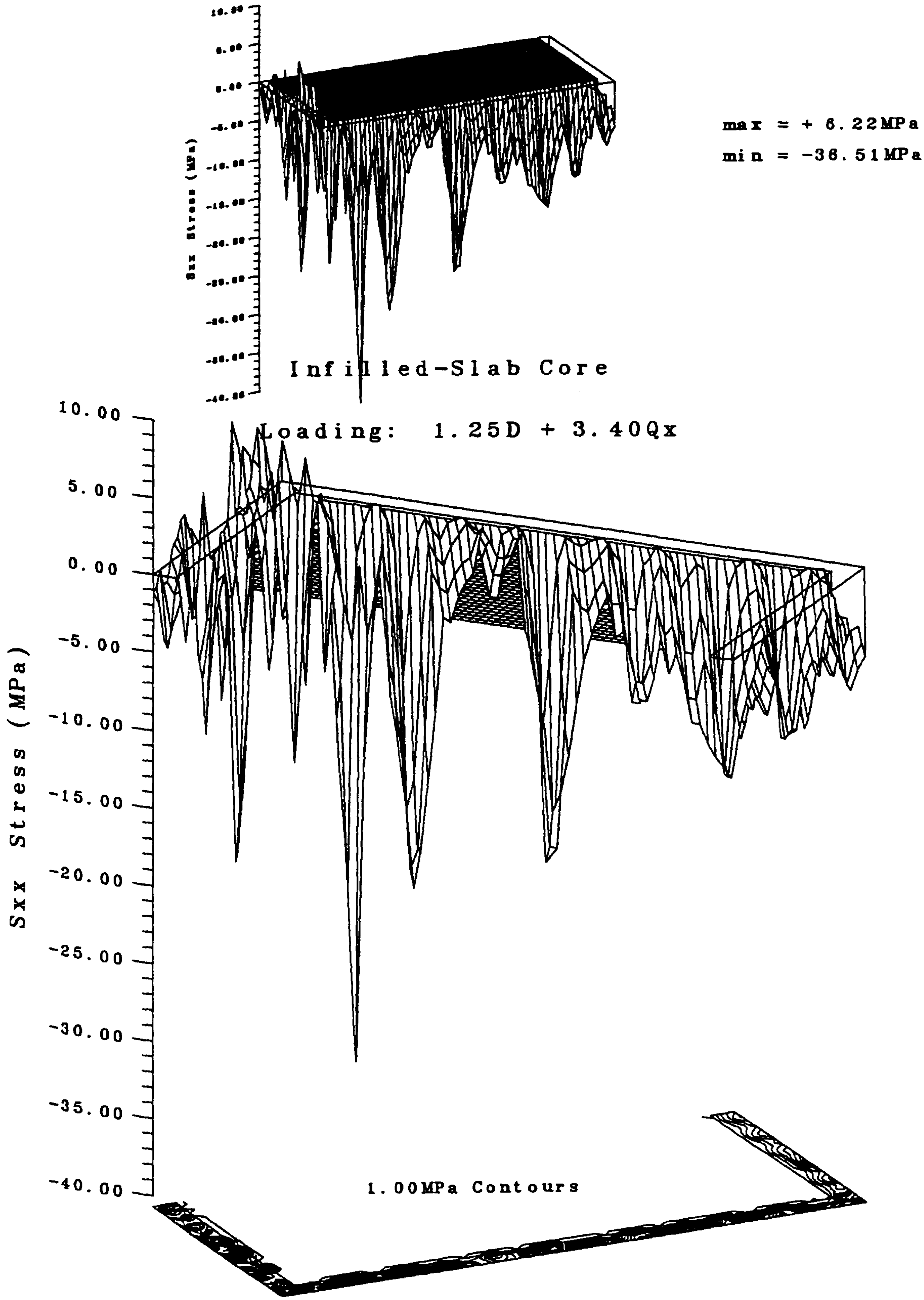

Figure 6.28 Distribution of the Concrete S_{xx} Stresses at the Infilled-Slab Core Base At Load Level $1.25\,D + 3.40\,Qx$ – Nonlinear Analysis DQX Model Results

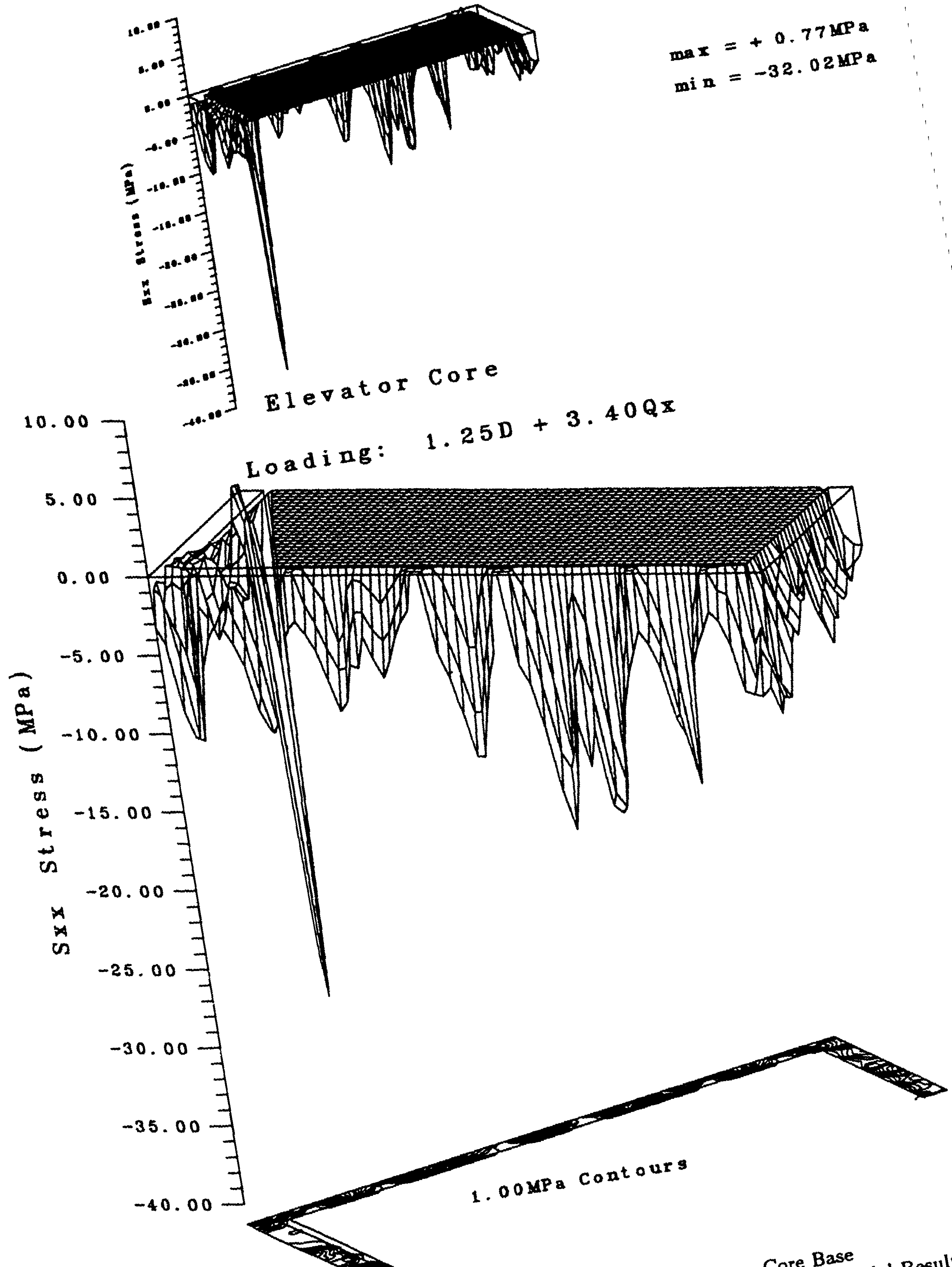

Figure 6.29 Distribution of the Concrete S_{xx} Stresses at the Elevator Core Base At Load Level $1.25\,D + 3.40\,Qx$ - Nonlinear Analysis DQX Model Results

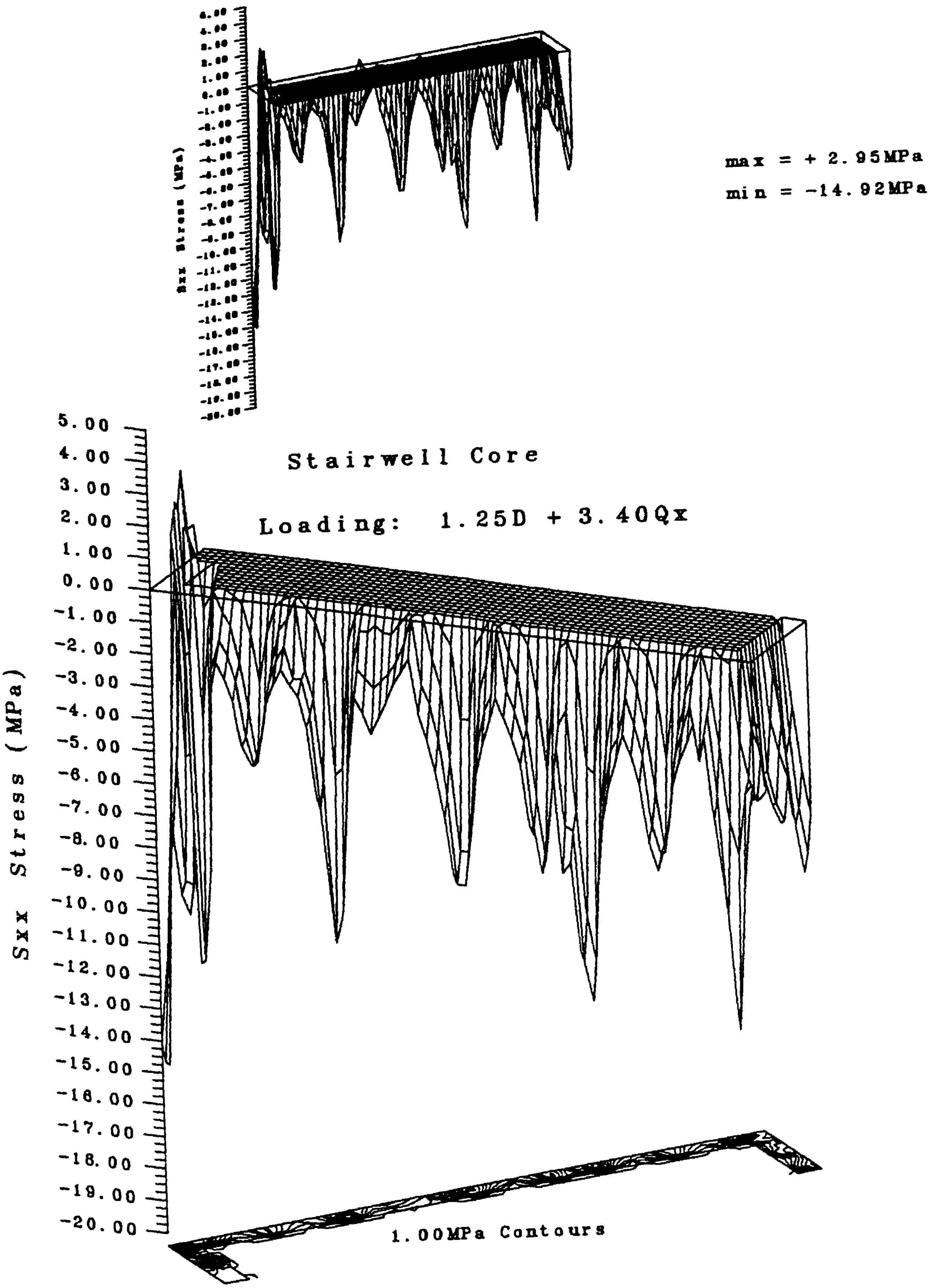

Figure 6.30 Distribution of the Concrete S_{xx} Stresses at the Stairwell Core Base At Load Level $1.25D + 3.40Qx$ – Nonlinear Analysis DQX Model Results

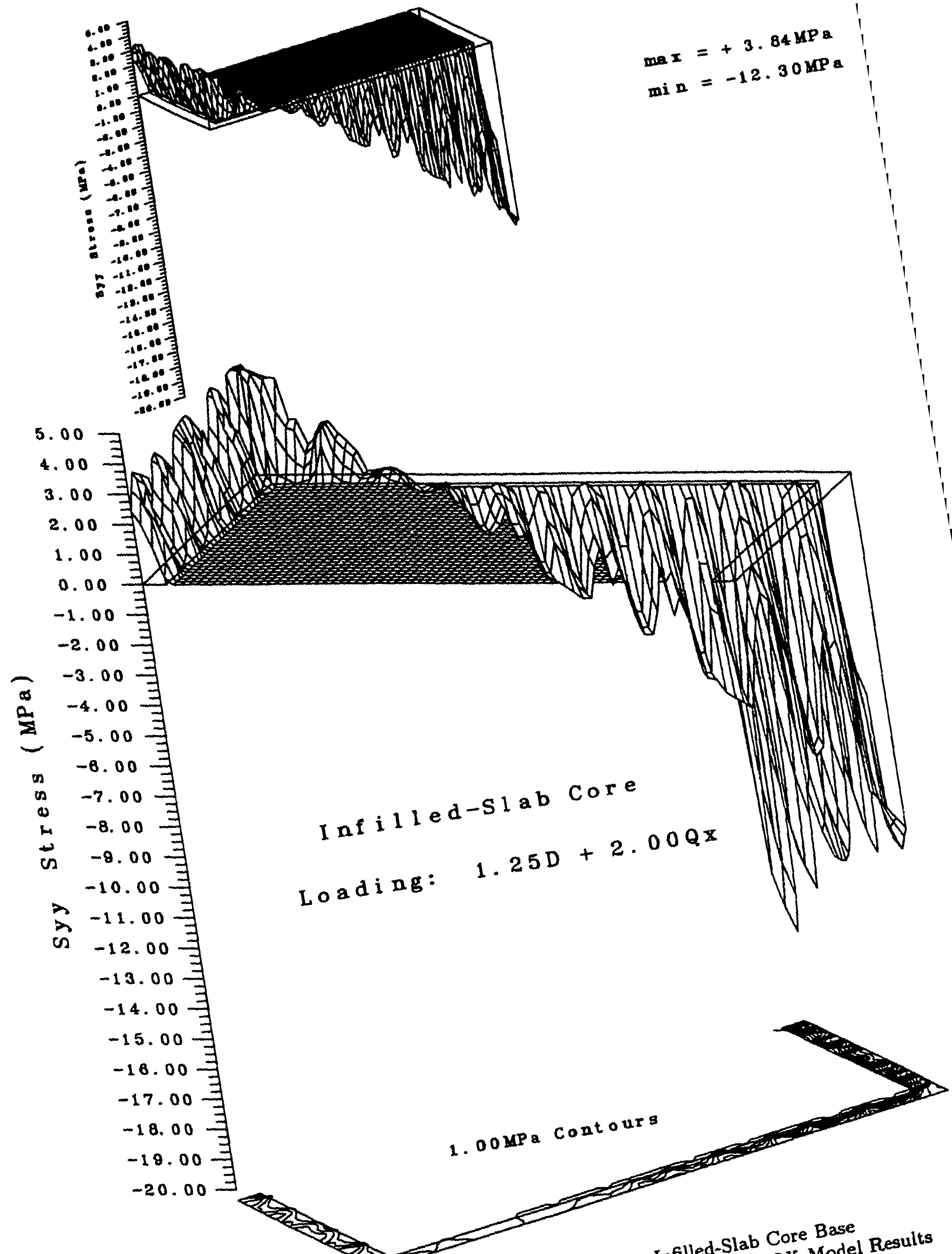

Figure 6.31 Distribution of the Concrete S_{yy} Stresses at the Infilled-Slab Core Base At Load Level $1.25\,D + 2.00\,Qx$ – Nonlinear Analysis DQX Model Results

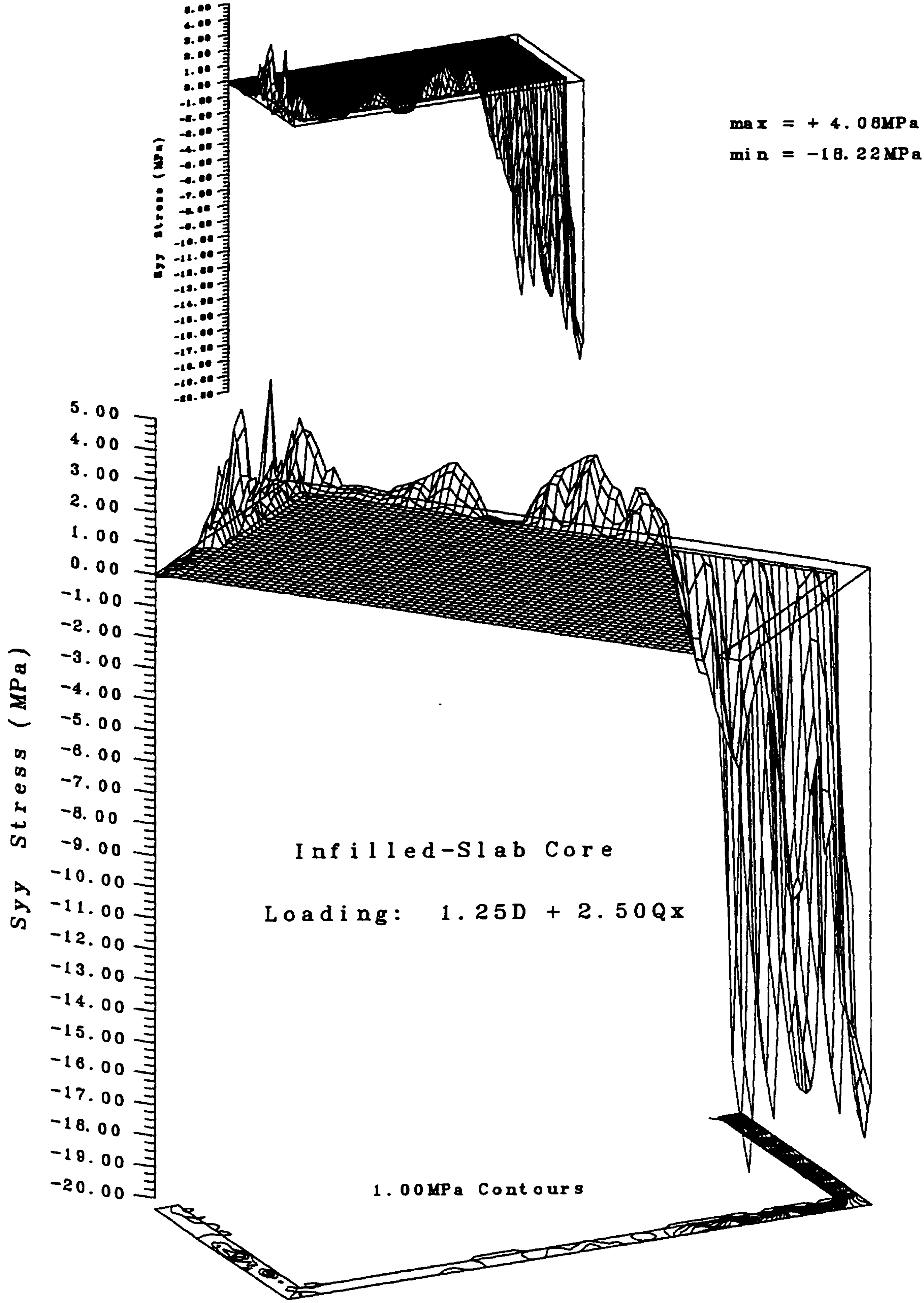

Figure 6.32 Distribution of the Concrete S_{yy} Stresses at the Infilled-Slab Core Base At Load Level $1.25D + 2.50Q_X$ – Nonlinear Analysis DQX Model Results

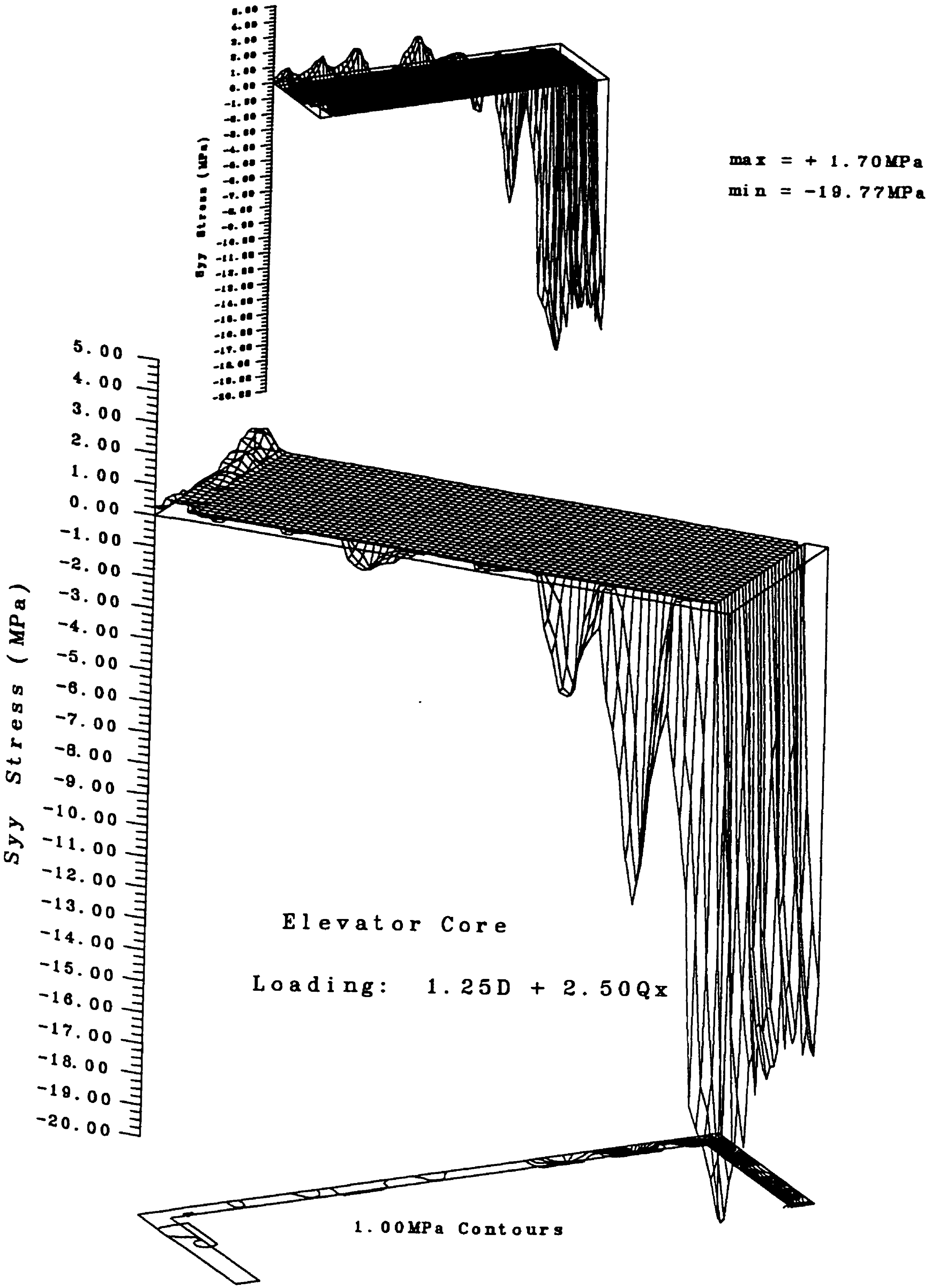

Figure 6.33 Distribution of the Concrete S_{yy} Stresses at the Elevator Core Base At Load Level $1.25\,D + 2.50\,Q_X$ - Nonlinear Analysis DQX Model Results

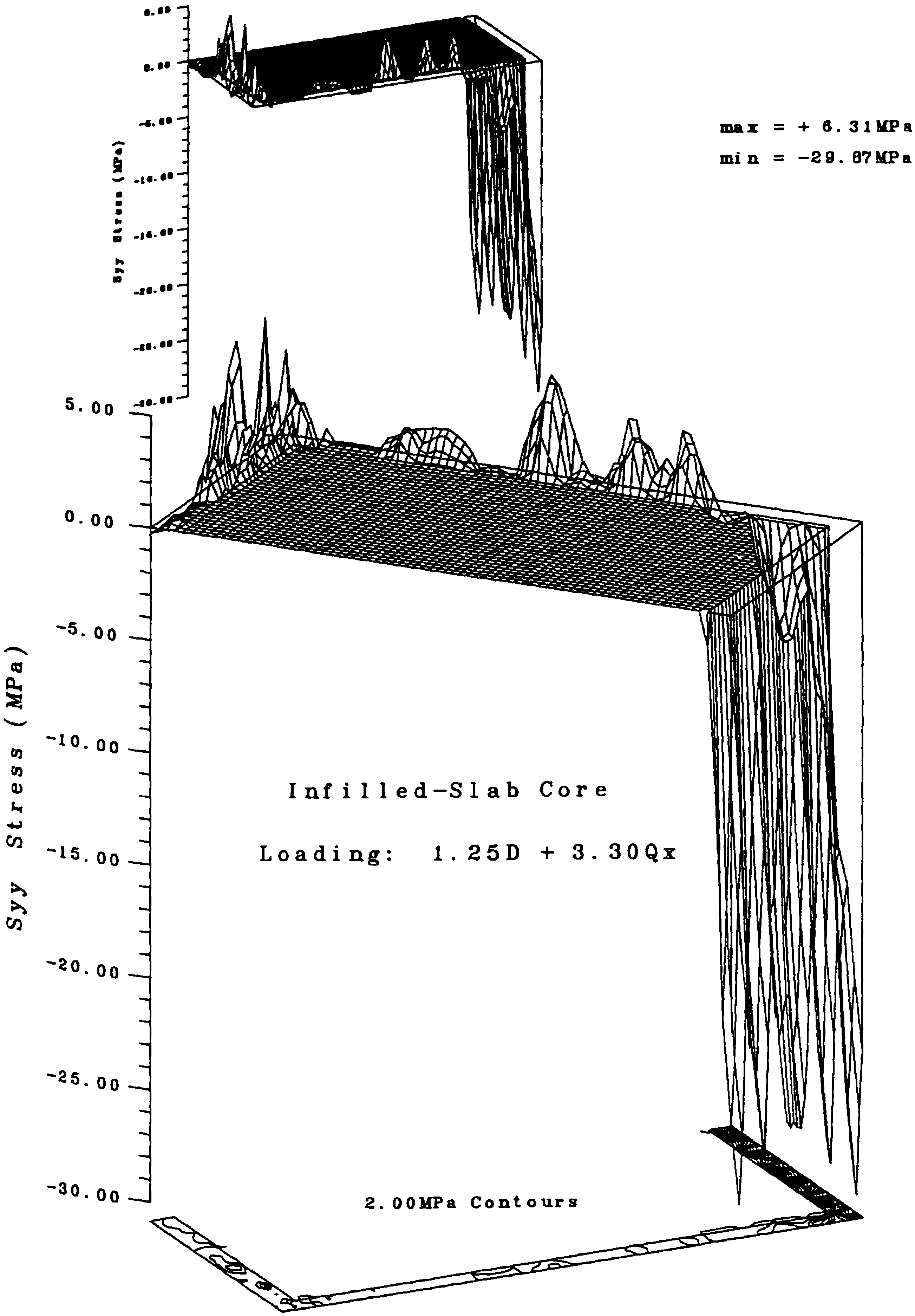

Figure 6.34 Distribution of the Concrete S_{yy} Stresses at the Infilled-Slab Core Base At Load Level $1.25\,D + 3.30\,Q_X$ – Nonlinear Analysis DQX Model Results

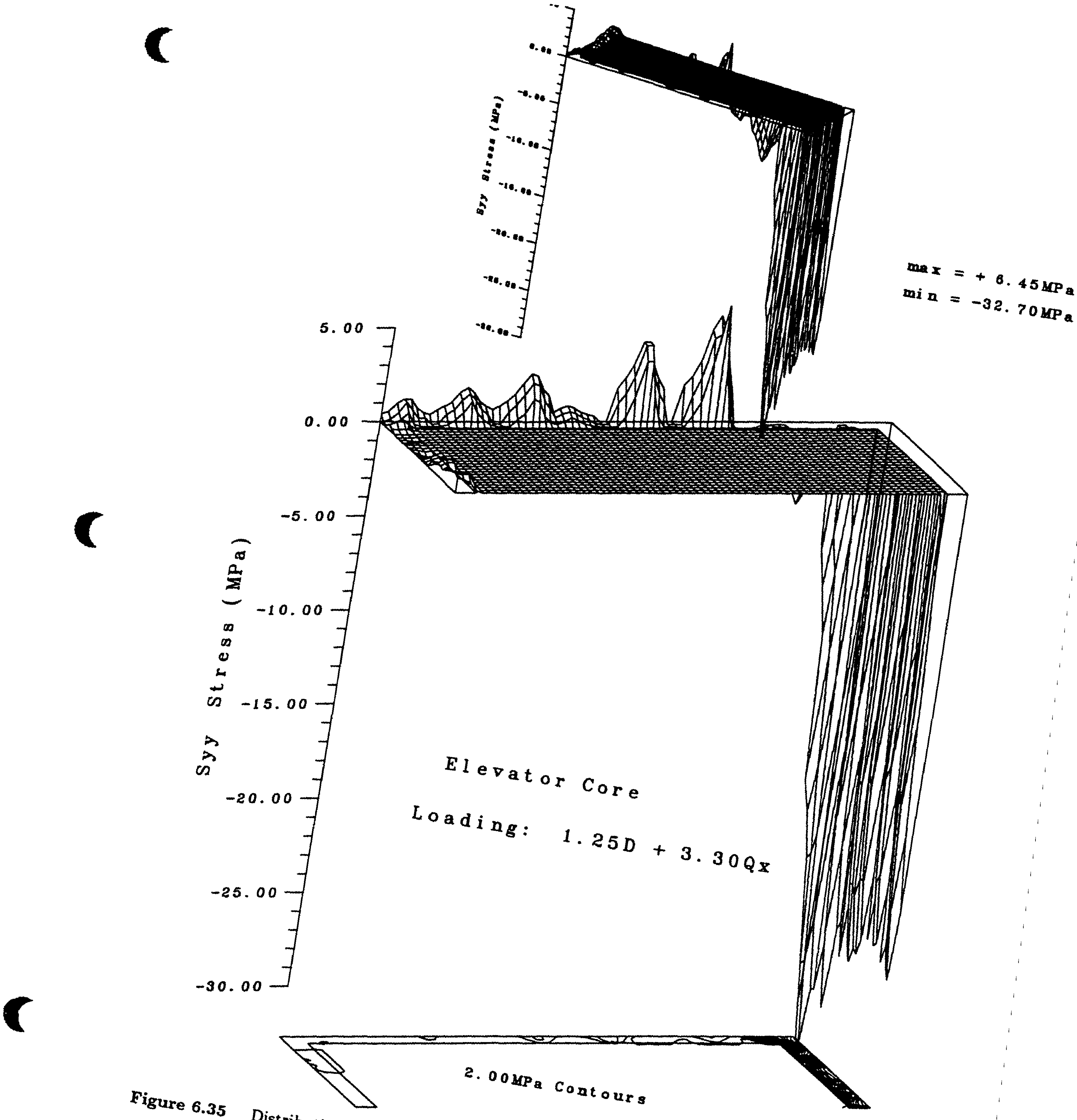

Figure 6.35 Distribution of the Concrete S_{yy} Stresses at the Elevator Core Base At Load Level $1.25D + 3.30Qx$ - Nonlinear Analysis DQX Model Results

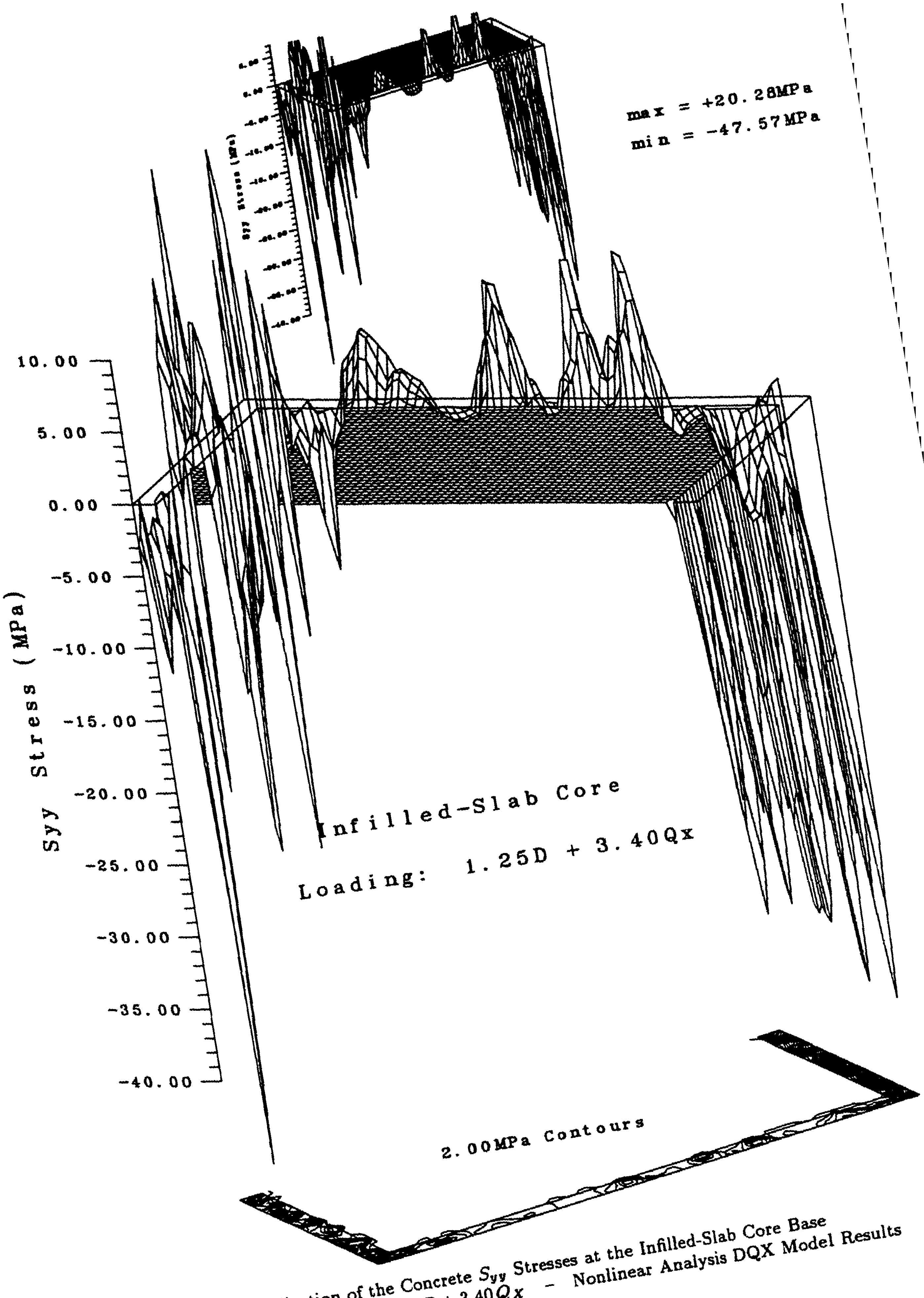

Figure 6.36 Distribution of the Concrete S_{yy} Stresses at the Infilled-Slab Core Base At Load Level $1.25D + 3.40Qx$ – Nonlinear Analysis DQX Model Results

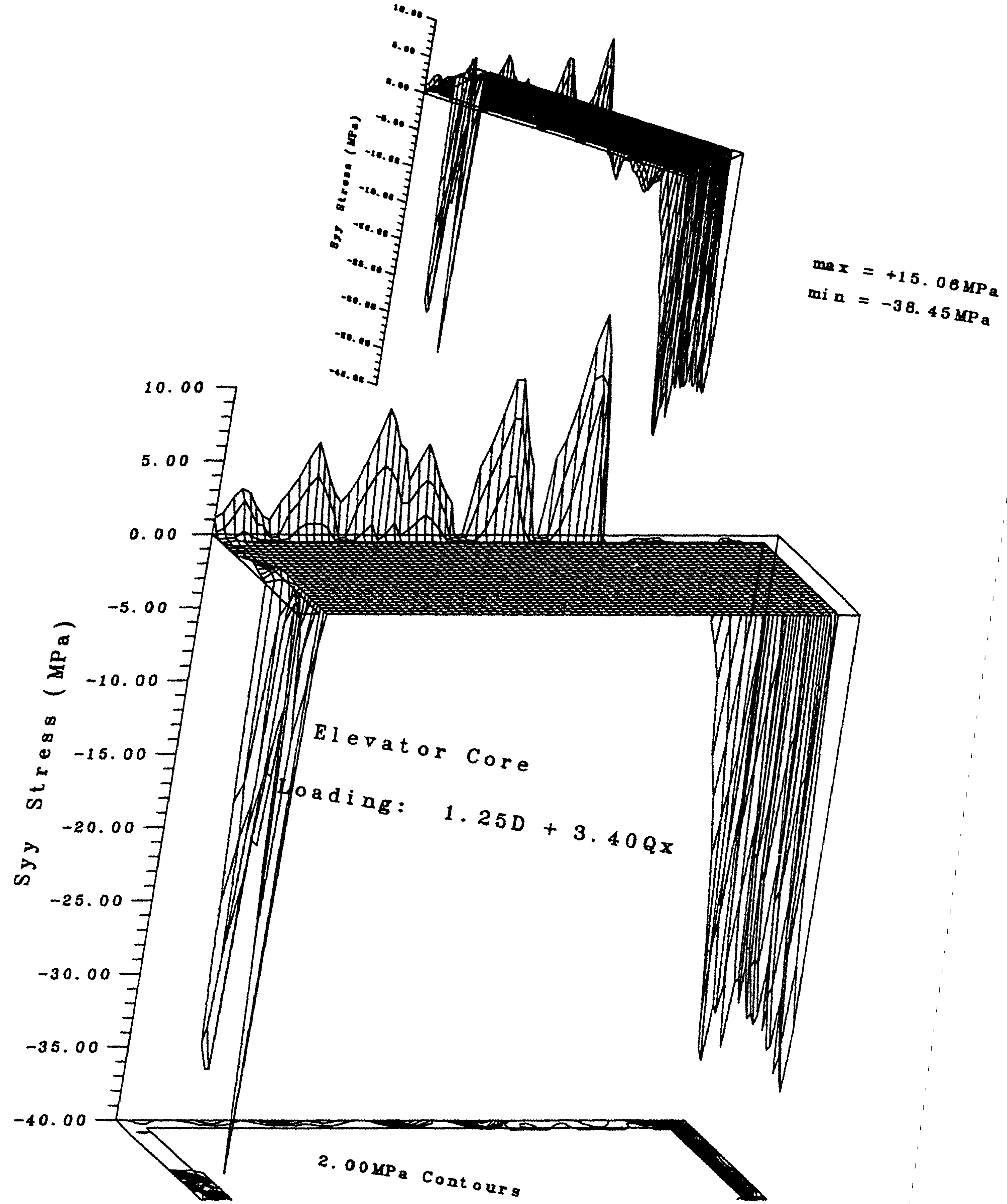

Figure 6.37 Distribution of the Concrete S_{yy} Stresses at the Elevator Core Base At Load Level $1.25D + 3.40Qx$ – Nonlinear Analysis DQX Model Results

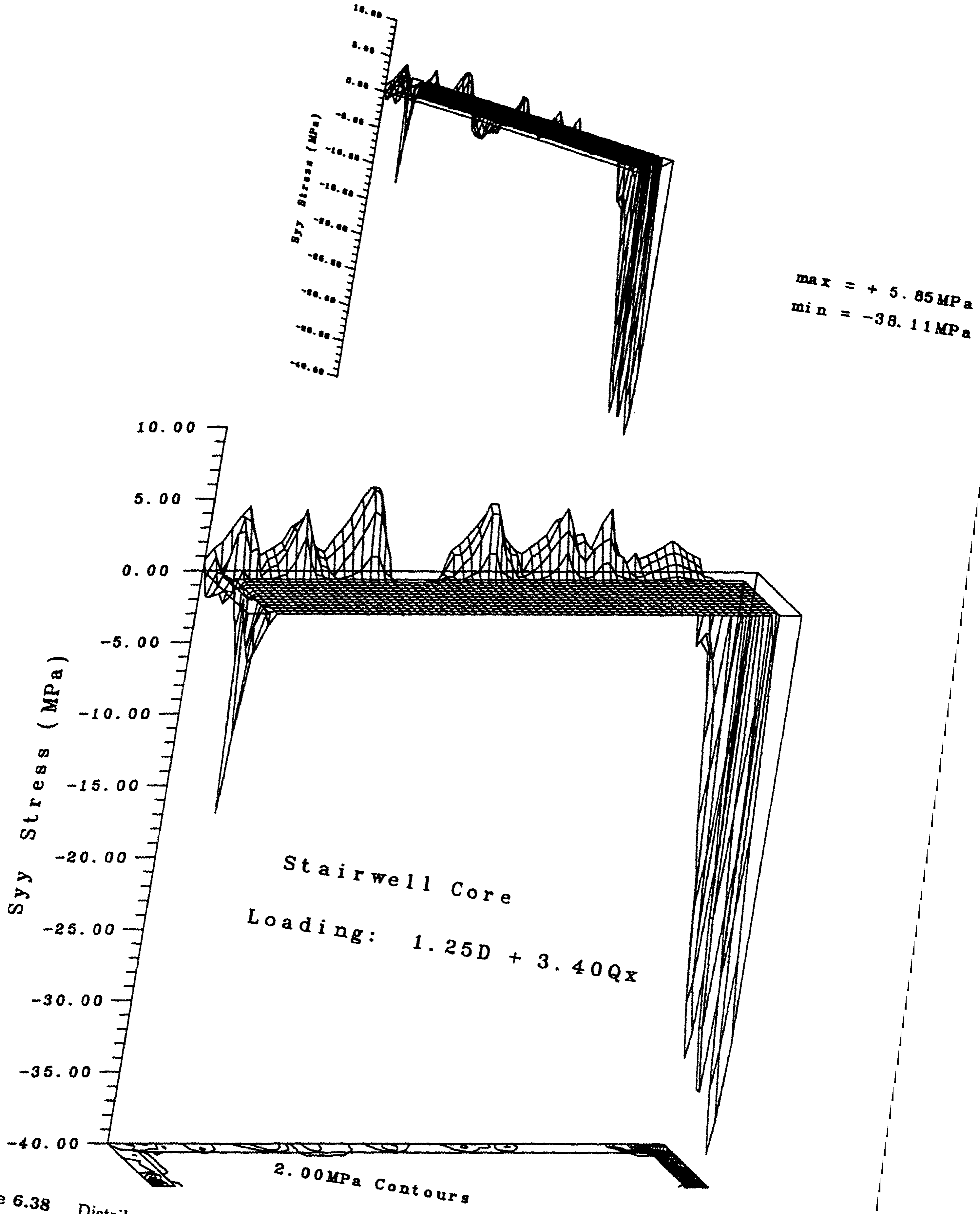

Figure 6.38 Distribution of the Concrete S_{yy} Stresses at the Stairwell Core Base At Load Level $1.25D + 3.40Qx$ – Nonlinear Analysis DQX Model Results

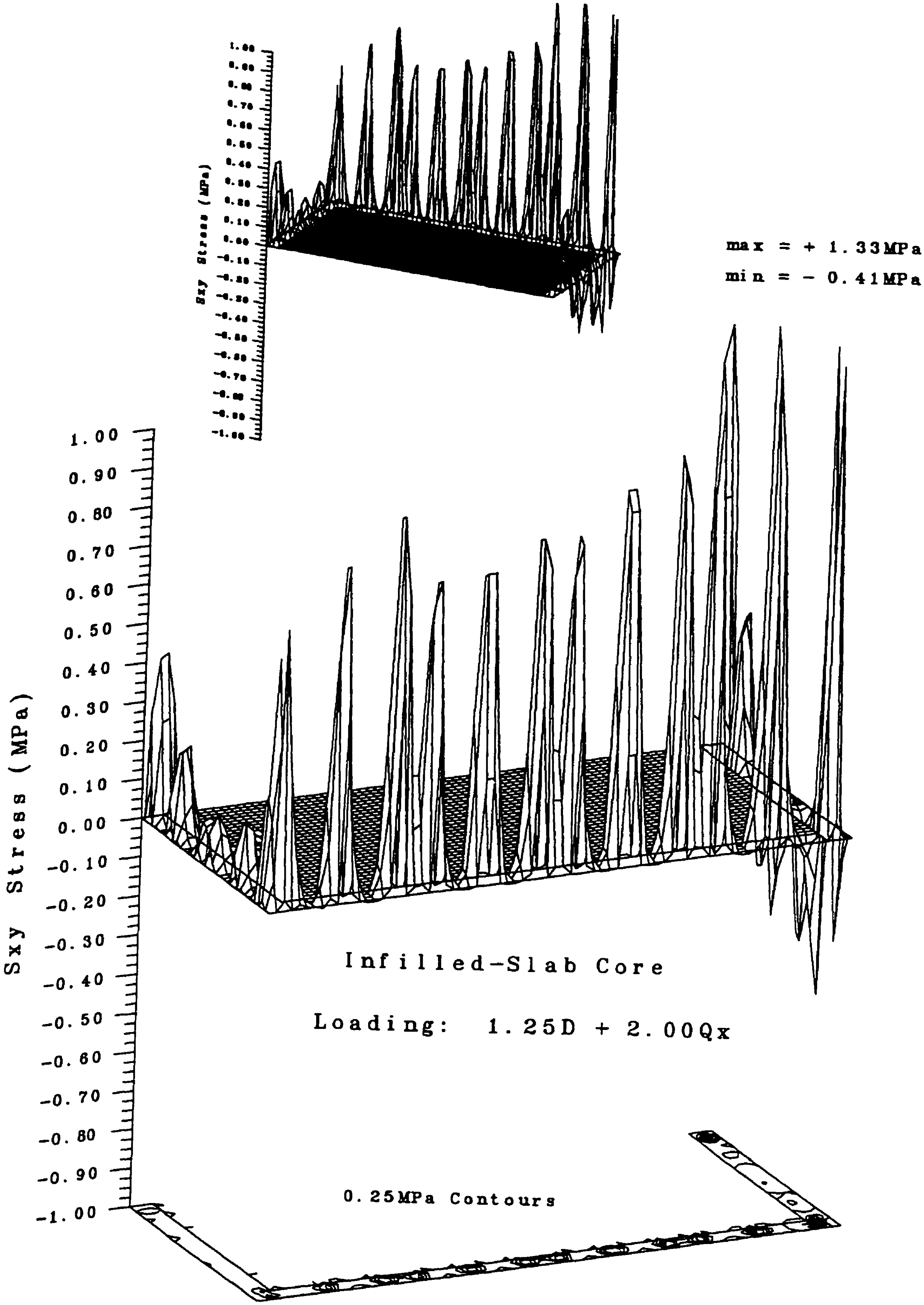

Figure 6.39 Distribution of the Concrete S_{xy} Stresses at the Infilled-Slab Core Base At Load Level $1.25\,D + 2.00\,Q_X$ – Nonlinear Analysis DQX Model Results

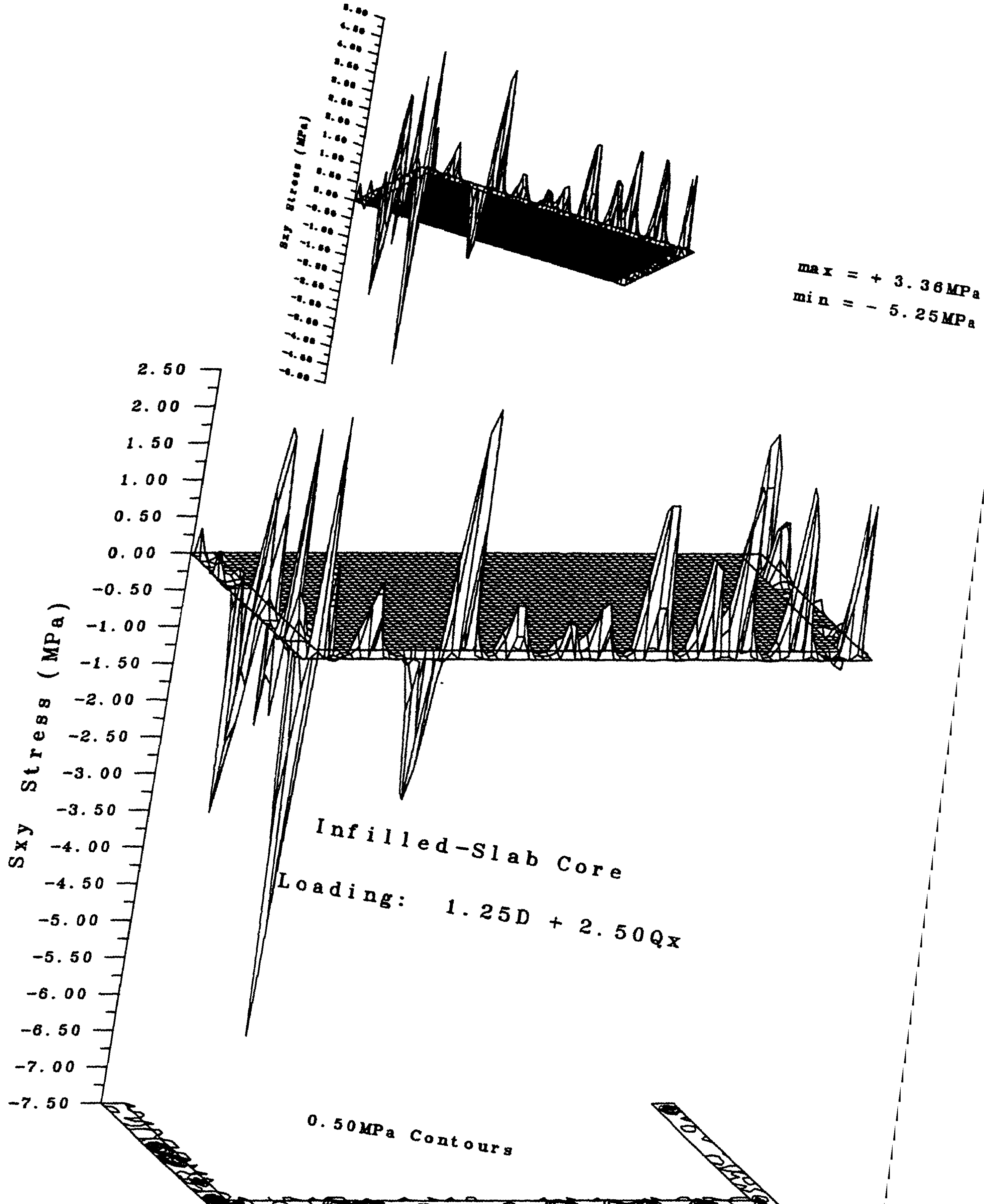

Figure 6.40 Distribution of the Concrete S_{xy} Stresses at the Infilled-Slab Core Base At Load Level $1.25D + 2.50Qx$ – Nonlinear Analysis DQX Model Results

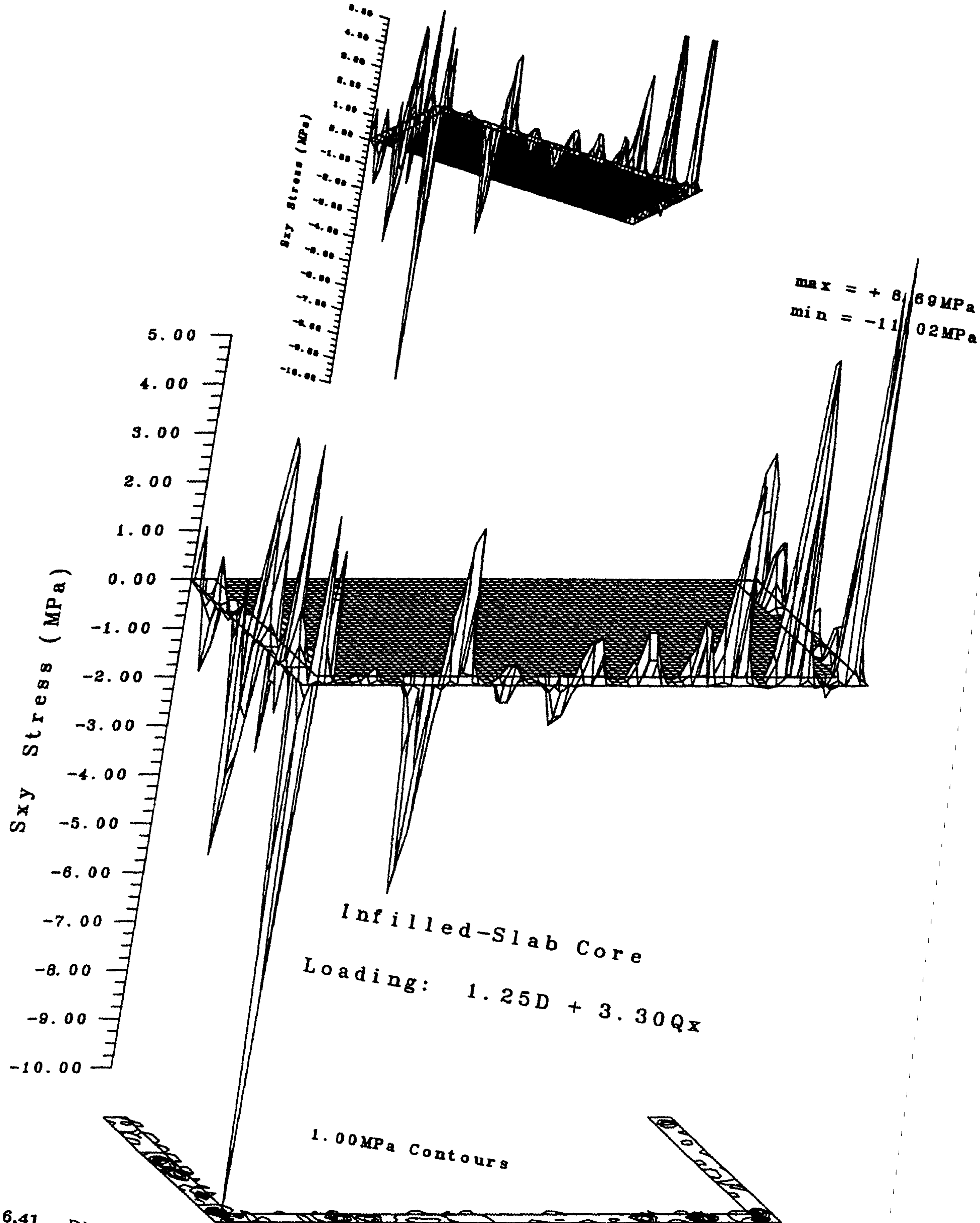

Figure 6.41 Distribution of the Concrete S_{xy} Stresses at the Infilled-Slab Core Base At Load Level $1.25\,D + 3.30\,Qx$ – Nonlinear Analysis DQX Model Results

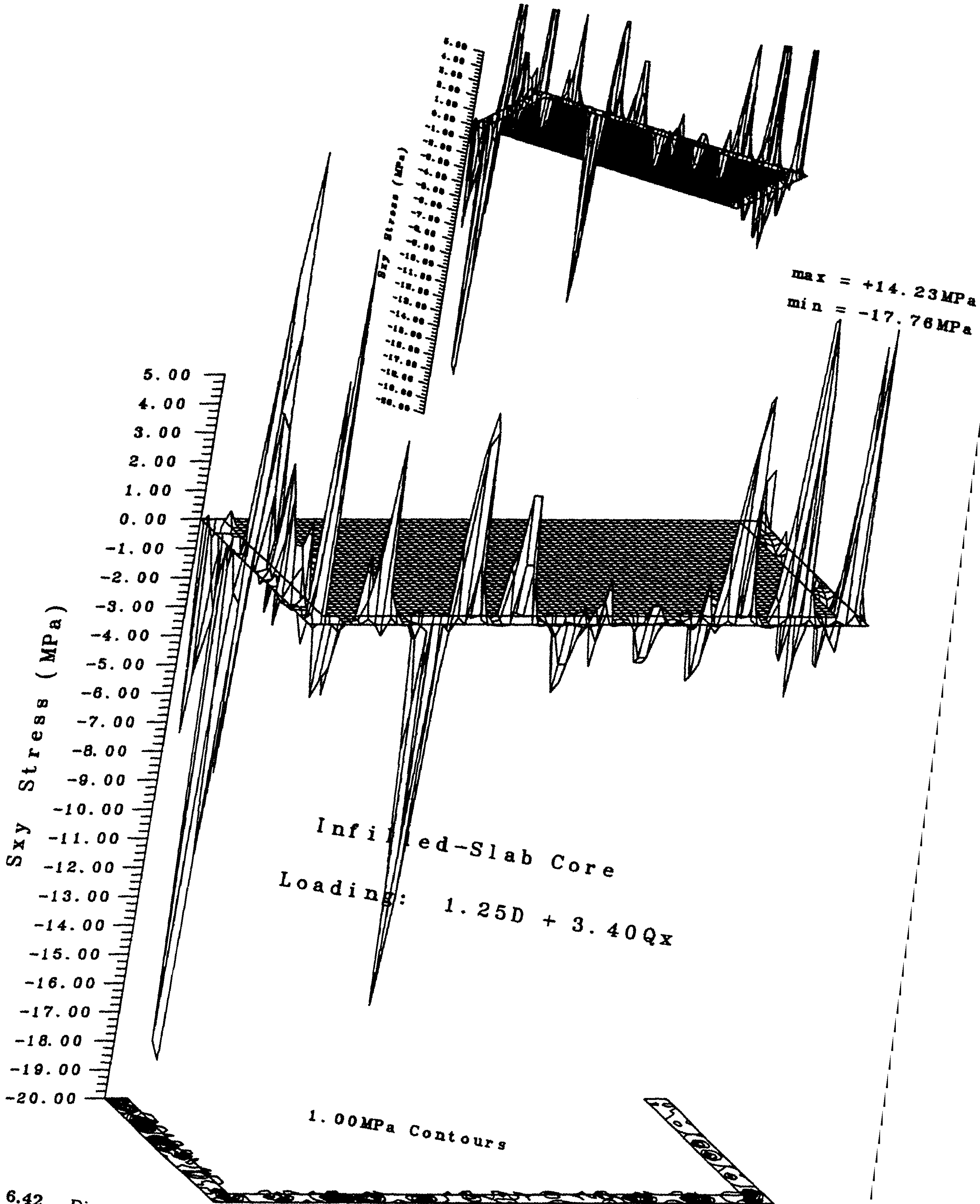

Figure 6.42 Distribution of the Concrete S_{xy} Stresses at the Infilled-Slab Core Base At Load Level $1.25D + 3.40Qx$ – Nonlinear Analysis DQX Model Results

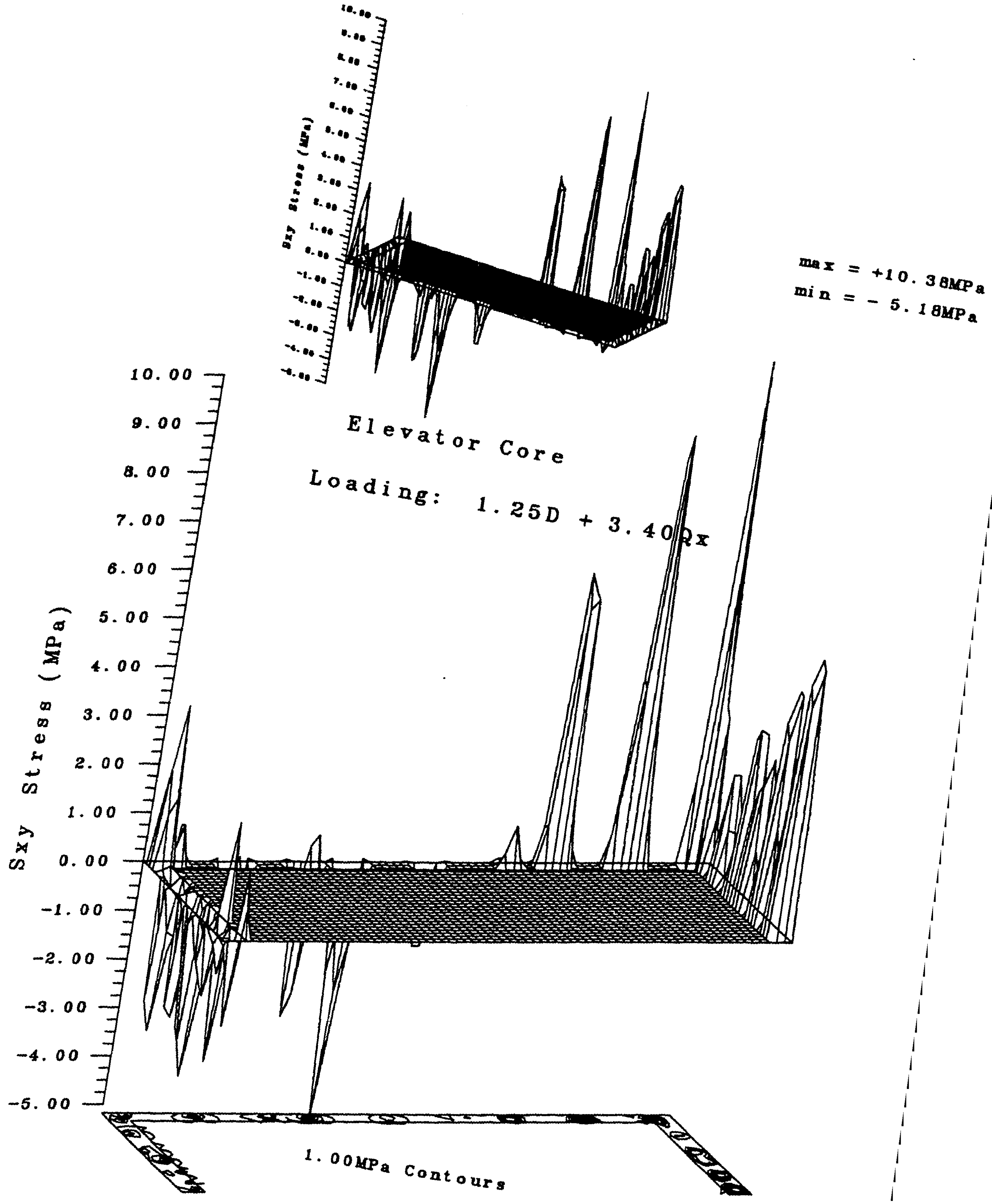

Figure 6.43 Distribution of the Concrete S_{xy} Stresses at the Elevator Core Base At Load Level $1.25\,D + 3.40\,Q_X$ – Nonlinear Analysis DQX Model Results

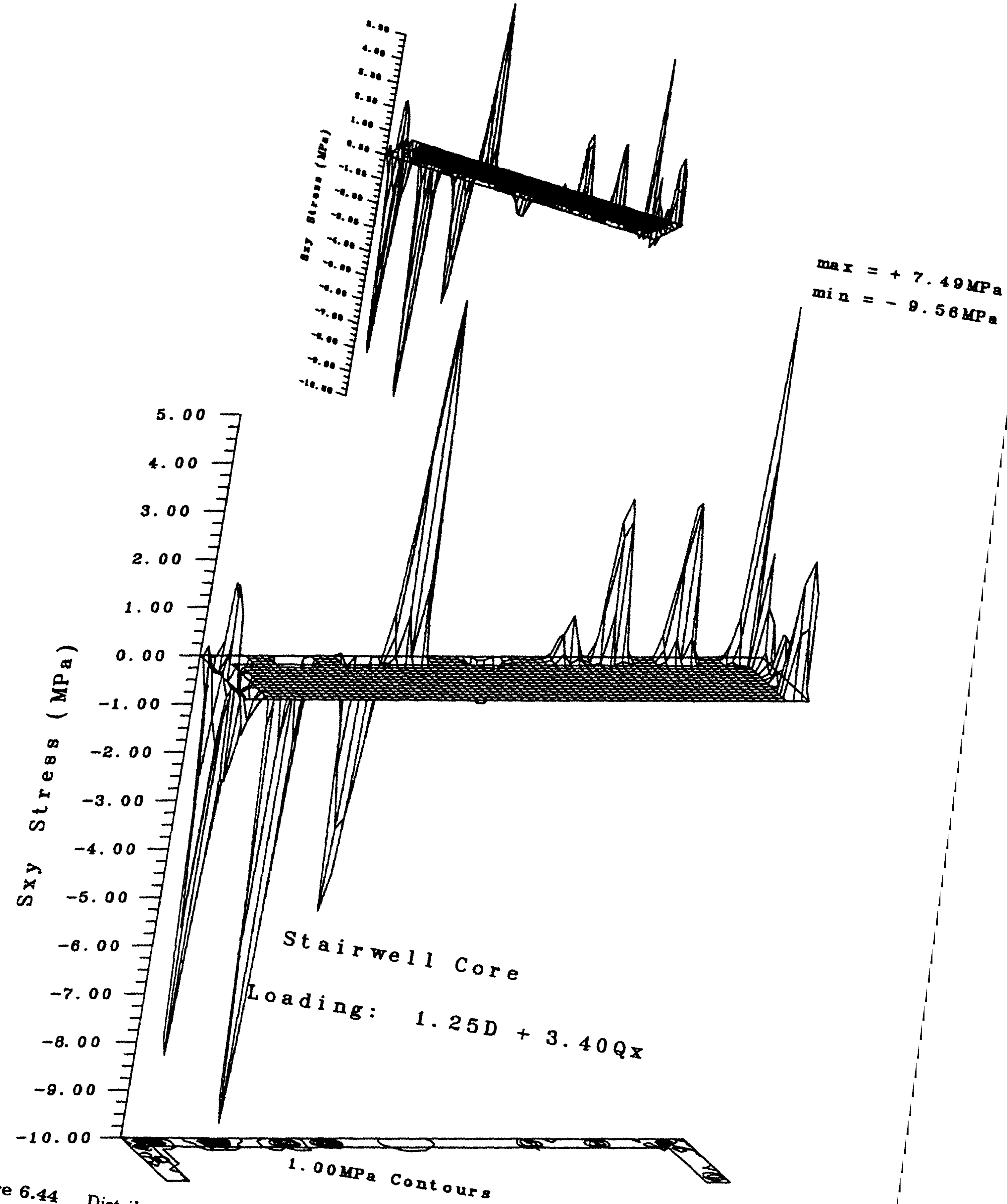

Figure 6.44 Distribution of the Concrete S_{xy} Stresses at the Stairwell Core Base At Load Level $1.25D + 3.40Q_X$ – Nonlinear Analysis DQX Model Results

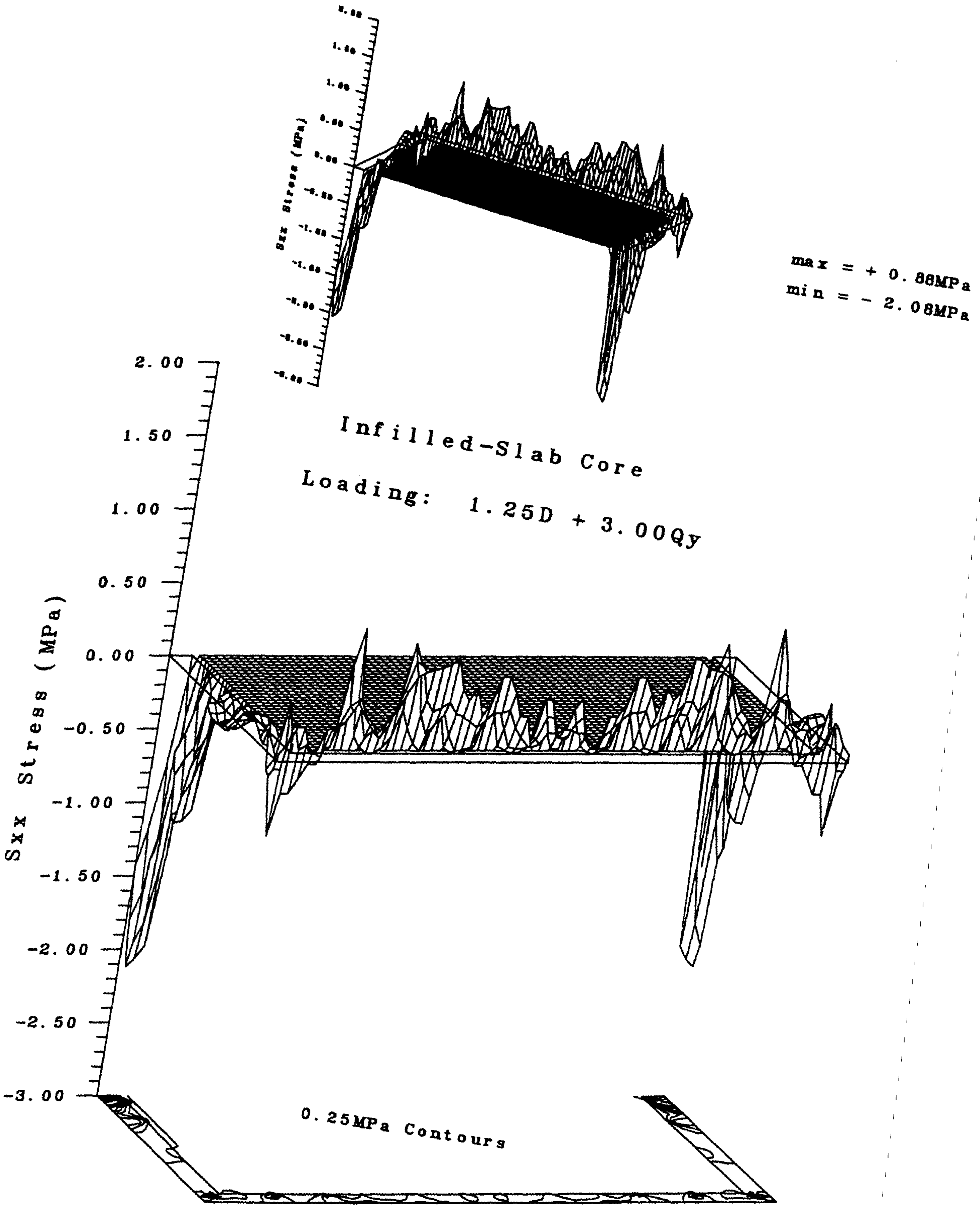

Figure 6.45 Distribution of the Concrete S_{xx} Stresses at the Infilled-Slab Core Base At Load Level $1.25D + 3.00Q_Y$ – Nonlinear Analysis DQY Model Results

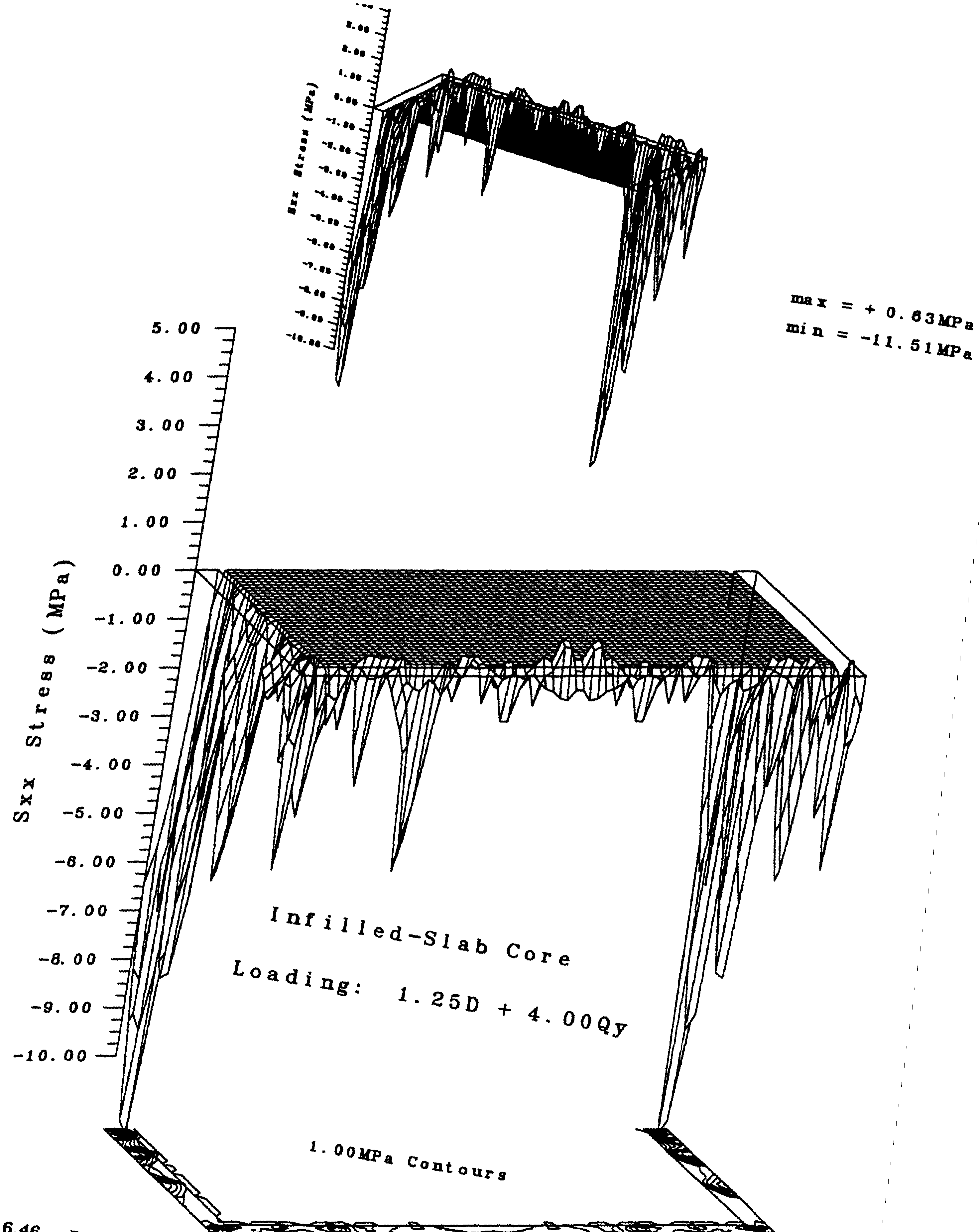

Figure 6.46 Distribution of the Concrete S_{xx} Stresses at the Infilled-Slab Core Base At Load Level $1.25\,D + 4.00Q_Y$ – Nonlinear Analysis DQY Model Results

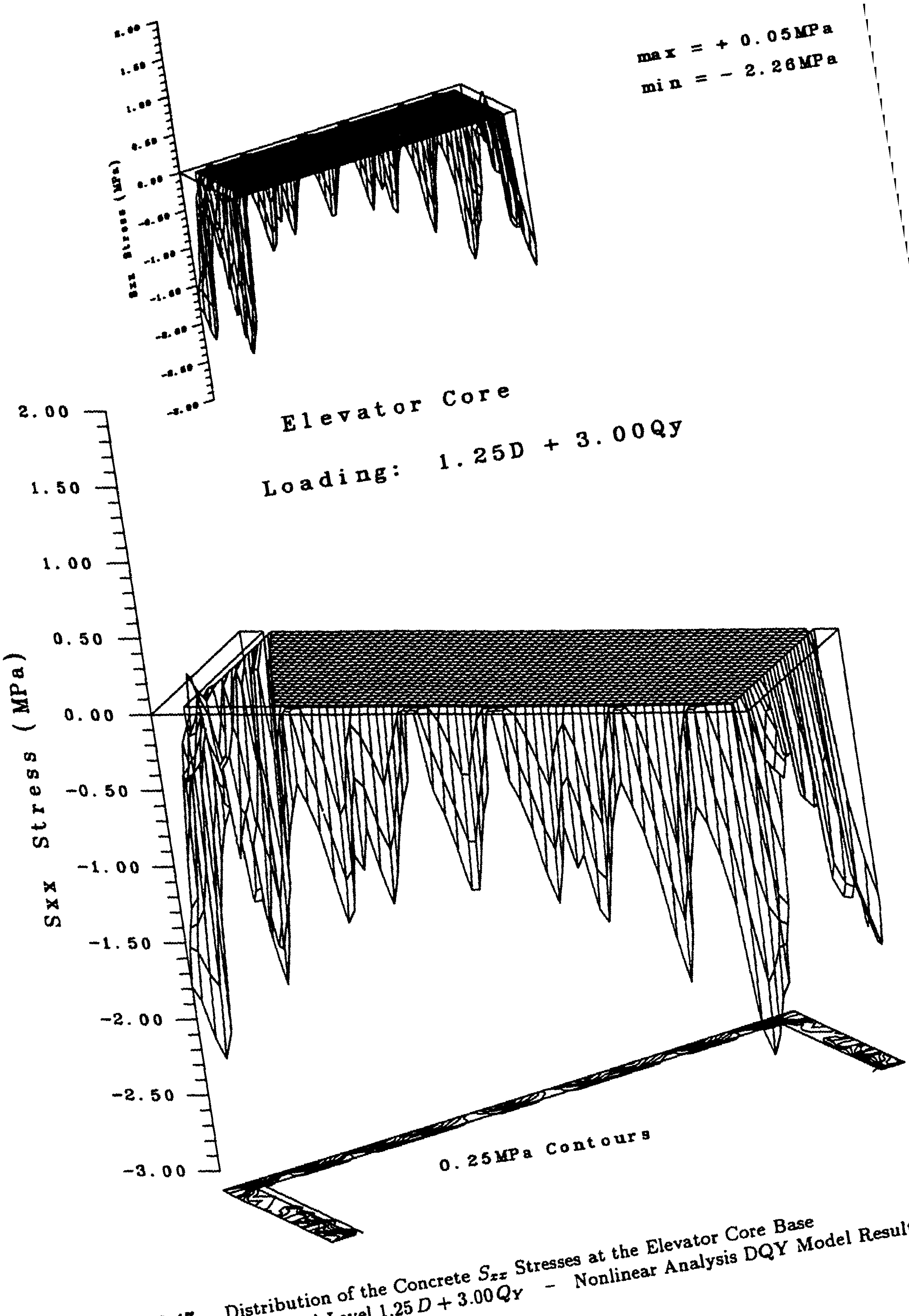

Figure 6.47 Distribution of the Concrete S_{xx} Stresses at the Elevator Core Base At Load Level $1.25\,D + 3.00\,Q_Y$ – Nonlinear Analysis DQY Model Results

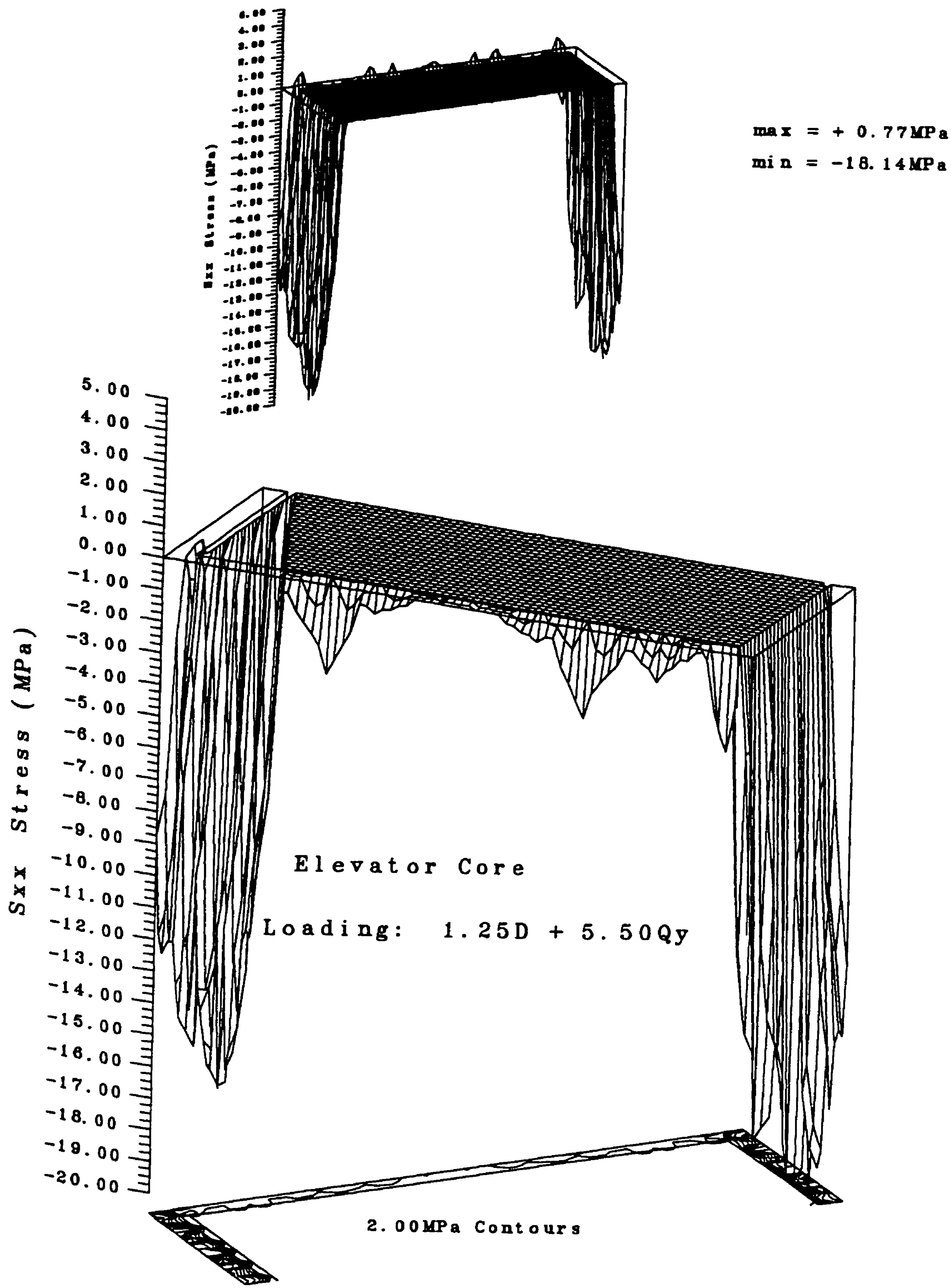

Figure 6.48 Distribution of the Concrete S_{xx} Stresses at the Elevator Core Base At Load Level $1.25\,D + 5.50\,Q_Y$ – Nonlinear Analysis DQY Model Results

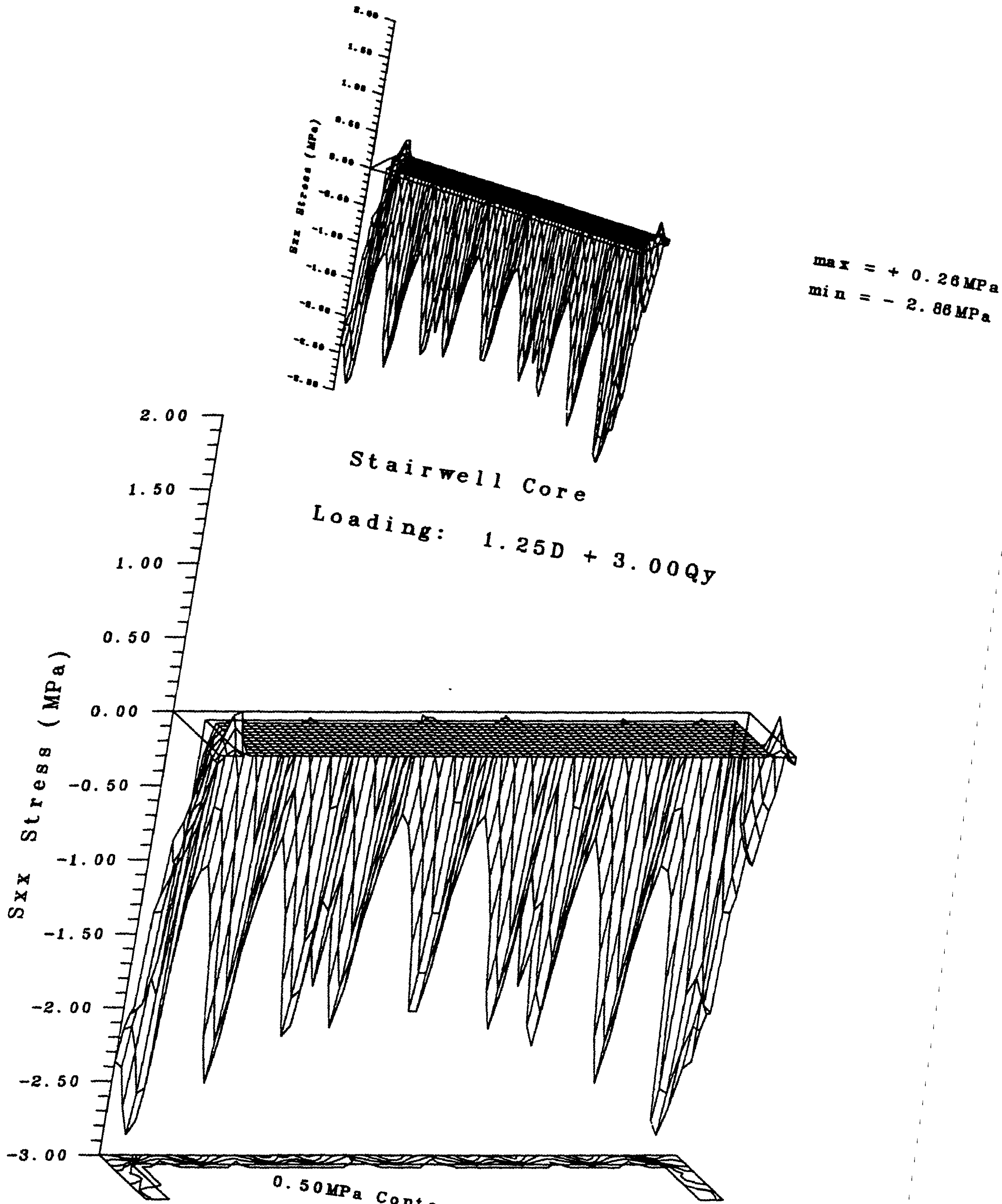

Figure 6.49 Distribution of the Concrete S_{xx} Stresses at the Stairwell Core Base At Load Level $1.25\,D + 3.00\,Q_Y$ – Nonlinear Analysis DQY Model Results

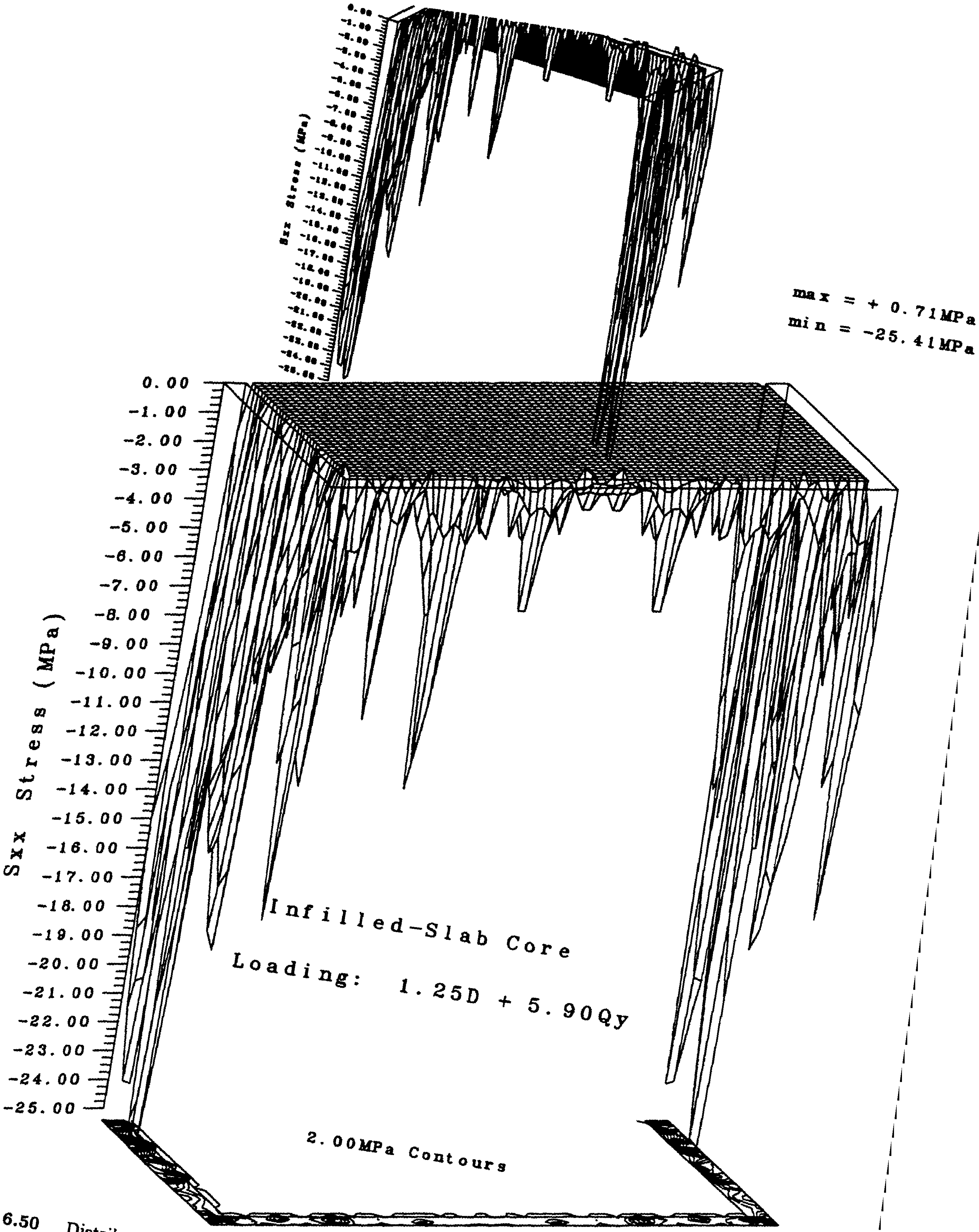

Figure 6.50 Distribution of the Concrete S_{xx} Stresses at the Infilled-Slab Core Base At Load Level $1.25\,D + 5.90\,Q_Y$ – Nonlinear Analysis DQY Model Results

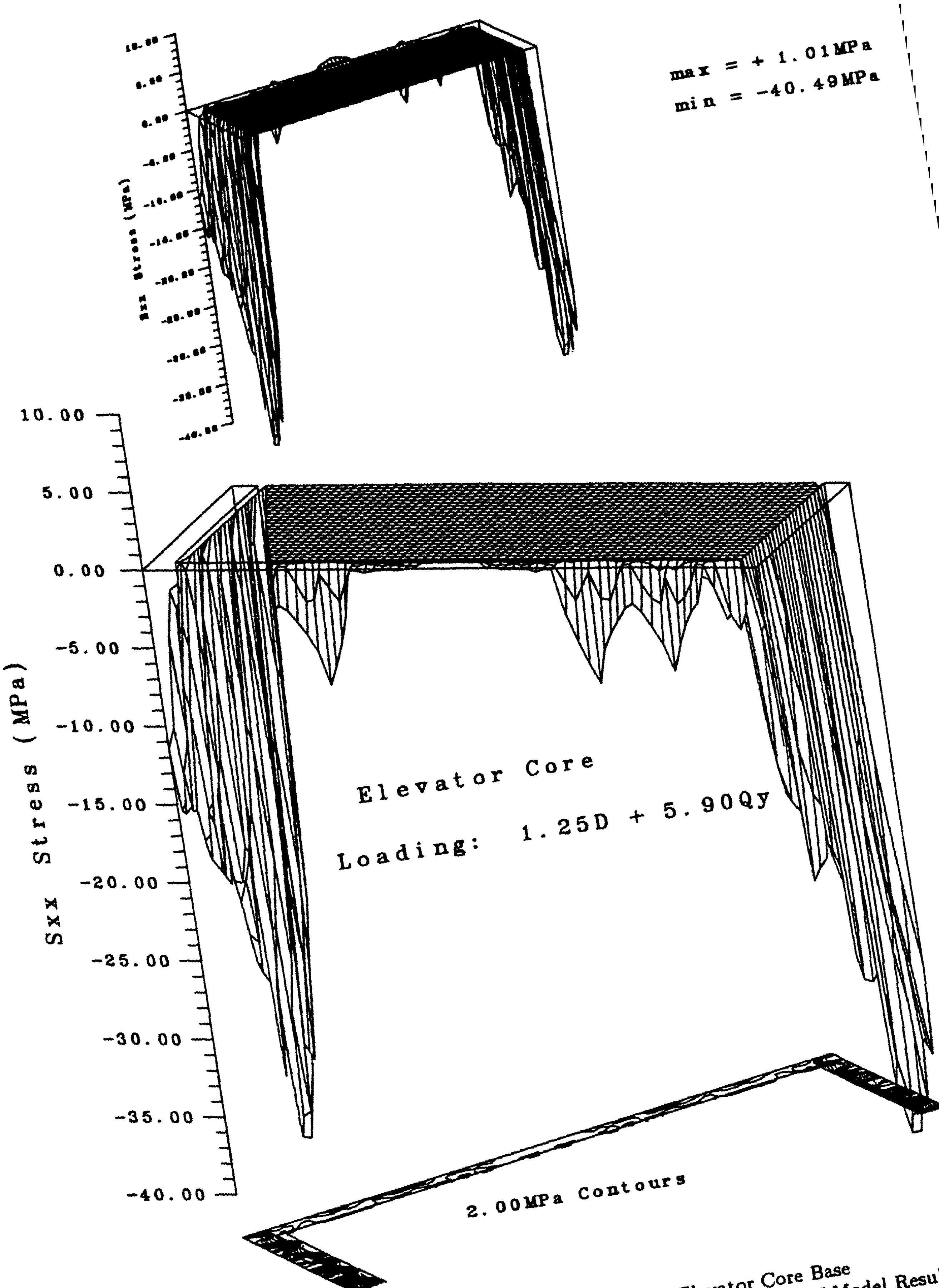

Figure 6.51 Distribution of the Concrete S_{xx} Stresses at the Elevator Core Base At Load Level $1.25\,D + 5.90\,Q_Y$ – Nonlinear Analysis DQY Model Results

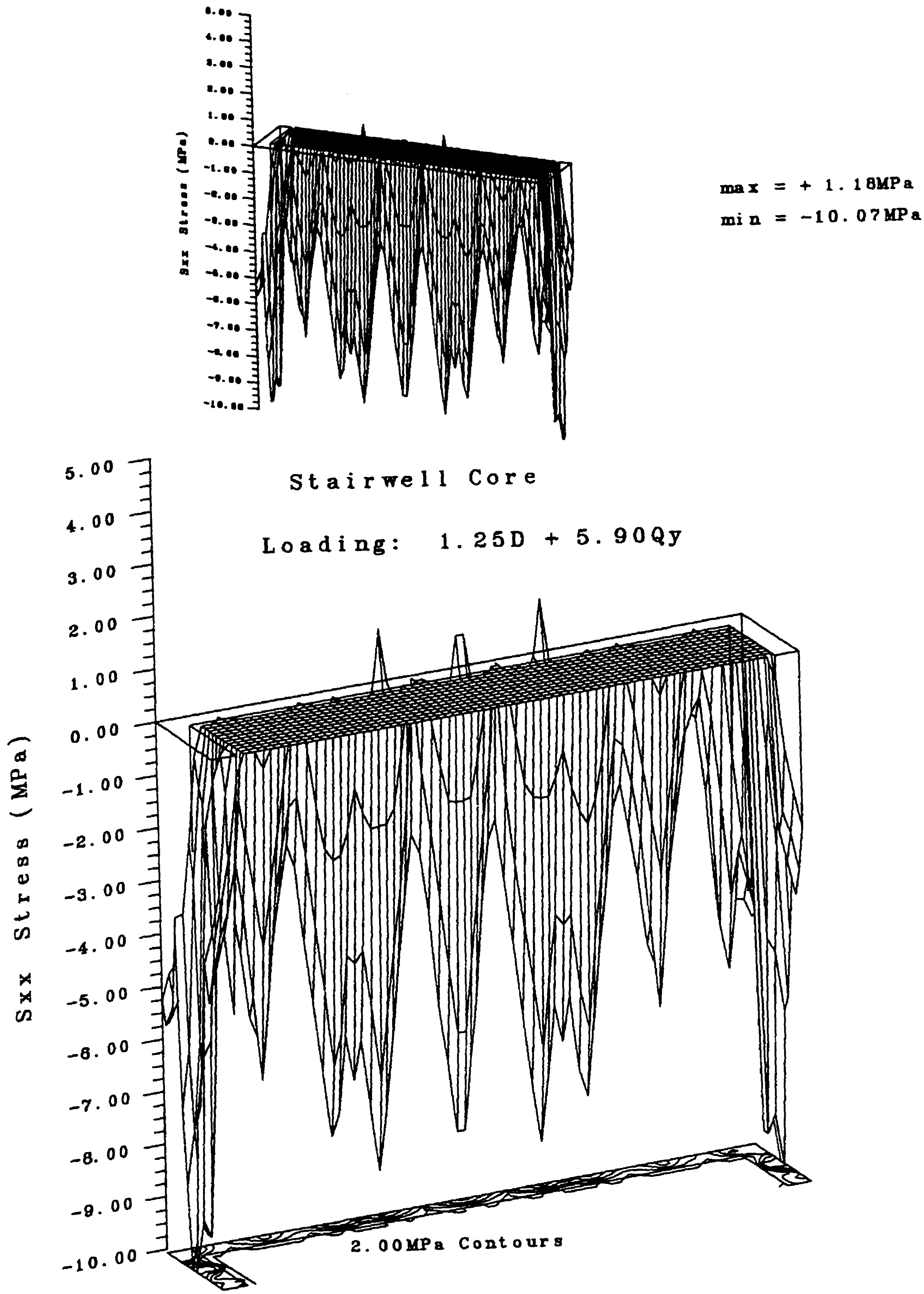

Figure 6.52 Distribution of the Concrete S_{xx} Stresses at the Stairwell Core Base At Load Level $1.25D + 5.90Q_Y$ – Nonlinear Analysis DQY Model Results

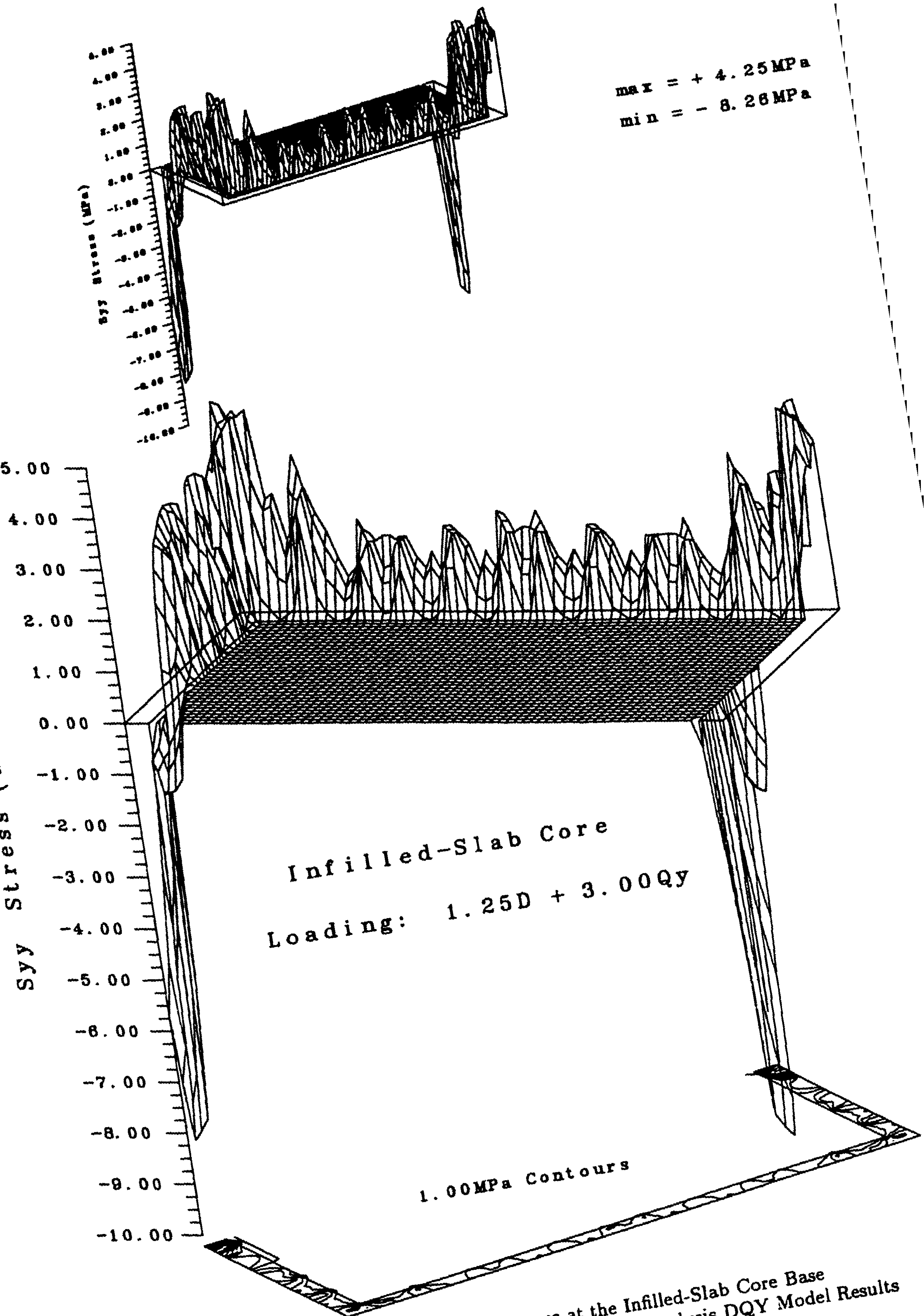

Figure 6.53 Distribution of the Concrete S_{yy} Stresses at the Infilled-Slab Core Base At Load Level $1.25\,D + 3.00\,Q_Y$ – Nonlinear Analysis DQY Model Results

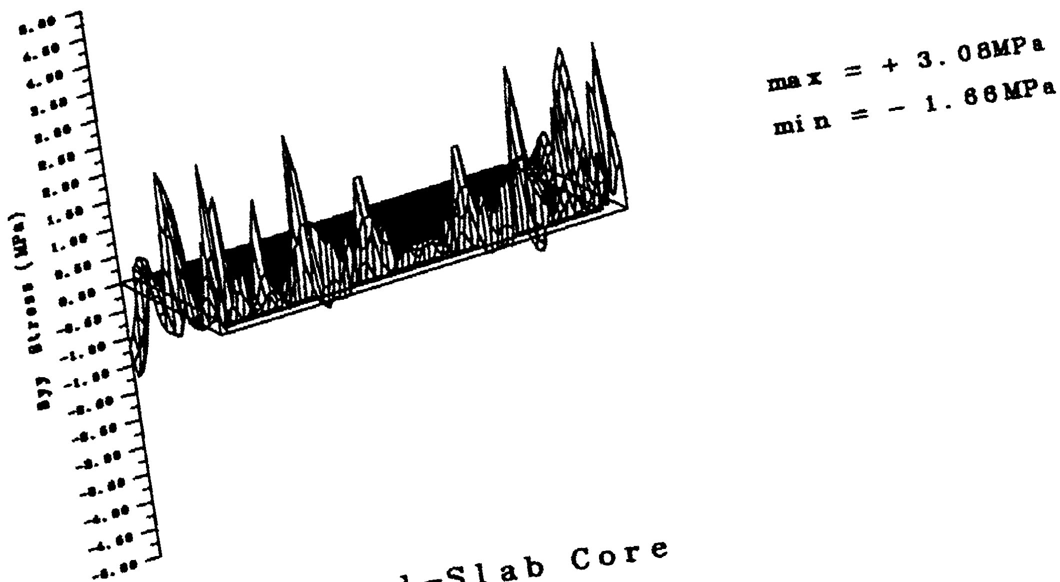

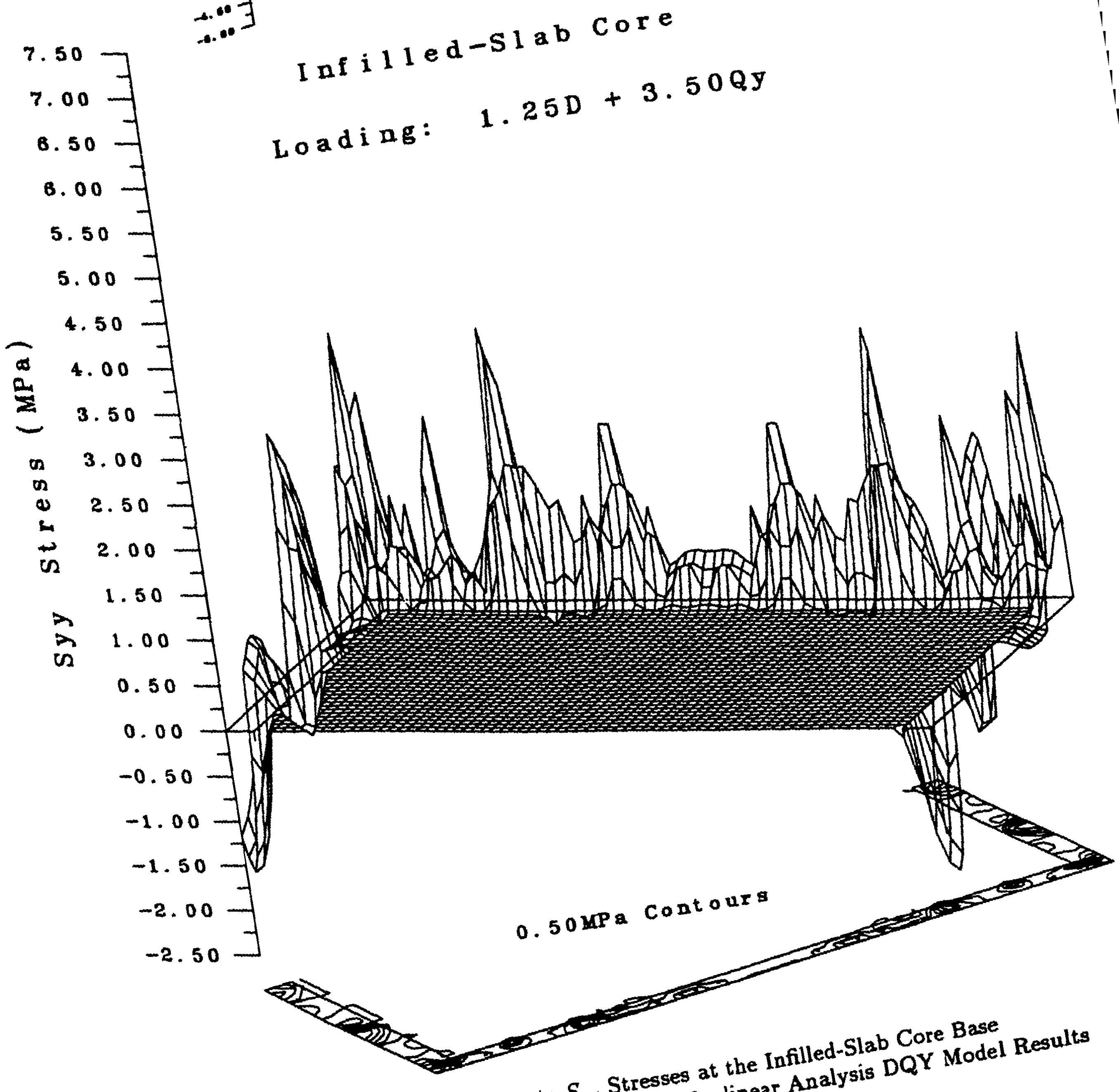

Figure 6.54 Distribution of the Concrete S_{yy} Stresses at the Infilled-Slab Core Base At Load Level $1.25\,D + 3.50\,Q_Y$ – Nonlinear Analysis DQY Model Results

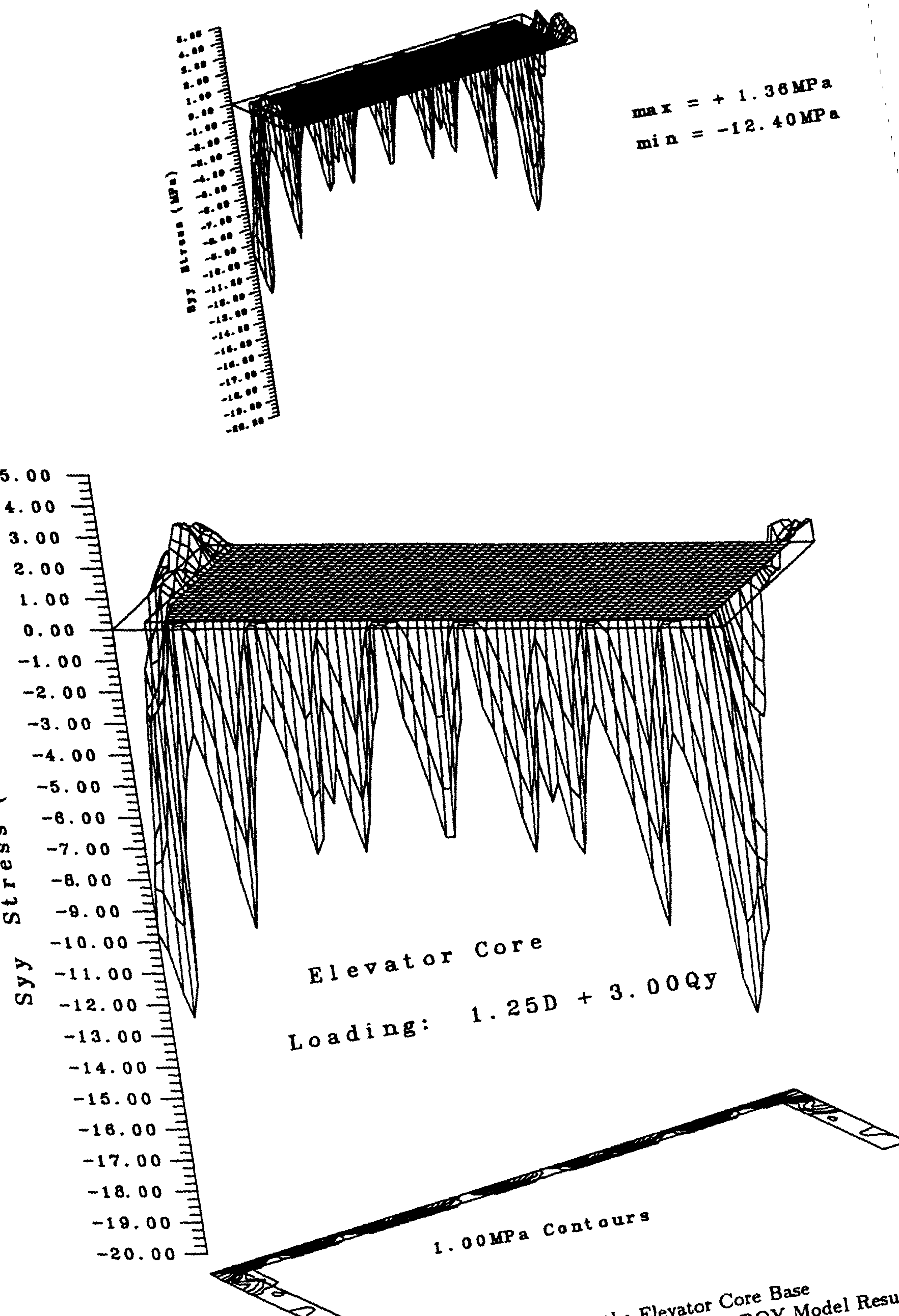

Figure 6.55 Distribution of the Concrete S_{yy} Stresses at the Elevator Core Base At Load Level $1.25\,D + 3.00\,Q_Y$ – Nonlinear Analysis DQY Model Results

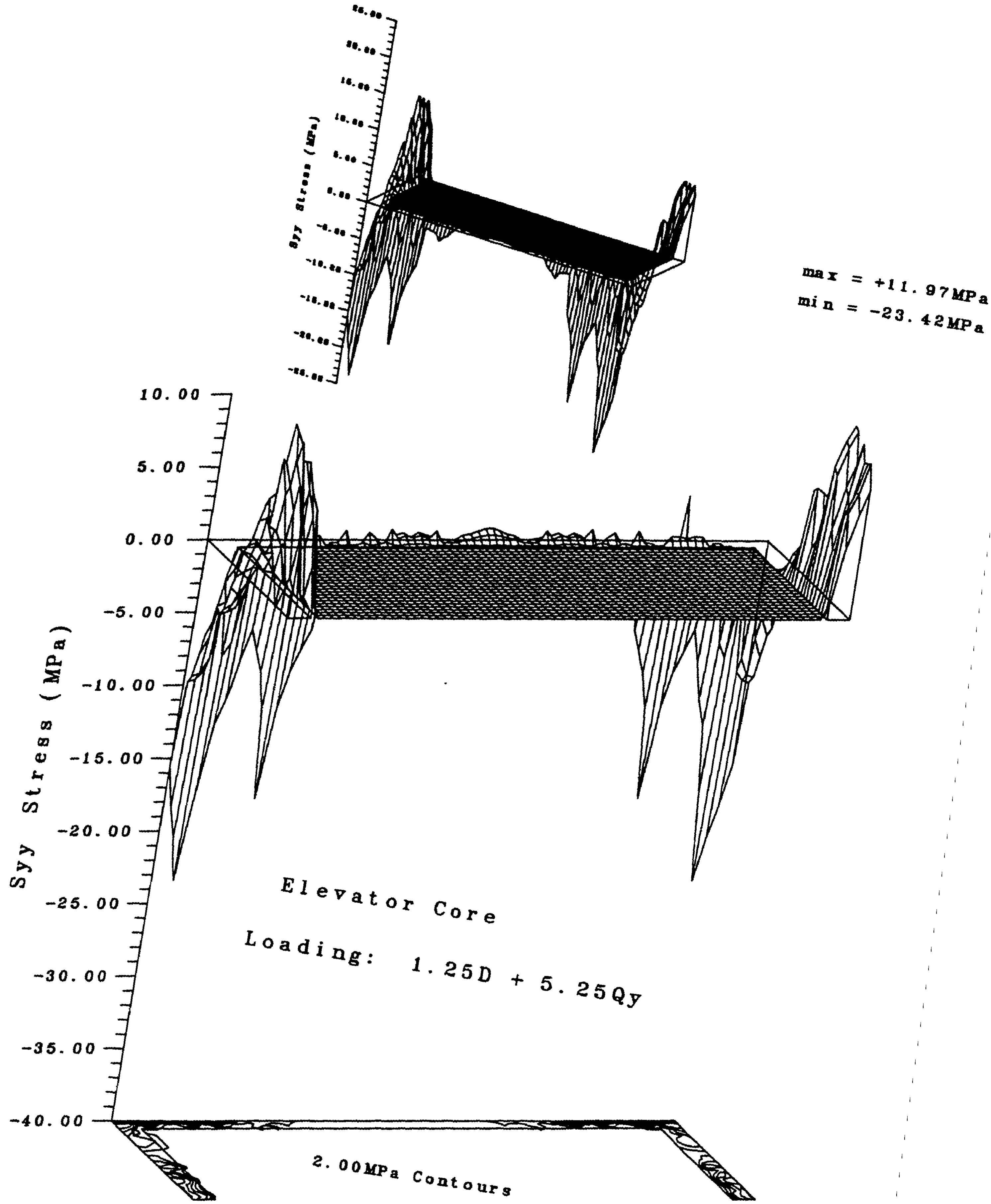

Figure 6.56 Distribution of the Concrete S_{yy} Stresses at the Elevator Core Base At Load Level $1.25\,D + 5.25\,Q_Y$ – Nonlinear Analysis DQY Model Results

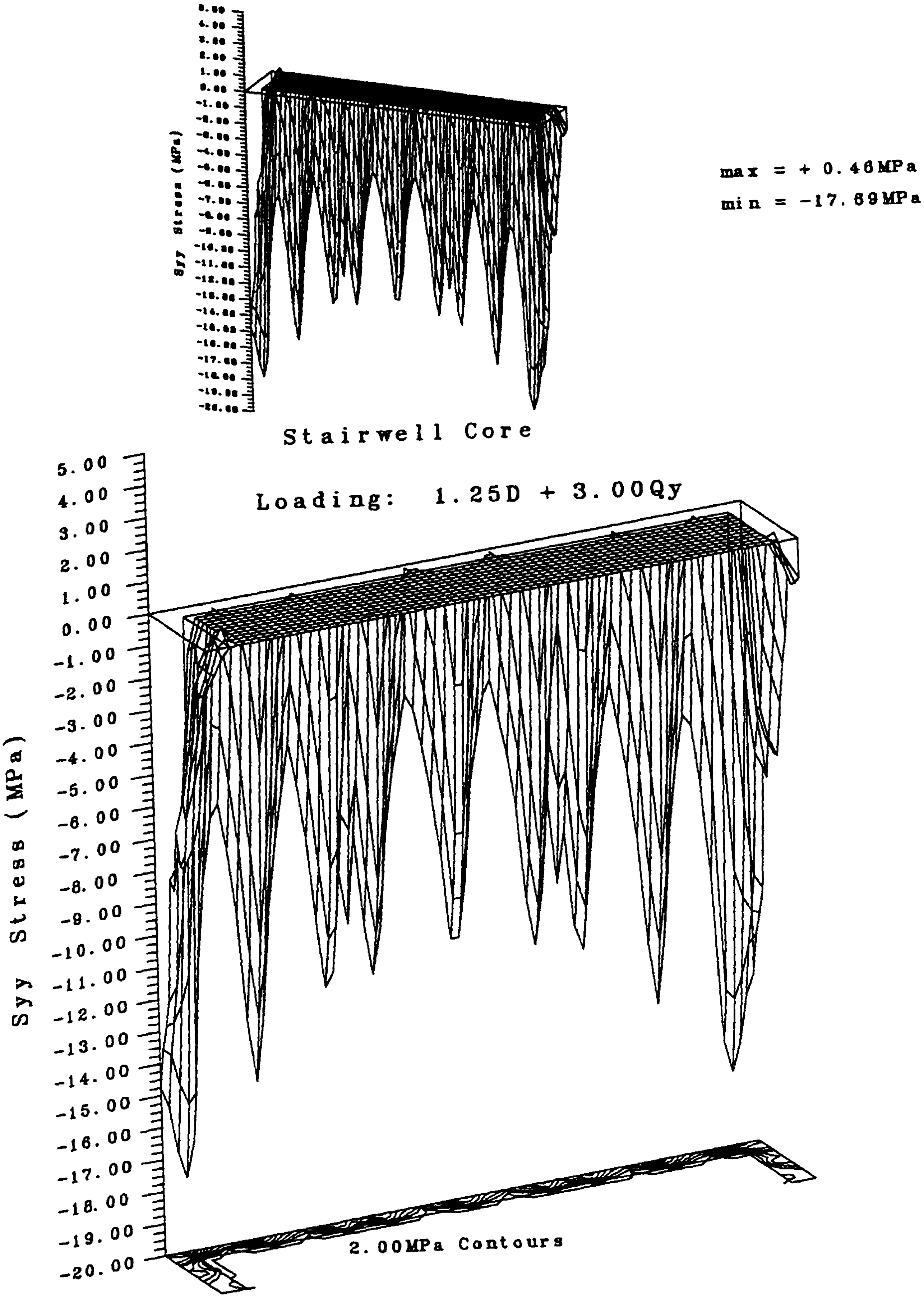

Figure 6.57 Distribution of the Concrete S_{yy} Stresses at the Stairwell Core Base At Load Level $1.25\,D + 3.00\,Q_Y$ – Nonlinear Analysis DQY Model Results

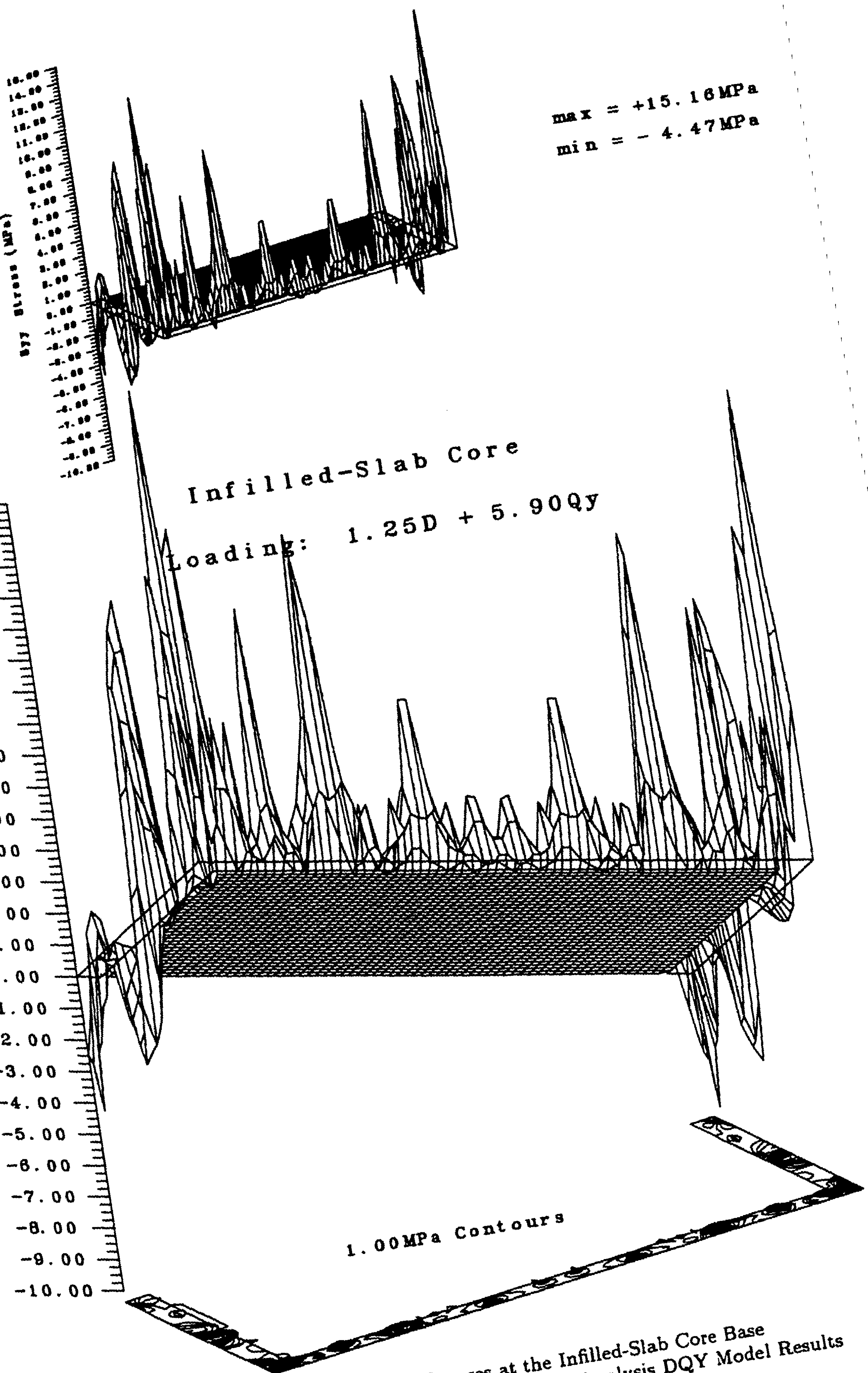

Figure 6.58 Distribution of the Concrete S_{yy} Stresses at the Infilled-Slab Core Base At Load Level $1.25\,D + 5.90\,Q_Y$ – Nonlinear Analysis DQY Model Results

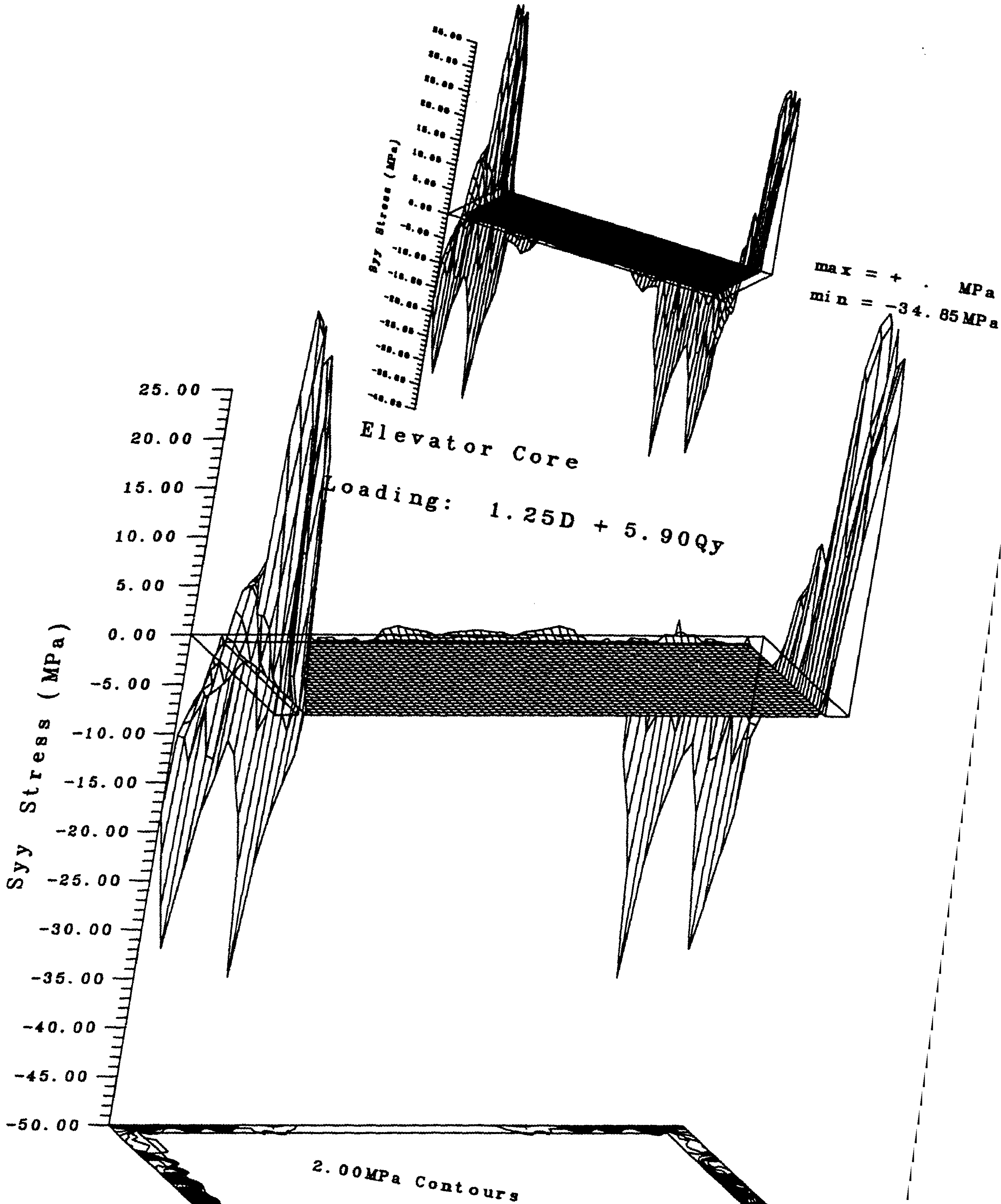

Figure 6.59 Distribution of the Concrete S_{yy} Stresses at the Elevator Core Base At Load Level $1.25D + 5.90Q_Y$ – Nonlinear Analysis DQY Model Results

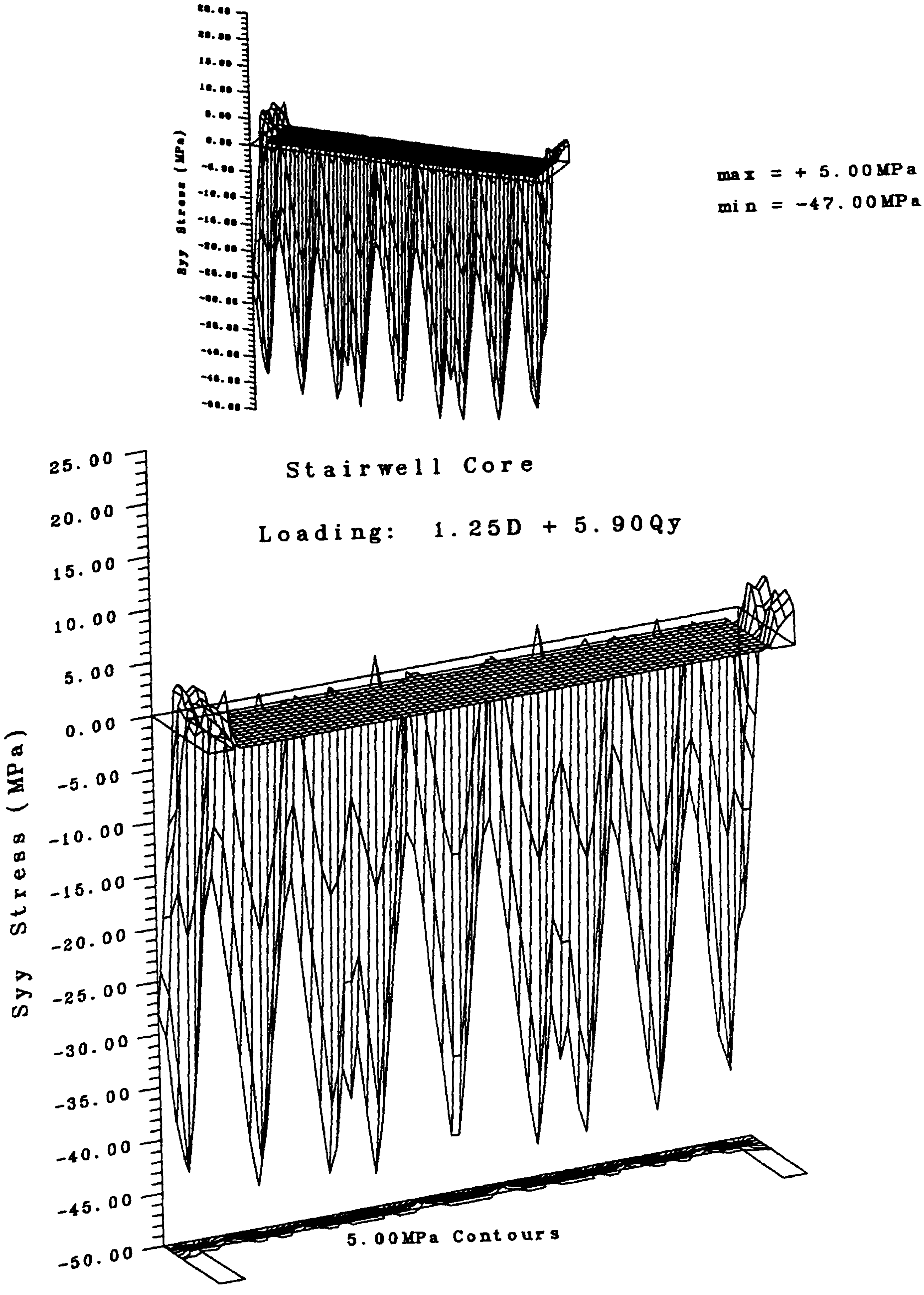

Figure 6.60 Distribution of the Concrete S_{yy} Stresses at the Stairwell Core Base At Load Level $1.25\,D + 5.90\,Q_Y$ – Nonlinear Analysis DQY Model Results

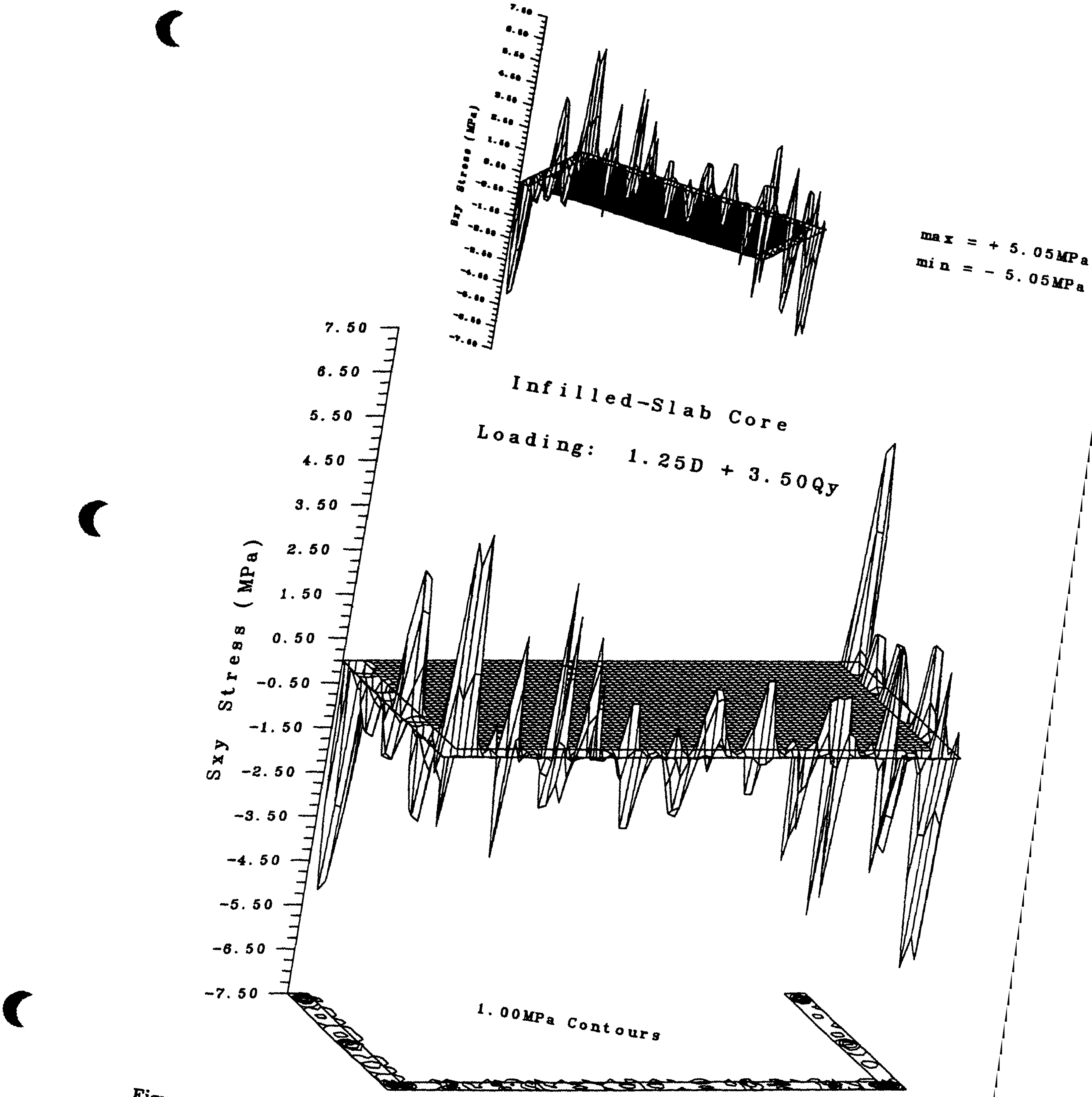

Figure 6.61 Distribution of the Concrete S_{xy} Stresses at the Infilled-Slab Core Base At Load Level $1.25D + 3.50Q_Y$ – Nonlinear Analysis DQY Model Results

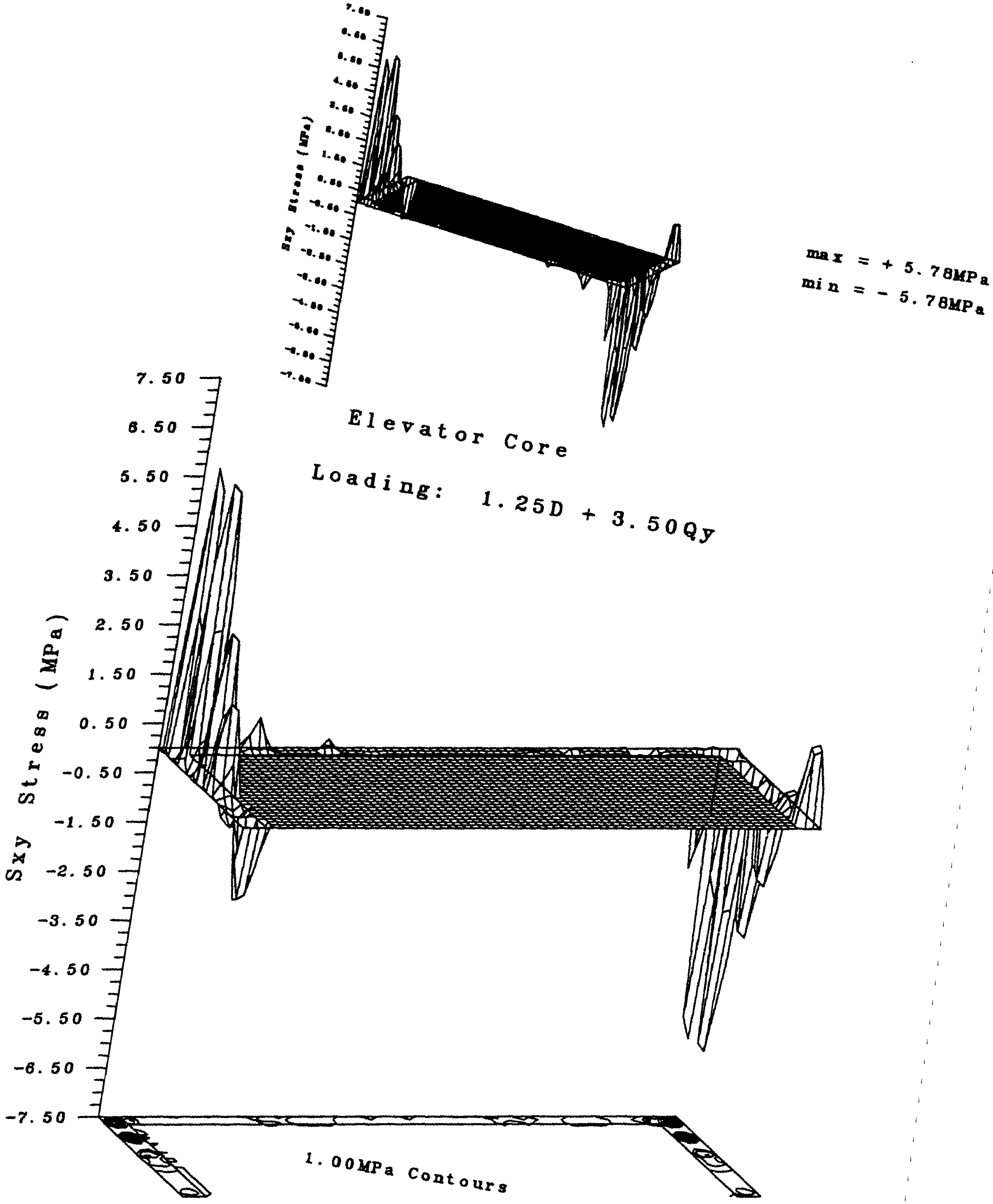

Figure 6.62 Distribution of the Concrete S_{xy} Stresses at the Elevator Core Base At Load Level $1.25\,D + 3.50\,Q_Y$ - Nonlinear Analysis DQY Model Results

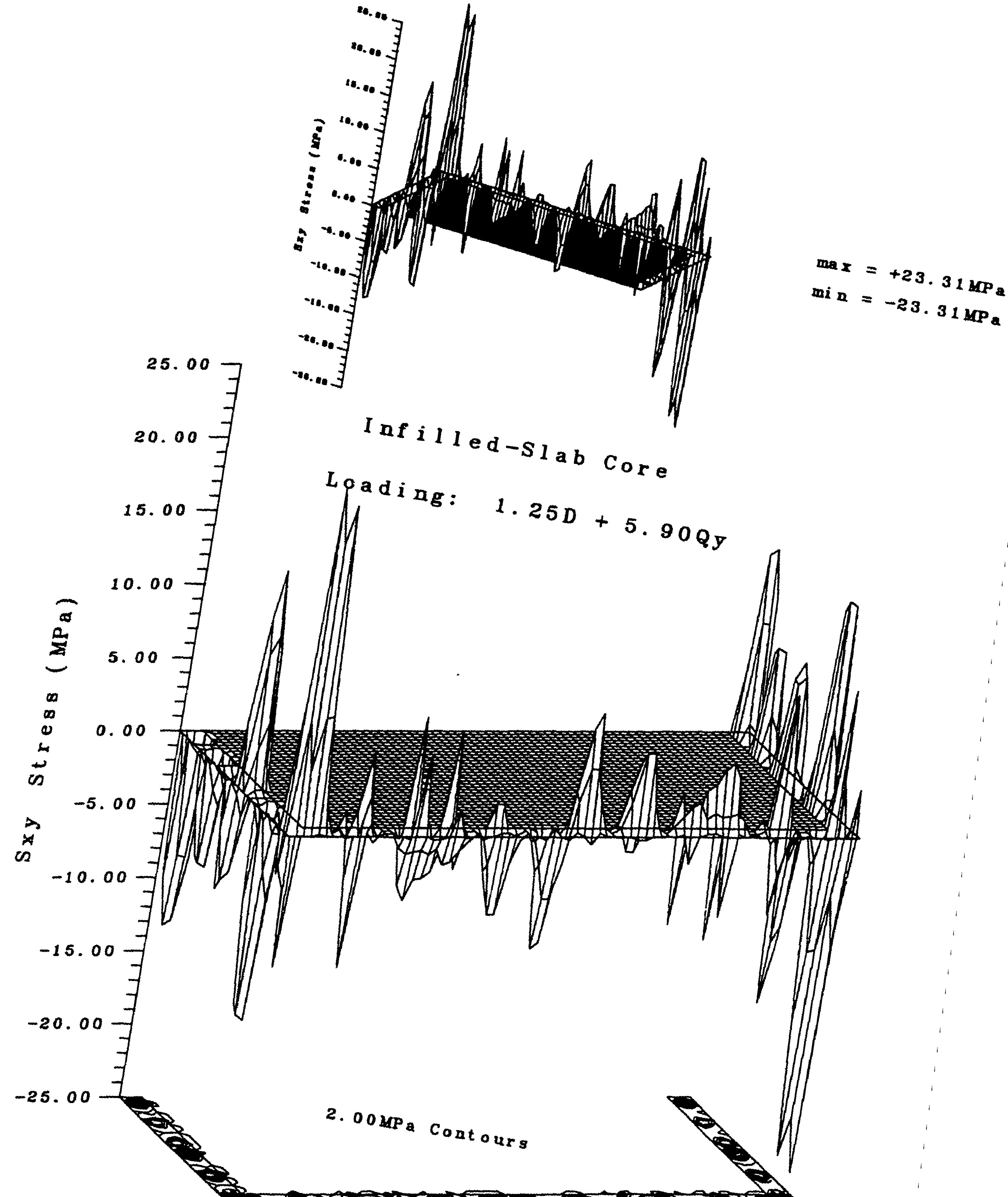

Figure 6.63 Distribution of the Concrete S_{xy} Stresses at the Infilled-Slab Core Base At Load Level $1.25\,D + 5.90\,Q_Y$ – Nonlinear Analysis DQY Model Results

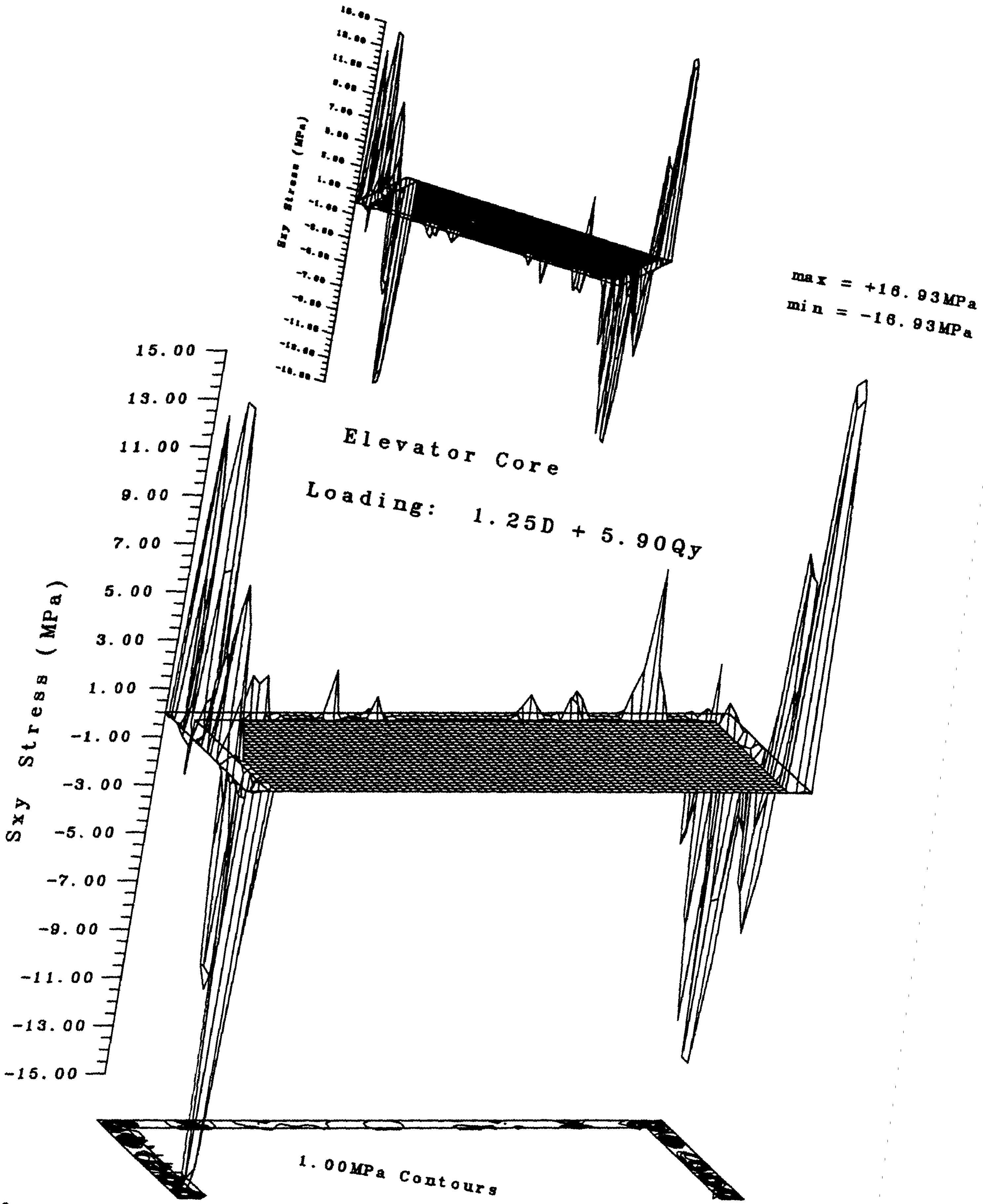

Figure 6.64 Distribution of the Concrete S_{xy} Stresses at the Elevator Core Base At Load Level $1.25\,D + 5.90\,Q_Y$ – Nonlinear Analysis DQY Model Results

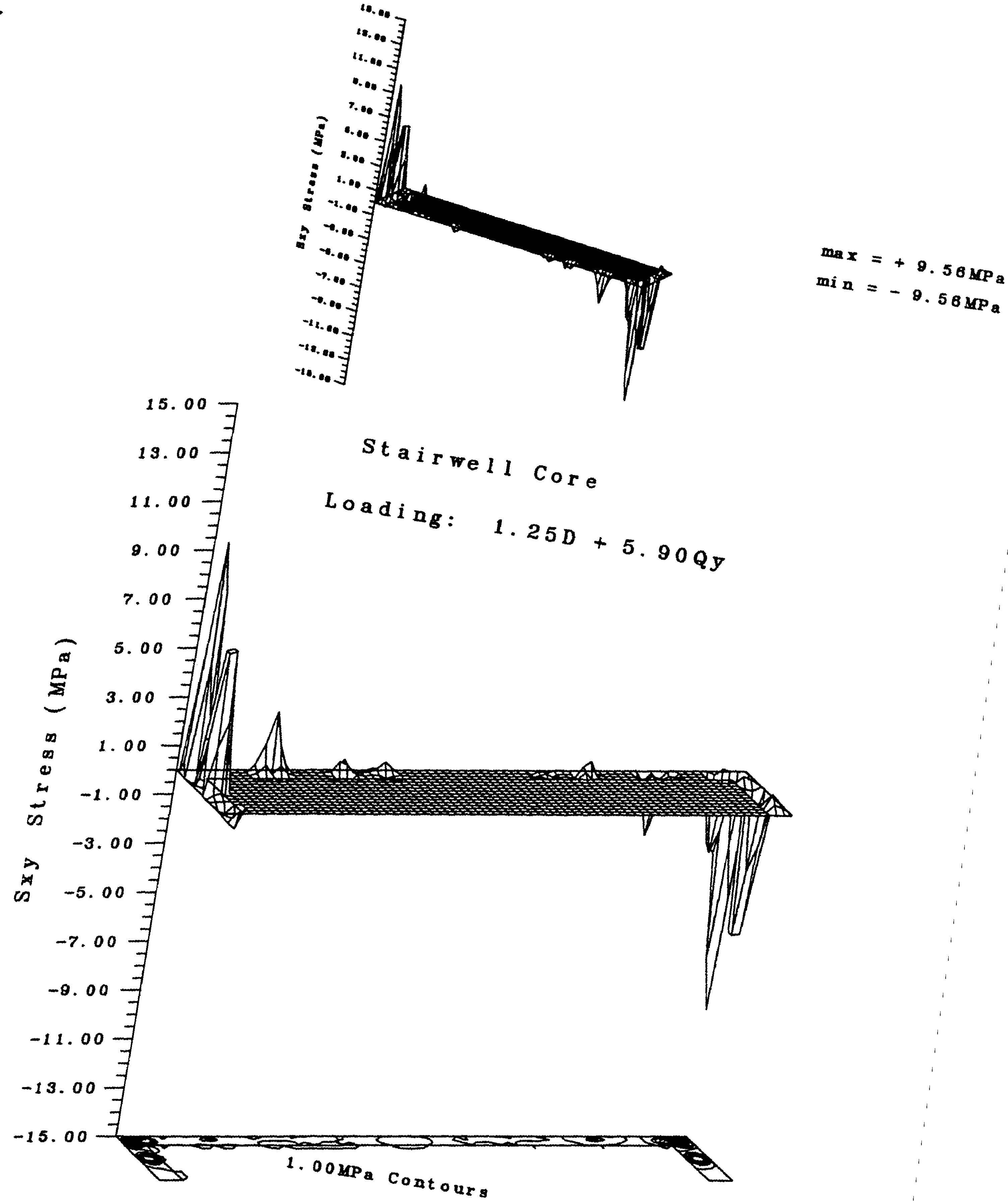

Figure 6.65 Distribution of the Concrete S_{xy} Stresses at the Stairwell Core Base At Load Level $1.25\,D + 5.90\,Q_Y$ – Nonlinear Analysis DQY Model Results

Chapter 7

Conclusions and Recommendations

7.1 Overall Structure Response

Typically, in analysis and design of core-slab-frame structures, the cores, coupling beams, columns and slab-band girders are considered as the lateral load resisting elements. Lintel beams stiffen enclosed slab edges along elevator core openings, surrounding and enclosed slabs are considered to transfer only in-plane axial forces between the cores and frames substructures; very short deep coupling beams, and slabs connecting the frames are not considered to be part of the lateral load resisting system and are designed for the gravity loads.

Present findings demonstrate that core-slab-frame structures subjected to earthquake and gravity loads, respond as a complex three-dimensional assemblage of cores, slabs and frames with interaction involving coupling and the associated stiffening effects, influencing the individual components and total structure response with an increased lateral stiffness by a factor of 2 to 3. Surrounding slabs connect the frame and core substructures creating a coupled core-slab-frame structure response causing the enclosed slabs to participate in the lateral loads resistance, thus, leading to large forces and load reversals transferred between the slabs and the cores. Combined with the coupling effects of the enclosed slabs within the cores, and the coupling and lintel beams, the cores respond as partially closed- and closed-sections. In addition to these actions, the fixed boundary conditions at the structure base further influence the lateral load structural response creating an overall stiffer lower 10% to 15% of the structure height.

The "actual" core-slab-frame structural response changes considerably from the elastic range to the nonlinear range to failure, with the stiffness of the structural components varying along the height. In the low load range, the cores substructure responds as a single coupled cores "box-action" unit showing uniform stress distributions in the core walls. As cracking and stiffness degradation of the core sections increases due to inelastic action in the lower storeys, at the higher load stages, the cores substructure response changes with a redistribution of stresses in the core walls demonstrating shear lag effects, tending to a individual linked core sections response as the structure approaches the ultimate load. As the earthquake load level increases, the concrete stress distributions in the cores lower region, become considerably nonlinear caused by the cracking of concrete and the yielding of reinforcement, demonstrating large stress peaks near the corner regions and the flange wall ends with several stress reversals occurring inbetween. At the ultimate load, the concrete stresses at the core base show very irregular distributions with stress concentrations of values exceeding the concrete compressive and tensile strengths indicating the effects of the three-dimensional core-slab structure response. Requirements of the various building codes for seismic design fall short of taking into consideration the "realistic" behaviour of the complete building structure. CSA Standard seismic design provisions are based on conditions of a concrete section subjected to uniaxial compression for typical members with a maximum compressive concrete strain of 0.003. The research findings show a more realistic value of the ultimate concrete compressive strain to be between 0.004 to 0.0045.

Core-slab-frame structures demonstrate tremendous stiffness and strength with large energy absorbing capability and ductile response when subjected to earthquake and gravity loads. Lateral load-deformation response until failure and the nonlinear inter-storey deformation profiles through the height of the structure demonstrate that concrete cracking, yielding of reinforcement and formation of plastic hinging extend over the lower 25% to 33% of the structure height. More importantly, the majority of damage occurs in the lower 10% to 15% of the structure height, indicating a large degradation in stiffness besides identifying the critical region for design. Critical areas are located in the surrounding and enclosed slab-core regions and junctions in the vicinity of the core flange/web wall corners, ends and junctions, and the slab-coupling and lintel beam connections where separation occurs between the slabs and the core walls resulting in the deterioration of slab-core wall-beam joint stiffness and integrity. Proper detailing is required for the slab-core wall-beam junctions, ends and corners, moreso in the bottom storeys, for ductility and seismic response.

7.2 Summary of the Present Investigation

Linear elastic and nonlinear inelastic analyses are performed for a typical core-frame-slab building structure examining the following:

1. Complete structural response to failure subject to earthquake and gravity loads.

2. Finite element modeling techniques and problems encountered for the structural components and material characteristics.

3. Contribution of the structural components: cores – open-, closed-, partially closed-sections, slabs – enclosed and surrounding cores, and coupling and lintel beams, on the overall structural response.

4. Analysis procedures are recommended.

5. Design procedures and reinforcement details are recommended for the various building components.

7.3 Summary of Analysis Findings

Response of core-slab-frame structures subject to earthquake and gravity loads demonstrate:

1. Complex three-dimensional behaviour with interaction occurring among the cores, beams, slabs and frames, which can only be determined employing three-dimensional finite element analysis techniques.

2. Enclosed and surrounding slabs, lintel and coupling beams do participate in the lateral load resistance. Also, the governing earthquake loading direction is not necessarily in the direction of the beam span, but is dependent on the structure configuration.

3. Response of core sections is altered to: infilled cores as closed box-sections, elevator cores as partially closed-sections, and stairwell cores as closed-sections.

4. Effective core flange/web wall lengths and slab widths participate in the lateral load resistance, varying between 10% to the entire wall length and slab width.

5. The above aforementioned actions result in an overall increased lateral and torsional stiffness of the structure by a factor of 2 to 3.

6. Combined with the fixed conditions at the base region, an additional 40% increase in the structural stiffness occurs in the lower 10% to 15% structure height.

7. Earthquake load effects are as significant as the gravity load effects.

8. Largest forces in the cores and slabs occur in the lower 10% to 15% structure height, demonstrating local concentrations and several reversals.

9. Critical areas for design include: slab-core wall ends, corners and junctions, around the slab-cores perimeter in a slab band width equal to 3 to 5 times the core wall thickness, and slab-coupling/lintel beam-core wall connections. Deterioration of the structural integrity of these regions due to inelastic actions occurs, requiring additional reinforcement and special detailing in these regions.

10. Plastic hinging region extends over the lower 25% to 33% height of the structure.

11. Majority of the inelastic action and damage is concentrated in the lower 10% to 15% structure height.

12. Considerable strength, ductility and energy absorption capabilities are demonstrated.

13. Failure mode includes local buckling of the cores in the lower region, being critical in the design.

7.4 Summary of Design Recommendations

Current CSA (ACI) concrete design codes are lacking for:

- cores - open-, closed- and partially closed-sections,
- slabs - "surrounding" and "enclosed" within cores,
- coupling and lintel beams, and
- critical core wall-beam-slab junctions, corners and regions.

Design procedures and reinforcement detailing are recommended taking into consideration the three-dimensional structural behaviour for the various building components, giving proposed code Clauses for the items listed below:

1. Cores:

   [i] Dimensional requirements

   [ii] Effective slab widths - lateral load resistance

   [iii] Concentrated reinforcement regions

   [iv] Confined core wall regions

   [v] Post-cracking behaviour of cores

   [vi] Plastic hinging regions

2. Enclosed and surrounding slabs:

   [i] Maximum bar sizes

   [ii] Maximum spacing of flexural reinforcement

   [iii] Maximum flexural reinforcement - ductility requirements

   [iv] Longitudinal reinforcement requirements

   - Critical slab-core wall corner and end regions

   [v] Hoop confinement of longitudinal reinforcement

3. Coupling beams:

   [i] Diagonal reinforcement limitations

   [ii] Development of diagonal reinforcement

   [iii] Hoop confinement of diagonal reinforcement

   [iv] Secondary cage reinforcement

4. Lintel beams

5. Core wall-beam-slab joints

7.5 Linear Elastic Response

Elastic analysis findings demonstrate that the contribution of the various structural components of core-slab-frame structures significantly influence the overall structural behaviour.

- For the structure deformations, eliminating the E-slabs, coupling and lintel beams doubles the maximum inter-storey twist. Ignoring the S-slabs flexural actions triples the maximum twist and in addition, elimination of the E-slabs and the coupling and lintel beams results in an increase of 45% for the top drift, a 30% larger inter-storey drift in the ground storey and a 4 fold increase in the maximum twist.

- Ignoring the E-slabs, lintel and coupling beams, increases the core corner stresses by 20% to 40% in the lower storeys, triples the slab stresses at the S-slabs-core corners at level 1, increases the S-slabs M_{yy} moments by 15% to 30% at the slab-Core flange wall end and slab-Stair corner regions indicating that the length of the Core flange walls combined with the interaction of the structural components increases the stiffness of the slab-core corner region. The S-slabs M_{xy} moments show a 25% decrease at the more flexible slab-Core flange wall end region, and a 3 fold increase at the slab-Elev corner due to the three-dimensional slab-core walls interaction stiffening the corner region.

- Elimination of the S-slabs flexural actions, increases the S-E-slabs S_{yy} and S_{xy} stresses by 25% to 50% at the slab-core corner regions at the ground storey. At the E-slabs-core corner regions, the M_{xx} moments are reduced to small values, the M_{yy} moments by 20% and the M_{xy} moments by 85%.

- Eliminating the S-slabs flexural actions, the E-slabs and the lintel and coupling beams, results in a 26% increase in the core S_{yy} stresses at the base, but has little effect on the shear stresses indicating approximately equal relative shear stiffnesses of the core sections. For the S-E-slabs, a 10% to 25% increase occurs in the stresses at the slab-core wall junctions, corners and flange wall end regions in the lower storeys.

Therefore, the core-slab-frame structure subject to earthquake load shows large inter-storey deformations and stresses in the cores and slabs in the lower 20% to 25% of the structure height, with maximum values occurring in the lower 10% of the structure height. Hence, the three-dimensional interaction of the surrounding and enclosed slabs, the coupling and lintel beams must be taken into consideration in the lateral load response resulting in an increase of about 1.5 to 3 times in the structural stiffness.

7.6 Nonlinear Inelastic Behaviour

7.6.1 Material Properties and Design Considerations

Examination of the Q_X earthquake load-drift response of the core-slab structure shows that:

• Tension-stiffening of the concrete and steel reinforcement improves the overall energy absorption characteristics by 25% for the Regions 2 and 3 of the structural response.

• Varying the amount of reinforcement through the height of the core walls to maintain a minimum steel content gives a better overall response with a 10% higher ultimate load, an improved Region 3, but with a reduced Region 4 predicting a 25% lower top drift, ductility and energy absorption capability, compared with using a uniform steel content throughout the height of the core walls.

• Considering the dead and live loads with a varying steel content through the height of the core walls for a minimum reinforcement, demonstrates the best earthquake load response predicting the largest ultimate load being 17% higher, a slower stiffness deterioration and the better energy absorption characteristics showing a well defined Region 3 and good ductility, with a 48% larger top drift, compared with the case when the dead loads are ignored.

• Uplift dead load conditions shows the shortest and lowest response giving a 25% lower ultimate load and top drift with about 50% lower ductility and energy absorption capacity, compared with considering the dead and live loads acting together with the earthquake loading.

7.6.2 Q_X Earthquake Loads Response

DQX model has an ultimate load of $3.40 Q_X$ and a top drift of $871\,mm$ with a ductility ratio of 9.90. At the ground storey, the maximum inter-storey drift is $40\,mm$, the slab-Core section corner inter-storey vertical deflection is equal to $53\,mm$, and the inter-storey twist response demonstrates a deterioration in the torsional stiffness to about one-tenth of the uncracked stiffness value. Plastic hinging extends over the lower 20% to 25% of the cores height.

At the ultimate load, very large strains are developed in the concentrated reinforcement at the ground level of the core sections at the flange wall end and the flange-web corner locations. Maximum tensile strains range from 0.0083 to 0.030 and the compressive strains are about 50% of the yield strain. Near the ultimate load, the concrete S_{xx}, S_{yy} and S_{xy} stresses in the core sections at the ground storey demonstrate very irregular nonlinear distributions composed of several jagged peaks at the web-flange corners and wall end regions, and stress reversals inbetween, with values of $-47\,MPa$ to $4\,MPa$. Concrete cracking in the corner regions results in separation of the slab-core web wall junctions, extending across the majority of the flange and web wall lengths at the ground level.

Failure mode of the DQX model consists of the rupture of the concentrated tension reinforcement at the Elev and Stair section flange-web corners and all core flange wall end locations, while the Core section flange-web corner tension reinforcement does not rupture at failure. Crushing of the concrete occurs at the compressive Core section flange-web wall corner region, the Elev section flange-web wall corner and end regions, and along the Stair section flange wall due to the partially closed-section configurations and short flange walls. This causes instability and deterioration of stiffness in each core section resulting in buckling of the flange walls in the lower 10% of the structure height.

7.6.3 Q_Y Earthquake Loads Response

DQY model has an ultimate load of $5.90\,Q_Y$ and a top drift of $1190\,mm$ with a ductility ratio of 25.87. At the ground storey, the largest inter-storey drift is equal to $81\,mm$ and the slab-Core section corner inter-storey vertical deflection is equal to $107\,mm$. Plastic hinging extends over the lower 33% of the cores height, basically due to the coupling action ot the core elements.

At the ultimate load, very large strains of 0.010 to 0.10 are developed in the concentrated tension reinforcement at the flange-web corner and flange wall end locations at the ground level of the core sections. Near the ultimate load, very irregular concrete S_{xx}, S_{yy} and S_{xy} stress distributions develop in the core sections at the ground storey, showing several stress peaks and jagged humps throughout the core walls and at the flange-web wall corners and flange wall ends with stress reversals inbetween these regions. Peak stresses are $-47\,MPa$ to $4\,MPa$ indicating both crushing and cracking of the concrete. The concrete S_{xy} stresses demonstrate that the core flange walls resist the majority of the shear.

Failure mode of the DQY model comprises of concrete crushing in the Stair section flange-web corner wall regions, causing rupture of the concentrated reinforcement at the Core web-flange corner locations and Elev flange wall ends. This results in tensile splitting and separation of the slab-Core section across one-half of the flange wall and one-third of the web wall lengths at the ground level. Consequently, concrete crushing occurs in the the Elev web-flange corner regions and the Core flange walls leading to instability and deterioration of stiffness in these core sections, with buckling of the web-flange wall corner regions occurring in the lower 10% of the structure height.

7.6.4 Contribution of the Structural Components

Nonlinear analysis findings demonstrate that the contribution of the various structural components of core-slab structures significantly influence the overall lateral load response.

• Consideration of the S-slabs flexural actions results in a similar lateral load response, giving the same ultimate load, but with a shorter Region 4 showing a 50% reduction in the top drift, and a 30% decrease in the energy absorption capacity and the ductility ratio.

• Consideration of the E-S-slabs improves the lateral load response showing a 20% increase in the lateral stiffness for the Regions 2 and 3, a 25% to 65% reduction in the top drift, the maximum inter-storey drift and twist, a 50% increase in the torsional stiffness in the lower 20% structure height, a 15% to 20% higher Region 3 and ultimate load, but demonstrates in a 20% to 45% decrease in the energy absorption capacity and the ductility ratio.

• Consideration of the dead loads improves the lateral load response doubling the ranges of Regions 2 and 3, the ultimate load and the energy absorption characteristics until failure, and increasing the maximum torsional deformation at the base by a factor of 5, showing upto a 20% increase for the top drift and the maximum inter-storey drift.

• Consideration of the three-dimensional interaction of the core sections, the E-S-slabs, and the coupling and lintel beams improve the lateral load-drift and twist response of the structure to failure, demonstrating a 65% increase in the lateral stiffness and a 30% increase in the torsional stiffness. The Region 2 and the ultimate load are increased by a factor of about 3, giving a Region 4 and increasing the total energy absorption capacity by about 10 to 12 times, and showing a 2 to 5 fold increase for the ductility ratio.

• The plastic hinging region increases in length from the lower 10% of the structure height when ignoring the dead loads, to the lower 20% of the height for the planar model to the lower 25% to 33% of the structure height when taking into consideration the three-dimensional response of the structure and the gravity loads.

Therefore, the three-dimensional interaction and associated coupling and stiffening effects of the surrounding and enclosed slabs, the coupling and lintel beams, and the core sections must be taken into consideration when evaluating the earthquake load response of core-slab-frame structures. These actions result in an increased lateral and torsional stiffness, total energy absorption capacity and ductility, and combined with the fixed conditions at the base significantly stiffen the lower region of the structure.

7.7 Core Response and Design

Analysis results for the core-slab-frame structure show that the influence of the core structural elements must be considered. converting the response of the cores to that of closed- and partially closed-sections. Core sections with enclosed slabs within their cross-section. combined with coupling and lintel beams. respond as closed box-sections. Elevator cores are stiffened by lintel beams and surrounding slabs. and respond as a partially closed-section. Stairwell cores typically have partial enclosed slabs within the web-flange wall regions and combined with beams. behave as closed-sections. In addition. combined with the fixed conditions at the ground level creates a large increase in the core stiffness in the lower 10% to 15% structure height. Resulting shear and interactive force distributions demonstrate that the cores resist a large portion of the total shear in the lower storeys. at the ground storey, with nearly equal shear stiffnesses.

Axial S_{xx}, S_{yy} and shear S_{xy} stresses and bending M_{xx}, M_{yy} and twisting M_{xy} moment distributions in the core sections due to earthquake loading are largest in the lower 20% to 25% of the structure height. Shear stresses decrease with reversals occurring between levels 1 to ground and the base, demonstrating the shear lag effect at the stiffer flange-web corners. At the lower core regions, the S_{xx}, S_{yy} and S_{xy} stresses due to dead loads are 50% to 2 times those due to earthquake loads. The resulting earthquake load M_{xy} moments are 25% to 2 times the M_{xx} and M_{yy} moments, while the M_{xx}, M_{yy} and M_{xy} moments due to dead loads are upto 5 times those due to earthquake loads.

Therefore. the critical region for seismic design is located in the lower 10% structure height with the largest core stresses and moments in the ground storey. demonstrating very irregular distributions across the core walls composed of concentrations of 2 to 4 larger values at the web-flange corners. flange wall ends and one-third web wall lengths with several reversals occurring inbetween these locations. These irregular distributions are caused by the three-dimensional interaction of the cores with long flexible web walls and stiffer flange-web corner regions and flange wall ends, the slabs and beams combined with the fixed conditions near the base region stiffening the structure in the lower storeys.

Core S_{xy} stress distributions demonstrate that the wall dimensions considerably influence these stresses with effective flange wall lengths participating with the web walls. Determination of the effective flange wall length is dependent on the three-dimensional behaviour of the core-slab-frame structure. One important factor not considered in determining the effective core flange wall width is the interaction of the slabs within and surrounding the core sections, resulting in an effective slab width participating with the core walls and beams in the lateral load resistance. In the higher load range, the nonlinear inelastic response must be taken into consideration in the design. Complex three-dimensional interaction between the core sections, beams, slabs and columns influences the effective core section cross-walls providing lateral support resulting in equivalent beams or effective slab widths participating in the lateral load response [Manatakos (1989)] which must be taken into consideration when determining the confined core wall regions and for the dimensional requirements. More research is required in this area.

7.7.1 Effective Core Flange/Web Wall Widths

Analysis findings for the structural lateral load response demonstrate complex interaction occurring between the surrounding and enclosed slabs, the coupling and lintel beams, and the core flange/web walls, resulting in effective flange/web wall widths participating with the web/flange walls of the core sections that influence the dimensional requirements in plastic hinging regions. Depending on the core configuration, between one-third to the entire core wall length is effective in the lateral load response. Further research is needed to study these effective wall lengths.

Dimensional requirements of planar structural walls in the CSA Standard (Cl 21.5.3) give conservative values for the wall thicknesses which are not based on consideration of the "actual" three-dimensional behaviour of a core section.

7.7.2 Confined Core Wall Regions

Concentrated reinforcement regions and confined compression regions at the core wall ends, corners and junctions should be designed as equivalent confined columns along plastic hinge lengths, to preserve their integrity at higher load levels.
Recommendations for confined core wall regions:

1. Confinement length of flange/web walls:
   - [i] $1/5^{th}$ of the adjoining web/flange wall.
   - [ii] Over any partially enclosed or surrounding slabs adjoining to the wall.
   - [iii] 3 to $5\,b_w$ (wall thickness)
     0.20 to 0.25 of the wall distance from beam joints.
2. Core walls of width $\leq$ 0.33 to 0.40 of the storey height, confine the entire wall width.

Suggested limits for the minimum wall compression zone:
(Add to Cl 21.5.3 and Cl 21.5.7 requirements)

$$c_{c_{\min}} \geq 3b_w \tag{7.1}$$

$$c_{c_{\min}} \geq l_w/5 \tag{7.2}$$

where l_w is the horizontal length of the core wall and b_w is the wall thickness.

Further research is needed to study the effective flange/web wall widths participating with the core web/flange walls along with the core wall components in determining the effective and confined cross-sectional area of a core section.

7.7.3 Concentrated Reinforcement Core Wall Regions

CSA Standard provides no guidance for determining the effective core flange/web wall cross-sectional area for the concentrated reinforcement requirements (Cl 21.5.6). Stress distributions in cores due to earthquake loading in plastic hinge regions, indicate a concentration of resistance at the wall end and corner regions. Three-dimensional interaction occurs between the flange and web walls. resulting in a part of the flange/web wall length at the ends and corners that participates beneficially in the lateral load resistance and must be considered in design.
Recommended concentrated reinforcement regions:

[i] 10% to 25% of core wall ends.

i.e. uniformly distributed reinforcement in the
central 75% to 80% of the wall cross-sectional area.

[ii] 3 to 5 b_w (wall thickness) at web/flange corners and junctions.

Further study is needed taking into consideration the three-dimensional core section response and the core configuration.

7.7.4 Cracked Strength of Core Sections

To ensure adequate post-cracking capacity of a core/wall section to prevent collapse. CSA Standard Cl 21.5.6.4.2 requires that the factored design core flexural resistance must be greater than the cracked core flexural strength.

$$M_{r_{core}} \geq M_{cr_{core}} \tag{7.3}$$

However. no guidance is given to determine the value of the cracked core flexural strength $I_{cr_{core}}$. Also. no provisions exist in the CSA Standard Cl 21 seismic provisions for the torsional post-cracking core behaviour. Nonlinear inelastic analysis results for earthquake and gravity loads demonstrate that the majority of cracking and damage occur in the lower 10% to 15% of the structure height due to plastic hinging, with separation between the core walls and the slab junctions, resulting in a considerable loss of stiffness near the ultimate load.
Recommend using values of:

$$I_{cr_{core}} = 40\% \text{ to } 25\% \ I_{\text{uncracked core}} \tag{7.4}$$

$$T_{cr_{core}} = 25\% \text{ to } 15\% \ T_{\text{uncracked core}} \tag{7.5}$$

For the:

[i] Individual core sections response.

[ii] Coupled cores substructure box-action response.

Further research is needed in the determination of the cracked flexural and torsional stiffness values for cores, which is very complex and is dependent on the core configuration, the connecting structural elements, and the type and level of loading.

7.7.5 Plastic Hinging Regions in Cores

Nonlinear analysis results demonstrate the plastic hinging region extending upto 25% to 33% of the lower height of core-slab-frame structures during a severe earthquake. This is larger than the CSA Standard (Cl 21.5.2.2) for uniform uncoupled planar walls, suggesting a plastic hinge length equal to $l_w \geq h_w/6$ and $\leq 2l_w$, which does not consider three-dimensional core response. Further study is needed examining the lower 10% to 15% of the structure height, where the majority of damage occurs due to earthquake loadings, being critical in design requiring proper reinforcement detailing and confinement of the concrete.

7.8 Lintel Beam Response and Design

Earthquake load response of core-slab-frame structures show lintel beams frame into elevator core confined flange wall ends which may also join with coupling beams, thus, converting the Elevator core into a partially closed-section. The resulting core torsional response causes the lintel beams to participate in the lateral load resistance, becoming an integral part of the structure. The resulting lintel beam forces due to earthquake loads are as significant as those due to the gravity loads. Therefore, lintel beams must be designed as ductile members following the seismic design provisions. The lintel beam forces due to Q_Y earthquake loads, in the direction perpendicular to the beams, are 2 to 5 times larger than the forces due to the Q_X earthquake loads. The forces due to dead loads are 2 to 5 times larger than those due to the earthquake loads. Hence, the lintel beam design is influenced by the lateral loading in the direction perpendicular to their span due to the three-dimensional coupled cores response.

An important factor influencing the seismic response of lintel beams is that typically a slab is present on one side converting the beams into equivalent L-beams across an elevator core. Further research is needed to determine and study the influence of the effective slab widths forming equivalent L-beams, the core flange walls combined with the slabs, and other structural components participating in the lateral load resistance on the overall response and seismic design of lintel beams. Also, no design provisions exist for lintel beam-core wall connections of partially closed sections, specifically at the flange wall ends where the out-of-plane flexural actions of the core walls are significant creating shear forces and bending moments in the lintel beams.

The lintel beams of the core-slab-frame structure do not satisfy the CSA Standard dimensional requirements of Cl 21.3.1 to qualify as ductile lateral load resisting elements and are not considered part of the lateral load resisting system. Typically lintel beams are designed following Cl 21.8 requirements to ensure that gravity load resisting members of a structure maintain their strength and integrity when subjected to earthquake loading. Dimensional requirements of Cl 21.3.1 do not take into consideration the three-dimensional structural behaviour.

Results show that torsional moments must be considered in the design of the lintel beams. No special provisions exist for ductile design of reinforced concrete members for torsion due to seismic loading in the CSA Standard (Cl 21).

7.9 Coupling Beam Response and Design

In the building short direction, the short span E-S coupling beams and the Stair section were originally designed for gravity loads only. However, the analysis results demonstrate that the cores substructure responds as a combined complex system of three core flange walls connected together by two sets of coupling beams spanning between the flange walls and web-flange corners. Therefore, all of the coupling beams must be designed using diagonal reinforcement for seismic ductility requirements. CSA Standard Cl 21 seismic provisions offer no specific guidelines for the design of deep coupling beams other than the requirement for diagonal reinforcement confined by hoops (Cl 21.5.8).

For the short, deep E-S coupling beams, the resulting forces due to Q_X earthquake loads are 2 to 3 times the forces due to dead loads which are 2 to 3 times the forces due to Q_Y earthquake loading. For the longer I-E coupling beams, the forces due to Q_Y earthquake loading are about equal to those due to dead loads, which are 4 to 5 times the forces due to Q_X earthquake loads. Maximum beam forces occur at the one-third and the mid-height structure level coupling beams for the Q_Y and Q_X earthquake loadings, respectively.

Further study is needed examining the effects of the core-slab-beam support conditions and the various configurations on the response of coupling beams subjected to earthquake loads. The governing earthquake loading direction for design is not necessarily in the direction of the span of the beam. Also, research is needed to investigate multiple coupled core substructures and the influence of the structural components present.

7.9.1 Diagonal Reinforcement Limitations

No limitations on the amount of diagonal reinforcement are provided in the CSA Standard Cl 21 seismic design provisions. By extension, from the seismic design provisions for ductile columns Cl 21.4.3.1 and beams Cl 21.3.2.1, the following requirements are recommended:

1. Minimum area of diagonal reinforcement:

$$A_{s_{\text{diag min}}} \geq 0.01 \left(\frac{A_g}{2}\right) \tag{7.6}$$

2. Maximum area of diagonal reinforcement:

$$A_{s_{\text{diag max}}} \leq 0.06 \left(\frac{A_g}{2}\right) \tag{7.7}$$

3. Minimum of 4 bars - One bar placed at each hoop corner.

Further research is needed in determining these diagonal reinforcement limits for seismic design taking into consideration the coupling beam-core wall joints response and reinforcement details.

7.9.2 Development of Diagonal Reinforcement

Recommend using the New Zealand Standard requirements (Cl 5.3.7. Section 5), which consider the hoop confinement provided in the core wall and give required development lengths of upto 40% longer compared with the CSA standard development lengths for tension reinforcement (Cl 12). Further research is needed taking into account the hoop confinement effects on the coupling beam diagonal reinforcement development length.

7.9.3 Hoop Confinement of Diagonal Reinforcement

CSA Standard Cl 21.5.8.2 requirements give hoop confinement spacings of $s_{\max} = 100\,mm$. Recommend using the New Zealand Standard requirements (Cl 6.5.3.3) which give more stringent hoop spacings of $s_{\mathrm{req'd}} = 55\,mm$ and $80\,mm$ for the I-E and E-S coupling beams. The latter requirements take into consideration the amount of diagonal reinforcement to be confined. Further research is required in this area to investigate the influence of the core wall configuration and reinforcement details.

7.9.4 Torsion Reinforcement Requirements

Analysis results demonstrate that the torsional moments in coupling beams due to earthquake and gravity loading can be significant. No provisions exist for ductile design of diagonally reinforced coupling beams for torsion due to seismic loading in the CSA Standard (Cl 21).

7.9.5 Cage Reinforcement

Recommended cage reinforcement requirements in diagonally reinforced coupling beams:

a) Transverse hoop maximum spacings are the smallest of:
[Cl 11.3.8.4, Cl 11.5.3.1 and Park and Paulay (1975)]

$$s = \frac{p_h}{8} \tag{7.8}$$

$$s = \frac{A_v}{0.002b_w} \leq \frac{d}{5} \tag{7.9}$$

$$s_{\max} = 150\,mm \tag{7.10}$$

b) Longitudinal bars distributed along the beam side faces:
[Cl 11.3.7.5, Cl 11.5.3.2 and Cl 10.6.7]

$$A_l = \frac{A_t p_h}{s} \tag{7.11}$$

$$s = \frac{A_{s_{\mathrm{total}}} \text{ per pair}}{0.002b_w} \leq \frac{d}{3} \tag{7.12}$$

$$s_{\max} = 200\,mm \tag{7.13}$$

where A_l is the total area of longitudinal reinforcement.

7.10 Core Wall–Beam Joint Ductility Requirements

Several types of joints are present in core-slab-frame structures including: beam-column, structural wall-coupling/lintel beam, core wall-slab, confined core wall end region-coupling/lintel beam, and various combinations of core wall-beam-slab ends, corners and junctions. All such joints must be designed for seismic ductility requirements of a "strong structural wall/column–weak beam-slab" philosophy. No specific ductility design provisions exist in the CSA Standard for such joints. The load carrying capacities of structural cores and the confined core flange and web wall regions must be determined from their corresponding axial load-moment (P-M) interaction diagrams.

Based on the research findings, it is recommended that P-M interaction diagrams be developed for individual core sections of various shapes, taking into consideration the three-dimensional core section behaviour due to the interaction of the web and flange walls and the slabs, and for coupled core structures of various configurations accounting for the "box-action" including the influence of lintel and coupling beams, and enclosed and surrounding slabs. The selected reinforcement arrangements can be presented in the form of tables for design purposes.

7.10.1 Core Wall-Coupling Beam Joints

Coupling beam-core flange wall joints consist of diagonally reinforced deep coupling beams framing into the core confined flange wall ends and web-flange corners. The inelastic behaviour of these joints is considerably different from that of a typical conventionally reinforced beam-column joint (Cl 21.4.2.2). More research is needed to study the behaviour of such joints.

7.10.2 Elevator Core Flange Wall-Lintel Beam Joints

Lintel beams span across an elevator core opening and connect with the flange wall ends, resulting in deep confined flange wall end-lintel beam joints. Thus, the behaviour is different from that involved in the ductility conditions for beam-column joints given by Cl 21.4.2.2 and Cl 21.6.

In determining the P-M interaction diagram for the Elev section flange wall, it is not realistic to consider only the confined column flange wall end region acting with the lintel beams. Analysis results for lateral load response demonstrate an effective flange wall width participating with the lintel beams, which ranges in length from the confined flange wall end column region to the entire flange wall width. Strong core flange wall-weak lintel beam ductility requirements are satisfied for the Elev section flange wall-lintel beam joint when taking into consideration the entire flange wall as being effective and properly confined. Further research is required to study the local effects and variations which occur at the confined column Elev section flange wall end region-lintel beam joints and their response to seismic loads.

7.11 Slab Response and Design

Findings of this research program and the previous work by Manatakos (1989) of core-slab-frame structures subjected to earthquake and gravity loads. show that the enclosed and surrounding slabs transfer not only in-plane forces but also out-of-plane forces between the cores and frames substructures. The slabs experience load reversals and are subjected to shearing stresses and twisting moments that are as significant as the direct stresses and the flexural moments. respectively. due to both earthquake and gravity loads. The resulting slab forces due to earthquake loading demonstrate that the in-plane axial S_{xx}. S_{yy} and shear S_{xy} stresses are largest in the lower 10% structure height showing local stress jumps of 8 to 10 times in magnitude and reversals occurring from levels 1 to ground, while the bending M_{xx}. M_{yy} and twisting M_{xy} moments demonstrate concentrations of upto 3 times larger values at the stiffer slab-core corner regions and flange wall ends. These irregular slab stresses and moments are caused by the varying slab support conditions and stiffness.

Therefore. critical slab regions are located at the slab-core web-flange corners interior and exterior regions. along slab-core wall lengths and junctions. at flange wall ends. and the most distressed regions are located at slab-coupling and lintel beam-core flange wall end regions. thus. requiring special slab reinforcement with a large reinforcement content. These irregular stresses and moments in the slabs are located within a slab band width equal to 3 to 5 times the core wall thickness adjacent to the slab-core wall junctions around the core perimeter.

No guidelines exist in the CSA Standard Cl 21 for seismic design of ductile two-way slabs subject to gravity and earthquake loads. The total slab moment consisting of the bending and twisting moments, must be considered in orthogonal X- and Y-directions and is typically determined [Park and Gamble (1979)] as:

$$|m_{xx}| + |m_{yx}| \quad \text{and} \quad |m_{yy}| + |m_{xy}| \tag{7.14}$$

Nonlinear post-cracking seismic response at the higher load stages result in a considerable reduction of the slab stiffness at the critical slab-core wall joints and regions. resulting in horizontal cracking and separation between the slabs and core walls. A 20% to 30% redistribution of the slab forces occurs [Park and Gamble (1979)], depending on the slab configuration. reinforcement details, support conditions and load level. This must be taken into consideration in design to ensure ductility and structural integrity of the slab-core regions.

Further research is needed to develop seismic design procedures for ductility of two-way slab structures which take into consideration the following factors: strain hardening of the reinforcement, the presence of compression steel, the provision of transverse hoop confinement around the longitudinal reinforcement in the critical slab regions over the effective slab band widths and plastic hinge lengths for lateral load resistance, biaxial and triaxial conditions in compression and tension, at the critical slab-structural wall corner and end regions, stress concentrations due to the various component structural elements, and the membrane compression and tension caused by the support conditions.

7.11.1 Maximum Bar Sizes in Two-Way Slabs

Recommend using Cl 21.5.4.4 requirements for structural walls:

$$d_{b_{\max}} \leq \frac{h_{\text{slab}}}{10} \tag{7.15}$$

7.11.2 Maximum Spacing of Flexural Reinforcement for Seismic Design of Two-Way Slabs

Recommend using Cl 21.5.5.1 requirements for structural walls:

[i] Within plastic hinging regions: $s_{\max} \leq 300\,mm$

[ii] Outside plastic hinging regions: $s_{\max} \leq 450\,mm$

7.11.3 Maximum Flexural Reinforcement for Ductility Requirements of Two-Way Slabs

Recommend limiting the ratios of the average negative to positive ultimate slab moments to:

$$m_{\text{ult}_x}^{-\text{ive}} \leq 1.5 \text{ to } 2.0\, m_{\text{ult}_x}^{+\text{ive}} \tag{7.16}$$

$$m_{\text{ult}_y}^{-\text{ive}} \leq 1.5 \text{ to } 2.0\, m_{\text{ult}_y}^{+\text{ive}} \tag{7.17}$$

$$m_{\text{ult}_x}^{+} \leq 1.0 \text{ to } 1.5\, m_{\text{ult}_y}^{+} \tag{7.18}$$

Limit the maximum tension reinforcement ratio to:

$$\rho_{\max} < 0.4\,\rho_{\text{bal}} \tag{7.19}$$

7.11.4 Longitudinal Reinforcement Requirements in Critical Slab-Core Wall Corner and End Regions

Recommendations to ensure plastic hinging in the vicinity of slab-core wall regions:

a) Maximum spacing of additional longitudinal reinforcement (Cl 13.4.2 and Cl 7.8.2 requirements):

$$s_{\max} \leq 2\,h_{\text{slab}} \leq 200\,mm \tag{7.20}$$

b) Provide 2 mats (orthogonal directions) over a distance the greater of:

[i] $1/5^{th}$ of the span in each direction

[ii] 3 to $5\,b_w$ (core wall thickness)

c) Maximum tension reinforcement ratio at critical corners:

$$\rho_{\max_{\text{critical region}}} < 0.6 \text{ to } 0.75\,\rho_{\text{bal}} \tag{7.21}$$

7.11.5 Hoop Confinement of Longitudinal Reinforcement in Slabs

At slab-core wall connections, must ensure structural integrity and ductility for plastic hinge formation allowing development of the cracked effective slab widths. Recommend confinement of the slab longitudinal reinforcement be provided in the form of closed hoops and cross-ties:

1. Minimum 4-legged hoop configuration

   Leg spacing $s \leq b_w$ (wall thickness) $\not> 300\,mm$

2. Minimum hoop width $=$ 1.5 to 3 b_w

   Maximum hoop width $=$ 3 to $5\,b_w$

3. Extend hoops outward from the slab-structural core wall face:

   0.20 to 0.30 of the span $\not<$ 4 to $6\,d$ (slab depth)

4. Maximum hoop spacings:

   [i] $d/2$ for a distance of $2d$ from the slab-core wall support

   [ii] (2/3) to (3/4) d for the remainder of the confinement length

Further research is needed in determining the "cracked" effective slab width due to earthquake loads developed at the critical slab-core wall end and flange-web corner regions.

7.11.6 Effective Slab Widths for Lateral Load Analysis

Findings of this research program and the previous work by Manatakos (1989) demonstrate that portions of enclosed and surrounding slabs participate in the lateral load resistance along with the core walls and beams, and their influence must be taken into consideration in evaluating the structural response. The effective slab width is influenced by the location of the span (end or interior), the slab location (upper, intermediate, or lower levels), characteristics of the adjacent spans, configuration of the core wall supports, and the interaction effects of the various structural components - cores, beams, slabs and frames. Values for the effective slab widths vary from one-tenth to the full panel width. The various charts and tables [Tso and Mahmoud (1977) and Pecknold (1977)] are suitable only for interior spans of interior panels in the interior floor levels. Further research is required in this area.

7.12 Recommendations for Future Research

The behaviour of reinforced concrete slab-core-frame building structures subjected to lateral and gravity loads is lacking. To realistically assess the behaviour of such structures, one must examine the strength and stiffness, distress and damage, ductility, energy absorption characteristics and failure modes when subjected to cyclic loads. Phenomena such as three-dimensional interaction, its effect on strength and stiffness and the influence of various structural components on the deformations and forces must be examined. In addition, a rational approach in selecting the type of finite element modeling technique of such structures is needed. Current concrete design codes have no provisions for the design of cores, frames and slab substructures taking into consideration the interaction phenomena mentioned above.

This investigation presents detailed findings for the complete behaviour of a typical core-slab-frame building subject to lateral and gravity loads, with design recommendations suggested for the various building components. Additional investigations are needed studying the behaviour of existing core-slab-frame buildings with various core configurations of C, U and Z shapes, core wall-slab/beam connections, frame substructures and slab systems. Presently, monotonically increasing earthquake loadings have been considered. The next step in the research program is to study the behaviour of core-slab-frame buildings subject to reversed cyclic earthquake loads, then to examine the dynamic response of such structures to failure. To complement the analytical work, experimental investigations of direct small scale models of selected subassemblages from core-slab-frame building structures and of the various connections are needed, to develop additional design recommendations.

Future research goals are aimed at developing a general applicability of the findings for the response and the design procedures recommended for reinforced concrete core-slab-frame building structures, to provide a better understanding of the complex behaviour of such structures.

Statement of Originality

Original contributions presented in this dissertation are summarized below.

1. Linear and Nonlinear Analysis of Core-Slab-Frame Structures:

Three-dimensional linear and nonlinear finite element analyses of modern reinforced concrete core-slab-frame buildings are performed for their complete response under monotonically increasing earthquake and gravity loads to failure.

Detailed information is derived for the first time for the following:

- Contribution of the structural components, cores, slabs and beams, on the overall structural response.
- Strength, ductility and energy absorption capabilities of such structures.
- Ultimate load and failure mode.
- Plastic hinging and damaged regions critical for design.
- Resultant deformations, strains and stresses, and forces at the various load levels.

Procedures are recommended for finite element modeling and analysis of core-slab-frame structures.

2. Design of Core-Slab-Frame Structures:

Design procedures and reinforcement detailing are recommended for the cores – open-, closed- and partially closed-sections, slabs – "surrounding" and "enclosed" within cores, coupling and lintel beams, and core wall-beam-slab connections taking into consideration the three-dimensional structural behaviour. Suitable clauses are developed for possible inclusion in the Canadian Concrete Design Code.

Bibliography

[1] ACI Committee 318. *Building Code Requirements for Reinforced Concrete (ACI 318-83).* American Concrete Institute, Detroit, 1983.

[2] ACI Committee 318. *Commentary on Building Code Requirements for Reinforced Concrete (ACI 318-83).* American Concrete Institute, Detroit, 1983. 155pp.

[3] ACI Committee 442. Response of buildings to lateral forces. *ACI Journal*, 68(2):81–106, Febuary 1971.

[4] F. Allen and P. LeP. Darvall. Lateral load equivalent frame. *ACI Journal Proceedings*, 74(7):294–299, July 1977.

[5] F. H. Allen and P. LeP. Darvell. Discussion of slab effective width for equivalent frame analysis by pecknold. *ACI Journal Proceedings*, 72(10):583–585, October 1975.

[6] ASCE Task Committee. *Finite Element Analysis of Reinforced Concrete.* State of the Art Report, ASCE, New York, USA, 1982.

[7] A. K. Basu and A. K. Nagpol. Frame-wall systems with rigidly jointed link beams. *Journal of the Structural Division, ASCE*, 106(ST5):1175–1192, May 1980.

[8] K. J. Bathe, E. L. Wilson, and F. E. Peterson. *A Structural Analysis Program for Static and Dynamic Response of Linear Systems.* Technical Report EERC 73-11, National Science Foundation, University of California, Berkeley, California, June 1973.

[9] J. R. Benjamin and N. C. Lind. A probablistic basis for a deterministic code. *ACI Journal Proceedings*, 66(72):857–865, November 1969. Third in a Series of Four Papers on Probablistic Concepts.

[10] J. R. Benjamin and B. E. Weinberg. Special introduction to series. *ACI Journal Proceedings*, 66(54):689, September 1969. Introduction to a Series of Four Papers on Probablistic Concepts.

[11] Canadian Standards Association. *National Building Code of Canada.* National Research Council of Canada, Ottawa, Ontario, 1985. NRC No. 30619.

[12] J. E. Carpenter. P. H. Kaar, and W. G. Corley. Design of ductile flat plate structures to resist earthquakes. In *Fifth World Conference on Earthquake Engineering*, Rome. Italy. 1973. Paper No. 250, Session 5D.

[13] J. E. Carpenter, P. H. Kaar, and N. W. Hanson. Discussion of proposed revision of aci 318-63: building code requirements for reinforced concrete. *ACI Journal Proceedings*, 67:696–697, September 1970.

[14] CEB-FIP. *CEB-FIP Model Code for Concrete Structures*. International System of Unified Standard Codes of Practice for Structures, Comité Euro-International du Béton Fédération International de la Précontrainte, Paris, France, April 1978. 348pp.

[15] CEB Recommendations Comité Européen du Béton. *Slabs and Plane Structures*. Comité Euro-International du Béton Fédération International de la Précontrainte, Paris, France, 1972. 180pp.

[16] W. F. Chen. *Plasticity in Reinforced Concrete*. McGraw-Hill Book Company, New York, first edition, 1982.

[17] S. F. Chew. *Behaviour of Core Substructures*. Master's thesis, Department of Civil Engineering and Applied Mechanics, McGill University, Montreal, Canada, September 1991.

[18] M. P. Collins, D. Mitchell, and J. G. MacGregor. *Explanatory Notes on CSA Standard CAN3-A23.3-M84 Design of Concrete Structures for Buildings*. Canadian Portland Cement Association (CPCA), Ottawa, Ontario, 1985. 140pp.

[19] R. D. Cook. *Concepts and Applications of Finite Element Analysis*. John Wiley and Sons, Inc., New York, second edition, 1981.

[20] R. J. Cope and L.A. Clark. *Concrete Slabs Analysis and Design*. Elsevier Applied Science, New York, first edition, 1984.

[21] W. G. Corley and J. O. Jirza. Equivalent frame analysis for slab design. *ACI Journal Proceedings*, 67(11):875–884, November 1970.

[22] W. G. Corley, M. A. Sozen, and C. P. Siess. *The Equivalent Frame Analysis for Reinforced Concrete Slabs*. Technical Report Structural Research Series No. 218, University of Illinois, Urbana, Illinois, June 1961. Department of Civil Engineering.

[23] C. A. Cornell. A probability-based structural code. *ACI Journal Proceedings*, 66(85):974–985, December 1969. Fourth in a Series of Four Papers on Probablistic Concepts.

[24] A. Coull. Distribution of shear forces in coupled shear wall structures. In *Response of Buildings to Lateral Forces SP 36*, pages 217–224, ACI Committee 442, Detroit, 1973. Paper No. 36-10.

[25] A. Coull and N. W. Adams. A simple method of analysis of the load distribution in multi-story shear wall structures. In *Response of Buildings to Lateral Forces SP 36*, pages 187–216, ACI Committee 442, Detroit, 1973. Paper No. 36-9.

[26] A. Coull and J. R. Choudhury. Analysis of coupled shear walls. *ACI Journal Proceedings*, 64(9):587–593, 1967.

[27] A. Coull and J. R. Choudhury. Stresses and deflections in coupled shear walls. *ACI Journal Proceedings*, 64(2):65–72, Febuary 1967.

[28] A. Coull and A. A. El Hag. Effective coupling of shear walls by floor slabs. *ACI Journal Proceedings*, 72(8):429–431, August 1975.

[29] A. Coull and R. D. Puri. Analysis of coupled shear walls of variable thickness. *Building Science*, 2:181–188, 1967.

[30] A. Coull and R. D. Puri. Analysis of pierced shear walls. *Journal of the Structural Division, ASCE*, 94(ST1):71–82, 1968.

[31] A. Coull and B. Stafford Smith. Analysis of shear wall structures (a review of previous research). In *Proceedings of a Symposium on Tall Buildings with Particular Reference to Shear Wall Structures*, pages 139–156, Pergamon Press, University of Southampton, April 1966.

[32] CPCA. *Concrete Design Handbook*. Canadian Portland Cement Association. Ottawa. Ontario. 1985.

[33] M. E. Criswell. Post punching resistance of flat plates. *ACI Journal Proceedings*, 80(28):229–235, September 1980.

[34] CSA Standard. *Design of Concrete Structures for Buildings, CAN3-A23.3-M84*. Canadian Standards Association, Ottawa, Ontario, 1984. 281pp.

[35] D. Darwin and D. A. Pecknold. Analysis of r/c shear panels under cyclic loading. *Journal of the Structural Division, ASCE*, 102(ST2):355–369, February 1976. Proc. Paper No. 11896.

[36] D. Darwin and D. A. Pecknold. Biaxial stress-strain relations for concrete. *Journal of the Structural Division, ASCE*, 98(ST5):1025–1034, May 1972.

[37] D. Darwin and D. A. Pecknold. Nonlinear biaxial stress-strain law for concrete. *Journal of the Engineering Mechanics Division, ASCE*, 103(EM2):229–241, April 1977. Proc. Paper No. 12839.

[38] A. T. Derecho. Frames and frame-shear wall systems. In *Response of Multistory Concrete Structures to Lateral Forces SP-36*, pages 13–27, ACI Committee 442, ACI Publication, Detroit, 1973.

[39] A. C. Eberhardt, E. S. Hoffman, J. C. Jofriet, and V. K. Handa. Discussion of equivalent frame analysis for slab design by corley, w. g. and jirza, j. o. *ACI Journal Proceedings*, 68(5):397–401, May 1971.

[40] Z. M. Elias. Flat slab analysis using equivalent beams. *ACI Journal Proceedings*, 76(8):1063–1078, October 1979.

[41] Z. M. Elias. Sidesway analysis of flat plate structures. *ACI Journal Proceedings*, 76(3):421–442, March 1979.

[42] B. Ellingwood. Reliability based criteria for reinforced concrete design. *Journal of the Structural Division, ASCE*, 105(ST4):713–727, April 1979. Proc. Paper No. 14480.

[43] B. Ellingwood. Reliability of current reinforced concrete designs. *Journal of the Structural Division, ASCE*, 105(ST4):699–712, April 1979. Proc. Paper No. 14479.

[44] B. Ellingwood, J. G. MacGregor, T. V. Galambos, and C. A. Cornell. Probability based load criteria: load factors and load combinations. *Journal of the Structural Division, ASCE*, 108(ST5):978–997, May 1982. Proc. Paper No. 17067.

[45] R. H. Evans and M. S. Marathe. Microcracking and stress-strain curves for concrete in tension. *Materiaux et Constructions*, 00(1):61–64, January-February 1968.

[46] M. Fintel. Deflections of high-rise concrete buildings. *ACI Journal*, 72(7):324–328, July 1975.

[47] M. Fintel. *Handbook of Concrete Engineering*. Van Nostrand Reinhold Company, New York, second edition, 1985.

[48] R. Fleming. *Wind Stresses in Buildings*. John Wiley and Sons Inc., New York, first edition, 1930.

[49] T. V. Galambos, B. Ellingwood, J. G. MacGregor, and C. A. Cornell. Probability based load criteria: assessment of current design practice. *Journal of the Structural Division, ASCE*, 108(ST5):959–977, May 1982. Proc. Paper No. 17067.

[50] G. A. M. Ghoneim. *Nonlinear Finite Element Analysis of Concrete Structures*. PhD thesis, Department of Civil Engineering, University of Calgary, Calgary, Canada, 1978.

[51] A. Girgis and B. Stafford Smith. The torsion analysis of tall building cores partially closed by beams. In *Symposium on the Behaviour of Building Systems and Components*, pages 223–252, Vanderbilt University, Nashville, Tennessee, 1979.

[52] J. E. Goldberg. Approximate analysis of tall building frames. In *Regonal Conference on Tall Buildings*, pages 177–194, IABSE ASCE AIA AIP IFHP VIA, Bankok, January 1974.

[53] J. E. Goldberg. Approximate elastic analysis. In *International Conference on Planning and Design of Tall Buildings Proceedings*, pages 169–183, ASCE-IASBE, Lehigh University, Bethlehem Pa., August 1972. Vol. 2, Paper No. 14-2.

[54] V. S. Gopalaratnam and P. S. Surendra. Softening response of plain concrete in direct tension. *ACI Journal Proceedings*, 82(27):310–323, May-June 1985.

[55] S. K. Gosh and M. Fintel. Modelling of frame-shear wall structures for static and dynamic analyses. *Journal of the Structural Division, ASCE*, 1978.

[56] A. C. Heidebrecht and B. Stafford Smith. Approximate analysis of open section shear walls subject to torsional loading. *Journal of the Structural Division, ASCE*, 99(ST12):2355–2373, December 1973.

[57] A. C. Heidebrecht and B. Stafford Smith. Approximate analysis of tall wall-frame structures. *Journal of the Structural Division, ASCE*, 99(ST2):199–221, Febuary 1973. Proc. Paper No. 9550.

[58] B. P. Hughes and G. P. Chapman. The complete stress-strain curve for concrete in direct tension. *RILEM Bulletin (Paris)*, 00(30):95–97, March 1966.

[59] S. Islam and R. Park. Tests on slab-column connections with shear and unbalanced flexure. *Journal of the Structural Division, ASCE*, 102(ST3):544–568, March 1976.

[60] J. C. Jofriet. Flexural cracking of concrete flat plates. *ACI Journal Proceedings*, 70:805–809, December 1973.

[61] A. F. Kabir. *Nonlinear Analysis of Reinforced Concrete Panels, Shells and Slabs for Time Dependent Effects*. PhD thesis, Division of Structural Engineering and Structural Mechanics, University of California, Berkeley, California, December 1976. US-SESM Report No. 76-6.

[62] G. A. Kani. *Analysis of Multistory Frames*. Frederick Ungar Publishing Co., Germany, fifth edition, 1957. Translated by C. J. Hyman, Crosby Lockwood and Son Ltd., London.

[63] M. F. Kaplan. Strains and stresses of concrete at initiation of cracking and near failure. *ACI Journal Proceedings*, 60(44):853–879, July 1963.

[64] F. Kerekes and H. B. Reid. Fifty years of development in building code requirements for reinforced concrete. *ACI Journal Proceedings*, 50(26):441–471, February 1954.

[65] A. H. Khan and B. Stafford Smith. A simple method of analysis for deflection and stresses in wall-frame structures. *Building and Environment*, 11:69–78, Febuary 1976.

[66] F. R. Khan. New structural systems for tall buildings and their scale effects on cities. In *Proceedings of the Symposium on Tall Buildings Planning, Design and Construction*, pages 99–128, Vanderbilt University, Nashville, Tennessee, 1974.

[67] F. R. Khan. On some special problems of analysis and design of shear wall structures. In *Symposium on Tall Buildings With Particular Reference to Shear Wall Structures*, pages 321–347, Oxford Pergamon Press, University of Southampton, April 1966.

[68] F. R. Khan and J. A. Sbarounis. Interaction of shear walls and frames. *Journal of the Structural Division, ASCE*, 90(ST3):285–335, June 1964. Proc. Paper No. 3957.

[69] M. A. H. Khan and B. Stafford Smith. Restraining action of bracing in thin-walled open section beams. *Proceedings of the Institute of Civil Engineers*, 59(Part 2):67–78, March 1975.

[70] C. F. Kollbrunner and K. Basler. *Torsion in Structures - An Engineering Approach*. Springer-Verlag, New York, english edition, 1969.

[71] H. Kupfer and K. H. Gerstle. Behaviour of concrete under biaxial stresses. *Journal of the Engineering Mechanics Division, ASCE*, 99(EM4):53–64, August 1973. Proc. Paper No. 9917.

[72] H. Kupfer, H. K. Hilsdorf, and H. Rusch. Behaviour of concrete under biaxial stresses. *ACI Journal Proceedings*, 66(52):656–666, August 1969.

[73] A. C. Liebenberg. Arch action in reinforced concrete slabs. In *Diamond Jubilee Convention of South African Institution of Civil Engineers*, pages 99–102, South Africa, 1963.

[74] A. K. W. Lim. *An Experimental Study of the Behaviour of Coupled Slab-Shear Wall Building Structures*. Master's thesis, Department of Civil Engineering and Applied Mechanics, McGill University, Montreal, Canada, June 1989.

[75] C. S. Lin and A. C. Scordelis. Nonlinear analysis of rc shells of general form. *Journal of the Structural Division, ASCE*, 101(ST3):523–538, March 1975. Proc. Paper No. 9917.

[76] S. C. Lin. *Nonlinear Analysis of Reinforced Concrete Slabs and Shells*. PhD thesis, Division of Structural Engineering and Structural Mechanics, University of California, Berkeley, California, April 1973. US-SESM Report No. 73-7.

[77] T. Y. Lin and S. D. Stotesbury. *Structural Concepts and Systems for Architectures and Engineers*. John Wiley and Sons Inc., New York, 1981.

[78] R. A. Link, A. E. Elwi, and A. Scanlon. Tension stiffening in concrete panels. In *Annual Conference of Canadian Society for Civil Engineering*, pages 664–678, Calgary, Alberta, 1988.

[79] T. C. Y. Liu, A. H. Nilson, and F. O. Slate. Stress-strain response and fracture of concrete in uniaxial and biaxial compression. *ACI Journal Proceedings*, 69(5):291–295, May 1972.

[80] A. E. Long and D. W. Kirk. Lateral load stiffness of slab-column structures. In *Reinforced Concrete Structures Subjected to Wind and Earthquake Forces*, pages 197–220, ACI Publication SP-63, Detroit, Michigan, April 1980.

[81] A. E. Long, E. W. Kirk, and D. J. Cleland. Moment transfer and the ultimate capacity of slab column structures. *The Structural Engineer*, 56A(4):304–322, April 1978.

[82] A. R. Lord. A test of a flat slab floor in a reinforced concrete building. *National Association of Cement Users (ACI)*, 7(11):156–179, November 1910.

[83] A. R. Lord. A test of a flat slab floor in a rienforced concrete building. *National Association of Cement Users (ACI)*, 7:156–179, March 1910.

[84] J. G. MacGregor. Load and resistance factors for concrete design. *ACI Journal Proceedings*, 80(27):279–287, July-August 1983.

[85] J. G. MacGregor. Safety and limit states design for reinforced concrete. *Canadian Journal of Civil Engineering*, 3(3):484–513, June 1976.

[86] I. A. MacLeod. Connected shear walls of unequal width. *ACI Journal Proceedings*, 67(5):408–412, May 1970.

[87] I. A. MacLeod. Lateral stiffness of shear walls with openings - discussion. In *Symposium on Tall Buildings With Particular Reference to Shear Wall Structures*, pages 223–244, Oxford Pergamon Press, University of Southampton, April 1966.

[88] I. A. MacLeod. *Shear Wall-Frame Interaction - A Design Aid with Commentary*. Portland Cement Association, April 1971. Special Publication.

[89] K. C. Manatakos. *Analysis of Low- and Medium-Rise Buildings*. Master's thesis, Department of Civil Engineering and Applied Mechanics, McGill University, Montreal, Canada, February 1989.

[90] K. C. Manatakos and M. S. Mirza. *Design of Reinforced Concrete Core-Slab-Frame Structures*. Technical Report Departmental Report No. 95-6, McGill University, Montreal, Canada, December 1995. Department of Civil Engineering and Applied Mechanics.

[91] K. C. Manatakos and M. S. Mirza. *Linear Behaviour of Reinforced Concrete Core-Slab-Frame Structures*. Technical Report Departmental Report No. 95-4, McGill University, Montreal, Canada, December 1995. Department of Civil Engineering and Applied Mechanics.

[92] K. C. Manatakos and M. S. Mirza. *Nonlinear Behaviour of Reinforced Concrete Core-Slab-Frame Structures*. Technical Report Departmental Report No. 95-5, McGill University, Montreal, Canada, December 1995. Department of Civil Engineering and Applied Mechanics.

[93] D. Micheal. Discussion of The bending stiffness of slabs connecting shear walls by Qadeer and Stafford Smith. *ACI Journal Proceedings*, 66(12):1021–1022, December 1969.

[94] M. S. Mirza and J. G. MacGregor. Variability of mechanical properties of reinforcing bars. *Journal of the Structural Division, ASCE*, 105(ST5):921–937, May 1979.

[95] L. J. M. Nelissen. Biaxial testing of normal concrete. *Heron (Delft), the Netherlands*, 18(1), 1972.

[96] New Zealand Standard. *Code of Practice for The Design of Concrete Structures NZS 3101*. Standards Association of New Zealand, Wellington, New Zealand, 1982. 127pp.

[97] New Zealand Standard. *Commentary on The Design of Concrete Structures NZS 3101*. Standards Association of New Zealand, Wellington, New Zealand, 1982. 156pp.

[98] J. R. Nichols. Statical limitations upon the steel requirement in reinforced concrete flat slab floors. *Transactions ASCE*, 77(3):1670–1681, March 1914. Discussion pp 1682–1736.

[99] M. E. Nofal. *Inelastic Load Distribution of Composite Concrete-Steel Slab-on-Girder Bridges - An Analytical and Experimental Study*. Master's thesis, Department of Civil Engineering, Carleton University, Ottawa, Canada, 1988.

[100] C. H. Norris and J. B. Wilbur. *Elementary Structural Analysis*, pages 309–315. McGraw-Hill Book Company Inc., New York, second edition, 1960.

[101] A. J. Ockleston. Arching action in reinforced concrete slabs. *The Structural Engineer*, 36(6):197–201, November 1958.

[102] A. J. Ockleston. Load tests on a three storey reinforced concrete building in johannesburg. *The Structural Engineer*, 33(10):304–322, November 1955.

[103] R. Park and W. L. Gamble. *Reinforced Concrete Slabs*. John Wiley and Sons, Inc., New York, first edition, 1980.

[104] R. Park and T. Paulay. *Reinforced Concrete Structures*. John Wiley and Sons, Inc., New York, first edition, 1975.

[105] T. Paulay. An elasto-plastic analysis of coupled shear walls. *ACI Journal Proceedings*, 67(11):915–922, November 1970.

[106] T. Paulay and M. J. N. Priestley. *Seismic Design of Reinforced Concrete and Masonry Buildings*. John Wiley and Sons, Inc., New York, first edition, 1992.

[107] PCA. *Continuity in Building Frames*. Portland Cement Association, Skokie, Illinois, 1985.

[108] D. A. Pecknold. Slab effective width for equivalent frame analysis. *ACI Journal Proceedings*, 72(4):135–137, April 1975.

[109] Portland Cement Association. *Design of Combined Frames and Shear Walls.* Portland Cement Association. 1965. Advanced Engineering Bulletin No. 14.

[110] A. Qadeer and B. Stafford Smith. Actions in slabs connecting shear walls. In *Proceedings of the Symposium on Tall Buildings Planning, Design and Construction*, pages 315–338. Vanderbilt University. Nashville, Tennesse. November 1974.

[111] A. Qadeer and B. Stafford Smith. The bending stiffness of slabs connecting shear walls. *ACI Journal Proceedings*, 66(6):464–473, June 1969.

[112] A. G. Razaqpur. Nonlinear analysis of shear transfer in concrete. In *Annual Conference of Canadian Society for Civil Engineering*, pages 237–254, Calgary. Alberta. 1988.

[113] A. G. Razaqpur and M. E. Nofal. *Transverse Load Distribution at Ultimate Limit States in Single Span Slab-on-Girder Bridges with Compact Steel Sections.* Technical Report MISC-88-01, The Research and Development Branch Ministry of Transportation, Ontario, Canada, September 1988.

[114] A. G. Razaqpur, M. E. Nofal, and M. S. Mirza. Nonlinear analysis of prestressed concrete box girder bridges under flexure. *Canadian Journal of Civil Engineering*. 16:845–853. June 1989.

[115] G. M. Sabnis, H. G. Harris, R. N. White, and M. S. Mirza. *Structural Modeling and Experimental Techniques.* Prentice-Hall Inc.. New Jersey, first edition, 1983.

[116] L. P. Saenz. Discussion of "equation for the stress-strain curve of concrete, by desayi and krishnan". *ACI Journal Proceedings*, 61(9):1229–1235, September 1964.

[117] D. M. Schultz and M. Fintel. Frame-shear wall systems for ultra high-rise concrete buildings– a case study. In *Proceedings of the Symposium on Tall Buildings Planning, Design and Construction*, pages 291–314, Vanderbilt University, Nashville, Tennessee, 1974.

[118] J. Schwaighofer and M. P. Collins. Experimental study of the behaviour of reinforced concrete coupling slabs. *ACI Journal Proceedings*, 74:123–127, March 1977.

[119] R. G. Sexsmith and M. F. Nelson. Limitations in application of probablistic concepts. *ACI Journal Proceedings*, 66(68):823–828, October 1969. Second in a Series of Four Papers on Probablistic Concepts.

[120] H. C. Shah. The rational probablistic code format. *ACI Journal Proceedings*, 66(54):690–697, September 1969. First in a Series of Four Papers on Probablistic Concepts.

[121] K. N. Shiu, G. B. Barney, A. E. Fiorato, and W. G. Corley. Reversing load tests of reinforced concrete coupling beams. In *Central American Conference on Earthquake Engineering*, pages 239–249, San Salvador, El Salvador, C. A., January 1978.

[122] S. H. Simmonds and J. Misic. Design factors for the equivalent frame method. *ACI Journal Proceedings*, 68(11):825–831, November 1971.

[123] A. Smith. Wind stresses in the steel frames of office buildings. *Journal of the Western Society of Engineers*, XX(4):341–364, April 1915.

[124] G. M. Smith and L. E. Young. Ultimate theory in flexure by exponential function. *ACI Journal Proceedings*, 52(3):349–359, November 1955.

[125] M. A. Sozen and C. P. Siess. Investigation of multiple-panel reinforced concrete floor slabs: design methods – their evolution and comparison. *ACI Journal Proceedings*, 60(8):999–1027, August 1963.

[126] B. Stafford Smith and B. S. Taranath. The analysis of tall core-supported structures subject to torsion. *Proceedings of the Institution of Civil Engineers*, 53(Part 2):173–187, September 1972.

[127] H. Sutherland and H. L. Bowman. *Structural Theory*. John Wiley and Sons Inc., New York, fourth edition, 1950.

[128] B. S. Taranath. Analysis of interconnected open section shear wall structures. *Journal of the Structural Division, ASCE*, 101(ST11):2367–2384, November 1975.

[129] B. S. Taranath. The effect of warping on interconnected shear wall-flat plate structures. *Proceedings of the Institute of Civil Engineers*, 61(Part 2):711–724, December 1976.

[130] S. Timoshenko and S. Woinowsky-Krieger. *Theory of Plates and Shells*. McGraw-Hill Book Company Inc., New York, first edition, 1959.

[131] W. K. Tso and J. K. Biswas. Analysis of core wall structure subject to applied torque. *Building Science*, 8(3):251–257, September 1973.

[132] W.K. Tso and A. A. Mahmoud. Effective width of coupling slabs in shear wall buildings. *Journal of the Structural Division, ASCE*, 103(ST3):573–586, March 1977.

[133] M. D. Vanderbilt. Equivalent frame analysis for lateral loads. *Journal of the Structural Division, ASCE*, 105(ST10):1981–1998, October 1979.

[134] M. D. Vanderbilt, M. A. Sozen, and C. P. Siess. Deflections of multiple-panel reinforced concrete floor slabs. *Journal of the Structural Division, ASCE*, 91(ST4):77–101, August 1965.

[135] V. Z. Vlasov. Thin-walled elastic beams. *National Science Foundation*, 2037–2047, 1961. English translation from Russian by the Israel Program for Scientific Translations, Jerusalem.

[136] V. Z. Vlasov. *Thin-Walled Elastic Beams.* English translation from Russian by the Israel Program for Scientific Translations Ltd., Jerusalem, second edition, 1961.

[137] C. K. Wang. *Statically Indeterminate Structures.* McGraw-Hill Book Company Inc., New York, first edition, 1953.

[138] C. K. Wang and C. G. Salmon. *Reinforced Concrete Design.* Harper and Row Inc., New York, third edition, 1979.

[139] H. M. Westergaard. Formulas for the design of rectangular floor slabs and the supporting girders. *ACI Journal Proceedings*, 22(3):26–46, March 1926.

[140] H. M. Westergard and W. A. Slater. Moments and stresses in slabs. *ACI Journal Proceedings*, 17(3):415–538, March 1921.

[141] J. B. Wilbur. A new method for analyzing stresses due to lateral forces in building frames. *Journal Boston Society of Civil Engineers*, 21(1):45–56, January 1934.

[142] A. C. Wilson. Wind bracing with knee braces or gusset plates. *The Engineering Record*, 58(10):272–274, September 1908.

[143] W. M. Wilson and G. A. Maney. *Bulletin No. 80 of the Engineering Experimental Station of the University of Illinios.* Technical Report, University of Illinios, Urbana Illinois, June 1915.

[144] W. M. Wilson and G. A. Maney. Wind stresses in the steel frames of office buildings. *Journal of the Western Society of Engineers*, XX(4):365–389, April 1915.

[145] G. Winter and A. H. Nilson. *Design of Concrete Structures.* McGraw-Hill Book Company Inc., New York, 9^{th} edition, 1979. p. 16.

[146] G. Wischers. Application of effects of compressive loads on concrete. *Betontech., Berlin*, 00(2 and 3), 1978. Duesseldorf.

[147] S. Wolfgang. *High-Rise Building Structures.* John Wiley and Sons Inc., New York, 1977. School of Architecture, Syracuse University.

[148] R. H. Wood and L. L. Jones. *Yield-Line Analysis of Slabs.* Thames and Hudson, Chatto & Windus, London, first edition, 1967.

[149] K. Zbirohowski-Kościa. *Thin Walled Beams - From theory to practice.* Crosby Lockwood and Son Ltd., London, first edition, 1967.

[150] O. C. Zienkiewicz. *The Finite Element Method.* McGraw-Hill Book Company Inc., New York, third edition, 1977.

End

IMAGE EVALUATION TEST TARGET (QA-3)

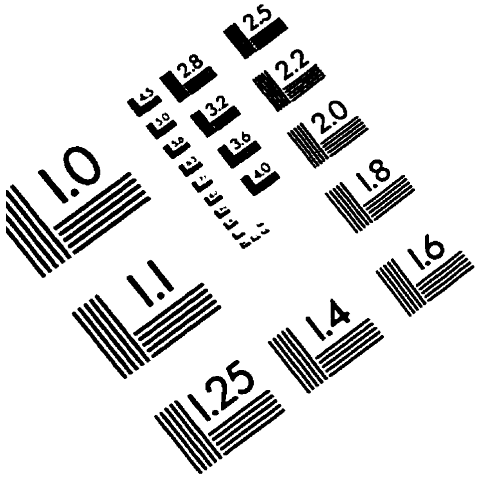

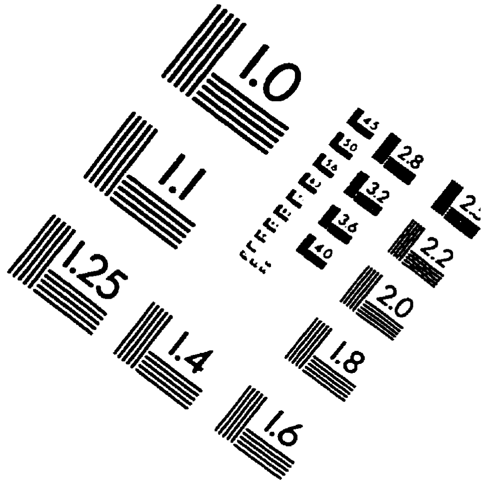

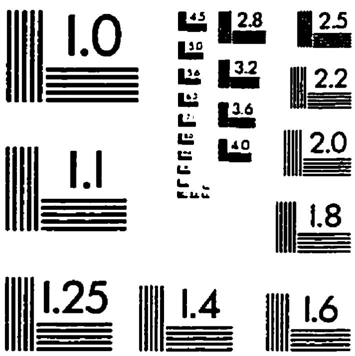

150mm

6"

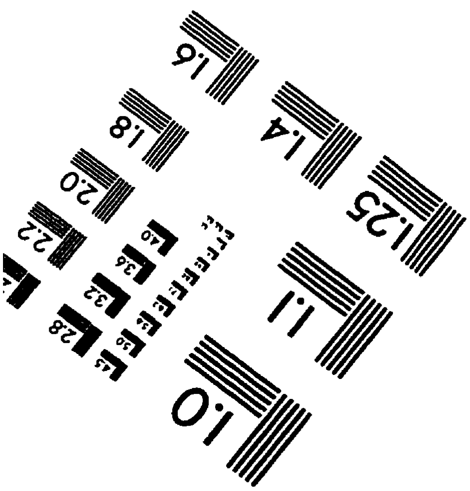

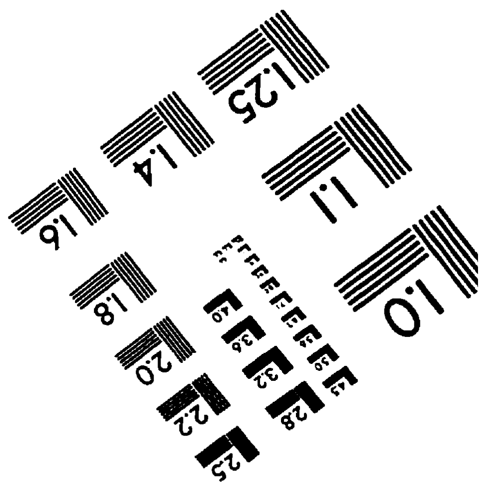

APPLIED IMAGE . Inc
1653 East Main Street
Rochester, NY 14609 USA
Phone: 716/482-0300
Fax: 716/288-5989